Development of a two-stroke, two-cylinder, spark-ignition UAV engine

MG Maree

orcid.org/ 0000-0002-9222-9042

Dissertation accepted in fulfilment of the requirements for the degree Master of Engineering in Mechanical Engineering at the North-West University

Supervisor: Prof CP Storm

Graduation: October 2020

Student number: 29188334

_____

DECLARATION

I, Marcel Gerhard Maree, hereby declare that this is my own work and that no plagiarism was committed.

23 November 2019

M.G. Maree | Date

ABSTRACT

The use of unmanned aerial vehicles (UAVs) for both civil and military applications has increased significantly throughout the world in recent years. The propulsion systems used in locally designed and manufactured, medium-range UAVs for the military are two-stroke internal combustion, spark-ignition (SI) engines that are imported from first world manufacturers at significant cost. This study investigates whether it is possible to design, manufacture and test a two-stroke, two-cylinder, horizontally-opposed, air-cooled, SI engine suitable for UAV application at a lower cost compared to imported products. In order to reduce design effort and assist in mitigating functional risk, appropriate commercially available motorbike components were used in critical areas of the engine. Most of the fundamental engine components, specifically the cylinders, cylinder heads, pistons and connecting rod assemblies, were sourced from a two-stroke Yamaha YFS 200 Blaster quad bike and integrated into the design. To design the remaining crankshaft and crankcase assembly structurally, a theoretical computer-based model was created to determine the forces generated by the engine mechanism, given the chosen cylinder arrangement. Essential input for the theoretical model was obtained experimentally by testing a two-stroke Yamaha DT 175 engine on a dynamometer and capturing the maximum cylinder pressure curves obtained throughout the usable speed range. No thermal, fluid, vibration or detailed structural analysis was done. The design was concluded by producing a complete set of detail drawings and bill of materials for the manufacturing process. Manufacturing of the crankcase required specialised tooling and a competent machinist, while the accurate alignment of the individual component press-fit crankshaft proved arduous. The assembly of the entire engine was, however, quickly accomplished. Once installed in the test cell, the UAV engine was successfully tested on a dynamometer while at full load. The prototype achieved the stated goal. Design refinement is, however, required to reduce the overall mass of the UAV engine, analyse critical components and apply cost-effective manufacturing methods.

KEYWORDS

Couples
Crankcase
Crankshaft
Design
Forces
Internal combustion engine
Manufacture
Testing
Two-cylinder
Two-stroke
Unmanned aerial vehicle

DEDICATION

I would like to dedicate this UAV engine to my Father in Heaven. Thank you for giving me this fascinating interest and for providing me with this splendid opportunity to conduct an engine design.

_____

ACKNOWLEDGEMENTS

I would like to express my sincere appreciation to all the people mentioned below for their individual contributions made throughout the course of this study:

Firstly, to Dr Andrew Taylor for giving me the opportunity to conduct this study at CAE. Without the finances and facilities provided by CAE for this extensive study, it would never have been concluded successfully. Special thanks to Willem Boshoff for all the technical assistance provided throughout the project. The machining and fabrication excellence displayed by Harold Bannister and Clinton Hulley while constructing all the UAV engine components proved most valuable. The rapid fabrication of numerous jigs and patient alignment assistance provided by Cornay Rabie are greatly appreciated. To all the other staff at CAE who assisted me with this project in too many ways to mention explicitly, all your contributions to making this project a success are sincerely appreciated.

Thank you to Cameron Davidson for proofreading the first iteration and assisting me with the subsequent grammatical editing, and to Willie Rabe for positive encouragement.

Special thanks to Prof Chris Storm for seeing the value in this study, for all his patient guidance and excellent advice. I would also like to extend my sincere gratitude to my family and friends, especially Leigh in Cape Town, for all their encouragement, support and faith in me.

TABLE OF CONTENTS

LIST OF TABLES

LIST OF FIGURES

NOMENCLATURE

A/F	Air/fuel ratio
ATDC	After top dead centre
ATE	Advanced Technologies and Engineering
bmep	Brake mean effective pressure
BC	Bottom centre
BDC	Bottom dead centre
BOM	Bill of materials
BTDC	Before top dead centre
cc	Cubic centimetres
CAM	Computer-aided manufacture
CAE	Cape Advanced Engineering
CDI	Capacitive discharge ignition
CFD	Computational fluid dynamics
CG	Centre of gravity
CI	Compression ignition
CNC	Computer numeric controlled
CP	Cylinder pitch
DH	Deck height
DVC	Disc valve close
DVO	Disc valve open
EC	Exhaust port close
ECE	Economic Commission for Europe
ECU	Electronic control unit
EO	Exhaust port open
ETA	Engine test analysis software
ETC	Electronic throttle control
EUR	Euro
F1	Formula One
FEA	Finite element analysis
FEM	Finite element methods
IC	Inlet close
IO	Inlet open
MHI	Mitsubishi Heavy Industries
MZ	Motorradwerk Zschopau
ppr	Pulses per revolution
PC	Personal computer
rpm	Revolutions per minute
RVC	Reed valve close
RVO	Reed valve open
sfc	Specific fuel consumption
spr	Samples per revolution
Sasol	South Africa Synthetic Oil Liquid
SANDF	South African National Defence Force
SI	Spark ignition
TC	Transfer port close, top centre
TDC	Top dead centre
TIG	Tungsten inert gas
TO	Transfer port open

TPS	Throttle position sensor
UAS	Unmanned aircraft system
UAV/s	Unmanned aerial vehicle/s
US	United States
USAF	United States Air Force
UTS	Ultimate tensile strength
ZAR	South African rand

LIST OF SYMBOLS

x	Distance	[m]
α	Crankshaft angular acceleration	[rad/s^2]
α	Coefficient of linear expansion	[°C^{-1}]
β	Bank angle	[°]
η_m	Mechanical efficiency	[%]
θ	Crank angle	[°]
θ_{ip}	Crank angle index point	[°]
θ_1	Crank angle for cylinder 1	[°]
σ_y	Yield stress	[Pa]
$\emptyset$	Connecting rod angle	[°]
$\emptyset_{ip}$	Connecting rod angle index point	[°]
Φ	Relative crank angle	[°]
ω	Crankshaft angular velocity, angular velocity	[rad/s]
ω_1	Minimum crankshaft angular velocity	[rad/s]
ω_2	Maximum crankshaft angular velocity	[rad/s]
Ω	Angular velocity of connecting rod	[rad/s]

LIST OF UNITS

a	Crank radius	[m]
a_b	Binomial series piston acceleration	[m/s^2]
a_p	Piston acceleration	[m/s^2]
AC	Reaction couple arm	[m]
A_p	Piston crown projected area	[m^2]
b	Number for bolts	-
B	Bore	[m]
C	Couple	[Nm]
CF	Perpendicular moment arm	[m]
C_p	Primary couple	[Nm]
C_r	Resultant couple	[Nm]
C_s	Secondary couple	[Nm]
d	Diameter of crank pin	[m]
d_p	Diameter of piston pin	[m]
δE	Surplus energy	[J]
F	Reaction force, centrifugal force	[N]
F_b	Force per bolt	[N]
F_{cr}	Crankcase seam bolt force	[N]
F_{cw}	Counterweight centrifugal force	[N]
F_{cy}	Cylinder flange bolt force	[N]
F_g	Piston gross force	[N]
F_i	Piston inertia force	[N]
F_p	Primary force	[N]
F_r	Resultant force	[N]
F_s	Secondary force	[N]
J_r	Total rotational inertia, polar moment of inertia	[kgm^2]
k	Radius of gyration	[m]
l	Connecting rod length	[m]
l_{cg}	Connecting rod length from big-end to CG	[m]
l_{cp}	Length of crank pin	[m]
l_{cpe}	Length of crank pin exposed	[m]
l_1-l_5	Length	[m]
L	Stroke	[m]
L_o	Original length	[m]
ΔL	Length increase	[m]
m	Mass	[kg]
$\dot{m}_a$	Air mass flow rate	[kg/s]
m_b	Mass allocated to big-end	[kg]
m_{be}	Mass of big-end bearing	[kg]
m_c	Mass of crankshaft and flywheel	[kg]
m_{cp}	Mass of crank pin	[kg]
m_{cr}	Connecting rod mass	[kg]
m_{cw}	Counterweight mass	[kg]
m_{cwa}	Counterweight mass approximation	[kg]
$\dot{m}_f$	Fuel mass flow rate	[kg/s]
m_o	Total reciprocating mass component	[kg]

m_p	Mass of piston	[kg]
m_{pc}	Mass of piston circlips	[kg]
m_{pp}	Mass of piston pin	[kg]
m_{pr}	Mass of piston rings	[kg]
m_r	Total rotational mass component	[kg]
m_{rp}	Mass of rotational parts	[kg]
m_s	Mass allocated to small-end	[kg]
m_{se}	Mass of small-end bearing	[kg]
m_w	Mass of big-end washer	[kg]
M	Bending moment	[Nm]
n	Number of cylinders	-
N	Piston side load	[N]
N_c	Crankshaft rotational speed	[rpm]
p	Cylinder pressure	[Pa]
P	Piston effort	[N]
P_b	Brake power	[W]
P_f	Friction power	[W]
P_i	Indicated power	[W]
Q	Connecting rod load, bearing load	[N]
r	Radius	[m]
r_{cg}	Geometric compression ratio	-
r_{ct}	Trapped compression ratio	-
r_{cw}	Counterweight radius	[m]
R	Connecting rod length/crank radius ratio	-
R_a	Bearing reaction at A	[N]
R_{ac}	Reaction at A due to couple	[N]
R_{ax}	Bearing A reaction in X-direction	[N]
R_{ay}	Bearing A reaction in Y-direction	[N]
R_b	Bearing reaction at B	[N]
R_{bc}	Reaction at B due to couple	[N]
R_{bs}	Bore/stroke ratio	-
R_{bx}	Bearing B reaction in X-direction	[N]
R_{by}	Bearing B reaction in Y-direction	[N]
R_x	Bearing reaction in X-direction	[N]
R_y	Bearing reaction in Y-direction	[N]
s	Piston displacement	[m]
s_b	Binomial series piston displacement	[m]
t	Time	[s]
T	Net indicated torque	[Nm]
T_g	Gross torque	[Nm]
T_i	Inertia torque	[Nm]
T_m	Mean output torque, mean resisting torque	[Nm]
T_{mb}	Mean brake torque	[Nm]
T_{mi}	Mean indicated torque	[Nm]
T_r	Reaction couple	[Nm]
ΔT	Resultant accelerating torque, resultant decelerating torque	[Nm]
ΔT	Temperature change	[°C]
v	Velocity	[m/s]
v_b	Binomial series piston velocity	[m/s]

v_p	Piston velocity	[m/s]
$\overline{v_p}$	Mean piston velocity	[m/s]
v_r	Rubbing velocity of crank pin	[m/s]
v_{rp}	Rubbing velocity of piston pin	[m/s]
V	Volume	[m^3]
V	Shear force	[N]
V_c	Clearance volume	[m^3]
V_d	Displaced cylinder volume	[m^3]
V_{dt}	Engine displacement	[cm^3]
V_t	Trapped cylinder volume	[m^3]
W_{comp}	Compression work per cycle	[J]
W_{exp}	Expansion work per cycle	[J]
W_i	Indicated work per cycle	[J]

1 INTRODUCTION

1.1 BACKGROUND

Currently the term “drone” is applied to all manner of unmanned aerial vehicles (UAVs) when spotted by the casual observer. And while the informal terminology is not strictly inaccurate, it does correctly identify that the use of UAVs has become ubiquitous. A UAV has been defined by the Joint Capability Group on Unmanned Aerial Vehicles (Valavanis & Vachtsevanos, 2015:44) as “a reusable aircraft designed to operate without an onboard pilot. It does not carry passengers and can be either remotely piloted or preprogrammed to fly autonomously.”

The tasks that UAVs currently perform are varied and dependent on the sector that uses them. The military initiated the use of UAVs and operations include aerial reconnaissance, surveillance, intelligence gathering and weapons delivery. Homeland security applications may include border patrol, search and rescue and law enforcement surveillance, to name a few. The development in micro-electronics, the civil application of the global positioning system, advances in wireless communication and improved battery technology have enabled the commercial application of UAVs. Some of their typical tasks are surveying, aerial photography, crop monitoring and game park patrols (DeGarmo, 2004:13-17).

Around 50 years ago, the Lightning Bug was the first significant UAV programme. This was used by the United States Air Force (USAF) for tactical reconnaissance during the Vietnam War and flew approximately 3500 sorties. Further UAV programmes were subsequently conducted, such as the D-21, but external political pressure and the development of surveillance satellites resulted in no significant pilotless programme being developed by the USAF until the early 1980s. This all changed in 1982, when Israel successfully used UAVs against Syria in the Bekaa Valley of Lebanon. This prompted the United States (US) to purchase Pioneer, the Israeli unmanned aircraft system (UAS), and to develop new pilotless aircraft. The RQ-1 Predator or Predator A was the result and it has been involved in every major US military operation between 1996 and 2004 (U.S. Air Force, 2005:1-2). The RQ-1 Predator was also the first UAV to carry Hellfire air-to-surface missiles in 2001, resulting in its designation changing to MQ-1 to reflect this (Office of the Secretary of Defense, 2002:6).

Today, UAVs are abundant. Small, relatively low-priced models, as illustrated by the DJI Mavic Pro in Figure 1.1 on the left, target the hobbyist and selected civil organisations, while certain military organisations, for instance the US, use large, complex, purpose-built UAVs such as the RQ-4 Block 30 Global Hawk, as illustrated in Figure 1.1 on the right (Zwijnenburg & Postma, 2018:8). The Mavic Pro is an electrically powered quadcopter that is 335 mm across diagonals, has an all-inclusive weight of 743 g and a maximum endurance of approximately 25 minutes (DJI, 2019). The Global Hawk is a gas turbine powered, fixed-wing reconnaissance aircraft that has a wingspan of 39.9 m, a gross take-off weight of 14.628 tons and a maximum endurance exceeding 32 hours (Northrop Grumman, 2016). The two figures below and the associated specifications above illustrate the diversity of the platforms available in the UAV sector.

FIGURE 1.1: DJI MAVIC PRO QUADCOPTER (LEFT) AND RQ-4 BLOCK 30 GLOBAL HAWK RECONNAISSANCE AIRCRAFT (RIGHT).
(Courtesy SZ DJI Technology Co., Ltd., Northrop Grumman Corporation)

A UAV cannot function in isolation, but is part of a UAS that is defined by the European Aviation Safety Agency (Valavanis & Vachtsevanos, 2015:45) as comprising "individual system elements consisting of an 'unmanned aircraft', the 'control system' and any other system elements necessary to enable flight."

The manufacturing of UAVs is categorised as either commercial or military. UAV Global estimated that by January 2018 there were more than 450 manufacturers, of which 300 were developing military UAVs (Zwijnenburg & Postma, 2018:9). With so many manufacturers and the illustrated diversity, suitable classification of UAVs is required.

Various classification schemes have been proposed and some are currently used. The variety of classification schemes arise owing to the diversity of the current UAV designs, capabilities and operational characteristics. Many metrics can be used and van Blyenburgh (2008:5) has compiled a comprehensive list for both UAV and the associated UAS classification and differentiation. The four main parameters used are mass, range, flight altitude and endurance. The Mavic Pro, as illustrated in Figure 1.1, would thus be categorised as a "micro (μ)" UAS and the Global Hawk as a "high-altitude long endurance (HALE)" UAS (Valavanis & Vachtsevanos, 2015:83-85).

In 1986 the Kentron Seeker 1 became the first operational UAV to be used in South Africa, by the then South African Defence Force or SADF. This platform provided aerial reconnaissance and weapons delivery guidance during the South African Border War and during this time three were downed by enemy fire. In November 1990, 10 Squadron ceased operations (Barnard, 2009:229-230; Martin, 2016).

Excluding the multitude of electrically powered micro-UAS currently operational in South Africa, the South African National Defence Force (SANDF) currently employs the Vulture UAS, as illustrated on the left in Figure 1.2. This UAV was designed by Advanced Technologies and Engineering, now Paramount Group, and mission functions include target acquisition, artillery fire correction and reconnaissance in support of the G5 and G6 Howitzer canons (van Blyenburgh & Butterworth-Hayes, 2006). Further development of the original Seeker 1 and 2 by Denel Dynamics, formerly Kentron, resulted in the Seeker 200 UAV, illustrated on the right in Figure 1.2. As of early 2016, the South African Air Force (SAAF) confirmed reactivation of 10 Squadron and it is rumoured that the Seeker 400, the latest evolution, will be the UAS used (Martin, 2016).

FIGURE 1.2: VULTURE UAV ACTIVE WITH SANDF (LEFT) AND DENEL DYNAMICS SEEKER 200 UAV (RIGHT).
(Courtesy Paramount Group, Denel Dynamics)

When the Vulture and Seeker 200 are subjected to the classification criterion proposed by van Blyenburgh (2008:5), both UAVs are categorised as medium-range (MR) UAS. This implies a UAV mass of between 150 and 500 kg, a range of 70 to 200 km, a flight altitude of up to 5000 m and an endurance of 6 to 10 hours.

For propulsion, the Vulture and the Seeker 1 UAVs use two-stroke, spark-ignition (SI), horizontally-opposed, air-cooled engines in a pusher configuration. The Vulture uses a Zanzottera 498i engine, as illustrated in Figure 1.3 on the left. This is a two-cylinder, 498 cc engine that produces 28 kW at 6700 rpm and has a mass of 15 kg (Zanzottera Technologies, 2004:12). The Seeker 1 is powered by a Limbach L550E, as illustrated on the right in Figure 1.3. This four-cylinder, 548 cc engine produces 38 kW at 7500 rpm and has a mass of 15 kg (Anon., s.a.). The engine models used in the Seeker 200 and 400 have not been publicly stated, although the two-stroke cycle has been confirmed.

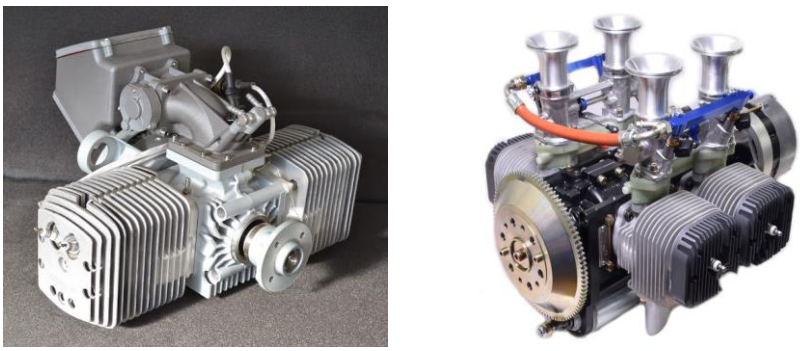

FIGURE 1.3: ZANZOTTERA 498I TWO-STROKE ENGINE USED IN THE VULTURE (LEFT) AND THE LIMBACH L550E TWO-STROKE ENGINE USED IN SEEKER 1 (RIGHT).
(Courtesy Zanzottera Technologies Srl, Limbach Flugmotoren GmbH)

Both engines pictured above, for the two South African MR class UAVs illustrated in Figure 1.2, are sourced internationally, since no local alternative is available. The Zanzottera is manufactured in Italy, while the Limbach is produced in Germany. These engines are purchased at significant cost. An April 2001 retail pricelist for Limbach two-stroke engines lists a cost of €9790 for a certified L550E engine, shipping included (Limbach Flugmotoren, 2001). Estimates made with the aid of a web-based inflation calculator, taking into account total inflation of 28.85% from 2001 to 2019 in Germany, results in a current cost of €12615, excluding tax (Inflation Tool, 2019). The resultant South African cost is R231 423 (Incl), given a 1 August 2019 exchange rate of 15.95 South African rand (ZAR) to the euro (EUR).

In 2007, 13 rhinos were poached in South Africa. By 2014 that figure had soared to 1 215, an increase of over 9 000%. From 2007 to the middle of 2019 a total of 7 912 rhinos were killed illegally in this country alone (Save the rhino, 2019). Had the available South African MR class UAVs, with a range and endurance of up to 200 km and 10 hours, been used, these appalling statistics may have been different. Moreover, there is an urgent need to patrol the vast South African border and coastal regions aerially against illegal migrants and fishing respectively.

The Teal Group, analysists that research and publish information on the aerospace and defence industry, projects that non-military UAS manufacture will increase from $4.9 billion in 2019 to $14.3 billion in 2028, with the commercial sector surpassing the consumer market in 2023 and becoming the largest segment (Teal Group, 2019).

1.2 PROBLEM STATEMENT

In view of the availability of the locally designed MR Vulture and various Seeker UAS platforms, the high international engine cost and the operational requirement, a suitably specified, reliable, locally manufactured UAV engine, available at a reasonable cost, could well present a viable alternative.

The problem statement is thus to develop a two-stroke, two-cylinder, horizontally-opposed, air-cooled, SI, UAV engine with a preferred engine displacement (V_{dt}) of 500 cc.

1.3 OBJECTIVES

The design, manufacturing and testing objectives for the UAV engine are as follows:

- Make use of as many suitable, commercially available engine parts as possible in critical areas, thus minimising design effort.
- The cost of the commercial items and manufacture of designed engine components is to be kept as low as possible.
- Maximum power and minimum weight for this class of engine are not paramount, since this design is considered a prototype demonstrator.
- While reliability is important, the longevity of the engine is not to be a primary design focus.
- The manufacturing complexity of the designed engine components and systems that require fabrication should be kept to a reasonable minimum.
- A full load power curve will suffice to characterise typical engine performance. Rigorous testing of the prototype engine throughout the operational speed and load range is not required.

1.4 RESEARCH METHODOLOGY

- Conduct a literature review to become aware of existing theory and current trends for the engine components and systems that are used in two-stroke, SI engines.
- Given the problem statement and the associated objectives, as seen in Sections 1.2 and 1.3 respectively, select a suitable commercial brand and purchase the engine parts that are to serve as donor components in the critical areas.
- Study the relevant theory and document the relationships, parameters and equations that characterise the reciprocating engine mechanism.
- Establish that the instantaneous cylinder pressure (p), cannot be calculated analytically and acquire an applicable two-stroke engine to obtain this data experimentally.
- Set up the experimental engine on a dynamometer and conduct the experiments, primarily to obtain the required instantaneous p curves at various increments throughout the engine speed range, while at full load.
- Construct a computer-based model, using Matlab, to read the experimental binary file input data and output the maximum p curves, for one cycle, at all the engine speeds tested.
- Model the four donor sub-assembly engine components, namely the cylinders, pistons, connecting rods and cylinder heads, using Pro Engineer Wildfire 3.0.
- Design the crankshaft and crankcase, with the aid of the solid modeller, based on the dimensional requirements of the donor components, while simultaneously applying the applicable engine theory.
- Write a further computer-based model, specifically for this UAV engine. Incorporate the experimentally obtained p curves, at various incremental engine speeds, with the relevant theoretical equations. The theoretical equations' independent variables can then be substituted with the UAV engine specifications and the results tabulated after running the Matlab programs.
- Design or specify all the required engine systems, with the aid of the solid modeller.
- Purchase the required raw materials; manufacture and assemble the crankshaft, crankcase and all the engine systems.
- Install the assembled UAV engine on a dynamometer and cautiously conduct the initial test runs. As confidence in the integrity of the prototype engine grows, proceed with a full load test, throughout the speed range, and tabulate the results.
- Evaluate and compare the UAV engine test results against the theoretical predictions and similar engines in the same market and document the findings.
- Conclude the dissertation and make recommendations.

1.5 SCOPE AND LIMITS

An internal combustion engine, when viewed as a complete system, is a complex device that is comprised of numerous systems and components. Given the number of mechanical engineering disciplines involved in designing, manufacturing and testing an entire prime mover, it is essential that the scope and limits of this study be clearly defined.

The scope of this dissertation includes the following:

- Selecting suitable donor engine components for the cylinders, pistons, connecting rods and cylinder heads of the engine sub-assembly.
- Designing the remaining two engine components of the engine sub-assembly, the crankshaft and crankcase.
- Specifying or designing the engine systems as required.
- Producing a full set of detail drawings and bill of materials (BOM) for the engine.
- Manufacturing, and assembly if required, of both the crankshaft and crankcase to the highest standard, adhering to stipulations in the relevant detail drawings.
- Restricting the manufacturing of the engine systems to “fit for purpose”.
- Installing the engine on a dynamometer and testing it.

The limits imposed on this project are the following:

- No thermo or fluid dynamic calculations or analyses of any kind will be conducted. This is based on the assumption that both fields have been correctly applied to the donor parts, by a reputable manufacturer, and thus require no further investigation.
- The theory and associated computer-based mathematical model will be primarily tasked with calculating the maximum forces and couples applied to the crankshaft and crankcase due to combustion and vibration directly associated with rotational and reciprocating balancing.
- In addition, the mathematical model will be restricted to determining some characteristic engine parameters and typical performance predictions.
- Besides some basic structural calculations, no detailed structural design, finite element analysis (FEA), or vibration analysis will be conducted on the crankshaft, crankcase or donor parts. The maximum forces and couples obtained can serve as inputs for a future FEA and vibration analysis and will not be addressed here, owing to the inherent scope and complexity of that topic.
- The engine systems that require design will be restricted to limited detail design only sufficient to obtain a functional, not optimised, system.
- The testing on a dynamometer will be restricted to full load, throughout the engine speed range, to characterise the performance of the UAV engine. No further testing will be conducted.

1.6 DISSERTATION STRUCTURE SUMMARY

This dissertation consists of eight chapters, as documented below:

1.6.1 CHAPTER 2: LITERATURE SURVEY AND EXISTING TECHNOLOGY

This chapter commences with the classification of reciprocating internal combustion engines. Subsequently a study of the two-stroke cycle, port timing, engine components and engine systems concludes this chapter.

1.6.2 CHAPTER 3: APPLICABLE RECIPROCATING ENGINE THEORY

The required geometric relationships and parameters that characterise the reciprocating engine mechanism is documented. This chapter closes with the derivation of analytical methods for balancing both rotary and reciprocating components.

1.6.3 CHAPTER 4: CYLINDER PRESSURE EXPERIMENTAL INVESTIGATION

The experimentally acquired instantaneous p curve, at various engine speed increments, is obtained in this chapter. The testing methodology, the systems used and the computer-based program written to extract the required data are detailed.

1.6.4 CHAPTER 5: THEORETICAL UAV ENGINE DESIGN

The theory defined in Chapter 3 is used to construct a computer-based model of the UAV engine. This model primarily comprises the forces and couples generated by a firing engine mechanism and those due to the balancing of the rotational and reciprocating systems.

1.6.5 CHAPTER 6: UAV ENGINE DESIGN, MANUFACTURE AND ASSEMBLY

The four donor engine components, in critical areas, initiate the design of the two remaining components, the crankshaft and crankcase. Subsequent to that, all the engine systems are designed. The designed engine components and systems are manufactured and assembled to finally produce the UAV engine.

1.6.6 CHAPTER 7: EXPERIMENTAL ENGINE TEST RESULTS AND ANALYSIS

The completed UAV engine is coupled to the dynamometer for testing. The most notable component and system failures are documented and rectified before the successful running of the prototype is possible. The test results are recorded and compared to those theoretically predicted and finally to two UAV engines manufactured by competitors.

1.6.7 CHAPTER 8: CONCLUSION AND RECOMMENDATIONS

The dissertation ends by stating the conclusion and recommendations.

1.6.8 REFERENCES

All the references used in this dissertation can be found in this section.

1.6.9 APPENDICES

This section contains all the experimental test results, all the UAV engine detail drawings and all Matlab computer programs that were written for this project.

---

2 LITERATURE SURVEY AND EXISTING TECHNOLOGY

2.1 RECIPROCATING INTERNAL COMBUSTION ENGINE CLASSIFICATION

Reciprocating internal combustion engines produce rotational output by the cyclic combustion of a pre-compressed fuel-air mixture. In 2018 it was estimated that there were about 1.2 billion passenger cars and 380 million commercial vehicles throughout the world (Kalghatgi, 2018:965). Most cars are powered by SI engines and commercial vehicles by compression-ignition (CI) engines (Duleep, 2004:497). These statistics do not include the reciprocating internal combustion engines used in shipping, aircraft, stationary generators, agricultural machines, recreational vehicles and small utility devices.

Given the sheer number of internal combustion engines in use and the variety of applications, it is evident that the classification of a prime mover for a specific task is essential. This chapter will commence with the classification of reciprocating internal combustion engines. The two-stroke cycle and port timing will follow. The two subsequent sections will document the primary two-stroke engine components and required peripheral systems that enable the working of a prime mover.

2.1.1 INTERNAL COMBUSTION ENGINE TYPE AND CYCLE

In 1860 Etienne Lenoir invented and built the first two-stroke engine (Noor *et al.*, 2008:1461). This engine had an efficiency of only 4%. Subsequent to that, in 1878 and 1897, Otto and Diesel respectively ran their engines (Degler, 1943:6-7). Otto's engine ran with his proposed four piston stroke design and Diesel with his liquid injection of fuel, directly into the cylinder, after being heated by compression (Heywood, 1988:2-4).

There are currently two main distinct types of reciprocating internal combustion engines: SI and CI engines. For SI engines, a homogeneous fuel-air mixture is ignited by a spark and a flame front propagates. CI engines rely on the auto-ignition of the injected fuel when exposed to the air heated in the cylinder by compression. Specific fuels have been developed for SI and CI engines, namely petrol and diesel respectively (Bae & Kim, 2017:3390).

Both SI and CI engines transform chemical energy into mechanical energy by converting the heat released by a thermodynamic cycle (Mollenhauer & Tschoeke, 2010:7). This thermodynamic cycle most commonly occurs in two or four strokes of the piston; thus, two- or four-stroke engines.

In a four-stroke engine, the piston moves through four strokes to complete a cycle (Brady, 2013:7). The induction of a fuel-air mixture, the compression, the combustion that results in expansion and the final exhausting thereof chronologically represent the four relatively distinct events that occur in the cylinder of a four-stroke engine. Thus, a four-stroke engine produces one power stroke for two crankshaft revolutions (Heywood, 1988:11).

In a two-stroke engine the entire cycle requires two piston strokes (Maleev, 1945:9). The sequence of gas exchange events that occur is identical to that of a four-stroke engine, but must occur within half the available number of strokes. Since four relatively distinct events, as described above, must occur within half the number of available strokes, certain gas exchange events must occur simultaneously. The detailed description thereof for an SI, two-stroke, crankcase-scavenge engine will be left for Section 2.2.1. A two-stroke engine thus has an advantage over a four-stroke engine by producing twice as many power strokes in the same time period, assuming that both engines rotate at the same speed (Stone, 1999:3).

Both SI and CI engines can function as either two- or four-stroke engines. However, Brady (2013:7) states that “four-stroke cycle gasoline and diesel engines predominate as the global prime mover of choice.” Everyday illustrations are the SI or CI four-stroke engines that power the motor vehicles we drive. Two-stroke SI and CI engines are generally used for different applications, as the following two illustrations will demonstrate.

Figure 2.1 illustrates a two-stroke, SI, O.S. Max GT15 model aircraft engine. This engine produces 1.8 kW at 15 000 rpm and has a bore of 27.7 mm and a stroke of 24.8 mm. Note that this engine weighs less than 1 kg (O.S. Engines, 2018:21).

FIGURE 2.1: O.S. MAX GT15 TWO-STROKE, SI, MODEL AIRCRAFT ENGINE.
(Courtesy O.S. Engines Mfg. Co., Ltd.)

A cut-away of the Mitsubishi Heavy Industries (MHI) 8UEC75LSII two-stroke, CI engine for super-tankers is illustrated in Figure 2.2. This eight-cylinder engine produces 24 000 kW at 84 rpm and has a bore of 750 mm and a stroke of 2 800 mm (Dragsted, 2011?:70). Note the foot-rungs inside the crankcase and the two walking platforms around the cylinders. Note the use of a crosshead attached to the connecting rod as well.

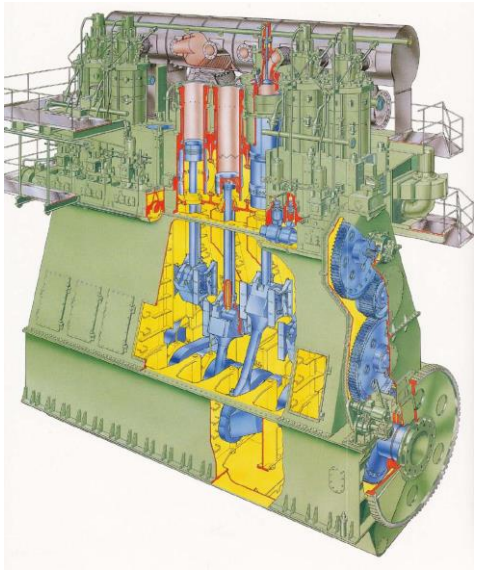

FIGURE 2.2: MHI 8UEC75LSII TWO-STROKE, CI, ENGINE FOR SUPER-TANKERS.
(Courtesy Mitsubishi Heavy Industries, Ltd.)

These two preceding figures and the related descriptions briefly illustrate some of the key differences between the applications for which two-stroke SI and CI engines are used. It will be left to Section 2.1.3 to define the applications for different types of engines in more detail.

2.1.2 RECIPROCATING ENGINE CONFIGURATION

During the last approximately 150 years, since Etienne Lenoir ran his gas engine, reciprocating internal combustion engines have been designed and manufactured in a wide variety of configurations. The term configuration, as applied here, refers broadly to the main physical attributes of the engine. Included in this definition is the number and layout of the cylinders, the location and functioning of the valve system and the method of cooling.

Figure 2.3 illustrates three common automotive and commercial engine layouts, in various states of assembly.

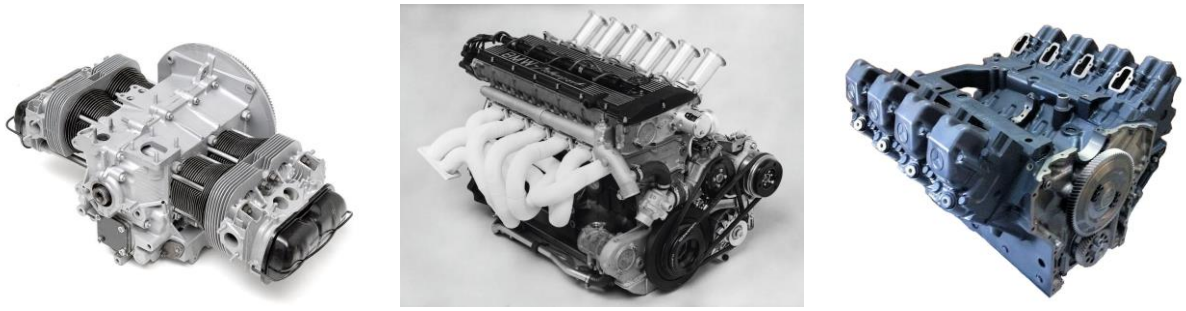

FIGURE 2.3: VW FOUR-CYLINDER, HORIZONTALLY-OPPOSED ENGINE (LEFT), BMW SIX-CYLINDER, IN-LINE ENGINE (CENTRE) AND MERCEDES-BENZ EIGHT-CYLINDER V ENGINE (RIGHT).

(Courtesy Volkswagen Motor Company LTM, Bayerische Motoren Werke AG, Daimler AG)

The engine on the left is a VW, SI, four-cylinder, horizontally-opposed, air-cooled, 1584 cc automotive engine (Fisher, 1970:9). The centre engine is a BMW M88, SI, six-cylinder, in-line, liquid-cooled, 3.5 L automotive engine (Catchpole, 2017). The engine on the right is a Mercedes-Benz OM442, CI, eight-cylinder, V, liquid-cooled, 14618 cc commercial engine (Service Department of Atlantis Diesel Engines, 1995?:6). Note that all three the engines are four-strokes.

Reciprocating internal combustion engines can have any number of cylinders, but currently the number typically ranges from one to 24 for light utility and heavy industrial applications respectively. The three engines pictured above illustrate the most popular contemporary cylinder count for automotive and commercial vehicles.

The number of cylinders can be combined with most layouts and is not restricted to that illustrated in Figure 2.3. For automotive and commercial applications, the in-line, four-cylinder engine is the most prominent. Currently six-cylinder engines are normally in a V layout for both SI and CI automotive engines and in-line for CI commercial engines, while eight-cylinder engines, for both SI and CI, are typically in the V layout as pictured. Other layouts such as radial, U and opposed-piston have previously also been built (Bosch, 2007:466).

The valves and related system to actuate the valves are an integral part of the engine architecture, as illustrated in Figure 2.4. on the following page.

The Saito FA-120, as pictured on the left, is a four-stroke, 19.95 cc model aircraft engine (Saito Seisakusho, s.a.:1). The camshaft gear, driven by the crankshaft below, actuates the intake and exhaust valves located within the cylinder head, by a pushrod and rocker assembly. A gear-driven camshaft, pushrod and rocker arrangement is similar to that used in the VW and Mercedes-Benz engines pictured in Figure 2.3. The BMW uses two overhead camshafts, one for the intake and the other for the exhaust valves, that are both driven by a chain. Since the camshafts are at the top of the engine, pushrods are not required.

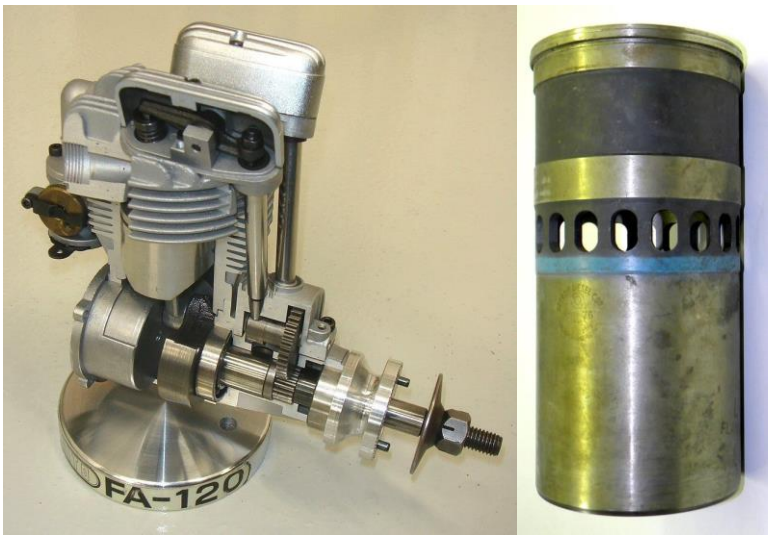

FIGURE 2.4: SAITO FA-120 FOUR-STROKE ENGINE (LEFT) AND DETROIT DIESEL 8V92 TWO-STROKE SLEEVE (RIGHT).

(Courtesy Saito Seisakusho Co., Ltd, Detroit Diesel Corporation)

The photo on the right is a Detroit Diesel 8V92 cylinder or more commonly called a sleeve. This is a commercial CI engine that utilises the uniflow, two-stroke cycle. The ports around the circumference of the sleeve are the intake ports, timed by the top edge of the piston position, and the exhaust gas exits through four poppet valves located in the cylinder head. These poppet valves utilise a gear-driven camshaft system similar to that of the Saito model engine (General Motors, 1979).

The poppet valve and the associated valve actuation system consist of numerous parts and as described above, form an integral part of the engine. Sleeve valves, by comparison, are simpler in operation, but restricted to the timing offered by the piston.

Maleev (1945:374) states that “methods of cooling may be divided into two main groups: direct, or air-cooling and indirect, or liquid-cooling.” The illustrations on the left of Figure 2.3, the VW automotive engine, and Figure 2.4, the Saito model aircraft engine, are both examples of air-cooled engines. Note that in both photos extensive cooling fins protrude around the cylinders and cylinder heads to improve heat dissipation by directed or direct airflow.

Liquid-cooled engines, such as the BMW M88 and Mercedes-Benz OM442 in Figure 2.3, do not have the expansive cooling fins. Instead a cavity is cast between the engine working surfaces and the exterior to allow for the flow of coolant through the engine. This heated fluid is then passed through a heat exchanger or radiator, cooled and recirculated back through the engine.

These two cooling methods require different manufacturing details (Maleev, 1945:374). Thus, this must be accounted for during the initial design phase of the engine.

2.1.3 RECIPROCATING INTERNAL COMBUSTION ENGINE APPLICATION

Degler (1943:8) states that “there is no universal internal combustion engine.” Every engine must be designed and manufactured to suit a particular task (Degler, 1943:8). This section will address the outstanding fundamental engine classification parameters and incorporate the knowledge gained from Sections 2.1.1 and 2.1.2 as required.

The application of a reciprocating internal combustion engine can be classified by:

- ***Utilisation*** determines whether the engine will be used for light, intermittent applications or continuous use.

  A two-stroke, SI engine might well be a suitable candidate as a low-utilisation engine. However, thermal efficiency, emissions and engine durability are drawbacks (Nora & Zhao, 2015:118). For continuous use a two-stroke, CI engine could be suitable. These low-speed engines are considered the most reliable reciprocating internal combustion engines (Mollenhauer & Tschoeke, 2010:600). These engines typically operate at around 100 rpm or less, as seen in Figure 2.2.

  Four-stroke engines occupy the utilisation middle ground, with SI engines being used for lighter duties, while CI engines are generally selected for applications that require higher utilisation.

- ***Application*** in this context is a broad term and includes engine operation speed range, engine displacement (V_{dt}), size and mass.

  The operational speed range requirement of an automotive engine, for example, is wide. Engine speed range from a smooth idle to maximum rated speed is used. An engine that is used to drive an electrical generator runs continuously at a single speed.

  The V_{dt} of different engines varies greatly. However, there are approximate engine capacity ranges for each application. For example, the O.S. Max model aircraft engines' capacities typically range from 1.79 cc for the Max-11AX, to 119.8 cc for the GT120T (O.S. Engines, 2018).

  Finally, the size and mass of the engine are critical in some applications, such as aviation. Military piston aeroplane engines require maximum possible power output from the smallest possible engine frame with a minimum weight (Ricardo & Hempson, 1968:279). This was said with reference to the Rolls-Royce Merlin engine used in the Second World War.

- ***Sophistication*** and cost are closely related. Should an engine be designed to be increasingly efficient or powerful, the unit cost will inevitably rise. Degler (1943:156) states that the best design is therefore an engine that will perform as required, while simultaneously having the lowest cost per unit. However, more stringent emission regulations have forced automotive companies to develop new engines. An example of this is Honda.

  The new 2016 Honda in-line, four-cylinder, 1.5 L and 2.0 L engines, known as "Earth Dreams Technology", had turbochargers, dual valve timing control and direct injection added to both engines. Honda states that the maximum thermal efficiency has improved from 34.8% for the normally aspirated 1.5 L to 38.0% for the turbocharged unit (Nakano *et al.*, 2016). Inevitably the cost of this new Honda engine, with the additional and more sophisticated hardware, is going to be higher than that of the old unit.

  The 2017 Formula One (F1), 1.6 L engines are good examples of sophisticated engines with high power outputs of over 598 kW that yet manage to attain thermal efficiencies of over 50% if energy recovery is taken into account (Bamsey, 2017:50-56). However, in 2017 this performance cost the Mercedes F1 engine manufacturing division a record $247 million, according to Forbes (Sylt, 2018).

The utilisation, application and sophistication of an internal combustion engine can only be successfully addressed in conjunction with the engine type, cycle and configuration.

2.2 TWO-STROKE ENGINE CYCLE AND PORT TIMING

The different types, cycles, layout configurations and applications of reciprocating internal combustion engines have been described in Section 2.1. With the overview complete, this section specifically addresses the two-stroke, SI, crankcase-scavenge engine, pictured in Figure 2.1.

This section will commence with a detailed description of the two-stroke engine cycle and conclude with an overview of the port timing events that determine the gas exchange processes.

2.2.1 TWO-STROKE ENGINE CYCLE

The major components required to convert the reciprocating motion into rotational output number only three for a two-stroke, SI, crankcase-scavenge engine. As stated in Section 2.1.1 the two-stroke engine cycle is named such because it requires two strokes of the piston, which is equivalent to a single crankshaft revolution, to produce one power stroke.

The two-stroke, SI, crankcase-scavenge engine operating cycle is depicted in Figure 2.5 by four separate diagrams marked A to D. The description of each is as follows:

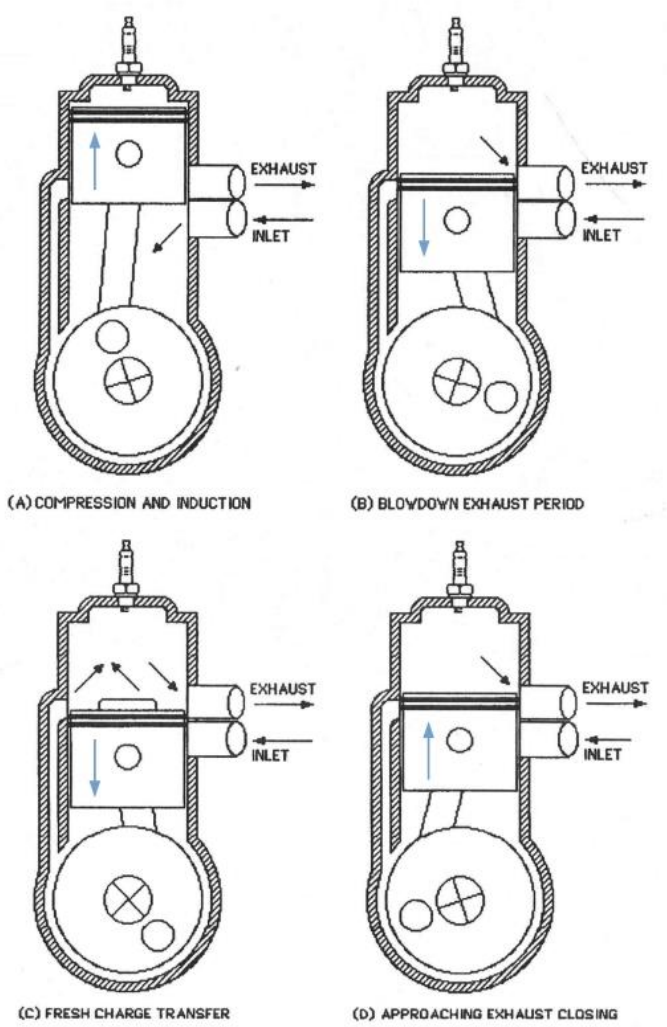

FIGURE 2.5: TWO-STROKE, SI, CRANKCASE-SCAVENGE ENGINE OPERATING CYCLE.
(Blair, 1996:6)

- ***Compression and induction (A)*** occur simultaneously by the upward movement of the piston within the cylinder. Compression of the fuel-air mixture inducted during the previous cycle occurs within the cylinder prior to combustion. Induction of fuel-air mixture or fresh charge through the intake system or inlet occurs within the crankcase owing to the partial vacuum created by the upward-moving piston (Blair, 1996:7). The two events described above occur in isolation of each other.
- ***Blowdown exhaust period (B)*** occurs after the mixture has combusted and expanded, producing the power stroke. It is important to note that of all the ports around the periphery of the cylinder the exhaust port is the first to open as the piston moves downward, producing the blowdown exhaust period (Heywood, 1988:12). The high-pressure products of combustion flow rapidly out of the exhaust port into the exhaust system owing to the high-pressure differential. This exhaust pulse can be used later in the engine cycle in a properly tuned exhaust system, as will be explained in Diagram D (Blair, 1996:400). In the crankcase of the engine the fresh charge inducted in Diagram A is compressed. Again, the events at the top and bottom of the piston occur in isolation.
- ***Fresh charge transfer (C)*** occurs within the cylinder as the transfer ports are exposed by the continual downward motion of the piston, in so doing increasing the pressure within the crankcase. When this exceeds the cylinder pressure, the fresh charge flows into the cylinder. This is called the scavenge process (Blair, 1996:7). An extremely complex fluid transfer process now takes place in the cylinder, since the induction and exhaust processes occur simultaneously. If the design of the transfer ports is not optimised, “short-circuiting” will occur and some fresh charge will be exhausted with the exhaust gas (Blair, 1996:8). The converse could also occur and significant exhaust gas could remain in the cylinder at the end of the scavenge process. The successful scavenging of the exhaust products out of the cylinder by the incoming fresh charge determines the performance of a two-stroke engine (Dekanski *et al.*, 1996:411).
- ***Approaching exhaust closing (D)*** signifies that the scavenging process is complete with the closure of the transfer ports and that the exhaust port is about to close at the “trapping” point (Blair, 1996:8). Since the exhaust port has not yet closed, excess fresh charge sucked into the exhaust system during the scavenging process can now be recovered by utilising the positive exhaust pressure pulse created in a tuned exhaust system during exhaust blowdown. The process requires that the reflected positive exhaust pressure pulse arrive at the exhaust port as the port is about to close, thus forcing the “spilt” fresh charge within the exhaust system back into the cylinder, and in so doing, increasing the mass of the trapped fresh charge within the cylinder prior to compression, resulting in greater engine output (Blair, 1996:437-438). It has been known for some time that the performance of a two-stroke engine is significantly influenced by the design of the exhaust system (Naito & Taguchi, 1966:185).

The two-stroke, SI engine operating cycle described above can only function effectively if all sequences of events relating to gas exchange within the engine and the environment are appropriately timed. The next section investigates these operating parameters.

2.2.2 TWO-STROKE CYCLE PORT TIMING

The obligatory gas exchange occurring during the two-stroke engine cycle, especially the gas transfer within the cylinder as described in the paragraphs of Section 2.2.1, is complex. The timing and duration of cylinder port events are of critical importance and are graphically illustrated in Figure 2.6. This diagram has been adapted from that found in Blair’s handbook (1996:18). Note that the induction method, timing and duration of the fuel-air mixture into the crankcase are not described here; more detail can be found in Section 2.4.3.

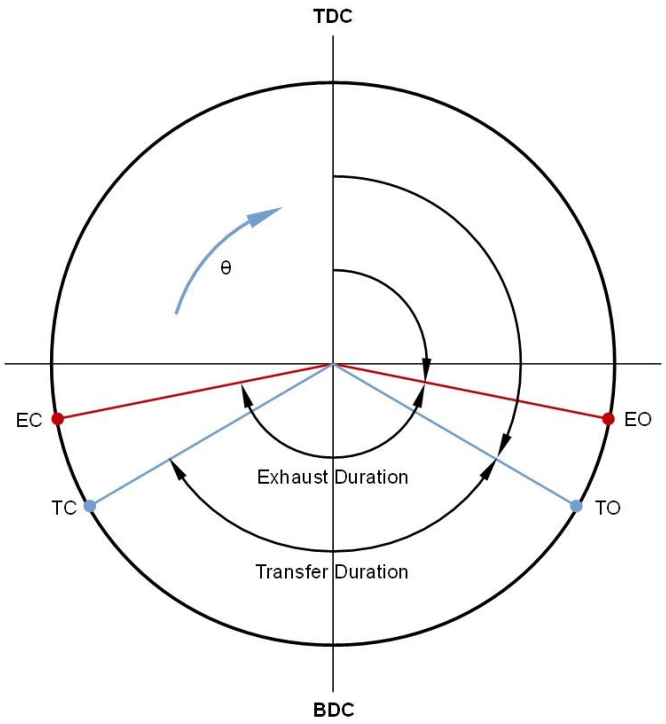

FIGURE 2.6: TWO-STROKE, SI ENGINE TRANSFER AND EXHAUST PORTS TIMING AND DURATION.

The direction of the crankshaft rotation is illustrated by the blue arrow and denoted by the crank angle (θ). Top dead centre (TDC) is the reference for both the exhaust (EO) and transfer (TO) port opening points, illustrated with red and blue markers respectively. Both ports remain open as the crank rotates through bottom dead centre (BDC), the transfer port (TC) being the first to close, followed by the exhaust port (EC). The duration for which both the exhaust and transfer ports remain open is illustrated graphically. Note that the timing for both the exhaust and transfer ports is symmetrical about the vertical TDC-BDC axis (Blair, 1996:18).

Typical values for the EO range between 110° and 82° after top dead centre (ATDC) for industrial to highly tuned engines respectively (Blair, 1996:19). From experimental results Yamaha found the optimum timing of the EO to be about 100° for a YA6 125 cc engine (Naito & Taguchi, 1966:184). The TO values range between 122° and 113° ATDC, again for conservative to high-performance engines respectively (Blair, 1996:19).

2.3 TWO-STROKE ENGINE SUB-ASSEMBLY MAIN COMPONENTS

A two-stroke, SI, crankcase-scavenge engine sub-assembly consists of three major components that transform linear motion into rotary motion, as stated in Section 2.2.1, and three additional components that house these working components. The engine sub-assembly thus forms the core of the entire engine and all six components are uniquely dimensioned and made from a variety of materials so that the task required of each component can be performed effectively.

The engine components that constitute the core workings of a two-stroke, SI, crankcase-scavenge engine, typically used in chainsaws and brush cutters, are illustrated in Figure 2.7 on the following page.

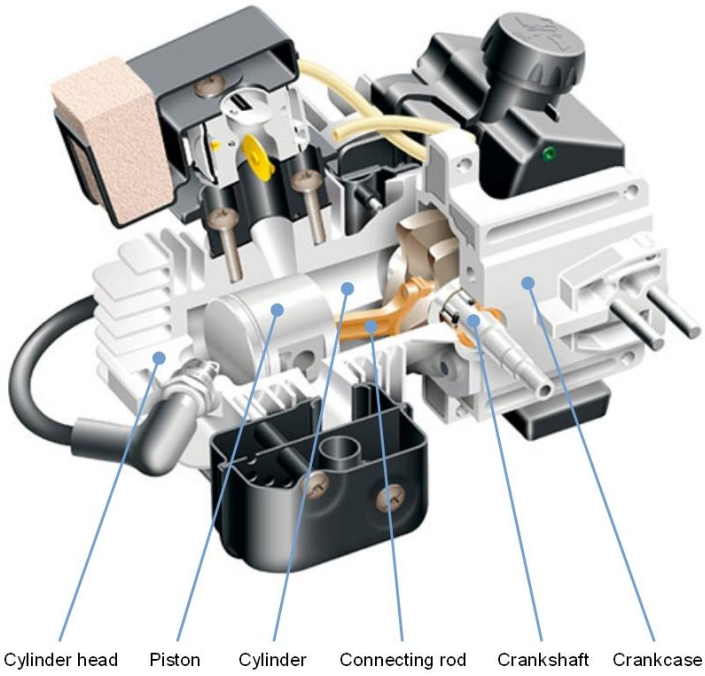

FIGURE 2.7: CUTAWAY DRAWING OF MCCULLOCH MAC 838S-AV TWO-STROKE, SI, CHAINSAW ENGINE. ENGINE DISPLACEMENT 38 CC, BORE 39 MM, STROKE 32 MM, MAXIMUM POWER 1.5 KW AT 12000 RPM.
(*Courtesy McCulloch Motors Corporation*)

The cutaway figure illustrates the crankshaft, crankcase, cylinder, piston, connecting rod and cylinder head that constitute the engine sub-assembly. The functioning, main design considerations, materials and manufacturing methods of all six components will be described next.

2.3.1 CRANKSHAFT

The crankshaft transforms the oscillating linear motion of the piston into rotation (Baragetti, 2015:272). This is done by making use of a connecting rod. The connecting rod is pinned to the piston at one end, while the other is connected to the crankshaft crankpin journals. These crankpin journals "are eccentric in relation to the longitudinal axis of the crankshaft" (Gomes *et al.*, 2018:466). The crankshaft illustrated in Figure 2.7, for a single-cylinder engine, consists of one eccentric crankpin journal or crank throw and is supported between two main bearings. The crankshaft for multiple-cylinder engines consists of numerous eccentric crank throws and main bearings, as illustrated in Figure 2.8.

FIGURE 2.8: SIX-CYLINDER, IN-LINE BMW S54 CRANKSHAFT.
(Courtesy Bayerische Motoren Werke AG)

The crankshaft is not only fundamental to the working of a reciprocating engine, but is also one of the first components requiring approximate dimensioning at the initiation of the design phase. The basic crankshaft configuration is determined by the engine layout, referring to the number of cylinders and cylinder orientation as defined in Section 2.1.2, the piston stroke (Citti *et al.*, 2018:487), the firing order (Degler, 1943:187) and the number of main bearings (Maleev, 1945:526).

Crankshaft loads during operation are primarily due to bending and torsion. Bending loads are applied by the cylinder pressure owing to combustion (Onda *et al.*, 2002:177) and inertia of the piston and connecting rod assembly (Niino *et al.*, 2000:135-136), while torsional loads are due to cyclic compression, combustion, inertia and a variable load (Mollenhauer & Tschoeke, 2010:250).

A resonant frequency or oscillation, in both bending and torsion, can be induced in a crankshaft when loaded, especially when operating at high engine speeds (Niino *et al.*, 2000:135). Crankshaft failures have resulted solely from torsional vibrations and owing to cracks initiating at stress concentrations due to bending and torsional loads (Gomes *et al.*, 2018:467). To counter this, the stiffness of the crankshaft can be increased by ensuring that the sections are sufficiently large, thus reducing stress (Degler, 1943:187), and/or by reducing the overall length of the crankshaft (Ricardo & Hempson, 1968:213).

Because of the cyclic loads that a crankshaft continuously has to endure, fatigue failures do occur and could initiate and propagate due to a residual stress in a fillet region (Gomes *et al.*, 2018:467). According to Baragetti (2015:271), suitable geometry and appropriate material selection, for a particular crankshaft, are not enough to guarantee fatigue resistance, which is also seriously affected by the load history, residual stresses arising from heat treatments, surface hardness and more. To assist in the prevention of crack initiation and propagation, processes exist that induce a residual compressive stress on the surface. These operations include nitriding, case-hardening, shot peening and rolling the necessary surface details.

The crankshaft must be correctly balanced, by using counterweights, engine vibration is significantly reduced (Baragetti, 2015:272). This is especially true for high-speed engines. The crankshaft must thus be both statically and dynamically balanced and if possible, use a crank throw arrangement that fundamentally provides better balance (Degler, 1943:186).

The multi-cylinder crankshaft pictured in Figure 2.8 is for an engine that has journal bearings and relies on forced lubrication. This is evident from the visible holes drilled into the crankshaft journals, circled in red, to allow for the flow of oil. Crankcase-scavenge two-stroke engines must, however, rely on a premix of fuel and lubricant of a certain ratio, typically 50:1, to lubricate all working components. In general, rolling element bearings function adequately despite poor lubrication (Naito & Taguchi, 1966:190). Thus, two-stroke crankshafts generally use deep groove ball bearings as main bearings and needle bearings for both the crank pin and piston pin, as illustrated in Figure 2.9.

FIGURE 2.9: YAMAHA XL 700 WAVE RUNNER TWO-STROKE, SI, TWO-CYLINDER CRANKSHAFT.

(Courtesy Yamaha Motor Company, Limited)

The two most important decisions regarding a crankshaft, according to Ricardo (1968:213), is to determine the dimensions and select the most appropriate material. Crankshafts are mostly manufactured from quenched and tempered steels that exhibit excellent mechanical and fatigue properties (Citti *et al.*, 2018:488). The alloy steel SAE-4340/AISI4340/EN24 has been extensively used for high-performance crankshafts and is manufactured by forging and billet machining (Kane, 2008:54). This steel is alloyed with approximately 0.8% Cr, 1.85% Ni and 0.25% Mo and has an ultimate tensile strength (UTS) of over 900 MPa (Citti *et al.*, 2018:488). The exceptional properties of this material can, however, not be fully exploited without proper heat treatment. Figure 2.10 graphically illustrates all the heat treatments and processes that must be applied to a forged quenched and tempered steel crankshaft to yield the final product, when typically using EN24. Note that the three red outlines each indicates a heating process. Other steel alloys and heat treatment cycles are used to manufacture crankshaft, but are far too numerous to expand on here.

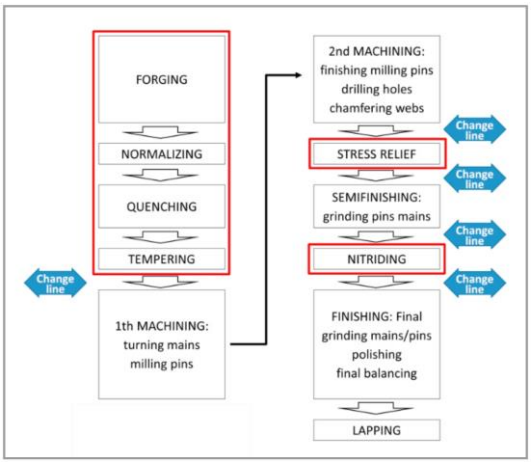

FIGURE 2.10: FLOW CHART FROM FORGING TO FINAL LAPPING FOR A QUENCHED AND TEMPERED STEEL CRANKSHAFT.
(Citti *et al.*, 2018:490)

The crankshaft of most engines are single-piece castings, forgings or machined from billet. The rough part is then heat-treated as required and subsequently finished to specification. These single-piece crankshafts are well suited to two-piece journal bearings, both main and crankpin bearings, when used in conjunction with forced lubrication.

However, two-stroke, crankcase-scavenge engines do not use forced lubrication and employ rolling element bearings throughout, as stated. Thus, the crankshaft can only be assembled once the needle bearings and connecting rods are in place, as illustrated in Figure 2.9. Both Yamaha (Naito & Taguchi, 1966:190) and Honda (Iwamoto & Saito, 2007:176) use crankshaft, for motorcycle engines that have been assembled by press-fitting the crankpin into the crank webs.

The press-fit margins that Honda uses are between 80 µm and 180 µm. These margins are typical of those seen in mass-production crankshafts (Iwamoto & Saito, 2007:177). According to Naito (1966:190), who is employed by Yamaha, a crankshaft that is supported between centres has a production accuracy of within 0.05 mm for a single-cylinder and between 0.05 and 0.08 mm for a two-cylinder engine.

Other crankshaft assembly techniques have been used in the past by both Pratt & Whitney and Porsche. In 1926 Pratt & Whitney designed a new crankshaft for the Wasp radial engine that used a split crankpin with male and female mating splines, all tied together by a bolt passing through the crankpin, as illustrated on the left in Figure 2.11 (McCutcheon, 1999?:5-1). The illustration on the right is of components of a Porsche 1500 roller bearing crankshaft manufactured by Hirth, using its patented serrated design (Hirth, 1924).

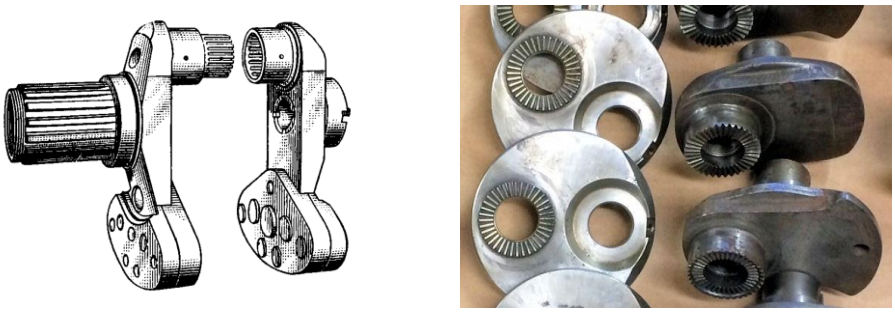

FIGURE 2.11: PRATT & WHITNEY WASP CRANKSHAFT (LEFT) AND PORSCHE 1500 ROLLER BEARING CRANKSHAFT MANUFACTURED BY HIRTH (RIGHT).
(Courtesy Pratt & Whitney, Dr.-Ing. h.c.F. Porsche AG)

2.3.2 CRANKCASE

The term crankcase or engine block refers to the structural mount in which engine components are housed and to which others are attached. The main functions of the crankcase are:

- It serves to transfer the force between the cylinder head and crankshaft due to combustion (Bosch, 2007:479).
- The engine block is a structural member and must withstand all manner of internal and external forces and moments due to engine operation.
- The crankcase-scavenge two-stroke engine uses the continuously changing crankcase volume, beneath the reciprocating piston, as a pump for the fresh charge (Blair, 1996:12).
- It houses the crankshaft, and depending on engine design, the camshaft.
- The engine block incorporates the cylinders, while the crankcase provides mounting points for the subsequent attachment of these.
- The engine block provides the base for the mounting of all manner of ancillary engine components (Bosch, 2007:479).
- Oil and water channels are often incorporated into the engine block (Bosch, 2007:479).

Figure 2.12 below illustrates three different crankcase designs.

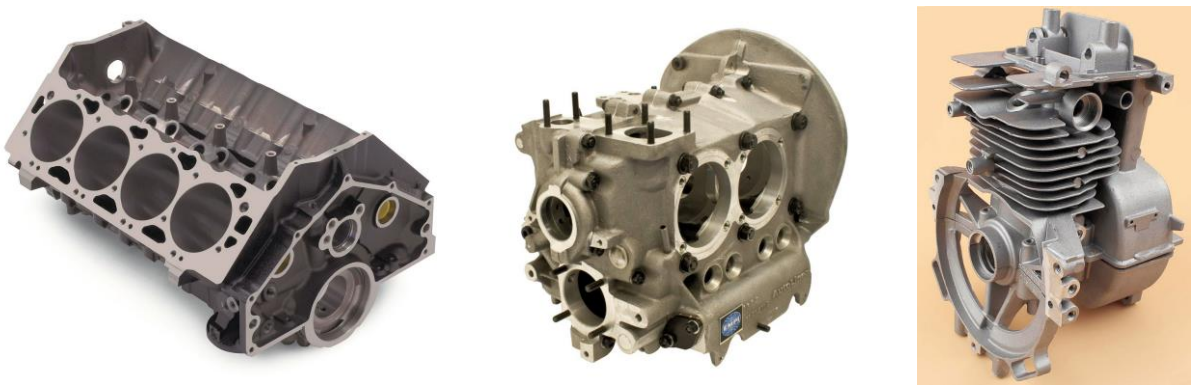

FIGURE 2.12: CHEVROLET 502, V8, CAST IRON ENGINE BLOCK (LEFT), VW, FOUR-CYLINDER, HORIZONTALLY-OPPOSED, ALUMINIUM CRANKCASE (CENTRE) AND A HONDA GX35, SINGLE-CYLINDER, ALUMINIUM ENGINE CASTING (RIGHT).
(Courtesy General Motors Company, Volkswagen Motor Company LTM, Honda Motor Co., Ltd)

The Chevrolet 502 in^3, cast iron engine block on the left incorporates the camshaft and the eight cylinders in a V-layout. The two-part VW, four-cylinder, horizontally-opposed, air-cooled crankcase in the centre includes the camshaft, but requires that the cylinders be bolted on. This is an aftermarket aluminium part, but since 1961 the VW crankcase has been made from magnesium (Kane, 2008:28). The figure on the right displays a two-piece Honda GX35 aluminium casting that incorporates many additional features over the other two castings.

The sizing of the crankcase is initially determined by the number of cylinders and the chosen engine layout. The bore, cylinder pitch, defined as the distance from one cylinder axis to the next, and the valve actuation drive determine the approximate length of the engine (Kondo *et al.*, 2009:45). Should the engine in question be a crankcase-scavenge two-stroke design, the valve drive train would not be required. The bore, stroke and sweep of the connecting rod big-end bearing sketches the engine boundary in the transverse plane (Ricardo & Hempson, 1968:205).

The engine must withstand all the internal and external forces and moments generated by engine operation, as stated, without compromising the accurate dimensional tolerances required for continuous successful engine operation. According to Degler (1943:260), it is essential during the design phase that the crankcase be detailed with adequate ribs and fasteners to ensure that it is rigid enough. In some applications, such as F1, the engine also forms an element in the stiffness of the vehicle by being connected to the monocoque at one end and to the gearbox at the other (Kondo *et al.*, 2009:48).

In 1943 Degler (1943:260) stated that “it is impossible to analyse with any degree of accuracy the effect of the various combinations of stresses present in many engine frames and crankcases” and that “for this reason but little analysis is usually attempted and the design is based on experiences with successful engines”. Structural design progressed, however, and 56 years later Stone (1999:452) stated, in his 1999 publication, that finite element methods (FEM) were extensively used to assist in design.

In certain applications, the mass of the prime mover must be kept to a minimum. Examples thereof would be aviation and motorsport. In 2005 the Honda F1, 3.0 L, V10 engine that produced an estimated 700 kW weighed less than 90 kg (Sakurahara, 2009:15)! Since the crankcase is the largest engine component, minimising mass by using lighter materials and optimising the design could render a significant saving.

Unlike a four-stroke engine that uses the crankcase volume only for lubrication purposes, the two-stroke, crankcase-scavenge engine also uses this alternating volume as a pump. Conducting tests, Yamaha found that to maximise speed and engine power, the crankcase volume should be made as small as possible (Naito & Taguchi, 1966:183).

Engine blocks are generally fabricated from cast iron, magnesium or aluminium, as illustrated in Figure 2.12 from left to right. Fan (2014:37) states that grey cast iron has been extensively used “due to its good castability, corrosion resistance and thermal conductivity, relatively low cost (20-40% less than steel), excellent vibration damping and abrasion resistance.” Stone (1999:445) adds that it is easily machined. Although VW has been using magnesium since 1961 for the fabrication of the air-cooled engine crankcase, as stated above, it is not commonly used. In the automotive industry aluminium has recently become a popular lightweight material choice. However, compared to cast iron there are drawbacks. Some of these are higher cost, lower strength, stiffness and less damping (Jhaveri *et al.*, 2018:1-2). Aluminium requires inserts for certain applications. Furthermore, the higher thermal conductivity makes aluminium more susceptible to distortion. The reduced stiffness due to the use of aluminium for engine blocks requires careful design with ribs and flanges to increase stiffness (Stone, 1999:451-452).

Figure 2.13 illustrates two automotive, six-cylinder, cast engine blocks. On the left is a Nissan RB26 cast iron engine block and on the right a BMW N54 aluminium engine block. Note the additional ribs used on the aluminium casting.

FIGURE 2.13: NISSAN RB26 CAST IRON ENGINE BLOCK (LEFT) AND A BMW N54 ALUMINIUM ENGINE BLOCK (RIGHT).

(Courtesy Nissan Motor Co., Ltd, Bayerische Motoren Werke AG)

Cast iron and aluminium engine blocks have traditionally been manufactured by means of sand casting. Aluminium crankcases have also been manufactured by gravity die cast, but this has fallen out of favour, primarily because of cost. Pressure die casting of aluminium components is optimal and low-cost, but there are technical limitations (Mollenhauer & Tschoeke, 2010:564). For small production runs or prototype engines it might be applicable to billet machine the crankcase. An example of this is Pipo Moteurs, based in France, that developed a Rallycross engine early in 2016. The 1997 cc, in-line, four-cylinder engine uses a machined aluminium crankcase that started life as a 100 kg billet and was then machined down to a final product of 15 kg. The aluminium alloy specification used is undisclosed, but stated to have properties superioir to that of 7075 (Mitchell, 2018:20-24)

Despite the crankcase being a complex part to design and manufacture, the manner and ease of engine component assembly into and onto the engine block must be taken into consideration.

2.3.3 CYLINDER

For all types of reciprocating internal combustion engines, the cylinder serves as part of the varying combustion chamber volume, as it guides the oscillating piston. For two-stroke engines the cylinder, or sleeve, has transfer and exhaust ports cut into it to facilitate the entry and exit of the working fluid.

The primary function of the cylinder is to facilitate the compression and expansion of the working fluid. To accomplish this successfully, the cylinder should be thick enough to withstand the combustion pressure, in both the radial and axial directions, and the additional piston side load (Degler, 1943:163).

The cylinder is either manufactured as part of the engine block, as shown in both illustrations in Figure 2.13, or fabricated as a separate component, a sleeve, as shown by the photo on the right in Figure 2.4. This separate cylinder could also include cooling fins or water channels if not housed within an engine block. This is illustrated in Figure 2.14 by the air-cooled Yamaha YFS 200 Blaster cylinder on the left and the liquid-cooled Yamaha YZ 250 cylinder on the right. Note that both these cylinder assemblies are for two-stroke, crankcase-scavenge, SI engines.

FIGURE 2.14: YAMAHA YFS 200 BLASTER AIR-COOLED CYLINDER (LEFT) AND A YAMAHA YZ 250 LIQUID-COOLED CYLINDER (RIGHT).
(Courtesy Yamaha Motor Company, Limited)

The intake ports, of equal size and height, around the circumference of the Detroit Diesel 8V92 sleeve, as illustrated on the right in Figure 2.4, are for a uniflow, two-stroke, CI engine. The sleeve of a two-stroke, crankcase-scavenge, SI engine is more complex, since transfer and exhaust ports are required. Figure 2.15 illustrates the two most common types of two-stroke, SI porting arrangements; cross-scavenge on the left and loop-scavenge on the right. Scavenging is defined as the simultaneous removal of the exhaust gas and induction of fresh charge (Heywood, 1988:235).

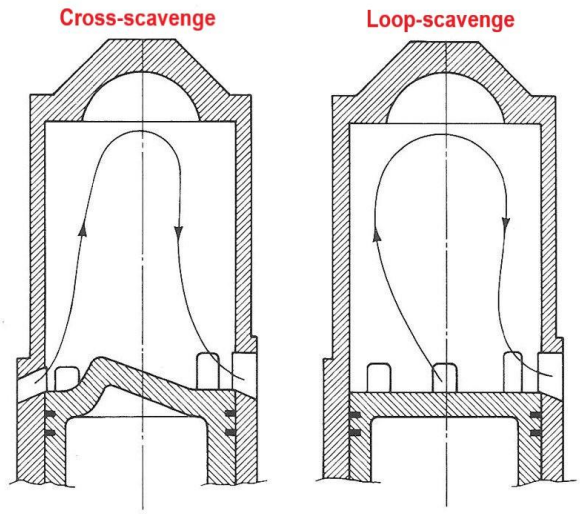

FIGURE 2.15: TWO-STROKE CROSS-SCAVENGE FLOW (LEFT) AND LOOP-SCAVENGE FLOW (RIGHT).
(Heywood, 1988:235)

Note that for the cross-scavenge layout, illustrated above on the left, to function correctly the piston crown requires a raised section, or deflector (Blair, 1996:10), adjacent to the transfer ports, as illustrated on the left in Figure 2.16. This piston is for a Vespa 125 cc moped engine. The photo on the right is a loop-scavenge sleeve for a high-performance Rossi Icarus 15 cc model helicopter engine and it illustrates the number and complexity of transfer and exhaust ports that can be used. The piston crown used in conjunction with this sleeve is flat.

FIGURE 2.16: VESPA 125 CC CROSS-SCAVENGE PISTON WITH DEFLECTOR (LEFT) AND ROSSI ICARUS 15 CC LOOP-SCAVENGE SLEEVE (RIGHT).
(Courtesy Piaggio & Co. SpA, Novarossi World s.r.l)

The two-stroke cycle and scavenging process are discussed in Section 2.2.1 and will thus not be repeated here. Instead, some of the complexities associated with scavenging and the different configurations will subsequently be documented.

For low throttle openings, mostly related to low speed and power settings, cross-scavenging has good scavenging characteristics, which is ideal for small outboard motors. However, at high throttle settings the cross-scavenge design exhibits poor scavenging efficiency and this results in lower specific power, coupled with poor fuel economy. The deflector piston, as seen above on the left, has a high surface-to-volume ratio and numerous hot edges that can initiate detonation and pre-ignition. The compression ratio used is consequently lower than that in comparable cross-scavenge designs (Blair, 1996:10).

Loop-scavenging was invented by Schnurle of Germany around 1926 (Blair, 1996:8) and according to Naito (1966:184), is now essentially the standard for small, two-stroke, SI engines. Schnurle's objective was to design a scavenging method that eradicated the detrimental hot edges of the deflector piston crown. This is done by two or more transfer ports, illustrated by the sleeve on the right in Figure 2.16, which direct the fuel-air mixture across an essentially flat top piston toward the sides and rear of the cylinder, away from the exhaust port. Various transfer port arrangements exist for loop-scavenging (Blair, 1996:8-9). The complexity associated with good loop-scavenge port design is far greater than that for a cross-scavenge engine (Blair, 1996:263).

Because of the ports cut into the lower section of a two-stroke, SI cylinder, the lower part of the piston stroke is forfeited to exhaust and ingest fresh charge. Compared to four-stroke engines, the gas exchange processes for a two-stroke engine occur in considerably less time. Thus, a greater volume of working fluid must flow through the cylinder in a shorter time span (Ricardo & Hempson, 1968:175), since ultimately the power output of any engine is related to the quantity of fresh charge retained within the cylinder (Ricardo & Hempson, 1968:177).

The port area can be altered by changing the width and height of the port. The width of each port is limited by piston ring ingress; if this happens, guide bars can be used (Ricardo & Hempson, 1968:179). The port timing is primarily determined by the port height, with the timing of the exhaust port contributing most to defining the character of a two-stroke engine (Naito & Taguchi, 1966:184). The transfer and exhaust port number and arrangement are thus critical.

Because of the numerous ports in the cylinder and the higher thermal loading of a two-stroke engine when compared to a four-stroke engine, the cylinder wall experiences thermal distortion (Naito & Taguchi, 1966:192; Waker, 1966:57). This distortion can largely be mitigated by selecting a proper material, complex machining and modified castings (Waker, 1966:57).

The selection of a suitable cylinder material is important and can be categorised as follows:

- Material selection for the sleeves and rings (Ricardo & Hempson, 1968:274)
- Surface treatment or coating applied to the cylinder
- The type of cylinder finish (Ricardo & Hempson, 1968:274).

Historically, cast iron cylinders have frequently been used. These offer some significant advantages. Cast iron has a porous structure and this allows oil to be retained. When any perceptible wear occurs, the free graphite cells are exposed and serve as a lubricant by releasing graphite (Ricardo & Hempson, 1968:274-275).

Steel cylinder liners are also used in large quantities, but without the proper surface treatment and finish are unsatisfactory. To resist abrasion, the surface hardness of a steel liner must be increased. This can be done by carburising, nitriding and hard chroming. However, these hard surfaces do not retain lubricant and require honing. This process leaves innumerable small oil reservoirs on the surface (Ricardo & Hempson, 1968:275-276).

Aluminium is now often used as a cylinder material, but must be treated. Electrolytic nickel plating, an alternative to chrome plating, can be combined with other elements to yield Nikasil, a Mahle trademark. The benefit is a hard, tough surface that has low friction. Thermal plasma-sprayed coatings have become widespread and even after honing will still contain multiple microscopic porous holes (Grant, 2017:48-52).

Naito (1966:192) states that since 1966 Yamaha has manufactured production motorcycle cylinders by either pressing the cast iron sleeve into the aluminium cylinder barrel or casting the barrel around the sleeve. Because of thermal distortion, an aluminium alloy cylinder is preferred and in racing engines these cylinders are used with a honed hard chrome bore.

2.3.4 PISTON

The piston oscillates within the cylinder, while the piston crown forms the bottom surface of the combustion chamber and subsequently transfers the force due to combustion to the piston pin. The piston in conjunction with the piston rings also provides a relatively gas-tight seal (Ricardo & Hempson, 1968:237).

Figure 2.17 illustrates a piston for a Honda F20C, four-stroke, SI engine on the left and that for a BMW M57, four-stroke, CI engine on the right. Note that both pistons are for cylinders of approximately 500 cc capacity and are used in automotive applications.

FIGURE 2.17: HONDA F20C, SI PISTON (LEFT) AND BMW M57, CI PISTON (RIGHT).
(Courtesy Honda Motor Co., Ltd, Bayerische Motoren Werke AG)

Although there are notable differences between the four-stroke SI and CI pistons, the similarities in function will first be stated. These are:

- The piston skirt, defined as the region below the third ring, aligns the piston in the cylinder (Heywood, 1988:729).
- Both the piston skirt and the piston lands, defined as the surface regions between the rings, transfer the piston side load to the cylinder (Heywood, 1988:729).
- Because of the inertia present in a reciprocating engine, it is desirable that the piston/assembly be as light as possible. This reduces the crank pin load and the inherent dynamic imbalance (Ricardo & Hempson, 1968:237).
- The piston and ring assembly accounts for the highest mechanical losses in an engine (Ricardo & Hempson, 1968:237). Sugimura (2007:97) states that approximately 40% of the mechanical losses can be attributed to the piston assembly.
- The piston crown is heated by both compression and notably combustion and must transmit and dispose of this heat (Ricardo & Hempson, 1968:237). The greatest heat flux is through the piston rings, while the piston skirt transmits very little (Ricardo & Hempson, 1968:243).
- Both these pistons have three rings in total. The first two are compression rings that provide the gas-tight seal, with the oil ring, the third ring, metering oil on the cylinder wall and returning the excess back to the sump (Heywood, 1988:730).

Note that the construction of the CI piston is more robust than that for the SI engine. This is also evident from the overall diameter of the CI piston pin. Heywood (1988:58) states that the highest typical brake mean effective pressure ($bmep$) of an SI, naturally aspirated engine is 10 bar, while that for a CI, turbo-charged unit is 18 bar. The turbo-charged BMW M57 CI piston is thus subjected to higher combustion pressures than the naturally aspirated Honda F20C SI piston.

One of the most noticeable differences between the two pistons is the design of the piston crowns. The SI piston, on the left, essentially has a flat crown with four recces cut into it for valve clearance. The CI piston on the right, utilises a bowl-in-piston chamber combustion system into which the diesel fuel is directly injected (Heywood, 1988:494). Since the combustion chamber is located within the piston crown, 15 to 20% of the heat generated, at full load, flows into the piston, whereas this figure drops to between 8 and 10% for an SI engine under the same conditions (Ricardo & Hempson, 1968:240).

Note that the piston skirt of the SI piston is shorter than that of the CI piston. This change has been made in recent years to reduce the mass and contact area (Heywood, 1988:733). The lighter construction of the SI piston allows the Honda F20C engine to attain maximum power at 8 300 rpm (Meaden, 2018). Figure 2.18 illustrates the piston, piston rings, piston pin and circlips for a Yamaha YZ 250 engine.

FIGURE 2.18: YAMAHA YZ 250, TWO-STROKE PISTON ASSEMBLY.
(Courtesy Yamaha Motor Company, Limited)

The Yamaha YZ 250 uses a two-stroke, single-cylinder, SI, liquid-cooled, 249 cc engine. The bore and stroke are 66.4 mm and 72.0 mm respectively (Yamaha, 2019). The notable differences between the YZ 250, two-stroke piston and the two four-stroke pistons, as seen in Figure 2.17, are:

- Of the three pistons, the two-stroke piston has the lightest construction. The YZ 250 piston pin is also evidence of that.
- The two-stroke piston skirt is the longest of all three pistons.
- Cast slots and holes are visible around the circumference of the two-stroke piston.
- Unlike the three-ring design of the SI and CI four-stroke pistons, the two-stroke piston uses only two thin compression rings.
- Pins in the piston ring grooves prevent the rings from turning.
- The hemispherical piston crown of the two-stroke piston is the simplest of the three, with no additional features cast or machined into it.

The functions previously listed that are common to both SI and CI four-stroke pistons are also applicable to a two-stroke piston, with the exception of the final point. A crankcase-scavenge, two-stroke piston does not require an oil ring, since there is no excess oil present on the cylinder wall.

Despite the similarities, two-stroke pistons for crankcase-scavenge, SI engines have the following unique design and operational issues:

- The lightest piston construction corresponds with the lowest maximum typical $bmep$ of approximately 6.7 bar (Heywood, 1988:887), when compared to that attained by the SI and CI examples used above.
- Since the crankcase is used as a pump, it is essential that the exhaust port is not uncovered at the top of the piston stroke. The piston skirt is thus slightly longer than the piston stroke (Ricardo & Hempson, 1968:178).
- The thermal loading on a two-stroke piston is high. In a four-stroke engine the piston benefits from the second half of the cycle, one revolution, when no heat is generated (Maleev, 1945:290). “Piston burn” can occur when the engine output is increased too much (Naito & Taguchi, 1966:193).
- To alleviate the risk of excessive thermal load on the piston, the actual, not geometric, compression ratio of a two-stroke engine is limited to 7.5 and 9.5 for production and racing engines respectively (Naito & Taguchi, 1966:185). Typical compression ratios for four-stroke SI and CI engines are 8 to 12 and 12 to 24 respectively (Heywood, 1988:43). Two-stroke, SI engines’ fuel conversion efficiency consequently suffers owing to the lower compression ratios used (Heywood, 1988:170).
- To aid heat transfer from the piston crown through the first compression ring, the piston land is made as short as possible. This minimum length is determined by structural limitations (Naito & Taguchi, 1966:193).
- Because of the high thermal loading on the piston and necessary holes and slots in both the piston and cylinder, thermal distorsion of both components occurs. The clearance between the piston and cylinder cannot be made too great or small to avoid risk of seizure (Naito & Taguchi, 1966:192).
- A two-stroke piston is manufactured to be elliptical in section, with this profile changing continuously thoughout the piston’s length. This complex profile is determined by trial and error for different types of engines (Naito & Taguchi, 1966:193).

A combustion chamber based on an oscillating piston within a cylinder cannot function effectively without suitable piston rings. As stated previously, the primary function of the piston rings is to provide a gas-tight seal.

The upper cylinder pressure enables the compression rings to seal by the working fluid acting across the top and rear of the ring. In doing so the ring seals radially against the cylinder wall and prevents the flow of working fluid to the crankcase by being forced against the bottom of the ring groove. Dykes discovered the circumstances under which ring collapse would occur. As a rule, owing to this and other factors, a narrower ring is used as the engine speed increases (Ricardo & Hempson, 1968:248-251). The design variations for compression rings are numerous, as are the possible surface coatings (Heywood, 1988:729).

The material of choice for the fabrication of pistons should be light and have high thermal conductivity. Aluminium has been that material for decades. The use of aluminium for pistons does, however, have drawbacks. When used in conjunction with cast iron or steel cylinders, the higher thermal expansion of the piston requires a large clearance. At high temperatures, aluminium's mechanical strength deteriorates catastrophically above 400°C and since aluminium is relatively soft, chafing, tearing and impact damage of the ring grooves, caused by the piston rings, may occur. Excessive ring groove wear can be addressed by including a cast iron insert into the piston for the first compression ring (Ricardo & Hempson, 1968:237-238). The BMW M57, CI piston in Figure 2.17 is evidence of this technique.

Numerous alloying elements are added to improve the properties of aluminium pistons. The aluminium alloy known as 2618, essentially the same as RR58 developed by Rolls-Royce for the Second World War Merlin aeroplane engines (Ward, 2010:40), is a copper-magnesium, low silicon alloy that is still in use today. The alloy 4032 has a beneficial lower coefficient of expansion due to its high silicon content, but inferior thermal conductivity (Kane, 2008:27-28).

Other materials have been used for pistons, with varied degrees of success. The 2009 Le Mans LMP1 champions Peugeot, running CI engines, are rumoured to have used steel pistons. The greatly increased fatigue strength and reduced wall thickness are reported advantages (Ward, 2010:41).

Pure beryllium and aluminium-beryllium alloy pistons have been used in motorsport for the Porsche 917 in the early 1970s and by McLaren-Mercedes from 1998 to 2000 respectively. The aluminium-beryllium alloy, AM162, consists of 62% beryllium and is an ideal material for pistons. AM162 has approximately three-quarters the density, three times the Young's modulus and 30% higher thermal conductivity than an aluminium alloy piston. However, the cost and manufacturing difficulties are significant drawbacks (Ward, 2010; Anon, 2008:74).

Aluminium alloy metal matrix composites pistons have also been used by Honda in F1. This material offers a 16% weight reduction over the 2618 alloy, high stiffness and better high temperature characteristics (Ishizuka *et al.*, 2009:246-247).

Pistons, piston rings and piston pins can be coated to reduce wear and friction. To improve running-in behaviour, polymer coatings are often applied to piston skirts. To reduce friction in racing applications diamond-like carbon coatings, also called DLC, can be applied to the piston, rings and piston pin, although fundamental changes must be made to the piston to accommodate the coating. Cast iron piston rings are still common, while steel ring faces are often sprayed with molybdenum. Titanium nitride and chromium nitride are also popular piston ring coatings (Ward, 2010:26-29).

The manufacture of pistons predominantly occurs as follows (Ward, 2010:40-45):

- Casting pistons for production runs has been and still is a manufacturing method used.
- Forged pistons are the most popular choice for production runs. The tooling required is not cheap, but the final product offers significant advantages. The grain flow due to forging is highly orientated and the forged product requires minimal post-machining.
- With the availability of four and five-axis machining centres, billet-machined pistons are now available. The process, however, is restricted to small production runs.

2.3.5 CONNECTING ROD

The connecting rod connects the oscillating piston to the rotating crankshaft and in so doing converts linear motion into rotary motion.

From the simple functional description above, the connecting rod might appear somewhat underwhelming. However, Figure 2.19 illustrates three different connecting rod designs for the same engine, a Ford four-stroke, SI, Ecoboost 2.0 L. The component on the left is the production version, with the two additional connecting rods, centre and right, manufactured for the aftermarket by Manley.

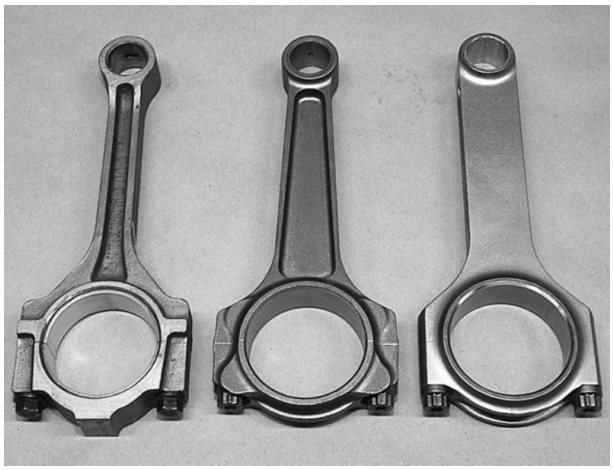

FIGURE 2.19: STANDARD PRODUCTION I-BEAM (LEFT), AFTERMARKET MANLEY I-BEAM (CENTRE) AND MANLEY H-BEAM (RIGHT) CONNECTING RODS USED IN A FORD FOUR-STROKE, SI, ECOBOOST 2.0 L.

(Courtesy Ford Motor Company, Manley Performance Products, Inc.)

The small-diameter hole at the top of the connecting rod is called the small-end and the large-diameter one the big-end. The piston pin is inserted through the small-end, that possibly uses a press-fit bronze bush (Stone, 1999:457), and the big-end is attached to the crank pin by extracting the two bolts and the separate bearing cap. These connecting rods use plain journal bearings, with forced lubrication.

For an engine to operate effectively at high speed and power, the stiffness, strength and mass of the connecting rod must be addressed concurrently (Minato & Mizogawa, 2009:251).

The connecting rod experiences a significant compressive load due to both the compression and power stroke of the engine. The beam between the small- and big-end bearings must have sufficient cross-sectional area, or be stiff enough, to withstand both buckling and bending (Okubo & Suzuki, 2014:215). The left and centre connecting rods, pictured in Figure 2.19, have an I-beam profile, while the component on the right uses an H-beam section. Note that the cross-sectional area of the Ford production I-beam connecting rod, on the left, is the lowest of the three throughout the component's length. Of the two aftermarket connecting rods, the H-beam on the right possibly has the largest cross-section. Mitchell (2017:51) states that if I- and H-beam connecting rods of equal weight were to be made, a higher buckling load would be tolerated by the H-beam component. In contrast, Ward (2009:68) reports seeing both I and H-beam profiles used in F1 engines, and surmises that a hybrid of the two designs is possibly best.

Decreasing the mass of the connecting rod results in lower main bearing loads, less friction and reduced engine vibration (Iida *et al.*, 2005:116).

The strength of the connecting rod and the two bolts that secure the bearing cap must be sufficient to withstand the tensile force, generated due to inertia, when the piston reaches TDC at maximum engine speed. An additional 30% over-speed should be allowed for if the engine acts as a brake. The load on the two bolts must also include the "end nip" of the bearing strip, should journal bearings be used (Ricardo & Hempson, 1968:206).

Since the connecting rod of a two-stroke engine is mostly in compression, because of the absence of a separate exhaust and induction stroke, the high tensile forces should not be a concern. Maleev (1945:523), however, states that should a two-stroke lose compression, high tensile forces would result and this should be accommodated.

The natural frequency of the connecting rod must be calculated and must lie outside the engine operational speed range. Should this not be possible, the engine should rapidly pass through the resonant frequency region (Mitchell, 2017:51).

For the big-end journal bearing to function correctly, the bearing cap must align with the connecting rod. This is primarily achieved by using dowel pins, more recently fracture splitting (Iida *et al.*, 2005:115) and serrations (Ricardo & Hempson, 1968:208).

The three connecting rods illustrated in Figure 2.19 are all for a four-stroke, SI engine. Figure 2.20 illustrates a connecting rod, needle bearings and thrust washers for a Yamaha DT 200, two-stroke, SI, motorcycle engine.

FIGURE 2.20: CONNECTING ROD, NEEDLE BEARINGS AND THRUST WASHERS FOR A YAMAHA DT 200, TWO-STROKE, SI, MOTORCYCLE ENGINE.
(Courtesy Yamaha Motor Company, Limited)

Unlike the four-stroke components that use a separate bearing cap, as seen in Figure 2.19, most two-stroke connecting rods are a single part. This eliminates the separate bearing cap and the inevitable compromises due to the bolted joint. However, this necessitates that the crankshaft be an assembly, as described in Section 2.3.1, which would possibly be more susceptible to damage than a single-part component.

The I-beam profile of the two-stroke connecting rod above is similar to the two illustrated in Figure 2.19, but seemingly smaller in comparable cross-sectional area. The reason could possibly be the lower typical $bmep$ values of 6.7 bar for a two-stroke engine when compared to 10 bar for a four-stroke, SI, naturally aspirated engine, as cited in Section 2.3.4.

Needle bearings are used for both the big- and small-end bearings, as illustrated above. This is due to the poor lubrication present in two-stroke crankcase-scavenge engines, as cited in Section 2.3.1. Note the two slots cut into the big-end bearing along the length of the connecting rod. The author suspects that this is done to aid the entry and exit of "lubricant". The rotating and oscillating needle bearings at the big and small-ends respectively are also subjected to shock loads and high operational temperatures (Naito & Taguchi, 1966:190-191).

The needle-bearing cage must be manufactured to within specified tolerances to prevent excessive axial loads arising at the big-end of the connecting rod. This is due to needles, within a poor tolerance cage, twisting and generating a side load. The two phosphor bronze thrust washers, seen in Figure 2.20, are inserted on either side of the big-end for this purpose. These washers are designed with oil-retaining dimples (Naito & Taguchi, 1966:191-192).

For the production of mass market vehicle connecting rods, non-heat-treated steel is generally used (Iida *et al.*, 2005:115). For the manufacture of two-stroke connecting rods, AISI 8620 steel is used and carburised before quenching (Naito & Taguchi, 1966:191). AISI 8620 is a low-carbon steel with approximately 0.5% chrome, 0.55% nickel and 0.2% molybdenum (Bringas, 2004:39). The copper plating visible in Figure 2.20 shields the beam of the connecting rod during carburising (Naito & Taguchi, 1966:191). The big and small-end require hard, ground inner surfaces, since these faces act as the outer races for the needle bearings.

The bearing cages were traditionally manufactured from phosphor bronze, but this has been surpassed by steel because of higher engine speeds. The steel cage is copper-plated to prevent galling by the needle roller bearings (Naito & Taguchi, 1966:191).

Aluminium and titanium are used for the fabrication of connecting rods in certain applications; however, the cost is high (Iida *et al.*, 2005:115). Aluminium alloys generally require increases in cross-sectional area when compared to steel equivalents, owing to their lower strength (Okubo & Suzuki, 2014:214-215).

Titanium was first used for connecting rods by Honda for the RC30/VFR750R motorcycle in 1987 (Ward, 2009:68). Because of titanium's lower density, a mass saving of approximately 40% can be achieved over an equivalent steel component, but some material must be added because of the lower UTS. The lower elastic modulus of 114 MPa, about half that of steel, also provides more damping (Mitchell, 2017:51-52).

Connecting rods are primarily manufactured by forging and machining (Stone, 1999:457). Whereas an I-beam connecting rod is forged and machined on the same plane, an H-beam requires more operations to complete. The component can be shot-peened to increase fatigue resistance (Mitchell, 2017:51-52).

Tight manufacturing tolerances are required for both roundness, 0.003 to 0.006 mm, and parallelism, 0.05 mm/100 mm, of and between the big- and small-end bores respectively (Naito & Taguchi, 1966:191).

2.3.6 CYLINDER HEAD

The cylinder head, with the aid of a head gasket, seals and forms the upper surface of the combustion chamber. The combustion chamber profile is determined by the cylinder head in conjunction with the piston crown. The spark plugs/injectors are also mounted in the cylinder head (Bosch, 2007:479).

The basic functional description of a cylinder head above suffices for a two-stroke crankcase-scavenge engine. However, should the engine be a current four-stroke, SI or CI unit, the fundamental definition would also include (Bosch, 2007:479):

- The cylinder head houses the intake and exhaust, ports and valves.
- The valve gear that actuates the valves is situated within the cylinder head.

Figure 2.21 illustrates the top and bottom of an assembled cylinder head for a Nissan RB26DETT four-stroke, SI, six-cylinder, in-line engine. The intake and exhaust, ports and valves are visible, as is the valve gear, in this case driven by two overhead camshafts.

FIGURE 2.21: TOP AND BOTTOM VIEW OF A NISSAN RB26DETT FOUR-STROKE, SI, SIX-CYLINDER ASSEMBLED CYLINDER HEAD.
(Courtesy Nissan Motor Co., Ltd)

Since the transfer of the working fluid for a two-stroke, crankcase-scavenge engine occurs owing to the ports within the cylinder, as described in Section 2.3.3, the four-stroke cylinder head functionality is not required and will not be discussed any further.

Figure 2.22 illustrates a Yamaha YZ 250 liquid-cooled cylinder head on the left and a Yamaha YFS 200 Blaster air-cooled component on the right for two-stroke engines. Note the simplicity of both components and the absence of moving parts when compared to that in Figure 2.21 for a four-stroke engine.

FIGURE 2.22: YAMAHA YZ 250 LIQUID-COOLED CYLINDER HEAD (LEFT) AND YAMAHA YFS 200 AIR-COOLED CYLINDER HEAD (RIGHT) FOR TWO-STROKE ENGINES.
(Courtesy Yamaha Motor Company, Limited)

The surface of the cylinder head above the piston crown will heat up owing to combustion. The cylinder heads must therefore be cooled by either liquid or air, as illustrated in Figure 2.22 on respectively the left and right (Ricardo & Hempson, 1968:231). Air-cooling is generally used on lower-output engines or when simplicity is advantageous (Stone, 1999:480). Liquid-cooling is chosen as a cooling medium when high-performance engines are designed, since the high power and speed specifications rely greatly on cooling (Naito & Taguchi, 1966:187-188).

Note that six bolts, of substantial diameter, secure both cylinder heads to the respective cylinders. For sealing of the joint, the thinnest gasket and the maximum permissible number of bolts should be used (Ricardo & Hempson, 1968:235). Heywood (1988:14) states that the construction of the cylinder heads must be substantial enough to distribute the forces uniformly due to combustion.

Figure 2.23 illustrates the underside, or the combustion face, of a Yamaha YZ 250 two-stroke, liquid-cooled cylinder head on the left; and a section view of the cylinder head and piston crown, when at TDC, that together form the combustion chamber on the right. Note that the combination of the YZ 250 piston, in Figure 2.18, and the YZ 250 cylinder head, on the left, replicates the combustion chamber profile on the right.

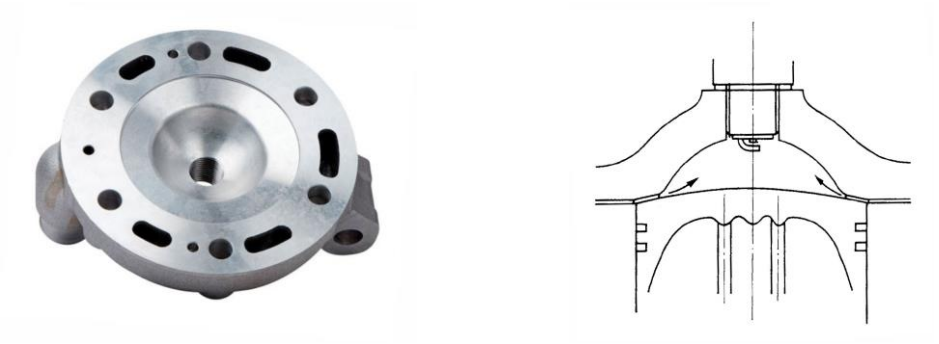

FIGURE 2.23: YAMAHA YZ 250 LIQUID-COOLED CYLINDER HEAD AS VIEWED FROM THE COMBUSTION CHAMBER (LEFT) AND COMBUSTION CHAMBER PROFILE (RIGHT).
(Courtesy Yamaha Motor Company, Limited, Naito & Taguchi, 1966:193)

“There has always been extensive debate over the optimum SI engine combustion chamber design.” (Heywood, 1988:844). Among the issues that constitute the debate are chamber compactness, flame travel path, squish and surface/volume ratio. Given that the profile of the piston crown, cylinder head and spark plug location are the primary variables, consensus has developed that major design combustion chamber objectives include the following (Heywood, 1988:844-846):

- A “fast burn” combustion process produces more robust combustion and improvements in both emissions and efficiency.
- Heat transfer to the entire combustion chamber should be kept to a minimum, since this substantially improves engine efficiency.
- There is high resistance to knock, since this limits the maximum compression ratio.

The diagram on the right in Figure 2.23, illustrates that Yamaha has opted to use a hemispherical combustion chamber, with the spark plug centrally located to shorten the flame path. Squish is also present between the outer piston crown and the cylinder head to increase turbulence and accelerate the combustion process. The upper compression ratio is not only limited by knock, but also by “piston burn”, as stated in Section 2.3.4 (Naito & Taguchi, 1966:185-193).

Both cast iron and aluminium are used in the manufacture of cylinder heads. Large CI engines often use individual cast iron cylinder heads to improve the head gasket sealing force and ease maintenance. Aluminium is generally used on both four- and two-stroke SI and CI engines. Aluminium has three times the thermal conductivity of cast iron, but is more susceptible to distortion (Stone, 1999:451). Multi-cylinder engines normally use the same cylinder head, although separate components can be used on air-cooled engines to improve cooling (Bosch, 2007:479).

2.4 TWO-STROKE ENGINE SYSTEMS

With the identification and description of the six components that constitute the engine sub-assembly completed in Section 2.3, the successful running of a two-stroke engine also depends on a number of systems. Some of the systems consist of a single component performing a seemingly simple task, while others comprise multiple components performing very complex functions. Irrespective of the perceived importance or complexity of a system, each is required to function as designed to ensure the smooth working of an engine.

Figure 2.24 illustrates a Hirth 4201 two-stroke, two-cylinder, SI, air-cooled UAV engine. The tags on the figure illustrate the cooling, intake, fuel, ignition and exhaust systems or parts thereof. The purpose and essential functioning of all these systems, including the lubrication system, will be described next.

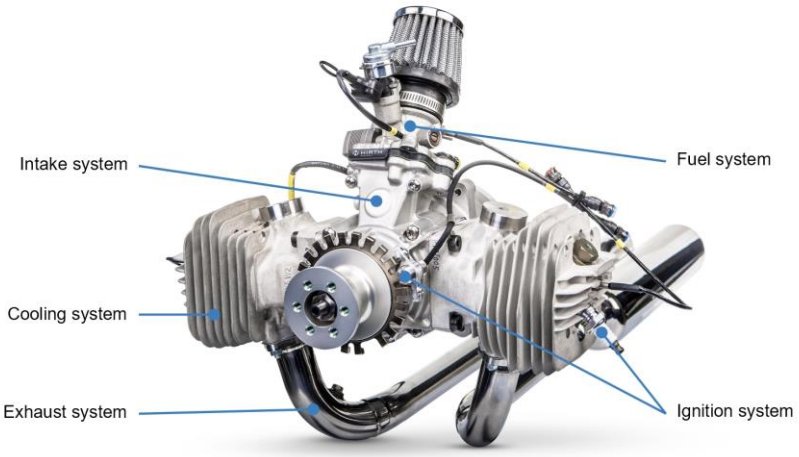

FIGURE 2.24: HIRTH 4201 TWO-STROKE, TWO-CYLINDER, SI, AIR-COOLED UAV ENGINE. ENGINE DISPLACEMENT 183 CC, BORE 54 MM, STROKE 40 MM, MAXIMUM POWER 11 KW AT 6500 RPM.
(Courtesy Göbler-Hirthmotoren GmbH)

2.4.1 COOLING SYSTEM

Of the energy liberated by the fuel owing to combustion, approximately 30%, in an SI engine, is transferred to the cooling system (Nomura *et al.*, 2015:89).

The transfer of heat within the combustion chamber is by (Heywood, 1988:670):

- Conduction through the piston, piston rings, cylinder and cylinder head;
- Forced convection due to the compression and expansion strokes and especially during the exhaust process of the working fluid; and
- Radiation from the high temperature flame front.

This heat is subsequently transferred to the environment, primarily by convection (Heywood, 1988:670), by making use of either liquid- or air-cooling.

Liquid-cooling utilises a water pump that pumps coolant through the cylinder block and head. The heated fluid then passes through a radiator, is cooled, and the cycle then repeats itself (Stone, 1999:452-453).

Air-cooled engines, as seen in Figure 2.24, transfer heat to the environment by air flowing across the horizontal and vertical cooling fins, cast as part of the cylinders and cylinder heads (Brusiani *et al.*, 2015:766).

The cooling fins generally have varying dimensional proportions because of the (Kiura *et al.*, 2005:101):

- Geometry of the cylinders and cylinder heads;
- Flow field of the cooling air; and
- Material properties and surface finish of the cooling fins.

The use of air-cooling enables a simplified layout, lower cost and less weight. However, liquid-cooled engines have higher heat transfer capacity (Brusiani *et al.*, 2015:766).

2.4.2 LUBRICATION SYSTEM

The introduction of oil between two surfaces in relative motion is known as lubrication and can perform the following functions (Heywood, 1988:740; Maleev, 1945:475):

- Reduce friction
- Decrease wear
- Cool surfaces and regions where heat due to friction is generated
- Wash away harmful impurities
- Assist the piston rings in guarding against excessive gas and oil leakage.

Most four-stroke and two-stroke CI engines use a forced-lubrication oil system. The oil is drawn from the sump by the pump and pumped through the oil filter, possibly an oil cooler, to the main oil gallery. The oil is subsequently diverted to the main, big-end, camshaft bearings and associated valve gear. Oil can also be diverted to other utilities, including nozzles that cool the underside of the pistons. All the oil is returned to the sump and the cycle is repeated (Heywood, 1988:740-741).

Crankcase-scavenge, two-stroke engines use a total-loss lubrication system that consumes the lubricant once it has been used (Bosch, 2007:495). A system like this was used during the 1960s by the SAAB Granturismo 850, SI, two-stroke, three-cylinder, 841 cc engine, as illustrated in Figure 2.25. The yellow arrows indicate the flow of lubricant from the pump, through the main and big-end bearings and final liberation into the crankcase (SAAB, 1962:8-1).

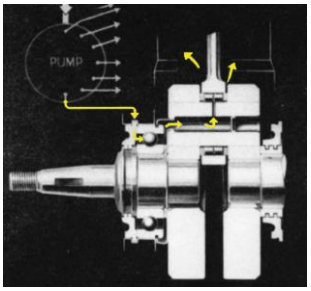

FIGURE 2.25: SAAB GRANTURISMO 850, SI, TWO-STROKE, THREE-CYLINDER, 841 CC TOTAL-LOSS CRANKSHAFT LUBRICATION SYSTEM.
(Courtesy SAAB Aircraft Co., Ltd)

Traditional crankcase-scavenge, two-stroke engines generally use less elaborate lubrication systems, with the oil often being mixed with the petrol in the fuel tank or metered into the engine by a variable volume pump (Bosch, 2007:495). Typical fuel-to-oil ratios vary from 25:1 to 200:1 for respectively older to current engines at light loads. Improvements in material properties and lubricants have made the reduction in lubricant consumption possible (Blair, 1996:470-471). Crankcase-scavenge, two-stroke engines do, however, not last as long as four-stroke engines, since the lack of a dedicated lubrication system leads to accelerated wear of components (Tan & Ripin, 2011:592).

2.4.3 INTAKE SYSTEM

The intake system provides a channel along which air initially flows through the air filter and is subsequently mixed with fuel, by the fuel system, before entering the crankcase, as seen in Figure 2.24.

The induction port of a two-stroke crankcase-scavenge engine can either be located on the crankcase, as seen in Figure 2.24, or on the lower circumference of the cylinder, as illustrated in Figure 2.14 in both the left- and right-hand photos. To accommodate the flow of the working fluid through the lower part of the cylinder and into the crankcase, the piston skirt requires that slots be cut through it, as seen in Figure 2.18.

Unlike a two-stroke crankcase-scavenge engine that initially inducts the working fluid into the crankcase, a four-stroke engine ingests the fuel-air mixture directly into the cylinders via an inlet manifold coupled to a cylinder head, as illustrated in Figure 2.21. The design of the intake manifold and cylinder head to flow correctly is extremely complex (Heywood, 1988:308), and a field of study on its own.

The mechanism used for the induction and timing of the working fluid into the crankcase is essential for the successful running of a two-stroke engine. Three methods are typically used. The simplest and most economical to manufacture is to allow the bottom edge of the piston skirt to expose and subsequently cover the inlet port by the oscillation of the piston, as seen in Figure 2.5 and Figure 2.7. However, this method confines the inlet port timing to symmetry about TDC (Blair, 1996:15).

To correspond more accurately to the pressure fluctuations within the crankcase, asymmetrical port timing is used (Blair, 1996:15). Figure 2.26 illustrates reed valves for a Yamaha RD 350 on the left and disc valves for a Suzuki RG 500 on the right. Both methods achieve asymmetrical port timing about TDC.

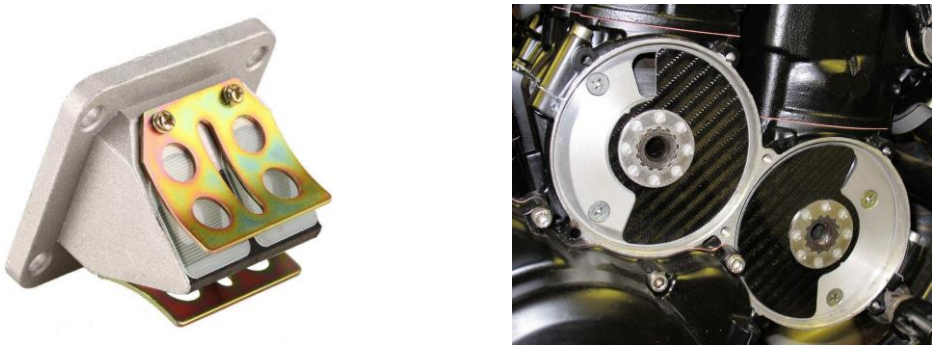

FIGURE 2.26: YAMAHA RD 350 REED VALVES (LEFT) AND SUZUKI RG 500 ROTARY VALVES (RIGHT).

(Courtesy Yamaha Motor Company, Suzuki Motor Company)

A reed valve, similar to the illustration above, would be inserted into the rectangular opening visible on both cylinders in Figure 2.14. Modern reed valves are mounted to a V-block design and use either spring steel or composite materials as reed petals (Blair, 1996:17). When designing reed valves, the designer must ensure that the effective port area of the deflected reed valve is sufficient. It must be confirmed that the stiffness of the reed petal is correct to enable the desired deflection and checked that the reed valves do not resonate throughout the engine speed range (Blair, 1996:451).

Disc valves, driven by the crankshaft, are mostly used in high-performance engines, although some mass production examples do exist (Blair, 1996:446), as seen in Figure 2.1. Disc valves can be manufactured from spring steel, although composite materials, as seen in Figure 2.26, are now common (Blair, 1996:16).

Currently reed valves are the most popular induction control method from small brush cutters to large outboard engines, unseating the piston-controlled inlet port (Blair, 1996:456). Disc valves were, however, still used in Grand Prix racing in 2008 by the Aprilia 125 cc engine that developed over 52 hp - that is 416 hp/l (Spalding, 2008:72-73).

The induction timing of the working fluid, by the three mechanisms described above, is illustrated in Figure 2.27 below.

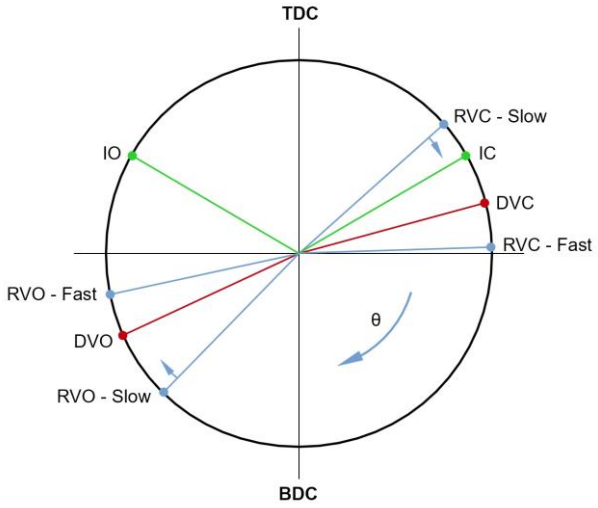

FIGURE 2.27: INDUCTION TIMING OPENING AND CLOSING ILLUSTRATION OF PISTON-CONTROLLED INLET PORTS (GREEN), REED VALVES (BLUE) AND DISC VALVE (RED).

The blue arrow, denoted by θ, indicates the crankshaft direction of rotation. TDC and BDC are marked at the top and bottom of the figure. The green, blue and red markers indicate the opening and closing points of the piston-controlled inlet port, reed valves and disc valve respectively. Note that the reed valves' opening and closing points change with engine speed. At low speed reed valves have asymmetrical timing, while being more symmetrical at high speeds (Blair, 1996:450).

Typical piston-controlled inlet open (IO) and inlet closed (IC) values are 75° BTDC and ATDC. Representative disc valve open (DVO) and disc valve close (DVC) values are 130° BTDC and 70° ATDC respectively. No specific values have been indicated for the opening and closing of the reed valves, denoted as RVO and RVC respectively. Suffice to indicate graphically the change in opening and closing points as the engine speed increases. For all three induction methods, increased power requirements imply increased porting durations (Blair, 1996:19).

2.4.4 FUEL SYSTEM

"The task of the engine induction and fuel systems is to prepare from ambient air and fuel in the tank an air-fuel mixture that satisfies the requirements of the engine over its entire operating regime" (Heywood, 1988:279). The fuel system for a two-stroke UAV engine, located between the air filter and the induction system, is illustrated in Figure 2.24.

The smooth and reliable running of an SI engine requires that a consistent and specific theoretical air-to-fuel (A/F) ratio of 14.4:1 and 14.7:1 be maintained. This relation is termed the stoichiometric ratio. The small variation in the ratio is due to the gasoline/petrol used (Heywood, 1988:280). However, in practice the mixture requirements vary depending on engine speed and load (Heywood, 1988:279), as illustrated in Figure 2.28.

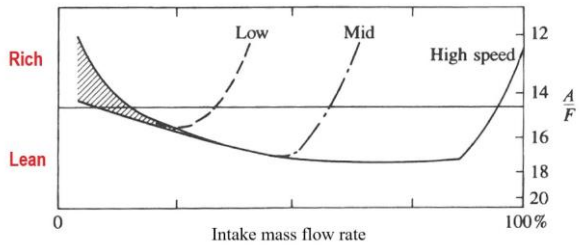

FIGURE 2.28: PRACTICAL AIR-TO-FUEL RATIOS AT LOW, MEDIUM AND HIGH ENGINE SPEEDS AS FUNCTION OF INTAKE MASS FLOW RATE.
(Heywood, 1988:281)

The figure illustrates the A/F ratio along the vertical axis with respect to the intake mass flow rate or load at low, medium and high engine speeds. Note that A/F values lower and higher than the stoichiometric ratio, of approximately 14.6, are rich and lean respectively.

The three distinct regions of the graph are (Heywood, 1988:280-281):

- For an engine to attain maximum power it is imperative that all the ***induced air*** be utilised. Thus, throughout the engine speed range as full throttle is approached, the mixture is enriched. Typical A/F ratios can be as low as 12 (Heywood, 1988:53).
- For maximum efficiency, it is essential that all the ***fuel*** is burnt. Thus, at part-load the combustion chamber is diluted with excess air. The quantity of excess air is, however, limited, since the reliable combustion of a homogeneous mixture is only possible within certain A/F ratio limits. Typical A/F ratio dilution can be as high as 18 (Heywood, 1988:53).
- To obtain a steady idle, the A/F ratio tends to be rich.

Engines running on diesel, using the CI cycle, are not restricted to the relatively narrow A/F ratio limits of SI engines. Typical A/F ratios are 18 at full load, increasing to 70 at idle (Heywood, 1988:53). The wide A/F ratios are possible, since the mixture formation is internal or heterogeneous and ignites due to auto-ignition. The load control for CI engines is thus performed by altering only the fuel supply (Bosch, 2007:501), while no throttle is required, since the air flow, at a fixed engine speed, remains unchanged (Heywood, 1988:25). Since SI engines require a homogeneous mixture constrained within a relatively narrow A/F ratio range, a throttle valve is required and this controls the combined flow of air and fuel into the engine (Heywood, 1988:17).

Regulating the fuel flow into the inducted air stream and providing a throttle valve to control the combined flow have traditionally always been the sole domain of carburettors (Heywood, 1988:282), and the devices are still used extensively. Fixed jet, or fixed venturi, and variable jet, or variable venturi, are the most common types (Stone, 1999:192).

For a fixed-jet carburettor, the air ingested from the air filter flows through a converging-diverging nozzle, or venturi. The resulting pressure drop, which is air flow rate dependent, between the carburettor inlet and the venturi draws the appropriate fuel quantity into the passing air stream. Finally, the adjustable throttle plate determines the flow rate of the fuel-air mixture (Heywood, 1988:282).

A Mikuni VM 34 variable jet carburettor, used for two-stroke engines, is illustrated on the left in Figure 2.29. A cable-operated throttle controls the opening, or venturi, of the piston valve that slides vertically within the carburettor housing. A taper jet needle, that is attached to the lower end of the piston valve, slides within the needle jet and consequently controls the fuel orifice, as illustrated on the right in Figure 2.29. The simultaneous action of the variable venturi and fuel orifice allows a constant A/F ratio throughout the operating range (Stone, 1999:194).

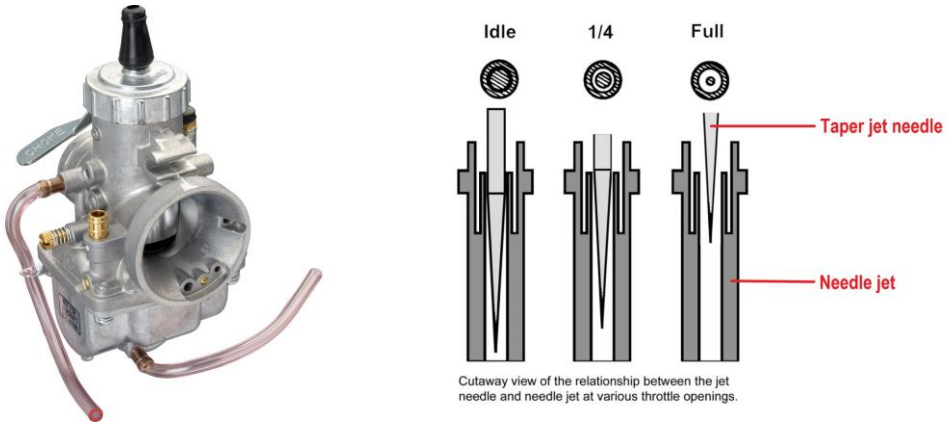

FIGURE 2.29: MIKUNI VM 34 CARBURETTOR (LEFT) AND IDLE TO FULL THROTTLE FUEL ORIFICE DUE TO THE TAPER JET NEEDLE AND NEEDLE JET (RIGHT).
(Courtesy Mikuni Corporation)

The use of carburettors, for many SI engine applications, has largely been replaced by intake port fuel injection systems, as illustrated in Figure 2.24 (Bosch, 2007:630). The advantages of fuel injection are "better fuel metering and fuel management" (Bosch, 2007:630). Since the first mechanical fuel injection systems, introduced in the early 1960s, much has changed and the rudimentary workings of only the current electronic systems will be described below.

The two fundamental inputs for the electronic control unit (ECU) are engine speed and air flow, or speed and load respectively. The engine speed is measured by the toothed encoder wheel, as illustrated in Figure 2.24. The air flow is measured by an air-flow sensor, of which numerous designs exist. A fuel pump and regulator supply petrol to a fuel rail at a constant pressure, typically around 3 bar, to which the fuel injector/s are mounted. The injection point and duration, typically 1.5 to 10 ms, is determined by the ECU based on the input data (Bosch, 2007:630; Heywood, 1988:294-297). In practice fuel-injection systems are far more complex and often employ closed loop lambda control in the exhaust system.

To this day, the development of fuel systems continues. Direct injection for SI, four-stroke engines have become more common place. For two-stroke engines, Evinrude has been using high-pressure direct injection, called ETEC, on outboard engines since 2003 (Foxhall *et al.*, 2015:7).

2.4.5 IGNITION SYSTEM

Before the ignition of the fuel-air mixture in an SI engine, compression occurs that raises both the pressure and temperature of the mixture to approximately 25 bar and 450 °C respectively. This is, however, still below the inception of mixture auto-ignition and an accurately timed spark is required to initiate combustion (Bosch, 2007:496). This is done by the ignition system, of which parts are pictured in Figure 2.24.

Despite being the final component in the ignition system, all the peripheral equipment has been purposely designed to ensure that the spark emitted by the spark plug is sufficient and correctly timed. A spark plug is subjected to an extreme operational environment and must withstand temperatures and pressures of up to 1000°C and 100 bar respectively. Typical operational temperatures are, however, between 500 and 900°C. To ignite a stoichiometric mixture, approximately 0.2 mJ of energy is required. However, lean and rich mixtures typically require 3 mJ or more. A traditional ignition system produces around 30 to 50 mJ. This is done by supplying an electrical pulse of up to 30 000 V to the spark plug (Bosch, 2007:648-649; Heywood, 1988:427-429).

To obtain maximum torque, maximum combustion pressure must occur just after TDC. For these conditions to be met, ignition of the mixture must occur before TDC. As the engine's rotational speed increases, or should a leaner mixture be present, the instant of ignition must be advanced further. For an SI engine the point of ignition is with reference to TDC, with the spark event typically occurring 10° to 50° BTDC. Knock limits the earliest possible point of ignition, while excessive exhaust gas temperatures restrict the latest. Ultimately, the spark plug creates a high temperature plasma kernel that ignites the compressed mixture and develops into a flame front that propagates across the combustion chamber (Bosch, 2007:639; Heywood, 1988:427).

Different ignition system designs have been used throughout the preceding decades to generate the required high voltage, at the correct moment. This includes magneto and capacitive-discharge ignition (CDI) systems. However, the most common conventional type of ignition system operates by means of a battery, coil and points, as illustrated in Figure 2.30.

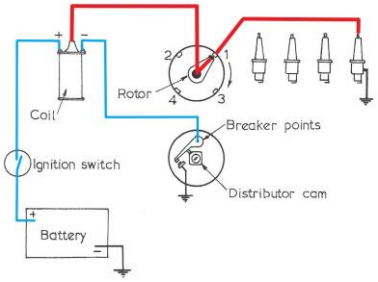

FIGURE 2.30: CONVENTIONAL COIL IGNITION SYSTEM.
(Bell, 1999:252)

The ignition system above consists of low- and high-voltage circuits, drawn in blue and red respectively. The sequence of events leading up to a spark event is as follows (Bell, 1999:252-253):

- Initially the breaker points are closed and current flows, in the low-voltage circuit, through the primary windings of the coil back to ground.
- The distributor cam rotates with the engine and determines the moment the breaker points open.
- The moment this occurs, current in the low-voltage circuit ceases to flow and the magnetic field in the coil starts to collapse.
- This induces current flow in the secondary windings and creates a voltage high enough to bridge the gap of the spark plug, thus creating a spark.
- The spinning rotor, in the red circuit, directs the high voltage to the correct cylinder.

The functional layout of a current automotive ECU-based ignition system is illustrated in Figure 2.31.

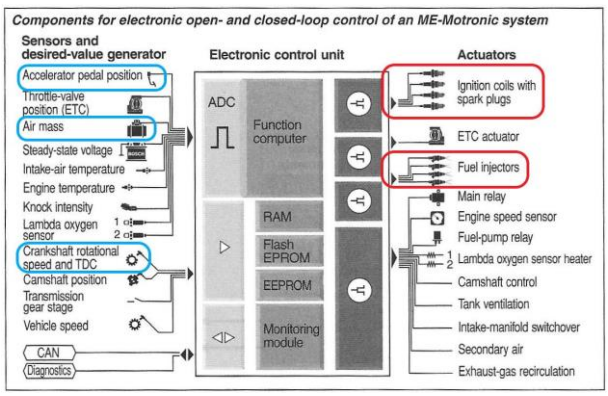

FIGURE 2.31: COMPONENTS FOR BOSCH ME-MOTRONIC SYSTEM.
(Bosch, 2007:655)

The Bosch Motronic automotive system was introduced in 1979; its original functionality combined electronic fuel injection and ignition in a single ECU. The Motronic system has undergone significant development since its inception and the layout of the ME-Motronic system pictured above is for current, port injected, SI engines. Note that this system controls many additional functions other than just fuel and ignition (Bosch, 2007:654-655).

However, the basic functional description of an ECU as stated in Section 2.4.4 is still valid. The three items on the left of the ECU, circled in blue, are the same basic inputs: air flow (air mass), engine speed (crankshaft rotational speed and TDC) and throttle position or load (accelerator pedal position). Based on this and other inputs, the ECU determines the quantity of fuel to inject and the most fitting time to initiate the spark. These two outputs are circled in red on the right of the figure (Bosch, 2007:655-656).

Figure 2.32 illustrates an ignition map stored in the ECU. The engine speed (speed) and air flow (relative air charge) data points are used as inputs, to determine the point of ignition BTDC (ignition angle) as an output for the ignition system. Since most current ECUs are closed-loop systems, ignition timing corrections can be made for temperature, lean operation, knock control and more. The fuel system in turn uses a fuel map (Bosch, 2007:639-640).

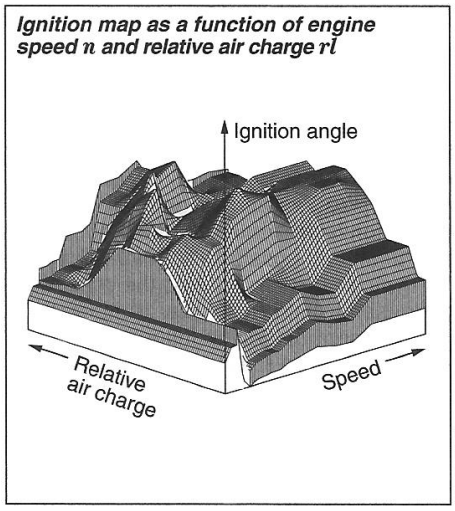

FIGURE 2.32: IGNITION MAP.
(Bosch, 2007:640)

2.4.6 EXHAUST SYSTEM

The exhaust system is the final path that the combustion products take before emission. However, the two-stroke exhaust system is of particular importance, since it serves not only to duct the exhaust gases, but by robust design it also ensures that the engine functions effectively throughout the desired speed range.

Figure 2.24 illustrates an un-tuned exhaust system for a two-stroke engine. To maximise the potential power that can be obtained from a two-stroke engine, a tuned exhaust system is required, as illustrated in Figure 2.33. This is for a two-stroke, SI, two-cylinder Yamaha RD 350 motorbike engine. Walter Kaaden, working for Motorradwerk Zschopau (MZ), applied the use of resonant harmonic techniques he had learnt at Peenemunde while working on the V1 weapons programme during the Second World War to the exhaust system of two-stroke engines. This resulted in the MZ 125 in 1961 and was the world's first naturally aspirated engine to produce 200 hp/l (Oxley, 2010).

FIGURE 2.33: AFTERMARKET TUNED EXHAUST SYSTEM FOR A TWO-STROKE, SI, TWO-CYLINDER YAMAHA RD 350 MOTORBIKE ENGINE.
(Courtesy Jollymoto)

The workings of a tuned exhaust system have been described in Section 2.2.1 under points B to D. To summarise, each exhaust system has a natural resonant frequency and it is desirable to "tune" that frequency to coincide with that of the scavenging process period. At the start of the scavenging process, or exhaust blowdown, it is desirable to have local low pressure in the exhaust to assist in the removal of the combustion products. Toward the end of the process, as the exhaust port is about to close, a local high pressure is required to force "spilt" fresh charge back into the cylinder and in so doing increase the charging efficiency (Naito & Taguchi, 1966:185).

What remains to be done is to briefly discuss the peculiar geometry of a tuned exhaust system, as seen in Figure 2.33. The entire exhaust system pictured above consists of two sections. The larger section is the tuned exhaust system, while the small cylindrical objects are the silencers. The diffuser of the tuned section gradually expands and this creates a wider, but less intense, suction reflection back to the exhaust port. The converging nozzle leading to the outlet is also slight, and purposely so, to reflect the compression waves back to the exhaust port through a wider engine speed range. The gradual angles used throughout thus result in a tuned exhaust that is more usable and less peaky. To conclude, two-stroke exhaust systems are extremely complex (Blair, 1996:435-445).

---

3 APPLICABLE RECIPROCATING ENGINE THEORY

A reciprocating two-stroke internal combustion engine contains numerous components and systems, as described in Chapter 2. The range of disciplines required to design these systems and components encompasses virtually every mechanical engineering field. This chapter is restricted to geometric relationships and parameters that characterise the reciprocating engine mechanism.

The numerous geometric relationships between the components of the engine mechanism and the operational environment are defined and derived, while the engine parameters deemed necessary to characterise engine operation are developed. Furthermore, the analytical methods for the resolution of both rotary and reciprocating unbalance are derived.

3.1 GEOMETRIC PROPERTIES OF THE ENGINE MECHANISM

The kinematic mechanism representing a two-stroke engine consists of three fundamental components: a crankshaft, connecting rod and piston. A reciprocating engine mechanism is graphically illustrated in Figure 3.1. Note that this graphic representation is specifically for two-stroke, SI engines, since the exhaust port is present at the lower region of the cylinder periphery.

Before defining relationships that characterise aspects of the engine mechanism, some important variables must first be stated:

B = Bore
L = Stroke
l = Connecting rod length
$\emptyset$ = Connecting rod angle
ω = Crankshaft angular velocity

The rotational speed of the crankshaft can be defined by either ω or by the crankshaft rotational speed (N_c) defined as:

$$N_c = \frac{60\omega}{2\pi} \tag{3.1}$$

The crank radius (a) and L are related by:

$$a = \frac{L}{2} \tag{3.2}$$

The ratio of the bore to stroke (R_{bs}) is:

$$R_{bs} = \frac{B}{L} \tag{3.3}$$

with typical values ranging from 0.8 to 1.2 for small to medium-sized engines (Heywood, 1988:43).

The ratio of the connecting rod length to the crank radius (R) is defined as:

$$R = \frac{l}{a} \tag{3.4}$$

Typical values are 3 to 4, again for small to medium-sized engines (Heywood, 1988:43).

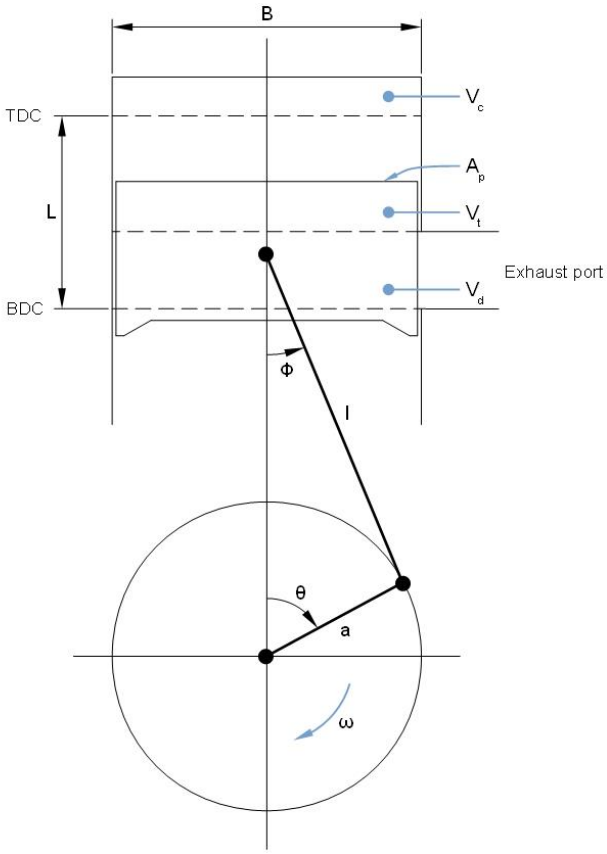

FIGURE 3.1: REPRESENTATION OF A RECIPROCATING ENGINE MECHANISM.

The projected area of the piston crown (A_p) is:

$$A_p = \frac{\pi}{4}(B)^2 \tag{3.5}$$

The displaced volume per cylinder (V_d) is defined as:

$$V_d = A_p L \tag{3.6}$$

This is graphically illustrated as the volume obtained when the piston sweeps from BDC to TDC.

The compression ratio for a two-stroke engine is defined in two ways. The geometric compression ratio (r_{cg}) is defined as:

$$r_{cg} = \frac{V_d + V_c}{V_c} \tag{3.7}$$

and the trapped compression ratio (r_{ct}), unique to two-stroke engines, is stated as:

$$r_{ct} = \frac{V_t + V_c}{V_c} \tag{3.8}$$

where:

V_c = Clearance volume
V_t = Trapped cylinder volume

The V_c is measured experimentally and represents the upper part of the cylinder volume that is not swept by the piston. The V_t is measured from the upper edge of the exhaust port to the upper limit of the piston when at TDC. The values obtained for r_{ct} are always below those obtained for r_{cg} that are typically between 8 and 12 for SI engines (Heywood, 1988:43).

The total displacement of an engine (V_{dt}) is calculated as:

$$V_{dt} = nV_d \tag{3.9}$$

where:

n = Number of cylinders

The fundamental variables and related equations of the reciprocating engine mechanism have been defined and formulated above. The resultant kinematics of the engine mechanism will be defined next.

3.2 MECHANISM KINEMATICS

With the basic variables and equations that constitute the essential parameters of the engine mechanism specified in Section 3.1, this section continues using the engine mechanism diagram to define essential mechanism kinematics.

A simple engine mechanism is illustrated in Figure 3.2. The piston displacement (s) of the piston pin axis from TDC is graphically illustrated.

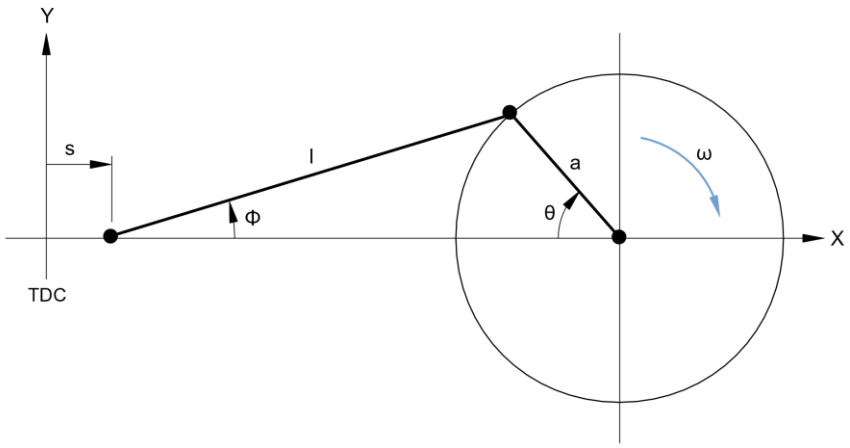

FIGURE 3.2: SIMPLE ENGINE MECHANISM.

To derive s with respect to θ, the following equation is formulated (Green, 1962:315-316):

$$s = a + l - [a\cos(\theta) + l\cos(\phi)]$$

After appropriate substitution and manipulation of the above equation, the resultant piston displacement is:

$$s = a\left[1 + R - \cos(\theta) - \sqrt{R^2 - [\sin(\theta)]^2}\right] \tag{3.10}$$

By taking the first and second derivative of Eq. (3.10) with respect to time (t) the piston velocity (v_p) and piston acceleration (a_p) can be obtained respectively and are given below by:

$$v_p = \omega a\left[\sin(\theta) + \frac{\sin(\theta)\cos(\theta)}{\sqrt{R^2 - [\sin(\theta)]^2}}\right] \tag{3.11}$$

$$a_p = \omega^2 a\left\{\cos(\theta) + \frac{R^2\cos(2\theta) + [\sin(\theta)]^4}{\{R^2 - [\sin(\theta)]^2\}^{\frac{3}{2}}}\right\} \tag{3.12}$$

With s, v_p and a_p for the piston defined above, the associated connecting rod angular displacement, which is equivalent to ϕ and angular velocity (Ω), will be stated.

The relationship between the angle that the connecting rod (ϕ), as seen in Figure 3.2, attains in relation to the angle of the crank (θ) is as follows (Green, 1962:320):

$$\phi = \sin^{-1}\left[\frac{a\sin(\theta)}{l}\right] \tag{3.13}$$

Differentiating Eq. (3.13) with respect to t results in Ω as defined below:

$$\Omega = \frac{\omega\cos(\theta)}{\sqrt{R^2 - [\sin(\theta)]^2}} \tag{3.14}$$

With the relevant kinematic equations for the engine mechanism derived above, formulations that are associated directly with the connecting rod follow in the next section.

3.3 CONNECTING ROD ENDS' RUBBING VELOCITIES

The connecting rod links the linear reciprocating motion of the piston to the rotary motion of the crankshaft. Because of this dual kinematic motion both the small- and big-end bearing faces do not experience constant tangential velocities, but fluctuating velocity profiles.

A connecting rod suspended about the axis of the piston pin A is illustrated in Figure 3.3, with both the piston pin and the crank pin sectioned. The crankshaft rotates at a constant angular velocity ω and consequently the illustrated crank pin as well. This induces an oscillating angular velocity Ω in the connecting rod, as graphically illustrated.

To calculate the tangential velocity on a bearing face, the following equation is used:

$$v = \omega r \tag{3.15}$$

where:

v = Velocity
r = Radius

The tangential velocity of the piston pin bearing face is:

$$v_{rp} = \Omega\frac{d_p}{2} \tag{3.16}$$

where:

v_{rp} = Rubbing velocity of the piston pin
d_p = Diameter of the piston pin

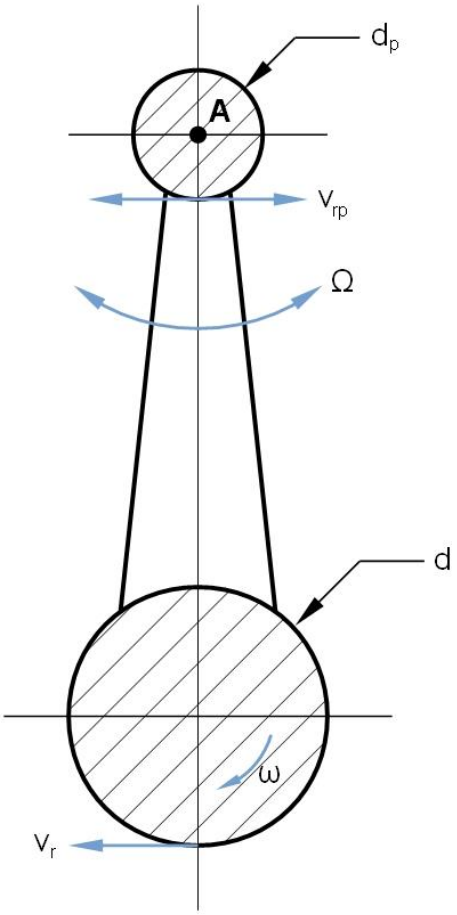

FIGURE 3.3: CONNECTING ROD RUBBING VELOCITIES FOR SMALL- AND BIG-ENDS.

The tangential velocity experienced by the crank pin is due to not only the constant angular velocity ω, but also the oscillating angular velocity Ω. Since the magnitude of Ω varies about zero, the resultant crank pin rubbing velocity oscillates about a fixed mean, defined as:

$$v_r = (\omega + \Omega)\frac{d}{2} \tag{3.17}$$

where:

v_r = Rubbing velocity of the crank pin
d = Diameter of the crank pin

Since the connecting rod experiences both linear and rotary motion, the mass allocation of the connecting rod due to both the aforementioned motions will be dealt with in the next section, along with the other associated engine components.

3.4 ROTATIONAL AND RECIPROCATING MASS ALLOCATION

The nature of the reciprocating engine mechanism, as illustrated in previous figures, implies that certain engine components will rotate and others oscillate, while the connecting rod will experience a mixture of both. This section assigns the components, or parts thereof, to the correct motion category.

Because of the motion of the connecting rod as already described, it is required that the point masses that will be allocated to either linear or rotational motion be calculated. The Bosch automotive handbook (2007:469) suggests that 1/3 of the total connecting rod mass be assigned as linear and the remaining 2/3 as rotational.

The methodology used by Green (1962:323) proposes that the point masses that are allocated as linear and rotational be inversely proportional to the distance from the centre of gravity (CG). This method is used and documented below.

A connecting rod with the CG marked is illustrated in Figure 3.4.

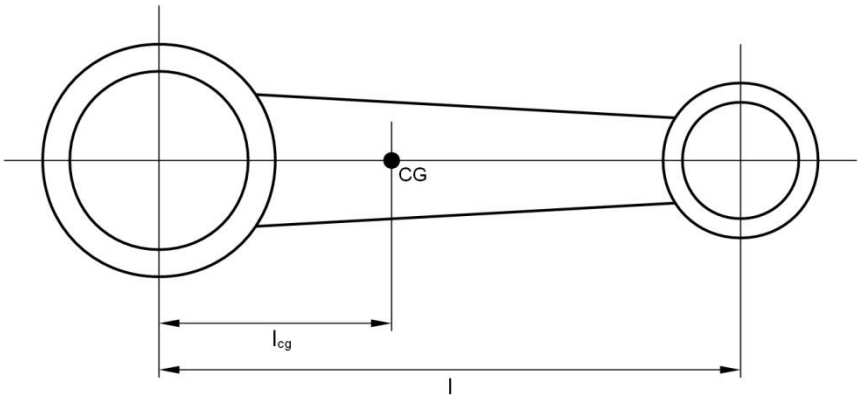

FIGURE 3.4: CONNECTING ROD SMALL- AND BIG-END MASS ALLOCATIONS.

The connecting rod mass allocated to the big-end is given by:

$$m_b = \left(\frac{l - l_{cg}}{l}\right) m_{cr} \tag{3.18}$$

where:

m_b = Mass allocated to the big-end
l_{cg} = Connecting rod length from big-end to CG
m_{cr} = Mass of the connecting rod

The connecting rod mass allocated to the small-end is:

$$m_s = \left(\frac{l_{cg}}{l}\right) m_{cr} \tag{3.19}$$

where:

m_s = Mass allocated to the small-end

The mass allocation for all the rotational components is:

$$m_r = m_c + m_w + m_{be} + m_b \tag{3.20}$$

where:

m_r = Total rotational mass component
m_c = Mass of the crankshaft and flywheel assembly
m_w = Mass of the big-end washers
m_{be} = Mass of the big-end bearing

The mass allocation for all the reciprocating components is:

$$m_o = m_p + m_{pr} + m_{pc} + m_{pp} + m_{se} + m_s \tag{3.21}$$

where:

m_o = Total reciprocating mass component
m_p = Mass of the piston
m_{pr} = Mass of all the piston rings
m_{pc} = Mass of both the piston circlips
m_{pp} = Mass of the piston pin
m_{se} = Mass of the small-end bearing

The total mass of both the rotational and reciprocating components influence the inertia and forces exerted on various engine components. The influence that the total reciprocating mass will have on forces within the engine is required for the next section.

3.5 PISTON, CONNECTING ROD AND BEARING FORCES

The combustion of the fuel-air mixture within the cylinder creates a sharp rise in pressure and forces the piston to displace. The engine mechanism is designed as such to facilitate the transfer of force from the piston, through the connecting rod and into the crank arm. This force is countered by a reaction force exerted by the main bearings.

Figure 3.5 illustrates an engine mechanism with numerous forces and reactions displayed. Note that the forces with solid lines represent forces experienced and exerted by/on components, whereas forces represented as dashed lines are for indication and are not required to balance the force diagram. Green (1962:320-323) formulated the arguments used in this section, although these are not presented in the same sequence as in the original text.

The piston effort (P) exerted by the piston is:

$$P = Q\cos(\phi) \tag{3.22}$$

where:

Q = Connecting rod load

If Eq. (3.22) is rewritten, the following results:

$$Q = \frac{P}{\cos(\phi)} \tag{3.23}$$

where Q is not only the connecting rod load, but also the bearing load (Q).

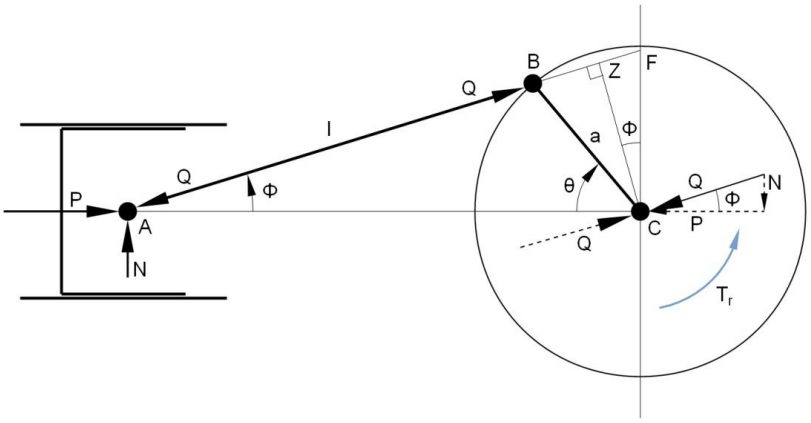

FIGURE 3.5: FORCES AND REACTIONS FOR THE RECIRPOCATING ENGINE MECHANISM.

The piston side load (N) transferred into the cylinder wall is:

$$N = Q\sin(\phi) \tag{3.24}$$

At point C in the figure above, Q acts as the bearing reaction force and can be broken up into two force components, namely P and N, as illustrated by the dashed lines and characterised mathematically by Eq. (3.22) and (3.24) respectively.

Equation (3.21) in Section 3.4 defines the mass component that must be allocated as the reciprocating point mass located on the piston pin axis, namely m_o. This mass must be taken into account when the force required to accelerate the piston is calculated. Figure 3.6 illustrates a piston within a sealed cylinder with a connecting rod attached. A cylinder pressure (p) is present within the cylinder and exerts a uniform pressure on the piston crown, as illustrated. The piston has displaced s from TDC and a_p is positive as per the X-axis direction.

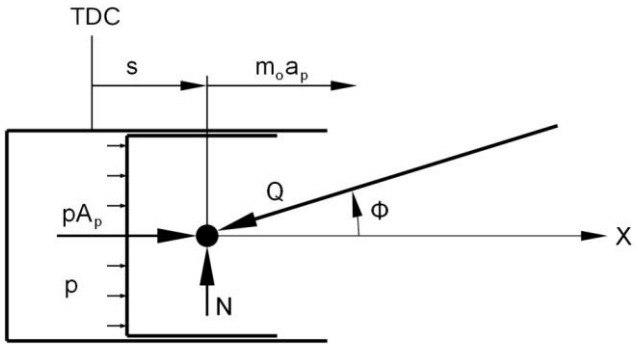

FIGURE 3.6: PISTON EFFORT FORCE DIAGRAM.

Based on Newton's second law, the following equation is formulated:

$$pA_p - Q\cos(\phi) = m_o a_p \tag{3.25}$$

Substitute Eq. (3.22) into Eq. (3.25) and rearrange:

$$P = pA_p - m_o a_p \tag{3.26}$$

Two important observations stemming from Eq. (3.26) are:

- It is ***imperative*** to note that both p and a_p are functions of θ.
- Should the engine piston have reciprocated in the vertical plane, the weight of m_o would have had to be added to the equation to account for the effects of gravity.

Equation (3.26) can be categorised into the following two equations:

$$F_g = pA_p \tag{3.27}$$

where:

F_g = Gross force

and:

$$F_i = m_o a_p \tag{3.28}$$

where:

F_i = Inertia force

Equation (3.27) is useful, since F_g indicates the force magnitude without the quantity lost or gained when m_o is accelerating or decelerating respectively. The F_i in turn represents the force magnitude required, or gained when, m_o is accelerating or decelerating respectively.

Using the equations derived in this section that define various aspects of the P exerted on the piston assembly, the next section will detail the couples created.

3.6 ENGINE TORQUE AND REACTION COUPLE

In order to use the P generated to create rotary motion, a couple is formed by the connecting rod linking the piston to the crank arm of the crankshaft. The torque that is generated is continuously fluctuating in magnitude, not only because of the ever changing p, but also because of the continuously varying length of the lever arm. The engine torque generated, the opposing reaction couple and the lever arms responsible for both couples are derived next.

Referring to Figure 3.5, the following observation is made:

$$T = Q \times CZ \tag{3.29}$$

here:

T = Net indicated torque

It is also geometrically observed that:

$$CZ = CF\cos(\phi) \tag{3.30}$$

Substitute Eq. (3.23) and (3.30) into Eq. (3.29) and simplify then:

$$T = P \times CF \tag{3.31}$$

here:

CF = Perpendicular moment arm

In order to calculate the torque for an entire crankshaft revolution, CF has to be derived for not only acute angles of θ as illustrated in Figure 3.5, but for obtuse angles too. An acute angle for θ is defined as any angle between 0° and ±90°, whereas an obtuse angle for θ varies from +90°, through 180° to -90°. The derivation for the acute and obtuse θ can be found in Appendices A.1 and A.2 respectively.

For acute θ the CF is:

$$CF = (l + a - s)\tan\left\{\sin^{-1}\left[\frac{1}{R}\sin(\theta)\right]\right\} \tag{3.32}$$

For obtuse θ the CF is:

$$CF = (l + a - s)\left[\frac{a\sin(\pi - \theta)}{(l + a - s) + a\cos(\pi - \theta)}\right] \tag{3.33}$$

Corresponding to both F_g and F_i, the equivalent turning moment equations are:

$$T_g = F_g \times CF \tag{3.34}$$

and:

$$T_i = F_i \times CF \tag{3.35}$$

where:

T_g = Gross torque
T_i = Inertia torque

The T defined in Eq. (3.31) can also be equated to:

$$T = T_g - T_i \tag{3.36}$$

To determine the reaction couple (T_r) of the engine assembly due to the T output of the crankshaft, reference is again made to Figure 3.5. At the main bearings, point C in Section 3.5, mention has been made of the fact that the bearing load (Q) can be broken up into components P and N, as illustrated.

Trigonometrically it is observed that:

$$P = \frac{N}{\tan(\phi)} \tag{3.37}$$

Substitute Eq. (3.37) into Eq. (3.31)

$$T = \frac{N}{\tan(\phi)} \times CF \tag{3.38}$$

Consider the triangle ACF then:

$$AC = \frac{CF}{\tan(\phi)} \tag{3.39}$$

Finally substitute Eq. (3.39) into Eq. (3.38) then:

$$T_r = N \times AC \tag{3.40}$$

where:

AC = Reaction couple arm

Note that:

$$T = T_r = P \times CF = N \times AC$$

Note that it can be observed that the output torque of the engine (T) must be equal to the resisting torque (T_r).

3.7 WORK DONE PER REVOLUTION

The area encapsulated within the pressure trace plotted by the p versus the corresponding incremental cylinder volume displacement (V) for one crankshaft revolution, can be used to determine the work done per revolution.

Figure 3.7 illustrates a cylinder pressure and the corresponding cylinder volume or p-V diagram for a single revolution, this diagram specifically for a two-stroke, SI engine.

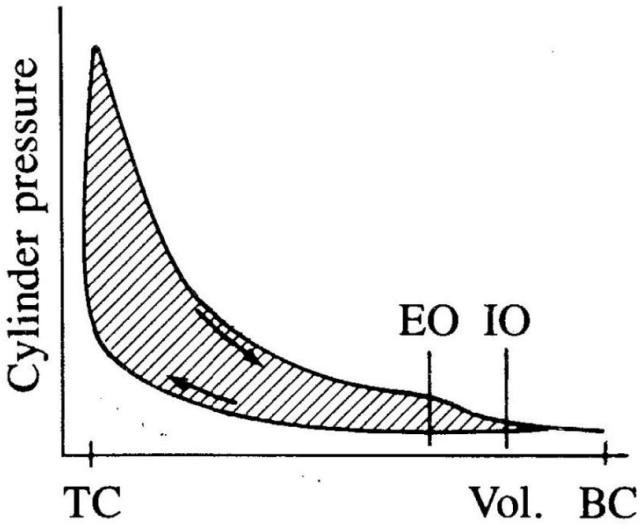

FIGURE 3.7: TWO-STROKE P-V DIAGRAM
(Heywood, 1988:47)

The introductory statement for this section can be numerically stated as:

$$W_i = \oint pdV \tag{3.41}$$

where:

W_i = Indicated work done per cycle

The circular integral of Eq. (3.41) can be mathematically stated as:

$$W_i = W_{exp} - W_{comp} \tag{3.42}$$

where:

W_{exp} = Area under the top curve from top centre (TC) to bottom centre (BC)
W_{comp} = Area under the bottom curve from TC to BC

Note that W_i refers to indicated work done as stated and *not* inertia. Also note that m_o does *not* influence the area encapsulated by the compressing and expansion curves. The effect of m_o, however, changes the shape of the p-V diagram (Green, 1962:333).

3.8 CRANKSHAFT ROTATIONAL SPEED FLUCTUATION APPROXIMATION

Because of the rising and falling pressures experienced within the cylinder, as illustrated graphically in Figure 3.7, the crankshaft output consists of a series of continuously fluctuating torque pulses. The fluctuating torque output is accompanied by a fluctuating crankshaft speed. In order to minimise the magnitude of the torque peaks and troughs and produce a more linear output, a flywheel is fitted, this reducing the influence of these pulsations.

Figure 3.8 illustrates the mean resisting torque (T_m) by a linear horizontal line. The T output that is available from the engine is drawn above and in this case, attempting to accelerate the crankshaft between θ_1 and θ_2 as sketched. The region between T and T_m, illustrated with hatch lines, represents the surplus energy available for crankshaft acceleration. The framework for this derivation methodology can be found in Green's book, *Theory of machines* (1962:337-339).

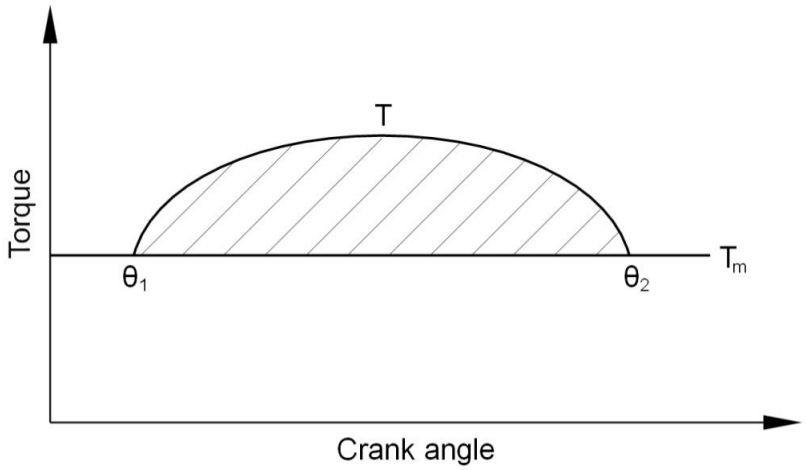

FIGURE 3.8: NET INDICATED AND MEAN CRANKSHAFT TORQUE INTEGRATION AREA.

The resultant accelerating/decelerating torque (ΔT) can be expressed as:

$$\Delta T = J_r \alpha \tag{3.43}$$

where:

J_r = Polar moment of inertia
α = Crankshaft angular acceleration

with:

$$J_r = m_r k^2 \tag{3.44}$$

where:

k = Radius of gyration

The ΔT can also be defined as:

$$\Delta T = T - T_m \tag{3.45}$$

Substitute Eq. (3.44) and (3.45) into (3.43) then:

$$T - T_m = m_r k^2 \frac{d^2\theta}{dt^2} \tag{3.46}$$

The completion of this derivation can be found in Appendix A.3.

The final equation representing the approximate crankshaft rotational speed fluctuation is:

$$\omega_2 - \omega_1 = \frac{\delta E}{m_r k^2 \omega} \tag{3.47}$$

where:

ω_2 = Maximum crankshaft angular velocity
ω_1 = Minimum crankshaft angular velocity
δE = Surplus energy

The tolerable crankshaft speed band, at a particular engine speed, must be determined and the inertia of the flywheel adjusted accordingly.

3.9 POWER PRODUCED

The rate at which work, as defined in Section 3.7, can be done is termed power and is a useful quantity to determine for any engine. The power derived from the piston due to the expanding gas mixture within the cylinder does not equate to the crankshaft output power, unless the power required to overcome all intrinsic inefficiencies and auxiliaries is added. These definitions of power are given next.

The indicated power (P_i) is:

$$P_i = W_i \frac{N_c}{60} \tag{3.48}$$

Since the P_i has been derived from the W_i, no operating losses have been accounted for and the rate of energy transferred from the expanding gas to the piston alone is calculated above.

The brake power (P_b) is defined as:

$$P_b = P_i - P_f \tag{3.49}$$

where:

P_f = Friction power

The P_b is the usable power generated by an engine, measured at the crankshaft. This quantity is obtained using a dynamometer that loads the engine at a certain N_c and then records the corresponding T. It is important to note that torque is the ability of an engine to do work, while the rate at which work is done is power (Heywood, 1988:46).

The P_f accounts for all power lost due to friction throughout the engine, the driving of all internal and external engine accessories and the pumping of air through the engine. This quantity is measured by conducting a motoring test on a non-firing engine, while maintaining conditions as if the engine was firing. The motoring test has inherent inaccuracies, since the gas forces on the piston and rings are lower than when the engine is running. It is essential that the throttle position be identical to when the engine is firing, to simulate pumping losses.

3.10 ENGINE CHARACTERISTICS

In the preceding sections of this chapter, numerous aspects and characteristics of the reciprocating engine mechanism have been specified and derived. While every effort was made to group the relevant variables together in a particular section, this was not always possible. The remaining definitions will now be discussed.

3.10.1 TRAPPED CYLINDER VOLUME

In Section 3.1, the term trapped cylinder volume (V_t) is defined. As stated, this is the cylinder volume that remains “trapped” within the cylinder, once the exhaust ports have closed. What remains is to define V_t mathematically below as:

$$V_t = A_p s \tag{3.50}$$

The term θ in Eq. (3.10), responsible for the magnitude of s, is that crank angle recorded at which the top edge of the piston is about to close the upper edge of the exhaust port.

3.10.2 MEAN PISTON VELOCITY

The mean piston velocity ($\overline{v_p}$) is an important parameter for correlating engine behaviour as a function of rotational speed. The parameter is defined as:

$$\overline{v_p} = 2L\frac{N_c}{60} \tag{3.51}$$

The significance of $\overline{v_p}$ is that for any type of reciprocating engine there are well-established norms. To limit the stress on the reciprocating components due to inertia, the $\overline{v_p}$ is limited to between 8 and 15 m/s, of which a small SI engine typically operates at the upper region of this range (Heywood, 1988:45).

3.10.3 MEAN TORQUE

The torque values specified in the preceding sections are all instantaneous values obtained at a particular θ. It is, however, generally more useful and easier to specify torque as an average value. The torque produced as a result of W_i is:

$$T_{mi} = \frac{W_i}{2\pi} \tag{3.52}$$

where:

T_{mi} = Mean indicated torque

The T_{mi} is analogous to W_i in the sense that no losses have yet been accounted for. Once losses have been acknowledged, the following formula is applicable:

$$T_{mb} = \frac{P_b 60}{2\pi N_c} \tag{3.53}$$

where:

T_{mb} = Mean brake torque

The T_{mb} is the average torque output measured at the crankshaft.

3.10.4 BRAKE MEAN EFFECTIVE PRESSURE

The brake mean effective pressure ($bmep$) is a useful relative engine performance measure. The effective use of the V_{dt} for a particular engine is measured. Dissimilar types of engines can also be compared to one another using this measure, defined as:

$$bmep = \frac{P_b 60}{V_{dt} N_c} = \frac{2\pi T_{mb}}{V_{dt}} \tag{3.54}$$

Typical maximum values of $bmep$ for naturally aspirated, four-stroke, SI engines range between 8.5 and 10.5 bar, at the engine rotational speed where maximum torque is produced (Heywood, 1988:50).

3.10.5 MECHANICAL EFFICIENCY

Mechanical efficiency (η_m) measures the ratio of the useful power output against the power obtained before losses and is defined as

$$\eta_m = \frac{P_b}{P_i} \tag{3.55}$$

The η_m depends on the throttle setting and the engine speed. Typical values are around 90% at full throttle, decreasing to 0% at idle (Heywood, 1988:49).

3.10.6 AIR/FUEL RATIO

The air-to-fuel ratio (A/F) compares the air mass flow rate ($\dot{m}_a$) to the fuel mass flow rate ($\dot{m}_f$) by making use of the following equation:

$$A/F = \frac{\dot{m}_a}{\dot{m}_f} \tag{3.56}$$

This ratio is useful, since all types of internal combustion engines operate with an A/F that resides within a certain range. For SI engines, this is typically between 12 and 18 (Heywood, 1988:53).

3.10.7 SPECIFIC FUEL CONSUMPTION

The $\dot{m}_f$ only indicates the fuel usage for the particular engine under investigation, which makes comparisons to other engines of different capacities and type impossible. A more useful measure is the specific fuel consumption (sfc), which measures how efficiently the fuel supplied is converted to power, defined as:

$$sfc = \frac{\dot{m}_f}{P_b} \tag{3.57}$$

The lower the sfc, the more effectively the fuel is used. Typical best values for SI and CI engines can go as low as 270 g/kWh and 200 g/kWh respectively (Heywood, 1988:52).

3.11 BALANCING A ROTATIONAL SYSTEM

All machinery, whether purely rotational or a combination of both rotational and reciprocating motion, such as a reciprocating internal combustion engine, must be balanced to operate smoothly. Balancing relates to the reduction, either partially or completely, of the vibration generated by machinery while in operation.

Rotary components can be satisfactorily balanced by the addition or removal of mass or masses at the appropriate location/s. For some components, rotational balancing is relatively easily accomplished, since the imbalance is due to an identical, diametrically opposed component being “out of balance” and mass is then either added or removed from it, an example being a two-bladed propeller.

Sometimes the geometry of the part does not allow balancing to be conducted as stated above and balancing-masses, offset along the axis of rotation, serve to balance the component. The counterweights found on engine crankshafts are an example thereof.

Rotational balancing encompasses both static and dynamic balancing; both are derived in the two sections that follow.

3.11.1 STATIC BALANCE

Static balance occurs when the summation of masses lie on the rotational axis (Green, 1962:375).

Figure 3.9 illustrates a rotating shaft, suspended between two bearing mounts, with two masses offset an identical distance from the axis of rotation along the shaft. Initially a single mass (m), at a radius (r) illustrated by solid lines, is attached to the shaft while rotating at an angular velocity (ω). The following equation is relevant for the force generated:

$$F = m\omega^2 r \tag{3.58}$$

where:

F = Centrifugal force

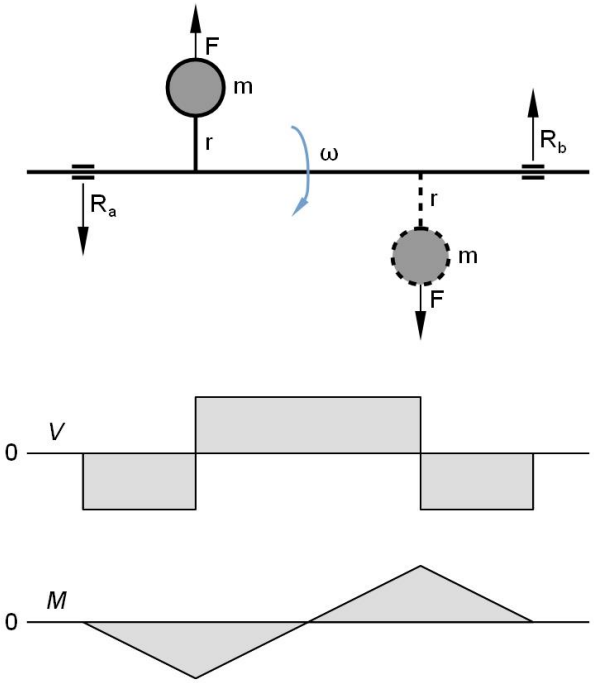

FIGURE 3.9: STATIC BALANCE OF A ROTATING SYSTEM.

In order to balance the assembly statically, a second identical mass (m), at a radius (r), illustrated with dashed lines, is added. This balancing mass is 180° opposed to the first, situated some distance along the shaft, as illustrated. A centrifugal force (F) of identical magnitude, but acting in the opposite direction, is generated.

Because of the F generated by both the mass and the balancing mass, bearing reactions (R_a) and (R_b) are created as illustrated. The shear force (V) and the bending moment (M) diagrams illustrate that the bearings experience a continuous rotating load and that the entire length of the shaft between the bearings is subjected to a bending moment respectively.

For a system to be statically balanced, the following condition must be met (Mabie & Reinholtz, 1987:505):

$$\sum F = \sum(m\omega^2 r) = 0 \tag{3.59}$$

Static balance thus occurs when the vector sum of the centrifugal forces is equal to zero.

3.11.2 DYNAMIC BALANCE

Dynamic balance ensues when in addition to the summation of masses being positioned on the rotational axis, no forces are present at the bearing mounts when operational (Green, 1962:376).

Figure 3.10 illustrates a rotating shaft, also suspended between two bearing mounts. To balance the single mass (m) at a radius (r), illustrated by solid lines, two identical counterweight masses (m_{cw}) are added at a counterweight radius (r_{cw}) and each at a distance (x) from m; these are illustrated by dashed lines.

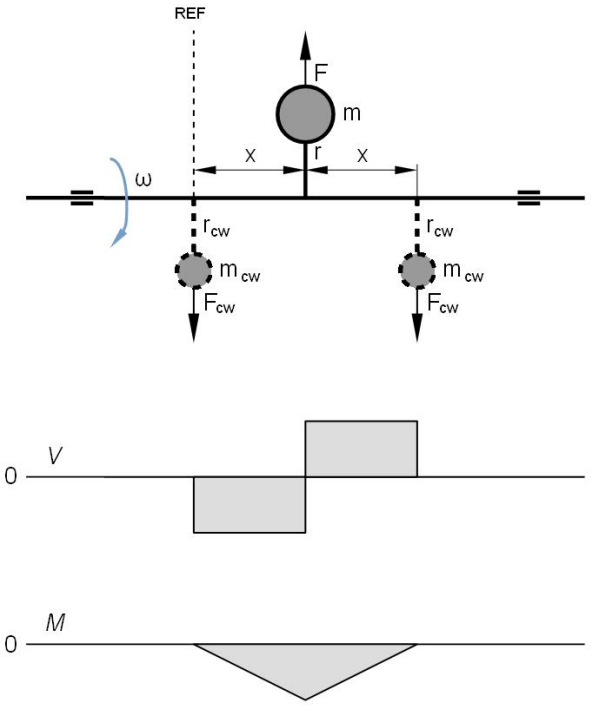

FIGURE 3.10: DYNAMIC BALANCE OF A ROTATING SYSTEM.

The first requirement for dynamic balance is that the system be statically balanced. Referring to Eq. (3.59) the following equation can be constructed and must hold true:

$$\sum F = m\omega^2 r - 2(m_{cw}\omega^2 r_{cw}) = 0$$

The second requirement is that the vector sum of the moments of the centrifugal forces be equal to zero (Mabie & Reinholtz, 1987:507). For the rotational shaft assembly above, the following equation can be written, using the dashed line marked *REF* as the origin:

$$m\omega^2 r(x) - m_{cw}\omega^2 r_{cw}(2x) = 0$$

Alternatively, the equation above can be written as:

$$F(x) - F_{cw}(2x) = 0$$

where:

F_{cw} = Centrifugal force due to counterweight

The two equations above can be rewritten as the following generic equation:

$$\sum C = \sum(m\omega^2 rx) = \sum(Fx) = 0 \tag{3.60}$$

where:

C = Couple

The V and M diagrams illustrate that the bearings do not experience any load and that the bending moment is restricted to the length of the shaft between the two counterweights.

Dynamic balance is thus achieved only when both the vector sum of the centrifugal forces and moments are equal to zero.

3.12 BALANCING A RECIPROCATING SYSTEM

For machinery with reciprocating components generating a rotary output, an effort must be made to balance not only the rotating components as described in Section 3.11, but the reciprocating components too, since “the shaking of a piston engine is due primarily to the inertia forces of the reciprocating masses located at the wrist pin” (Mabie & Reinholtz, 1987:513).

Reciprocating systems can, however, not always be balanced and a certain degree of vibration is tolerated, provided it is not near a resonant frequency that will cause failure or large enough to cause discomfort (Mabie & Reinholtz, 1987:504).

Balancing a reciprocating system, or at least determining the unbalance, involves calculating the primary and secondary forces and couples associated with the mechanism, aided by the binomial series.

3.12.1 BINOMIAL SERIES APPROXIMATION

The unbalance of a reciprocating mechanism is usually confined to the first and second harmonics. All the higher order harmonics do exist, but their influence is considered negligible (Mabie & Reinholtz, 1987:516).

In order to derive the first two harmonics mathematically, Eq. (3.10), defining the piston displacement, can be approximated by making use of the binomial series and then differentiated twice to yield acceleration. The outcome will only be presented here, while this important derivation can be found in Appendix A.4 (Mabie & Reinholtz, 1987:36).

After making use of the binomial series, the resultant piston acceleration is:

$$a_b = a\omega^2\left[\cos(\theta) + \frac{a}{l}\cos(2\theta)\right] \tag{3.61}$$

where:

a_b = Piston acceleration due to binomial series

The piston acceleration equation has now been broken up into the first and second harmonic terms.

3.12.2 PRIMARY AND SECONDARY FORCES

As in rotating systems, reciprocating systems also experience both forces and couples that contribute to operational vibration and both have to be accounted for. The forces due to the first and second harmonics or primary and secondary forces are derived first (Mabie & Reinholtz, 1987:516-517).

The inertia force defined by Eq. (3.28) can have a_p substituted by a_b, as derived in the binomial series, as stated in Eq. (3.61) and the following results:

$$F_r = m_o a\omega^2 \cos(\theta) + m_o \frac{a^2}{l}\omega^2 \cos(2\theta) \tag{3.62}$$

with:

$$F_p = m_o a\omega^2 \cos(\theta) \tag{3.63}$$

$$F_s = m_o \frac{a^2}{l}\omega^2 \cos(2\theta) \tag{3.64}$$

where:

F_r = Resultant force
F_p = Primary force
F_s = Secondary force

Equation (3.62) is relevant when the engine in question is a single-cylinder ***and*** for this two-cylinder, horizontally-opposed UAV engine, that will have the engine configuration specified in Chapter 5, for the following reasons:

- For in-line, multiple-cylinder engines the θ term, for both $\cos(\theta)$ and $\cos(2\theta)$, has to be expanded to include the relative crank angle (Φ) of the subsequent crank throws relative to the first. The inclusion of Φ is, however, not required, since each bank of the UAV engine consists of only a single cylinder.
- Engine configurations such as V or opposed-engines are analysed as two separate in-line engines, with a bank angle (β) between the banks. The resultant forces and couples of the two in-line, or in this case the two single-cylinder engines are then due to the vector sum (Mabie & Reinholtz, 1987:526).

The two statements above then account for how Eq. (3.62), that is relevant for single-cylinder engines, can be used unaltered for this two-cylinder, horizontally-opposed UAV engine.

3.12.3 PRIMARY AND SECONDARY COUPLES

The rocking couples generated by the reciprocating masses of a two-cylinder, horizontally-opposed engine will now be investigated for both the first and second harmonics.

Refer to Figure 3.11 of a two-cylinder, horizontally-opposed engine with the *REF* plane passing through cylinder 1. Consider the primary couple (C_p) created by the F_p of the second cylinder that is located a distance of x from the *REF* plane, then:

$$C_p = F_p x \tag{3.65}$$

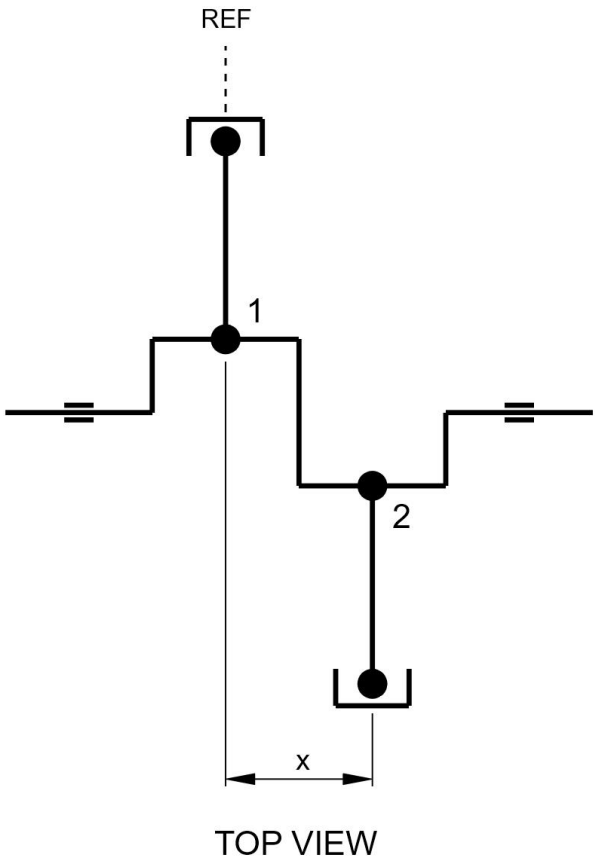

FIGURE 3.11: TWO-CYLINDER, HORIZONTALLY OPPOSED ENGINE LAYOUT.

Substitution of Eq. (3.63) into Eq. (3.65) results in:

$$C_p = \omega^2 (m_0 a x) \cos(\theta) \tag{3.66}$$

The secondary couple (C_s) is derived in the same manner

$$C_s = \omega^2 \left(m_0 \frac{a^2}{l} x \right) \cos(2\theta) \tag{3.67}$$

The resultant couple (C_r) is then:

$$C_r = C_p + C_s$$

or:

$$C_r = \omega^2 (m_0 a x) \left[\cos(\theta) + \frac{a}{l} \cos(2\theta) \right] \tag{3.68}$$

The balance/unbalance experienced by a two-cylinder, horizontally-opposed reciprocating system due to both primary and secondary forces and couples has been derived.

3.13 ENGINE FORCES

Because of the cyclic combustion process occurring in a reciprocating internal combustion engine, a fluctuating p as defined in Section 3.5 is created. This p interacts with the volume within the enclosed cylinder, generating forces that not only drive the crankshaft, but also create forces that are transferred through major engine components.

The largest forces experienced by the crankcase and associated components are documented, while the bearing reaction forces due to the combustion process are derived. This section does not include all forces and couples, but only those that have not yet been detailed elsewhere.

3.13.1 CRANKCASE AND CYLINDER FORCES

The peak force experienced by the cylinder head, cylinder and crankcase due to the p generated by combustion is significant and the components must be robust enough to withstand many such cycles.

Figure 3.12 illustrates a single-cylinder, internal combustion engine schematic with F_g, defined in Section 3.5, marked and the reaction force (F) of equal magnitude illustrated on the underside. The hoop stress generated within the cylinder is confined to the cylinder and is not transferred elsewhere.

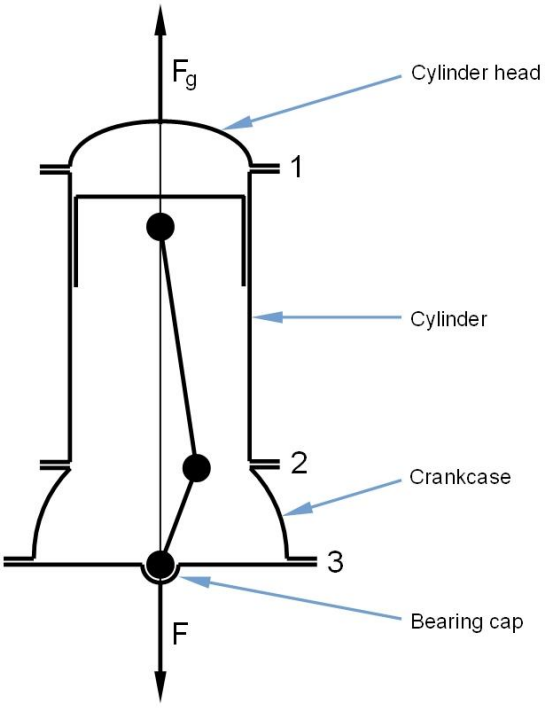

FIGURE 3.12: SINGLE-CYLINDER SCHEMATIC ILLUSTRATING MAJOR STRUCTURAL FORCES DUE TO COMBUSTION.

Two important observations are:

- The forces described above are internal; although the external engine mounts do not experience any force, the components mentioned above do.
- The F_g fluctuates continuously, since it is a function of p, as defined in Eq. (3.27).

The force path of F_g is documented as it progresses through the engine components and joints marked 1 to 3 as follows:

- The F_g initially exerts an upward force on the cylinder head.
- The cylinder in turn experiences F_g, also in an upward direction.
- The F_g once transferred to the crankcase has F, exerting a downward force on the bearing caps, thus completing the force path.

The tensile force experienced per bolt, should the interface be symmetrical, is:

$$F_b = \frac{F_g}{b} \tag{3.69}$$

where:

F_b = Force/bolt
b = Number of bolts

For a non-symmetrical bolted interface, the above equation would provide an indication of the F_b.

3.13.2 BEARING REACTION FORCES

The p generated by combustion that drives the crankshaft, so producing useful torque, also creates a force on the crankshaft that is opposed by the crankshaft bearings, as demonstrated in Section 3.5.

Since P is a function of p and Q a function of P as stated in Eq. (3.26) and (3.23) respectively, Q is a function of p that also varies in magnitude continuously per cycle.

Figure 3.13 illustrates an in-line, two-cylinder engine with the crank throws opposed at 180°. The side view illustrates cylinder 1 producing a power stroke due to p and Q generating a downward force on crank arm 1. The front view illustrates the ϕ at which Q attains a maximum value. The crankshaft pictured in the side view is thus also tilted at ϕ.

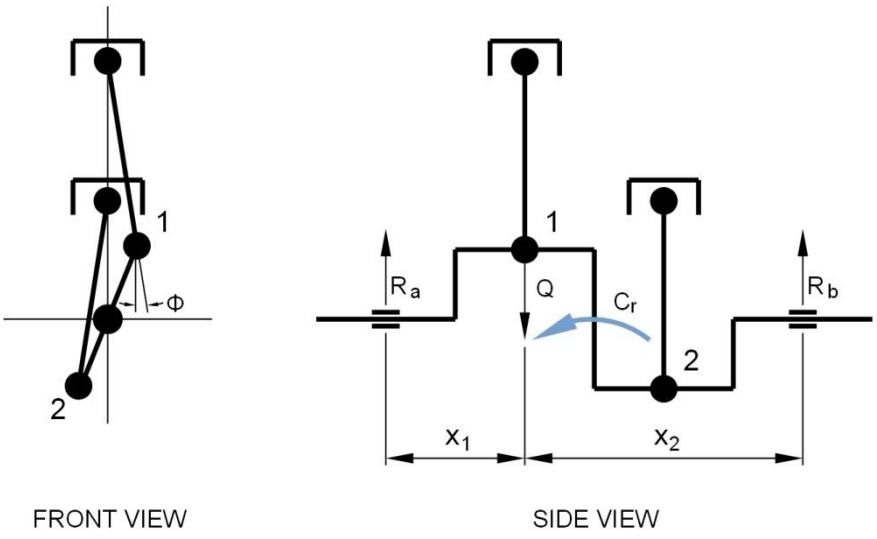

FIGURE 3.13: BEARING REACTIONS DUE TO CONNECTING ROD FORCES AND BALANCING COUPLES.

The R_b is calculated by taking moments about a as follows:

$$Q(x_1) = R_b(x_1 + x_2)$$

Thus:

$$R_b = \frac{Q(x_1)}{x_1 + x_2} \tag{3.70}$$

The R_a is calculated in a similar manner.

Figure 3.14 represents the R_a, broken up into X and Y component forces as follows:

$$R_x = R_a \sin(\phi) \tag{3.71}$$

and

$$R_y = R_a \cos(\phi) \tag{3.72}$$

where:

R_x = Bearing reaction component in the X-direction
R_y = Bearing reaction component in the Y-direction

Similar methodology is applied to calculate the component reaction forces of R_b.

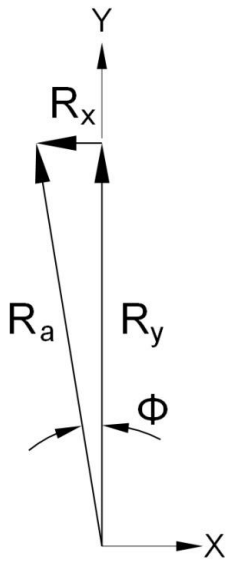

FIGURE 3.14: BEARING REACTION COMPONENTS IN THE X AND Y DIRECTIONS.

Should a C_r, as derived in Section 3.12.3, be present due to unbalance, as depicted in Figure 3.13, a corresponding R_a and R_b would be created (not depicted in figure).

Equation (3.70) would be used to determine the main bearing reactions by substituting $Q(x_1)$ with C_r for calculating both R_a and R_b.

4 CYLINDER PRESSURE EXPERIMENTAL INVESTIGATION

Suitable facilities are required and resources are consumed, if accurate and repeatable results are to be obtained from internal combustion engines tested on dynamometers, since the number of variables that can adversely influence the experimental outcome is considerable.

In the following chapter, the effort required to obtain comprehensive experimental data is justified. The engine to be used in the experiments is specified and the test cell installation and instrumentation are described. Finally, the experimental techniques and results are detailed.

4.1 EXPERIMENTAL JUSTIFICATION

Following the detailed explanation and derivation of some fundamental aspects of reciprocating engine operation in Chapter 3, this material might be considered sufficient to apply directly to a new engine design.

However, Eq. (3.26) defines P as a function of both p and a_p and both variables are functions of θ, as stated in Section 3.5. But unlike a_p that can be solved for any θ by application of Eq. (3.12), no equation for p can be derived. This is due to the extremely complex processes, both thermo and fluid dynamic, that govern engine performance (Heywood, 1988:749). “At present, it is not possible to construct models that predict engine operation from basic governing equations alone.” (Heywood, 1988:749). An analytical equation for p does thus not exist. Computer simulation packages that utilise sophisticated modelling techniques to predict engine performance based on supplied input criteria do exist, but are virtually/exclusively for four-stroke engines.

Thus, no other viable alternative remained but to obtain the p with respect to θ experimentally, and provided that the engine characteristics are not dissimilar to those of the proposed experimental engine, the p curve obtained should be a fairly good approximation.

The test engine selection and specifications for the dynamometer experiments are discussed in the next section.

4.2 TEST ENGINE SPECIFICATIONS

The requirements for the project are that a two-stroke, two-cylinder, horizontally-opposed, air-cooled engine be designed and constructed. As stated in Section 4.1, the engine characteristics of the test engine should not be too dissimilar from those of the proposed experimental engine.

A Yamaha DT 175 SI engine was selected as a suitable test engine. It is a two-stroke, single-cylinder, air-cooled motorbike engine that is often used in the recreational motorbike environment. Unlike two-stroke engines that are highly tuned to be used in a racing environment, this type of engine is relatively conservatively tuned, suiting the proposed engine characteristics. The engine type is still readily available and spare parts are stocked by the agents. Two engines were acquired, one for dynamometer testing and the other for measurement purposes.

Before the specification sheet could be tabulated, two workshop experiments first had to be conducted to obtain test engine information not supplied by the manufacturer.

4.2.1 PORT TIMING

The two-stroke cycle port timing, as described in Section 2.2.2, was determined for the DT 175 engine by conducting the following experiment.

The test engine acquired for measurement purposes was stripped of all excess components and placed on a workbench, as illustrated in Figure 4.1. A degree wheel with 1° increments was attached to the crankshaft, while a pointer was constructed and secured to the crankcase. A dial gauge was affixed to an aluminium beam secured by bolts to the cylinder and located at the centre of the piston crown, to avoid piston rock influencing the reading. The documented testing procedure can be found in Appendix B.1.

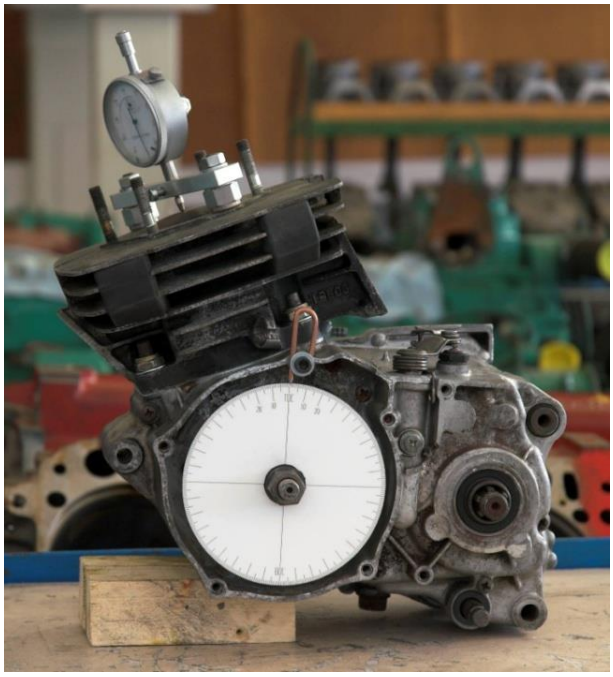

FIGURE 4.1: PORT TIMING ESTABLISHED BY A DEGREE WHEEL AND DIAL GAUGE.

The resultant port timing was:

- EO at 92° ATDC
- TO at 121° ATDC

With the port timing established, the V_c was measured.

4.2.2 CLEARANCE VOLUME

As stated in Section 3.1, the V_c represents the upper part of the cylinder volume that is not swept by the piston and owing to the geometrical complexity of this volume, the simplest method to determine the clearance volume is by experimental methods.

Three items influence the V_c, namely:

- The V_c increases since the thickness of the cylinder head gasket contributes additional volume.
- The V_c is reduced by the protruding volume of the domed piston crown when at TDC.
- The volume of the cylinder head with the spark plug installed increases the V_c.

The first point is calculated theoretically, whereas items two and three are measured experimentally, as illustrated in Figure 4.2 when viewed from left to right. The listed experimental procedure can be found in Appendix B.2.

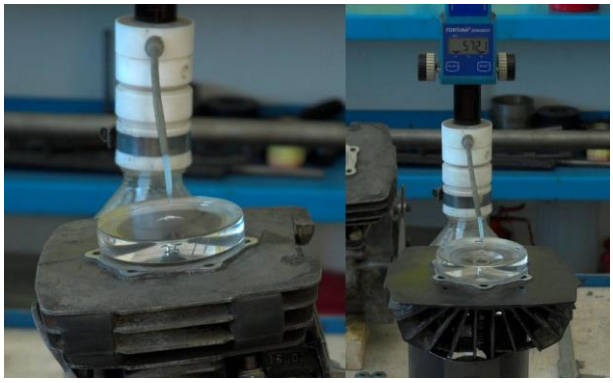

FIGURE 4.2: VOLUMETRIC CONTRIBUTIONS TO THE V_C MEASURED FOR BOTH (LEFT) THE PROTRUDING PISTON CROWN AND (RIGHT) THE CYLINDER HEAD.

The calculations done to determine the volume for each item will not be displayed, but rather the summation of the final volumes obtained for items one to three, which is as follows:

$$V_c = \frac{3.42-6.99+21.41}{1000} = 17.84\times10^{-3}\ \text{m}^3$$

The V_c can now be used to calculate both r_{cg} and r_{ct}, as defined by Eq. (3.7) and Eq. (3.8) respectively.

4.2.3 EXPERIMENTAL ENGINE SPECIFICATIONS

The specifications for the test engine can be found in the following table.

TABLE 4.1: YAMAHA DT 175 ENGINE SPECIFICATIONS.

Engine type	Yamaha DT 175
Cycle	Two-stroke
Cooling	Air
Number of cylinders	1
Bore	66.00 mm
Stroke	50.00 mm
Connecting rod length	105.00 mm
Bore-to-stroke ratio	1.32
Connecting rod length-to-crank radius ratio	4.20
Displaced cylinder volume	171.06 cc
Clearance volume	17.84 cc
Geometric compression ratio	10.59
Trapped compression ratio	6.54
Exhaust port open	92° ATDC
Transfer port open	121° ATDC
Maximum power	12.8 kW at 7000 rpm
Maximum torque	18.6 Nm at 5500 rpm
Fuel system	Mikuni VM26SS carburettor
Ignition system	CDI
Induction system	Reed valve
Lubrication system	Autolube
Transmission	6-speed gearbox
Final drive output	Chain

The engine specifications provide a good indication of not only the physical dimensions of the engine and selected components; if the individual enquiring is equipped with fair knowledge of internal combustion engine operational aspects, then a reasonable forecast of the engine performance is likely too.

With the engine specifications of the Yamaha DT 175 engine tabulated, the report will subsequently describe the test cell setup.

4.3 TEST CELL SETUP

A sound test cell setup is essential to achieve effective engine dynamometer testing, since the number of variables that can adversely influence the outcome is substantial and care must be taken to ensure that the results are accurate.

The following sections will describe the test cell layout, the mechanical installation of the test engine and the peripheral equipment required for this setup.

4.3.1 TEST CELL LAYOUT

Test cell 7 at Cape Advanced Engineering (CAE), as illustrated in Figure 4.3 below, is an enclosed area with the operator-controlled computer interface and associated electrical equipment located on the outside of the test cell. A large sliding door provides access to the test cell and a sound-proof observation window allows visual monitoring of the engine.

FIGURE 4.3: CAE TEST CELL 7.

The test cell is adequately ventilated, with forced air blowing in through vents above the sliding door and two lower vents at the opposite end to the access door, painted light blue in the figure above, extracting air. This ensures that the heat generated during testing is continuously dissipated.

A steel structure in the centre of the test cell has been anchored to the floor and provides the test bed for the test engine, dynamometer and related equipment.

The power generated is dissipated by a Froude EC 38 Eddy current dynamometer. Continuous water circulation through the dynamometer dissipates the heat generated internally by the Eddy currents. The specifications of the dynamometer are tabulated in Table 4.2 below.

TABLE 4.2: FROUDE EC 38 DYNAMOMETER SPECIFICATIONS.

Dynamometer description	Froude EC 38
Classification	Eddy current dynamometer
Maximum power	164 kW
Maximum rotational speed	10000 rpm
Maximum torque	477 Nm
Maximum torque speed	3300 rpm
Rotor inertia	0.101 kgm^2

The engine is normally coupled to the dynamometer by means of a driveshaft. A 40 kW electrical motor, controlled by a variable speed drive, can be coupled to the other end of the dynamometer, should a friction motoring test or more complex experiments require this.

4.3.2 TEST ENGINE INSTALLATION

The physical installation of the engine onto the test bed and the mechanical connection to the dynamometer are detailed next.

The engine had front and rear mounting points on the bottom of the crankcase and a steel cradle frame was constructed to house the engine. Threaded rods with lock-nuts at either end tied the engine to the cradle frame. Two rubber mounts were installed beneath the cradle frame to dampen vibration and were in turn attached to circular tube pedestals, which were bolted to the test bed, as illustrated in Figure 4.4 below.

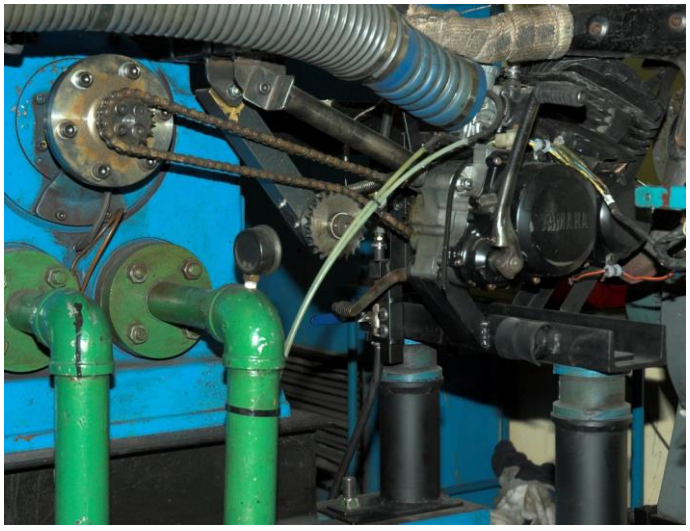

FIGURE 4.4: TEST ENGINE MOUNTED TO TEST BED AND CHAIN DRIVE COUPLING.

To account for the twisting of the assembly about the rubber mounts, a tube was inserted with one end attached to an upper, rear mounting point on the engine and the other to the dynamometer frame. To ensure that no bending stress was induced when twisting occurred, both ends were constructed as pinned joints.

Since the final drive output of the test engine was a chain drive, as listed in Table 4.1, it was deemed appropriate to abandon the traditional shaft coupling method and to couple the test engine to the dynamometer by using a chain drive, as illustrated above.

An adapter was fabricated to attach a motorbike sprocket to the dynamometer. The chain tension on the slack side of the chain was controlled by a spring-loaded idler gear on a pivot mechanism and the ideal chain tension was obtained by altering the spring tension.

4.3.3 ENGINE PERIPHERALS

The test cell layout is illustrated in Figure 4.5. The major peripheral equipment required to enable the test engine to run is as follows:

- *The cooling fan* was positioned in front of the engine and blew air directly across both the cylinder and cylinder head.
- *The exhaust system* used was the factory-fitted Yamaha exhaust, with flexible steel ducting transporting the exhaust gas to the extraction air vents of the test cell. The test cell exhaust ducting could not be used because of excessive back pressure.
- *The ignition system* and original wiring loom were used and adapted so that the test cell emergency stop, when activated, would cut the engine ignition.
- The engine was *started* by means of the incorporated kick-starter, while an assistant disengaged the clutch.
- *Throttle control* was accomplished by a remotely controlled electrical actuator, pulling the throttle cable.

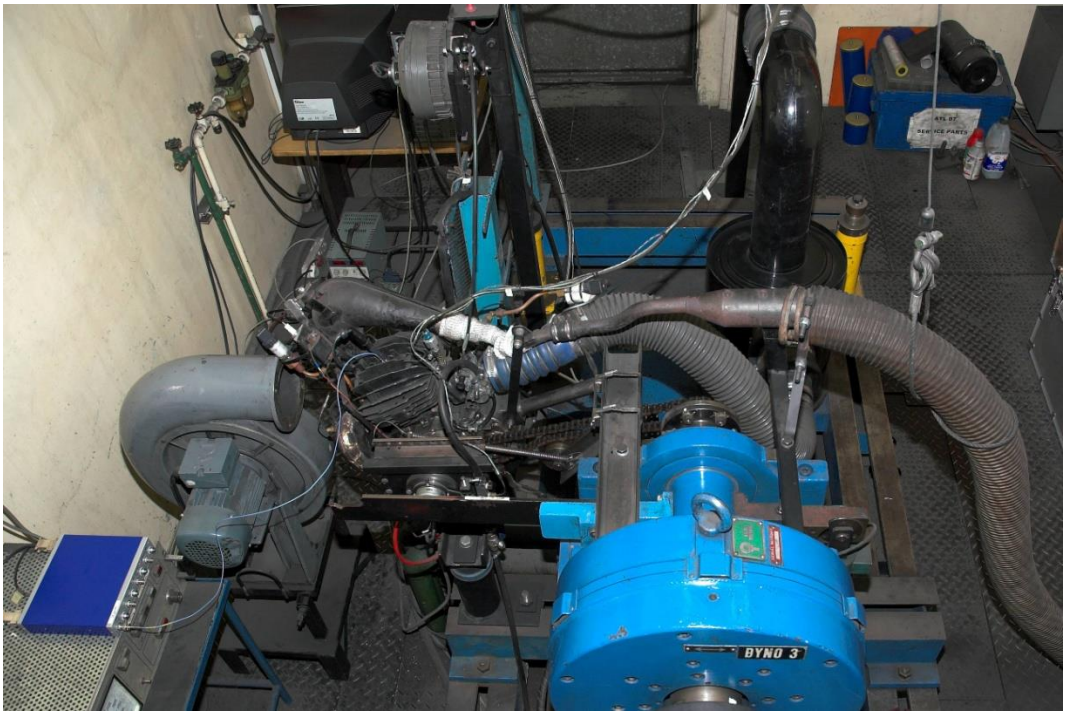

FIGURE 4.5: TEST CELL LAYOUT.

4.4 TEST CELL INSTRUMENTATION

Purposeful dynamometer testing and evaluation of results cannot be conducted successfully without reliance on accurate and reliable instrumentation. Test cell 7 has been designed for a great variety of experiments and consequently numerous outputs are available; however, only the data deemed directly relevant to this project will be discussed.

The instrumentation used and the outputs generated by both the test cell system and the crucial high-frequency logging system will be described next.

4.4.1 TEST CELL SYSTEM

The test cell system refers to the installed CAE test equipment necessary for not only the running of the entire test cell, but also the monitoring and recording of sensory inputs required for this experiment, as schematically illustrated in Figure 4.6.

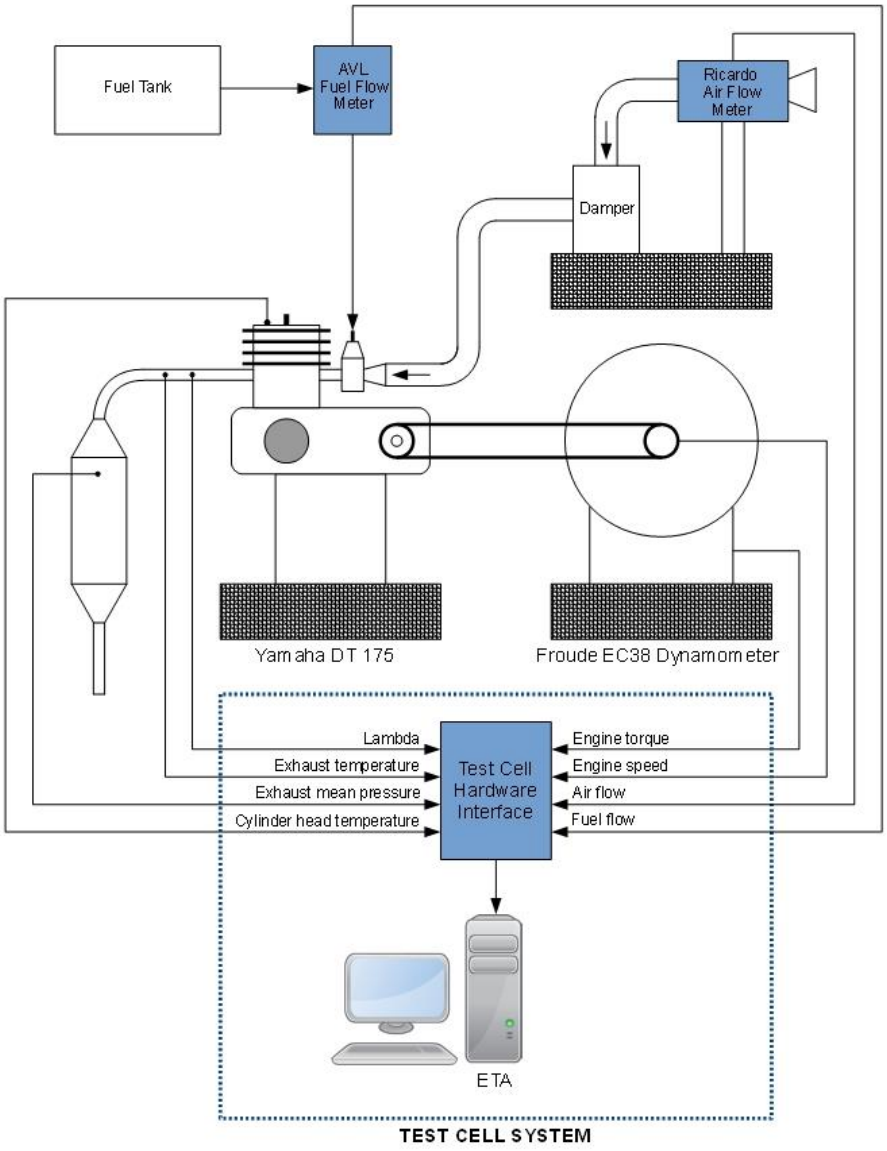

FIGURE 4.6: TEST CELL SYSTEM SCHEMATIC LAYOUT.

The schematic above illustrates the test engine coupled to the dynamometer with some peripheral equipment attached, as seen in Figure 4.5. Eight sensory inputs are received and measured by the test cell hardware interface and then logged by the CAE proprietary software package, Engine Test Analysis (ETA) at a fixed rate of 2 Hz. The instrumentation used and functioning thereof is as follows:

- *The engine torque* was measured by a load cell and multiplied by the acting lever arm length.
- *The engine speed* measured by the proximity incremental sensor attached to the dynamometer had to be multiplied by 3.517, because of fourth gear being selected on the test engine. This reduction of the test engine output speed proportionally increased the maximum dynamometer input torque favourably to 65.4 Nm, thus allowing the oversized dynamometer, for this test engine, to operate at 13.7% of the maximum rated torque, as tabulated in Table 4.2.
- *The air flow* was measured by a Ricardo viscous air flow meter, number P 7023 1087H. The air flow was initially directed through a large truck air filter with the filter element installed to dampen resonant frequencies, before being attached to the test engine carburettor filter element, also left in place to mitigate resonance.
- *The fuel flow* rate was obtained from the installed AVL dynamic fuel balance, type 7130. The autolube system for throttle variable volume two-stroke lubricant dosing as listed in Table 4.1 was disabled in favour of a constant premix ratio of 50:1 fuel-to-lubricant mixture under all speed and load conditions.
- A *lambda* sensor, as illustrated in Figure 4.7, was installed in the exhaust to assist in verification of the A/F ratio obtained by the air flow and fuel flow meters.
- An *exhaust temperature* J-type thermocouple measured the exhaust gas temperature, as seen in Figure 4.7.
- *The cylinder head temperature* thermocouple was installed to monitor the cylinder head temperature. The temperature was allowed to reach 100°C before the cooling fan was manually activated. The maximum cylinder head temperature allowed was 140°C before testing at those parameters had to cease.
- *The exhaust mean pressure*, the outlet point illustrated in Figure 4.7, was measured using a Wika S-10, 0 - 2.5 bar pressure transducer with a fixed canister volume fitted prior to the sensor, thus damping the exhaust pulses.

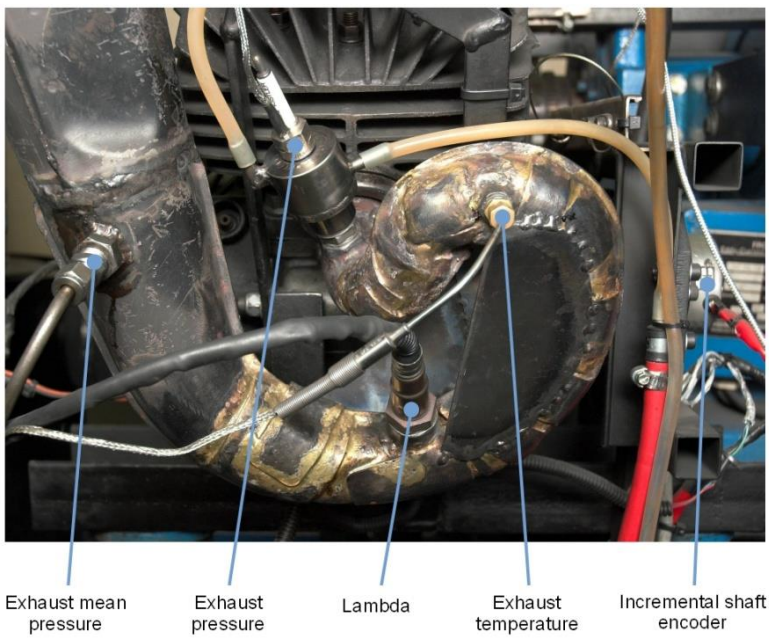

FIGURE 4.7: EXHAUST SENSOR LAYOUT.

Prior to the experiment commencing, all the transducers listed above were first calibrated. The calibration techniques and equipment used for this purpose are not within the scope of this dissertation.

4.4.2 HIGH-FREQUENCY LOGGING SYSTEM

The high-frequency logging system is an independent data-capturing system that samples at a far higher rate than the test cell system is capable of. The high rotational speed of the engine, together with the high rate of change of the signals to be sampled, necessitated a high-frequency logging system, as schematically illustrated in Figure 4.8. The system consisted of three transducers producing four signals, two of which were first conditioned before being delivered to a data acquisition device for binary storage by a computer.

Because of the rapid pressure fluctuations, thermal loading and hostile environment in a combustion chamber, a specialised transducer was required to measure the cylinder pressure. Measuring spark plugs are manufactured for this purpose and in addition to being a functional spark plug, these also encompass a piezo-electric pressure sensor that has been designed to function effectively in the aforementioned environment.

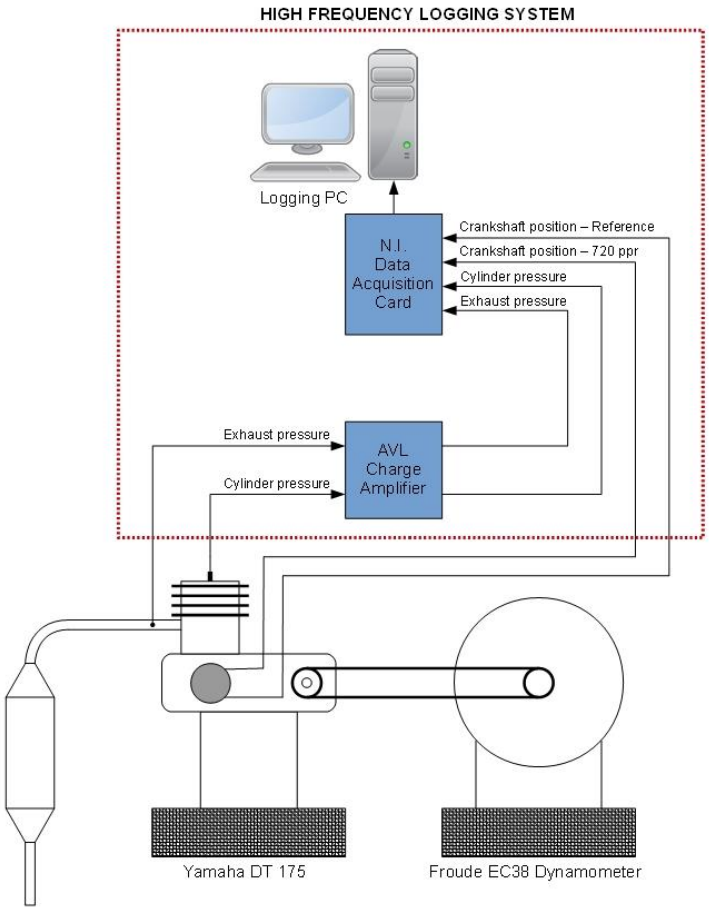

FIGURE 4.8: HIGH-FREQUENCY LOGGING SYSTEM SCHEMATIC LAYOUT.

The cylinder pressure transducer used was a Kistler measuring spark plug, Type 6117A67U25. An aluminium cylindrical adapter was manufactured to enable the conical seat of the Kistler measuring spark plug to be mounted against the flat seat of the cylinder head spark plug mount, while maintaining the original sparkplug intrusion depth into the cylinder.

The exhaust pressure transducer used was an identical Kistler measuring spark plug, as mentioned above. Because of the sustained high gas temperatures in the exhaust system and the ideal mounting location being as close as possible to the exhaust port, a steel mount with a conical seat, surrounded by a water jacket, was constructed, as illustrated in Figure 4.7, the inlet and outlet silicon hoses for the water jacket cooling being clearly visible.

Because both the cylinder and exhaust pressure transducers are piezo-electric sensors, an AVL MicroIFEM piezo charge amplifier was used to measure and condition the signals received with a sensor sensitivity of 200 pC/bar and 50 pC/bar per channel respectively. For both channels data loss was undesirable, so the highest low-pass filter of 100 kHz was used and cyclic drift compensation was enabled.

In order to ascertain the relationship between the cylinder and exhaust pressures as a function of the crankshaft angular position, a BEI L25 incremental optical shaft encoder with a disc resolution of 720 pulses per revolution (ppr), as seen in Figure 4.7, was attached to the crankshaft by means of a torsionally stiff flexible coupling. Two channels were used, the first producing only a single reference pulse per revolution, the second 720 ppr. The orientation of the encoder to the crankshaft was such that the single reference pulse corresponded exactly with BDC, the identical orientation technique as described in Appendix B.1 being used, only now with a 180° offset. The offset was selected to accurately capture the combustion pressure trace about the θ TDC vicinity.

Four channels of the National Instruments, M Series, Multifunction DAQ Device, Number 190 996B-02 data acquisition card were used to capture the two pressure and two encoder signals. The Nyquist rate is the minimum sampling frequency required to avoid aliasing and is equal to twice the highest frequency within that signal (Stone, 1999:542). To avoid aliasing occurring within the sampled 720 ppr signal with the test engine running at a maximum rotational speed of 6500 rpm, a minimum sampling frequency of 156 kHz was required. Thus, a sampling rate of 250 kHz per channel was utilised. Finally, the logging PC stored the generated binary file.

Failures that occurred, some critical, and the solutions implemented that rectified the problems will be described in the next section.

4.5 TESTING FAILURES AND RECTIFICATION

Despite the best efforts to construct a robust test cell installation upon the first attempt, inevitable technical difficulties arose once the system was run and these problems had to be dealt with. Some were completely solved and others accepted.

The major technical difficulties experienced and the proposed solutions reached while conducting the dynamometer tests on the test engine will be described next.

4.5.1 EXCESSIVE ENGINE VIBRATION

Initially the test engine cradle frame, as described in Section 4.3.2, was rigidly attached to the circular tube pedestals, as illustrated in Figure 4.9 on the left, *without* two rubber mounts. This was done deliberately, since the mounting points of the engine had rubber inserts preinstalled by Yamaha and this was thought sufficient to dampen operational vibration.

However, when the test engine was first run, catastrophic vibration resulted at more than one engine speed and although no damage occurred, it was clear that further damping of the installation had to be implemented.

FIGURE 4.9: THE ORIGINAL TUBE PEDESTALS (LEFT) AND (RIGHT) THOSE MODIFIED WITH RUBBER MOUNTS.

The circular tube pedestals were modified to accommodate rubber mounts, as illustrated in Figure 4.9 on the right, and a tube to constrain the twisting of the assembly owing to the output torque, as mentioned in Section 4.3.2, was installed. All subsequent testing occurred free of any noticeable resonant vibration.

4.5.2 EXHAUST FAILURES

The original exhaust system of the test engine was used for all testing, as stated in Section 4.3.3. The mounting points of the exhaust system used when installed in a Yamaha DT 175 motorbike frame were all replicated, as illustrated in Figure 4.5.

However, shortly after testing commenced, the first of many fractures of the exhaust system occurred in the vicinity of the exhaust port region, as illustrated in Figure 4.10 below.

FIGURE 4.10: FIRST AND SECOND EXHAUST FAILURES IN THE VICINITY OF THE EXHAUST PORT.

The affected region was repeatedly repaired by bending and brazing steel plates over the cracks. Additional stiffening ribs were also added and the final result can be seen in Figure 4.7.

The root cause of this continuous cracking was never isolated, but was thought to relate mainly to inaccurate mounting points, resulting in undue stress induced in the exhaust system.

4.5.3 AIRFLOW METER RESONANCE

The Ricardo viscous air flow meter was originally not connected as described in Section 4.4.1 and illustrated in Figure 4.11, but connected directly to the carburettor filter element by a single flexible pipe.

FIGURE 4.11: AIR FLOW METER WITH IN-LINE TRUCK FILTER ATTACHED.

This initial direct connection resulted in the test engine abruptly ceasing operation as soon as the throttle was set to open at 40%. Numerous attempts were made to solve the problem, including testing Helmholtz resonators of various volumes, but to no avail. It appeared that the problem was due to a resonant frequency being generated within the single flexible pipe, entirely disrupting engine charge induction.

The resonant frequency concern was successfully addressed, as previously described, by the addition of the truck filter element in the air flow meter line.

4.5.4 ERRONEOUS LAMBDA READINGS

The lambda sensor installed in the exhaust system, as described in Section 4.4.1, consistently recorded different A/F ratios when compared to the quotient of $\dot{m}_a$ and $\dot{m}_f$ as measured by the Ricardo viscous air flow meter and the AVL dynamic fuel balance respectively.

It was assumed that the individually measured $\dot{m}_a$ and $\dot{m}_f$ quantities were correct and the lambda sensor readings erroneous. Since the lambda sensor measures oxygen content in the exhaust gas (Bosch, 2007:151), the “spilt” fresh charge within the exhaust system, high in oxygen content, flowing back into the cylinder under the influence of the reflected positive exhaust pressure as described in Section 2.2.1, possibly contributed to the inaccurate readings.

This problem was not solved and the lambda readings for all the experiments were discarded.

4.5.5 ALTERNATIVE EXHAUST PRESSURE TRANSDUCER

Initially the Kistler measuring spark plug, finally installed as the exhaust pressure transducer described in Section 4.4.2, was not used. Instead a Wika S-10 pressure transmitter for general applications was installed, as illustrated in Figure 4.12. Note that in the figure below the Wika pressure transducer has been connected in parallel with a fitting for a Kistler measuring spark plug. This was done during the fault-finding phase.

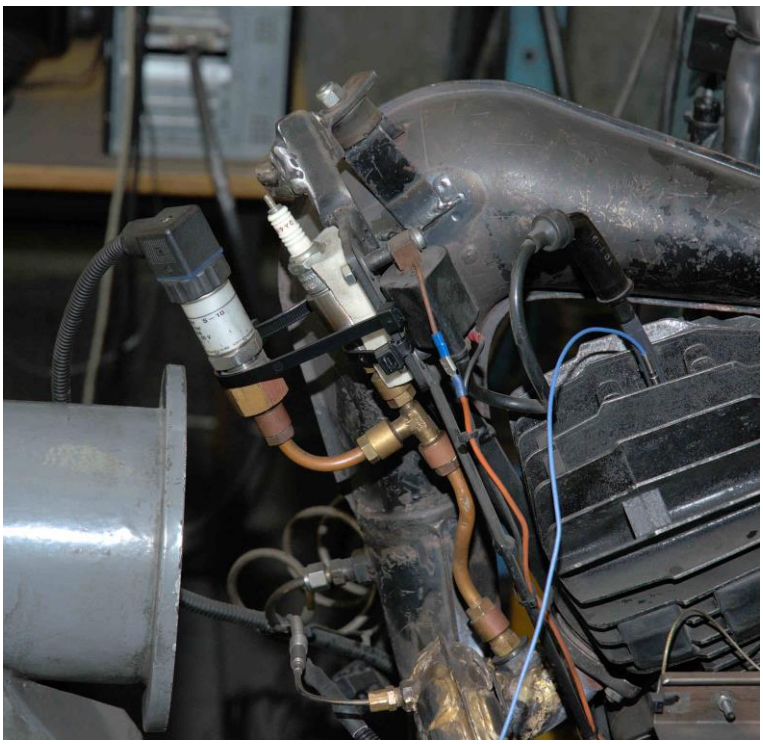

FIGURE 4.12: WIKA S-10 EXHAUST PRESSURE TRANSDUCER.

The Wika transducer was initially intentionally used, since the Kistler piezo-electric cylinder pressure transducer can only respond to the rate of change in pressure and requires an absolute reference pressure for correction; this was to be provided by the Wika exhaust pressure transducer (Stone, 1999:515). However, the maximum permissible temperature of the medium for the Wika transducer is 80°C, well below the exhaust gas temperature. The same location on the exhaust as for the Kistler transducer, surrounded by the water jacket as in Figure 4.7 was used, but instead of the aforementioned assembly, a 20 cm copper tube was used to offset the Wika transducer from the hot exhaust gas, as illustrated.

The initial results were, however, suspect and fault finding commenced with the output of the Wika pressure transducer compared to that of the Kistler piezo-electric pressure transducer. Upon analysis of the logging PC results, with both transducers subjected to the exhaust pressure, the Wika S-10 pressure transmitter displayed a significant phase shift in the pressure trace, coupled with a questionable rate of response.

There was no alternative but to use another Kistler piezo-electric pressure transducer for the exhaust pressure, as previously described, and then first to reference this pressure to the exhaust mean pressure, as described in Section 4.4.1, before finally correcting the cylinder pressure. The methodology used to accomplish this will be described in Section 4.7.4.

4.6 TEST CELL SYSTEM EXPERIMENTAL RESULTS

The first experimental results analysed the data obtained from the test cell system, but before the results can be analysed, the correction factors used must be defined.

4.6.1 CORRECTION FACTORS

The correction factors adjust T to standard atmospheric conditions so that direct comparisons between engines can be made.

The variables that influence the correction factors are ambient pressure, temperature and humidity of the air inducted into the engine. Numerous standards exist for the measurement and correction of T, CAE using the Economic Commission for Europe (ECE) standard.

The formulation of the ECE standard was embedded in the test cell system and will not be derived. This correction factor is used in the section that follows.

4.6.2 TEST CELL EXPERIMENTAL RESULTS FOR YAMAHA DT 175

The ETA software package of the test cell system wrote all recorded output data to a spreadsheet at a set rate of 2 Hz, as described in Section 4.4.1. The sampling time used per set point was 20 seconds to allow flow meters and temperatures to stabilise, resulting in a data string of 40 entries per channel, of which the average was then used. The test cell experimental results for the Yamaha DT 175 can be found in Appendix E.1.

The columns in black print illustrate the average transducer readings for each set point. The columns in blue represent calculated values, derived from the transducer readings as per the formulae in Chapter 3. Noteworthy comments are as follows:

- *The engine speed* differed slightly from the speed set point by 0.34 to 0.95%, from the lowest to the highest percentage error respectively.
- *The correction factor* was almost identical at all eight speed set points, thus resulting in a minor engine torque correction.
- *The friction power* was experimentally obtained as described in Section 3.9.
- *The air flow/fuel flow* ratio for the test engine ranged between 10.4 and 14.3. If the range is as defined by Heywood in Section 3.10.6 to be between 12 and 18, then this engine generally ran with a low air-to-fuel ratio, termed rich.
- *The specific fuel consumption* ranged between 412.0 and 680.8 g/kWh, an increase of 53 to 152% above the best value of 270 g/kWh that can be obtained by an SI engine, as stated in Section 3.10.7.
- *The brake mean effective pressure* at peak torque was 5.8 bar, below the 8.5 to 10.5 bar stated by Heywood in Section 3.10.4 for four-stroke, SI engines.
- *The mean piston velocity* attained a maximum value of 10.8 m/s, well within the upper limit of 15 m/s, as stated in Section 3.10.2.

With the test cell experimental results documented, the high-frequency logging system test procedure will be described next.

4.7 HIGH-FREQUENCY LOGGING SYSTEM RESULTS ANALYSIS

The culmination of the experimental investigation is the transfer of the sampled data from the high-frequency logging system for the subsequent manipulation thereof to yield the anticipated results.

The PC-based program specifically written to read, manipulate, correct and extract the maximum cylinder pressure cycle will be described in the sections that follow.

4.7.1 CYLINDER PRESSURE PROGRAMME

Because of the high sampling rate of the high-frequency logging system, as described in Section 4.4.2, reading and manipulation of the generated data was simply not possible using available spread sheet packages, owing to the vast number of entries. In total, 1.25 million data points were generated per channel, for an equivalent five-second run, and a bespoke program had to be written. The structure of the program is best understood by referring to the flow chart in Figure 4.13 below.

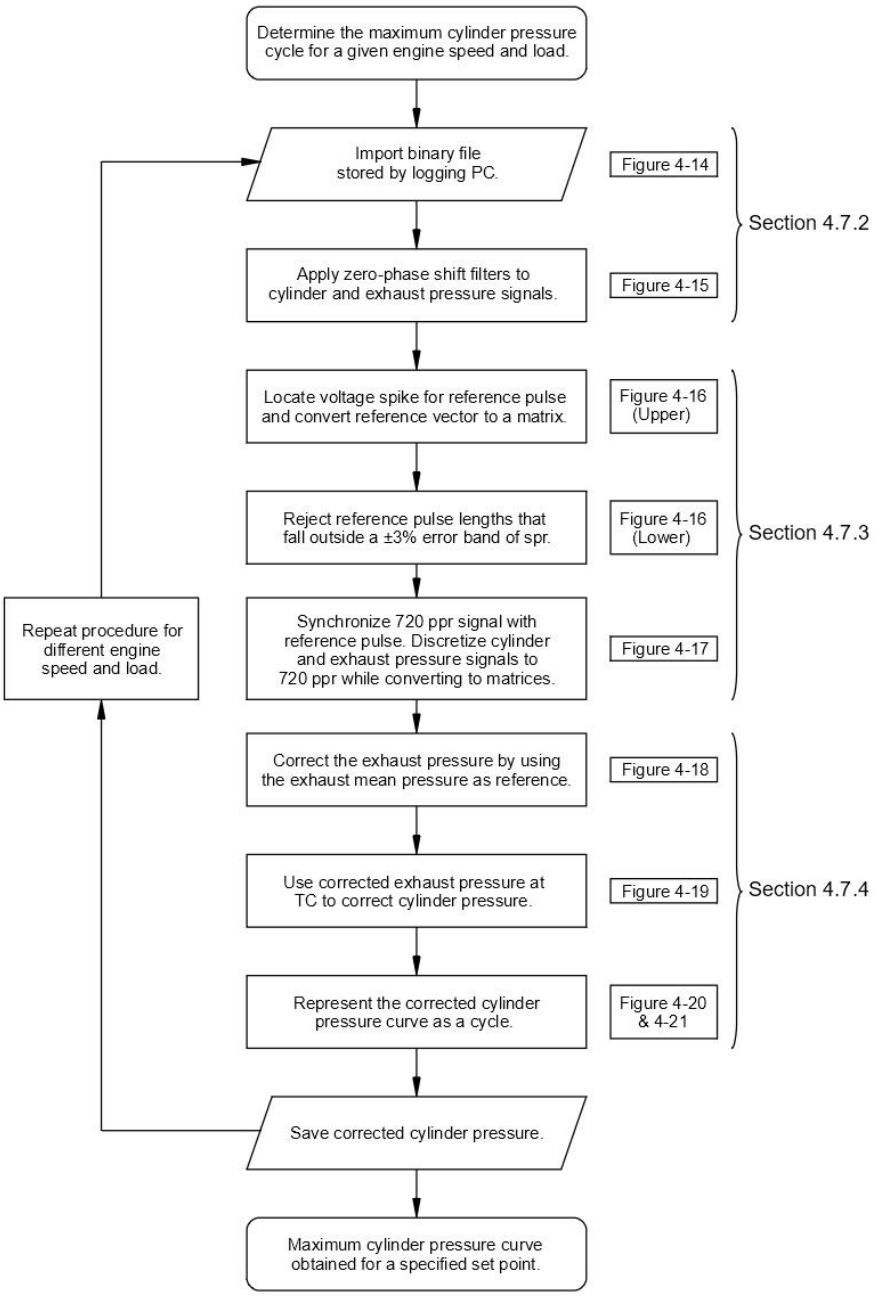

FIGURE 4.13: FLOW CHART OF MATLAB PROGRAM TO EXTRACT THE MAXIMUM CYLINDER PRESSURE CYCLE FOR A SPECIFIED ENGINE SPEED AND LOAD.

A scientific and engineering package called Matlab by The MathWorks was selected as the software capable of reading and manipulating the data recorded by the high-frequency logging system. The goal of the program was to isolate the cylinder pressure cycle that attained the greatest peak combustion pressure, since this would result in the highest internal forces within the structure of the engine. This specific cylinder pressure and important related attributes would then be saved and used in future programs. This is to be detailed in Chapter 5.

The program structure has been broken up into three sections, as can be seen in Figure 4.13. The functioning of each will be described and illustrated by figures in the sections that follow. The entire program written to determine the maximum cylinder pressure cycle can be found in Appendix G.1.

4.7.2 EXPERIMENTAL DATA

The P_b output of the engine is a product of both T and ω. To increase T, P must be increased as defined by Eq. (3.31) and maximum P is generated when p, as defined in Eq. (3.26), is greatest when at full throttle. Secondly, ω can be raised and lowered, in so doing proportionally altering P_b. All testing was thus conducted at full throttle, at eight speed set points in 500 rpm increments, beginning at 3000 rpm and ending with 6500 rpm.

Firstly, the binary file stored by the logging PC for a specified set point was imported and all four recorded channels, as yet unfiltered, are displayed in Figure 4.14. All the figures that follow in this section illustrate the engine when tested at full throttle and 5500 rpm.

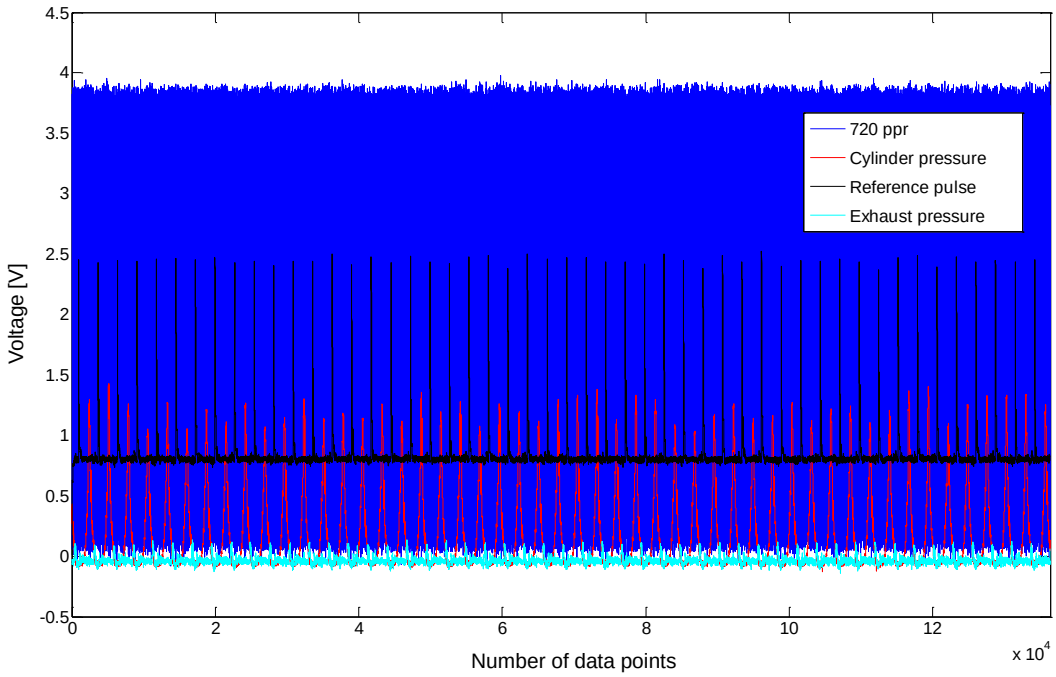

FIGURE 4.14: OUTPUT VOLTAGE OF ALL FOUR CHANNELS UNFILTERED AS FUNCTION OF NUMBER OF DATA POINTS FOR 50 CYCLES AT 5500 RPM.

The filtering of both the cylinder and exhaust pressure signals was next, by designing a low-pass, fourth order Butterworth filter with a cut-off frequency of 1.375 kHz. A zero–phase shift digital filtering technique in Matlab, called 'filtfilt', was used. The reference pulse and the 720 ppr signals were not filtered, since no wave content was of interest, only the high-voltage peaks.

Figure 4.15 illustrates five cycles output voltage for all four channels, upper left. The filtered cylinder and exhaust pressure signals are displayed in the right column and the reference pulse in the lower left corner. For the sake of clarity, the densely populated 720 ppr signal is not illustrated, but oscillates about +2 V, producing 720 complete square waves per revolution.

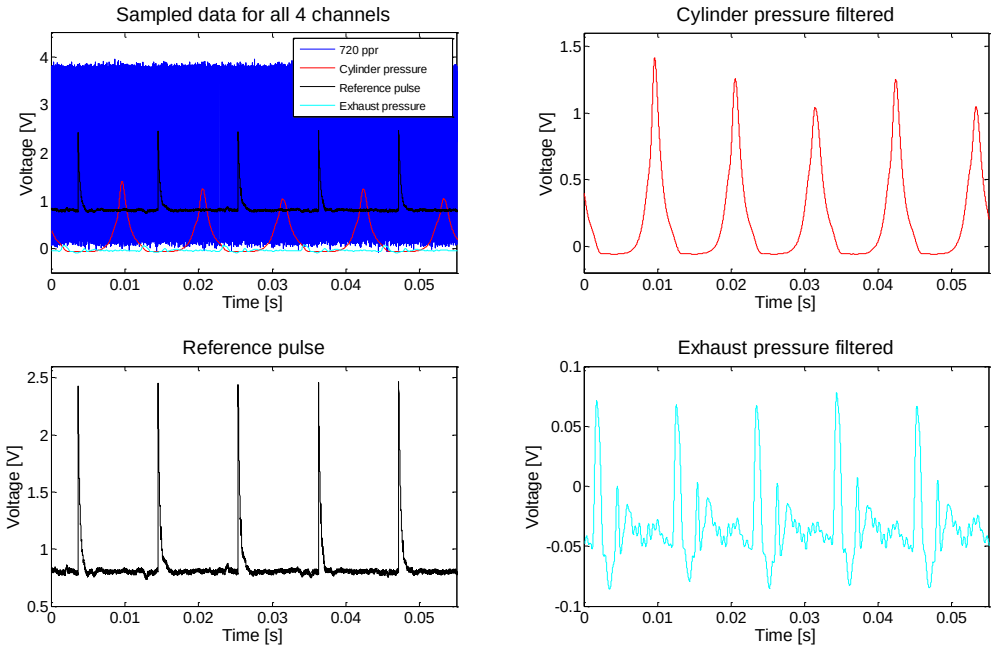

FIGURE 4.15: SAMPLED DATA FOR ALL AND INDIVIDUAL CHANNELS AS FUNCTION OF TIME FOR FIVE CYCLES AT 5500 RPM.

4.7.3 DATA MANIPULATION

The precise location of the voltage spike, clearly visible in the reference pulse plot displayed in Figure 4.15, was important, since this indicated BDC from one revolution to the next, as described in Section 4.4.2.

To detect the voltage spike, the slope of the curve between two adjacent sample points had to be steeply positive and with the first and second sampling points below and above 2 V respectively. With all the BDC *index* location points known, the reference pulse vector was converted to a matrix, to allow the analysis of individual cycles. The upper plot of Figure 4.16 illustrates the result. The horizontal axis indicates the number of sample points per revolution (spr) and this is calculated with the engine running at 5500 rpm and the sampling rate fixed at 250 kHz per channel; the theoretical spr is thus 2727.27, rounded to 2727. Any reference pulse that did not comply with a theoretical spr error band criterion of ±3% was discarded. The reconstructed reference pulse is displayed in the lower plot of Figure 4.16.

The 720 ppr signal was then synchronised with that of the reference pulse *index* location points, so that the start and end of the 720 square wave cycles had the same *index* location points (BDC) as those of the reference pulse. In practice, the error was never more than a single spr, or an equivalent time span of 4 µs at 5500 rpm.

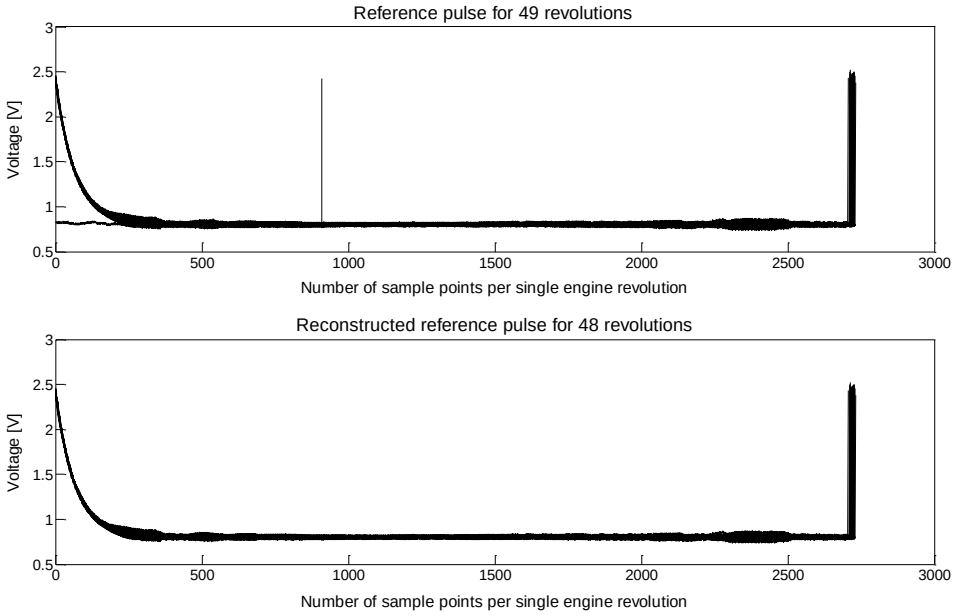

FIGURE 4.16: REFERENCE AND RECONSTRUCTED REFERENCE PULSE VOLTAGE AS FUNCTION OF SAMPLE POINTS AT 5500 RPM.

All four input vector signals were then discretised to 720 ppr and converted to matrices of 720 rows with each new column initiated by a BDC *index* point. Each row entry corresponded to a positive vertical voltage spike of the 720 ppr signal, representing a ½° of crankshaft revolution.

The upper plot of Figure 4.17 represents all the columns/revolutions of the newly created cylinder pressure matrix, while the lower plot illustrates the cycle that attained the greatest peak cylinder pressure.

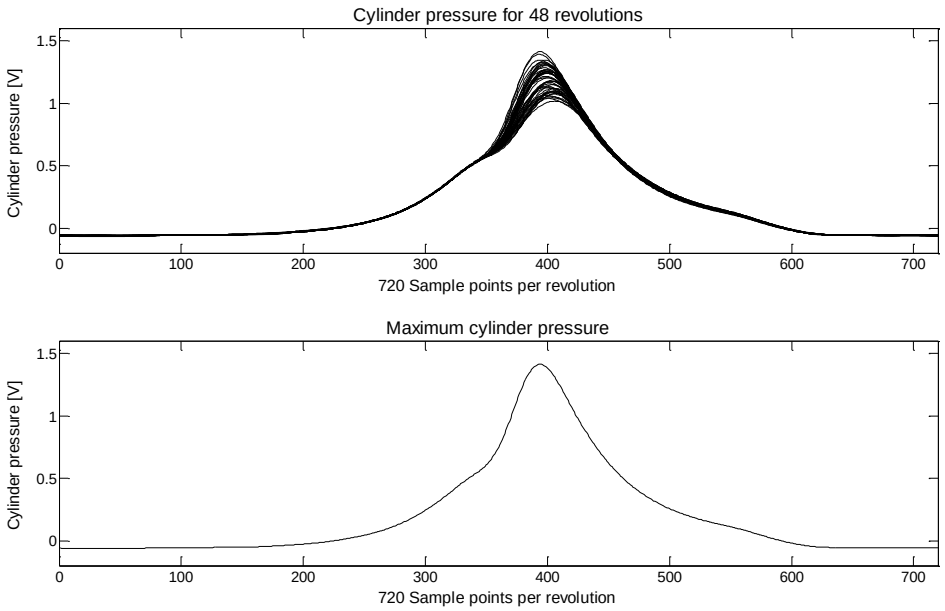

FIGURE 4.17: CYLINDER AND MAXIMUM CYLINDER PRESSURE CURVE AS FUNCTION OF 720 SAMPLE POINTS AT 5500 RPM.

4.7.4 SIGNAL CORRECTION

As stated in Section 4.5.5, there was no alternative but to use a Kistler piezo-electric pressure transducer for the exhaust pressure and the signal correction thereof is illustrated in Figure 4.18.

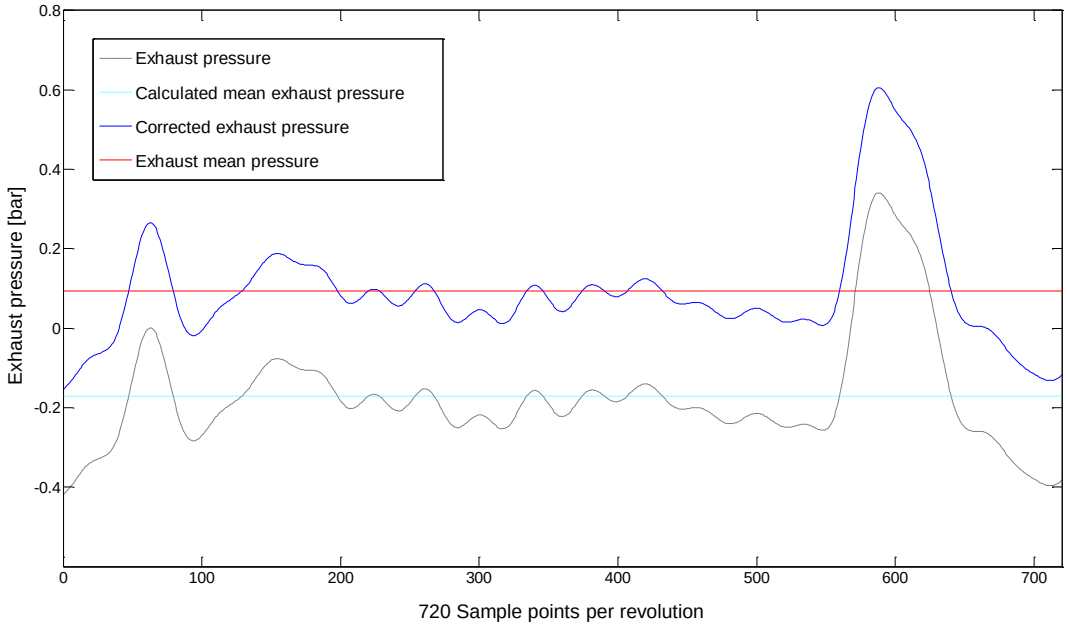

FIGURE 4.18: CORRECTED EXHAUST PRESSURE AND ADJUSTMENT CURVES AS FUNCTION OF 720 SAMPLE POINTS AT 5500 RPM.

In order for the exhaust pressure correction procedure to commence, the Y-axis voltage scale had to be converted to pressure. Each Kistler measuring spark plug is calibrated by the factory and this calibration factor converts output voltage to pressure.

The exhaust pressure cycle that corresponds to the maximum cylinder pressure, as illustrated in the lower plot of Figure 4.17, is illustrated in the figure above by black dashes. The calculated mean exhaust pressure is the average of the 720 data points of the exhaust pressure; this value is graphically represented by a cyan dashed horizontal line. The difference of 0.265 bar between the exhaust mean pressure represented by a horizontal red line and the calculated mean exhaust pressure is used to shift the exhaust pressure upward to become the corrected exhaust pressure plotted in blue.

The corrected exhaust pressure is then used to correct the cylinder pressure, as displayed in Figure 4.19. In four-stroke engines, the pressure in the inlet plenum at the moment of inlet valve closure is used as the reference pressure for the correction of the cylinder pressure. However, this method is not feasible for two-stroke engines, since cylinder induction occurs via the crankcase and not the intake system. The most appropriate moment to equate the corrected exhaust pressure in red to the cylinder pressure in black was selected as TC. This required that the cylinder pressure be raised by 1.172 bar, as displayed by the corrected cylinder pressure in blue.

To equate the exhaust and cylinder pressures at EC is not feasible, since very intense pressure waves can be present in a tuned exhaust system, as described in Section 2.2.1, and this would consequently distort the correction factor.

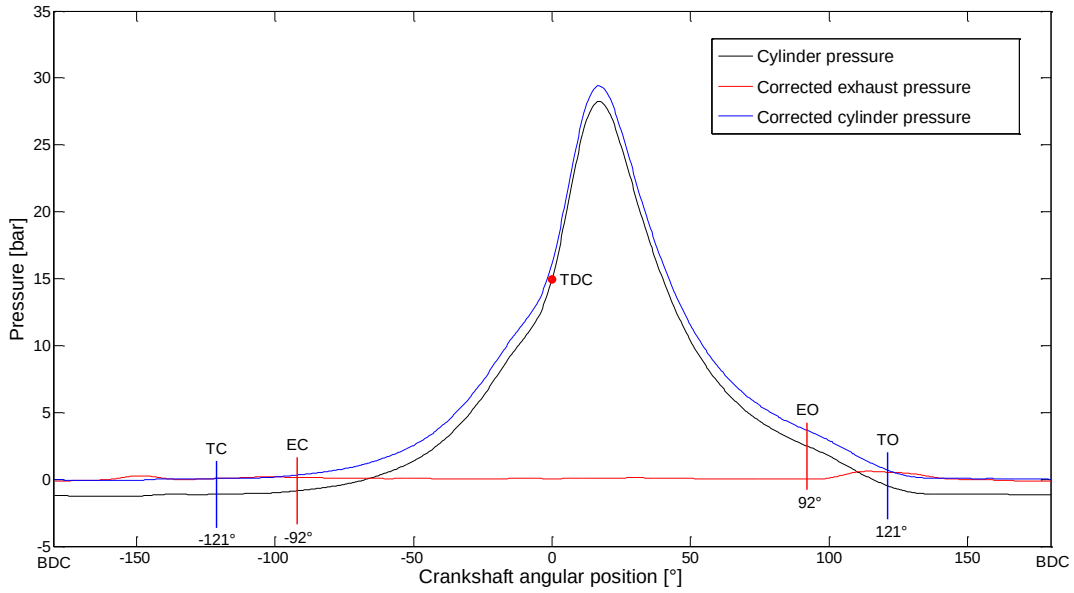

FIGURE 4.19: CORRECTED CYLINDER AND EXHAUST PRESSURE CURVES AS FUNCTION OF CRANKSHAFT ANGULAR POSITION AT 5500 RPM.

Figure 4.20 plots the corrected cylinder pressure, now again referred to as the cylinder pressure, as a function of a single crankshaft revolution, denoted in angular position, while Figure 4.21 plots the p-V diagram as displayed in Figure 3.7 for comparative purposes.

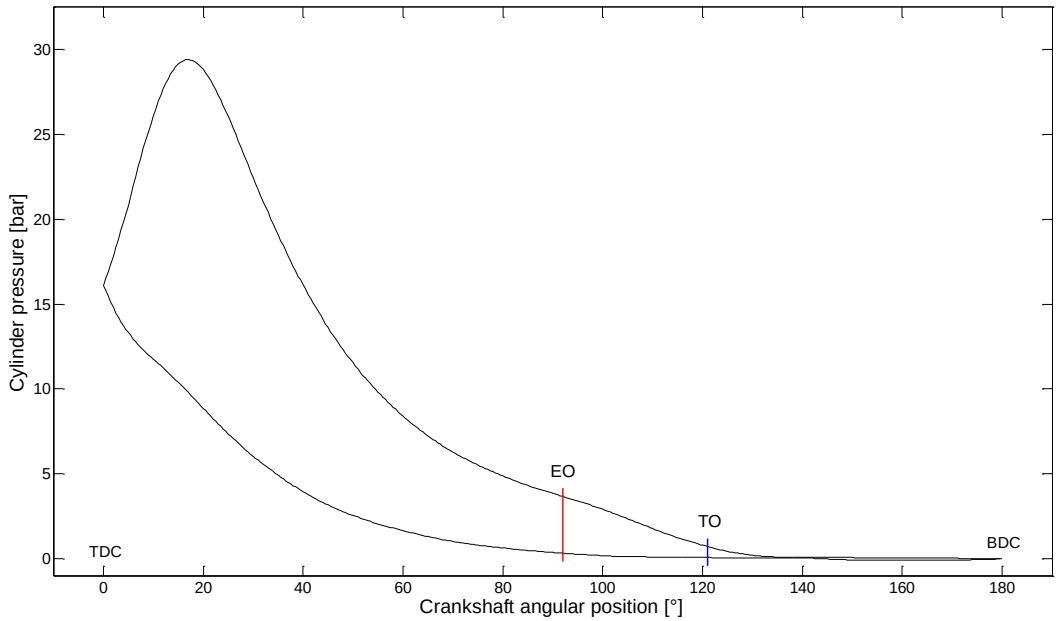

FIGURE 4.20: CYLINDER PRESSURE AS FUNCTION OF CRANKSHAFT ANGULAR POSITION AT 5500 RPM.

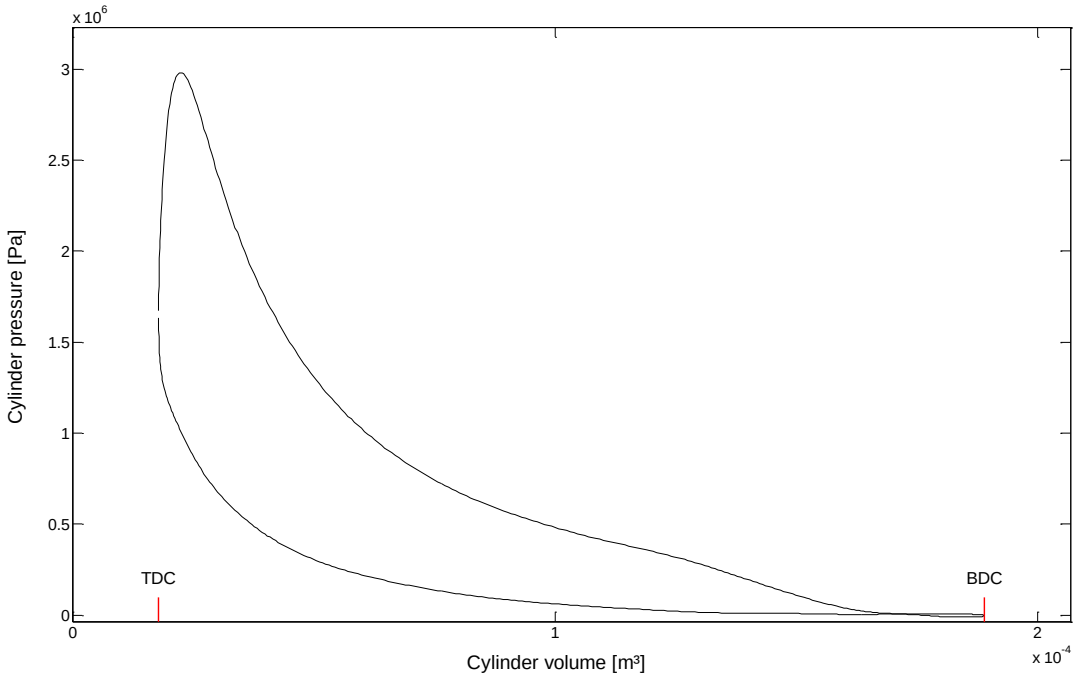

FIGURE 4.21: P-V DIAGRAM.

The proposal stipulated in Section 4.1 has been achieved by obtaining p with respect to θ for any desired engine speed and load.

These experimental results are now carried over to Chapter 5 to be used in conjunction with the theory of Chapter 3 to design the required aspects of the engine theoretically.

5 THEORETICAL UAV ENGINE DESIGN

A detailed design of the entire engine or substantial parts thereof will not be attempted in this chapter for reasons stated in the introduction. Instead, the theory defined in Chapter 3 will be used to construct a suitable engine model.

In this chapter the engine configuration will be described, the design brief and objectives reiterated and the engine specifications defined. The forces and couples generated by the firing reciprocating engine mechanism, combined with the balancing of the rotational and reciprocating system, will ultimately be summed to yield the engine forces and couples.

5.1 UAV ENGINE DESIGN SYNOPSIS

It is imperative before the initiation of any project, that the design objectives and constraints are clearly communicated and understood. The design brief, the implicit design parameters and the resultant engine specifications will be outlined in the sections that follow.

5.1.1 UAV ENGINE DESIGN OBJECTIVES

The design brief is to provide propulsion for a UAV, typically using a 500 cc sized engine with the following fundamental parameters:

- A two-stroke cycle, SI engine has been stipulated, thus minimising engine complexity and weight.
- A two-cylinder engine is specified to increase the overall engine displacement.
- The horizontally-opposed cylinder configuration can better accommodate aircraft fuselage profiles, improve engine balance and will ensure adequate cooling for both cylinders.
- An air-cooled engine ensures simplicity and lower weight when compared to liquid-cooled equivalents.

The design objectives for the UAV engine, as stated in Section 1.3, are the following:

- Make use of as many suitable, commercially available engine parts as possible in critical areas, thus minimising design effort.
- While reliability is important, the longevity of the engine is not to be a primary design focus.
- Maximum power and minimum weight for this class of engine are not paramount, since this design is considered a prototype.
- The cost of the commercial items and manufacture of designed engine components is to be kept as low as possible.

Since commercial parts are to be used in the design, it is essential to select a suitable engine early in the design that will act as the donor and to identify all the parts that will be incorporated. As stated in Section 4.2, the engine characteristics of the Yamaha DT 175 test engine had to be similar to that of the UAV engine in order for the experimental data obtained in Chapter 4 to be of use. The maximum capacity, two-stroke, air-cooled engine with similar characteristics that can easily be obtained is the Yamaha YFS 200 Blaster, a quad-bike engine with V_d of 195.01 cc, producing P_b of 15 kW at 7000 rpm. Weight is always carefully monitored in aeronautical applications and by using motorbike components it is anticipated that the engine parts selected will exhibit a higher power-to-weight ratio than automotive equivalents.

The most important parts that will be incorporated into the design are four critical engine components, as stated in Section 1.5, namely the:

- Cylinder assembly
- Piston assembly
- Connecting rod assembly
- Cylinder head

The remaining two engine components of the six described in Section 2.3, which will have to be designed to suit the proposed engine configuration, are the:

- Crankshaft
- Crankcase

The main theoretical objective of this dissertation is to calculate the forces and couples applied to both the crankshaft and crankcase throughout the engine speed range and then to determine the greatest force component in both magnitude and direction at all the specified loading points/areas. Ultimately, this data will serve as load input for an FEA model and the two designed parts can then be structurally optimised using this technique, but this, as stated in the introduction, is beyond the scope of this dissertation. The connecting rod ends' rubbing velocities and the crankshaft rotational speed fluctuation are also investigated.

The use of commercially available engine parts is also extended to the engine systems, as described in Section 2.4, wherever possible. However, a detailed explanation of the engine systems and the commercial parts incorporated will be left for the practical design of the UAV engine as described in Chapter 6.

5.1.2 UAV ENGINE DESIGN PARAMETERS

In order to achieve the theoretical design objectives stated in Section 5.1.1, the theory derived in Sections 3.2 to 3.10 will be applied, ***in the same sequence***, but now with the independent variables substituted by the UAV engine specifications combined, where required, with the experimental results obtained in Chapter 4 to yield the theoretical UAV engine design parameters.

As in Section 4.7, the graphs plotting a dependent variable as a function of crankshaft angular position (θ) will for illustrative purposes also be at N_c = 5500 rpm (ω = 575.96 rad/s, rounded to 576 rad/s). The maximum value/s obtained per revolution at this crankshaft rotational speed will be displayed. For selected sections, the maximum values achieved throughout the engine speed range will also be plotted, if considered informative.

To assist in achieving the stated theoretical design objective, a separate Matlab program was written for Sections 5.2 to 5.10, which can be found in Appendix G.2. The structure of this program is less complex than the cylinder pressure program used in Chapter 4 and the methodology employed will be restricted to the following points:

- For a selected set point, the maximum cylinder pressure curve obtained in Chapter 4 for that engine speed is imported into the program, to be used as required.
- All the required UAV engine specifications are entered and, using the applicable reciprocating engine theory of Sections 3.1 to 3.10, the required maxima and graphs for the same eight speed set points beginning at 3000 rpm and ending at 6500 rpm, in 500 rpm increments, are generated.
- At the end of the program, the maxima of interest are all exported to a Microsoft Excel spread sheet as tabulated in Appendix C.1.

After the identification of the Yamaha YFS 200 Blaster and the engine components that are to be incorporated into the UAV engine, the specifications of the proposed engine follow.

5.1.3 EXPERIMENTAL ENGINE SPECIFICATIONS

The UAV engine specifications will subsequently be documented using the equations defined in Section 3.1 as required, before commencing with the applicable reciprocating engine theory of Sections 3.2 to 3.10, since all the required engine data must first be known.

The four Yamaha Blaster engine components that are to be used as stipulated in Section 5.1.1 provide most of the required data. Since the donor cylinder/piston assembly relies on the stroke length of the original crankshaft in order to function correctly, as described in Section 2.2.1, this is thus retained. The UAV engine specifications can be found in Table 5.1 below.

TABLE 5.1: UAV ENGINE SPECIFICATIONS.

UAV Engine Layout and Systems		
Engine type		CAE UAV engine
Cycle		Two-stroke
Engine configuration		Horizontally-opposed
Cooling		Air
Fuel system		Fuel-injection
Ignition system		ECU
Induction system		ETC and reed valves
Lubrication system		Premix
Exhaust system		Un-tuned
Final drive output		Direct drive propeller
UAV Engine Geometric Properties		
Number of cylinders	n	2
Bore	B	66.00 mm
Stroke	L	57.00 mm
Crank radius	a	28.50 mm
Ratio of bore to stroke	R_{bs}	1.16
Piston crown projected area	A_p	3.42 x 10^{-3} m^2
Engine displacement	V_{dt}	390.02 cc
Displaced cylinder volume	V_d	195.01 cc
Clearance volume	V_c	20.33 cc
Geometric compression ratio	r_{cg}	10.59
Connecting rod length	l	110.00 mm
Connecting rod length from big-end to CG	l_{cg}	45.00 mm
Ratio of connecting rod length to crank radius	R	3.86
Diameter of crank pin	d	22.00 mm
Diameter of piston pin	d_p	16.00 mm
Total rotational inertia	J_r	27.30 x 10^{-3} kgm^2

The specification omissions are r_{ct}, EO, TO, P_b and T_{mb}. The first three values require the assembled engine, so that physical measurements can be taken, and the last two values are predicted in the sections that follow. The exception is V_c; this parameter is required and is estimated by scaling from the value obtained in Table 4.1 for the Yamaha DT 175. Clarification with respect to the tabulated engine systems will be developed further in Chapter 6.

Note the following: for the inertia forces to counteract one another in a horizontally-opposed, two-cylinder engine, the crankshaft configuration requires a 180° crank pin offset from one another. This, however, results in the simultaneous firing of both cylinders for a two-stroke engine, producing a single torque pulse per revolution.

The first of the engine design parameters to be detailed using the engine specifications above is the UAV engine mechanism kinematics.

5.2 TWO-CYLINDER ENGINE MECHANISM KINEMATICS

With the required equations of the mechanism kinematics derived in Section 3.2, the first of the engine design parameters can be calculated and plotted.

The s, v_p and a_p are defined by Eq. (3.10), (3.11) and (3.12) respectively. After substitution of the appropriate values tabulated in Table 5.1 with ω = 576 rad/s (N_c = 5500 rpm), θ is swept through a complete revolution starting at 0° (TDC) and Figure 5.1 is obtained.

The maximum s, v_p and a_p are 57.00 mm at 180°, 16.96 m/s at 76.5° and 11.9 km/s^2 at 0° respectively. The maximum s remains 57.00 mm for any N_c, whereas an increase in ω generates a linear and quadratic increase in v_p and a_p respectively. Irrespective of ω, maximum v_p and a_p always occur at 76.5° (283.5°) and 0° respectively, as tabulated in Appendix C.1.

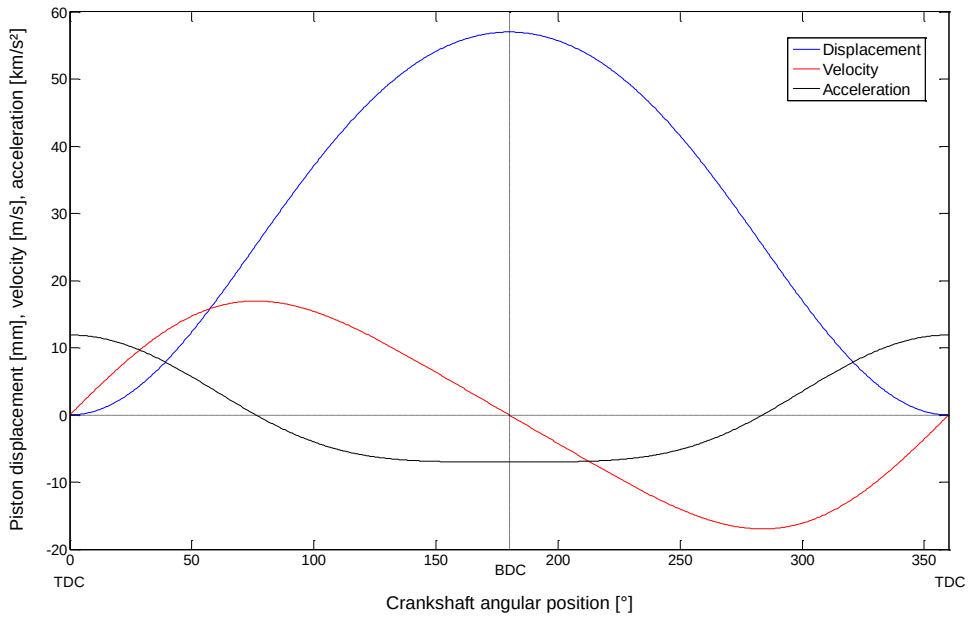

FIGURE 5.1: PISTON DISPLACEMENT, VELOCITY AND ACCELERATION AS FUNCTION OF CRANKSHAFT ANGULAR POSITION AT 5500 RPM.

5.3 UAV CONNECTING ROD ENDS' RUBBING VELOCITIES

Aspects of the dual rotary and reciprocating motion experienced by the connecting rod are described by Ω, v_{rp} and v_r, as defined by Eq. (3.14), (3.16) and (3.17) respectively.

The crankshaft rotates at a constant ω = 576 rad/s for an entire revolution, as illustrated by the blue horizontal line in the upper plot, titled angular velocity, in Figure 5.2. By comparison the Ω denoted by the red curve oscillates about ω. When θ = 90° and 270° both ω and Ω are equal. This corresponds with the moment that the connecting rod oscillation about the piston pin alters direction.

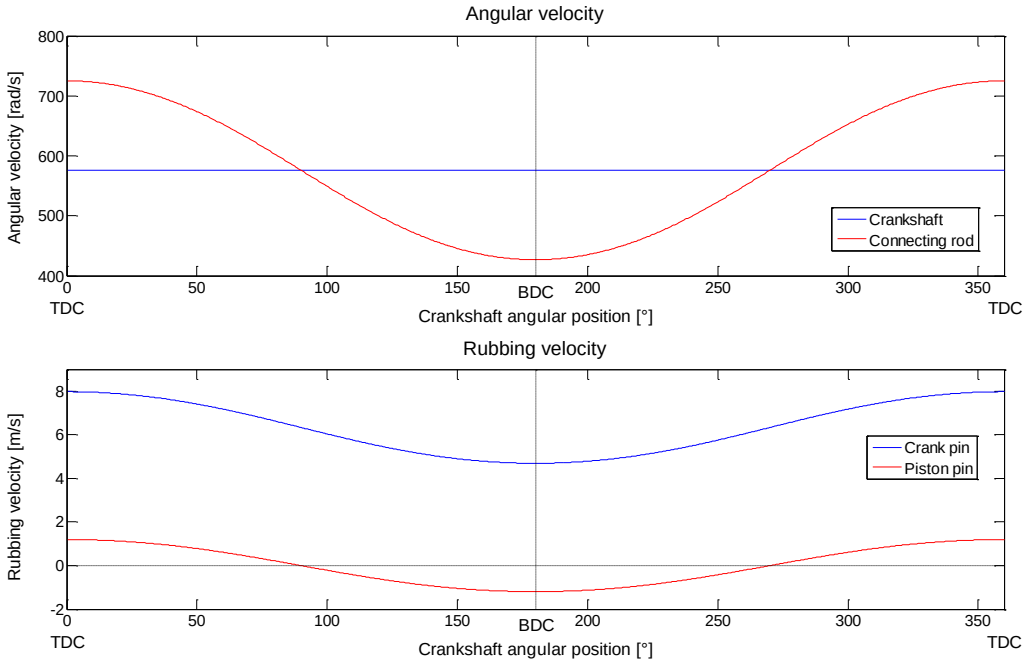

FIGURE 5.2: ANGULAR VELOCITY OF CRANKSHAFT AND CONNECTING ROD WITH RUBBING VELOCITY OF CRANK PIN AND PISTON PIN AS FUNCTION OF CRANKSHAFT ANGULAR POSITION AT 5500 RPM.

The lower plot, titled rubbing velocity, illustrates v_r and v_{rp} curves plotted in blue and red respectively. The v_{rp} fluctuates about zero with the alteration in the sign of the Y-axis corresponding to a change in direction of the connecting rod oscillation. The v_r oscillates in phase with the v_{rp} about a mean of 6.34 m/s; however, always retaining a positive rubbing velocity.

5.4 UAV ROTATIONAL AND RECIPROCATING MASS ALLOCATION

The mass allocation is the sum of all the rotating and reciprocating components as defined by Eq. (3.20) and (3.21) respectively.

With m_{cr} = 139.77 g and substituting the appropriate values as listed in Table 5.1 into Eq. (3.18) and (3.19), the connecting rod mass distribution is m_b = 82.59 g and m_s = 57.18 g. Thus 59.1% and 40.9% of m_{cr} are assigned to the big- and small-ends respectively.

For this UAV engine, m_r comprises the single crankshaft assembly and additional big-end associated masses for both cylinders, as listed in Table 5.2 on the following page.

TABLE 5.2: SUM OF ALL ROTATIONAL MASSES.

ROTATIONAL MASS COMPONENTS				
Item	**Symbol**	**Mass of Item [g]**	**Quantity**	**Mass Totals [g]**
Mass of crankshaft and flywheel	m_c	3681.80	1	3681.80
Mass of big-end washer	m_w	5.46	4	21.84
Mass of big-end bearing	m_{be}	21.97	2	43.94
Mass allocated to big-end	m_b	82.59	2	165.18
Total rotational mass component (m_r)				**3912.76**

The m_o is the sum of all the components required to complete a single piston assembly as tabulated in Table 5.3.

TABLE 5.3: SUM OF ALL RECIPROCATING MASSES FOR A SINGLE PISTON ASSEMBLY.

RECIPROCATING MASS COMPONENTS				
Item	**Symbol**	**Mass of Item [g]**	**Quantity**	**Mass Totals [g]**
Mass of piston	m_p	192.98	1	192.98
Mass of piston rings	m_{pr}	4.03	2	8.06
Mass of piston circlips	m_{pc}	0.28	2	0.56
Mass of piston pin	m_{pp}	44.97	1	44.97
Mass of small-end bearing	m_{se}	18.07	1	18.07
Mass allocated to small-end	m_s	57.18	1	57.18
Total reciprocating mass component (m_o)				**321.82**

5.5 UAV PISTON AND CONNECTING ROD FORCES

The forces transferred to and by the piston on the cylinder wall, connecting rod and bearings are due to the p generated by combustion. The experimental results obtained in Chapter 4 will subsequently be used to calculate these forces.

The maximum cylinder pressure curves obtained with the Yamaha DT 175 test engine at full throttle from 3000 rpm, in 500 rpm increments, to 6500 rpm are illustrated in Figure 5.3 with key observations applicable to all eight curves as follows:

- The gradual increase in p from 92° before top dead centre (BTDC) occurs at EC, signifying the start of mixture compression.
- The initiation of combustion is indicated by the sharp increase in the positive slope of p, occurring between 10° BTDC and TDC.
- Despite the increase in cylinder volume, p continues to rise ATDC due to combustion.
- After 92° ATDC there is a slight increase in the negative slope of p. This corresponds with EO and the subsequent accelerated drop in p.
- The gas exchange processes occurring between TO at 121° and TC at -121° are too low in magnitude to be observed in this figure.

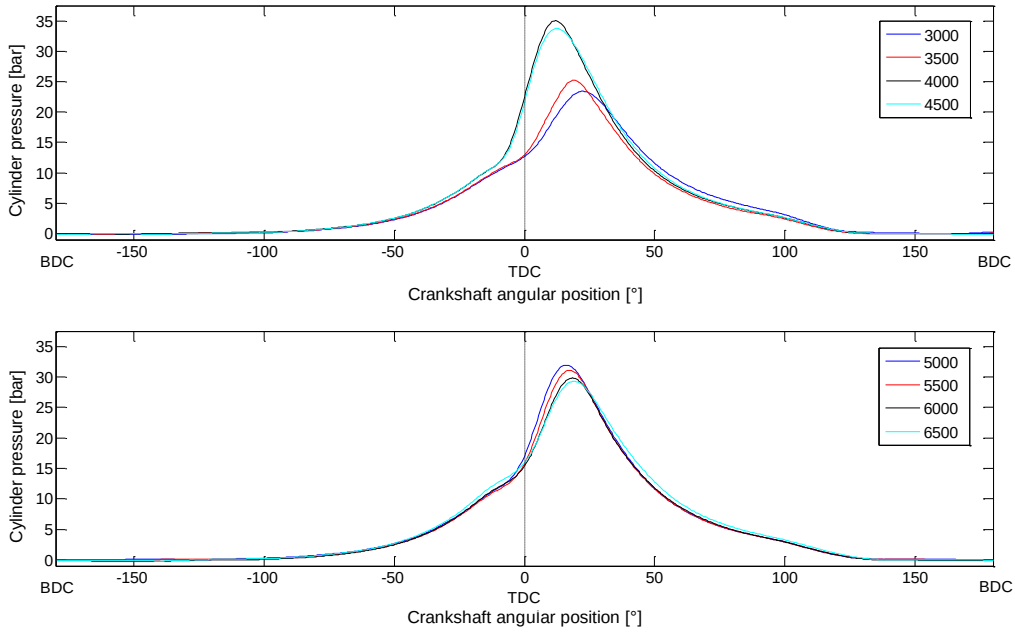

FIGURE 5.3: MAXIMUM CYLINDER PRESSURE CURVES OBTAINED ON THE YAMAHA DT 175 AT FULL THROTTLE IN 500 RPM INCREMENTS FROM 3000 RPM TO 6500 RPM AS FUNCTION OF CRANKSHAFT ANGULAR POSITION.

Figure 5.4 below illustrates the magnitude and associated θ of the cylinder pressure peaks obtained in Figure 5.3 and is of interest because of the main theoretical objective stated in Section 5.1.1.

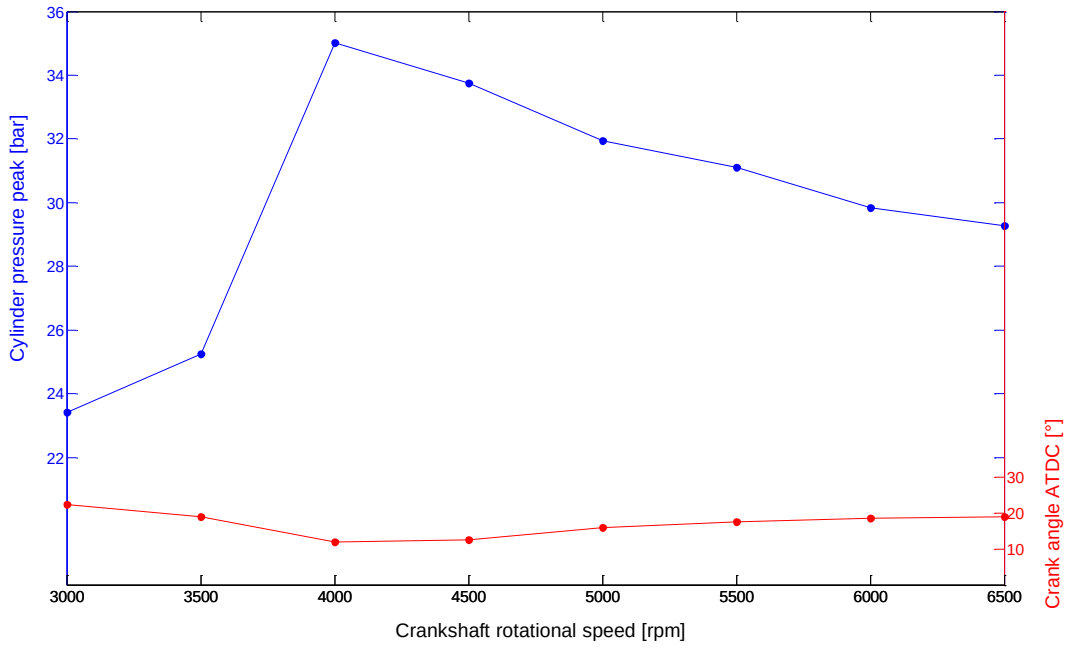

FIGURE 5.4: CYLINDER PRESSURE PEAKS AND ASSOCIATED CRANK ANGLE ATDC OBTAINED EXPERIMENTALLY AS FUNCTION OF CRANKSHAFT ROTATIONAL SPEED.

The highest and lowest cylinder pressure peaks obtained are 35.02 bar at 4000 rpm and 23.77 bar at 3000 rpm respectively. The θ corresponding to the cylinder pressure peak varies with each N_c. An average value of θ = 17.1° ATDC is achieved.

Figure 5.5 illustrates the F_g, F_i and P exerted on the piston as defined by Eq. (3.27), (3.28) and (3.26) respectively for a single revolution at 5500 rpm. Before the p curves illustrated in Figure 5.3 can be used, the θ must first be rearranged so that the pressure traces start at 0° (TDC) and end at 360° (TDC).

The blue F_g curve mimics the trend of the red p curve at 5500 rpm in Figure 5.3, but now plotted as a force due to the multiplication by A_p.

The red F_i curve illustrates the m_o calculated in Table 5.3, multiplied by a_p as plotted in Figure 5.1. The F_i curve follows the same trajectory as a_p, now mirrored about the X-axis.

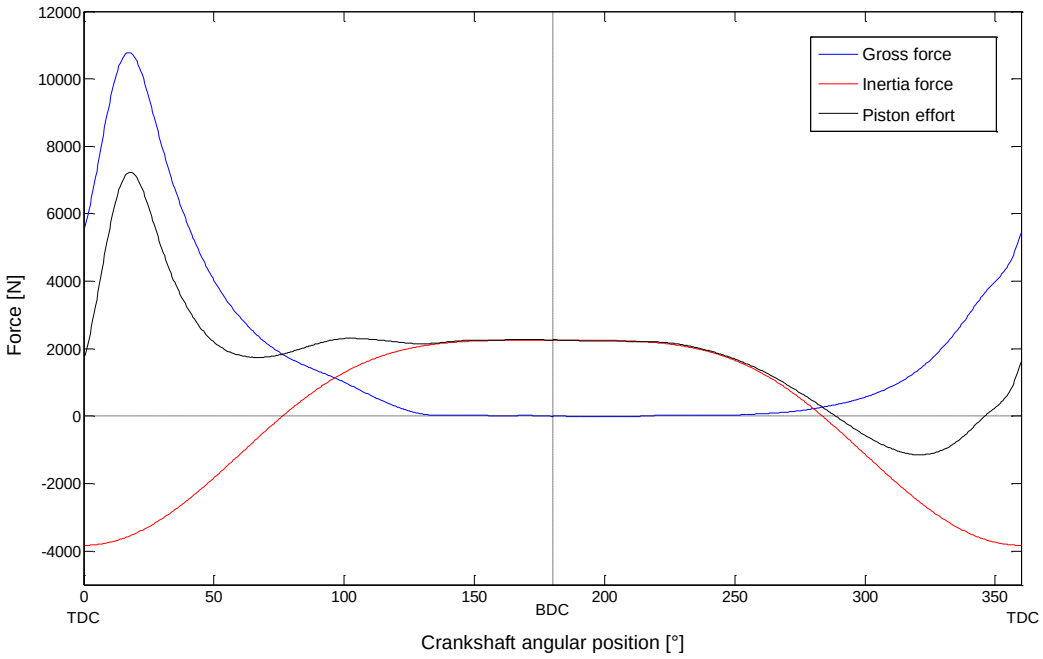

FIGURE 5.5: PISTON GROSS FORCE, INERTIA FORCE AND PISTON EFFORT AS FUNCTION OF CRANKSHAFT ANGULAR POSITION AT 5500 RPM.

The P illustrated in black is the sum of both F_g and F_i and the following can be noted:

- The P available from TDC to 76.5° ATDC is lower in magnitude than F_g because of the F_i required to accelerate m_o.
- After 76.5° ATDC to BDC the F_i required to now decelerate m_o contributes to raising P above the available F_g.
- At BDC the stationary piston is again accelerated, now at a lower rate to 76.5° BTDC, and F_i is required. The negligible magnitude of F_g makes a minimal contribution to the sum of P.
- From 76.5 BTDC to TDC, m_o must again be decelerated, now at a higher rate, and the F_i required to do so contributes to the F_g required to compress the inducted mixture.

The difference in acceleration/deceleration rates at TDC and BDC is due to the geometry of the engine mechanism. Although not illustrated for other values of N_c, the P curve shape for an entire revolution can vary immensely, primarily owing to F_i.

The influence of F_i on P as a function of N_c is illustrated in Figure 5.6.

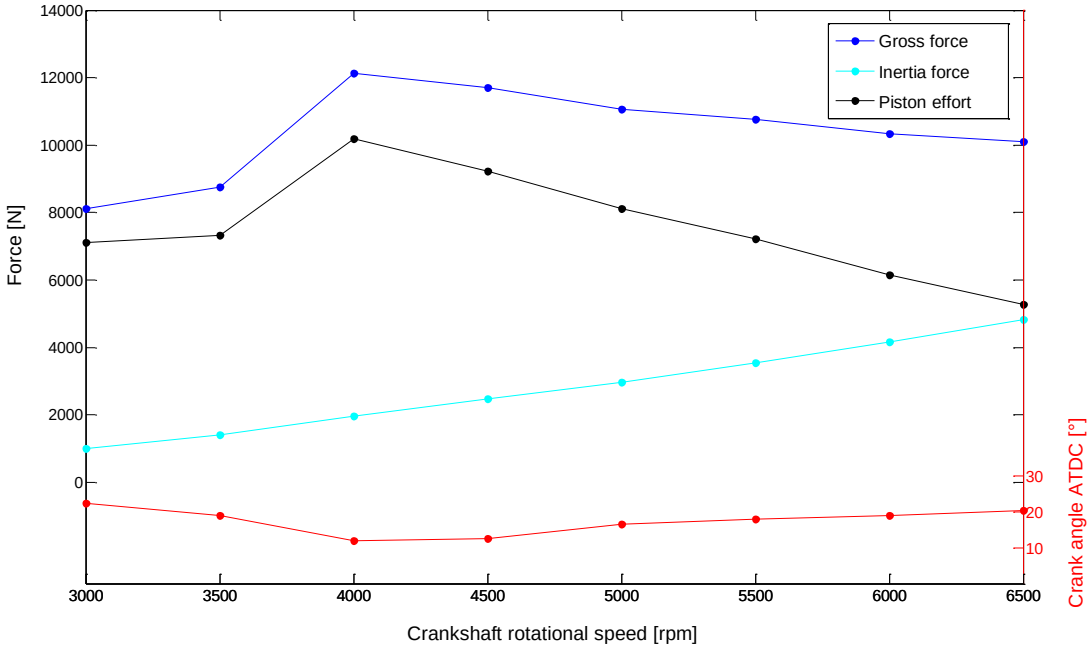

FIGURE 5.6: PISTON GROSS FORCE, INERTIA FORCE AND MAXIMUM PISTON EFFORT AT SPECIFIED CRANK ANGLE ATDC AS FUNCTION OF CRANKSHAFT ROTATIONAL SPEED.

The θ drawn in red is associated with the maximum P attained plotted in black and is likewise the reference point used for both the blue F_g and cyan F_i curves displayed above. The θ obtained differs slightly from that of Figure 5.4 for maximum p, since P is the sum of both F_g and F_i.

As stated for Figure 5.5, F_g now again mimics the p curve of Figure 5.4 because of the relationship exhibited in Eq. (3.27).

From 1005 N at 3000 rpm to 4623 N at 6500 rpm, the increase in the F_i requirements to accelerate m_o at the θ displayed above increases almost linearly with N_c.

The resultant decrease in P as N_c increases to 6500 rpm is evident from the graph. Note that this initial decrease in P is regained when m_o starts to decelerate 76.5° ATDC/BTDC.

Figure 5.7 illustrates the P curve obtained in Figure 5.5, now used to determine both Q and N, as defined by Eq. (3.23) and (3.24) respectively for a single revolution at 5500 rpm.

For the geometry of this engine mechanism, ϕ oscillates about 0° and ±15.02° for θ = 0° and ±90° respectively. This results in $Q = P$ and $1.035P$ when for θ = 0° and ±90° respectively, as illustrated by the red Q curve.

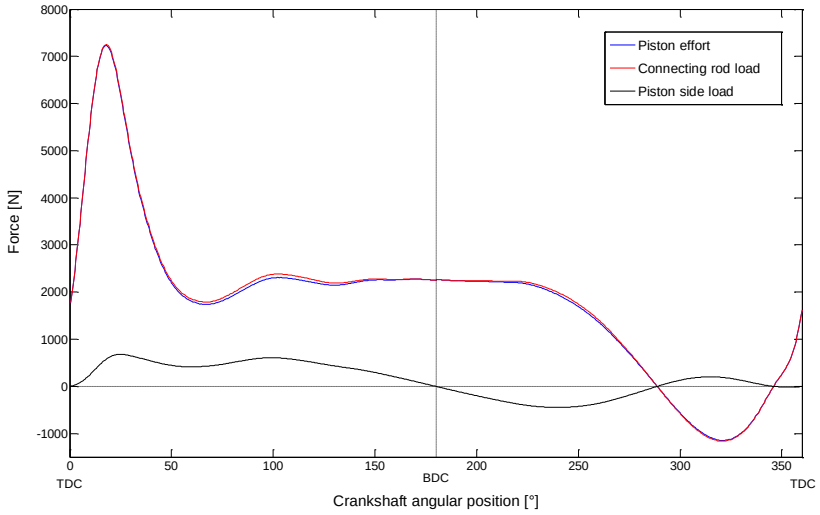

FIGURE 5.7: PISTON EFFORT, CONNECTING ROD LOAD AND PISTON SIDE LOAD AS FUNCTION OF CRANKSHAFT ANGULAR POSITION AT 5500 RPM.

Between θ = 0°and 180° both Q and ϕ are greater than zero, thus the resultant N curve as plotted in black acts against the cylinder wall in the direction illustrated in Figure 3.5 for the power stroke. From BDC to θ = 289° the N acts in the opposite direction and continues further to oscillate about zero, dependent on the sign of Q.

5.6 EXPERIMENTAL ENGINE MOMENT ARM AND OUTPUT TORQUE

The various force curves obtained in Section 5.5 will be used in combination with the CF to determine the engine torque and associated reaction couple.

Before the resultant torque curves are displayed, the CF for a complete revolution with acute and obtuse angles, as defined by Eq. (3.32) and (3.33) respectively, is plotted by the blue curve in Figure 5.8. The additional red curve is the Y-axis pin displacement when viewed along the X-axis in Figure 3.2.

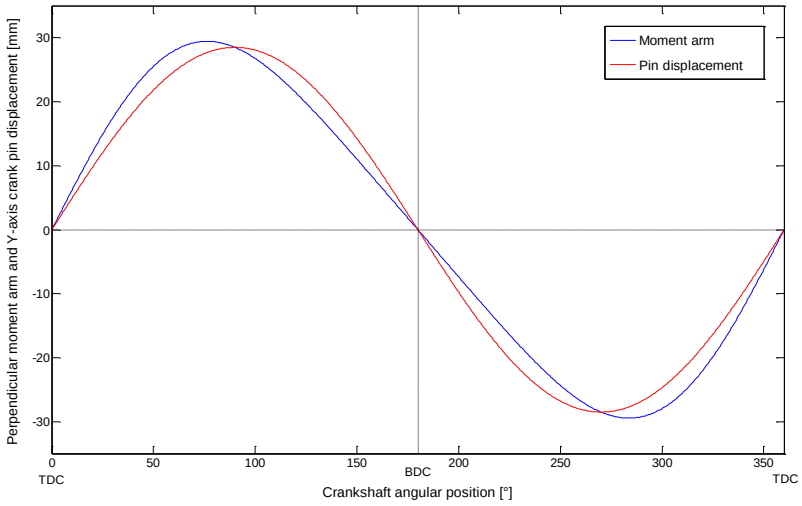

FIGURE 5.8: PERPENDICULAR MOMENT ARM AND Y-AXIS CRANK PIN DISPLACEMENT AS FUNCTION OF CRANKSHAFT ANGULAR POSITION.

The Y-axis crank pin displacement is a sinusoidal oscillation about the X-axis. The maximum Y-axis crank pin displacement of 28.5 mm occurs at 90° ATDC/BTDC and corresponds with a, as tabulated in Table 5.1.

The CF also oscillates about the X-axis with identical X-axis intercepts at 0°, 180° and 360°. The maximum CF = 29.44 mm is obtained when θ = 76.5° ATDC and BTDC. When compared to the Y-axis crank pin displacement, the CF curve initially has a steeper positive slope to 76.5°, followed by a gentler negative slope to 76.5° BTDC (283.5°).

Figure 5.9 plots the instantaneous T_g, T_i, T and average T_{mi} per cylinder as defined by Eq. (3.34), (3.35), (3.31) and (3.52) respectively for a single revolution at 5500 rpm.

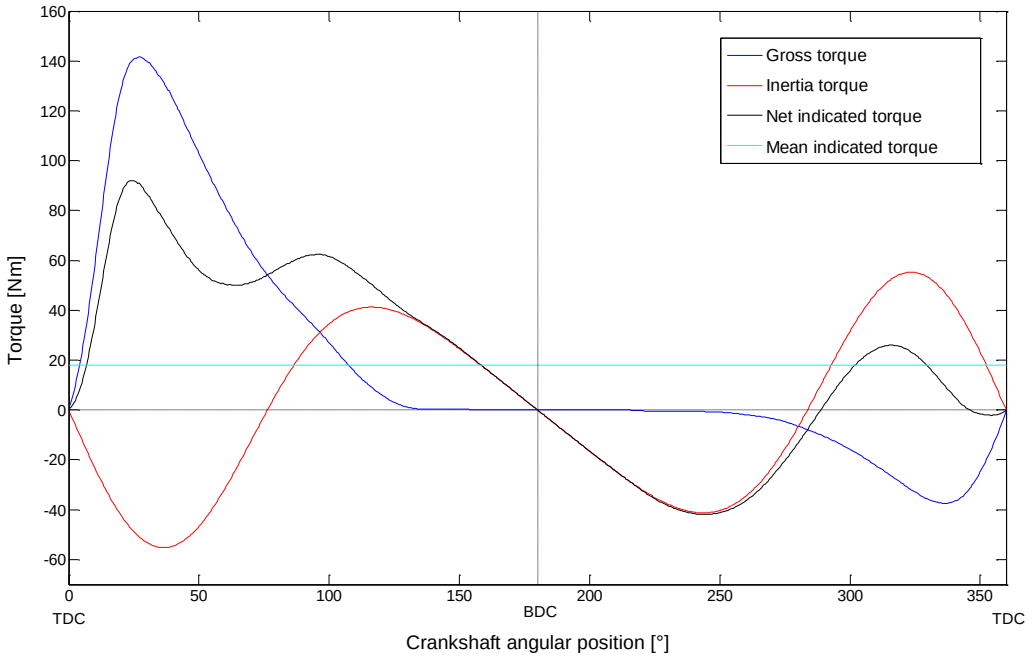

FIGURE 5.9: GROSS TORQUE, INERTIA TORQUE, NET INDICATED TORQUE AND MEAN INDICATED TORQUE PER CYLINDER AS FUNCTION OF CRANKSHAFT ANGULAR POSITION AT 5500 RPM.

All three instantaneous torque curves pass through zero at TDC and BDC. This result is expected, since CF is the second term present in all three equations and is also zero at both TDC and BDC, as illustrated in Figure 5.8.

The T_g, plotted in blue, has the following characteristics:

- From TDC to approximately 130° ATDC, T_g delivers positive driving torque due to the power stroke.
- When TC occurs at 239° (121° BTDC) the T_g required by the crankshaft steadily increases as mixture compression commences, decreasing to zero at TDC.

The T_i maps the torque required to accelerate and decelerate m_o, as described in Section 5.5 with regard to F_i, in summary:

- Negative T_i is required to accelerate m_o from TDC to 76.5° ATDC and again from BDC to 76.5° BTDC (283.5°).
- Inertia torque is added to the crankshaft when m_o decelerates from 76.5° ATDC to BDC and again from 76.5° BTDC to TDC.

The T is defined by Eq. (3.31) as stated and Eq. (3.36). By making use of the second equation, T_i is subtracted from T_g and T, as displayed by the black curve, is the result and the following can be noted:

- From TDC to BDC a positive T driving the crankshaft is present.
- From BDC to 289° ATDC torque is extracted from the crankshaft.
- From 289° ATDC to TDC, T oscillates about zero, providing mostly positive torque.
- Although not plotted for other values of N_c, the T curve profile can fluctuate considerably, since T is a function of P.

Although W_i will only be determined in the next section, it was considered informative to plot the cyan horizontal line illustrating T_{mi} per cylinder in this figure to illustrate that the peak high and low T of 92.1 Nm and -41.9 Nm when θ = 24° and 244.5° respectively are 5.1 and 3.3 times greater than the T_{mi} = 18.0 Nm average.

As stated in Section 5.1.3, the crankshaft configuration is such that both cylinders fire simultaneously; the T as plotted above for a single cylinder is thus multiplied by two, with no change in phase.

The T_r is defined by Eq. (3.40) and is equal to T, as stated in Section 3.6. Thus the T_r curve per revolution is identical in profile to T, however, acting in the opposite direction.

5.7 PROPOSED ENGINE WORK DONE PER REVOLUTION

The W_i per cylinder is obtained by calculating the circular integral of the p-V diagram as defined by Eq. (3.41) for the experimental engine, as illustrated in Figure 5.10 below.

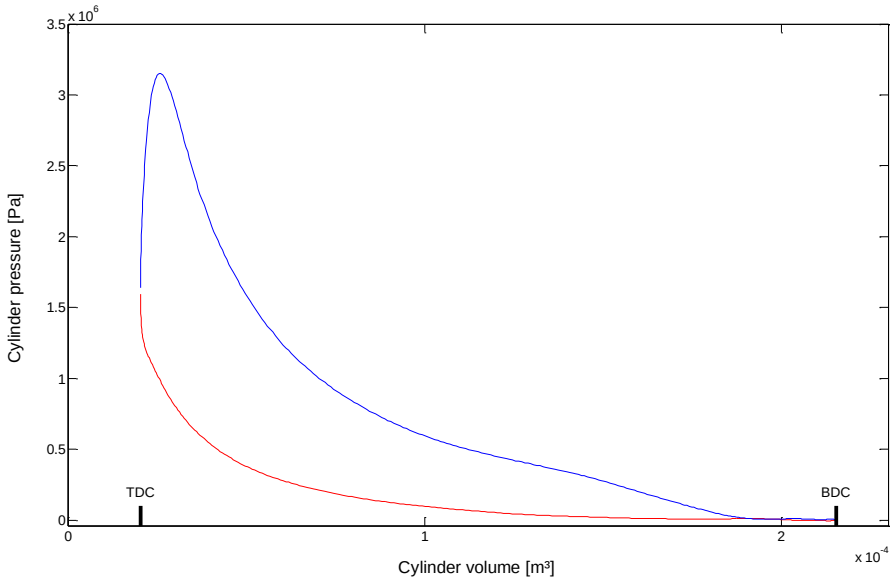

FIGURE 5.10: EXPERIMENTAL ENGINE P-V DIAGRAM AT 5500 RPM.

The upper blue expansion curve originates at TDC and extends to BDC, while the lower red compression curve starts at BDC and terminates back at TDC. Using Eq. (3.42) and an integral function in Matlab termed 'trapz' between the regions stated, the following values are obtained at 5500 rpm:

- W_{exp} = 146.6 J
- W_{comp} = 34.1 J
- W_i = 112.5 J

The percentage of the W_i available when compared to the W_{exp} is 76.7%, while 23.3% of W_{exp} is expended by the W_{comp}. The T_{mi} = 18.0 Nm per cylinder can now be calculated using Eq. (3.52), as illustrated in Figure 5.9.

5.8 UAV CRANKSHAFT ROTATIONAL SPEED FLUCTUATION

Calculating the crankshaft rotational speed fluctuation as described in Section 3.8 requires that the influence of both cylinders on the crankshaft be considered.

As stated in Section 5.6, for both cylinders firing simultaneously the black single cylinder T curve of Figure 5.9 is multiplied by two, with no phase change. Figure 5.11 below illustrates the blue T curve for both cylinders and the red horizontal line represents the total T_{mi} = 36.0 Nm for a single revolution at 5500 rpm.

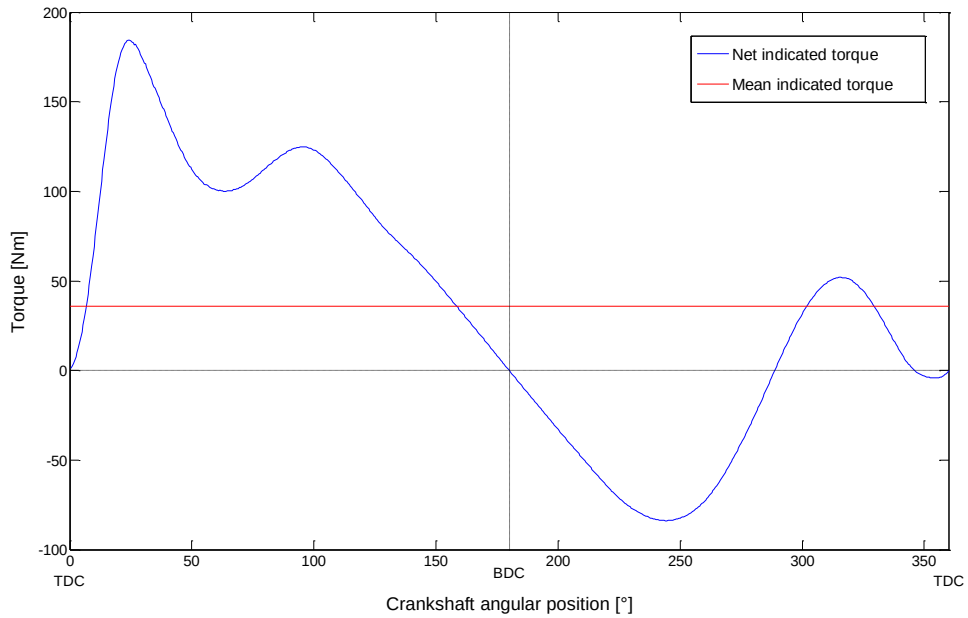

FIGURE 5.11: NET INDICATED TORQUE AND MEAN INDICATED TORQUE FOR BOTH CYLINDERS AS FUNCTION OF CRANKSHAFT ANGULAR POSITION AT 5500 RPM.

The methodology of the Matlab subroutine used to obtain the δE required by Eq. (3.47) to calculate the crankshaft rotational speed fluctuation is as follows:

- Determine the points on the X-axis where T and T_{mi} intercept.
- Integrate T between the intercepts obtained to establish the areas below and above T_{mi}.
- Use the largest area, since it correlates to the greatest surplus energy available to alter rotational speed.

The maximum area calculated is δE = 189.46 J between θ = 6.5° and 158.0°. By Eq. (3.44) the product of m_r and k^2 is equal to J_r, that is 27.30 x 10^{-3} kgm^2 as tabulated in Table 5.1. Then for ω = 576 rad/s, ω_2 - ω_1 = 12.05 rad/s (115.1 rpm).

Since the mean N_c = 5500 rpm, ω_1 = 5442.5 rpm occurs at θ = 6.5° and once the positive δE has been expended, ω_2 = 5557.6 rpm at θ = 158.0°. This relates to approximately 1% variation in rotational speed for the engine with an appropriately sized 32” wooden propeller fitted.

Should the 32” wooden propeller of 618 g with a polar moment of inertia equal to 24.3 x 10^{-3} kgm^2 be removed and only the entire crankshaft assembly inertia of 3 x 10^{-3} kgm^2 be used, the resultant speed fluctuation of ω_1 = 4976.9 rpm and ω_2 = 6023.1 rpm, also at θ = 6.5° and 158.0° respectively, occurs. The approximate rotational speed variation is then 9.5%.

The crankshaft rotational speed fluctuation with the propeller fitted decreases from 3.5% to 0.8% as the crankshaft rotational speed increases from 3000 rpm to 6500 rpm, as tabulated in Appendix C.1.

5.9 TWO-CYLINDER ENGINE POWER AND TORQUE

Two important UAV engine specifications that still have to be quantified are the useful power output at the crankshaft or P_b and T_{mb}.

To obtain the W_i for both cylinders, W_i per cylinder calculated in Section 5.7 is multiplied by two, thus W_i (both cylinders) = 225.0 J. By Eq. (3.48) the P_i = 20.6 kW at N_c = 5500 rpm.

Figure 5.12 below displays the graph of the estimated P_i, P_f and P_b for the UAV engine from 3000 rpm to 6500 rpm in 500 rpm increments.

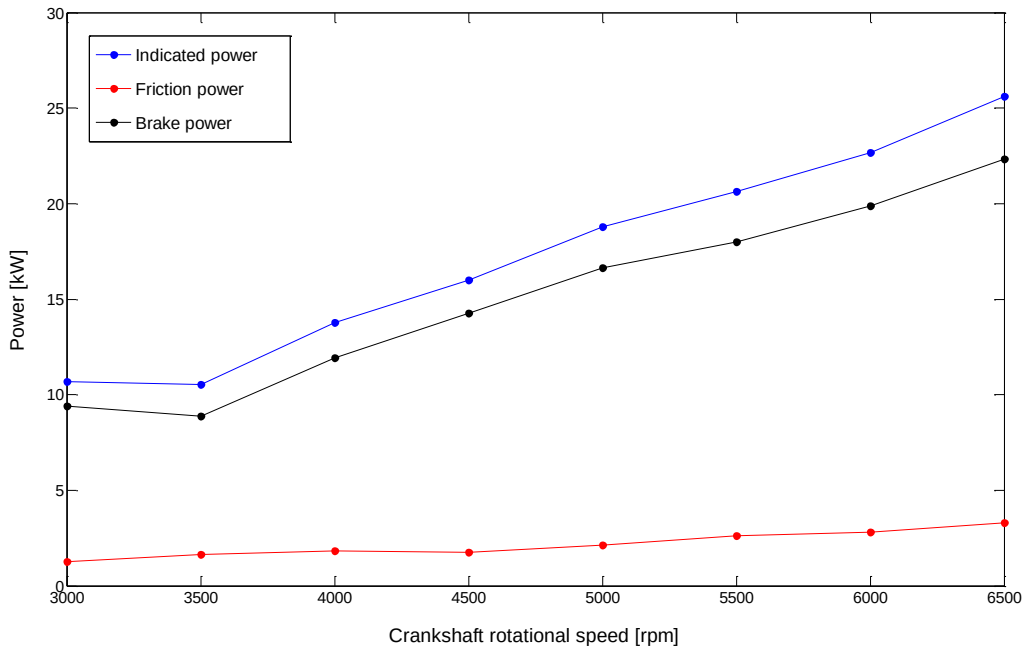

FIGURE 5.12: INDICATED POWER, FRICTION POWER AND BRAKE POWER OF THE UAV ENGINE AS FUNCTION OF CRANKSHAFT ROTATIONAL SPEED.

The P_f of the Yamaha DT 175 tabulated in Appendix E.1 is used as the reference value that is then adapted to estimate the P_f of the UAV engine using the following methodology:

- A factor of 0.85 reduces the tabulated P_f of the test engine, since it is assumed that the gearbox and chain drive is 85% efficient.
- The V_d of the proposed engine is 1.14 times greater per cylinder than that of the test engine, increasing the P_f.
- A factor of 2 is introduced to represent the two cylinders of the proposed engine.

The P_f of the UAV engine is thus 1.35 x 0.85 x 1.14 x 2 = 2.6 kW at 5500 rpm. To determine the P_b, the P_f must be deducted from the P_i, as defined by Eq. (3.49). Thus P_b = 18.0 kW at 5500 rpm.

The percentage of the indicated power lost to friction is 12.1% at 3000 rpm and increases slightly to 12.9% at 6500 rpm.

The T_{mb} is defined by Eq. (3.53) and is plotted in Figure 5.13 below with the P_b throughout the engine speed range.

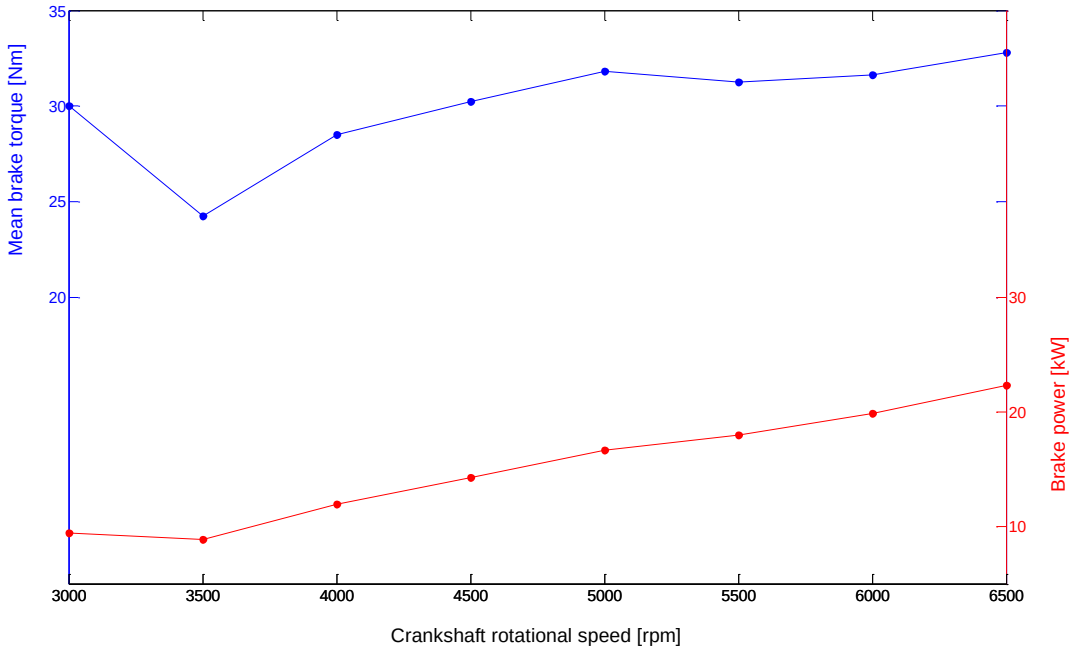

FIGURE 5.13: MEAN BRAKE TORQUE AND BRAKE POWER OF THE UAV ENGINE AS FUNCTION OF CRANKSHAFT ROTATIONAL SPEED.

The maximum T_{mb} and P_b is 32.8 Nm at 6500 rpm and 22.3 kW at 6500 rpm respectively, while the minimum values attained are 24.2 Nm at 3500 rpm and 8.9 kW at 3500 rpm.

5.10 UAV ENGINE CHARACTERISTICS

The remaining engine characteristics that will be detailed are $\overline{v_p}$, $bmep$ and η_m in the paragraphs that follow. All the values stated refer to Appendix C.1.

The highest $\overline{v_p}$ obtained is 12.35 m/s at 6500 rpm. This value is within the 8 to 15 m/s parameters stated for small SI engines in Section 3.10.2.

The $bmep$ ranges from 3.9 bar at 3500 rpm to 5.2 bar at 6500 rpm. The maximum $bmep$ of 5.2 bar is obtained at maximum torque but below the 8.5 to 10.5 bar pressure range for a four-stroke, SI engine stated in Section 3.10.4.

As stated in Chapter 4, all testing was conducted at full throttle with the resultant average η_m = 87.4% throughout the engine speed range. The highest η_m = 89.1% at 4500 rpm correlates well with the typical value of 90%, as stated in Section 3.10.5.

5.11 HORIZONTALLY-OPPOSED ENGINE BALANCE

With the UAV engine design parameters completed in the previous section, the balancing of the proposed engine is conducted.

The two-cylinder crankshaft is both statically and dynamically balanced, while the primary and secondary forces and couples will be calculated for the two horizontally-opposed assemblies of reciprocating components.

To assist in rotary and reciprocating balancing of the engine for all rotational speeds, a Matlab program was developed and can be found in Appendix G.3.

5.11.1 MANUFACTURED CRANKSHAFT BALANCE

The static and dynamic balancing theory applicable for any rotational system as derived in Section 3.11 will be applied to the UAV engine crankshaft illustrated in Figure 5.14 below.

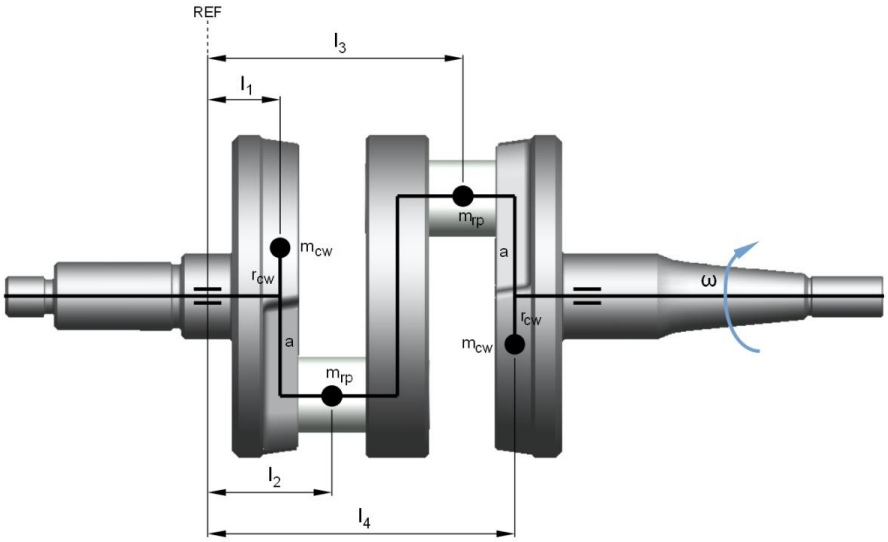

FIGURE 5.14: MODEL OF MANUFACTURED TWO-CYLINDER UAV CRANKSHAFT WITH BEARINGS, POINT MASSES, RADII AND LENGTHS FROM REF PLANE SUPERIMPOSED.

The details regarding the design and manufacture of the crankshaft pictured above will only be described in Chapter 6. However, in order to balance the rotational system of the UAV engine, the four point masses, radii and lengths from the REF plane, as illustrated by the superimposed sketch, are required, hence the inclusion of this illustration at this point.

The crankshaft is supported by two bearings on either side, as illustrated. The m_{cw} at r_{cw} and mass of rotational parts (m_{rp}) at a, have lengths l_1 = 21.05 mm, l_4 = 89.70 mm, l_2 = 36.50 mm and l_3 = 74.25 mm respectively from the REF plane that has been established through the centre of the left bearing. Note that the crank pins of the two-cylinder crankshaft are offset at 180° from one another, as discussed in Section 5.1.3.

Before applying the relevant equations to determine m_{cw} and r_{cw}, m_{rp} must first be obtained. The m_{rp} is not to be confused with m_r as tabulated in Table 5.2, since the latter represents the entire rotational mass of the engine and not the summed mass of the individual components connected to a single big-end. The m_{rp} is defined as:

$$m_{rp} = m_b + 2m_w + m_{be} + \left(\frac{l_{cpe}}{l_{cp}}\right) m_{cp} \tag{5.1}$$

where:

l_{cpe} = Length of crank pin exposed
l_{cp} = Length of crank pin
m_{cp} = Mass of crank pin

The values of the first three terms for the equation above are tabulated in Table 5.2. The last term represents the mass of the crank pin between the two webs of the crankshaft, calculated using the values tabulated in Table 5.4 below.

TABLE 5.4: CRANK PIN SPECIFICATIONS.

Length of crank pin exposed	l_{cpe}	19.5 mm
Length of crank pin	l_{cp}	56.5 mm
Mass of crank pin	m_{cp}	131.16 g

Applying Eq. (5.1) and substituting the appropriate values from both Table 5.2 and Table 5.4 results in: m_{rp} = 160.75 g with a = 28.5 mm.

To statically balance the crankshaft, Eq. (3.59) is used in conjunction with Figure 5.14 to yield the following:

$$\sum F = \omega^2\left(m_{cw}r_{cw} - m_{rp}a + m_{rp}a - m_{cw}r_{cw}\right) = 0 \tag{5.2}$$

All four terms within the brackets cancel one another and the summation is thus equal to zero, as stated above. This crankshaft configuration is thus statically balanced for all rotational speeds and any values of both m_{cw} and r_{cw}.

To dynamically balance the crankshaft Eq. (3.60) is used, again in conjunction with Figure 5.14, to develop the following equation (a clockwise couple is positive.):

$$\sum C = \omega^2\left(-m_{cw}r_{cw}l_1 + m_{rp}al_2 - m_{rp}al_3 + m_{cw}r_{cw}l_4\right) \tag{5.3}$$

Since both m_{cw} and r_{cw} are unknown, with only one equation formulated, an iterative approach is used to solve for the two variables. Equation (3.60) states that to achieve dynamic balance, the sum of all the couples must equate to zero. Thus, equating the above equation to zero and simplifying yields:

$$m_{cwa} = \frac{m_{rp}a(l_2 - l_3)}{r_{cw}(l_1 - l_4)} \tag{5.4}$$

where:

m_{cwa} = Counterweight mass approximation

Note that the ω^2 term is absent when the sum of the couples is equal to zero. The ideal m_{cwa} value is compared to m_{cw} and the error value obtained determines whether m_{cw} is to increase or decrease. The final step of the iterative process is to calculate if the proposed m_{cw} and r_{cw} combination results in Eq. (5.3), equating to zero.

The final values obtained by using both the solid model illustrated and the appropriate Matlab code found in Appendix G.3 are m_{cw} = 149.81 g and r_{cw} = 16.81 mm.

The crankshaft is thus both statically and dynamically balanced.

5.11.2 TWO-CYLINDER RECIPROCATING BALANCE

The horizontally-opposed, two-cylinder engine with the crank pins offset at 180° from one another will now have the primary and secondary forces and couples for the reciprocating components calculated using the theory derived in Sections 3.12.2 and 3.12.3. Figure 5.15 illustrates the UAV engine layout.

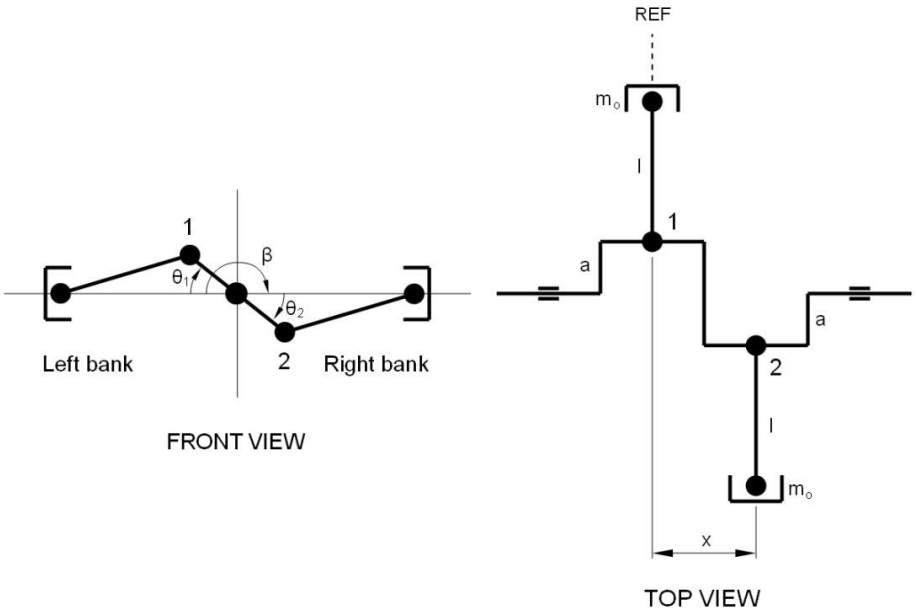

FIGURE 5.15: FRONT AND TOP VIEW OF THE UAV, HORIZONTALLY-OPPOSED, TWO-CYLINDER ENGINE WITH CRANK PINS OFFSET AT 180°.

To determine the F_p, Eq. (3.63) is applied to the figure above subject to the following criteria:

- As stated in Section 3.12.2, a horizontally-opposed engine is analysed as two separate in-line engines, with β = 180°. The resultant forces and couples are then due to the vector sum.
- The 180° crank pin offset of the two-cylinder crankshaft implies that θ_1 and θ_2, representing the left and right cylinder banks respectively, are equal, thus $\theta = \theta_1 = \theta_2$. This is illustrated in the front view of the figure above.

Thus, by applying Eq. (3.63) twice, initially to the left bank and then to the right bank, the following equation results:

$$\sum F_p = m_o a\omega^2 \cos(\theta) - m_o a\omega^2 \cos(\theta) = 0 \tag{5.5}$$

Because of the vector sum the second term of the equation is negative, since the reciprocating masses are equal in magnitude but opposite in direction.

To calculate the F_s, Eq. (3.64) is used, and is again subject to the above stated criteria. This equation is also applied twice, resulting in the following:

$$\sum F_s = m_o \frac{a^2}{l}\omega^2 \cos(2\theta) - m_o \frac{a^2}{l}\omega^2 \cos(2\theta) = 0 \tag{5.6}$$

Both the primary and secondary forces are thus equal to zero for all rotational speeds.

To determine the C_p and C_s, consider the top view of Figure 5.15 above. A REF plane is drawn such that it passes through the axis of cylinder 1 as illustrated. The distance from the axis of cylinder 1 to 2 or cylinder pitch (CP) is calculated by referring to Figure 5.14, substituting the necessary lengths and the following results:

$$x = CP = l_3 - l_2 = 37.75\ mm \tag{5.7}$$

For calculating both the C_p and C_s, the above stated criteria remain valid. By applying Eq. (3.66) to cylinder 2, the resulting equation is formulated for any ω as:

$$C_p = \omega^2 (346.24\times10^{-6}) \cos(\theta) \tag{5.8}$$

The m_o = 321.82 g is obtained from Table 5.3, with a and x as stated. A primary rocking couple thus exists.

By making use of Eq. (3.67), again applied to cylinder 2, the C_s for any engine speed is calculated as:

$$C_s = \omega^2 (89.71\times10^{-6}) \cos(2\theta) \tag{5.9}$$

A secondary rocking couple also exists, with l = 110 mm as tabulated in Table 5.1.

To obtain the resultant rocking couple the C_p and C_s are summed as stated by Eq. (3.68) to yield:

$$C_r = \omega^2 (m_0 a x)\left[\cos(\theta) + \frac{a}{l}\cos(2\theta)\right]$$

$$C_r = \omega^2 (346.24\times10^{-6})\left[\cos(\theta) + 0.259[\cos(2\theta)]\right] \tag{5.10}$$

With N_c still at 5500 rpm for illustrative purposes, Figure 5.16 displays the graphs of the C_p, C_s and C_r plots obtained.

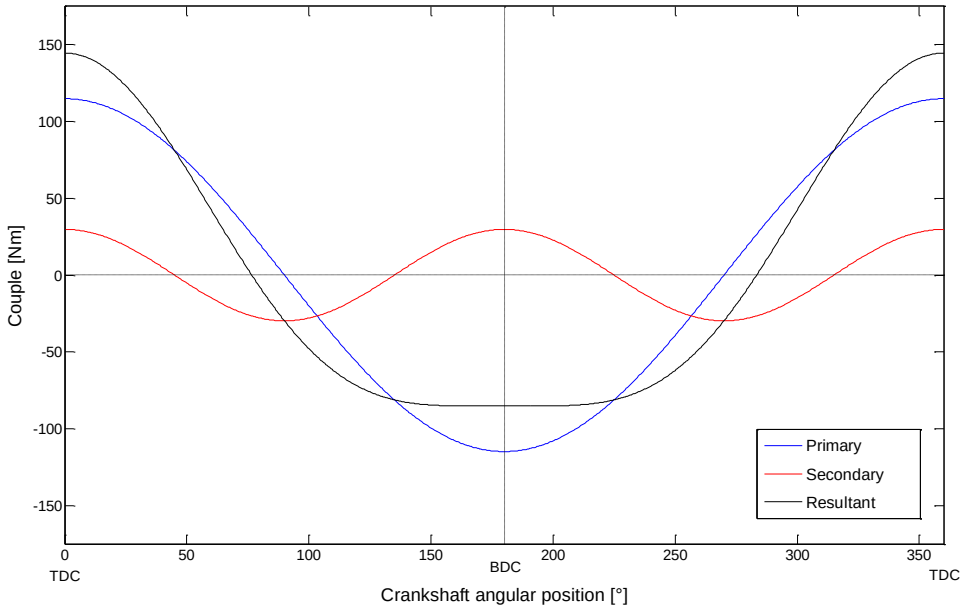

FIGURE 5.16: PRIMARY, SECONDARY AND RESULTANT COUPLES FOR THE RECIPROCATING BALANCE AS FUNCTION OF CRANKSHAFT ANGULAR POSITION AT 5500 RPM.

The frequency of the C_s is double that of the C_p, while the amplitude of the C_p is more than double that of the C_s. The C_r curve is dominated by the C_p characteristics, with the peak amplitude at TDC and wave form at BDC influenced by C_s. The C_r thus induces a rocking couple on the engine when viewed from the top, which increases in amplitude as the engine speed increases, while the period of C_r remains constant. The maximum C_r attained for each consecutive N_c is tabulated in Appendix C.1.

Note that the equations defining the primary and secondary forces and couples are ***not related to engine load***, but to the geometry and in the case of the primary and secondary couples, the N_c of the horizontally-opposed engine as well. The C_r curve will thus remain consistent at a fixed N_c, regardless of P.

5.12 UAV ENGINE FORCES AND COUPLES

The culmination of this chapter is the determination of all the relevant forces and couples acting on the experimental engine to yield the greatest values, at all eight speed set points.

The tensile bolt forces at the cylinder flange and crankcase seam are obtained. The reaction and resultant couples due to torsional crankshaft output and reciprocating balance respectively are then calculated. Lastly, the crankshaft, main bearing reaction forces and verification of applied maxima are determined.

To accomplish the stated objectives, a Matlab program was written for this section and can be found in Appendix G.4.

5.12.1 COLLATING FORCES AND COUPLES METHODOLOGY

In order to collate the maximum relevant forces and couples, at a specific N_c, the instant when these maxima occur during a crankshaft revolution has to be identified.

The red curve of Figure 5.7 illustrates the Q for a single crankshaft revolution at N_c = 5500 rpm. Since the highest forces and couples exerted on both the crankshaft and crankcase are of interest, the maximum Q = 7250.6 N obtained during the power stroke was considered the reference point or crank angle index point (θ_{ip}) = 18° for all relevant forces and couples at 5500 rpm while at full throttle. Using Eq. (3.13), the corresponding ϕ or connecting rod angle index point (ϕ_{ip}) = 4.6° was calculated.

The above procedure was conducted for all eight speed set points from 3000 rpm to 6500 rpm by using the appropriate Matlab program. The theoretical results obtained for this section are tabulated in Appendix C.2.

5.12.2 TWO-CYLINDER CRANKCASE AND CYLINDER INTERFACE FORCES

The forces experienced by the bolts at both the cylinder flange and crankcase seam will be calculated below.

The blue curve of Figure 5.5 illustrates the F_g for a single revolution at 5500 rpm, with θ_{ip} = 18°, the corresponding F_g = 10.77 x 10^3 N.

The upward force on the cylinder at joint 2, as illustrated in Figure 3.12, during the power stroke due to F_g, is defined by Eq. (3.69). The cylinder flange of the Yamaha YFS 200 Blaster requires four bolts, as illustrated below on the left, in Figure 5.17 by the four red circles.

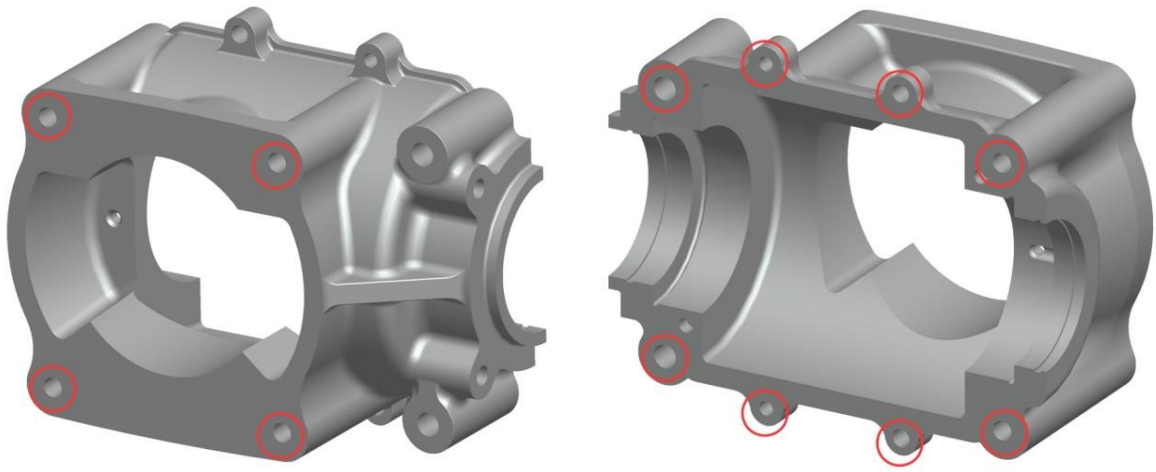

FIGURE 5.17: CRANKCASE CYLINDER FLANGE JOINT 2 (LEFT) AND SEAM BOLT JOINT 3 DISPLAYED (RIGHT).

Note: As in the case of the crankshaft, the design and manufacture of the crankcase will only be described in Chapter 6 but, because of necessity, are illustrated now.

The relevant equation is:

$$F_{cy} = \frac{F_g}{4} = 2691.3\ N \tag{5.11}$$

where:

F_{cy} = Cylinder flange bolt force

Again, referring to the single-cylinder schematic of Figure 3.12, the horizontally-opposed UAV engine has another single-cylinder engine attached, mirrored about joint 3. Since both cylinders fire simultaneously, the F_g is multiplied by two. By again applying Eq. (3.69), now with eight crankcase seam bolts as illustrated in Figure 5.17 on the right by the eight red circles, the equation becomes:

$$F_{cr} = \frac{2F_g}{8} = 2691.3\ N \tag{5.12}$$

where:

F_{cr} = Crankcase seam bolt force

Note that the bolt loads for both the cylinder and crankcase are assumed to be evenly distributed. In practice this will not necessarily be the case, especially for the crankcase seam bolts.

The mass of both the cylinder heads and cylinders could be included in both calculations; however, the effect thereof when compared to F_{cy} and F_{cr} is negligible for static calculation purposes.

5.12.3 REACTION AND RESULTANT COUPLES

The reaction couple due to the crankshaft output torque and the resultant balancing couple due to the reciprocating masses will subsequently be detailed.

For a single-cylinder engine, T_r is defined by Eq. (3.40), while for this two-cylinder engine where both cylinders fire simultaneously, the equation is modified as:

$$T_r = n(N \times AC) \tag{5.13}$$

At θ_{ip}, N = 580.5 N and AC = 138.5 mm, as illustrated in Figure 5.7 and Figure 3.5 respectively. This results in T_r = 160.8 Nm for both cylinders firing simultaneously. A rocking couple is generated about the crankshaft axis, as illustrated in Figure 5.18 by the blue arrows around the X-axis. This couple is subsequently transferred through the crankcase into the engine mounts. Should the engine misfire on a cylinder, the T_r is halved.

The C_r as calculated in Section 5.11.2 is illustrated in the figure on the next page by the red arrows acting about the Z-axis. The C_r = 133.3 Nm at θ_{ip} as plotted by the black curve in Figure 5.16, with the length between the two main bearings denoted by l_5 = 110.75 mm.

Note that the axis of C_r (representing both the primary and secondary couples) "is always perpendicular to the plane of stroke" (Green, 1962:404), in this case the XY-plane.

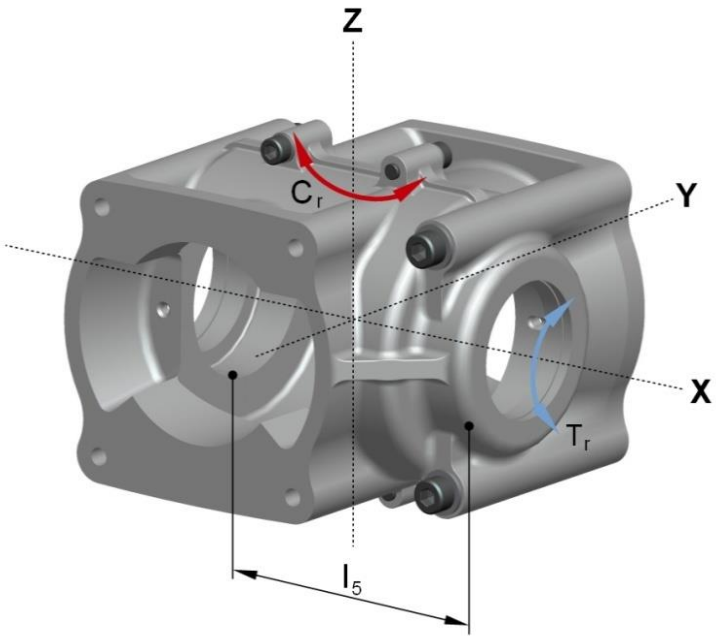

FIGURE 5.18: CRANKCASE REACTION COUPLE ABOUT THE X-AXIS AND RESULTANT BALANCING COUPLE ABOUT THE Z-AXIS.

As stated in Section 3.13.2 for calculating the bearing reaction forces due to C_r, Eq. (3.70) can be rewritten as:

$$R_{ac} = R_{bc} = \frac{C_r}{l_5} = 1203.7\ N \tag{5.14}$$

where:

R_{ac} = Reaction at A due to couple
R_{bc} = Reaction at B due to couple

Both R_{ac} and R_{bc} are equal in magnitude but opposite in direction. This will be detailed in the next section.

5.12.4 UAV CRANKSHAFT AND BEARING REACTION FORCES

Ultimately, the forces due to both combustion and balancing couples transmit loads through the connecting rods and crankshaft into the two main bearings.

Figure 5.19 illustrates the bearing reaction force diagram for both Q and C_r coloured blue and red respectively. The main bearing reaction forces at θ_{ip} due to Q, as specified in Section 5.12.1, on bearing A as illustrated in the top view, are calculated by applying Eq. (3.70) and taking moments about bearing B to yield the following:

$$R_a = R_b = \frac{Q(l_3 - l_2)}{l_5} = 2471.4\ N \tag{5.15}$$

Similarly, the main bearing reaction forces at bearing B are calculated and, owing to symmetry, $R_a = R_b$. Note that the bearing reaction forces are identical in magnitude but opposite in direction.

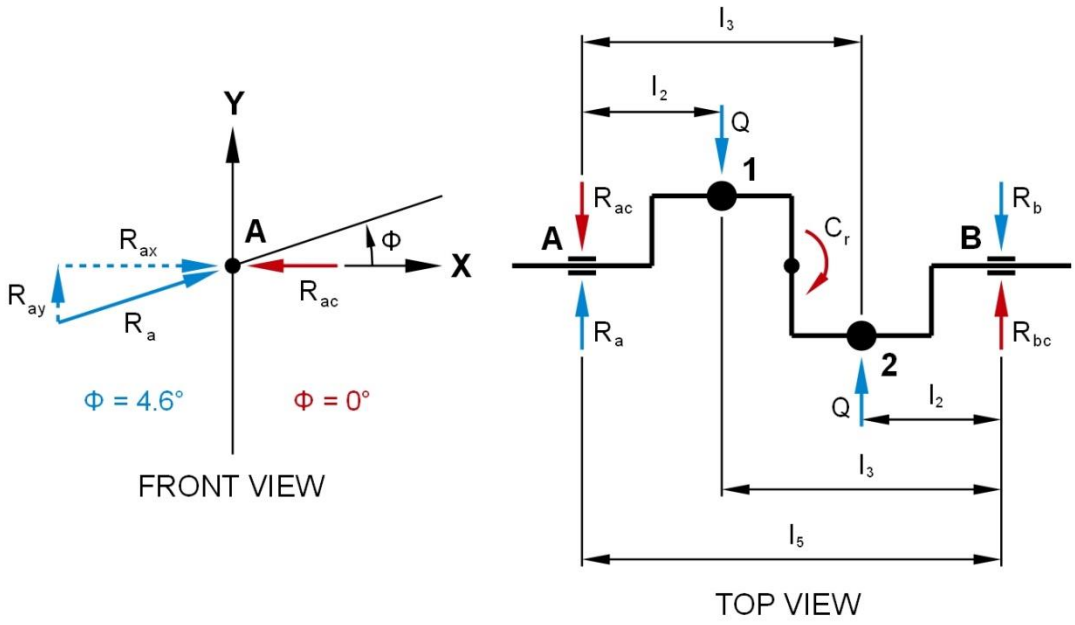

FIGURE 5.19: MAIN BEARING REACTION FORCE DIAGRAM FOR BOTH Q AND C_R.

The orientation of the crankshaft in the top view is such that m_o for cylinders 1 and 2 generate a clockwise C_r as indicated by the red arc. To counter C_r, R_{ac} and R_{bc} as calculated in Section 5.12.3 are generated, as illustrated by the red arrows at bearings A and B respectively.

The reaction forces on bearing A due to R_a and R_{ac} are illustrated in the front view by the blue and red arrows respectively. To determine the resultant forces on bearing A, the X and Y component forces are calculated by using and modifying Eq. (3.72) and (3.71) as follows:

$$R_{ax} = R_a \cos(\phi_{ip}) - R_{ac} = 1259.8\ N \tag{5.16}$$

and

$$R_{ay} = R_a \sin(\phi_{ip}) = 197.9\ N \tag{5.17}$$

where:

R_{ax} = Bearing A reaction in X-direction
R_{ay} = Bearing A reaction in Y-direction

The reaction forces on bearing B are calculated using the same equations and yield the following results:

$$R_{bx} = -1259.8\ N$$

$$R_{by} = -197.9\ N$$

where:

R_{bx} = Bearing B reaction in X-direction
R_{by} = Bearing B reaction in Y-direction

The forces on bearing B are equal in magnitude to A, but both act in the negative X and Y directions.

Should the engine misfire on cylinder 2, Q for that cylinder would not be present. Consequently, the bearing reactions would change with bearing A loads increasing to R_{ax} = 3641.7 N and R_{ay} = 389.2 N. The forces for bearing B remain relatively similar with R_{bx} = -1178.2 N and R_{by} = -191.3 N.

Both the forces and couples illustrated in the front and top views of Figure 5.19 can be used as force and couple inputs for crankshaft-related calculations.

5.12.5 UAV FORCE AND COUPLE SUMMARY

All the forces and couples referred to in the sections above apply to the experimental engine at a rotational speed of 5500 rpm while at full throttle. The graphs that follow examine the reference points, bolt forces, couples and bearing forces at all eight speed set points. The final graph displays the applied maxima used at 5500 rpm.

The reference points or θ_{ip} and the corresponding ϕ_{ip} for all eight speed set points are illustrated by the blue and red curves respectively in Figure 5.20 below.

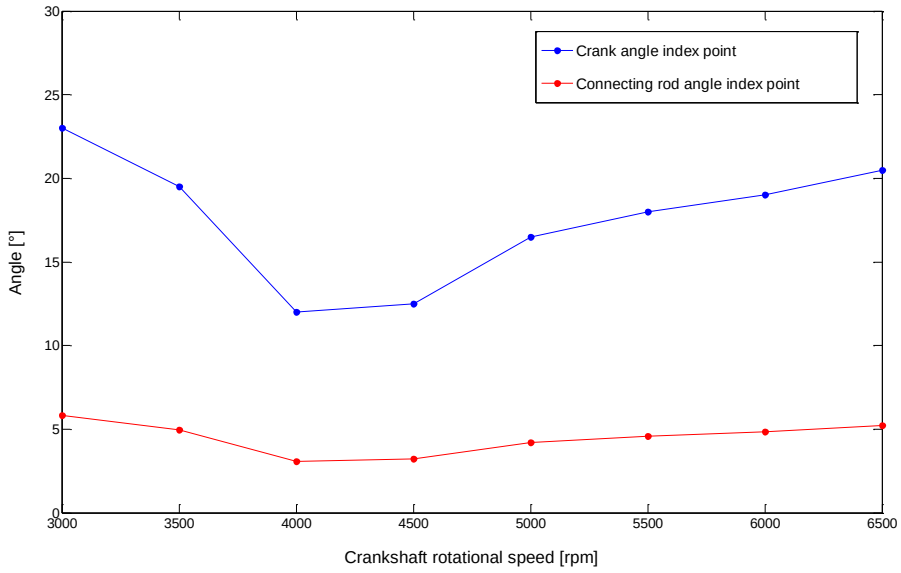

FIGURE 5.20: CRANK ANGLE INDEX POINTS AND CONNECTING ROD ANGLE INDEX POINTS AT MAXIMUM CONNECTING ROD LOAD AS FUNCTION OF CRANKSHAFT ROTATIONAL SPEED.

As stated in Section 5.12.1, the θ_{ip} at a particular N_c represents the crank angle when the maximum Q for that particular cycle is obtained. At each N_c the θ_{ip} varies, with a minimum of 12.0° at 4000 rpm and a maximum of 23.0° at 3000 rpm. The ϕ_{ip} is a function of θ_{ip} and varies accordingly, with a minimum of 3.1° at 4000 rpm and a maximum of 5.8° at 3000 rpm.

As previously stated, θ_{ip} and ϕ_{ip} at each N_c constitute the reference points for the calculation of all the relevant forces and couples at that particular engine speed.

Since F_{cy} and F_{cr} are identical for this particular engine, a single curve illustrating both variables for all eight speed set points is plotted in Figure 5.21 below.

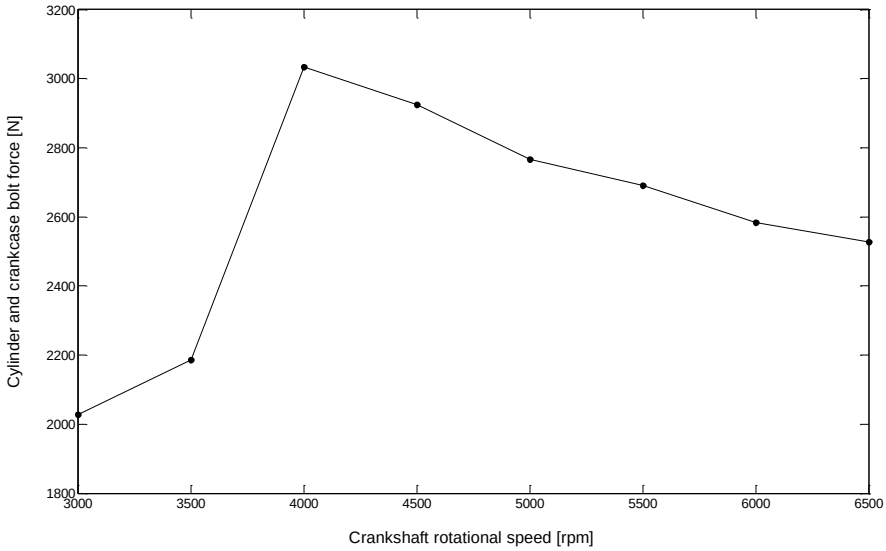

FIGURE 5.21: CYLINDER FLANGE BOLT FORCE AND CRANKCASE SEAM BOLT FORCE AT MAXIMUM CONNECTING ROD LOAD AS FUNCTION OF CRANKSHAFT ROTATIONAL SPEED.

Minimum and maximum forces of 2028.1 N and 3034.5 N at 3000 rpm and 4000 rpm respectively are obtained at each respective θ_{ip}. Notice that the trend of this curve is identical to that of Figure 5.4. This is to be expected, since F_g is a function of p, as stated in Eq. (3.27).

Both T_r and C_r, illustrated in blue and red respectively, at all eight N_c for each corresponding θ_{ip} are displayed in Figure 5.22.

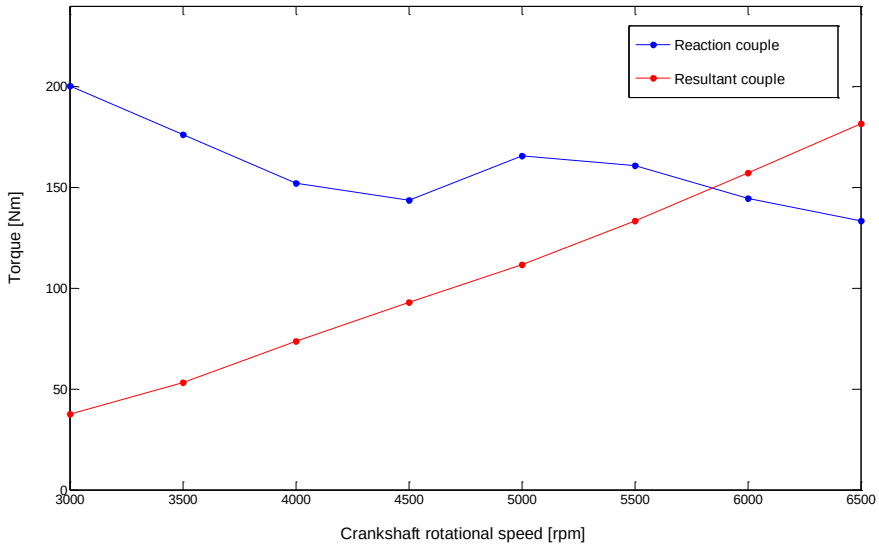

FIGURE 5.22: REACTION COUPLE AND RESULTANT COUPLE AT MAXIMUM CONNECTING ROD LOAD AS FUNCTION OF CRANKSHAFT ROTATIONAL SPEED.

The T_r varies from a minimum of 133.3 Nm at 6500 rpm to a maximum of 200.5 Nm at 3000 rpm. The C_r increases almost linearly as the engine speed increases, initiating from a minimum of 37.6 Nm at 3000 rpm and ending at a maximum of 181.6 Nm at 6500 rpm.

Thus, despite θ_{ip} variations at each N_c as displayed in Figure 5.20, C_r is strongly dependent on ω^2, as stated in Eq. (5.10).

Since the main bearing forces at A and B are identical in magnitude but opposite in direction, only the forces for bearing A are plotted. Figure 5.23 illustrates the X and Y component forces for bearing A at each incremental speed set point for the corresponding θ_{ip}, coloured blue and red respectively.

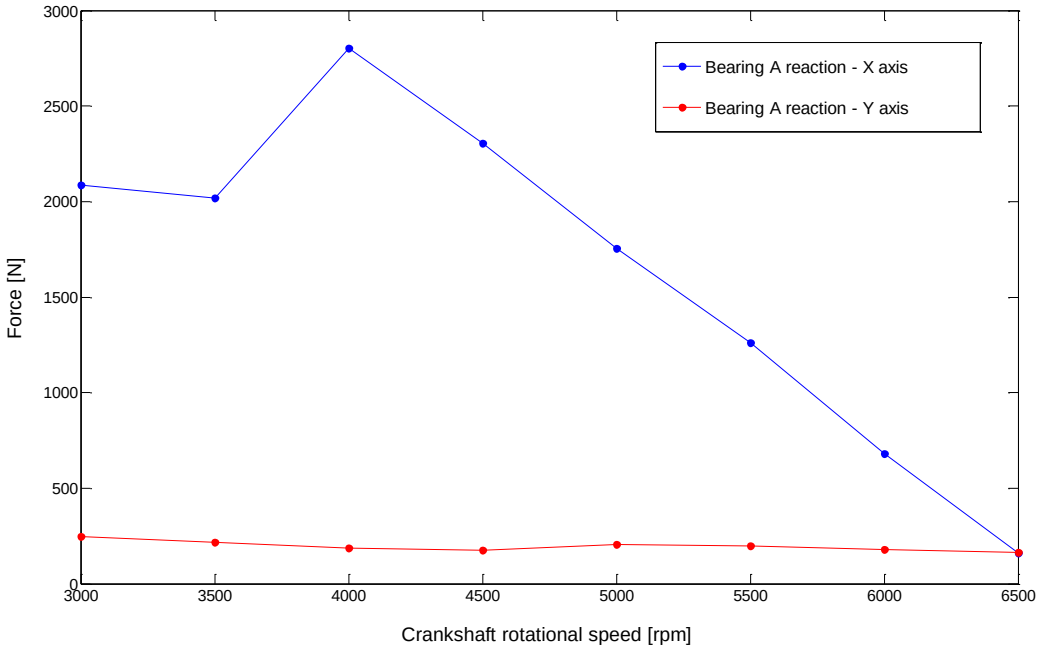

FIGURE 5.23: BEARING A REACTION IN THE X AND Y-DIRECTION AT MAXIMUM CONNECTING ROD LOAD AS FUNCTION OF CRANKSHAFT ROTATIONAL SPEED.

The figure illustrates that from a peak force of 2804.0 N at 4000 rpm, R_{ax} decreases almost linearly to 160.9 N at 6500 rpm. This is due to the influence of R_{ac} that acts in the opposite direction to R_{ax}, as illustrated in Figure 5.19. Appendix C.2 tabulates that from 4000 rpm to 6500 rpm R_{ac} increases from -666.4 N to -1640.0 N respectively, thus opposing R_{ax}.

The R_{ay} force maintains an almost horizontal trend with an average value of 196.4 N for all eight speed set points, since Eq. (5.17) is not influenced by R_{ac}.

Figure 5.24 displays the F_g, Q, N and C_r for a single revolution at 5500 rpm. Note that some of the curves have been scaled to increase resolution and that the Y-axis is purposefully left dimensionless, since curves with different units have been plotted on the same vertical axis.

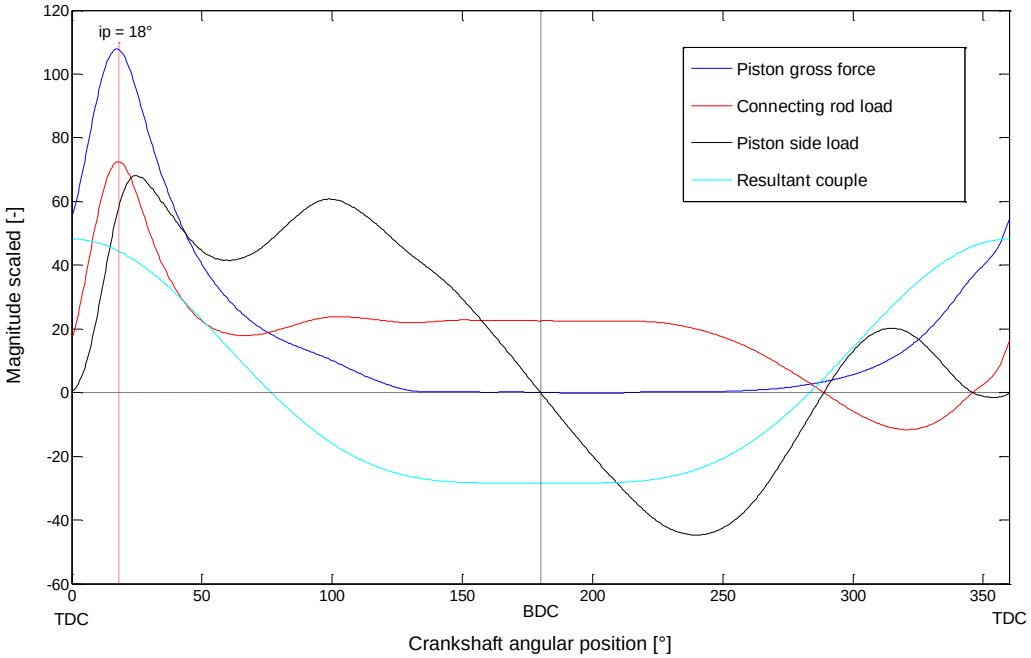

FIGURE 5.24: PISTON GROSS FORCE, CONNECTING ROD LOAD, PISTON SIDE LOAD AND RESULTANT COUPLE AS FUNCTION OF CRANKSHAFT ANGULAR POSITION AT 5500 RPM.

All calculations throughout Chapters 4 and 5 have been conducted with N_c = 5500 rpm, while Section 5.12 has used θ_{ip} = 18°, denoted by the red dashed vertical line.

This graph illustrates the error associated across all four curves, by applying θ_{ip} = 18° universally. The percentage errors are as follows:

- F_g lower by 0.1% - Blue curve
- Q lower by 0.0% - Red curve
- N lower by 14.7% - Black curve
- C_r lower by 7.8% - Cyan curve

The percentage error for all other speed set points can be found in Appendix C.2.

The dynamic nature of the forces and couples experienced by the UAV engine is clearly illustrated in Figure 5.24 and numerous other plots throughout this chapter. The next step would be to conduct a detailed FEA study of both the crankshaft and crankcase using the tabulated data, but as previously stated, this is beyond the scope of this dissertation. However, without conducting a FEA to verify and optimise the structural integrity of the crankshaft and crankcase, the strength, longevity and reliability of both components are unknown.

The greatest force components in both magnitude and direction for all the specified loading points/areas have been tabulated in Appendix C.2. Using the techniques specified in this section, the theoretical objective stated in Section 5.1.1 has been accomplished.

---

6 UAV ENGINE DESIGN, MANUFACTURE AND ASSEMBLY

With the applicable engine theory, required experimental investigation and subsequent theoretical design completed in Chapters 3, 4 and 5 respectively, the actual or practical design of the UAV engine can commence.

Commercially sourced engine parts will be used to initiate the design of the remaining engine components. Subsequent to that, the engine systems will be detailed. The designed/engine components and systems will then be manufactured and assembled to produce the UAV engine.

6.1 EXPERIMENTAL ENGINE DESIGN METHODOLOGY

The experimental engine includes both engine components and systems. The engine components as listed in Section 2.3 are the central elements of any two-stroke, SI engine, around which the engine systems as described in Section 2.4 are developed.

The methodology employed for the design of the experimental engine is as follows:

- Four of the six engine components are donor parts from a Yamaha YFS 200 Blaster as stated in Section 5.1.1. Since the dimensional and functional specifications of the parts are fixed, these parts form the foundation of the initial design.
- The two remaining engine components that require design are the crankshaft and the crankcase. Both parts will be designed to comply with the dimensional requirements of the donor parts and functional requirements for the intended task.
- Once all the engine components have been designed and integrated, the engine systems will be developed to suit the experimental engine, again paying attention to both form and function.

As previously stated in the preceding chapters, a detail design of the entire experimental engine will not be attempted. Instead, the above methodology statement will direct activity and best practice will be applied to both the engine components and systems that require design. Should an item be designed by making use of a reference, a citation will be noted.

The entire UAV engine was designed using Pro Engineer Wildfire 3.0 and all the assembly, sub-assembly, detail drawings and BOM can be found in Appendix F.

6.2 UTILISING EXISTING ENGINE COMPONENTS

To initiate the design process, the four donor components and related parts from a Yamaha YFS 200 Blaster were purchased, assessed and drawn. The sections below describe and illustrate the relevant parts. All-important engine specifications not stated can be found in Table 5.1.

6.2.1 THE CYLINDER

The first of the four donor parts assessed is the cylinder. The cylinder is constructed from cast aluminium and uses a steel sleeve insert, as illustrated in Figure 6.1.

The approximate outer dimensions of the large cooling fins are 223 mm by 190 mm when viewed from above, while the exact distance between the crankcase and cylinder head mounting faces is 98.45 mm. The cylinder is attached to the crankcase by four M8 studs, as illustrated in the right figure, while the cylinder head is secured by six M8 studs.

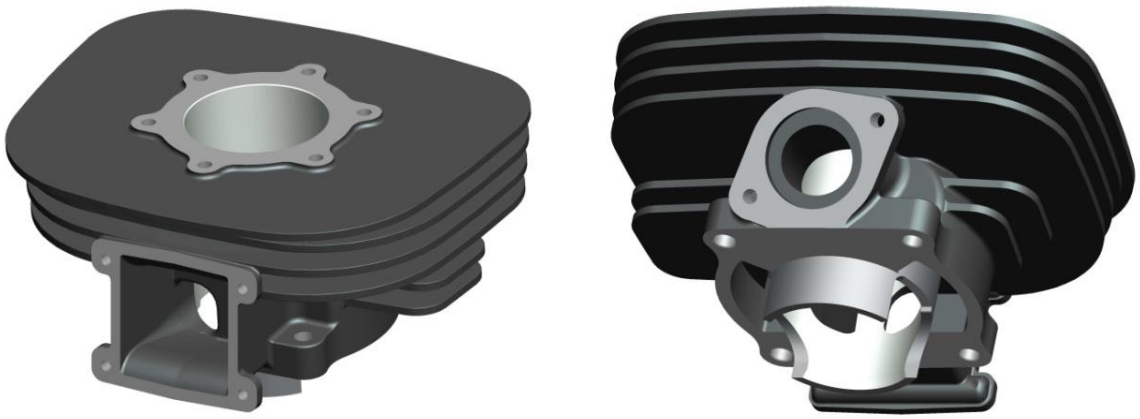

FIGURE 6.1: CYLINDER FROM A YAMAHA YFS 200 BLASTER.

The left figure illustrates the almost square inlet port that houses the reed valve of the intake system. The fresh fuel-air mixture is inducted through the oval shaped inlet ports of the sleeve, into the crankcase and up through the transfer ports. The right figure illustrates the two transfer ports that are visible on the cylinder-crankcase mounting face. The spent gas is dispelled though the round exhaust port.

6.2.2 THE CYLINDER HEAD

The second donor part used is the cylinder head, as displayed in Figure 6.2 below.

FIGURE 6.2: CYLINDER HEAD FROM A YAMAHA YFS 200 BLASTER.

Cast aluminium is also the material used for fabrication. The top view of the part's dimensional bounds is similar to that of the cylinder, while the maximum height of the cooling fins is approximately 74 mm. The six studs used to secure the cylinder head to the cylinder are visible around the periphery of the centrally located spark plug hole, with the upper part of the symmetrical combustion chamber being visible on the right.

6.2.3 THE PISTON AND CONNECTING ROD ASSEMBLIES

The piston and connecting rod assemblies are the last two of the four listed donor parts used. An exploded view of both assemblies is illustrated in Figure 6.3, with the corresponding assembly drawing AAB561MA0300 available in Appendix F.5.

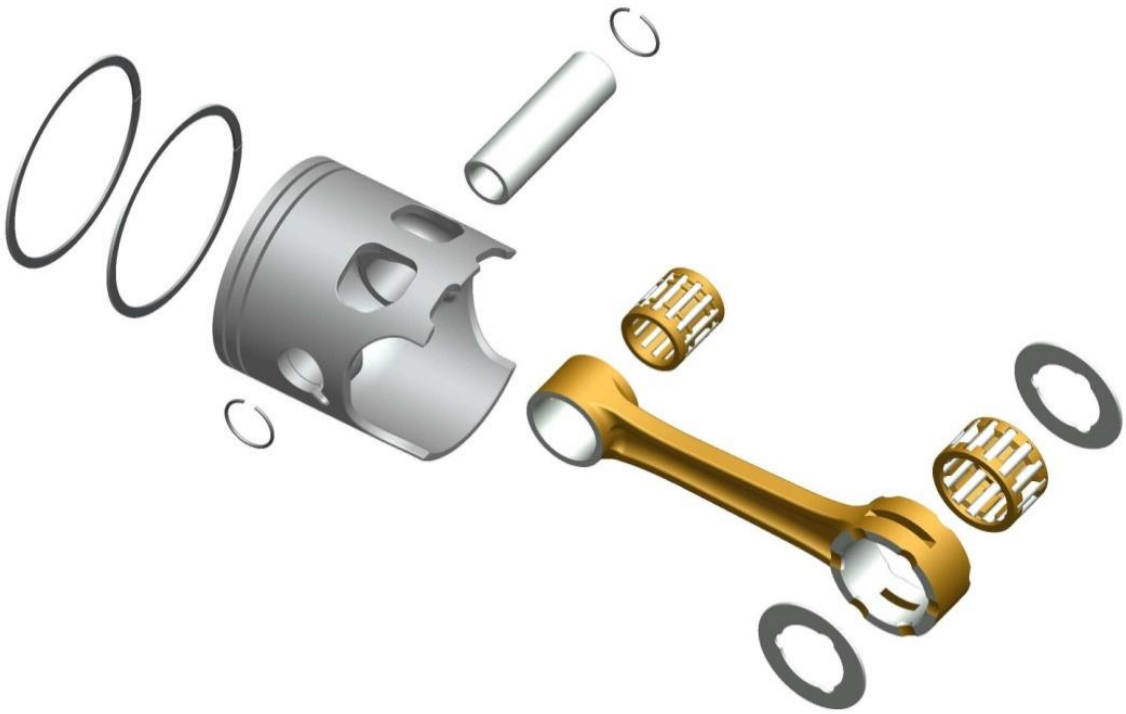

FIGURE 6.3: PISTON AND CONNECTING ROD ASSEMBLIES FROM A YAMAHA YFS 200 BLASTER.

The aluminium piston uses two compression rings and has a slightly domed piston crown. The two visible cut-outs in the piston skirt are inlet ports and match the dimensions of those in the sleeve of the cylinder in Figure 6.1. The steel piston pin is hollow, with a ground outer surface. The piston pin is secured in position by circlips on either side.

The connecting rod is a forged steel component that has been copper-plated to increase corrosion resistance. This connecting rod is a single component and this implies that the crankshaft will be a press-fit assembly. The inner faces of both the small- and big-ends are ground and serve as the outer races for the needle bearings used at both ends. Dimpled white-metal washers are fitted on both sides of the big-end to avoid contact between similar materials used for manufacturing the connecting rod and crankshaft.

6.3 DESIGN AND MANUFACTURE OF THE CRANKSHAFT

The two remaining engine components that require design and manufacture are the crankshaft and the crankcase.

The crankshaft configuration and dimensions direct numerous aspects regarding the crankcase layout and the former will thus be designed first. Once the assembly of the crankshaft has been completed, the crankcase will be designed and manufactured.

6.3.1 CRANKSHAFT DESIGN

The crankshaft is central to any simple engine mechanism, since the reciprocating motion of components is converted into useful rotary motion by this device.

Before commencing with the design of the crankshaft, consideration was given to the manufacturing effort involved in fabricating a complex component that operates under very demanding loads, as established in numerous figures throughout Chapter 5. The male/female crankpin spline crankshaft used by Pratt & Whitney and the Hirth serrated design, both illustrated in Figure 2.11, were possible options but were rejected because of manufacturing complexity.

It was thus considered prudent to use a press-fit, Yamaha YFS 200 Blaster crankshaft as donor for the two outer crankshaft throws/output shaft components and then to design and fabricate only the central crankshaft throw.

This arrangement is beneficial, since the design and manufacturing time is decreased, with the assurance that Yamaha used appropriate strength steel with suitable machining tolerances while fabricating the components. The adverse consequences are that some design options might then be somewhat restricted.

An exploded view of the crankshaft assembly is illustrated in Figure 6.4 below. The corresponding drawing AAB561MA0100 can be found in Appendix F.3. Each of the four main components, namely the crankshaft, main bearings, bearing sleeves and lip seals, will be designed or specified in the text that follows.

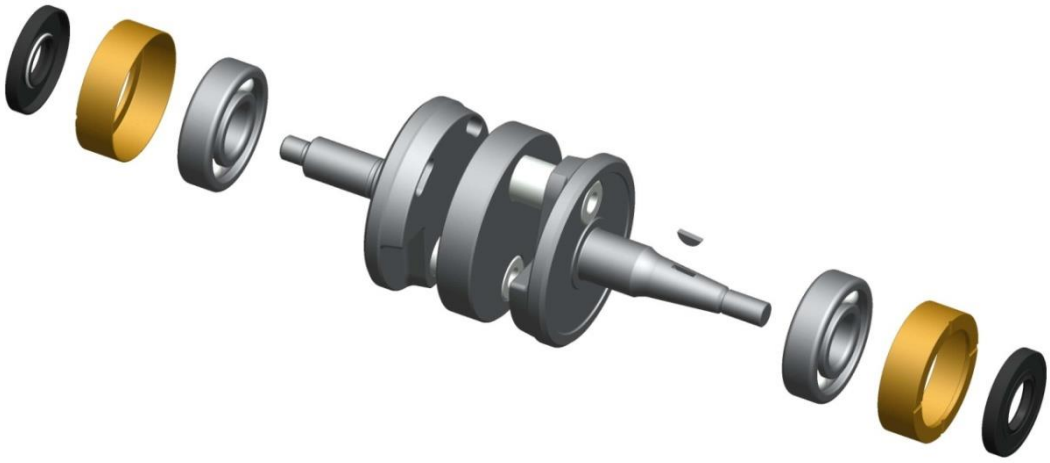

FIGURE 6.4: EXPLODED VIEW OF THE CRANKSHAFT ASSEMBLY.

To initiate the crankshaft design process and provide reference data for the future design of the crankcase in Section 6.4.1, the following crankshaft specifications are fundamental:

- *The crankshaft configuration* is such that the two crank pins are 180° offset one from the other as stated in Section 5.1.3.
- *The crank radius* is fixed at 28.50 mm, as tabulated in Table 5.1, since both the donor crankshaft throws and cylinder stroke are innate.
- *The cylinder pitch* is 37.75 mm, as stated in Eq. (5.7). This distance is purposefully kept as short as possible to minimise the out-of-balance forces of the unsupported central crankshaft throw.
- *The length between the two main bearings centres* is 110.75 mm, as stated in Section 5.12.3. This distance is determined by the geometry of the proposed crankshaft.

The first crankshaft component to be designed is the crankshaft centre or central crankshaft throw, with detail drawing number AAB561MM0201 as found in Appendix F.4. The 93.80 mm outer diameter is identical to that of the crankshaft donor parts, while the 18.25 mm thickness is appropriate, since the two Yamaha crank pins were originally pressed in on the donor crankshaft to that depth. The material used is EN24 in condition T with a yield stress (σ_y) = 650 MPa. The machining tolerance for the pitch circle diameter of the two crank pins is 57.000 ± 0.010 mm.

The last important consideration with regard to the central crankshaft throw is the appropriate machining tolerance of the two holes for the press-fit crank pins. Honda uses press-fit margins of between 80 µm and 180 µm for mass production crankshafts, as stated in Section 2.3.1. Both Yamaha crank pins have a measured outer diameter of 21.995 mm, while the two Yamaha crankshaft throws both have an identical crank pin hole diameter of 21.950 mm. This equates to a positive interference fit of +0.045 mm. It was decided to use the Yamaha interference fit, instead of that specified by Honda, since it seemed excessive. The same mean interference fit of +0.045 mm is thus specified for both crank pin holes, since twisting of the crankshaft under load cannot be tolerated.

The two outer crankshaft throws must be machined in order to dynamically balance the crankshaft as calculated in Section 5.11.1. The counterweights of both crankshaft donor throws are identical, as illustrated in Figure 6.5 below.

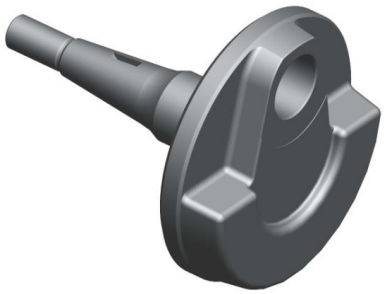

FIGURE 6.5: ONE ORIGINAL OUTER CRANKSHAFT DONOR THROW.

To achieve the calculated m_{cw} at r_{cw}, both counterweights were machined, as shown in Figure 6.6. The applicable detail drawings are AAB561MM0202 and AAB561MM0203 in Appendix F.4.

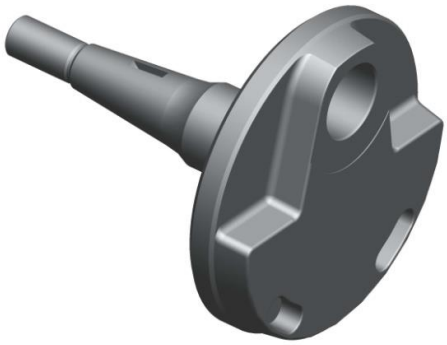

FIGURE 6.6: THE SAME OUTER CRANKSHAFT DONOR THROW POST-MACHINING TO BALANCE THE CRANKSHAFT DYNAMICALLY.

The two main bearings are located on either side of the crankshaft, as illustrated in Figure 6.4, and fit flush up against the crankshaft when pressed home. The “selection of bearing type” section in the SKF general catalogue (2003:33-193) was used as a guide for selecting the most appropriate bearing for this task. Note that certain topics in this section have been deemed irrelevant for this application and are thus omitted. The following points are, however, applicable in selecting the main bearings:

- Both main bearings are the same size, since Section 5.12.4 proves that the radial loads at both ends are equal in magnitude.
- Non-separable bearings are used.
- The radial forces vary continuously throughout a crankshaft revolution, as illustrated by Q in Figure 5.7. The maximum radial force attained throughout the engine speed range also varies, as seen in Figure 5.23, with a maximum resultant force of 2810.2 N for θ = 12° at N_c = 4000 rpm.
- An axial force is exerted on the main bearing nearest the drive hub owing to the thrust of the propeller, estimated at 500 N when operating at full throttle.
- Because of the two points above, the dominant load is in the radial direction.
- The inner diameter of the bearing is fixed, since it must conform to the 25 mm diameter shaft of both outer crankshaft throws. The outer diameter of the bearing is not space-restricted. The breadth is, however, restricted by the two output shaft bearing faces being 14.7 mm and 20.0 mm wide.
- Misalignment is not a concern, since the crankcase will be line-bored.
- The maximum operational speed is 6500 rpm.
- No integral seals are required, since the fuel-oil mixture will lubricate and cool the bearings during operation.

After due consideration, a single row deep groove ball bearing 6305 was selected with an outer diameter = 62 mm and breadth = 17 mm. This is wider than the available bearing face of one output shaft. The overhang of 2.3 mm is unwelcome, but considered tolerable.

The bearing selected can be quantified using the SKF life equations (2003:52-75), but this is regarded as being outside the scope of this dissertation.

The two main bearings are encapsulated by two aluminium bronze bearing sleeves, as pictured in Figure 6.4. The applicable detail drawing is AAB561MM0101 in Appendix F.3.

The primary function of the sleeve is to allow for both radial and axial tolerance refinement should it be required, instead of modifying or replacing the intricate crankcase. A secondary function is to assist in channelling the fuel-oil mixture through the bearings, but this will be described in Section 6.5.2.

Finally, two rotary lip seals are used at both ends to ensure that the compressed fresh charge within the crankcase flows to the cylinders without leakage to the environment. The lip seals also prevent the ingress of foreign matter into the crankcase.

6.3.2 CRANKSHAFT ASSEMBLY AND ALIGNMENT

The assembly and subsequent alignment of the press-fit crankshaft will be described in this section. The relevant detail drawing illustrating the crankshaft components and assembly tolerances is AAB561MA0200, Sheet 1 and 2 respectively in Appendix F.4.

The central crankshaft throw was manufactured and upon inspection it was established that both holes for the press-fit crank pins were out of specification, providing a +0.010 mm and +0.025 mm interference fit instead of the required +0.045 mm fit as stated in the previous section.

The compromised part was used because of time constraints in the full knowledge that using this component as is could result in twisting of the crankshaft while running and that this could lead to a catastrophic engine failure. To remedy the situation, the following was done: With the crank pins pressed into the central crankshaft throw, both pins were tungsten inert gas (TIG) welded to the central throw on a single side only, as illustrated on the left in Figure 6.7. Both sides of the crank pin could not be welded, since one of the dimpled white-metal washers of the connecting rod assembly rubs against the outer surface of the central throw.

FIGURE 6.7: THE TIG WELDING APPLIED TO THE CRANK PINS ONCE PRESSED INTO THE CENTRAL CRANKSHAFT THROW (LEFT) AND THE ASSEMBLED CRANKSHAFT (RIGHT).

The visible discolouration of the central throw is due to pre-heating applied to the part before both press operations commenced. The use of this remedial action does not suggest that the solution is ideal.

Before the two outer crankshaft throws were heated and pressed onto the central crankshaft throw, simple jigging was manufactured to aid both concentric alignment and crank pin press depth. The procedure used was as follows:

- The central crankshaft throw was placed on the press bed and a steel spacer with a width of 19.50 mm was rested on the sub-assembly to limit the press depth. This width provided a 0.50 mm big-end clearance between two opposing crank throws and the big-end connecting rod assembly. The Yamaha YFS200P service manual specifies a lower and upper clearance of 0.2 and 0.7 mm respectively (2001:3). The resultant average of 0.45 mm is similar to that obtained.
- A close-fitting, thick-walled sleeve with a long upward-facing slot to allow for connecting rod access was dropped around the sub-assembly and functioned as a concentric guide.
- The connecting rod assembly for the big-end, consisting of two dimpled washers, a needle bearing and connecting rod, was fitted over the exposed crank pin.
- The outer crankshaft throw was then heated and placed in position above the sub-assembly, suspended by a long-threaded rod screwed to the thread on the end of the output shaft.
- Finally, the outer throw was rapidly pressed home to prevent excessive heat conduction occurring between the hot and cold components.

Despite pre-heating the outer crankshaft throws, considerable force was still required to press the parts home. The assembled crankshaft is illustrated on the right in Figure 6.7, with heat discolouration visible on the output shaft.

The objective of the crankshaft alignment procedure is to comply with the concentric specification of 0.03 mm for surfaces A and B, as stipulated in drawing AAB561MA0200, Sheet 2. The Yamaha YFS200P service manual also specifies 0.03 mm (2001:3). This concentric specification was complied with by ensuring that all three crankshaft throws were concentric to one another and perpendicular to the rotational axis.

Independently aligning the outer throws to the central throw was considered the most effective methodology and was accomplished as follows:

- The crankshaft was initially clamped vertically in a three-jaw chuck, secured to the bed of the computer numeric controlled (CNC) mill as illustrated in Figure 6.8 left, with the blue dot indicating the outer throw that was to be aligned. The central throw was firstly aligned, by means of a dial gauge, to the axis of the vertical mill spindle for both concentricity and perpendicularity. The misalignment of the top outer crankshaft throw was then measured, recorded and marked on the blue dot throw.
- Next, the crankshaft was transferred to the manual mill three-jaw chuck with the blue dot throw ***now clamped***, as illustrated in the right figure. To reduce the possibility of the crankshaft shifting in the jaws owing to the impact loads required to straighten the crankshaft, a bracing beam was placed over the top of the blue dot throw and secured to the mill bed as shown.
- The clamped orientation of the crankshaft was such that the maximum concentric deflection point marked on the blue dot throw was opposite the copper mallet strike point. The hammer impact was ***always applied only to the central throw***, as indicated by the red arrow marked 1. A dial gauge, which was withdrawn from the surface during hammer blows, tracked the incremental progress of concentric alignment, signified by the curved blue arrows. The perpendicular alignment required was then applied to the central throw, directly opposite the crank pin, as indicated by the double-headed red arrow marked 2.
- The crankshaft was then returned to the CNC mill and the dial gauge measurement repeated to validate the progress. The entire procedure was continuously repeated until the blue dot throw was aligned to the centre throw. The above procedure was repeated to align the other outer crankshaft throw.

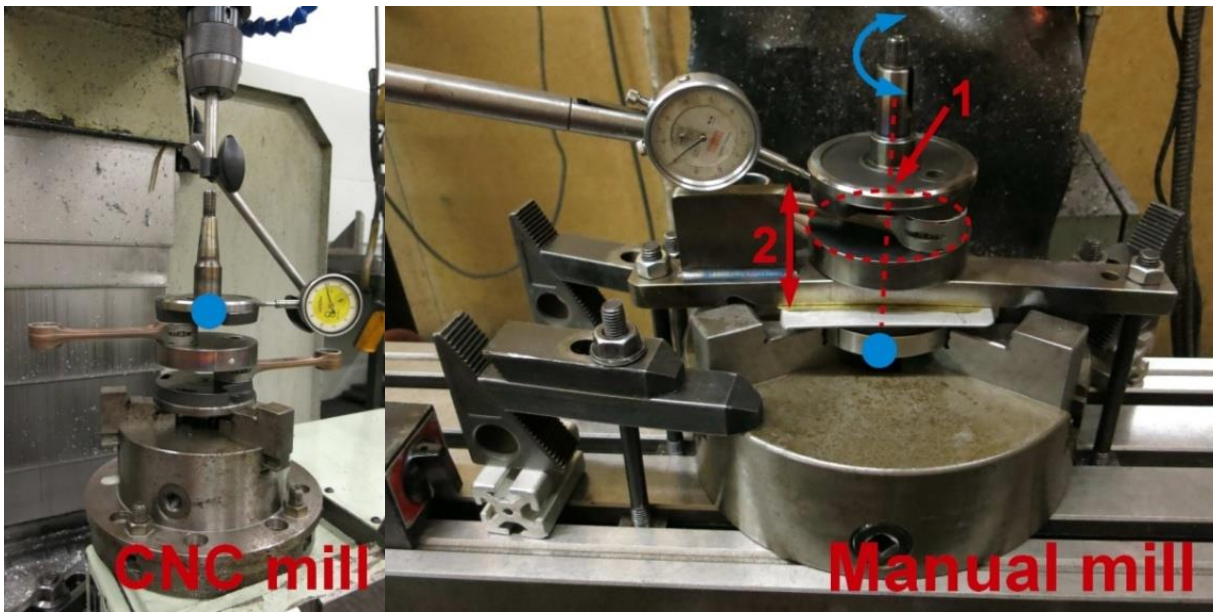

FIGURE 6.8: THE CRANKSHAFT CLAMPLED IN A THREE-JAW CHUCK ON THE CNC MILL (LEFT) AND MANUAL MILL (RIGHT).

Several difficulties encountered while aligning the crankshaft had to be overcome. Continuous incremental modifications were made to the bracing jig assembly anchoring the outer crankshaft throw in the chuck of the manual mill, since the impact loads would incrementally lift and rotate the crankshaft, thus rendering the progress tracking by the dial gauge useless. The entire alignment procedure was also extremely time-consuming, because of the repeated clocking of the crankshaft on the CNC mill to assess progress.

All the tooling and jigs used to assemble and align the crankshaft are illustrated on the left in Figure 6.9. To verify the accuracy of the crankshaft, the assembly was clocked between centres and the run-out of the main bearing faces A and B was measured, as illustrated on the right.

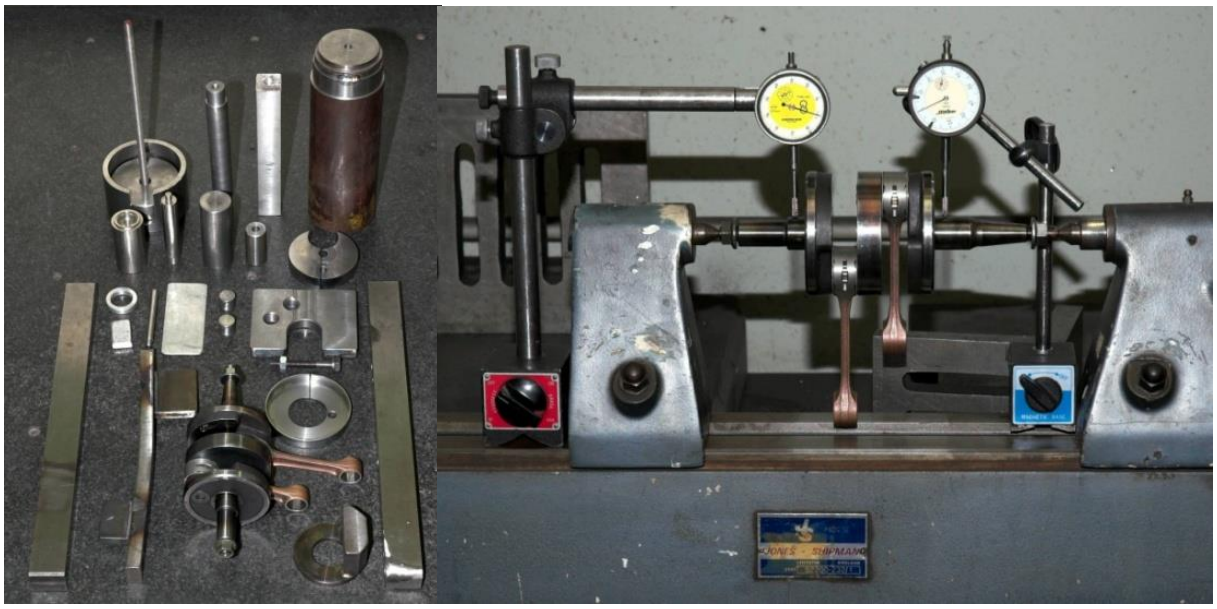

FIGURE 6.9: TOOLING AND JIGS FOR ASSEMBLING AND ALIGNING THE CRANKSHAFT (LEFT) AND ALIGNMENT OF THE CRANKSHAFT CHECKED BETWEEN CENTRES BY DIAL GAUGES (RIGHT).

The maximum recorded run-out for main bearing A and B is 0.030 mm and 0.065 mm respectively. The maximum run-out for bearing B is out of specification, but was left as such because of resource and time constraints. These tolerances, practically attained, are outside the desired specifications of 0.03 mm throughout, but within that specified by Naito (1966:190) of between 0.05 mm and 0.08 mm for a two-cylinder engine. The recorded radial and axial deflections for the crankshaft at 90° rotation increments between centres can be found in Appendix D.1.

6.4 DESIGN AND MANUFACTURE OF THE CRANKCASE

With the design and manufacture of the crankshaft complete, attention now turns to the crankcase that houses the crankshaft and related components.

As for the crankshaft, the design and manufacture of the crankcase will also be documented in two separate sections, starting with the design of the crankcase.

6.4.1 CRANKCASE DESIGN

While the crankshaft forms the nucleus of the moving components for a reciprocating engine, the crankcase encapsulates the crankshaft and provides a secure foundation for it and the associated engine components to operate in. A section view of the crankcase, crankshaft, connecting rods, pistons, cylinders and cylinder head assemblies is illustrated in Figure 6.10 below.

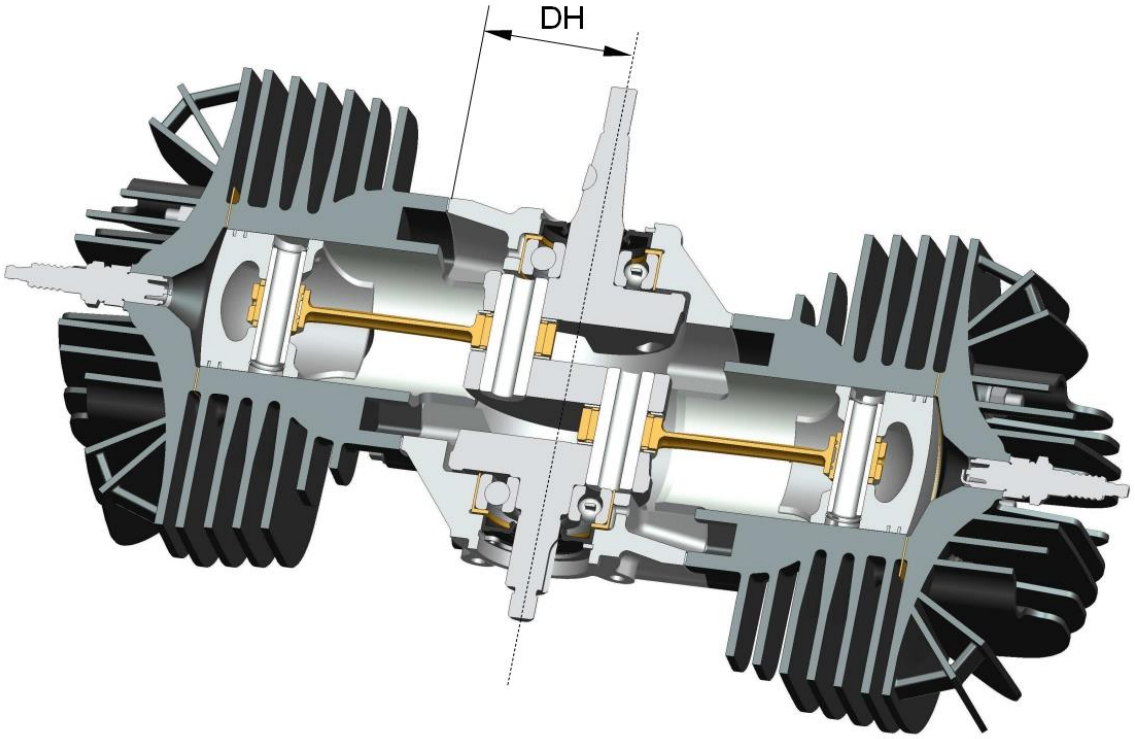

FIGURE 6.10: LONGITUDINAL SECTION OF THE UAV ENGINE ILLUSTRATING THE SIX MAJOR ENGINE COMPONENTS.

The figure illustrates the interaction between the six major engine components, specifically pertaining to the relationship of each with the crankcase. The detail drawings for the right (Crankcase 1) and left (Crankcase 2) crankcase components when viewing the engine from the front are AAB561MM0401 and AAB561MM0501, as found in Appendix F.6 and Appendix F.7 respectively. The crankcase design is conducted subject to the following criteria:

- The designated cylinder configuration is horizontally-opposed, as specified in Section 5.1.1.
- A CP of 37.75 mm between the cylinder axis centrelines is mandatory, as stated in Section 6.3.1.
- The distance between the two main bearing centres is 110.75 mm. This value is also stipulated in Section 6.3.1.
- The deck height (DH) = 69.75 mm, as illustrated in Figure 6.10, is set as such when the outer edge of the piston crown, while at TDC, is flush with the top edge of the cylinder. Note that the thickness of 0.8 mm for the cylinder gasket, as illustrated in the exploded view of drawings AAB561MA0400 and AAB561MA0500, is taken into account.

- The detail drawings AAB561MM0201 and AAB561MA0200 Sheet 2, as found in Appendix F.4, assign an outer diameter of 93.80 mm and length of 95.75mm to the crankshaft throws respectively. The crankcase inner diameter and length are both specified as 98.0 mm. Thus a clearance of 2.1 mm and 1.13 mm per side exists in diameter and length respectively between the crankshaft and crankcase. Since two-stroke SI engines rely on crankcase compression for fresh charge transfer, as detailed in Section 2.2.1, the gaps were kept to a practical minimum. (Jennings, 2007:95-97).
- The main bearing area dimensional requirements are determined by the main bearing, bearing sleeve, crank seal and circlip.
- The orientation of the cylinder intake and exhaust ports are determined by the cut-outs in the piston skirt, as illustrated in Figure 6.3, which must align with the inlet ports of the cylinder. Figure 6.11 shows that the chosen orientation is such that the inlet port faces upward and the round exhaust port downward.
- Section 6.2.1 designates that four M8 studs are required to bolt the cylinder to the crankcase. Figure 5.17 on the left circles the four M8 holes in the crankcase that are used to make this attachment.
- The cylinder transfer ports, as seen on the right in Figure 6.1 at the crankcase bolt interface, determine the cut-out shape required by the crankcase, as illustrated on the left in Figure 5.17.
- Because of the bearing reaction forces determined in Section 5.12.4, the main bearings require an opposing force to remain stationary. Two M8 bolts on either side of the crankcase clamp the main bearings in position, as illustrated in Figure 6.11 below. Owing to geometrical constraints, the bolts could not be ideally positioned directly over the main bearings.
- In addition to the bearing reaction forces, the four M8 bolts must withstand F_g together with the four M6 crankcase seam bolts, as detailed in Section 5.12.2. The four smaller seam bolts also assist in increasing the stiffness of the bolted crankcase assembly.
- The crankcase is designed so that it can be split through the middle, as illustrated in Figure 5.18, to allow for the fitment of parts. This does, however, complicate the manufacturing process.
- The crankcase is given an average skin thickness of 5.1 mm in the crankshaft region and 7.5 mm for the cylinder region. Ribs and generous radii are used wherever deemed necessary, to minimise stress concentrations, which may result in fatigue cracks.

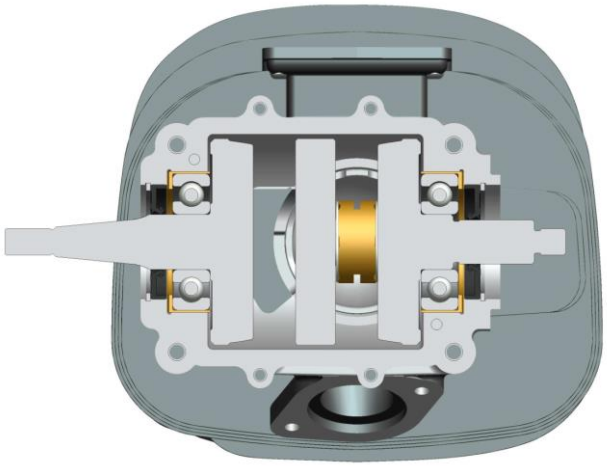

FIGURE 6.11: SECTIONAL VIEW OF THE UAV ENGINE COMPONENTS ALONG THE CRANKCASE SPLIT.

Ideally, the designed crankcase should be subjected to an FEA to evaluate the validity of the proposed design, but as mentioned previously, scope constraints prevented this on both the crankshaft and crankcase.

6.4.2 CRANKCASE MANUFACTURE

The inherent complexity of the crankcase is not restricted to structural design considerations, but extends to the manufacturing of the component. The material selected, specified tolerances, thermal expansion considerations and manufacturing methods will be described in the paragraphs that follow.

The material used for the manufacture of the two crankcase halves is 6082 aluminium in condition T, with a σ_y = 255 MPa. Grade 7075 aluminium, with a σ_y = 480 MPa was originally specified, but was unavailable. Aluminium is used for the crankcase in order to optimise strength-to-weight and stiffness-to-weight ratios.

The manufacturing tolerances of the assembled crankcase and crankshaft assembly must be considered, since the manufactured parts must fit upon assembly. The detail drawings specifying the manufacturing tolerances of the bearing sleeve, both crankcase halves and crankshaft, are AAB561MM0101 (Appendix F.3), AAB561MM0401/0501, Sheet 2 (Appendix F.6 and F.7) and AAB561MA0200, Sheet 2 (Appendix F.4) respectively. The length, specified tolerances and cumulative tolerance totals for the bearing sleeves and crankcase are tabulated in Table 6.1.

TABLE 6.1: SPECIFIED AND CUMULATIVE TOLERANCES FOR THE BEARING SLEEVES AND CRANKCASE.

Item	Dimension Length [mm]	Tolerance [mm]		Quantity	Tolerance [mm]	
		Lower	Upper		Lower	Upper
Bearing sleeve	2.50	-0.05	-0.10	2	+0.10	+0.20
Crankcase	48.50	+0.05	+0.10	1	+0.05	+0.10
	86.25	+0.05	+0.10	1	+0.05	+0.10
Total cumulative tolerance					**+0.20**	**+0.40**

The crankshaft length of 95.75 mm specifies a lower and upper tolerance of 0.00 mm and +0.10 mm respectively. Should the crankshaft be manufactured to the lower tolerance, the lower and upper clearance upon assembly would be +0.20 mm and +0.40 mm respectively. Conversely, if the crankshaft is manufactured to the upper tolerance, the assembly clearance is +0.10 mm and +0.30 mm. Thus, the crankshaft assembly will fit into the crankcase upon assembly.

The detail drawings for crankcase 1 and 2 specify that the two bores that house the bearing sleeves be machined to Ø64.00 mm with an H7 fit that specifies a lower and upper tolerance of +0.001 mm and +0.030 mm respectively. The Ø76.00 mm bore that provides access and accurate location for the steel cylinder sleeve is also specified as an H7 fit.

An internal combustion engine operates at an elevated temperature to that of the surroundings and consequently the engine components experience thermal expansion defined as (Sears *et al.*, 1985:288-289):

$$\Delta L = \alpha L_o \Delta T \tag{6.1}$$

where:

ΔL = Length increase
α = Coefficient of linear expansion
L_o = Original length
ΔT = Temperature change

The α for respectively steel and aluminium is 1.2 x 10^{-5} °C^{-1} and 2.4 x 10^{-5} °C^{-1}. Approximating the crankshaft as a steel rod with $L_o = l_5$ = 110.75 mm, the following thermal expansion occurs if both the crankcase and crankshaft operate at a temperature that is 50°C higher than ambient: $\Delta L_{Crankshaft}$ = 0.066 mm. Since the aluminium crankcase has a α that is double that of steel, the approximate thermal expansion for the same original length will also be double at $\Delta L_{Crankcase}$ = 0.13 mm. It is thus required that the main bearing opposite the drive hub, that experiences the axial force as stated in Section 6.3.1, be free to slide to accommodate thermal expansion. The bores of both the bearing sleeve and crankcase are specified as H7, to meet this requirement.

The detail drawings of the two crankcase halves convey important information to the machinist about those features of the part that require accurate manufacture, as documented in the paragraphs above. However, because of the complexity of the two components the detail drawings do not/cannot present all the information required to manufacture the parts.

Since the entire UAV engine model is assembled from Pro Engineer parts, the computer-aided manufacturing (CAM) extension of Wildfire 3.0 is used to generate the toolpaths for the CNC mill so that the crankcase halves can be machined. Because of the nature of the work that CAE regularly does, the company has the required tooling and skilled machinists for this complex manufacturing task.

The left-hand picture in Figure 6.12 shows the two crankcase halves with the machining for the first setup complete. The right-hand photograph illustrates a crankcase half with the machining for the second setup, to remove the excess inner material from the underside, in progress. Each part requires a further three setups to machine the two sides and the rear detail for the engine mount.

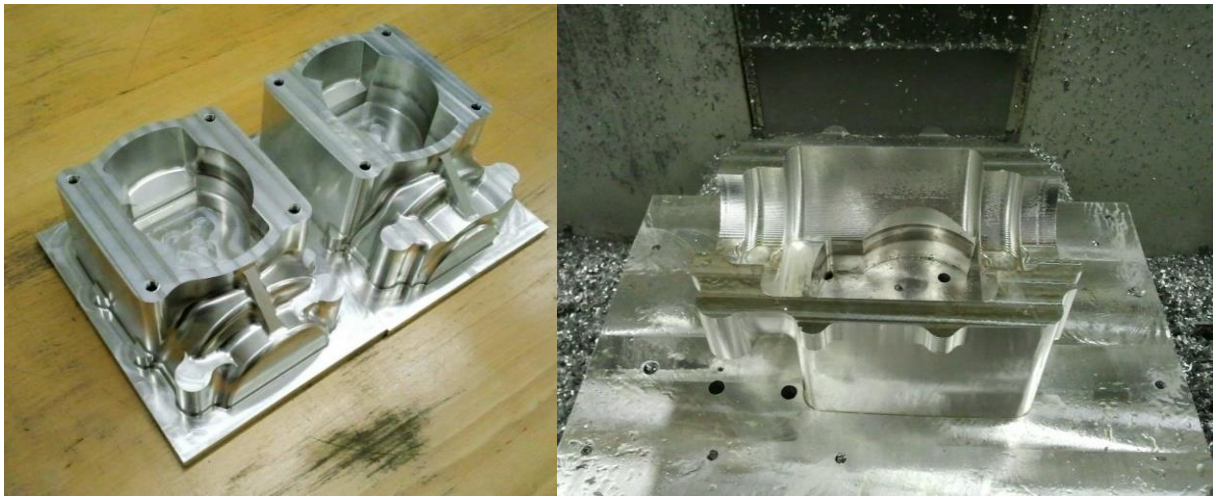

FIGURE 6.12: THE CRANKCASE HALVES WITH THE MACHINING OF THE FIRST SETUP COMPLETE (LEFT) AND THE SECOND SETUP IN PROGRESS (RIGHT).

Before the two halves are bolted together for the final line-boring of the two main bearing regions, their accurate alignment is ensured by the two diagonally opposed Ø5 mm dowel pins. The mating surfaces must also comply with the flatness and parallelism specifications of 0.020 µm and 0.04 µm respectively, since an uneven surface would compromise the integrity of the final crankcase assembly.

The picture in Figure 6.13 shows the completed crankcase, with the two halves bolted together, undergoing trial fitment of both cylinders, cylinder heads and engine mount.

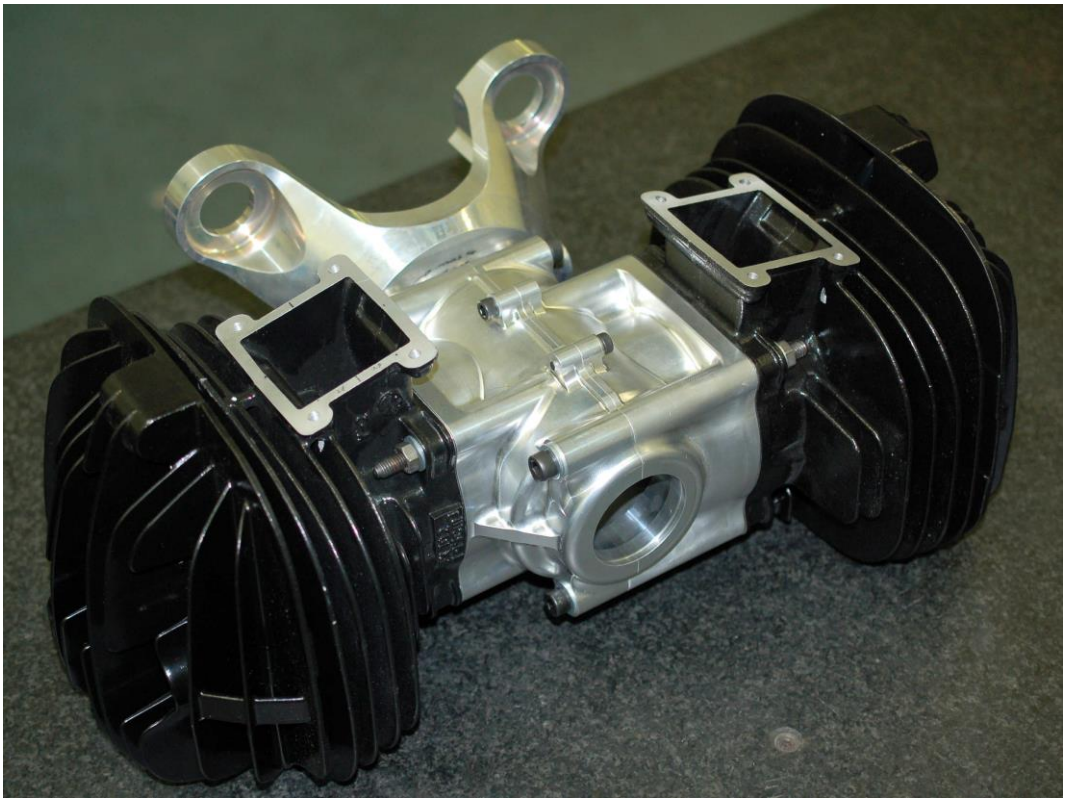

FIGURE 6.13: COMPLETED CRANKCASE UNDERGOING TRIAL FITMENT.

6.5 ENGINE SYSTEMS DESIGN AND MANUFACTURE

With the design and manufacture of the crankshaft and crankcase complete, the six engine systems required by a two-stroke, SI engine, as described in Section 2.4, will now be documented.

The design and manufacture of the cooling and lubrication systems will initiate this section. The intake, fuel, ignition and exhaust systems follow the sequence of the fuel-air mixture from induction to exhaust and will consequently conclude the UAV engine systems.

As stated in the introduction, the number of mechanical engineering disciplines involved when considering all the engine systems is numerous and a detailed theoretical design of the six systems will not be performed. Instead, the methodology statement in Section 6.1 will guide the detailed design process of each system.

6.5.1 COOLING SYSTEM

The design brief in Section 5.1.1 states that the UAV engine is to use air-cooling as the cooling system. The selection of the Yamaha YFS 200 Blaster engine components as donor parts for the experimental engine includes this requirement.

The cylinder and cylinder head, pictured in Figure 6.1 and Figure 6.2 respectively, illustrate the large cooling fins of both components. The cooling fins are long when viewed in cross-section and decrease in thickness as the fin tapers from root to tip.

The heat transfer from the cooling fins to the surroundings is mainly by forced convection as the propeller blows air across the exposed cooling surfaces. Heat is also exchanged to the surroundings by thermal radiation. The dimensions of the cooling fins have been left unchanged for this application. Comprehensive testing of the cooling requirements might indicate that the cooling of the UAV engine once at speed and altitude is excessive, since these two components were originally designed for terrestrial-based applications with higher ambient temperatures and lower forced convection air velocity. Amendments could then possibly be made by trimming off excess cooling fin length.

The two cylinder heads illustrated in Figure 6.13 do not allow the flow of forced air in the direction of flight. This is due to the bolt pattern of the cylinder/cylinder head interface that allows only this particular orientation for fitment.

6.5.2 LUBRICATION SYSTEM

The lubrication system of the UAV engine relies on the fuel-oil mixture inducted into the crankcase to lubricate the engine components.

The two main bearings, as illustrated in Figure 6.11, are shielded on one side by the face of the crank throw and on the other by the impervious lip seal. Since no forced lubrication occurs, an alternative arrangement is required to allow a portion of the fuel-oil mixture to flow through the main bearings, as illustrated by the sketched red path in Figure 6.14.

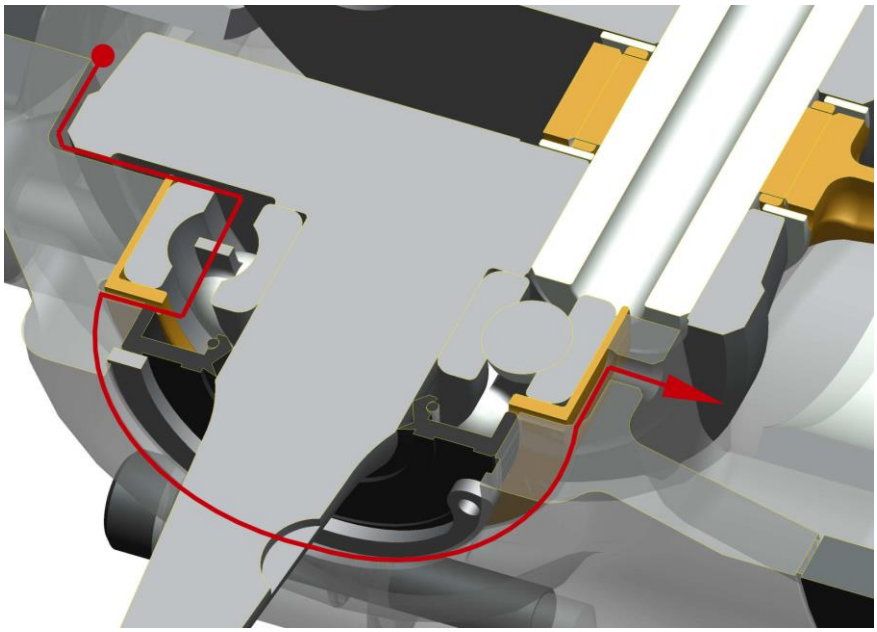

FIGURE 6.14: LUBRICATION PATH OF FUEL-OIL MIXTURE THROUGH MAIN BEARING.

The positive pressure created within the crankcase during the scavenge process, as described in Section 2.2.2, creates a pressure gradient for the fuel-oil mixture to flow through the main bearing, along one of the four recesses cut into the bearing sleeve, into the flow channel specifically machined into the crankcase for this purpose and out, through a Ø4 mm hole in the lower region of the transfer port, so completing the flow path. This method of inducing mixture flow through the main bearings is also found on the Yamaha DT 175 and in the book, *Two-stroke performance tuning* (Bell, 1999:147).

The connecting rod, big- and small-end needle bearings also require lubrication. The lower plot of Figure 5.2 traces the rubbing velocities of the crank pin in blue and the piston pin in red. The tangential velocity of the needle rollers at the big-end is far higher than that of the bearings at the small-end that oscillate about zero. Figure 6.3 illustrates the donor connecting rod, with two slits cut into opposite sides of the big-end only. Presumably, this is done by Yamaha to assist in allowing fresh fuel-oil mixture into the big-end bearings, while the small-end does not require this intervention owing to the low tangential velocity. The piston rings and bore interface are lubricated by the churning of the newly inducted charge during each cycle.

As used for the testing of the Yamaha DT 175 in Chapter 4, a premix ratio of 50:1 fuel-to-lubricant mixture will also be used for the UAV engine.

6.5.3 INTAKE SYSTEM

The first system to initiate the flow of fuel-air mixture through the UAV engine is the intake system.

The UAV engine specifications tabulated in Table 5.1 point to the fact that the induction system will include an ECU to regulate air flow and a fuel system that utilises fuel injection. Thus, a single centrally mounted throttle body (ETC) is to be used and the air will then be directed to the two inlet ports that house the reed valves. This is illustrated in Figure 6.13 by the two square upward-facing ports attached to the cylinder.

The air flow is initially inducted through a K&N air filter that is attached to the top of a Visteon ETC, as illustrated in the exploded view of the assembly drawing AAB561MA1200, found in Appendix F.14. Correct sizing of the throttle body is essential and is done as follows: Table 4.1 specifies that the Yamaha DT 175, with an V_{dt} of 171.06 cc, uses a Mikuni VM26SS carburettor with a venturi throat diameter of 26 mm, which equates to a venturi throat area of 5.31 x 10^{-4} m^2. The UAV engine specifications tabulated in Table 5.1 specify a V_{dt} of 390.02 cc. Since both cylinders fire simultaneously, the air flow through the throttle body is equivalent to a single-cylinder engine of 390.02 cc. By using linear interpolation with the engine displacements and venturi throat areas as the independent and dependent variables respectively, the venturi throat area for the UAV engine is 1.21 x 10^{-3} m^2. This equates to a venturi diameter of 39.3 mm. The Visteon throttle body, VR2S6U-9E927-FC has a throat diameter of 45.0 mm, which is 14.5% larger in diameter than required.

The throttle body is attached to the top of the inlet manifold that is illustrated in Figure 6.15; the equivalent assembly drawing is AAB561MW1600, which can be found in Appendix F.18. The top surface of the inlet manifold is purposely displayed slightly transparent, so that the inner workings can be seen.

The throttle body adapter with drawing number AAB561MM1608, to which the throttle body is screwed, has a divergent inner section profile to guide the air flow into a central plenum of 500 cc capacity. The plenum that directs air to the two inlet ports is deliberately this large, after the problems described in Section 4.5.3 with the abrupt engine operation due to resonant frequencies generated in long, constant diameter pipes. This large central plenum thus eliminates any substantial pipe lengths from the throttle body to the inlet ports.

FIGURE 6.15: INLET MANIFOLD OF UAV ENGINE.

The inlet manifold trumpets and the inlet manifold adapter, as seen in drawings numbered AAB561SL1605/1606 and AAB561MM1601, are all given continuous gentle curves to duct air flow from the central plenum into the two inlet ports. The inlet trumpet frontal area is 1.85 times that of the square inlet port area, into which the reed valves are inserted, as seen in drawing number AAB561MA1000, which can be found in Appendix F.12.

The entire manifold should ideally be fabricated from a composite material, with brass inserts to accommodate the fasteners, since the shape of the manifold could then be optimised without the vertically mounted ETC and air filter, while simultaneously reducing the mass. However, ease of manufacture and more importantly, correct functionality, outweighed the previous consideration. The entire inlet manifold is manufactured from 304 stainless steel and TIG welded together, using the assembled engine pictured in Figure 6.13 as the assembly jig.

Should this UAV engine be used in flight, a functional composite manifold would have to be designed and manufactured, ideally with the aid of computational fluid dynamics (CFD).

6.5.4 FUEL SYSTEM

Before air enters the reed valves, the two fuel-injectors located on both sides of the intake manifold, as demarcated by the two holes in Figure 6.15 and the inlet manifold top drawing number AAB561SL1604, inject fuel into the air stream. This drawing can be found in Appendix F.18.

A fuel-injector and mounting assembly is illustrated in Figure 6.16 and drawing number AAB561MA1300 illustrates an exploded view of the injector assembly; this can be found in Appendix F.15. Note that transparency has been applied to the model on the next page to aid visualisation.

FIGURE 6.16: FUEL-INJECTOR AND MOUNTING ASSEMBLY.

The injector assembly is mounted to the inlet manifold by TIG-welding the lower injector boss to the inlet manifold top plate. The upper fuel-rail mounting position is secured and maintained by the two vertical aluminium columns, called an injector standoff. The specific arrangement of the cap screws, as seen above, allows for assemblage of the injector assembly. The two o-rings located on either side of the fuel-injector prevent fuel that is under pressure from leakage.

The calculation done to determine the capacity of the two fuel injectors is as follows: In Appendix E.1, it is reported that the fuel flow of the Yamaha DT 175 when tested at 6500 rpm and 100% throttle opening is 5.46 kg/hr. By applying the same linear interpolation methodology as used in Section 6.5.3, the equivalent fuel flow rate for the 390.02 cc UAV “single-cylinder” engine is 12.45 kg/hr or 207.5 g/min. The Bosch automotive fuel injectors with VW part number 06A906031AS can deliver fuel at 109.3 g/min when subject to a 3 bar line-pressure and 80% duty cycle. The number of injectors required is thus: 207.5 g/min divided by 109.3 g/min, to yield 1.9. The flow rate of the two VW injectors will thus suffice.

In order to maintain a fuel-rail pressure of 3 bar, a fuel circuit will be used and this will contain the following stated elements: A fuel pump will pump fuel from a tank, through a fuel filter and into the fuel-rail of the first injector assembly that is coupled to the second injector assembly by a fuel line. A fuel pressure regulator that maintains the 3 bar pressure will be located at the exit of the second fuel-rail and the unused fuel will be circulated back to the tank.

The fuel injectors are actuated simultaneously by an electrical signal that is received from an ECU, as stated in Section 2.4.4, with a description of the functioning thereof in Section 6.5.5.

6.5.5 IGNITION SYSTEM

The ignition system of an SI engine determines the instant when the high voltage spark that initiates combustion is produced.

Both the ignition and fuel systems of modern internal combustion engines rely on an ECU and all the associated transducers to provide inputs and outputs for the engine to function correctly and efficiently. A detailed description of this entire system is beyond the scope of this section. Instead, a basic functional description of an elementary system will be given. The ECU receives three important inputs. The first is the throttle input by the user, the second is the feedback that the throttle position sensor (TPS) provides to the ECU about the butterfly angle of the ETC and the third is the feedback regarding the engine speed and position with respect to TDC that is provided by the crank sensor, as illustrated in Figure 6.17 below.

FIGURE 6.17: TOOTHED ENCODER WHEEL AND CRANK SENSOR ATTACHED TO THE ENGINE MOUNT.

The Bosch crank sensor, with part number 261 210, can also be seen in the exploded view of the assembly drawing number AAB561MA0600. This drawing can be found in Appendix F.8.

The crank sensor relies on this toothed encoder wheel, termed a 30-2, as seen in the detail drawing number AAB561SL0702 and found in Appendix F.9, to transmit pulses by magnetic induction to the ECU. Note that this 30-2 encoder wheel tooth profile was modified to 36-1, as stated in Section 7.2.1. The missing tooth enables the ECU to identify TDC. The ECU in turn provides the driving signals to both fuel injectors and the coil that provides the high voltage required by both sparkplugs.

To enable the ECU to provide the correct outputs, a three-dimensional map/matrix is created by arduous engine testing that assigns the correct fuel-injection duration and sparkplug timing to the assigned transducers, based on engine speed and load requirements.

6.5.6 EXHAUST SYSTEM

The exhaust system is used to expel the spent exhaust gas to the surroundings. The exhaust system of the two-cylinder UAV engine is pictured in Figure 6.18, with the drawing AAB561MA0800 illustrating an exploded view of the assembly. This can be found in Appendix F.10.

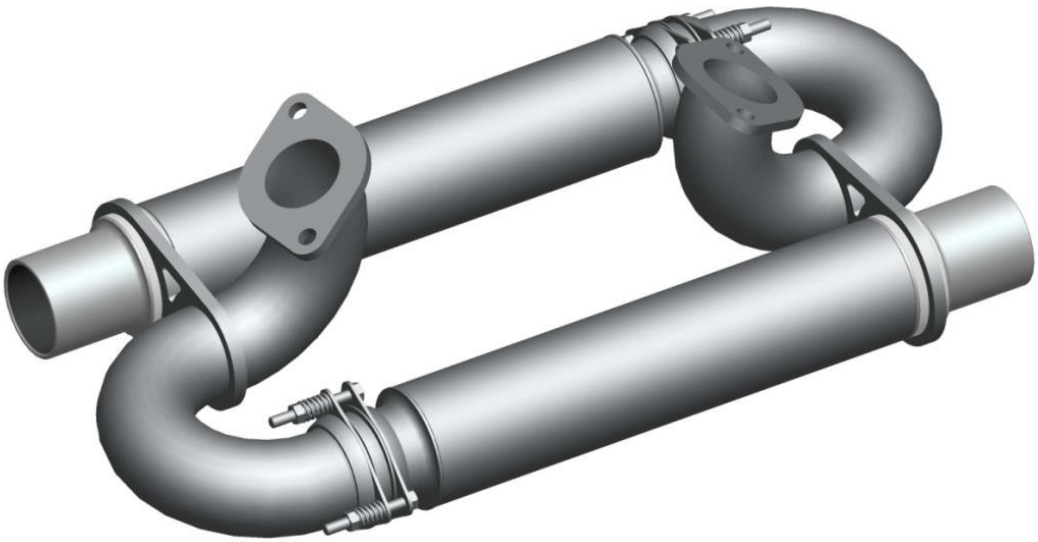

FIGURE 6.18: EXHAUST SYSTEM OF THE UAV ENGINE.

Each cylinder ducts exhaust gas through the exhaust header pipe that is constructed from 316 stainless steel, as seen in drawing AAB561MW1500. This detail can be seen in Appendix F.17.

To minimise the bending stress that the exhaust flange exerts on the exhaust port studs of the cylinder, an exhaust ball joint that is held together by three compression springs is used. Unlike the tuned exhaust systems pictured in Figure 2.33 and Figure 4.5, the silencer used is an un-tuned exhaust silencer from a Zanzottera 498i UAV engine. The use of a tuned exhaust system for two-stroke engines is ideal, but because of space and mass constraints this has been omitted.

The two separate exhaust systems are held in place by the four exhaust port studs and two exhaust brackets, as seen in drawing number AAB561SL1501, these securing the rear end of the silencers.

6.6 UAV ENGINE ASSEMBLY

With the required engine components and systems specified, designed and manufactured in Sections 6.2, 6.3, 6.4 and 6.5, the UAV engine is ready to be assembled.

The completed solid model of the experimental engine will be presented, along with a brief description of the two remaining components that will complete the assembly. All the physical components that constitute the UAV engine will then be displayed and assembled, concluding with the mass and cost of the engine.

6.6.1 ASSEMBLY OF UAV ENGINE MODEL

Before displaying the UAV engine model, two remaining engine components must be described to complete the experimental engine model.

The engine mount, after the first machining setup and once complete, is displayed in Figure 6.19 on the left and right respectively. The detail drawing of the engine mount, AAB561MM0601, can be found in Appendix F.8. The mount is billet-machined from 6082 aluminium. Four radially mounted M8 bolts attach the engine mount to the crankcase rear, guided into position by a Ø61.0 mm hole that locates on a 4.6 mm protruding shoulder. The four legs of the engine mount extend backward with sufficient length to allow for the fitment of an alternator onto the rear of the crankshaft, should this be required. Drawing number AAB561MA0600 illustrates an exploded view of the engine mount assembly. The four large holes at the rear of the engine mount accommodate two 50 Shore hardness rubber engine mounts per hole. These two polyurethane engine mounts are compressed during installation by the two large washers on either side until the centrally located mount crush tube stops compression. The mounting bolt is then finally torqued to the correct specification.

FIGURE 6.19: UAV ENGINE MOUNT AFTER FIRST MACHINING SETUP (LEFT) AND ONCE COMPLETE (RIGHT).

The final component required to complete the UAV engine is the 6082 aluminium propeller flange, as seen in drawing number AAB561MM0901, found in Appendix F.11. This part is attached to the front of the crankshaft, identified by the taper output shaft in Figure 6.7 on the right, and allows for the fitment of a propeller to the experimental engine. The propeller flange face overhangs the nearest main bearing by 73.5 mm. This is visible in the assembly drawing AAB561MA0000, Appendix F.2, in both the side and top views. The large cooling fins of both the cylinder and cylinder head of the nearest bank require this overhang for propeller clearance. However, should the propeller be unbalanced, a bending moment will be created and excessive vibration or catastrophic crankshaft failure could result.

This design could be improved by adding a third main bearing further forward along the taper shaft. This will, however, increase design complexity, mass and cost. Furthermore, the donor output taper shaft is difficult to modify.

With all the engine components and systems designed and manufactured, the assembled UAV engine model is now complete, as seen in Figure 6.20. An exploded view of all the engine sub-assemblies is displayed in drawing number AAB561MA0000.

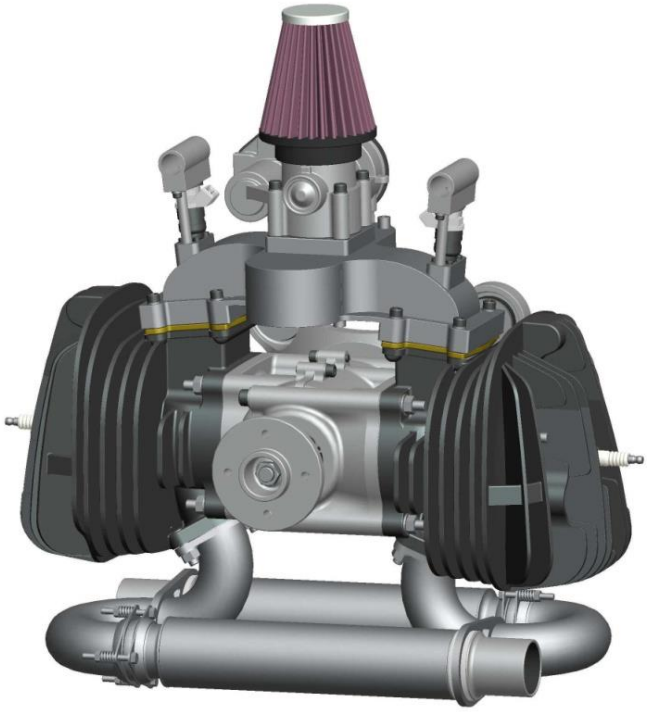

FIGURE 6.20: COMPLETE ASSEMBLED UAV ENGINE MODEL.

6.6.2 ASSEMBLED UAV ENGINE

With the design, drawing of the solid model, detail drawings, procurement and manufacture of all the required engine components and sub-assemblies completed, the assembly of the UAV engine can commence. All the engine components and systems required for the assembly of the UAV engine are pictured in Figure 6.21 below.

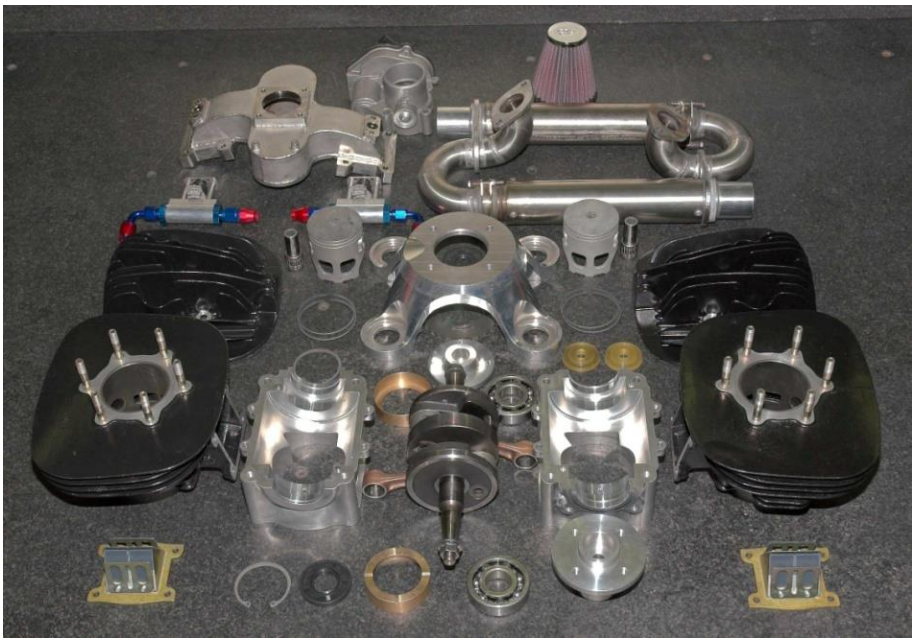

FIGURE 6.21: ENGINE COMPONENTS AND SYSTEMS OF THE UAV ENGINE.

The assembly sequence commences with the two main bearings pressed onto the crankshaft and the bearing sleeves and lip seals slid into position. The crankshaft assembly is then dropped into one of the crankcase halves and the eight crankcase bolts torqued to specification once the opposite half is in place. The pistons are then attached to the small-end of the connecting rods by inserting the piston pins. The pistons and cylinders are well lubricated and the latter slid over the former and tightened using the four flange studs. The last remaining engine components, the cylinder heads, are installed on top of the cylinders. The remaining engine systems are assembled and attached to the UAV engine as required. No re-work of components was required while assembling the engine.

The mass of the assembled engine model as illustrated in Figure 6.20 is 30.71 kg, while the mass of the actual engine is 26.6 kg. The 15.5% disparity in mass of the solid model is due to the omission of some of the finer details in complex components and not modelling all the cavities in parts such as the cylinders and throttle body.

The completed assembly of the two-stroke, two-cylinder, horizontally-opposed, air-cooled, SI UAV engine is displayed in Figure 6.22.

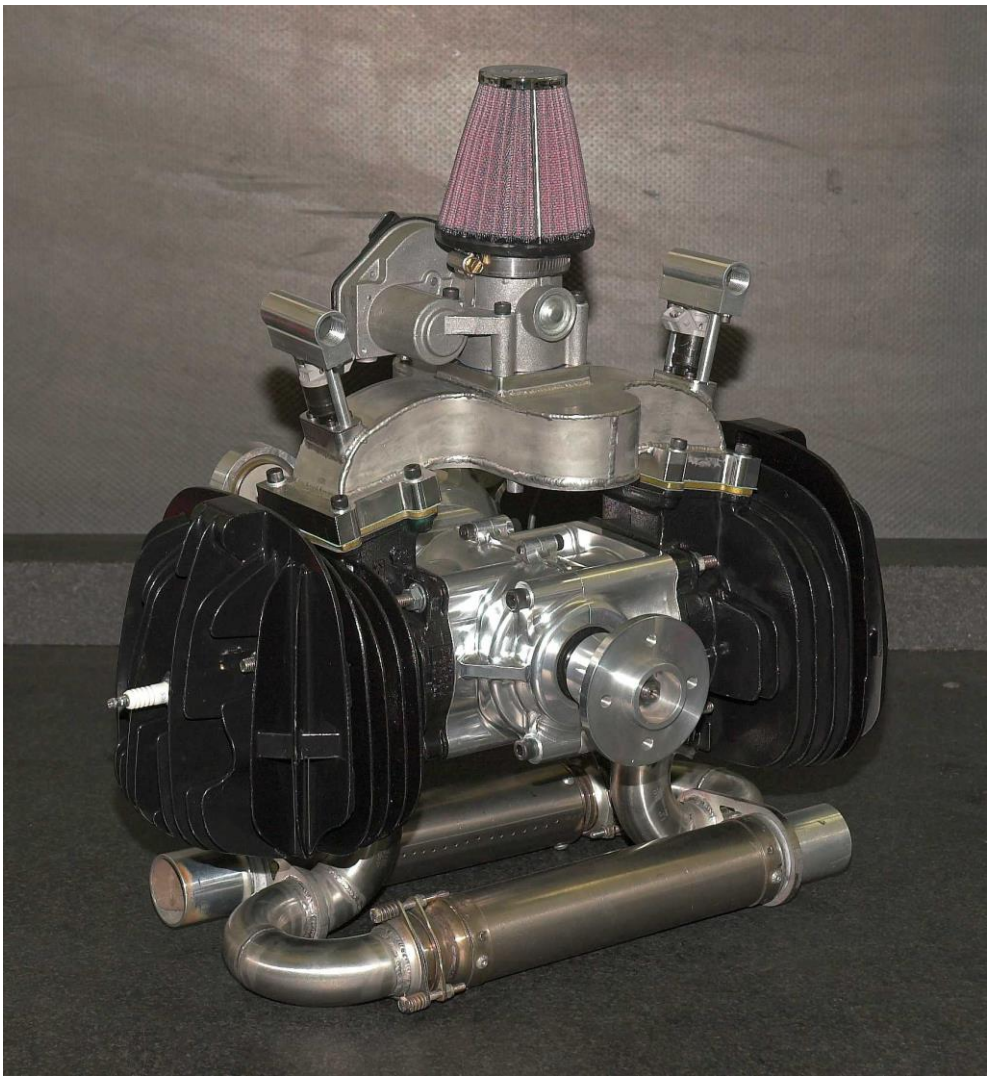

FIGURE 6.22: COMPLETED ASSEMBLY OF THE UAV ENGINE.

The cost of procuring, manufacturing and assembling the UAV engine can be found in Table 6.2 below.

TABLE 6.2: UAV ENGINE COMPONENTS AND SYSTEMS PURCHASE, MANUFACTURE AND ASSEMBLY COST.

ENGINE COMPONENTS			
Item	**Description**	**Cost %**	**Cost**
Cylinder	Purchase of two cylinders and cylinder gaskets.	11.5	R8938.80
Cylinder head	Purchase of two cylinder heads and head gaskets.	2.6	R2020.80
Piston	Purchase of two pistons, piston pins, small-end bearings and two sets of piston rings and circlips.	2.4	R1859.10
Crankshaft and connecting rods	Purchase of two crankshafts with connecting rod attached. Manufacture of crankshaft centre and assembly of crankshaft. Purchase of all accessories.	8.8	R6863.77
Crankcase	Purchase of aluminium and manufacture of two crankcase halves.	14.6	R11400.00
ENGINE SYSTEMS			
Item	**Description**	**Cost %**	**Cost**
Intake system	Purchase of air-filter, throttle body, two reed valves and gaskets. Purchase and machining of stainless steel and fabrication of intake manifold.	14.8	R11536.45
Fuel system	Purchase of two fuel injectors, one fuel pump, filter, regulator and all Goodrich fuel hoses and fittings. Machine injector assembly parts.	14.7	R11454.17
Ignition system	Purchase of Perfect Power ECU, Ford ignition module, Bosch crank sensor and two NGK spark plugs.	5.8	R4548.08
Exhaust system	Purchase of stainless-steel bends, laser-cut parts and two exhaust gaskets. Fabrication of exhaust system.	9.1	R7094.10
ADDITIONAL COMPONENTS			
Item	**Description**	**Cost %**	**Cost**
Engine mount	Purchase of material and manufacture of engine mount and washers. Polyurethane purchase and manufacturing of mould for casting.	8.8	R6823.20
Propeller flange and encoder hub	Purchase of aluminium and manufacturing of propeller flange, encoder hub.	4.2	R3300.00
Fasteners	Purchase of all studs, bolts, nuts and washers.	2.6	R2038.96
TOTAL COST		**100**	**R77877.43**

Note that the connecting rod has been grouped with the crankshaft, since Yamaha only sells these two components as an assembly. The cooling and lubrication systems are not tabulated, since both are included in specific engine components and thus incur no quantifiable cost.

The total cost of R77 877.43 for the complete, assembled UAV engine can also be broken up into R34 691.89 for procurement of all required components, R36 824.64 for the purchase of raw material and machining of parts and R6 360.90 for the fabrication and assembly of components. The CAE hourly rate used for machining and fabrication of components is R350/hour and R300/hour respectively.

Note that the cost associated with the design of the UAV engine has not been included in the total cost.

7 EXPERIMENTAL ENGINE TEST RESULTS AND ANALYSIS

With the UAV engine assembly complete, the engine is ready to be tested. Before the test run can commence, the experimental engine and peripheral systems must first be fitted and subjected to numerous rigorous checks.

The coupling of the UAV engine to the dynamometer and subsequent fitment of the engine to the test stand will firstly be described. The installation and testing of peripheral systems, along with the most notable component/system failures, will then be detailed. Subsequently, the running of the UAV engine will be conducted and the resultant performance curves plotted. Finally, the test results obtained will be compared to those theoretically predicted and analysed.

7.1 UAV ENGINE TEST CELL SETUP

The UAV engine will be set up in the same test cell at CAE, test cell 7, as was used for the testing of the Yamaha DT 175 described in Chapter 4. A detailed description of the test cell layout will thus be omitted. Instead, the two sections that follow will describe the unique points of this engine setup.

Before this particular test cell installation is described, the design of the driveshaft assembly that links the experimental engine to the dynamometer follows.

7.1.1 UAV ENGINE DRIVESHAFT ASSEMBLY

Unlike the Yamaha DT 175 test engine that was linked to the dynamometer by means of a chain drive, as illustrated in Figure 4.4, the UAV engine is coupled to the Froude EC 38 dynamometer by means of a drive shaft. The driveshaft assembly and detail drawings can be found in Appendix F.16.

Since a propeller will not be attached to the engine while in the test cell, a flywheel was designed, manufactured and installed instead of the propeller flange, as seen in detail drawing AAB561MM1404.

The inertia of the flywheel, at 24.3 x 10^{-3} kgm^2, is equal to that of the 32” wooden propeller as described in Section 5.8 and will ensure that the rotational speed variation of the engine remains within the calculated band, as tabulated in Appendix C.1. Note that the design of the flywheel is such that the CG is as close as possible to the nearest main bearing to ensure that if a bending moment is exerted on the crankshaft output shaft, because of imbalance, it will remain as low as possible.

The selection of suitable couplings and the design of the coupling shaft for the driveshaft assembly are a complex task. Erroneous coupling selection or a poorly designed coupling shaft may lead to numerous failures, some catastrophic (Plint & Martyr, 1995:116).

In Chapter 8 of *Engine testing: theory and practice* (Plint & Martyr, 1995:116-135) it is stated that the fundamental theory of this topic is complex. It is also beyond the scope of this dissertation. However, the reference text presents an abbreviated version of the fundamental theory and although not presented here, is used to design the driveshaft assembly illustrated in Figure 7.1, with drawing number AAB561MA1400 illustrating an exploded view of the assembly.

The two Centaflex, CF-A-04-1, torsional couplings are linked to a Ø24.5 mm, EN24 grade steel coupling shaft, as seen in detail drawing AAB561MM1402. One torsional coupling bolts to the flywheel by means of a three-bolt interface and the other to a steel flange at the opposite end of the driveshaft, as seen in detail drawing AAB561MM1403. This provides the attachment interface between the torsional coupling and the dynamometer.

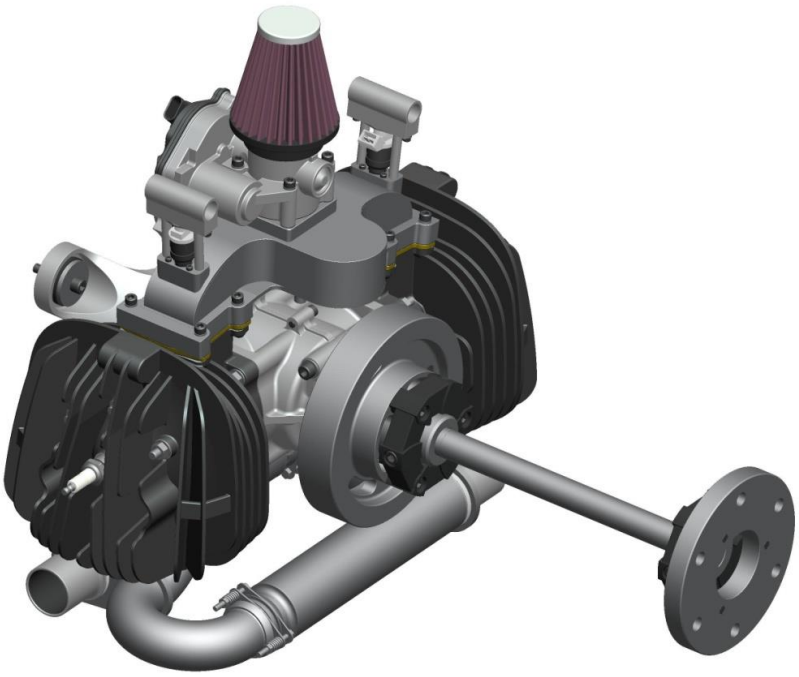

FIGURE 7.1: UAV ENGINE WITH FLYWHEEL AND DRIVESHAFT ASSEMBLY ATTACHED.

7.1.2 ENGINE ALIGNMENT AND PERIPHERAL SYSTEMS

A new engine mount, as illustrated by the blue engine test stand in Figure 7.2 below, was constructed to couple the UAV engine to the dynamometer, enable the accurate alignment of the engine and fit the required system peripherals.

FIGURE 7.2: UAV ENGINE TEST STAND AND INSTALLED PERIPHERAL EQUIPMENT.

The test cell layout for the testing of the UAV engine required that the following major points, typically in this order, be attended to:

- *The test stand alignment* required that the distance along the Y-axis, as illustrated in Figure 7.2, between the engine flywheel and dynamometer input flange be set to within 1 mm. A subtle, combined manipulation of displacement along and rotation about the X- and Z-axes served to ensure that both parallel and angular misaligment would be minimised. This tedious procedure resulted in a radial and axial misalignment, when measured with a dial gauge, of under 0.15 mm and 0.1 mm respectively.
- *The 25 kg counterweight,* painted green in the foreground of the above figure, was added when the initial alignment attempts proved futile owing to the moment introduced by the engine about the X-axis. The counterweight introduced a moment of essentially the same magnitude in the opposite direction and stabilised the engine mount.
- *The electric starter motor* function was performed by the same 40 kW electrical motor, controlled by a variable speed drive, as mentioned in Section 4.3.1. The electric motor is located behind the dynamometer and coupled to it by a torsional shaft with a one-way bearing at one end. This then performs the same function as that of a starter motor, since when the engine fires, the one-way bearing starts to disengage/slip and the engine can then continue to accelerate while the electric motor is switched off.
- *The exhaust system*, as seen in Figure 7.3, required the fabrication of two exhaust ducts, similar to that used when testing the Yamaha engine in Section 4.3.3, to duct the exhaust gas to the extraction air vents at the back of the test cell. The tail pipe outer diameter of the Zanzottera 498i silencer is 45 mm, while the inner diameter of the exhaust duct is 72.2 mm, resulting in a 13.6 mm air gap all round, as seen in Figure 7.4. This was purposely done to prevent the exhaust duct from functioning as an additional tuned exhaust pipe. The air gap also allowed the flow of test cell air, at ambient temperature, to flow down the exhaust duct, thus lowering the surface temperature of the duct.
- *Two cooling fans*, as seen in both the upper and lower figures, direct a forced draft of air at ambient temperature onto the cylinder heads of both cylinders. The fans were manually controlled by the operator and turned on when the cylinder head temperature exceeded 70°C.

FIGURE 7.3: ENGINE TEST STAND LAYOUT AS SEEN FROM THE TOP.

FIGURE 7.4: EXPERIMENTAL ENGINE TEST CELL EXHAUST SYSTEM.

- *Throttle control* was accomplished in the same manner as stated in Section 4.3.3, by an electrical actuator that pulled the throttle cable when remotely selecting a larger throttle opening.
- *The ignition system's* main components that were used were identical in function to those described in Section 6.5.5. The user-programmable, aftermarket automotive ECU selected was a Perfect Power XMS5A-4A, as seen mounted against the blue stand in the centre in Figure 7.5. The ECU received two inputs. The first was from the crank sensor, a Bosch 261 210, detecting the magnetic pulses from the toothed encoder wheel, as illustrated on the left. Note the slots in the encoder wheel; these enable the adjustment of TDC of the wheel to correspond with TDC of the piston as measured by a dial gauge. The second input was the TPS feedback that was artificially generated by using a remotely stationed potentiometer, controlled by the operator. This allowed the ignition timing to be retarded or advanced, 0° to 30° BTDC respectively, in order to maximise performance by noting the engine output. The ECU provided a single output voltage pulse, with the duration determined by the stipulated dwell time of between 2 ms and 4 ms, to charge the primary side of the coil. This is illustrated on the right in the figure below, and provides a spark to both cylinders simultaneously. The requirement for an ignition map, as stated in Section 6.5.5, was thus nullified by the operator manually adjusting the timing for each speed set point.

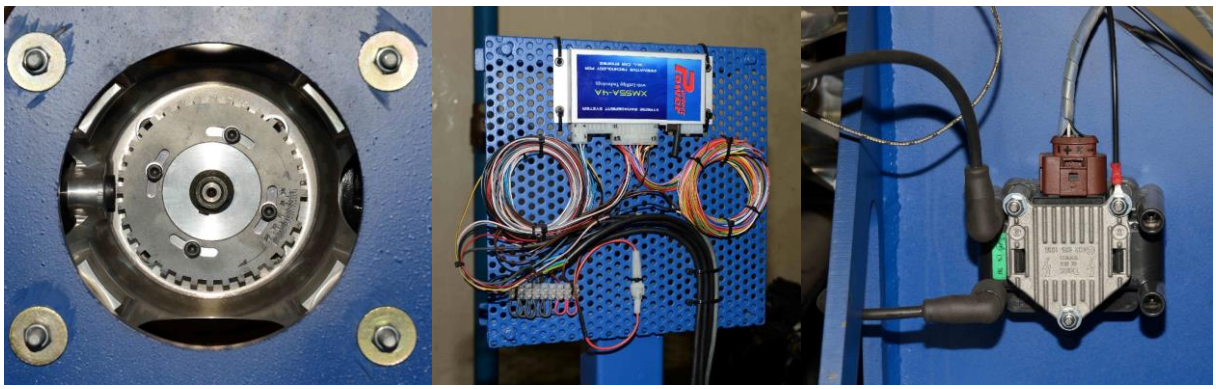

FIGURE 7.5: IGNITION ENCODER WHEEL (LEFT), ECU (CENTRE) AND COIL (RIGHT).

7.2 UAV ENGINE TESTING FAILURES AND RECTIFICATION

Before the UAV engine is run, numerous problems associated with a variety of systems and components have to be solved.

Modifications to the ignition system and the subsequent erratic operation thereof will firstly be documented. The alterations to the fuel system will then be described. Finally, the driveshaft failure, the resultant damage to peripheral engine components and the redesign thereof will conclude this section.

7.2.1 ERRATIC IGNITION

Initially the ignition system hindered the UAV engine from starting and running smoothly. Numerous modifications and subtle adjustments were made to most of the system in an attempt to rectify the problems.

The encoder wheel was the first item that required modification. The tooth profile of 30-2, as shown in drawing number AAB561SL0702 in Appendix F.9, had to be changed to 36-1. A single-tooth output encoder wheel was also tested with varying success.

The Perfect Power XMS5A-4A ECU, as described in the previous section, proved difficult to program and operate despite helpful assistance from the South African agents. Poor wiring layout of the low voltage trigger signal and high tension side, as described in Section 2.4.5, by the author initially resulted in low-voltage trigger pulses with erratic magnitudes, as illustrated in Figure 7.6 on the left. The solution was to separate the low- and high-tension systems and make the low-voltage trigger pulse line as short as possible. The upper right-hand photo in Figure 7.6 displays a stable magnetic inductive trigger pulse that has increased in magnitude, from approximately 0.6 V to 20 V peak-to-peak, at the same rotational speed.

FIGURE 7.6: TRIGGER PULSE VOLTAGE BEFORE (LEFT) AND AFTER REWIRING (RIGHT).

The manually operated TPS feedback, as described in Section 7.1.2, proved very effective at fine-tuning the timing to obtain maximum torque at a particular speed set point.

However, despite numerous attempts to resolve the problematic issues stated above, the UAV engine ignition system proved to be unreliable throughout the duration of the test.

7.2.2 FUEL INJECTION OMISSION

The UAV engine was initially designed to operate using fuel injection, as documented in Section 6.5.4. The entire fuel injection system was scrapped in favour of a single carburettor, as seen in Figure 7.7 below. Obtaining a fuel map requires substantial engine run time, as stated in Section 6.5.5, and the risk of possibly damaging the untested, experimental UAV engine was not deemed worthwhile.

The figure below displays a Mikuni VM26SS carburettor, the factory-fitted carburettor for the Yamaha DT 175, attached to a short intake runner that in turn is bolted to the large central plenum. From the knowledge gained about induction resonance, as stated in Section 4.5.3, the runner was kept as short as possible.

FIGURE 7.7: MIKUNI VM26SS CARBURETTOR AND INTAKE RUNNER BOLTED TO THE CENTRAL PLENUM.

Section 6.5.3 details the calculations used to estimate the ideal venturi throat diameter of 39.3 mm for the UAV engine carburettor. Since the Mikuni VM26SS carburettor has a throat diameter of 26 mm, a reduction in air flow at full throttle will result. This is, however, not considered too serious, since Section 5.1.1 states that obtaining maximum power output for this prototype engine is not paramount.

To ensure that the engine did not run lean and possibly sustain damage, the main jet of the carburettor was sized by monitoring the average exhaust temperatures, throughout the speed range while at full throttle, and comparing the results to those attained by the Yamaha DT 175, as tabulated in Appendix E.1. A #170 sized main jet was found to be optimal. Note that the fuel injectors and fuel rails remained fitted throughout testing but were never used.

7.2.3 DRIVESHAFT FAILURE

The design of the original driveshaft is documented in Section 7.1.1 and the associated assembly drawing AAB561MA1400, that can be found in Appendix F.16. Because of modifications to the original flywheel, erractic iginition and a poorly designed torsional coupling connection, the driveshaft failed, resulting in damage to the driveshaft and the engine crankshaft.

The original flywheel seen in detail drawing AAB561MM1404 had an inertia, of 24.3 x 10^{-3} kgm^2, as stated in Section 7.1.1, that is equivalent to a 32" wooden propeller. The author feared that the possible bending moment exerted on the crankshaft output shaft, due to the centrifugal force as defined by Eq. (3.58), might become excessively high in response to imbalance as the engine speed increased. It was considered prudent to decrease the mass, and unavoidably also the inertia, of the flywheel by turning off excessively thick sections on a lathe. The mass and inertia of the flywheel were decreased by 47% and 58% respectively to 2.65 kg and 10.5 x 10^{-3} kgm^2.

The erratic ignition, described in Section 7.2.1, especially at low engine speeds, resulted in high crankshaft rotational speed fluctuations. The crankshaft rotational speed fluctuation, as tabulated in Appendix C.1, decreases from 3.5% to 0.8% as the engine speed increases from 3000 rpm to 6500 rpm. The lower the engine speed, especially during startup and initial engine acceleration, the greater the rotational speed fluctuation and so too δE, T and θ as defined in Section 3.8. The resultant increase in ΔT results in greater forces in the coupling bolts. Figure 7.8 below shows two of the three hub bolts of the coupling, ripped out of the hub at the flywheel end of the driveshaft. This occurred at engine speeds well below 3000 rpm.

FIGURE 7.8: RADIAL CENTAFLEX COUPLING BOLTS RIPPED OUT OF HUB.

Thus, because of the lower inertia of the flywheel, the erratic ignition and a poorly designed/inappropriate torsional coupling, the failure of the coupling hub, as illustrated above, resulted in the unsuccessful torsional driveshaft constructed from two Centaflex, CF-A-04-1, torsional couplings, as illustrated in Figure 7.9.

FIGURE 7.9: FAILED CENTAFLEX TORSIONAL DRIVESHAFT.

This sudden failure of the driveshaft, on the flywheel side, resulted in bending the crankshaft out of alignment about the press-fit crank pins. Consequently, the engine had to be stripped, the crankshaft re-aligned and the UAV engine mounted back in position.

While stipping the engine, the researcher noted that the woodruff key, that secures the flywheel and the crankshaft, had been partly sheared, as illustrated in Figure 7.10. This was due to either the rotational speed fluctuations mentioned above or an insuffienctly torqued nut that allowed relative movement between the flywheel and the taper shaft.

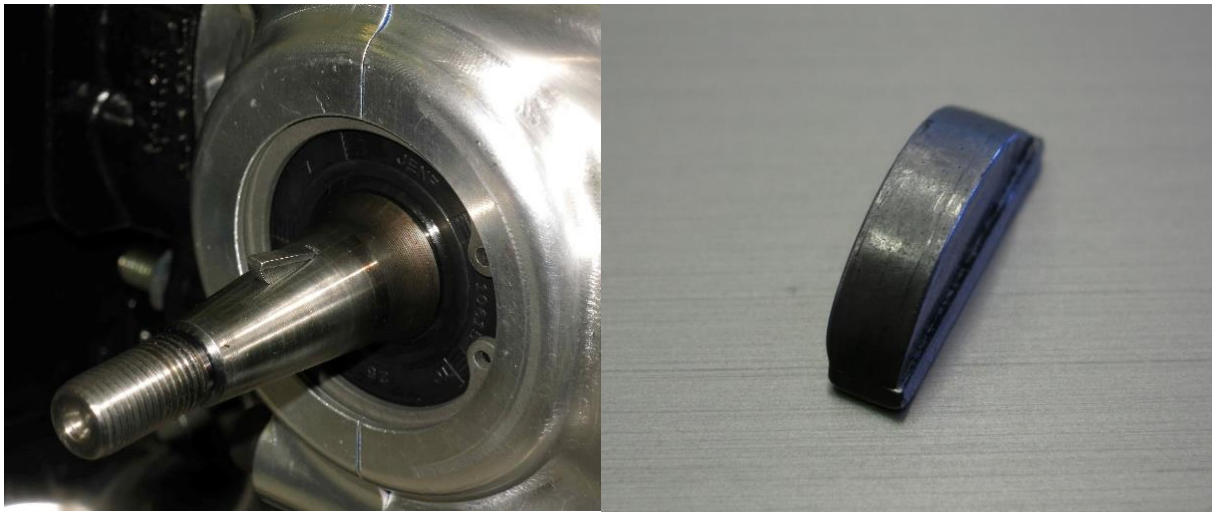

FIGURE 7.10: PARTLY SHEARED WOODRUFF KEY.

7.2.4 ALTERNATIVE SASOL DRIVESHAFT

After the catastrophic failure of the original driveshaft, as documented in Section 7.2.3, a torsional transmission based on a different design was required. The fundamental change in the philosophy of the new driveshaft will be described below, along with the importance of maintaining the original flywheel inertia and ease of fitment.

Since the old driveshaft failed catastrophically and consequently damaged the engine crankshaft, a new driveshaft design was required. The Centaflex torsional coupling used for this application, as seen in Figure 7.8, exhibited two problems. Firstly, the three axial bolts that bolt into the flywheel could not maintain the concentricity of the coupling with the flywheel under high torsional impulses. Secondly, the three radial bolts that secure the coupling to the shaft were ripped out because of insufficient thread depth into the hub.

An entirely new design had to be implemented, with two fundamental changes. Firstly, the coaxial alignment of the driveshaft would be maintained by the fitment of spherical bearings at both ends. These bearings allow angular movement about a central point, but prevent radial deflection. The outer ring of the bearing supports the driveshaft, while the inner ring is located on a spigot at both the flywheel and dynamometer ends, as illustrated by the solid model sectional view in Figure 7.11. The right of the shaft represents the dynamometer end with a commercially available spherical bearing fitted. The left illustrates the flywheel end and due to limited space uses a custom designed and manufactured spherical bearing. The assembly and detail drawings for this alternative driveshaft can be found in Appendix F.19. Note that both the old and new driveshaft retain the assembly section number 14.

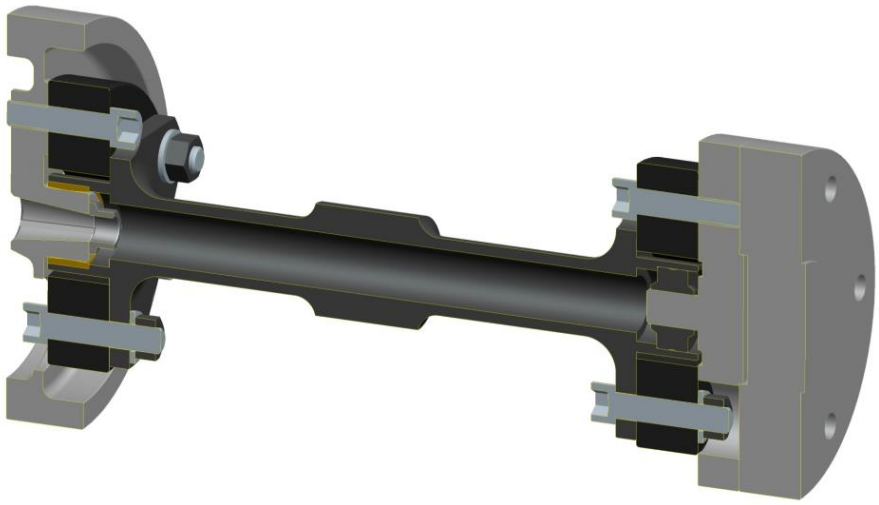

FIGURE 7.11: SOLID MODEL SECTIONAL VIEW OF THE NEW TORSIONAL DRIVESHAFT.

The second fundamental change required that the torsional rubbers would serve no function other than transferring torque and providing damping between the engine and dynamometer. Figure 7.12 below illustrates all the parts that comprise the new torsional driveshaft. Note that the driveshaft and torsional rubbers were kindly supplied by Sasol.

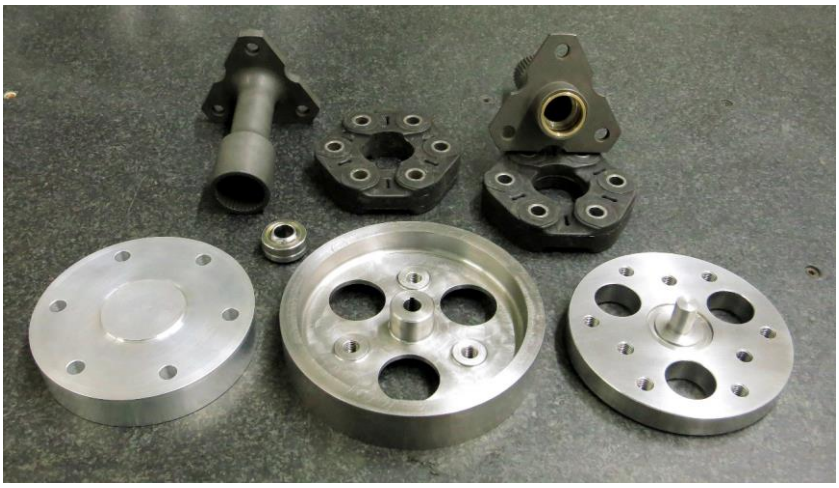

FIGURE 7.12: ALL MANUFACTURED PARTS IN FRONT AND SASOL-SUPPLIED DRIVESHAFT AND TORSIONAL RUBBERS AT THE BACK.

The lower inertia of the modified flywheel and the erractic ignition, as described in Section 7.2.3 and Section 7.2.1 respectively, together possibly introduced torsional loads on the old driveshaft for which it was not designed.

In an effort to reduce the magnitude of the torsional impulses, it was decided that the inertia of the new flywheel at 20.7 x 10^{-3} kgm^2, as seen above, would approach that of a typical 32” wooden propeller, as stated in Section 7.1.1. The inertia of this new flywheel is 13.8% lower than the original. However, this flywheel, with a mass of 3.46 kg, is 30.3% lighter than the original.

Another important consideration while designing the flywheel was to ensure that the overhanging moment, as stated in previous sections, was kept to a minimum. This was done by placing approximately half of the torsional coupling within the flywheel as close to the main bearing of the engine as possible, as illustrated in Figure 7.11. This resulted in the new flywheel having a length of 48.8 mm from its CG to the nearest main bearing when compared to the 66.3 mm of the original, bringing about an improvement of 26.4%.

The two-part spigot and spacer arrangement of the driveshaft connection to the dynamometer flange, as illustrated in Figure 7.11, was especially designed like that. The alignment of the engine to the dynamometer, as described in Section 7.1.2, is tedious and very time-consuming. Because of insufficient spline length and spigots at both ends of the driveshaft, this arrangement allows the fitment and removal of the shaft without disrupting the alignment of the engine.

Figure 7.13 below illustrates the new torsional driveshaft, fitted and aligned to the dynamometer. The flywheel end is displayed on the left, while the dynamometer connection is illustrated on the right.

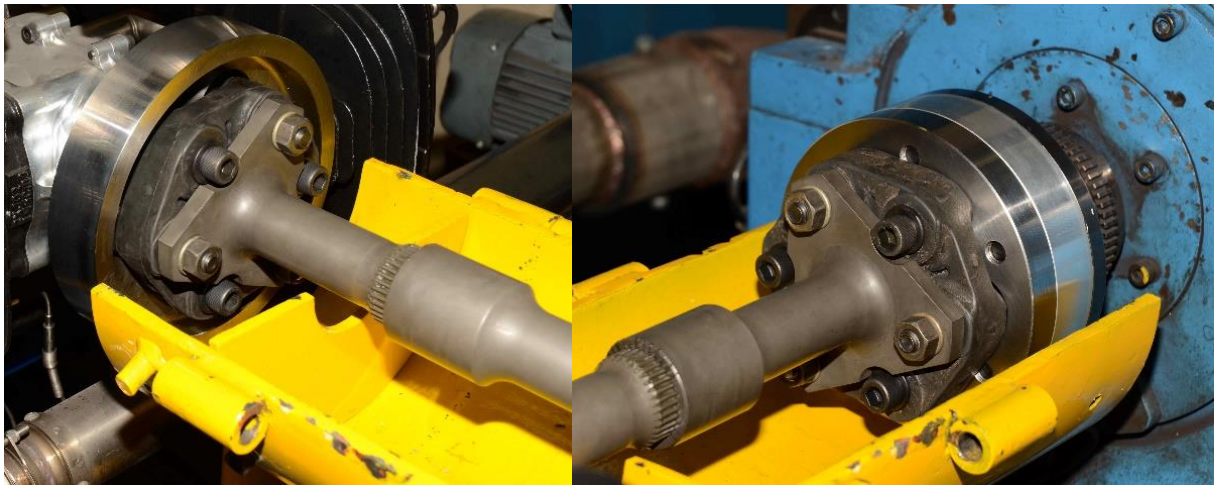

FIGURE 7.13: NEW TORSIONAL DRIVESHAFT FITTED TO THE ENGINE (LEFT) AND THE DYNAMOMETER (RIGHT).

7.3 UAV ENGINE TEST RUN AND RESULTS

At this stage the UAV engine is finally ready for the first test run, following the identification and rectification of the problems associated with various systems and components, as documented in the previous section.

This section will commence with a brief description of the sensory inputs and data-logging procedure that will be used to record the engine runs. This will be followed by listing the important pre-start checks that must first be done on the entire test cell installation prior to starting the engine. Lastly, the UAV engine test results will be documented and plotted.

7.3.1 EXPERIMENTAL ENGINE INSTRUMENTATION

The test cell system based on ETA, as detailed in Section 4.4.1, was once again used for the running of the UAV engine. The recording of data, as described in the first paragraph of Section 4.6.2, was again conducted at a fixed rate of 2 Hz for 40 data points per set point.

The sensory inputs and outputs used for this test are as follows:

- *Both engine torque and speed* were measured by the dynamometer.
- *The fuel flow*, but not the air flow, was recorded by the AVL fuel balance.
- *Both exhaust temperatures* were measured as illustrated in Figure 7.4. It is important that both be measured, since this provides combustion and A/F mixture information.
- *A single cylinder head temperature* was measured. This provided the operator the temperature information required to operate the two cooling fans manually.

Compared to the testing of the Yamaha DT 175, as detailed in Chapter 4, the number of recorded data channels might seem insufficient. However, bearing in mind the design objectives stated in Section 5.1.1, the aim of this dynamometer test is to establish that the prototype engine runs.

7.3.2 PRE-START CHECKS

After ensuring that the entire test cell installation was mechanically sound, the following pre-start checks were done:

- The *rotation direction* of the electric starter motor had to be checked. Since this engine is a reed valve, two-stroke engine, it can run in either direction. However, there is a preferred direction and that is dictated by the engaged direction of the one-way bearing. The engine thus runs in the counter-clockwise direction when viewed from the flywheel end.
- *Mechanical runs* on the engine were conducted at low speed, 250 rpm to 750 rpm, by engaging the electric starter motor. The initial runs were conducted with no fuel flow, omitted sparkplugs and the ignition switched off to verify the mechanical working of the engine and associated dynamometer systems.
- *The ignition system* was checked next. With the sparkplugs still omitted and the ignition turned on, the engine was again rotated at low speed by the starter motor. By using a timing light, the ignition timing was verified by ensuring that the ECU timing setting correlated with the corresponding timing marks on the flywheel. The dwell time was also checked, by using an oscilloscope connected to the primary side of the coil, to confirm the charge time. The correct functioning of the secondary side of the coil was visually established by the sparking of the sparkplugs.
- *The fuel system*, although much simplified since the omission of the fuel injection system, still required checks. The zero-to-100% throttle actuation was verified, as was the fuel flow into the carburettor once the supply tap was opened.
- *The peripheral systems* as mentioned in Section 7.1.2 were the last to be checked for correct functioning.

These checks were done to ensure that all known risks to the prototype were mitigated.

7.3.3 UAV ENGINE TEST RESULTS

With the pre-start checks completed, the UAV engine was ready to be started. To minimise the initial structural stress on the engine, and enable smooth running due to some dynamometer load, the first run was conducted at 3000 rpm with a throttle position of 30%. To minimise the risk of damage to the prototype, the maximum engine speed was incrementally increased, from 3000 rpm to a maximum of 5500 rpm, only once a thorough external inspection of the engine had been done. The throttle position for all the engines runs, except the first run, was 100%, since the engine's part-throttle performance is not required for this dissertation. The experimental results for the UAV engine can be found in Appendix E.2.

Figure 7.14 plots the T_{mb}. for the UAV engine from 2500 rpm to 5500 rpm, in 500 rpm increments, while at full throttle. Note that the correction factors as described in Section 4.6.1, have been applied to both the T_{mb} and P_b plots.

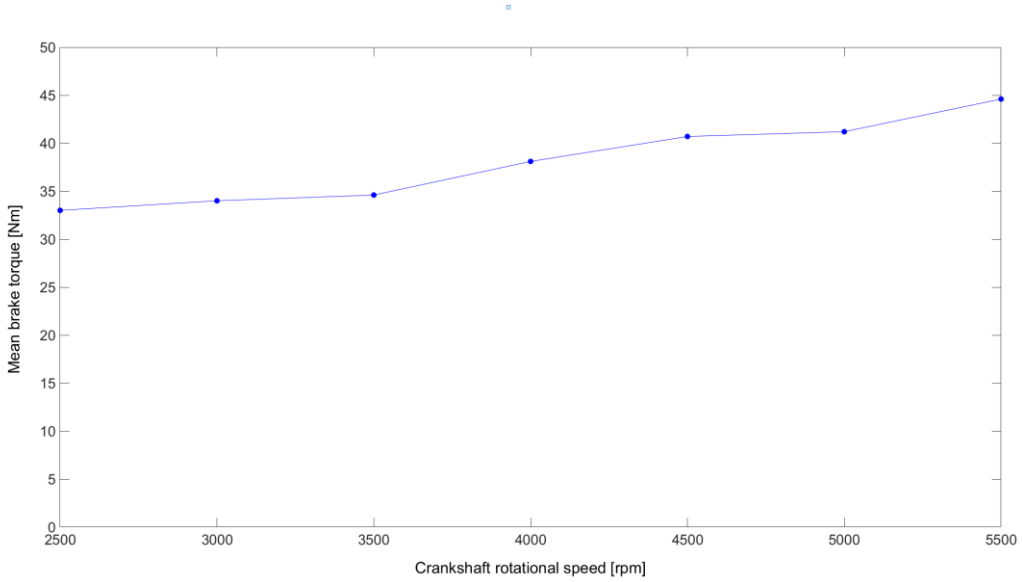

FIGURE 7.14: EXPERIMENTAL MEAN BRAKE TORQUE OF THE UAV ENGINE AS FUNCTION OF CRANKSHAFT ROTATIONAL SPEED.

The minimum and maximum T_{mb} are 33.0 Nm and 44.6 Nm at 2500 rpm and 5500 rpm respectively. Note that the torque curve upward trend is almost linear through the engine speed range, with no peaks or troughs. Figure 7.15 is a graph depicting the P_b for the UAV engine from 2500 rpm to 5500 rpm at full throttle.

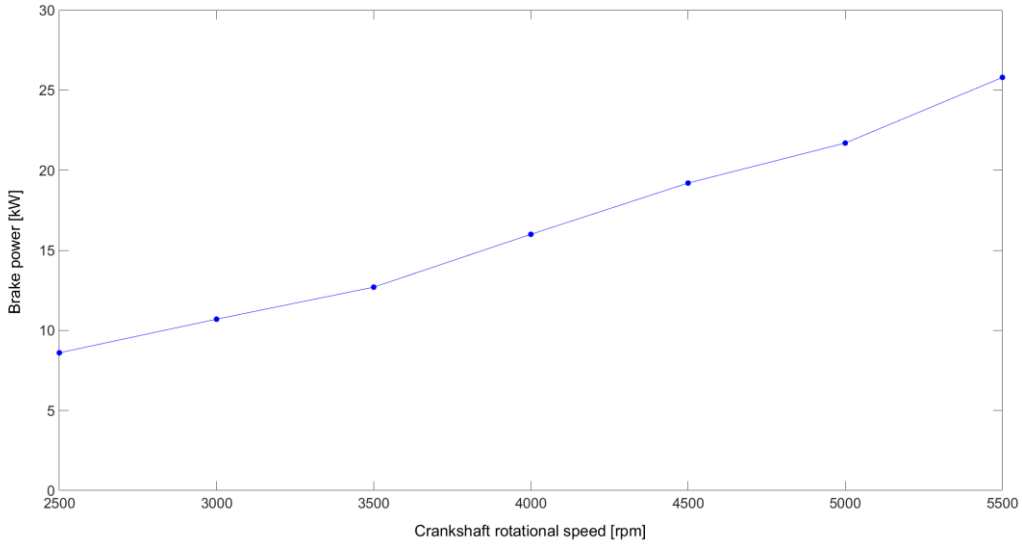

FIGURE 7.15: EXPERIMENTAL BRAKE POWER OF THE UAV ENGINE AS FUNCTION OF CRANKSHAFT ROTATIONAL SPEED.

The corrected P_b for the engine increases steadily from a minimum of 8.6 kW at 2500 rpm to a maximum of 25.8 kW at 5500 rpm. Note that both the torque and power curves exhibit an upward trend at 5500 rpm, potentially indicating that the point of maximum power has not yet been attained.

Figure 7.16 plots the two exhaust temperatures for the left- and right-hand cylinder banks. The left bank temperature rises steadily from 417.7°C to 563.4°C as the engine speed increases, while that of the right bank remains at about an average temperature of 490.0°C. The maximum temperature for the right bank is 502.5°C at 5500 rpm, 60.9°C less than that of the left bank at the same engine speed.

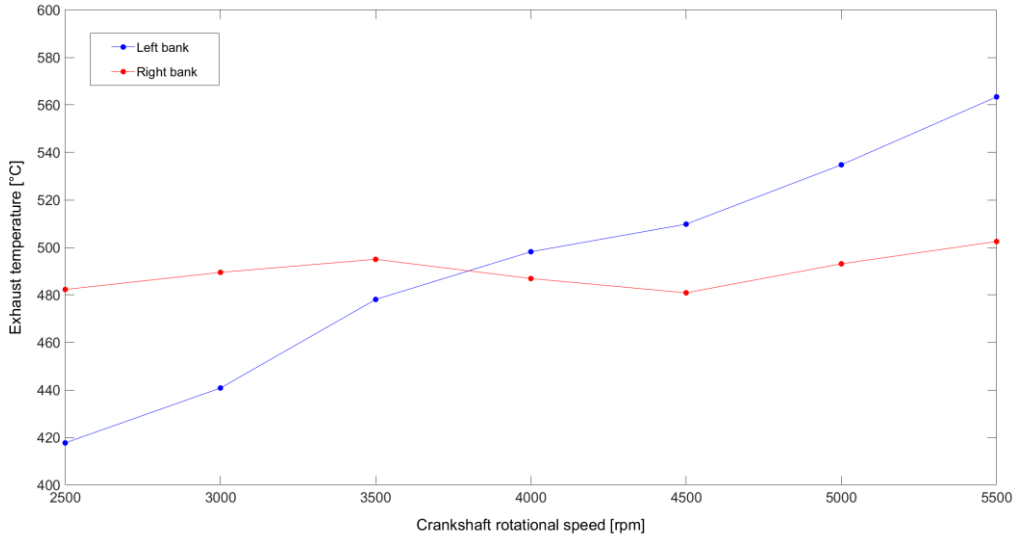

FIGURE 7.16: LEFT AND RIGHT BANK EXHAUST TEMPERATURES OF THE UAV ENGINE AS FUNCTION OF CRANKSHAFT ROTATIONAL SPEED.

The $bmep$ of the UAV engine from 2500 rpm to 5500 rpm, at full throttle, is plotted in Figure 7.17. The $bmep$ increases continually from 5.32 bar at 2500 rpm to 7.19 bar at 5500 rpm. Note that the trend of this curve will be identical to that of Figure 7.14, since $bmep$ is directly proportional to T_{mb}, as stated in Eq. (3.54).

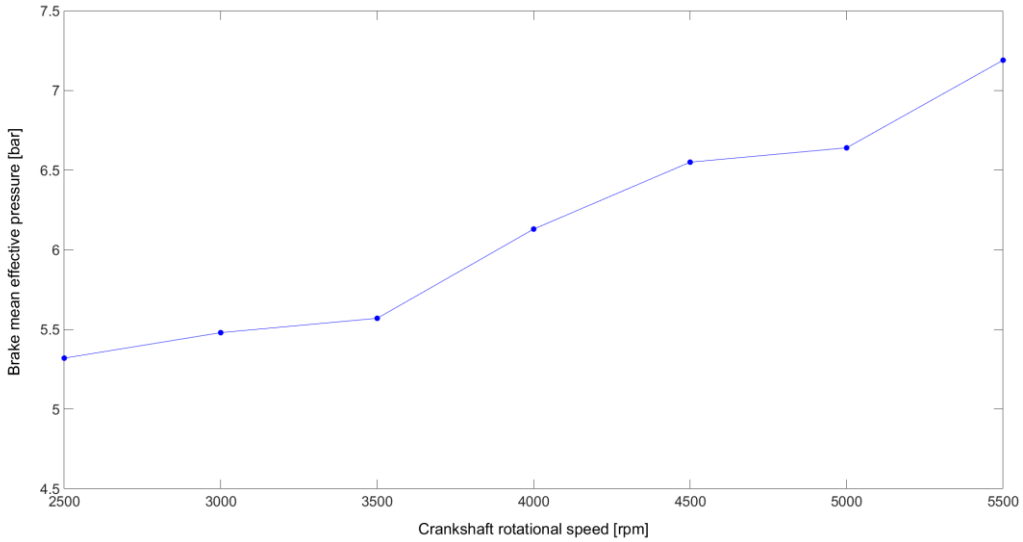

FIGURE 7.17: EXPERIMENTAL BRAKE MEAN EFFECTIVE PRESSURE OF THE UAV ENGINE AS FUNCTION OF CRANKSHAFT ROTATIONAL SPEED.

The sfc for the UAV engine is plotted in Figure 7.18 below. The sfc averages 600.0 g/kWh from 2500 rpm to 3500 rpm and then consistently drops to 341.7 g/kWh at 5500 rpm. The fuel efficiency of the experimental engine thus decreases slightly from 2500 rpm to 3500 rpm and then continuously improves to 5500 rpm.

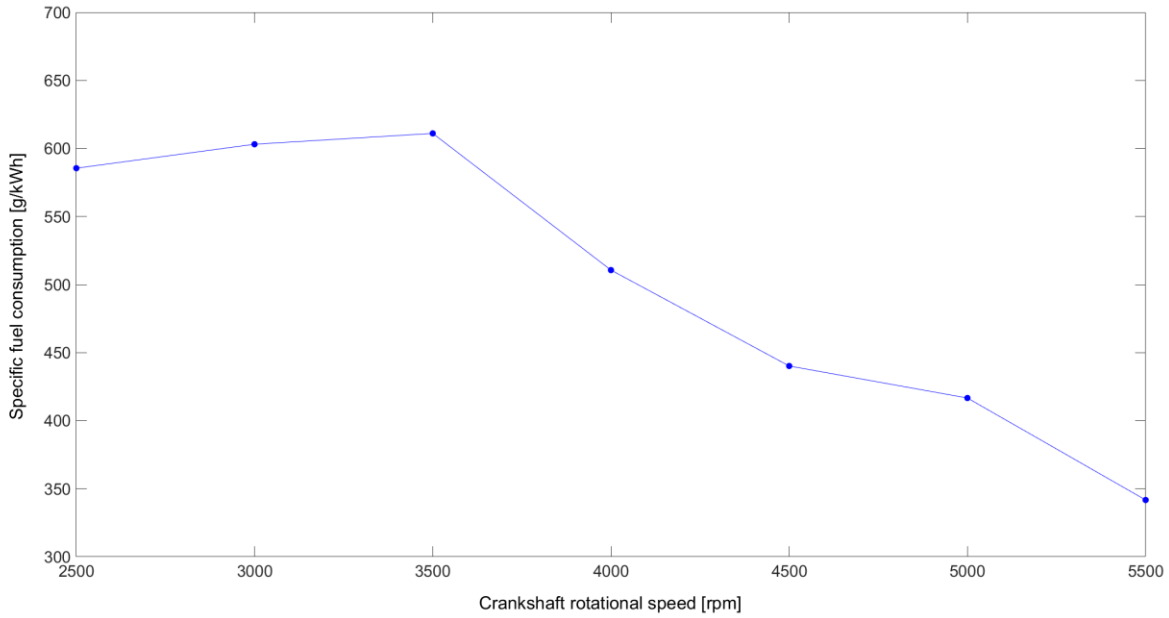

FIGURE 7.18: SPECIFIC FUEL CONSUMPTION OF THE UAV ENGINE AS FUNCTION OF CRANKSHAFT ROTATIONAL SPEED.

This concludes the documentation of the experimental UAV engine test results. The analysis and interpretation of the above results will follow in Section 7.4.

7.4 CALCULATION AND INTERPRETATION OF RESULTS

With the testing of the UAV engine completed and documented in the previous section, this section will examine how effectively the prototype test engine has performed.

The analysis and interpretation of the UAV engine test results will be detailed in the three sections that follow. The first will compare the prototype experimental results to those theoretically calculated. The second will scrutinise the performance aspects of the UAV engine that should be compared to those attained by the Yamaha DT 175 that was tested in Chapter 4. The third and last section will compare selected test results to those attained by two similar UAV engines and conclude with comments.

7.4.1 COMPARISON OF UAV EXPERIMENTAL AND THEORETICAL RESULTS

The combination of Chapters 3, 4 and 5 provided the methodology and input data to construct a theoretical UAV engine model. The accuracy of the UAV engine performance predictions, as seen in Appendix C.1, will now be compared to the experimental results. The comparative plots that follow start at 3000 rpm, since the Yamaha DT 175 was not tested at 2500 rpm.

Figure 7.19 plots the experimental and theoretical T_{mb} in blue and red respectively from 3000 rpm to 5500 rpm, in 500 rpm increments, at full throttle. The third plot, in dashed black at the top of the figure, indicates the percentage increase of the experimental results over the theoretical predictions.

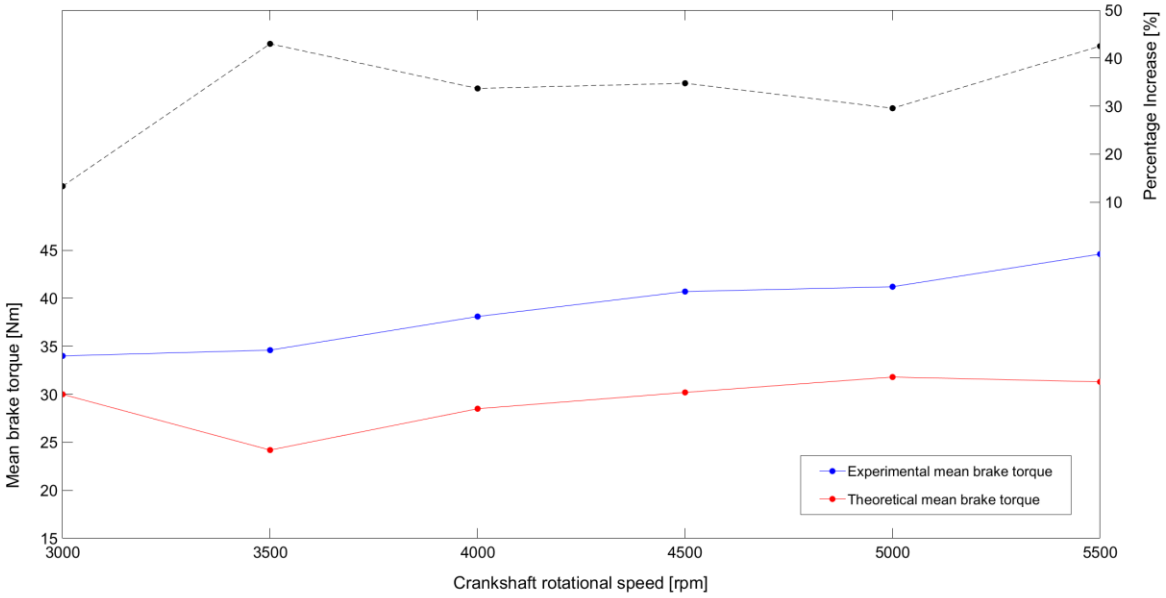

FIGURE 7.19: EXPERIMENTAL AND THEORETICAL MEAN BRAKE TORQUE COMPARISON OF UAV ENGINE AS FUNCTION OF CRANKSHAFT ROTATIONAL SPEED.

When studying the two T_{mb} curves, the following points emerge:

- There is a substantial percentage increase in the experimental T_{mb} over the theoretical, as indicated throughout the N_c range by the top black dashed curve. The average percentage increase is 32.8% throughout, with a minimum of 13.3% at 3000 rpm and a maximum of 43.0% at 3500 rpm.
- The 32.8% average experimental T_{mb} increase over the theoretical curve renders the theoretical prediction inaccurate. In addition, the upward and downward trends of the theoretical curve at 3000, 3500 and 5500 rpm do not correlate with the experimental curve, as indicated by the steep positive and negative slope changes of the comparative percentage curve.
- The approximately 33% higher T_{mb} throughout the N_c range implies greater moments and forces throughout the engine. This renders the theoretical results that are based on the experimental engine data, as tabulated in Appendix C, numerically inaccurate.
- The experimental results of T_{mb} are surprising, but not at all disappointing. As stated previously, the continuous upward trend from 34.0 Nm at 3000 rpm to 44.6 Nm at 5500 rpm and possibly still climbing beyond is a tremendous result. Should a propeller be connected and swung between the plotted N_c range the increasing load, as the engine speed is increased, is countered by more T_{mb}.

The comparative P_b plots of the experimental and theoretical results, from 3000 rpm to 5500 rpm, are displayed in Figure 7.20 in blue and red respectively. The third plot, in black dashes, again illustrates the percentage increase of the experimental results over the theoretical estimate.

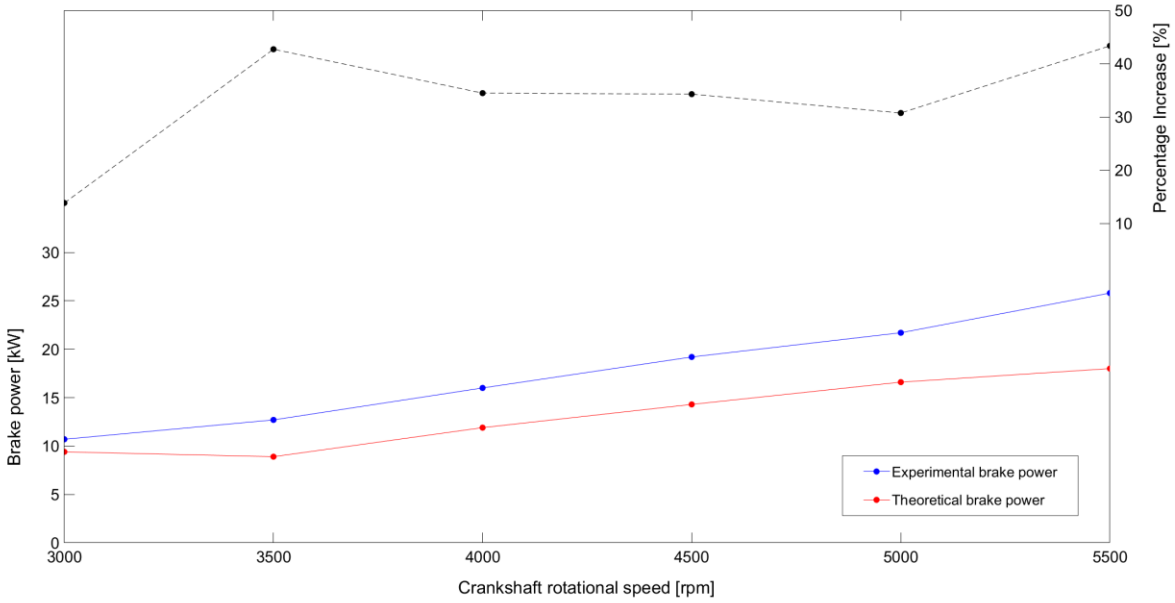

FIGURE 7.20: EXPERIMENTAL AND THEORETICAL BRAKE POWER COMPARISON FOR THE UAV ENGINE AS FUNCTION OF CRANKSHAFT ROTATIONAL SPEED.

The following points are worth noting:

- The black dashed percentage increase curve for P_b is identical to T_{mb}; it should be, since Eq. (3.53), when P_b is made the subject, indicates that P_b is directly proportional to T_{mb} and N_c. Thus, the commentary for Figure 7.19 regarding the curve illustrating the percentage increase also applies to this figure.
- The 32.8% average increase in P_b throughout the N_c range also renders the theoretically predicted values for brake power inaccurate.
- As for the previous T_{mb} figure, this approximately 33% increase in P_b thoughout the N_c range is not unwelcome. The corrected P_b starts at 10.7 Kw at 3000 rpm and continues to climb smoothly to 25.8 kW at 5500 rpm. This substantial increase in P_b, over the theoretical estimate, increases the energy density, kW per kg, of the UAV engine. In the aviation industry, this is a pleasing finding, since piston aeroplane engines "call for the utmost possible power output from the minimum weight" (Ricardo & Hempson, 1968:279).

Figure 7.21 on the following page displays the $bmep$ of the experimental and theoretical curves for the UAV engine in blue and red respectively as a function of N_c from 3000 rpm to 5500 rpm.

The following points are applicable:

- The trend of both the blue and red $bmep$ curves are identical to the two T_{mb} curves and this should be so, since Eq. (3.54) indicates that $bmep$ is directly proportional to T_{mb}.
- The percentage increase curve of the experimental over the theoretical results is then also identical to that for the T_{mb}. Thus, all comments made for Figure 7.19 in this regard are applicable here.
- The $bmep$ of the UAV engine from a low of 5.48 bar at 3000 rpm to a high of 7.19 bar at 5500 rpm is once again better than expected.
- The average $bmep$ of the theoretical prediction, from 3000 to 5500 rpm, is 4.7 bar, while that of the experimental results is 6.3 bar.

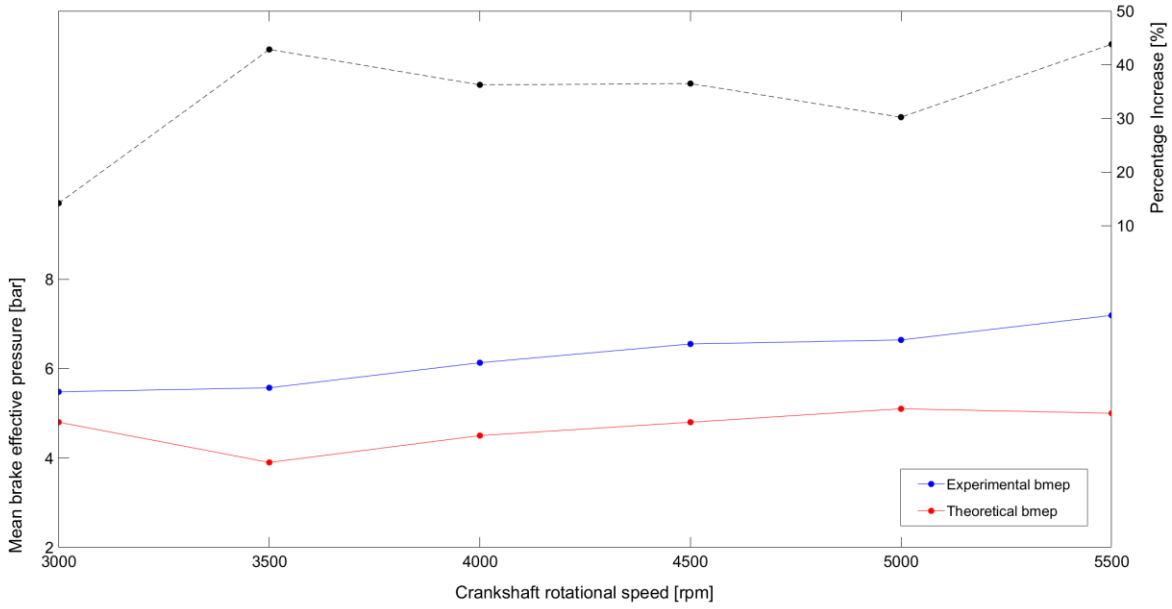

FIGURE 7.21: EXPERIMENTAL AND THEORETICAL BRAKE MEAN EFFECTIVE PRESSURE COMPARISON FOR THE UAV ENGINE AS FUNCTION OF CRANKSHAFT ROTATIONAL SPEED.

The figure above does, however, explain why the theoretical estimates for T_{mb} and P_b, and by implication then all the associated values in Appendix C, are inaccurate. This is due to the following:

- Throughout the engine speed range, 3000 rpm to 5500 rpm, there is an average of 32.8% increase in $bmep$, as with T_{mb} and P_b.
- Thus, the average combustion pressure throughout a single crankshaft revolution is approximately 32.8% higher than that experimentally measured/theoretically predicted.
- The correction that must be made to the instantaneous p, the cylinder pressure curve, as illustrated in Figure 4.19 to accommodate the average 32.8% increase, is unknown.

Blair states: From experimental work for various types of two-stroke engines, the potential levels of attainment of brake mean effective pressure are well known within quite narrow limits. Blair (1996:43) also tabulates that an untuned-silenced and tuned-silenced exhaust system for a single-cylinder, two-stroke engine should produce $bmep$ around 4.5 to 6 bar and 8.0 to 9.0 bar respectively.

The author thus assumed that the cylinder pressure curves of the Yamaha DT 175, a well-established, reputable brand, would be a fair representation for a similar SI, two-stroke engine design. Yamaha specifies a maximum torque, assumed to be at the flywheel, of 18.6 Nm at 5500 rpm and 20.6 Nm at 7000 rpm for the DT 175 and YFS 200 Blaster respectively. The resultant maximum $bmep$ values for the DT 175 and YFS 200 are 6.83 bar and 6.64 bar respectively. Admittedly this does not occur at the same engine speed, but the difference is 2.8% with respect to the DT 175. Thus, according to the author, the differences in the two $bmep$ curves should have been within a few percentage points either way, not 32.8%.

The theoretical and experimental average $bmep$ values of 4.7 bar and 6.3 bar respectively for the UAV engine is a difference of 1.6 bar or 32.8% and one or more of the following points on the following page might apply:

- The Yamaha DT 175 that was tested was possibly in poor condition. The Yamaha specifications, as seen in Table 4.1, for the DT 175 state a maximum torque of 18.6 Nm at 5500 rpm. The test engine attained 15.1 Nm at 5500 rpm. This is lower than the factory-stated claim by 19%.
- The port timing of the cylinders of the UAV engine, thus the Yamaha YFS 200 Blaster, has possibly been designed for highly tuned applications. Although the port timing of the YFS 200 cylinders has not been measured, this seems unlikely, given that the maximum calculated/specified $bmep$ is 6.64 bar, which correlates very well with the DT 175 maximum $bmep$ of 6.83 bar. This possibly indicates similar states of "tune".
- The DT 175, as illustrated in Figure 4.5, was tested with the factory-fitted exhaust system that does include a tuned length and silencer section. The UAV engine, as illustrated in Figure 7.4, was fitted with two untuned and silenced exhaust systems. Given that the maximum $bmep$ ratings for both engines are essentially identical, the fitted tuned exhaust system of the DT 175 should in theory have allowed this engine to attain higher performance than the UAV engine. The opposite outcome has occurred, with the maximum $bmep$ of 7.19 bar at 5500 rpm improving the factory-stated maximum of 6.64 bar at 7000 rpm for the UAV engine. The reason is unknown.
- The UAV engine test cell exhaust system, as pictured in Figure 7.4, possibly acted as a tuned exhaust system. This seems highly unlikely, since the photo clearly illustrates the gap between the UAV exhaust outlet and the test cell ducting. This air gap would dissipate the pressure pulse generated by the exhaust. In addition, the $bmep$ increase would only feature within a certain engine speed band, not over the entire N_c range.
- The inlet manifold of the UAV engine is unique to two-stroke engines, for the reasons described in Section 6.5.3. From the experimental results, it is clear that the intake manifold design and carburettor combination did not detract from the performance. However, the possible benefits to be had from this design configuration are untested.

7.4.2 COMPARISON OF UAV AND YAMAHA DT 175 EXPERIMENTAL RESULTS

Two experimental results obtained by both the UAV and Yamaha DT 175 engines, that are noteworthy and comparable, will be investigated. Firstly, the exhaust temperatures and secondly the specific fuel consumption, throughout the engine speed range while at full throttle, will be compared.

Figure 7.22 compares the UAV left- and right-hand cylinder bank exhaust temperatures, in blue and red respectively, to the Yamaha DT 175, in dashed black, from 3000 rpm to 5500 rpm while at full throttle.

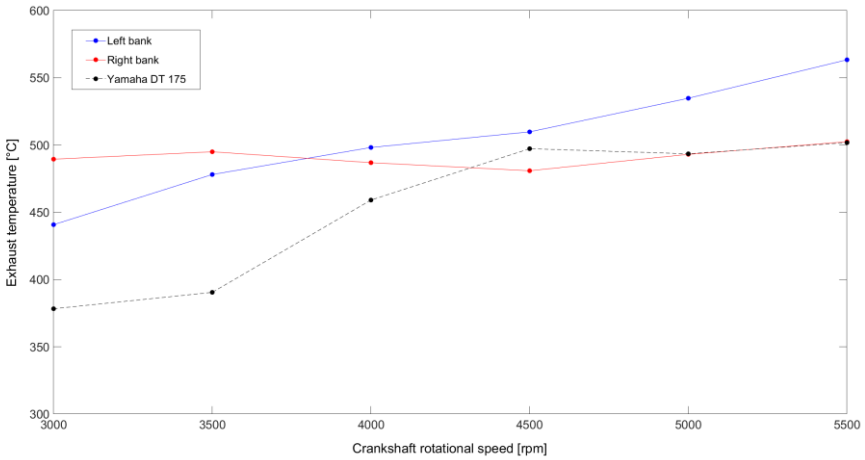

FIGURE 7.22: UAV ENGINE AND YAMAHA DT 175 EXHAUST TEMPERATURES AS FUNCTION OF CRANKSHAFT ROTATIONAL SPEED.

A benefit of having first run the Yamaha DT 175 test engine in standard tune was that the full load exhaust temperature throughout the speed range was obtained. This information was useful when the UAV engine was first run to ensure that the engine did not run too hot, indicating that the carburettor jetting was incorrect, as stated in Section 7.2.2.

From studying the figure, the following observations emerged:

- The left- and right-hand cylinder banks of the UAV engine do not follow the same trend. The left-hand bank temperature follows an upward trend, from 440.8°C to 563.4°C as the speed increases, that is similar to that of the DT 175, whereas the right-hand bank averages an exhaust temperature of about 491.3°C. The reason for this is unknown, since there is a loose relationship between exhaust temperature and $bmep$ (Blair, 1996:442). Thus, as the $bmep$ increases through the N_c range, as seen in Figure 7.21, so should the exhaust temperature.
- According to Blair, typical exhaust temperature ranges for engines below 5 bar $bmep$ are between 350°C and 450°C (Blair, 1996:436). He also states that the anticipated exhaust temperatures of Enduro and Grand Prix motor cycle racing engines can be 500°C to 600°C respectively (Blair, 1996:442). With the minimum and maximum temperatures of 441°C and 563°C, for both banks of the UAV engine throughout the speed range, the measured exhaust temperatures do not seem unreasonable.
- The correlation between the DT 175 and UAV engine exhaust temperatures is good, from 4000 to 5500 rpm. The two DT 175 exhaust temperatures at 3000 and 3500 rpm are lower than that of both banks of the UAV engine, but not outside the range stated by Blair in the previous point.

The sfc of the UAV and DT 175 engines, at full throttle, is plotted in Figure 7.23 in blue and red respectively from 3000 rpm to 5500 rpm. The percentage change, when compared to the Yamaha DT 175, is illustrated by a black dashed line at the top of the figure.

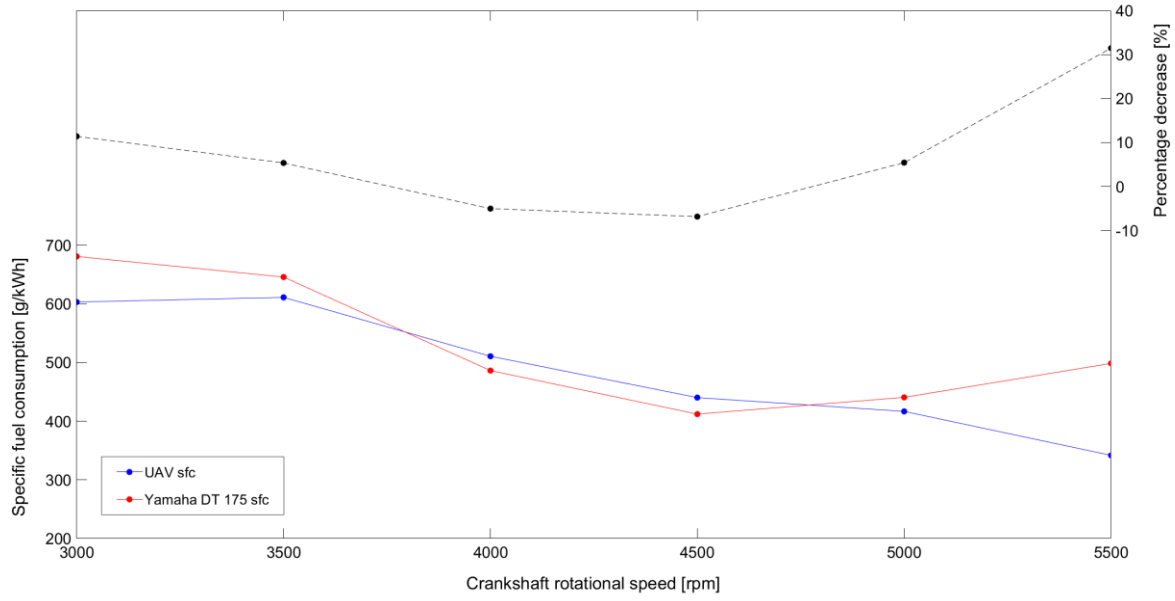

FIGURE 7.23: EXPERIMENTAL ENGINE AND YAMAHA DT 175 SPECIFIC FUEL CONSUMPTION AS FUNCTION OF CRANKSHAFT ROTATIONAL SPEED.

The following points are worth noting:

- The sfc of the UAV engine is at its highest of 611.1 g/kWh at 3500 rpm and drops to its lowest of 341.7 g/kWh at 5500 rpm. The trend of the DT 175 sfc curve is nearly identical at all points except at 5500 rpm.
- The two sfc curves have excellent correlation from 3500 rpm to 5000 rpm; the maximum difference is 6.8% at 4500 rpm. This is a welcome finding, since both engines are SI, two-stroke engines in what is believed to be a similar state of tune.
- Blair specifies that a 200 cc Batoni two-stroke engine, which is used in Vespa scooters, obtains its best and worst sfc of 456 g/kWh and 670 g/kWh at full throttle (Blair, 1996:476-477). Thus, all the sfc values attained by the UAV engine, except one, are typical for engines of this class. The sfc of 342 g/kWh at 5500 rpm seems better than average.

7.4.3 UAV ENGINE PERFORMANCE COMPARED TO COUNTERPARTS

With the comparative analysis of the UAV engine experimental results against the theoretical predictions and test engine outcomes complete, one final investigation remains. The T_{mb}, P_b and sfc of the experimental engine will be compared to those of two similar UAV engines and the chapter will conclude with comments.

The two UAV engines to be compared are the Zanzottera 498H and the Limbach L550E, seen in Figure 1.3. Both are two-stroke, SI, horizontally-opposed, air-cooled engines. The Zanzottera is an Italian-manufactured two-cylinder engine of 490 cc capacity, while the Limbach is a German-produced four-cylinder engine of 548 cc. The manufacturers' datasheets for the Zanzottera 498H and the Limbach L550E can be found in Appendices H.1 and H.2 respectively.

Figure 7.24 plots the T_{mb} for the UAV engine, Zanzottera and Limbach in blue, red and black respectively from 2500 rpm to 7500 rpm. Note that none of the engines uses the entire engine speed range and that each curve only displays the available data.

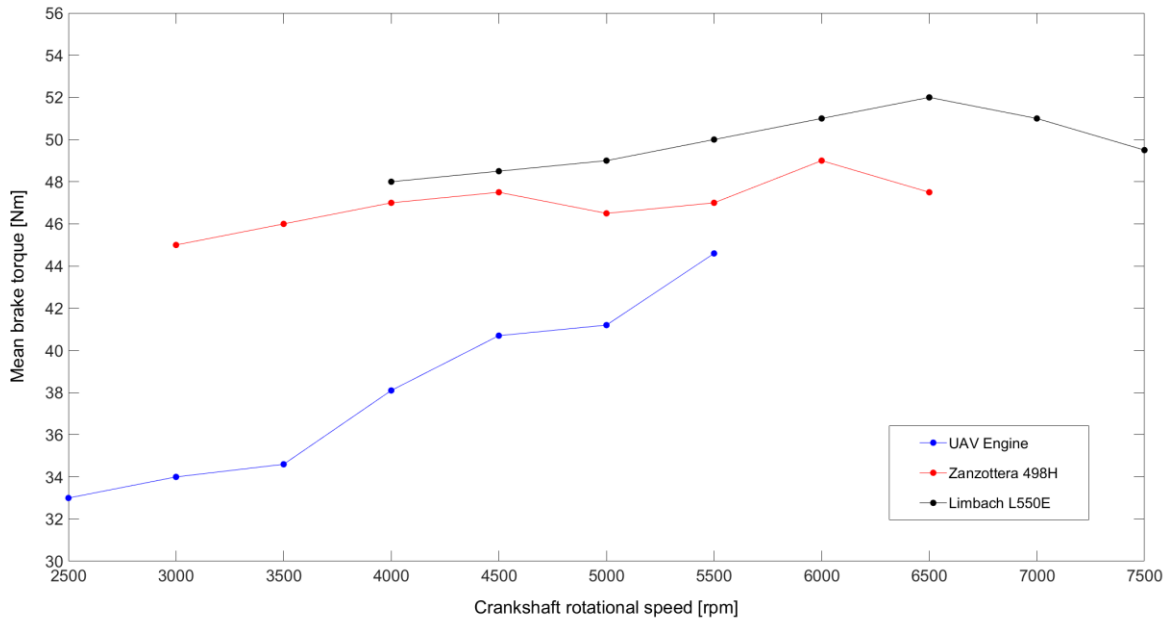

FIGURE 7.24: UAV, ZANZOTTERA AND LIMBACH ENGINES MEAN BRAKE TORQUE AS FUNCTION OF CRANKSHAFT ROTATIONAL SPEED.

The red and black T_{mb} curves of the Zanzottera and Limbach engines respectively generally follow the same trend and are similar in magnitude. The T_{mb} values of the Limbach engine are the highest of the three engines, but all things being equal, this should be the case, since it has the greatest capacity.

The T_{mb} of the UAV engine is the lowest throughout the N_c range, but then again it has the smallest capacity of 390 cc. This is 20.4% and 28.8% lower than the Zanzottera and Limbach engines respectively. Raising the UAV engine T_{mb} curve by 24.6%, the average of the two engines being compared, the brake torque values are similar to those of the two engines compared, except at 5500 rpm, where the T_{mb} is raised well above the other two.

The P_b for the UAV, Zanzottera and Limbach engines is reflected in the graph in blue, red and black respectively from 2500 rpm to 7500 rpm in Figure 7.25.

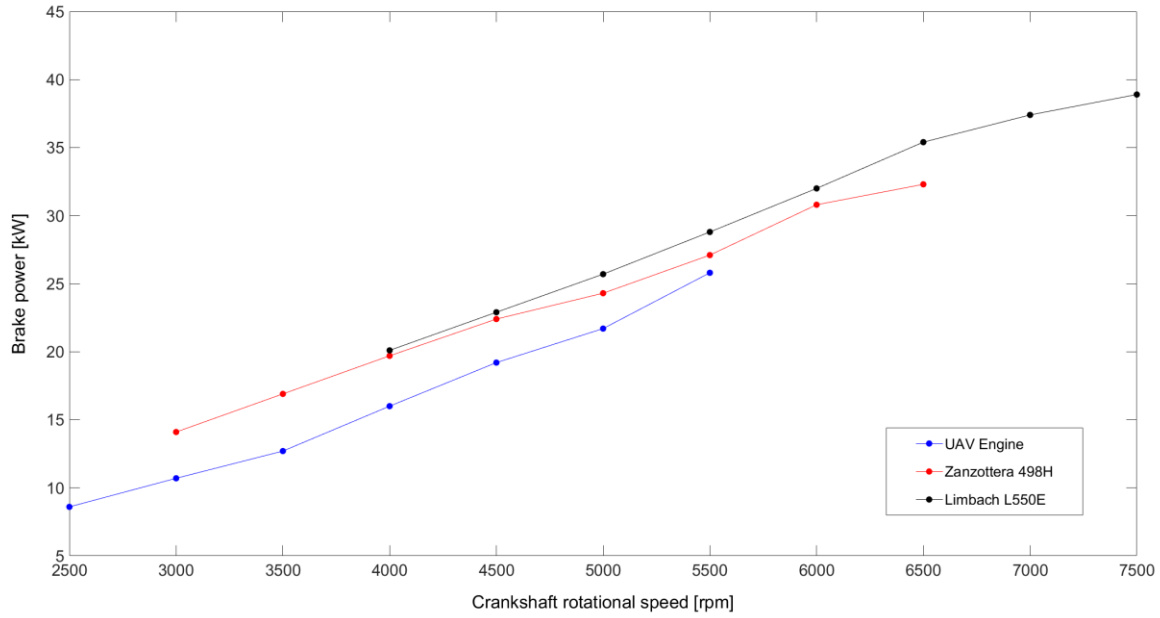

FIGURE 7.25: UAV, ZANZOTTERA AND LIMBACH ENGINES' BRAKE POWER AS FUNCTION OF CRANKSHAFT ROTATIONAL SPEED.

The red and black P_b curves of the Zanzottera and Limbach engines are again similar in trend and magnitude. The UAV engine P_b curve is lower in magnitude throughout the N_c range. However, as stated previously, this engine is approximately 25% smaller in cubic capacity. The maximum P_b values of the Limbach Zanzottera and UAV engines are 38.9 kW at 7500 rpm, 32.3 kW at 6500 rpm and 25.8 kW at 5500 rpm respectively.

Figure 7.26 plots the sfc for the UAV, Zanzottera and Limbach engines throughout the N_c range in blue, red and black respectively.

Unlike the previous two comparative figures, the sfc trends and magnitudes differ for all three these engines. The Zanzottera generally has the best sfc, while the Limbach possibly has the worst. The UAV engine has an sfc curve that is somewhat similar to that of the Limbach except at 5500 rpm, where it drops to the best of all three curves at 341.7 g/kWh. The spread of the sfc for the UAV engine falls just outside the high of the Limbach at approximately 600 g/kWh and the low of the Zanzottera at roughly 350 g/kWh.

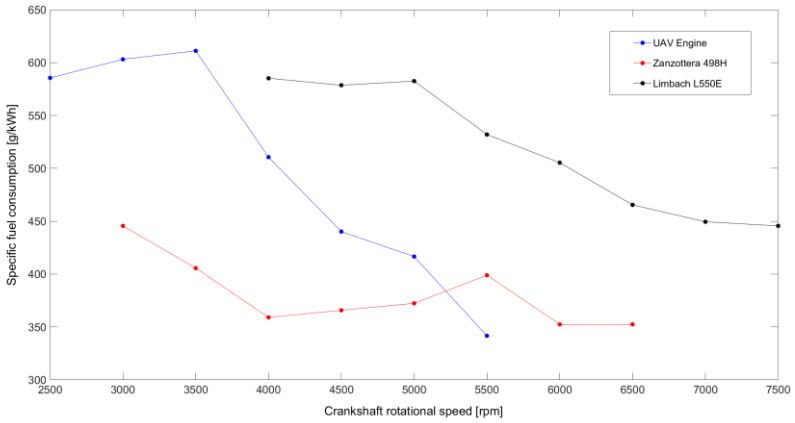

FIGURE 7.26: UAV, ZANZOTTERA AND LIMBACH ENGINES' SPECIFIC FUEL CONSUMPTION AS FUNCTION OF CRANKSHAFT ROTATIONAL SPEED.

Table 7.1 compares some noteworthy engine specifications and performance criteria of the UAV, Zanzottera 498H and Limbach L550E engines.

TABLE 7.1: COMPARISON OF UAV, ZANZOTTERA 498H AND LIMBACH L550E ENGINES' SPECIFICATIONS AND PERFORMANCE FIGURES.

Description	Symbol	UAV Engine	Zanzottera 498H	Limbach L550E	Units
Engine displacement	V_{dt}	390.02	490	548	cc
Engine mass	m	26.6	15	15	kg
Mean brake torque	T_{mb}	44.6 @ 5500 rpm	49 @ 6000 rpm	52 @ 6500 rpm	Nm
Brake power	P_b	25.8 @ 5500 rpm	32.3 @ 6500 rpm	38.9 @ 7500 rpm	kW
Brake mean effective pressure	bmep	7.2	6.3	6.0	bar
Power–to-capacity	P_b / V_{dt}	88.7	88.4	95.2	hp/l
Power–to-weight	P_b / m	0.97	2.15	2.59	kW/kg

As seen in the figures accompanying this section, and remarked on, the Limbach is the engine with the largest capacity and consequently produces the highest P_b and T_{mb}, followed by the Zanzottera and lastly the UAV engine with the smallest capacity. The UAV engine is the heaviest at 26.6 kg, 77.3% heavier than the other two engines weighing 15 kg each, with no accessories attached. The UAV engine, however, has the highest $bmep$ at 7.2 bar, 12.5% and 16.7% higher than the Zanzottera and Limbach engines respectively. The power-to-capacity ratio indicates how well the available engine displacement is used. The P_b to V_{dt} ratio of the UAV engine at 88.7 hp/l (note the units) is nearly identical to that of the Zanzottera at 88.4 hp/l. The Limbach is the highest at 95.2 hp/l. Finally, the power–to-weight ratio of the UAV engine is disappointingly low at 0.97 kW/kg. This is 122% and 167% worse than the Zanzottera and Limbach engines respectively.

With the comparison of the UAV engine to equivalent counterparts complete, the UAV engine fares well in all tests except mass and the consequent power-to-weight ratio. With an average of 145% lower power-to-weight ratio, compared to the other two UAV engines, the experimental engine is very overweight.

8 CONCLUSION AND RECOMMENDATIONS

The purpose of this study was to design, manufacture and test a two-stroke, two-cylinder, horizontally-opposed, air-cooled, spark-ignition (SI), unmanned aerial vehicle (UAV) engine. The engine was a new development, subject to a number of objectives with a preferred engine displacement (V_{dt}) of 500 cc.

Developing an entire reciprocating internal combustion engine encompasses virtually every mechanical engineering field. Thus, at the initiation of this study, very definite bounds, in the form of scope and limits, had to be specified.

This conclusion will firstly review both the theoretical and practical objectives that were achieved. The UAV engine development's successes and shortcomings will then be summarised and proposed recommendations will close this final chapter.

8.1 THEORETICAL OBJECTIVES

8.1.1 CRANKSHAFT AND CRANKCASE FORCES AND COUPLES

The primary theoretical objective of this dissertation was to calculate the forces and couples applied to both the crankshaft and crankcase, throughout the engine speed range, and then to determine the greatest force component, in both magnitude and direction, at all the specified loading points/areas.

Researching the applicable theory, the researcher understood that a significant number of independent inputs and dependent variables are required to mathematically describe all the forces and couples present in the proposed UAV engine. It was considered prudent to create a computer-based mathematical model that incorporated all the theoretical objectives of this study. The Matlab-based computer programs used the theory derived in Chapter 3 and combined the required experimental results of Chapter 4 to generate the UAV engine model, described in Chapter 5. The four programs, summarised in the paragraphs that follow, exchanged data if required and generated the requested tabulated output.

The first program, as documented in Chapter 4, was written to record, evaluate and extract the maximum cylinder pressure (p) curve for a single crankshaft revolution, at 500 rpm increments of the test engine from 3000 rpm to 6500 rpm. This was achieved by experimentally measuring the instantaneous p of a Yamaha DT 175 single-cylinder, two-stroke engine at full throttle. This data could only be obtained experimentally, since no analytical equation for p exists. This crucial data, for the second program, was acquired and clearly illustrate that the peak p occurs just after top dead centre (TDC) due to combustion.

The second program used formulae and characteristics primarily derived from the simple engine mechanism, as documented in Chapter 3. The required input variables were substituted by the appropriate UAV engine specifications. After importing the p curves, obtained in the first program, this program was run and the bulk of the theoretical engine design data was calculated at all eight speed set points. The cyclical nature, with often high peak values of the crankshaft perpendicular moment arm (CF), forces, couples, torque, power and other variables as a function of the crankshaft angular position (θ), clearly illustrates the dynamic nature of the UAV engine. This aforementioned trend was plotted in many graphs throughout Chapter 5.

The third program performed both rotational and reciprocating balancing of the crankshaft and the oscillating piston/connecting rod assemblies respectively. This was done by using the applicable theory derived in Chapter 3 and applying it in Chapter 5 to the horizontally-opposed, two-cylinder engine where the two crank pins of the crankshaft are offset at 180° from one another. The crankshaft was successfully balanced both statically and dynamically.

This was done by running this third program alongside a solid model of the crankshaft and iterating to the solution. This resulted in both outer crankshaft throws having material removed from the counterweights. The primary and secondary reciprocating forces of this horizontally-opposed engine are zero for all rotational speeds. The primary and secondary reciprocating couples are, however, both continuously present and increase in amplitude as the crankshaft rotational speed (N_c) increases, while the period to complete one resultant couple (C_r) cycle always remains the same. It is noteworthy that the C_r is not influenced by p, but by the engine geometry and N_c. Thus, there was no need to import the maximum p curves obtained in the first program.

The fourth and final program imported the required theoretical UAV engine design data and appropriate reciprocating balance results from the second and third programs respectively. The imported data along with the appropriate theory, as found in Chapter 5, was used successfully to calculate the forces and couples on both the crankshaft and crankcase, along/about the applicable axes and at all the designated load points. By selecting the peak of the connecting rod load during the power stroke as the reference point or crank angle index point (θ_{ip}) for all the data, the maximum forces and couples at all the relevant load points/areas could finally be tabulated, at eight increments, from 3000 rpm to 6500 rpm.

8.1.2 ENGINE CHARACTERISTICS AND PERFORMANCE PREDICTIONS

The secondary theoretical objective was the derivation of selective characteristic engine parameters and performance predictions, as found in Chapter 3, and applying this theory to the UAV engine, as seen in Chapter 5. A separate Matlab program was not written, but the above stated objectives were incorporated into the second, third and fourth programs, as described in Section 8.1.1.

In addition to calculating the forces and couples used in attaining the primary theoretical objectives, velocities, accelerations, energy, torque and power were determined to achieve the following:

- The connecting rod ends' different and fluctuating rubbing velocity profiles allowed for lubrication assessment.
- In order to minimise the fluctuating torque peaks and troughs on the crankshaft, the work done due to the power and compression strokes of the piston had to be calculated. This was essential in determining the inertia of the flywheel for the future dynamometer testing of the UAV engine.
- The prototype engine torque and power output predictions were made in 500 rpm increments, from 3000 rpm to 6500 rpm.
- The reaction couple of the engine mount was calculated.

This section was concluded by predicting various characteristics of the UAV engine, namely mean piston velocity ($\overline{v_p}$), brake mean effective pressure ($bmep$) and mechanical efficiency (η_m). Generally, the comparison of these parameters with similar engines was favourable.

8.2 PRACTICAL OBJECTIVES

8.2.1 DEVELOPMENT OF CRANKSHAFT AND CRANKCASE

One of the primary objectives of this study, as stated in Section 1.3, was to make use of as many suitable, commercially available engine parts in critical areas as possible. The Yamaha YFS 200 Blaster two-stroke, single-cylinder, air-cooled quad bike, with a displaced cylinder volume (V_d) of 195 cc, was identified as a suitable donor engine. Two sets of cylinders, pistons, connecting rods and cylinder heads were purchased, measured and modelled using Pro Engineer Wildfire 3.0. The crankshaft and crankcase were designed to comply with both the dimensional requirements of the donor parts and functional requirements for the intended task. A full set of detail drawings and bill of materials (BOM), for the manufacture and assembly of all engine components and systems were produced.

The crankshaft was designed using two Yamaha YFS 200 outer crankshaft throws, to decrease both design time and manufacturing effort; only the central crankshaft throw, that accommodates the two 180° offset crank pins, was fabricated using EN24 steel. The press-fit assembly required that both big-end bearings and connecting rods be assembled with the crankshaft. Aligning the crankshaft within the stated specifications proved extremely time-consuming and the limited length of the Yamaha output shaft restricted main bearing arrangements and propeller output flange options.

The crankcase houses the crankshaft, accommodates the two bolted on, horizontally-opposed cylinders and allows for the attachment of the rear engine mount. The crankcase was designed in two halves, split along the vertical plane of the crankshaft centreline. Numerous aspects of the crankcase had to be thoughtfully designed. These included the cylinder pitch (CP), deck height (DH), the main bearing/lip seal layout and the crankcase seam bolting arrangement. The crankcase was skilfully CNC machined from two 6082 aluminium billets. Two diagonally opposed dowel pins, located on the common mounting faces, and final line-boring of the two main bearing regions ensured accurate alignment once the two crankcase halves were bolted together.

The aforementioned Yamaha engine parts could then be assembled with the two manufactured engine components to form the engine sub-assembly, with an V_{dt} of 390 cc.

8.2.2 DESIGN AND MANUFACTURE OF ENGINE SYSTEMS

With the engine sub-assembly complete, the six engine systems required by a two-stroke, SI engine could be specified or developed as required.

The cooling system required no intervention, since the acquired Yamaha cylinders and cylinder heads were both air-cooled. The original dimensions of the large cooling fins were left unchanged for this application. This did, however, require the working face of the propeller flange to be moved forward, to allow for the swing of the propeller to clear the cooling fins. Moreover, should the propeller not be well balanced, an undesirable bending moment would be generated on the crankshaft output shaft.

The lubrication system of the UAV engine relies on a 50:1 fuel-to-lubricant mixture, initially inducted into the crankcase during each revolution, to lubricate all the engine components. To aid in the lubrication of the two main bearings, a passage was designed to allow some fuel-oil mixture to be drawn through the bearings and into the transfer ports owing to the pressure gradient present during the scavenge process.

The intake system consists of a single throttle body (ETC) that is vertically mounted on a large central plenum. Two short runners, on either side of the plenum, direct the working fluid to the two inlet ports of the cylinders that house the reed valves. Continuous gentle curves were used throughout the intake design. The large central plenum of 500 cc, which acts as an accumulator and damper, and the two short runners were purposely designed after the experimental investigation required to measure p, using the Yamaha DT 175 as described in Section 8.1.1, suffered abrupt engine operation failure at throttle openings above 40%. This was due to a long, constant diameter pipe that connected the Ricardo viscous air flow meter to the carburettor and consequently generated disruptive resonant frequencies. The issue was successfully resolved by breaking the continuous pipe midway and inserting a large truck filter. For ease of construction, stainless-steel plates were used to fabricate the intake manifold, but this resulted in a heavy component.

The fuel system was originally designed to use two fuel injectors, actuated by an electronic control unit (ECU), mounted on the intake system and located above each reed valve. The entire fuel-injection system was, however, discarded and replaced by a single Mikuni VM26SS carburettor, because of the UAV engine run time required to obtain a fuel map for the ECU. The possible risk of damage to the prototype engine was deemed too high.

The ignition system was based on the knowledge that a Perfect Power XMS5A-4A aftermarket ECU would be used. This unit required two fundamental inputs, namely crankshaft rotational speed and engine load. The crankshaft rotational speed was captured by a Bosch crank sensor, bolted to the engine mount, that worked in conjunction with a 36-1 toothed encoder wheel mounted to the rear of the crankshaft. The engine load was artificially generated by a potentiometer controlled by the operator. This allowed the ignition timing to be retarded or advanced, 0° to 30° before top dead centre (BTDC), until maximum mean brake torque (T_{mb}) was indicated on the dynamometer. Given the required inputs, the ECU would initiate a low voltage signal to charge the coil, with a user-specified dwell time of between 2 ms and 4 ms, which would in turn generate the high voltage required by the spark plugs. The 180° crank pin offset resulted in the simultaneous firing of both cylinders once per revolution.

The exhaust system is located beneath the engine. Two un-tuned Zanzottera 498i silencers were used in conjunction with strategically placed 316 stainless-steel bends and were tungsten inert gas (TIG) welded together. Each exhaust pipe incorporated a ball joint, held together by three compression springs, at the end of the pipework and a sliding-fit joint at the end of the silencer to minimise stress on the structure due to thermal expansion.

8.2.3 TESTING OF UAV ENGINE

With the engine sub-assembly of Section 8.2.1 built, and all the engine systems of Section 8.2.2 complete, the entire UAV engine could be assembled, ready for testing.

A new engine test stand was constructed to allow the UAV engine and the required peripheral systems to be mounted. To align the centreline of the crankshaft to that of the dynamometer, the test stand was designed to be manipulated along and about both the horizontal and vertical axes. The most noteworthy peripheral system was the 40 kW electrical motor, controlled by a variable speed drive, coupled to the other side of the dynamometer and incorporating a one-way bearing. This enabled the pre-start testing and starting of the UAV engine. The exhaust gases were extracted by two fabricated exhaust ducts. The engine was cooled by two operator-controlled cooling fans directed at each cylinder head. Some basic instrumentation, to monitor the exhaust gas and cylinder head temperatures, was mounted to the prototype engine along with that already provided by the test cell.

The prototype engine was coupled to a Froude EC 38 Eddy current dynamometer by using a torsional driveshaft. Since no propeller would be used, a flywheel with an inertia equivalent to that of a 32” wooden propeller was substituted. This would ensure that the rotational speed variation of the engine, due to the torque pulses, remained within calculated bounds. The initial Ø24.5 mm, EN24 steel driveshaft used two appropriately sized Centaflex-A flexible couplings at either end.

Before the UAV engine could be run, problems associated with some systems and components first had to be resolved. The two most significant were:

- The ignition system was erratic. In an attempt to rectify this, numerous modifications were made. The initial wiring layout was altered so that the low- and high-voltage signal lines were separated. This resulted in the magnetic inductive trigger pulse increasing significantly from 0.6 V to 20 V peak-to-peak. The 36-1 toothed encoder wheel count and tooth profile were altered with varying success. Furthermore, the Perfect Power ECU proved difficult to programme. Despite numerous attempts to resolve the problematic issues, this system remained unreliable.
- The original driveshaft, using the Centaflex-A couplings, failed catastrophically owing to a poorly designed torsional coupling connection and the erratic ignition. This resulted in damage to the driveshaft that bent the press-fit crankshaft. There was no alternative but to design a new torsional coupling arrangement. A new driveshaft was kindly lent by Sasol and consequently a new flywheel and shaft mounting arrangement had to be designed. The new driveshaft performed flawlessly.

Before the prototype engine was started, a number of pre-start checks were done, which included:

- Checking the direction of rotation;
- Setting TDC with a timing light and verifying the functioning of the ignition system;
- Confirming that fuel flowed to the carburettor and calibrating the remote throttle actuation; and
- Electrically turning the engine over at 250 rpm to 750 rpm to confirm mechanical integrity.

The first engine run was conducted at 3000 rpm with a throttle opening of 30%, to confirm that the prototype actually ran. To minimise the risk of catastrophic engine failure, the engine speed was increased in 500 rpm increments from 2500 rpm to a maximum of 5500 rpm. The throttle opening for all engine runs, except the first, was 100%. After every run the engine was given a thorough external inspection.

The UAV engine ran successfully throughout the entire test period and achieved the following performance figures at full throttle:

- The minimum and maximum mean brake torque (T_{mb}) was 33.0 Nm at 2500 rpm and this steadily increased to 44.6 Nm at 5500 rpm.
- The minimum and maximum brake power (P_b) values were 8.6 kW and 25.8 kW at 2500 rpm and 5500 rpm respectively.
- The maximum brake mean effective pressure ($bmep$) was 7.2 bar at 5500 rpm.
- The left- and right-hand cylinder bank exhaust temperatures did not follow the same trend. From 2500 rpm to 5500 rpm the right bank remained at an average temperature of 490.0°C, while the left bank temperature steadily increased from 417.7°C to 563.4°C.
- The specific fuel consumption (sfc) averaged 600.0 g/kWh from 2500 rpm to 3500 rpm and then consistently dropped to 341.7 g/kWh at 5500 rpm.

8.3 UAV ENGINE DEVELOPMENT EFFECTIVENESS

A two-stroke, two-cylinder, horizontally-opposed, air-cooled, SI, UAV engine with a V_{dt} of 390 cc has been designed, manufactured and tested as stated in the problem statement of Section 1.2. However, the accomplishments and limitations of this study have yet to be determined and these will be addressed in the following two sections.

8.3.1 PROJECT ACCOMPLISHMENTS

This study achieved the following stated goals:

- The donor cylinders, pistons, connecting rods and cylinder heads of a Yamaha YFS 200 Blaster quad bike were successfully integrated into the design of a UAV engine.
- All the theoretical forces and couples on the crankshaft and crankcase due to combustion and balancing were tabulated for the possible future application of finite element analysis (FEA). The design, practical integration with the donor parts, manufacture and assembly of both the crankshaft and crankcase were also achieved.
- Secondary theoretical objectives of selective engine parameters were successfully calculated.
- All engine systems required by the prototype engine were successfully specified, designed and manufactured despite setbacks that were nearly all resolved.
- The UAV engine achieved full power test runs from 2500 rpm to 5500 rpm. At 5500 rpm both maximum T_{mb} of 44.6 Nm and P_b of 25.8 kW were attained.

This study achieved the following goals in terms of comparison:

- The maximum T_{mb} of 44.6 Nm for the UAV engine compares favourably to that generated by the Zanzottera 498H and Limbach L550E UAV engines when taking into account that the V_{dt} of both engines compared is 20.4% and 28.8% larger respectively.
- The maximum P_b of 25.8 kW for the UAV engine is on par with that produced by both the Zanzottera and Limbach engines if the power-to-capacity ratios are considered. The UAV engine's P_b / V_{dt} specification is 88.7 hp/l compared to 88.4 hp/l and 95.2 hp/l for the other two engines respectively.
- The sfc of the UAV engine when compared to that attained by the Yamaha DT 175 from 3000 rpm to 5500 rpm is nearly identical at four of the six measured points. Furthermore, the upper and lower sfc bounds of approximately 600 g/kWh to 350 g/kWh throughout the engine speed range is valid for this prototype, the Zanzottera and Limbach UAV engines.
- The fact that the performance of the UAV engine is comparable to that of both the Zanzottera and Limbach UAV engines justifies the assumption that if the donor parts were to be sourced from a reputable manufacturer, no thermal or flow calculations would be required for this study.
- The comparative performance figures also illustrate that the "fit for purpose" design methodology of the engine systems was satisfactory for this project.
- The total cost of R77 877.43 for the UAV engine, excluding design time, is well below the estimated 2019 cost of R231 423 for a Limbach L550E imported UAV engine.

8.3.2 PROJECT LIMITATIONS

The shortcomings of this study are the following:

- No static or dynamic structural calculations or FEA were done on either the crankshaft or crankcase. This dissertation clearly demonstrates the dynamic nature of the forces and couples applied to both these untried components and conducting no structural investigation or vibration analysis, to probe for resonant frequencies, was a significant risk. In the absence of any structural investigation the reliability and longevity of both components are unknown.
- With the engine systems designs limited to functional ones and the manufacturing thereof restricted to "fit for purpose", the effective functioning of the engine systems, especially the dynamic ones such as the intake and exhaust, is unknown.
- The use of Yamaha YFS 200 donor parts for the two outer crankshaft throws, the cylinders and cylinder heads imposed detrimental limitations on the propeller output flange placement due to the short output shaft and the large cooling fins of the cylinder/cylinder head assembly. The two inlet ports of the donor cylinders are located on each cylinder. Thus, a suitable inlet manifold had to be designed and fabricated. A single inlet port located on the crankcase would have been ideal.
- The maximum predicted theoretical values for T_{mb}, P_b and $bmep$ of the UAV engine are all lower by an average of 32.8%, from 3000 rpm to 5500 rpm, when compared to the experimental results. While the experimental results are not at all disappointing, the inaccurate theoretical prediction is.
- Because of the 32.8% greater experimental T_{mb} values throughout the engine speed range, the theoretical magnitude of the forces and couples acting on all the engine sub-assembly components is inaccurate.
- At 26.6 kg, the prototype is far heavier than the Zanzottera 498H and Limbach L550E UAV engines that weigh 15 kg each. Thus, the power-to-weight ratio of the UAV engine is 0.97 kW/kg compared to 2.15 kW/kg and 2.59 kW/kg for the Zanzottera and Limbach engines respectively.

8.4 RECOMMENDATIONS

This dissertation demonstrates that it is possible to design a locally manufactured UAV engine, using suitable donor engine components in critical areas. However, for this prototype engine to be competitive and effective in the local medium range (MR) UAV market, further development would be required.

Further theoretical investigations could include the following:

- Conduct a detailed structural analysis, using FEA, of both the crankshaft and crankcase.
- Examine, understand and optimize the performance of the engine systems, especially the dynamic ones such as the intake and exhaust systems, possibly by using CFD techniques.
- The excessive mass of the current prototype engine can be reduced by structural, flow and thermal optimisation of both engine components and systems. For example, the seemingly excessively large cooling fins of both the Yamaha cylinders and cylinder heads for this application could possibly be trimmed after a detailed flow and thermal study has been conducted, thus reducing engine mass.
- To obtain a more accurate p representation for the UAV engine, experimentally run a Yamaha YFS 200 Blaster engine and record the instantaneous p instead of using the Yamaha DT 175.

Further practical refinement could include the following:

- To assist in mass reduction of the UAV engine, alternative materials could be used in certain areas. For example, the intake manifold could be manufactured from a composite material instead of stainless steel plates.
- For the accurate and effective assembly and alignment of the press-fit crankshaft, proper tooling and jigging are required.
- Use better quality products in certain areas, for example the erratic Perfect Power ECU in the ignition system and the inadequate Centaflex-A couplings of the original driveshaft.
- Rigorous testing of the UAV engine would be required to validate the final product.

Despite the scope and limits applied to this study, designing, manufacturing and testing an entire reciprocating internal combustion engine is a substantial undertaking owing to the number of mechanical engineering disciplines involved. These suggested theoretical and practical topics that require further investigation are recommendations based on the author's experience with this study, but this is by no means a comprehensive list.

---

9 REFERENCES

Anon. 2008. Now, here's a thing: aluminium beryllium. *Race engine technology*, 6(3):74. (Issue 031 June/July 2008).

Anon. s.a. SAAF: the unofficial website on the South African Air Force: Seeker 1. https://www.saairforce.co.za/the-airforce/aircraft/160/seeker-1 Date of access: 30 July. 2019.

Bae, C. & Kim, J. 2017. Alternative fuels for internal combustion engines. (*In*: Proceedings of The Combustion Institute. p. 3389–3413).

Bamsey, I. 2017. Half-time team talk: British Grand Prix 2017. *Race engine technology*, 15(5):50-56. (Issue 105 September/October 2017).

Baragetti, S. 2015. Design criteria for high power engines crankshafts. *The open mechanical engineering journal*, 9(1):271-281.

Barnard, L. 2009. Cross-border operations of the SAAF in Angola: 1987-1989. Prelude to the final stages of the war. *Journal for contemporary history*, 34(1):223-236.

Bell, A. Graham. 1999. Two-stroke performance tuning. 2nd ed. s.l.: Haynes.

Blair, Gordon. P. 1996. Design and simulation of two-stroke engines. Warrendale: SAE.

Bosch. 2007. Automotive handbook. 7th ed. Plochingen: Robert Bosch GmbH.

Brady, R. N. 2013. Internal combustion engines: gasoline and diesel. (*In*: Reference module in earth systems and environmental sciences. p. 1-59).

Bringas, J. E., *ed*. 2004. Handbook of comparative world steel standards. 3rd ed. s.l.: ASTM.

Brusiani, F., Falfari, S., Forte, C., Cazzoli, G., Verziagi, P., Ferrari, M. & Catanese, D. 2015. Definition of a CFD methodology to evaluate the cylinder temperature distribution in two-stroke air cooled engines. (*In*: Energy Procedia. p. 765-774).

Catchpole, H. 2017. BMW M5 E28 - history, review and specs of an icon. https://www.evo.co.uk/reviews/19887/bmw-m5-e28-history-review-and-specs-of-an-icon Date of access: 15 May. 2019.

Citti, P., Giorgetti, A. & Millefanti, U. 2018. Current challenges in material choice for high-performance engine crankshaft. *Procedia structural integrity*, 8:486-500.

DeGarmo, M. T. 2004. Issues concerning integration of unmanned aerial vehicles in civil airspace. Virginia: Mitre Corporation.

Degler, Howard. E. 1943. Diesel engines: theory and design. Chicago: American Technical.

Dekanski, C. W., Bloor, M. I. G. & Wilson, M. J. 1996. A parametric model of a 2-stroke engine for design and analysis. *Computer methods in applied mechanics and engineering*, 137:411-425.

DJI. 2019. Mavic Pro: specs. https://www.dji.com/mavic/info#specs Date of access: 2019 July. 26.

Dragsted, Jorn. 2011? The first 50 years of turbocharged 2-stroke, crosshead, marine diesel engines. Frankfurt: CIMAC. (Historical booklet).

Duleep, K. G. 2004. Internal combustion engine vehicles. (*In*: Encyclopedia of energy. p. 497-513).

Fan, K. L., He, G. Q., She, M., Liu, X. S., Lu, Q., Yang, Y., Tian, D. D. & Shen, Y. 2014. High-temperature low cycle fatigue behavior of a gray cast iron. *Materials characterization*, 98:37-46.

Fisher, Bill. 1970. How to hotrod VW engines. Los Angeles: HP Books.

Foxhall, N., Hinterberger, W., Winkler, F., Oswald, R. & Schogl, O. 2015. Potential of different injection systems for high performance two-stroke engines. (BRP. p. 1-25.)

General Motors. 1979. Service manual Detroit Diesel engines: series 92. 3rd ed. Detroit.

Gomes, J., Gaivota, N., Martins, R. F. & Silva, P. P. 2018. Failure analysis of crankshafts used in maritime V12 diesel engines. *Engineering failure analysis*, 92:466-479.

Grant, M. 2017. Finishing school: cylinder liners. *Race engine technnology*, 15(6):46-54. (Issue 106 November 2017).

Green, W. G. 1962. Theory of machines. 2nd ed. Glasgow: Blackie.

Heywood, John. B. 1988. Internal combustion engine fundamentals. New York: McGraw-Hill.

Hirth, A. 1924. Crank shaft. Patent: (US 1514768).

Iida, Z., Takada, K., Suzuki, S. & Sato, C. 2005. Development of light weight connecting rod. *Honda R&D technical review*, 17(2):115-121.

Inflation Tool. 2019. Inflationtool. https://www.inflationtool.com/euro-germany/2001-to-present-value?amount=9790 Date of access: 1 August. 2019.

Ishizuka, K., Kusakai, K. & Imai, N. 2009. Development of metal matrix composite piston. *Honda R&D technical review*, F1 special:246-247.

Iwamoto, T. & Saito, J. 2007. Development of simulation technology for dynamic behavior of assembled crankshaft systems in single-cylinder engines. *Honda R&D technical review*, 19(1):176-183.

Jennings, Gordon. 2007. Two-stroke tuner's handbook. s.l.: H.P. Books.

Jhaveri, K., Lewis, G. M., Sullivan, J. L. & Keoleian, G. A. 2018. Life cycle assessment of thin-wall ductile cast iron for automotive lightweighting applications. *Sustainable materials and technologies*, 15:1-8.

Kalghatgi, G. 2018. Is it really the end of internal combustion engines and petroleum in transport? *Applied energy*, 225:965-974.

Kane, J. 2008. Choice metals: advanced metals. *Race engine technology*, 6(6):26-36. (Issue 034 November 2008).

Kane, J. 2008. Coping with torture: crankshafts. *Race engine technology*, 6(5):46-59. (Issue 033 September/October 2008).

Kiura, T., Kushibiki, T. & Shiomi, K. 2005. Research on prediction of cooling air flow in small air-cooled utility engines. *Honda R&D technical review*, 17(1):100-106.

Kondo, K., Endo, H. & Gotou, T. 2009. Technical description of formula one engine structural design. *Honda R&D technical review*, F1 special:44-53.

Limbach Flugmotoren. 2001. Retail pricelist 2-stroke engines: valid from 02 April 2001. http://www.reaa.ru/yabbfiles/Attachments/limbach.pdf Date of access: 1 August. 2019.

Mabie, Hamilton. H. & Reinholtz, Charles. F. 1987. Mechanisms and dynamics of machinery. 4th ed. s.l.: Wiley.

Maleev, V. L. 1945. Internal-combustion engines. 2nd ed. New York: McGraw-Hill.

Martin, G. 2016. SAAF confirms reactivation of 10 Squadron. https ://www.defenceweb.co.za/aerospace/aerospace-aerospace/saaf-confirms-reactivation-of-10-squadron Date of access: 29 July. 2019.

McCutcheon, K. 1999? No short days: the struggle to develop the R-2800 "Double Wasp" crankshaft. s.l.: s.n. http://www.enginehistory.org/engines.shtml Date of access: 22 May. 2019.

Meaden, D. 2018. Honda S2000: review, history and specs of an icon. https://www.evo.co.uk/honda/s2000 Date of access: 6 June. 2019.

Minato, S. & Mizogawa, K. 2009. Development of hollow titanium connecting rod. *Honda R&D technical review*, F1 special:251-253.

Mitchell, S. 2017. Mass reducer: motocross con rod design. *Race engine technology*, 15(3) (Issue 103 June/July 2017).

Mitchell, S. 2018. Specific power: Pipo Moteurs rallyx rallycross engine. *Race engine technology*, 15(7):20-32. (Issue 107 December/January 2018).

Mollenhauer, Klaus. & Tschoeke, Helmut., *eds*. 2010. Handbook of diesel engines. Heidelberg: Springer.

Naito, H. & Taguchi, M. 1966. Some developments aspects of two-stroke cycle motorcycle engines. (s.l.: Yamaha. p. 181-196.)

Nakano, K., Wada, Y., Jono, M. & Narihiro, S. 2016. New in-line 4-cylinder gasoline direct injection turbocharged downsizing engine. *Honda R&D technical review*, 28(1):139-146.

Niino, T., Iwamoto, T. & Ueda, S. 2000. Development of simulation technology for the dynamic behaviour of crankshaft systems in motorcycle engines. *Honda R&D technical review*, 12(2):135-140.

Nomura, T., Matsushita, K., Fujii, Y. & Fijiwara, H. 2015. Estimation technology establishment for temperature distributions of engine based on thermal balance under vehicle running conditions. *Honda R&D technical review*, 27(2):89-102.

Noor, M. M., Kadirgama, K., Devarajan, R., Sani, M. S. M., Nawi, M. F. M. & Yusaf, T. F. 2008. CFD simulation and validation of the in-cylinder within a motored two stroke SI engine. (*In*: International conference on science & technology: applications in industry & education. p. 1461-1468).

Nora, M. D. & Zhao, H. 2015. High load performance and combustion analysis of a four-valve direct injection gasoline engine running in the two-stroke cycle. *Applied energy*, 159:117-131.

Northrop Grumman. 2016. RQ-4 Block 30 Global Hawk: high-altitude, long-endurance unmanned aircraft system. (Brochure).

O.S. Engines. 2018. Power transfer: vol 37. s.l. (O.S. Max all products line-up).

Office of the Secretary of Defense. 2002. Unmanned aerial vehicles roadmap: 2002-2027.

Okubo, M. & Suzuki, M. 2014. Study of optimization of reciprocating parts for general-purpose engine with aluminium-alloy connecting rods. *Honda R&D technical review*, 26(2):214-219.

Onda, H., Asai, T., Fujiki, K., Kudo, H. & Murofushi, K. 2002. Development of high-strength induction hardened crankshaft. *Honda R&D technical review*, 15(2):175-182.

Oxley, M. 2010. Degler's fast stroke. https://www.motorsportmagazine.com/archive/article/august-2010/37/degners-fast-stroke Date of access: 06 July. 2019.

Plint, M. & Martyr, A. 1995. Engine testing: theory and practice. Oxford: Butterworth-Heinemann.

Ricardo, H. R. & Hempson, J. G. G. 1968. The high-speed internal-combustion engine. 5th ed. London: Blackie.

SAAB. 1962. Service manual for Saab "Granturismo 850". Trollhattan (Ordering number: 787898).

Saito Seisakusho. s.a. Instructions for Saito FA-120S/120SH/120SGK (AAC) 4-stroke engines. Chiba (Instruction booklet).

Sakurahara, K. 2009. Summary of Honda Formula One engine in third-era activities. *Honda R&D technical review*, F1 special:14-18.

Save the rhino. 2019. Poaching stats: the latest from South Africa. https://www.savetherhino.org/rhino-info/poaching-stats/ Date of access: 1 August. 2019.

Sears, Francis. W., Zemansky, Mark. W. & Young, Hugh. D. 1985. College physics. 6th ed. Reading: Addison-Wesley.

Service Department of Atlantis Diesel Engines. 1995? Operator's handbook: industrial ADE. Cape Town: Atlantis Diesel Engines.

SKF. 2003. General catalogue. s.l.: s.n.

Spalding, N. 2008. Frantic flyweight flight: motorcycle 125 cc grand prix. *Race engine technology*, 6(5):70-73. (Issue 033 September/October 2008).

Stone, Richard. 1999. Introduction to internal combustion engines. 3rd ed. Warrendale: SAE.

Sugimura, K. 2007. Development of piston surface treatment for internal combustion engine. *Honda R&D technical review*, 19(1):97-102.

Sylt, C. 2018. Mercedes' F1 engine investment accelerates to $250 million. https://www.forbes.com/sites/csylt/2018/09/23/mercedes-f1-engine-investment-accelerates-to-250-million/#3f04a5615fe7 Date of access: 17 May. 2019.

Tan, Y. & Ripin, Z. M. 2011. Frictional behavior of piston rings of small utility two-stroke engine under secondary motion of piston. *Tribology International*, 44:592-602.

Teal Group. 2019. Teal Group predicts worldwide civil drone production will almost triple over the next decade. https://www.tealgroup.com/index.php/pages/press-releases/60-teal-group-predicts-worldwide-civil-drone-production-will-almost-triple-over-the-next-decade Date of access: 1 August. 2019.

U.S. Air Force. 2005. The U.S. Air Force remotely piloted aircraft and unmanned aerial vehicle strategic vision. (Article).

Valavanis, K. P. & Vachtsevanos, G. J., *eds*. 2015. Handbook of unmanned aerial vehicles. Dordrecht: Springer.

van Blyenburgh, P. 2008. Unmanned aircraft systems: the current situation. (Paris: UVS International. p. 1-31.)

van Blyenburgh, P. & Butterworth-Hayes, P., *eds*. 2006. Successful conclusion of the Vulture UAV development programme. (*In*: UAV systems: the global persepctive 2006/2007. Paris: Blyenburgh. p. 105-107).

Waker, C. 1966. The present-day efficiency and the factors governing the performance of small two-stroke engines. (s.l.: Fichtel & Sachs. p. 40-58.)

Ward, W. 2009. Vital connections: con rods. *Race engine technology*, 7(4):64-72. (Issue 040 August 2009).

Ward, W. 2010. Aluminium-beryllium: advanced materials. https://www.highpowermedia.com/blog/2939/aluminium-beryllium Date of access: 10 June. 2019.

Ward, W. 2010. Film review: coatings. *Race engine technology*, 8(3):26-36. (Issue 047 June/July 2010).

Ward, W. 2010. Reciprocating ideas: pistons. *Race engine technology*, 7(7):40-48. (Issue 043 December/January 2010).

Yamaha. 2019. YZ250: specifications. https://www.yamahamotorsports.com/motocross/models/yz250/specifications Date of access: 2019 June. 07.

Yamaha Motor Corporation. 2001. Yamaha YFS200P: supplementary service manual. s.l.

Zanzottera Technologies. 2004. Use and maintenance instructions: 498i engine. Como (Document No. 1001012 Issue 00).

Zwijnenburg, W. & Postma, F. 2018. Unmanned ambitions: security implications of growing proliferation in emerging military drone markets. Utrecht: Pax.

10 APPENDICES

A CALCULATIONS AND DERIVATIONS

A.1 ACUTE PERPENDICULAR MOMENT ARM

The Figure A.1 below illustrates θ when at an acute angle. Trigonometrically it can be stated that:

$$CF = CA\tan(\phi) \tag{10.1}$$

and geometrically:

$$CA = (l + a) - s \tag{10.2}$$

Substitute Eq. (10.1) into Eq. (10.2)

$$CF = (l + a - s)\tan(\phi)$$

Finally, using Eq. (3.13) and substituting the above results in:

$$CF = (l + a - s)\tan\left\{\sin^{-1}\left[\frac{1}{R}\sin(\theta)\right]\right\}$$

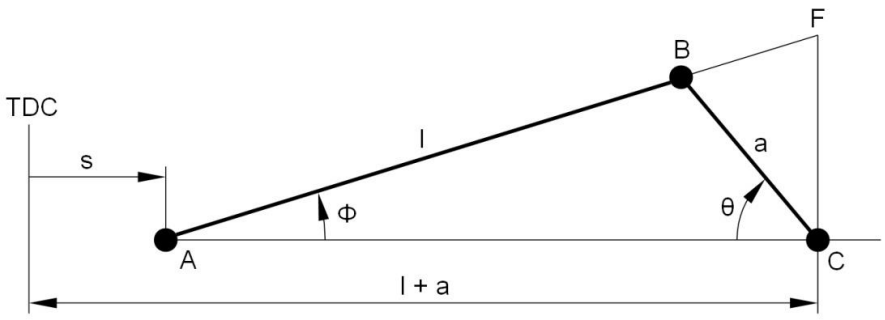

FIGURE A.1: ACUTE MOMENT ARM

A.2 OBTUSE PERPENDICULAR MOMENT ARM

When θ is an obtuse angle Figure A.2 below applies. Trigonometrically:

$$\frac{CF}{CA} = \frac{BO}{AO}$$

rearranging:

$$CF = CA\frac{BO}{AO} \tag{10.3}$$

with:

$$\varepsilon = \pi - \theta \tag{10.4}$$

Trigonometrically:

$$BO = a\sin(\varepsilon) \tag{10.5}$$

and:

$$CO = a\cos(\varepsilon) \tag{10.6}$$

Geometrically:

$$AO = CA + CO$$

Substitute Eq. (10.6) and rewrite as:

$$AO = (l + a) - s + a\cos(\varepsilon) \tag{10.7}$$

and finally substitute Eq. (10.4), (10.5) and (10.7) into Eq. (10.3) then:

$$CF = (l + a - s)\left[\frac{a\sin(\pi - \theta)}{(l + a - s) + a\cos(\pi - \theta)}\right]$$

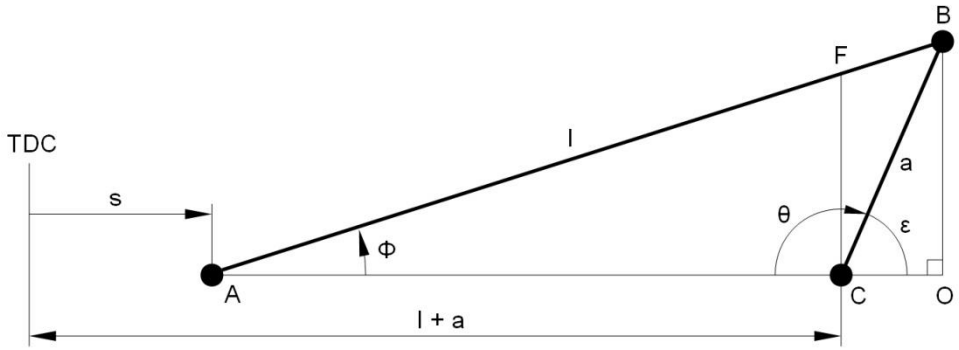

FIGURE A.2: OBTUSE MOMENT ARM

A.3 APPROXIMATE CRANKSHAFT ROTATIONAL SPEED FLUCTUATION

The last term of Eq. (3.46), equal to α, can be written as:

$$\frac{d^2\theta}{dt^2} = \frac{d\omega}{dt} = \frac{d\omega}{d\theta}\frac{d\theta}{dt} = \omega\frac{d\omega}{d\theta} \tag{10.8}$$

Substitute Eq. (10.8) into Eq. (3.46) and

$$T - T_m = m_r k^2 \omega\frac{d\omega}{d\theta} \tag{10.9}$$

Integrating Eq. (10.9) between θ_1 and θ_2, as illustrated in Figure 3.8, with respect to θ is:

$$\int_{\theta_1}^{\theta_2}(T - T_m)\,d\theta = \int_{\theta_1}^{\theta_2} m_r\,k^2\omega\frac{d\omega}{d\theta}d\theta \tag{10.10}$$

The left-hand side of Eq. (10.10) represents the surplus energy and can be written as δE. Conducting the integration on the right-hand side and rearranging results in:

$$\delta E = m_r k^2(\omega_2 - \omega_1)\frac{(\omega_2 + \omega_1)}{2} \tag{10.11}$$

An approximation for the average crankshaft rotational speed is used as:

$$\omega \cong \frac{(\omega_2 + \omega_1)}{2}$$

Finally, substituting the above equation into Eq. (10.11) and rearranging then:

$$\omega_2 - \omega_1 = \frac{\delta E}{m_r k^2 \omega}$$

A.4 BINOMIAL SERIES APPROXIMATION

Equation (3.10) can be expanded as follows:

$$s = a[1 - \cos(\theta)] + l\left\{1 - \sqrt{1 - \left(\frac{a}{l}\right)^2 [\sin(\theta)]^2}\right\} \tag{10.12}$$

The binomial series is:

$$(1 \pm B^2)^{\frac{1}{2}} = 1 \pm \frac{1}{2}B^2 - \frac{B^2}{2 \cdot 4} \pm \cdots$$

of which only the first two terms are used with:

$$B = \left(\frac{a}{l}\right)\sin(\theta)$$

Considering only the term under the square root of Eq. (10.12) yields:

$$\sqrt{1 - \left(\frac{a}{l}\right)^2 [\sin(\theta)]^2} = 1 - \frac{1}{2}\left(\frac{a}{l}\right)^2 [\sin(\theta)]^2 \tag{10.13}$$

then substituting Eq. (10.13) into Eq. (10.12) is:

$$s_b = a[1 - \cos(\theta)] + l\left[1 - \left\{1 - \frac{1}{2}\left(\frac{a}{l}\right)^2 [\sin(\theta)]^2\right\}\right]$$

and simplifying results in:

$$s_b = a[1 - \cos(\theta)] + \frac{a^2}{2l}[\sin(\theta)]^2 \tag{10.14}$$

where:

s_b = Piston displacement due to binomial series

Taking the first derivative of Eq. (10.14) and simplifying yields:

$$\frac{ds_b}{dt} = v_b = a\omega\left[\sin(\theta) + \frac{a}{2l}\sin(2\theta)\right] \tag{10.15}$$

where:

v_b = Piston velocity due to binomial series

Finally, taking the first derivative of Eq. (10.15) and simplifying results in:

$$\frac{dv_b}{dt} = a_b = a\omega^2\left[\cos(\theta) + \frac{a}{l}\cos(2\theta)\right]$$

B EXPERIMENTAL METHODS

B.1 PORT TIMING PROCEDURE

The procedure to establish TDC is as follows:

- To determine TDC accurately the crankshaft must be rotated by at least 20° to either side of the initial TDC estimate, while observing the dial gauge and ceasing rotation at the point where the dial gauge alters direction.
- The degree wheel is then gently rotated while holding the crankshaft stationary until the 0°/TDC marking corresponds with the pointer.
- The above procedure is repeated until TDC has been accurately established.

The procedure to determine the port timing can then commence:

- With the degree wheel accurately indicating TDC, the dial gauge assembly is removed. The crankshaft is slowly rotated until the edge of the piston crown uncovers the top edge of the exhaust port. The corresponding degree wheel reading for the exhaust port is representative for both EO and EC.
- The crankshaft is then rotated further in the same direction, until the top edge of the uppermost transfer port is revealed as the piston continues to descend. This reading indicates both TO and TC.

This completes the port timing procedure.

B.2 MEASURING CLEARANCE VOLUME

The experimental procedure to determine the volumes is as follows:

- A Perspex cover of known volume, with a small, centrally located hole for allowing fluid access, is placed on top of the item to be measured. The top inner face is manufactured with a slight relief angle to prevent bubble entrapment.
- A thin layer of petroleum jelly is used at the interface of the Perspex cover and any other component that requires a water-tight seal.
- Using a burette, a known volume of distilled water is added until the meniscus just protrudes above the Perspex cover.
- The volume added is then subtracted from the known volume and the difference represents the final volume.

That concludes this measuring methodology.

C THEORETICAL RESULTS

C.1 THEORETICAL RESULTS FOR UAV ENGINE

Crankshaft rotational speed	N_c	**3000**	**3500**	**4000**	**4500**	**5000**	**5500**	**6000**	**6500**	rpm
Throttle setting	-	100	100	100	100	100	100	100	100	%
Description	**Symbol**	**Yamaha DT 175 Recorded Data**								**Units**
Cylinder pressure peak	p	23.42	25.24	35.02	33.74	31.95	31.10	29.83	29.28	bar
@ Crank angle ATDC	θ	22.5	19.0	12.0	12.5	16.0	17.5	18.5	19.0	°
Experimental cycle number	-	21	140	216	132	51	103	197	263	-
Description	**Symbol**	**Experimental Engine Design Data**								**Units**
Piston velocity (Maximum)	v_p	9.25	10.79	12.33	13.88	15.42	16.96	18.50	20.04	m/s
@ Crank angle ATDC	θ	76.5	76.5	76.5	76.5	76.5	76.5	76.5	76.5	°
Piston acceleration (Maximum)	a_p	3541.6	4820.5	6296.2	7968.6	9837.8	11903.8	14166.5	16625.9	m/s^2
@ Crank angle ATDC	θ	360.0	360.0	360.0	360.0	360.0	360.0	360.0	360.0	°
Connecting rod angular velocity (Maximum)	Ω	81.40	94.96	108.53	122.09	135.66	149.23	162.79	176.36	rad/s
@ Crank angle ATDC	θ	360.0	360.0	360.0	360.0	360.0	360.0	360.0	360.0	°
Crank pin rubbing velocity (Maximum)	v_r	4.35	5.08	5.80	6.53	7.25	7.98	8.70	9.43	m/s
@ Crank angle ATDC	θ	360.0	360.0	360.0	360.0	360.0	360.0	360.0	360.0	°
Piston pin rubbing velocity (Maximum)	v_{rp}	0.65	0.76	0.87	0.98	1.09	1.19	1.30	1.41	m/s
@ Crank angle ATDC	θ	360.0	360.0	360.0	360.0	360.0	360.0	360.0	360.0	°
Piston effort (Maximum)	P	7113.6	7330.5	10181.5	9226.6	8106.2	7227.3	6162.0	5283.4	N
@ Crank angle ATDC	θ	22.5	19.0	12.0	12.5	16.5	18.0	19.0	20.5	°
Piston gross force (Maximum)	F_g	8118.5	8750.0	12138.2	11695.7	11074.4	10779.8	10341.3	10148.8	N
@ Crank angle ATDC	θ	22.5	19.0	12.0	12.5	16.0	17.5	18.5	19.0	°
Piston gross force @ Piston effort (Maximum)	F_g	8118.5	8750.0	12138.2	11695.7	11068.3	10765.4	10333.6	10106.2	N
Piston inertia force (Maximum)	F_i	1139.8	1551.3	2026.2	2564.5	3166.0	3830.9	4559.0	5350.5	N
@ Crank angle ATDC	θ	360.0	360.0	360.0	360.0	360.0	360.0	360.0	360.0	°

Crankshaft rotational speed	N_c	**3000**	**3500**	**4000**	**4500**	**5000**	**5500**	**6000**	**6500**	rpm
Throttle setting	-	100	100	100	100	100	100	100	100	%
Description	**Symbol**	**Experimental Engine Design Data**								**Units**
Piston inertia force @ Piston effort (Maximum)	F_i	1005.0	1419.5	1956.7	2469.1	2962.1	3538.1	4171.6	4822.8	N
Connecting rod load (Maximum)	Q	7150.1	7357.7	10196.3	9241.2	8128.2	7250.6	6184.1	5305.3	N
@ Crank angle ATDC	θ	23.0	19.5	12.0	12.5	16.5	18.0	19.0	20.5	°
Piston side load (Maximum)	N	856.6	739.1	800.0	773.0	752.2	680.6	677.7	782.5	N
@ Crank angle ATDC	θ	32.5	28.5	25.0	26.5	26.0	24.5	102.5	104.5	°
Piston side load @ Piston effort (Maximum)	N	708.8	620.6	549.3	518.2	598.1	580.5	521.6	481.4	N
Net indicated torque per cylinder (Maximum)	T	114.0	99.2	108.1	104.6	101.5	92.1	81.8	78.7	Nm
@ Crank angle ATDC	θ	32.0	27.0	25.0	24.5	26.0	24.0	25.0	100.5	°
Gross torque per cylinder (Maximum)	T_g	130.1	120.3	134.0	137.9	143.1	141.8	141.5	146.5	Nm
@ Crank angle ATDC	θ	32.0	28.5	26.5	26.5	27.5	27.0	28.0	29.0	°
Inertia torque per cylinder (Maximum)	T_i	16.4	22.4	29.2	37.0	45.7	55.2	65.7	77.2	Nm
@ Crank angle ATDC	θ	323.5	323.5	323.5	323.5	323.5	323.5	323.5	323.5	°
Mean indicated torque per cylinder	T_{mi}	17.1	14.5	16.6	17.1	18.0	18.0	18.2	18.9	Nm
Indicated work per cycle per cylinder	W_i	106.8	90.3	103.3	106.6	112.7	112.5	113.4	118.2	J
Expansion work done per cycle per cylinder	W_{exp}	137.1	122.0	138.2	141.1	149.0	146.6	146.3	154.9	J
Compression work done per cycle per cylinder	W_{comp}	30.3	31.7	34.8	34.4	36.3	34.1	32.9	36.7	J
Compression work vs. Expansion work	-	22.1	26.0	25.2	24.4	24.4	23.3	22.5	23.7	%
Maximum crankshaft angular velocity	ω_2	3105.0	3579.1	4076.9	4568.8	5065.1	5557.5	6052.7	6554.7	rpm
@ Crank angle ATDC	θ	119.0	134.5	141.0	148.5	154.0	158.0	161.0	163.5	°
Minimum crankshaft angular velocity	ω_1	2895.0	3420.9	3923.1	4431.2	4934.9	5442.5	5947.3	6445.3	rpm
@ Crank angle ATDC	θ	6.0	5.5	3.0	3.5	5.5	6.5	297.0	295.5	°
Crankshaft rotational speed fluctuation	-	3.5	2.3	1.9	1.5	1.3	1.0	0.9	0.8	%

Crankshaft rotational speed	N_c	**3000**	**3500**	**4000**	**4500**	**5000**	**5500**	**6000**	**6500**	rpm
Throttle setting	-	100	100	100	100	100	100	100	100	%
Description	**Symbol**	**UAV Engine Performance Predictions**								**Units**
Mean indicated torque	T_{mi}	34.0	28.7	32.9	33.9	35.9	35.8	36.1	37.6	Nm
Mean brake torque	T_{mb}	30.0	24.2	28.5	30.2	31.8	31.3	31.6	32.8	Nm
Indicated power	P_i	10.7	10.5	13.8	16.0	18.8	20.6	22.7	25.6	kW
Friction power	P_f	1.3	1.6	1.8	1.7	2.1	2.6	2.8	3.3	kW
Brake power	P_b	9.4	8.9	11.9	14.3	16.6	18.0	19.9	22.3	kW
Mean piston velocity	$\bar{\upsilon}_p$	5.70	6.65	7.60	8.55	9.50	10.45	11.40	12.35	m/s
Brake mean effective pressure	bmep	4.8	3.9	4.5	4.8	5.1	5.0	5.0	5.2	bar
Mechanical efficiency	η_m	88.2	84.4	86.6	89.1	88.6	87.3	87.6	87.1	%
Description	**Symbol**	**Balancing of Horizontally-Opposed Engine**								**Units**
Maximum summation couple	C_r	43.0	58.6	76.5	96.8	119.5	144.6	172.1	202.0	Nm
@ angle	θ	360.0	360.0	360.0	360.0	360.0	360.0	360.0	360.0	º

C.2 THEORETICAL FORCES AND COUPLES FOR UAV ENGINE

Crankshaft rotational speed	N_c	**3000**	**3500**	**4000**	**4500**	**5000**	**5500**	**6000**	**6500**	rpm
Throttle setting	-	100	100	100	100	100	100	100	100	%
Description	**Symbol**	**Reference Angles**								**Units**
Crank angle index point	θ_{ip}	23.0	19.5	12.0	12.5	16.5	18.0	19.0	20.5	º
Corresponding connecting rod angle index point	Φ_{ip}	5.8	5.0	3.1	3.2	4.2	4.6	4.8	5.2	º
Description	**Symbol**	**Forces and Couples**								**Units**
Piston gross force at index point	F_g	8112.4	8742.7	12138.2	11695.7	11068.3	10765.4	10333.6	10106.2	N
Cylinder flange bolt force	F_{cy}	2028.1	2185.7	3034.5	2923.9	2767.1	2691.3	2583.4	2526.6	N
Crankcase seam bolt force	F_{cr}	2028.1	2185.7	3034.5	2923.9	2767.1	2691.3	2583.4	2526.6	N
Connecting rod load at index point	Q	7150.1	7357.7	10196.3	9241.2	8128.2	7250.6	6184.1	5305.3	N
@ Connecting rod angle	Φ	5.8	5.0	3.1	3.2	4.2	4.6	4.8	5.2	º
Bearing A reaction (No misfire)	R_a	2437.2	2507.9	3475.5	3149.9	2770.6	2471.4	2107.9	1808.3	N
Bearing B reaction (No misfire)	R_b	-2437.2	-2507.9	-3475.5	-3149.9	-2770.6	-2471.4	-2107.9	-1808.3	N
Bearing A reaction (Misfire)	R_a	4793.6	4932.8	6835.9	6195.5	5449.4	4861.0	4146.0	3556.8	N
Bearing B reaction (Misfire)	R_b	-2356.5	-2424.9	-3360.4	-3045.6	-2678.8	-2389.6	-2038.1	-1748.5	N
Piston side load at index point	N	723.8	636.3	549.3	518.2	598.1	580.5	521.6	481.4	N
Reaction couple (No misfire)	T_r	200.5	176.3	152.1	143.5	165.7	160.8	144.5	133.3	Nm
Reaction couple (Misfire)	T_r	100.3	88.1	76.1	71.8	82.8	80.4	72.2	66.7	Nm
Resultant couple	C_r	37.6	53.2	73.8	93.1	111.6	133.3	157.1	181.6	Nm
@ Crank angle ATDC	θ	0.0	0.0	0.0	0.0	0.0	0.0	0.0	0.0	º
Bearing A reaction due to resultant couple	R_{ac}	-339.6	-480.4	-666.4	-840.8	-1008.0	-1203.7	-1419.0	-1640.0	N
Bearing B reaction due to resultant couple	R_{bc}	339.6	480.4	666.4	840.8	1008.0	1203.7	1419.0	1640.0	N

Crankshaft rotational speed	N_c	**3000.0**	**3500.0**	**4000.0**	**4500.0**	**5000.0**	**5500.0**	**6000.0**	**6500.0**	rpm
Throttle setting	-	100.0	100.0	100.0	100.0	100.0	100.0	100.0	100.0	%
Description	**Symbol**	**Bearing Forces Summation**								**Units**
Bearing A reaction - X axis (No misfire)	R_{ax}	2085.1	2018.1	2804.0	2304.2	1755.0	1259.8	681.4	160.9	N
Bearing A reaction - Y axis (No misfire)	R_{ay}	246.7	216.9	187.2	176.6	203.9	197.9	177.8	164.1	N
Bearing B reaction - X axis (No misfire)	R_{bx}	-2085.1	-2018.1	-2804.0	-2304.2	-1755.0	-1259.8	-681.4	-160.9	N
Bearing B reaction - Y axis (No misfire)	R_{by}	-246.7	-216.9	-187.2	-176.6	-203.9	-197.9	-177.8	-164.1	N
Bearing A reaction - X axis (Misfire)	R_{ax}	4429.4	4433.9	6159.6	5345.0	4426.6	3641.7	2712.2	1902.2	N
Bearing A reaction - Y axis (Misfire)	R_{ay}	485.3	426.6	368.2	347.4	401.0	389.2	349.7	322.7	N
Bearing B reaction - X axis (Misfire)	R_{bx}	-2004.8	-1935.4	-2689.1	-2200.0	-1663.5	-1178.2	-611.9	-101.3	N
Bearing B reaction - Y axis (Misfire)	R_{by}	-238.6	-209.7	-181.0	-170.8	-197.1	-191.3	-171.9	-158.6	N
Description	**Symbol**	**Maxima Verification**								**Units**
Piston gross force lower by	-	0.1	0.1	0.0	0.0	0.1	0.1	0.1	0.4	%
Connecting rod load lower by	-	0.0	0.0	0.0	0.0	0.0	0.0	0.0	0.0	%
Piston side load lower by	-	15.5	13.9	31.3	33.0	20.5	14.7	23.0	38.5	%
Resultant couple lower by	-	12.6	9.1	3.5	3.8	6.6	7.8	8.7	10.1	%

D MANUFACTURING RESULTS

D.1 CRANKSHAFT RADIAL AND AXIAL DEFLECTION

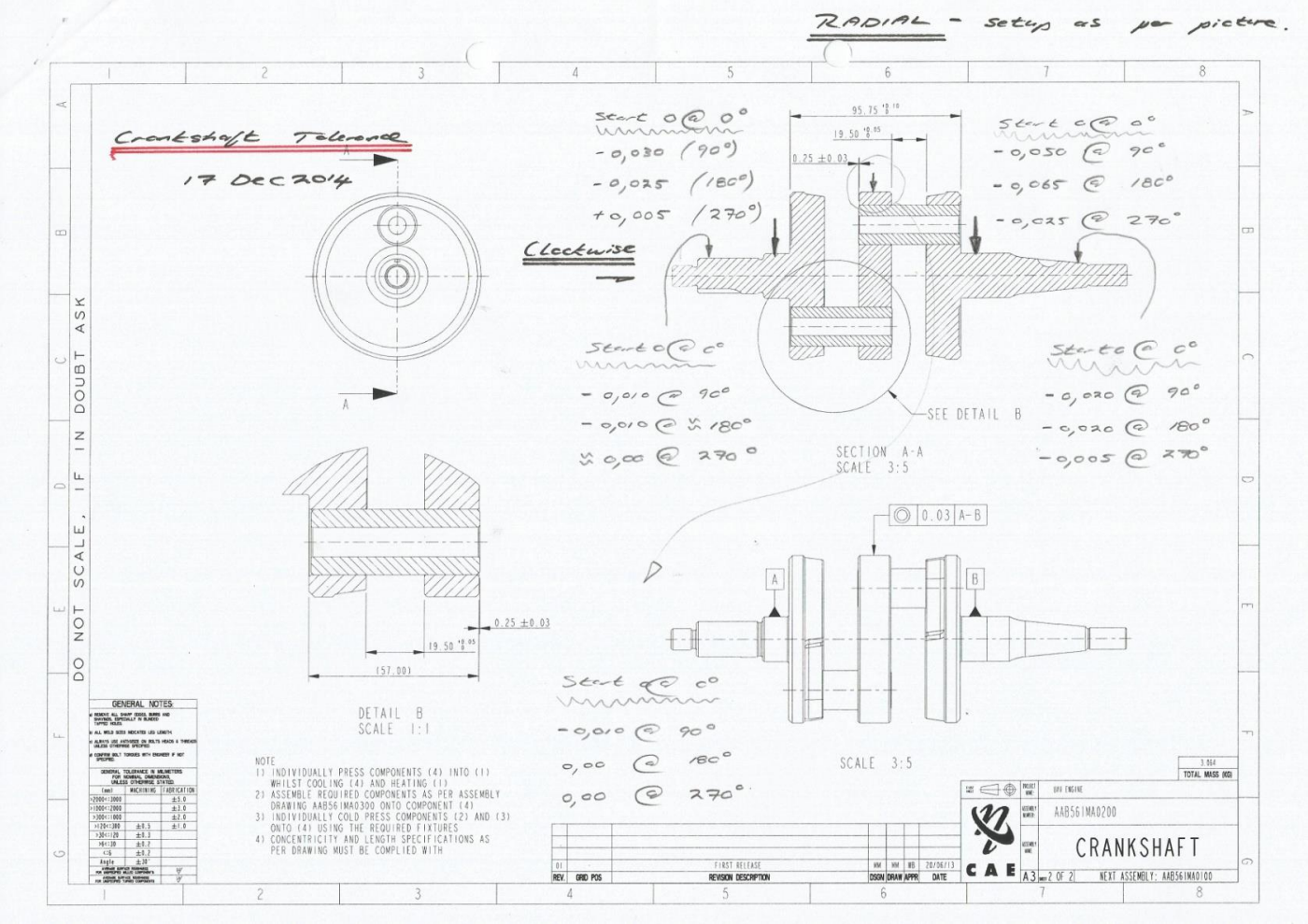

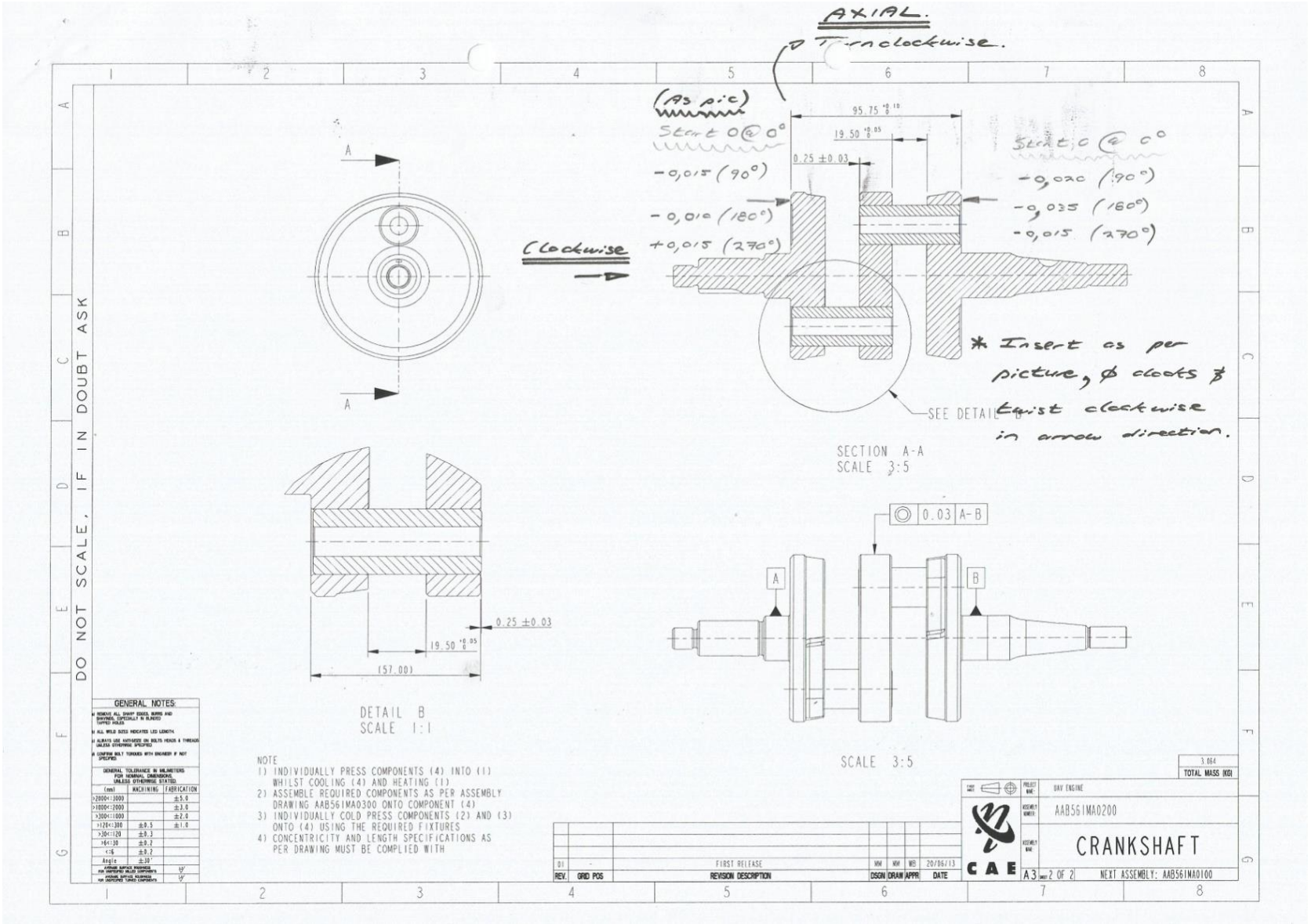
AXIAL.
Turn clockwise.
(As pic)
Start 0 @ 0°
-0,015 (90°)
-0,010 (180°)
+0,015 (270°)
Clockwise
95.75 +0.10 -0.10
19.50 +0.05 -0.05
0.25 ±0.03
Start 0 @ 0°
-0,020 (90°)
-0,035 (180°)
-0,015 (270°)
* Insert as per picture, Ø clocks & twist clockwise in arrow direction.
SEE DETAIL B
SECTION A-A
SCALE 1:5
0.03 A-B
A
B
SCALE 3:5
DETAIL B
SCALE 1:1
0.25 ±0.03
19.50 +0.05 -0.05
(57.00)
DO NOT SCALE, IF IN DOUBT ASK
GENERAL NOTES:
GENERAL TOLERANCE IN MILIMETERS FOR NOMINAL DIMENSIONS UNLESS OTHERWISE STATED
(mm) MACHINING FABRICATION
>2000<3000 ±5.0
>1000<2000 ±3.0
>300<1000 ±2.0
>120<300 ±0.5 ±1.0
>30<120 ±0.3
>6<30 ±0.2
<6 ±0.1
Angle ±10'
NOTE
1) INDIVIDUALLY PRESS COMPONENTS (4) INTO (1) WHILST COOLING (4) AND HEATING (1)
2) ASSEMBLE REQUIRED COMPONENTS AS PER ASSEMBLY DRAWING AAB561MA0300 ONTO COMPONENT (4)
3) INDIVIDUALLY COLD PRESS COMPONENTS (2) AND (3) ONTO (4) USING THE REQUIRED FIXTURES
4) CONCENTRICITY AND LENGTH SPECIFICATIONS AS PER DRAWING MUST BE COMPLIED WITH
REV. GRID POS REVISION DESCRIPTION DSGN DRAW APPR DATE
01 FIRST RELEASE MM MM MB 20/06/13
3.664 TOTAL MASS (KG)
PROJECT NAME: UAV ENGINE
ASSEMBLY NUMBER: AAB561MA0200
ASSEMBLY NAME: CRANKSHAFT
CAE
A3 SHEET 2 OF 2 NEXT ASSEMBLY: AAB561MA0100

E EXPERIMENTAL RESULTS

E.1 TEST CELL EXPERIMENTAL RESULTS FOR YAMAHA DT 175

Item	Throttle	Speed set point	Engine speed	Correction factor	Engine torque	Brake power	Friction power	Exhaust temperature	Cylinder head temperature
	[%]	[rpm]	[rpm]		[Nm]	[kW]	[kW]	[°C]	[°C]
1	100	6500	6478	0.988	15.8	10.7	1.7	509.1	129.4
2	100	6000	5976	0.989	15.2	9.5	1.5	503.2	137.8
3	100	5500	5469	0.989	15.1	8.6	1.4	501.8	139.0
4	100	5000	4970	0.989	15.3	8.0	1.1	493.5	139.1
5	100	4500	4461	0.990	12.2	5.7	0.9	497.3	132.0
6	100	4000	3964	0.990	10.6	4.4	1.0	459.1	121.7
7	100	3500	3467	0.990	10.3	3.7	0.9	390.5	120.0
8	100	3000	2972	0.990	8.4	2.6	0.7	378.3	122.5

The columns in black print illustrate the average transducer readings for each set point. The columns in blue represent calculated values.

Item	Throttle	Speed set point	Air flow	Fuel flow	Air flow/Fuel flow	Specific fuel consumption	Brake mean effective pressure	Mean piston velocity	Exhaust mean pressure
	[%]	[rpm]	[kg/hr]	[kg/hr]		[g/kWh]	[bar]	[m/s]	[mbar]
1	100	6500	56.68	5.46	10.4	509.1	5.8	10.8	135.3
2	100	6000	52.51	4.93	10.6	518.7	5.6	10.0	117.1
3	100	5500	47.56	4.30	11.1	498.5	5.5	9.1	93.3
4	100	5000	41.43	3.51	11.8	440.6	5.6	8.3	72.6
5	100	4500	33.69	2.35	14.3	412.0	4.5	7.4	45.7
6	100	4000	29.54	2.13	13.9	486.2	3.9	6.6	34.8
7	100	3500	26.60	2.41	11.0	645.7	3.8	5.8	31.3
8	100	3000	23.66	1.78	13.3	680.8	3.1	5.0	25.0

E.2 EXPERIMENTAL RESULTS FOR UAV ENGINE

Item	Throttle	Speed set point	Engine speed	Correction factor	Engine torque	Brake power	Left exhaust temperature	Right exhaust temperature
	%	rpm	rpm		Nm	kW	°C	°C
1	100	2500	2488	0.928	33.0	8.6	417.7	482.3
2	100	3000	2994	0.928	34.0	10.7	440.8	489.5
3	100	3500	3498	0.928	34.6	12.7	478.1	495.0
4	100	4000	4004	0.927	38.1	16.0	498.2	486.9
5	100	4500	4512	0.927	40.7	19.2	509.8	480.9
6	100	5000	5019	0.927	41.2	21.7	534.8	493.1
7	100	5500	5526	0.927	44.6	25.8	563.4	502.5

The columns in black print illustrate the average transducer readings for each set point. The columns in blue represent calculated values.

Item	Throttle	Speed set point	Average exhaust temperature	Cylinder head temperature	Fuel flow	Specific fuel consumption	Brake mean effective pressure	Mean piston velocity
	%	rpm	°C	°C	kg/hr	g/kWh	bar	m/s
1	100	2500	450.0	57.0	5.04	585.50	5.32	4.73
2	100	3000	465.2	72.5	6.43	603.10	5.48	5.69
3	100	3500	486.5	69.2	7.74	611.06	5.57	6.65
4	100	4000	492.5	69.7	8.15	510.63	6.13	7.61
5	100	4500	495.3	72.5	8.46	440.17	6.55	8.57
6	100	5000	513.9	76.3	9.02	416.65	6.64	9.54
7	100	5500	533.0	78.9	8.83	341.72	7.19	10.50

F UAV ENGINE DETAIL DRAWINGS

The drawing number convention used is as specified below.

The drawing numbers used conform to the CAE design office guidelines. The drawing number *AAB561MM0702,* for example, consists of four elements:

- *AAB561* – Represents the CAE project number.
- *MM* – Designates the type of drawing of which four are used.
- *07* – Assembly or sub-assembly section.
- *02* – Assembly, sub-assembly or part number, starting at 00 for the assembly/sub-assembly drawing.

The four types of drawings that can be used are designated within the drawing number as:

- MA: Assembly or sub-assembly that might require assembly.
- MW: Assembly or sub-assembly that requires welding.
- MM: Components requiring machining.
- SL: Parts requiring laser cutting.

All the components and quantities required to manufacture the entire engine is listed in the bill of material tables on the assembly and sub-assembly drawings.

F.1 ASSEMBLIES AND SUB-ASSEMBLIES OF THE UAV ENGINE

Item	Assembly and Sub-assembly Description	Drawing Number	Quantity
1	Engine assembly	AAB561MA0000	1
2	Crankshaft assembly	AAB561MA0100	1
3	Crankshaft	AAB561MA0200	1
4	Piston assembly	AAB561MA0300	2
5	Case 1 assembly	AAB561MA0400	1
6	Case 2 assembly	AAB561MA0500	1
7	Engine mount assembly	AAB561MA0600	1
8	Encoder wheel	AAB561MA0700	1
9	Exhaust assembly	AAB561MA0800	2
10	Propeller assembly	AAB561MA0900	1
11	Reed valve assembly	AAB561MA1000	2
12	Inlet manifold assembly	AAB561MA1100	1
13	Throttle body assembly	AAB561MA1200	1
14	Injector assembly	AAB561MA1300	2
15	Driveshaft assembly	AAB561MA1400	1
16	Exhaust pipe assembly	AAB561MW1500	2
17	Inlet manifold	AAB561MW1600	1
18	Alternative driveshaft assembly	AAB561MA1400	1

F.2 ENGINE ASSEMBLY

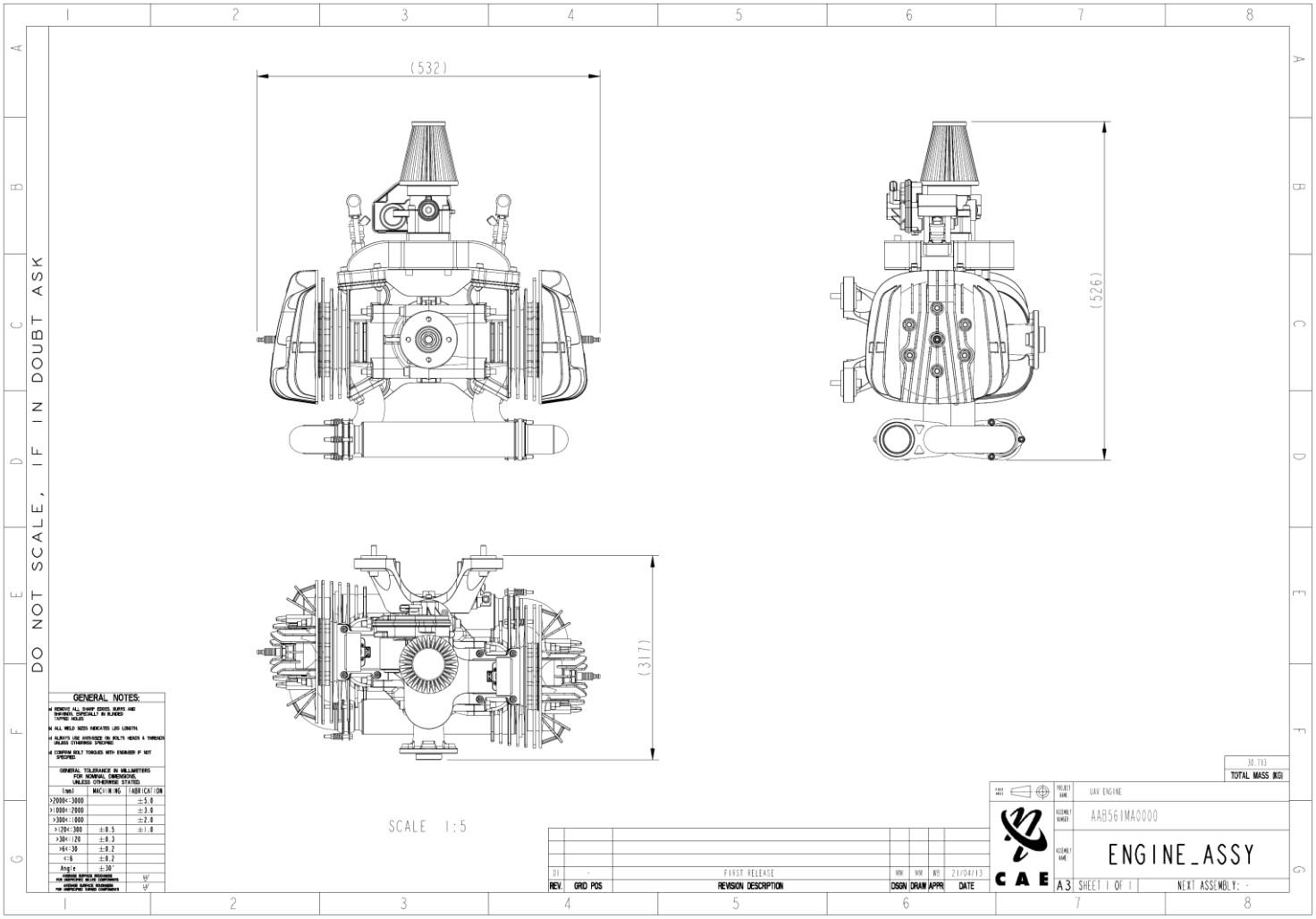

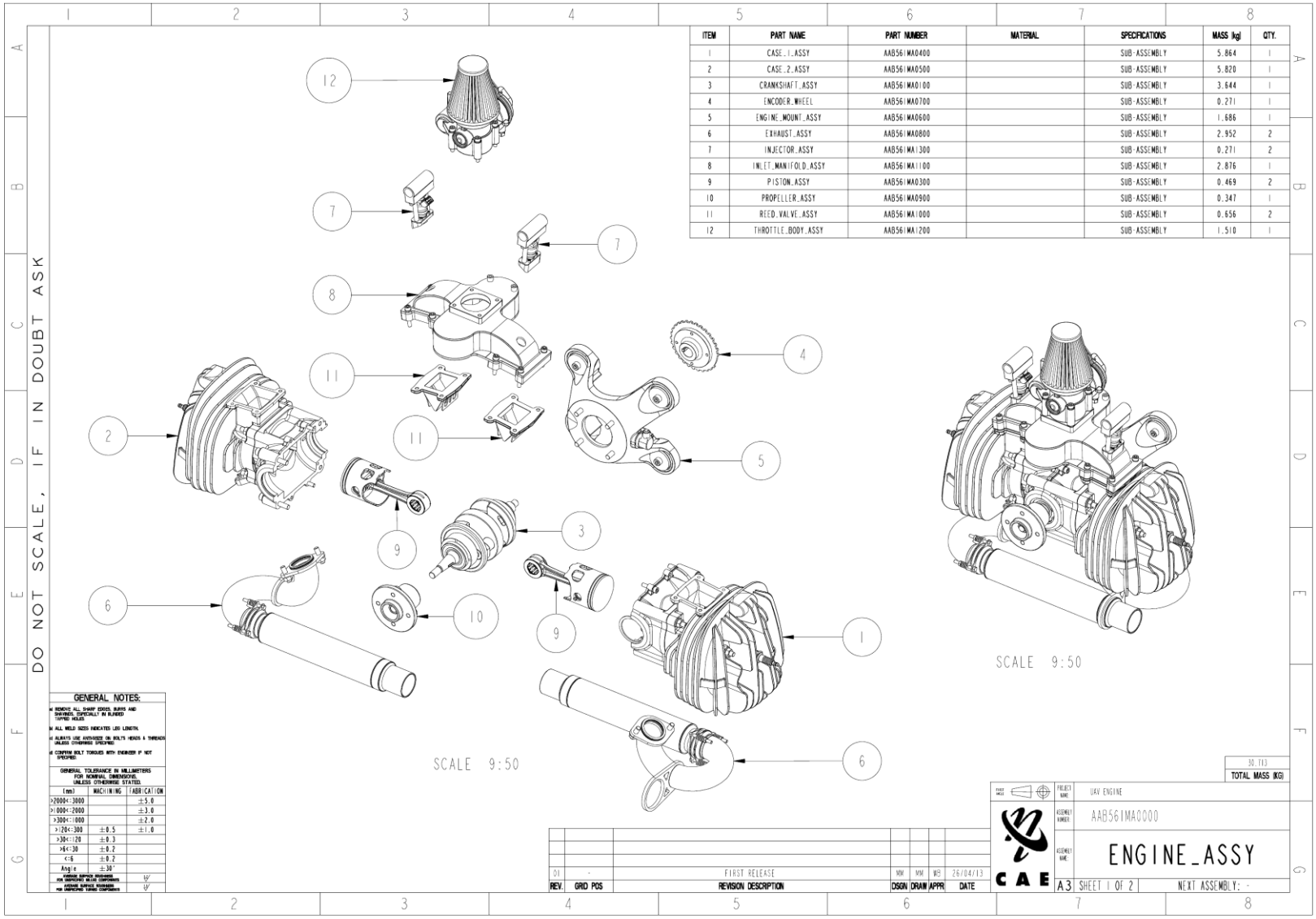

ITEM	PART NAME	PART NUMBER	MATERIAL	SPECIFICATIONS	MASS (kg)	QTY.
1	CASE_1_ASSY	AAB561MA0400		SUB-ASSEMBLY	5.864	1
2	CASE_2_ASSY	AAB561MA0500		SUB-ASSEMBLY	5.820	1
3	CRANKSHAFT_ASSY	AAB561MA0100		SUB-ASSEMBLY	3.644	1
4	ENCODER_WHEEL	AAB561MA0700		SUB-ASSEMBLY	0.271	1
5	ENGINE_MOUNT_ASSY	AAB561MA0600		SUB-ASSEMBLY	1.686	1
6	EXHAUST_ASSY	AAB561MA0800		SUB-ASSEMBLY	2.952	2
7	INJECTOR_ASSY	AAB561MA1300		SUB-ASSEMBLY	0.271	2
8	INLET_MANIFOLD_ASSY	AAB561MA1100		SUB-ASSEMBLY	2.876	1
9	PISTON_ASSY	AAB561MA0300		SUB-ASSEMBLY	0.469	2
10	PROPELLER_ASSY	AAB561MA0900		SUB-ASSEMBLY	0.347	1
11	REED_VALVE_ASSY	AAB561MA1000		SUB-ASSEMBLY	0.656	2
12	THROTTLE_BODY_ASSY	AAB561MA1200		SUB-ASSEMBLY	1.510	1

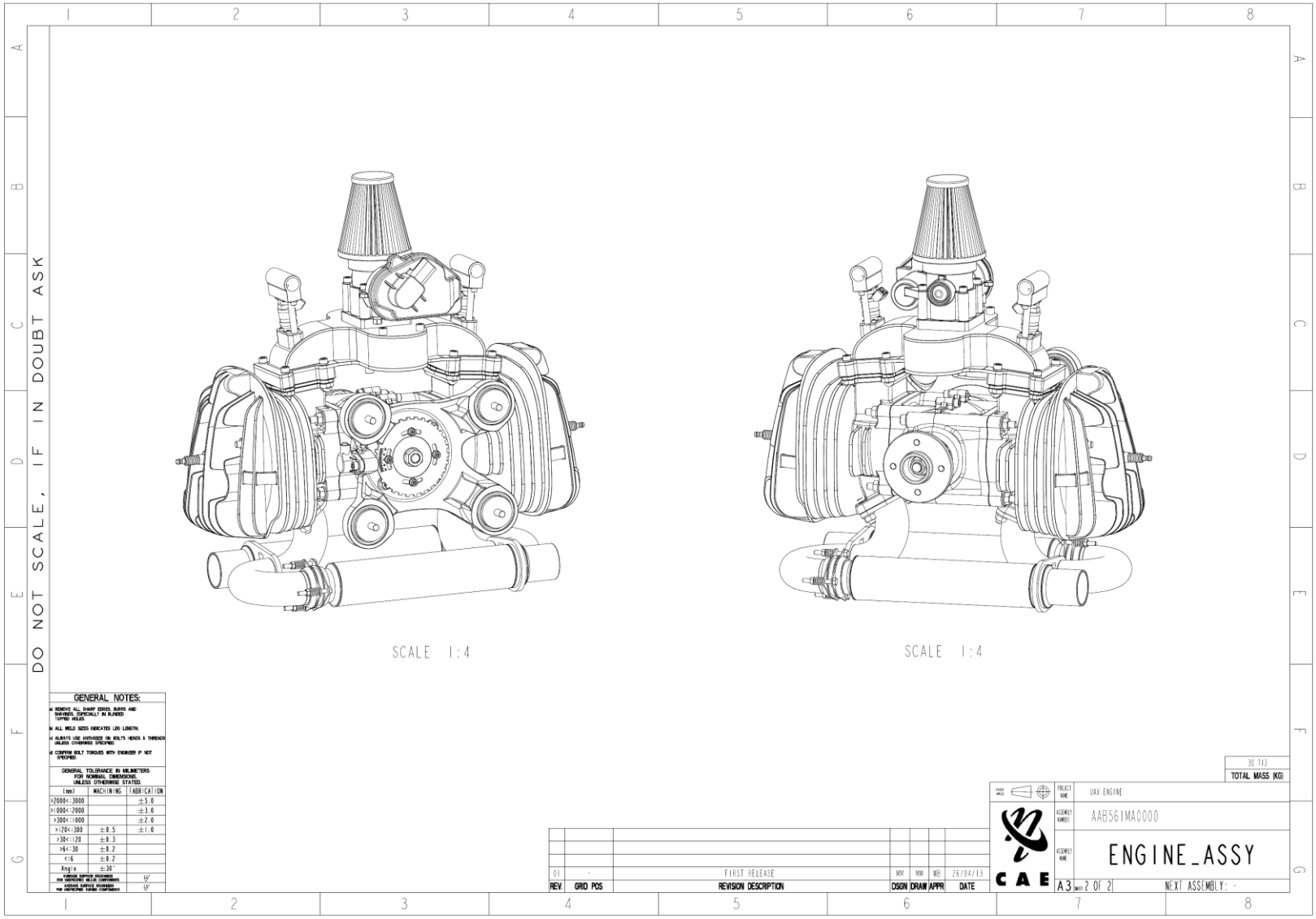
DO NOT SCALE, IF IN DOUBT ASK
SCALE 1:4
SCALE 1:4
GENERAL NOTES:
GENERAL TOLERANCE IN MILIMETERS FOR NOMINAL DIMENSIONS, UNLESS OTHERWISE STATED.
TOTAL MASS (KG)
UAV ENGINE
AAB561MA0000
ENGINE_ASSY
FIRST RELEASE
CAE

F.3 CRANKSHAFT ASSEMBLY

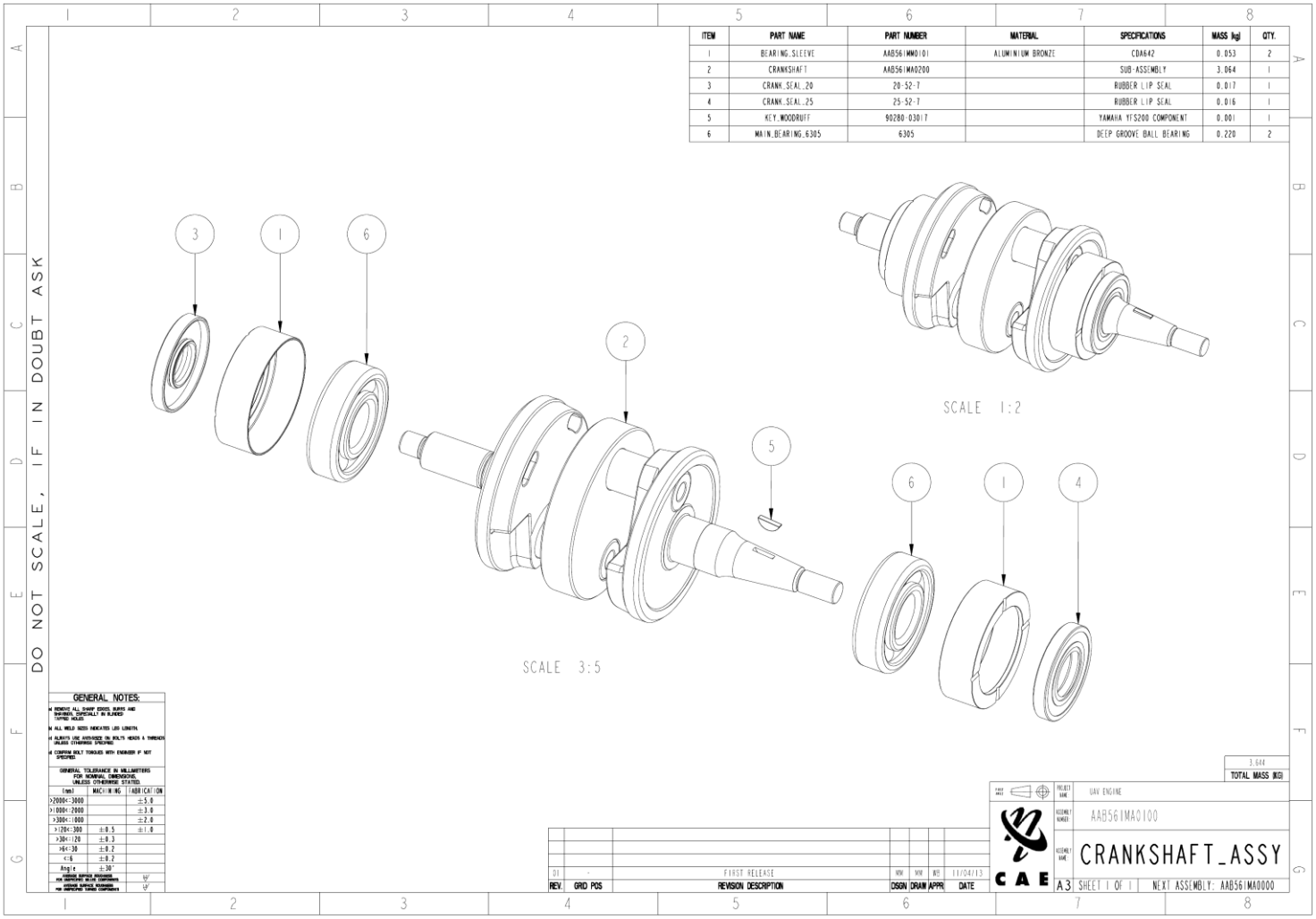

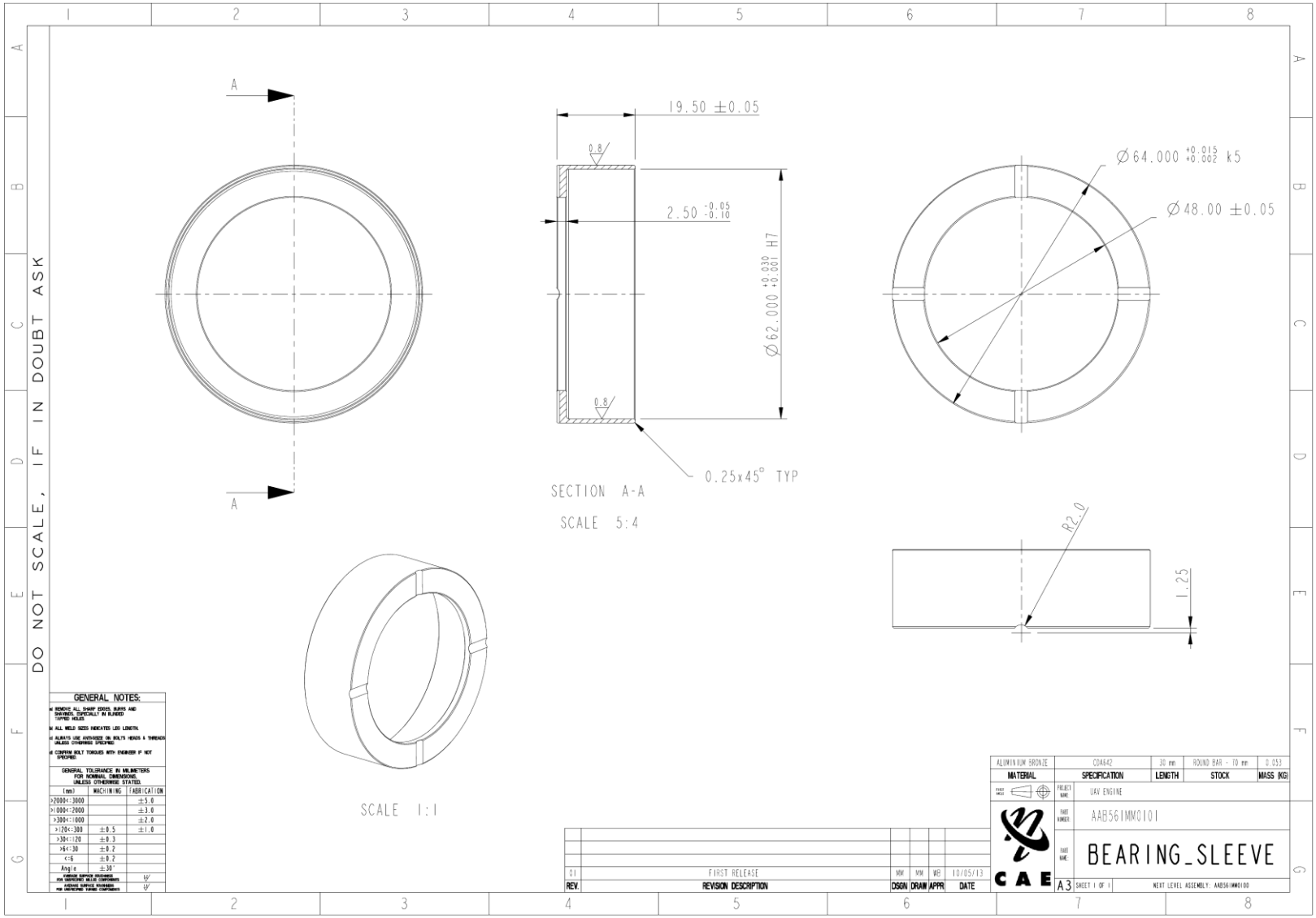
DO NOT SCALE, IF IN DOUBT ASK
A
A
19.50 ±0.05
0.8
2.50 -0.05 -0.10
Ø62.000 +0.030 +0.001 H7
0.8
0.25x45° TYP
SECTION A-A
SCALE 5:4
Ø64.000 +0.015 +0.002 k5
Ø48.00 ±0.05
R2.0
1.25
SCALE 1:1
GENERAL NOTES:
GENERAL TOLERANCE IN MILIMETERS FOR NOMINAL DIMENSIONS, UNLESS OTHERWISE STATED
ALUMINIUM BRONZE
CDA642
30 mm
ROUND BAR - TO mm
0.053
MATERIAL
SPECIFICATION
LENGTH
STOCK
MASS (KG)
UAV ENGINE
AAB561MM0101
BEARING_SLEEVE
A3
01 FIRST RELEASE 10/05/13
REV. REVISION DESCRIPTION DSGN DRAW APPR DATE

F.4 CRANKSHAFT

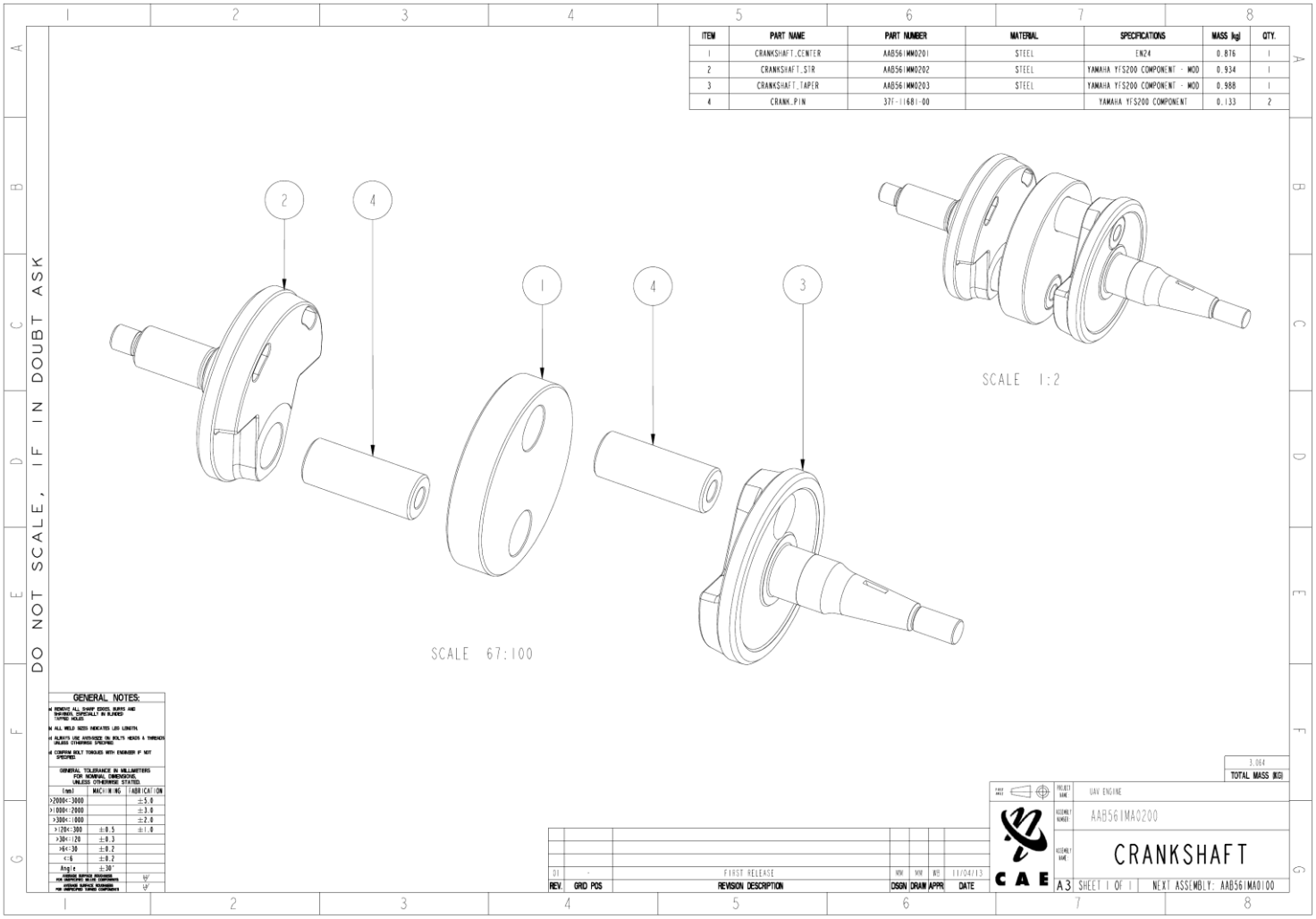

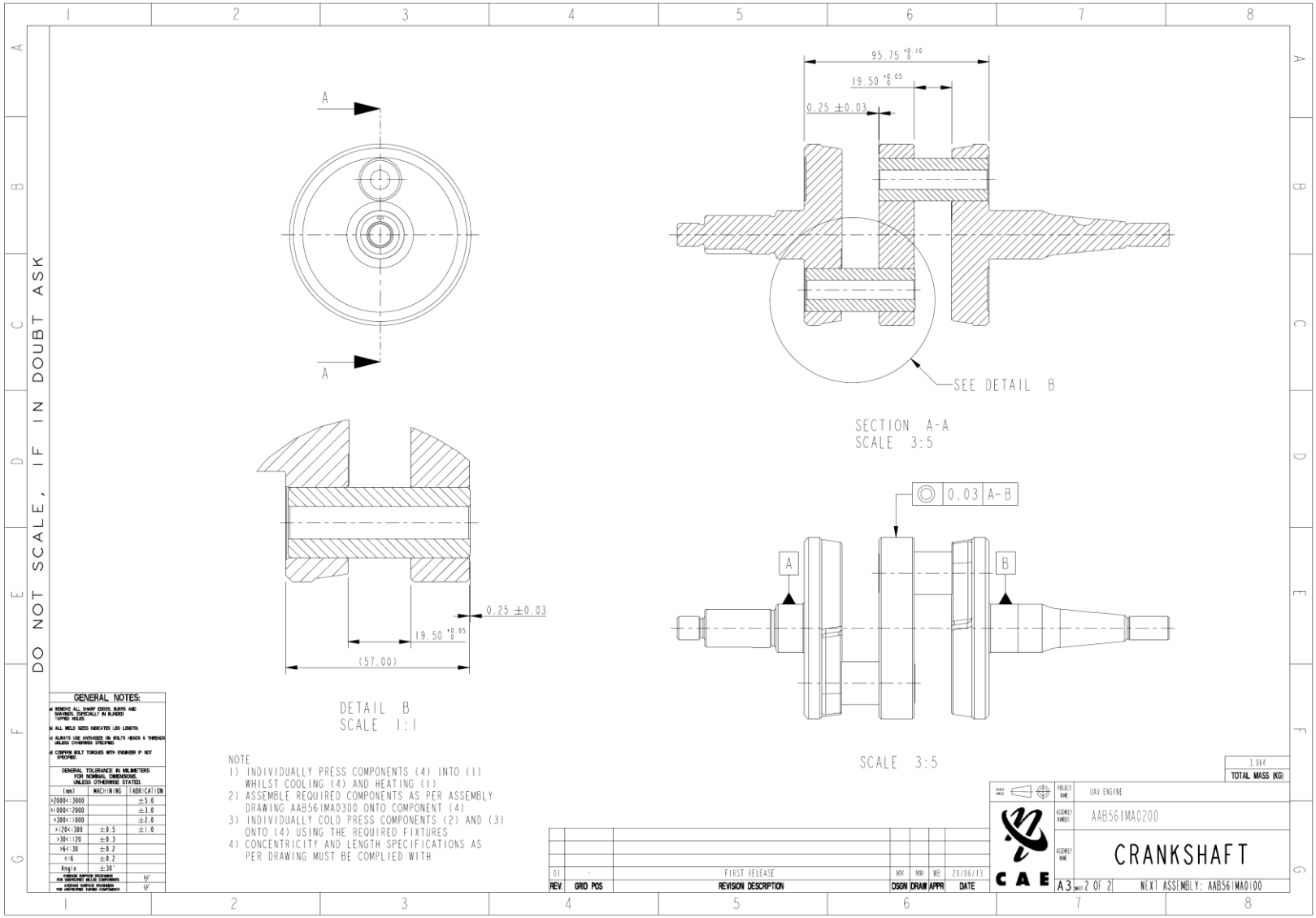
DO NOT SCALE, IF IN DOUBT ASK
95.75 +0.10 0
19.50 +0.05 0
0.25 ±0.03
SEE DETAIL B
SECTION A-A
SCALE 3:5
0.03 A-B
A
B
SCALE 3:5
DETAIL B
SCALE 1:1
0.25 ±0.03
19.50 +0.05 0
(57.00)
GENERAL NOTES:
GENERAL TOLERANCE IN MILIMETERS FOR NOMINAL DIMENSIONS, UNLESS OTHERWISE STATED
NOTE
1) INDIVIDUALLY PRESS COMPONENTS (4) INTO (1) WHILST COOLING (4) AND HEATING (1)
2) ASSEMBLE REQUIRED COMPONENTS AS PER ASSEMBLY DRAWING AAB561MA0300 ONTO COMPONENT (4)
3) INDIVIDUALLY COLD PRESS COMPONENTS (2) AND (3) ONTO (4) USING THE REQUIRED FIXTURES
4) CONCENTRICITY AND LENGTH SPECIFICATIONS AS PER DRAWING MUST BE COMPLIED WITH
3.064
TOTAL MASS (KG)
UAV ENGINE
AAB561MA0200
CRANKSHAFT
A3 SHEET 2 OF 2
NEXT ASSEMBLY: AAB561MAD100
01 - FIRST RELEASE MW MW WB 20/06/13
REV. GRD POS REVISION DESCRIPTION DSGN DRAW APPR DATE

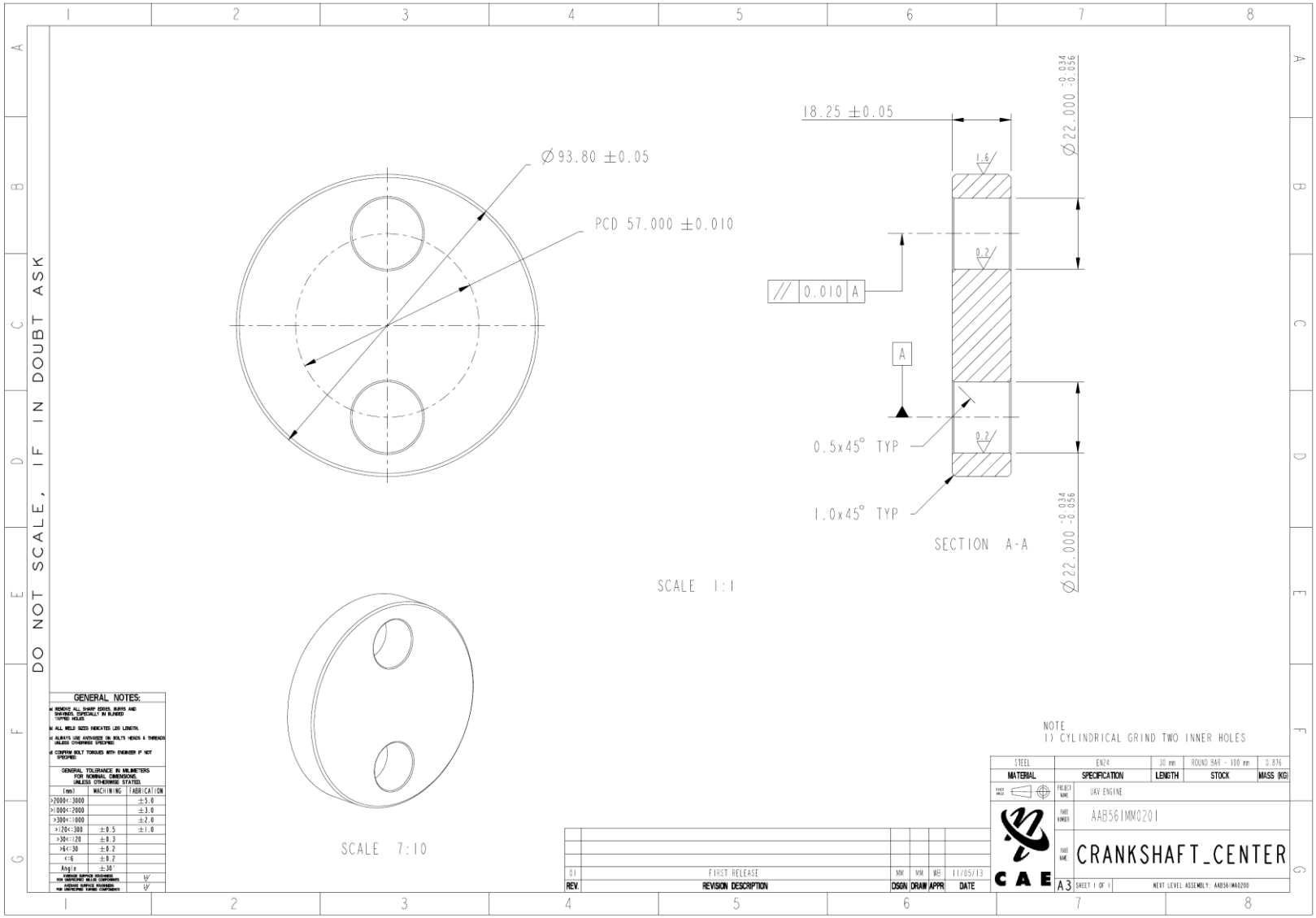
DO NOT SCALE, IF IN DOUBT ASK
Ø93.80 ±0.05
PCD 57.000 ±0.010
18.25 ±0.05
Ø22.000 -0.034 -0.056
0.010 A
A
0.5x45° TYP
1.0x45° TYP
SECTION A-A
SCALE 1:1
SCALE 7:10
NOTE
1) CYLINDRICAL GRIND TWO INNER HOLES
GENERAL NOTES:
GENERAL TOLERANCE IN MILIMETERS FOR NOMINAL DIMENSIONS, UNLESS OTHERWISE STATED
STEEL
EN24
30 mm
ROUND BAR - 100 mm
0.876
MATERIAL
SPECIFICATION
LENGTH
STOCK
MASS (KG)
UAV ENGINE
AAB561MM0201
CRANKSHAFT_CENTER
CAE
A3
01 FIRST RELEASE MM MM WB 11/05/13
REV. REVISION DESCRIPTION DSGN DRAW APPR DATE

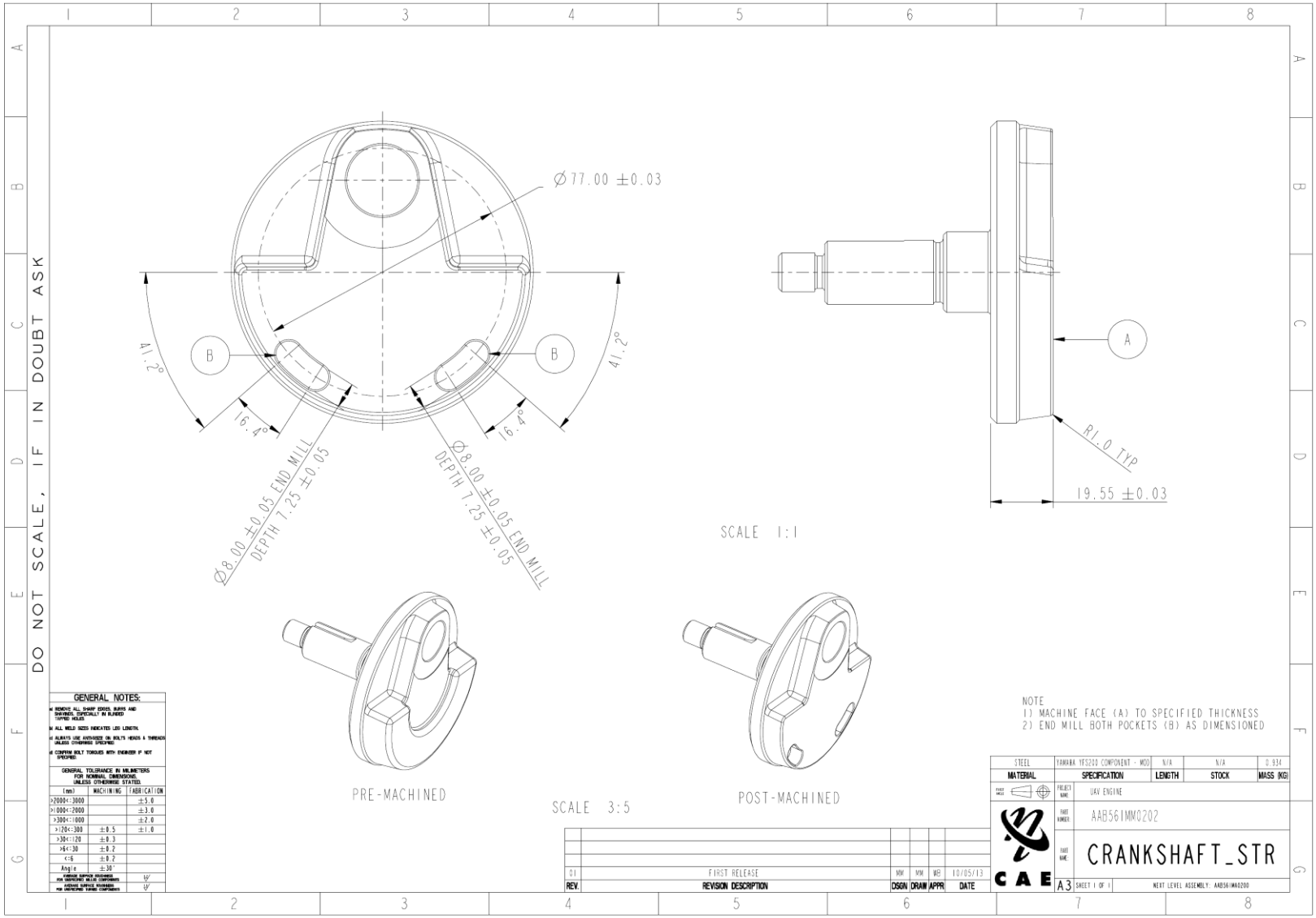
DO NOT SCALE, IF IN DOUBT ASK
Ø77.00 ±0.03
41.2°
41.2°
16.4°
16.4°
B
B
Ø8.00 ±0.05 END MILL
DEPTH 7.25 ±0.05
Ø8.00 ±0.05 END MILL
DEPTH 7.25 ±0.05
A
R1.0 TYP
19.55 ±0.03
SCALE 1:1
PRE-MACHINED
POST-MACHINED
SCALE 3:5
NOTE
1) MACHINE FACE (A) TO SPECIFIED THICKNESS
2) END MILL BOTH POCKETS (B) AS DIMENSIONED
GENERAL NOTES:
GENERAL TOLERANCE IN MILLIMETERS FOR NOMINAL DIMENSIONS, UNLESS OTHERWISE STATED
Item | MACHINING | FABRICATION
>2000<:3000 | ±5.0
>1000<:2000 | ±3.0
>300<:1000 | ±2.0
>120<:300 | ±0.5 | ±1.0
>30<:120 | ±0.3
>6<:30 | ±0.2
<:6 | ±0.2
Angle | ±30'
STEEL | YAMAHA YFS200 COMPONENT - MOD | N/A | N/A | 0.934
MATERIAL | SPECIFICATION | LENGTH | STOCK | MASS (KG)
UAV ENGINE
AAB561MM0202
CRANKSHAFT_STR
A3
01 FIRST RELEASE MM MM WB 10/05/13
REV. REVISION DESCRIPTION DSGN DRAW APPR DATE

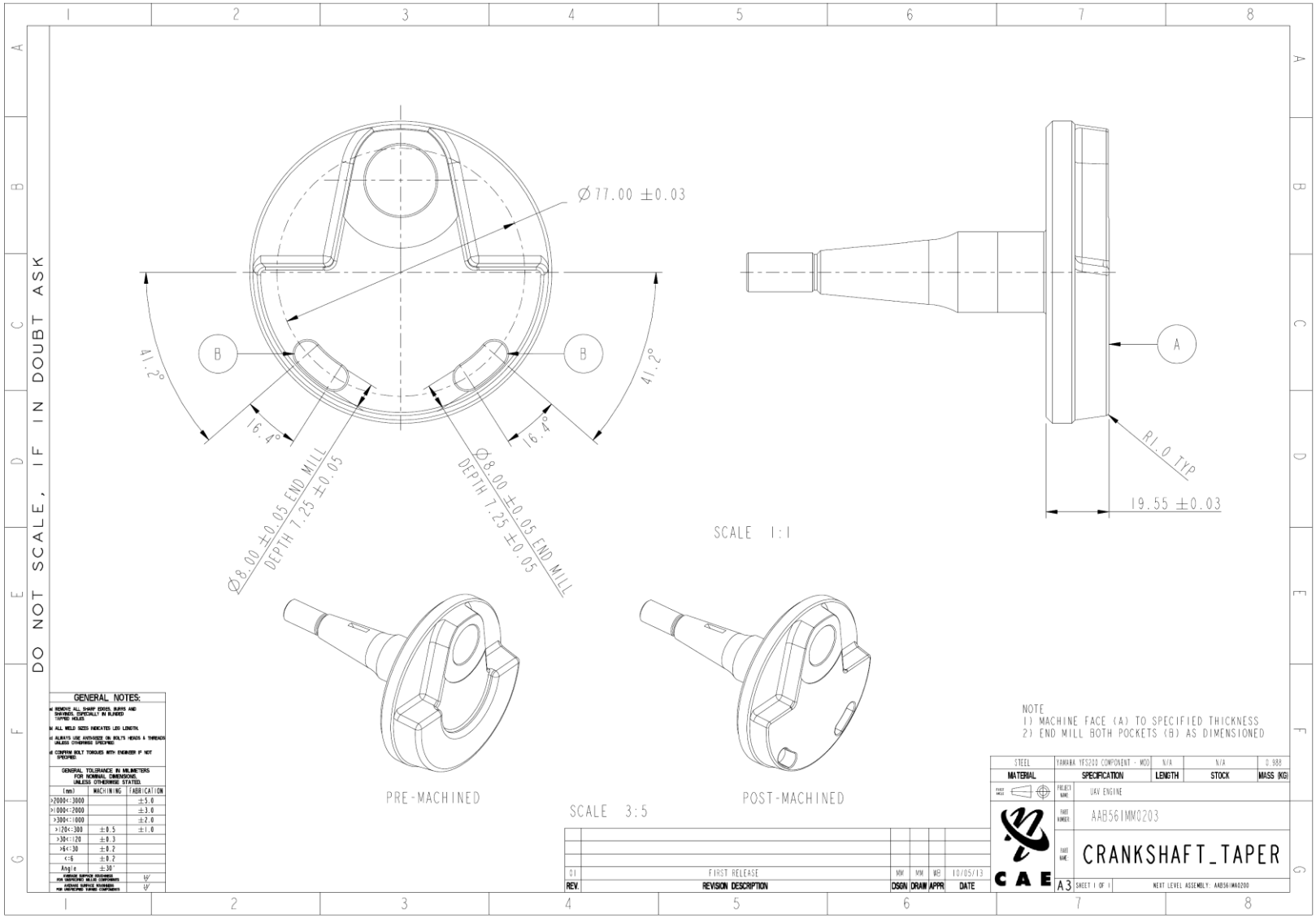
DO NOT SCALE, IF IN DOUBT ASK
Ø77.00 ±0.03
41.2°
41.2°
16.4°
16.4°
B
B
Ø8.00 ±0.05 END MILL
DEPTH 7.25 ±0.05
Ø8.00 ±0.05 END MILL
DEPTH 7.25 ±0.05
A
R1.0 TYP
19.55 ±0.03
SCALE 1:1
PRE-MACHINED
POST-MACHINED
SCALE 3:5
NOTE
1) MACHINE FACE (A) TO SPECIFIED THICKNESS
2) END MILL BOTH POCKETS (B) AS DIMENSIONED
GENERAL NOTES:
GENERAL TOLERANCE IN MILLIMETERS FOR NOMINAL DIMENSIONS, UNLESS OTHERWISE STATED
Item | MACHINING | FABRICATION
>2000<=3000 | ±5.0
>1000<=2000 | ±3.0
>300<=1000 | ±2.0
>120<=300 | ±0.5 | ±1.0
>30<=120 | ±0.3
>6<=30 | ±0.2
<=6 | ±0.2
Angle | ±30'
REV. | REVISION DESCRIPTION | DSGN | DRAW | APPR | DATE
01 | FIRST RELEASE | MM | MM | WB | 10/05/13
MATERIAL | STEEL | SPECIFICATION | YAMAHA YFS200 COMPONENT - MOD | LENGTH | N/A | STOCK | N/A | MASS (KG) | 0.988
PROJECT NAME | UAV ENGINE
PART NUMBER | AAB561MM0203
PART NAME | CRANKSHAFT_TAPER
A3 | SHEET 1 OF 1 | NEXT LEVEL ASSEMBLY: AAB561MA0200
CAE

F.5 PISTON ASSEMBLY

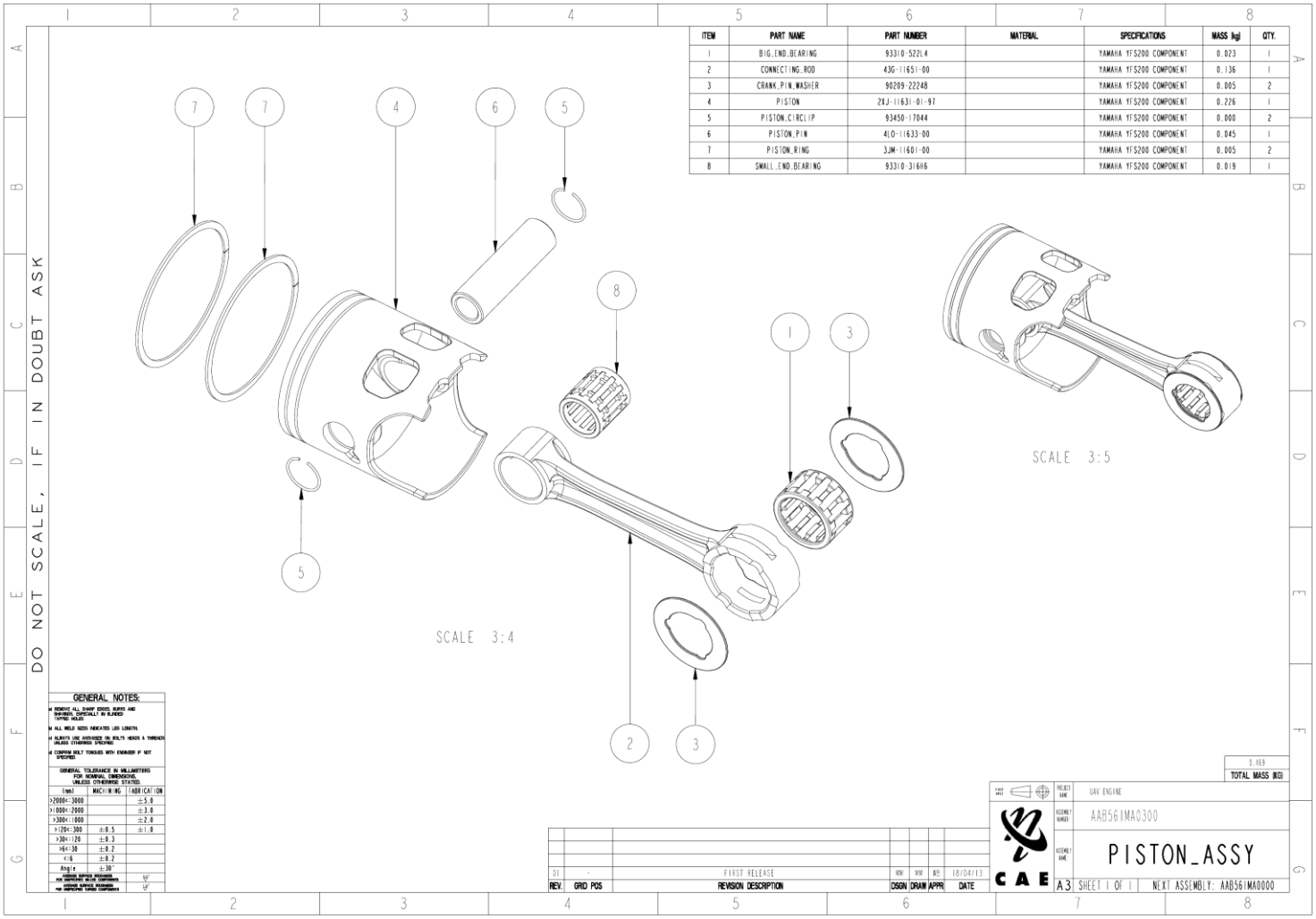

ITEM	PART NAME	PART NUMBER	MATERIAL	SPECIFICATIONS	MASS (kg)	QTY.
1	BIG_END_BEARING	93310-522L4		YAMAHA YFS200 COMPONENT	0.023	1
2	CONNECTING_ROD	43G-11651-00		YAMAHA YFS200 COMPONENT	0.136	1
3	CRANK_PIN_WASHER	90209-22248		YAMAHA YFS200 COMPONENT	0.005	2
4	PISTON	2XJ-11631-01-97		YAMAHA YFS200 COMPONENT	0.226	1
5	PISTON_CIRCLIP	93450-17044		YAMAHA YFS200 COMPONENT	0.000	2
6	PISTON_PIN	4LO-11633-00		YAMAHA YFS200 COMPONENT	0.045	1
7	PISTON_RING	3JM-11601-00		YAMAHA YFS200 COMPONENT	0.005	2
8	SMALL_END_BEARING	93310-316H6		YAMAHA YFS200 COMPONENT	0.019	1

REV.	GRID POS	REVISION DESCRIPTION	DSGN	DRAW	APPR	DATE
01		FIRST RELEASE	MM	MM	MS	18/04/13

F.6 CASE 1 ASSEMBLY

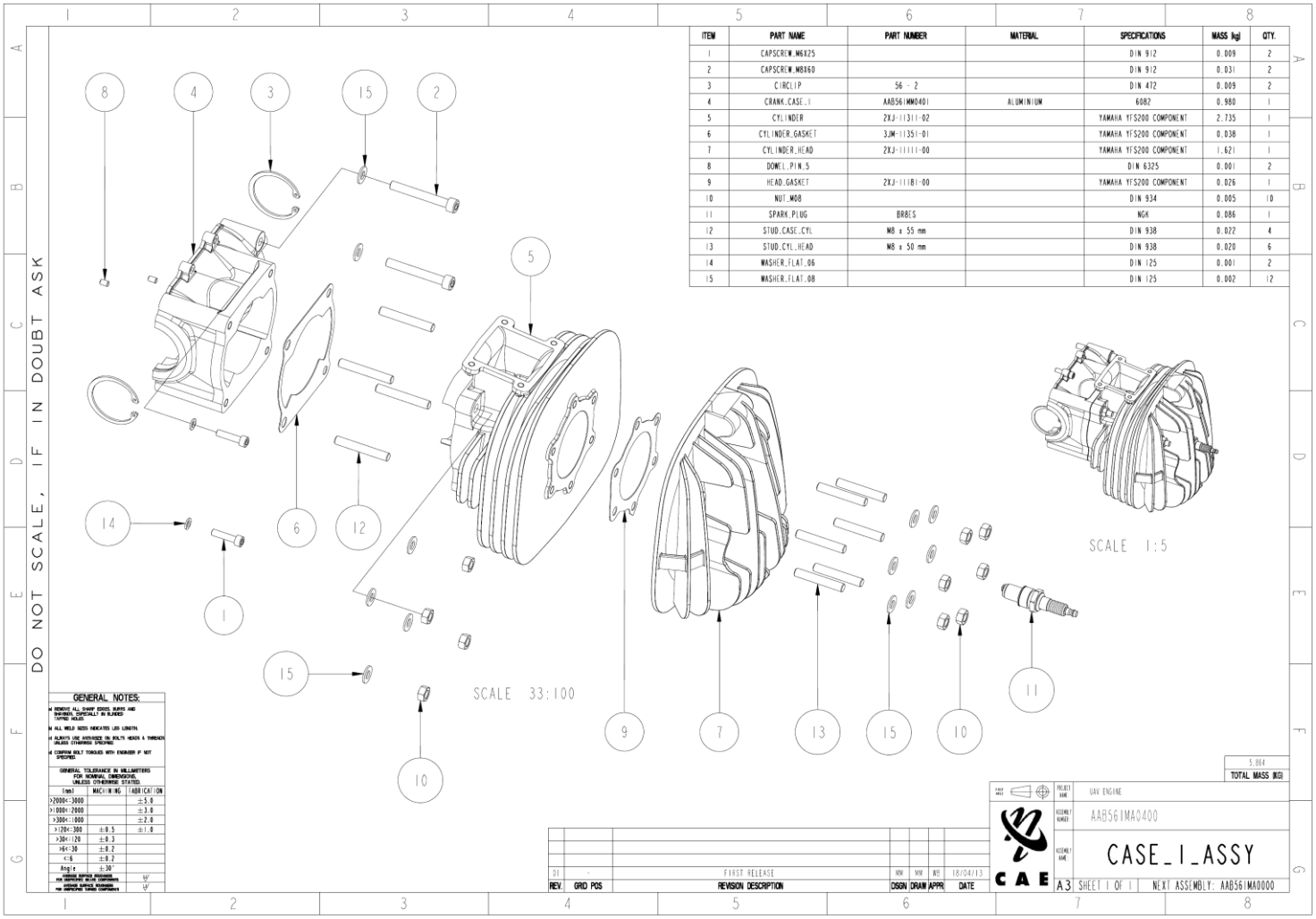

ITEM	PART NAME	PART NUMBER	MATERIAL	SPECIFICATIONS	MASS (kg)	QTY.
1	CAPSCREW_M8X25			DIN 912	0.009	2
2	CAPSCREW_M8X60			DIN 912	0.031	2
3	CIRCLIP	56 - 2		DIN 472	0.009	2
4	CRANK_CASE_1	AAB561MM0401	ALUMINIUM	6082	0.980	1
5	CYLINDER	2XJ-11311-02		YAMAHA YFS200 COMPONENT	2.735	1
6	CYLINDER_GASKET	3JM-11351-01		YAMAHA YFS200 COMPONENT	0.038	1
7	CYLINDER_HEAD	2XJ-11111-00		YAMAHA YFS200 COMPONENT	1.621	1
8	DOWEL_PIN_5			DIN 6325	0.001	2
9	HEAD_GASKET	2XJ-11181-00		YAMAHA YFS200 COMPONENT	0.026	1
10	NUT_M08			DIN 934	0.005	10
11	SPARK_PLUG	BR8ES		NGK	0.086	1
12	STUD_CASE_CYL	M8 x 55 mm		DIN 938	0.022	4
13	STUD_CYL_HEAD	M8 x 50 mm		DIN 938	0.020	6
14	WASHER_FLAT_06			DIN 125	0.001	2
15	WASHER_FLAT_08			DIN 125	0.002	12

GENERAL TOLERANCE IN MILLIMETERS FOR NOMINAL DIMENSIONS UNLESS OTHERWISE STATED		
(mm)	MACHINING	FABRICATION
>2000<:3000		±5.0
>1000<:2000		±3.0
>300<:1000		±2.0
>120<:300	±0.5	±1.0
>30<:120	±0.3	
>6<:30	±0.2	
<:6	±0.2	
Angle	±30'	

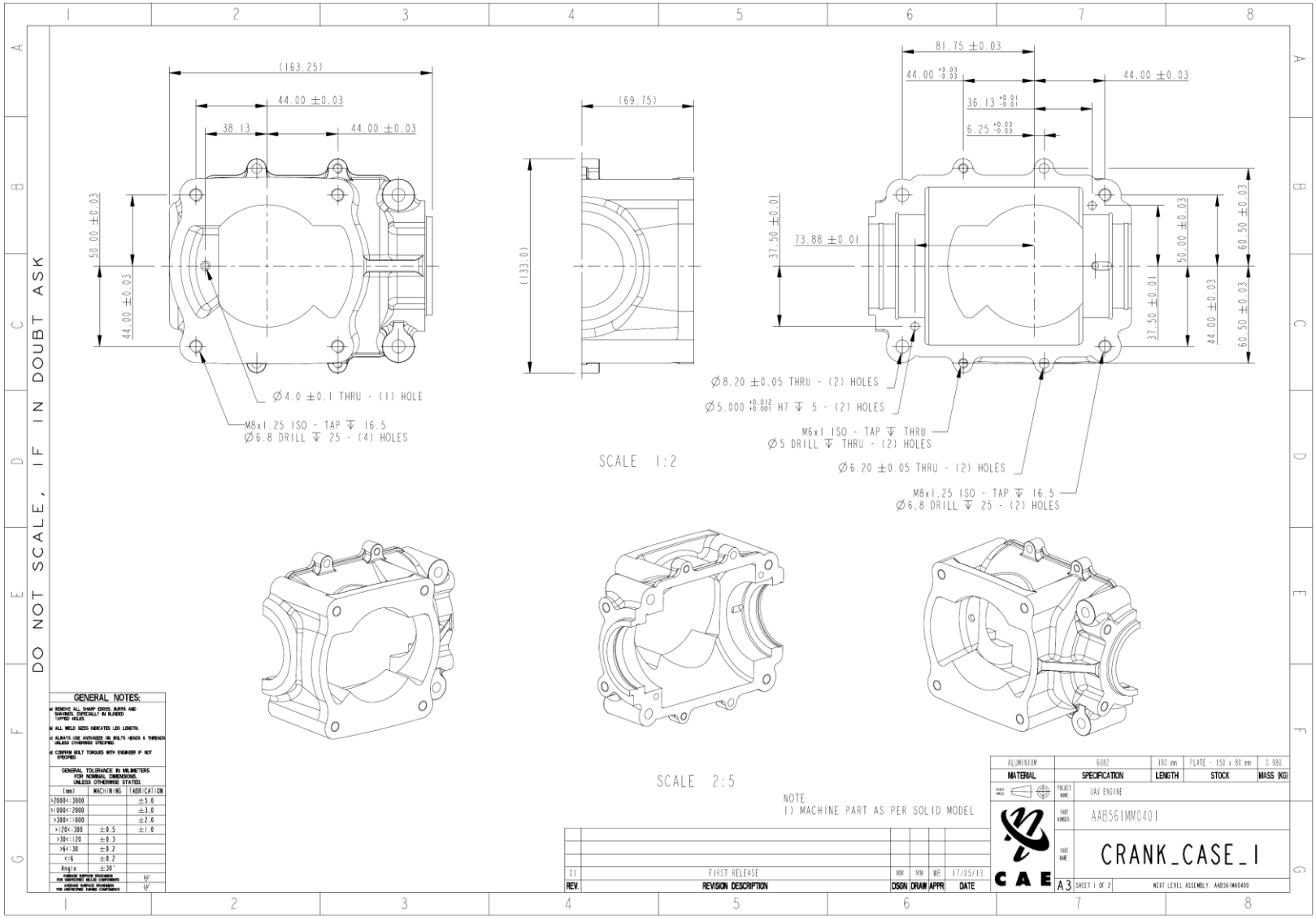
DO NOT SCALE, IF IN DOUBT ASK
(163.25)
44.00 ±0.03
38.13
44.00 ±0.03
50.00 ±0.03
44.00 ±0.03
Ø4.0 ±0.1 THRU - (1) HOLE
M8x1.25 ISO - TAP ↧ 16.5
Ø6.8 DRILL ↧ 25 - (4) HOLES
(69.75)
(133.0)
SCALE 1:2
81.75 ±0.03
44.00 +0.03 -0.03
44.00 ±0.03
36.13 +0.01 -0.01
6.25 +0.03 -0.03
37.50 ±0.01
73.88 ±0.01
50.00 ±0.03
44.00 ±0.03
37.50 ±0.01
60.50 ±0.03
60.50 ±0.03
Ø8.20 ±0.05 THRU - (2) HOLES
Ø5.000 +0.012 +0.001 H7 ↧ 5 - (2) HOLES
M6x1 ISO - TAP ↧ THRU
Ø5 DRILL ↧ THRU - (2) HOLES
Ø6.20 ±0.05 THRU - (2) HOLES
M8x1.25 ISO - TAP ↧ 16.5
Ø6.8 DRILL ↧ 25 - (2) HOLES
SCALE 2:5
NOTE
1) MACHINE PART AS PER SOLID MODEL
GENERAL NOTES:
GENERAL TOLERANCE IN MILIMETERS FOR NOMINAL DIMENSIONS, UNLESS OTHERWISE STATED.
Item | MACHINING | FABRICATION
>2000<:3000 | | ±5.0
>1000<:2000 | | ±3.0
>300<:1000 | | ±2.0
>120<:300 | ±0.5 | ±1.0
>30<:120 | ±0.3 |
>6<:30 | ±0.2 |
<:6 | ±0.2 |
Angle | ±30'
01 FIRST RELEASE MM MM WB 17/05/13
REV. REVISION DESCRIPTION DSGN DRAW APPR DATE
ALUMINIUM | 6082 | 180 mm | PLATE - 150 x 80 mm | 0.980
MATERIAL | SPECIFICATION | LENGTH | STOCK | MASS (KG)
PROJECT NAME: UAV ENGINE
PART NUMBER: AAB561MM0401
PART NAME: CRANK_CASE_1
CAE
A3 SHEET 1 OF 2
NEXT LEVEL ASSEMBLY: AAB561MA0400

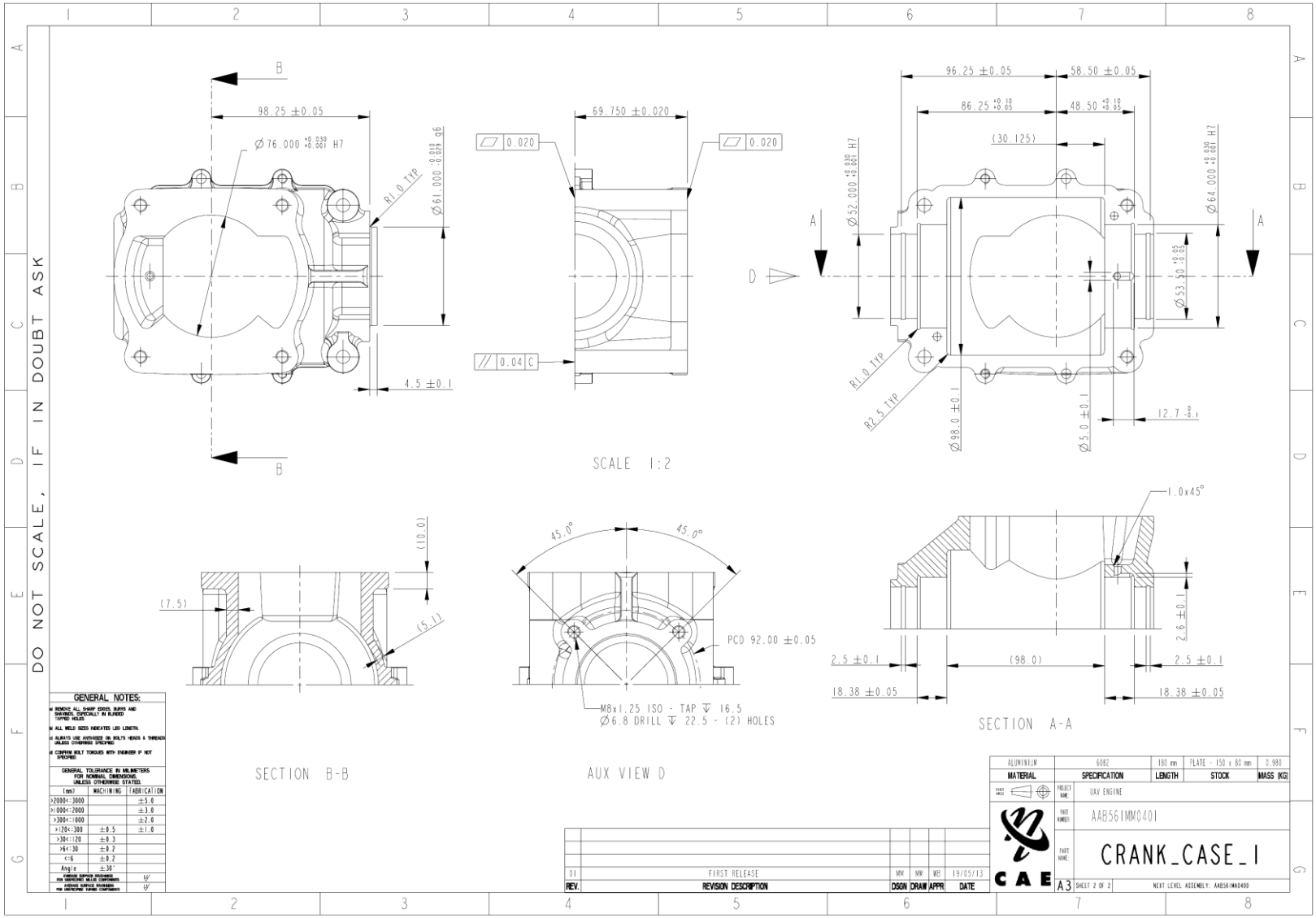
DO NOT SCALE, IF IN DOUBT ASK
SCALE 1:2
SECTION B-B
AUX VIEW D
SECTION A-A
GENERAL NOTES:
CRANK_CASE_1
AAB561MM0401
UAV ENGINE
ALUMINIUM
6082
180 mm
PLATE - 150 x 80 mm
0.980
FIRST RELEASE
19/05/13

F.7 CASE 2 ASSEMBLY

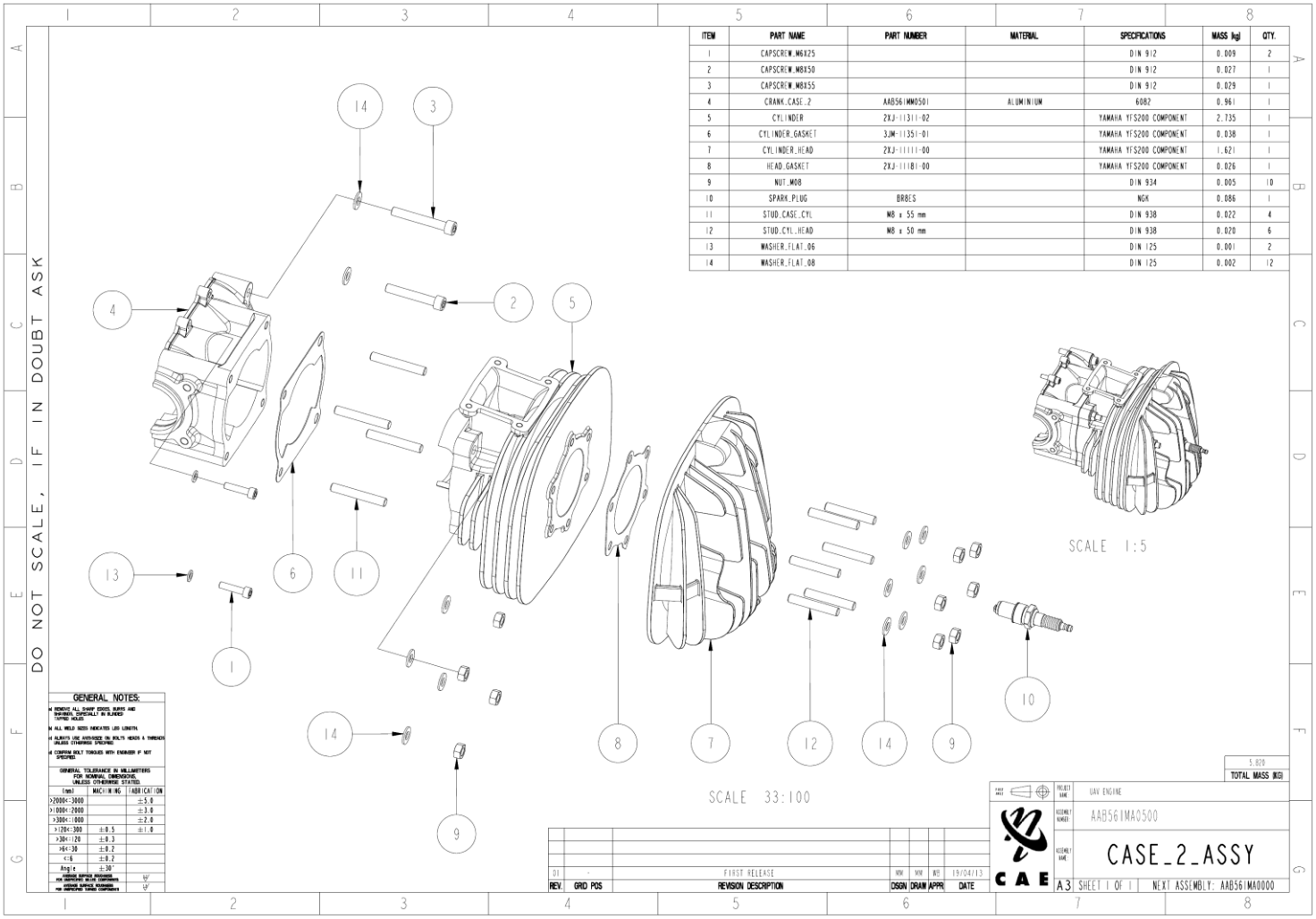

ITEM	PART NAME	PART NUMBER	MATERIAL	SPECIFICATIONS	MASS (kg)	QTY.
1	CAPSCREW_M6X25			DIN 912	0.009	2
2	CAPSCREW_M8X50			DIN 912	0.027	1
3	CAPSCREW_M8X55			DIN 912	0.029	1
4	CRANK_CASE_2	AAB561MM0501	ALUMINIUM	6082	0.961	1
5	CYLINDER	2XJ-11311-02		YAMAHA YFS200 COMPONENT	2.735	1
6	CYLINDER_GASKET	3JM-11351-01		YAMAHA YFS200 COMPONENT	0.038	1
7	CYLINDER_HEAD	2XJ-11111-00		YAMAHA YFS200 COMPONENT	1.621	1
8	HEAD_GASKET	2XJ-11181-00		YAMAHA YFS200 COMPONENT	0.026	1
9	NUT_M8			DIN 934	0.005	10
10	SPARK_PLUG	BR8ES		NGK	0.086	1
11	STUD_CASE_CYL	M8 x 55 mm		DIN 938	0.022	4
12	STUD_CYL_HEAD	M8 x 50 mm		DIN 938	0.020	6
13	WASHER_FLAT_06			DIN 125	0.001	2
14	WASHER_FLAT_08			DIN 125	0.002	12

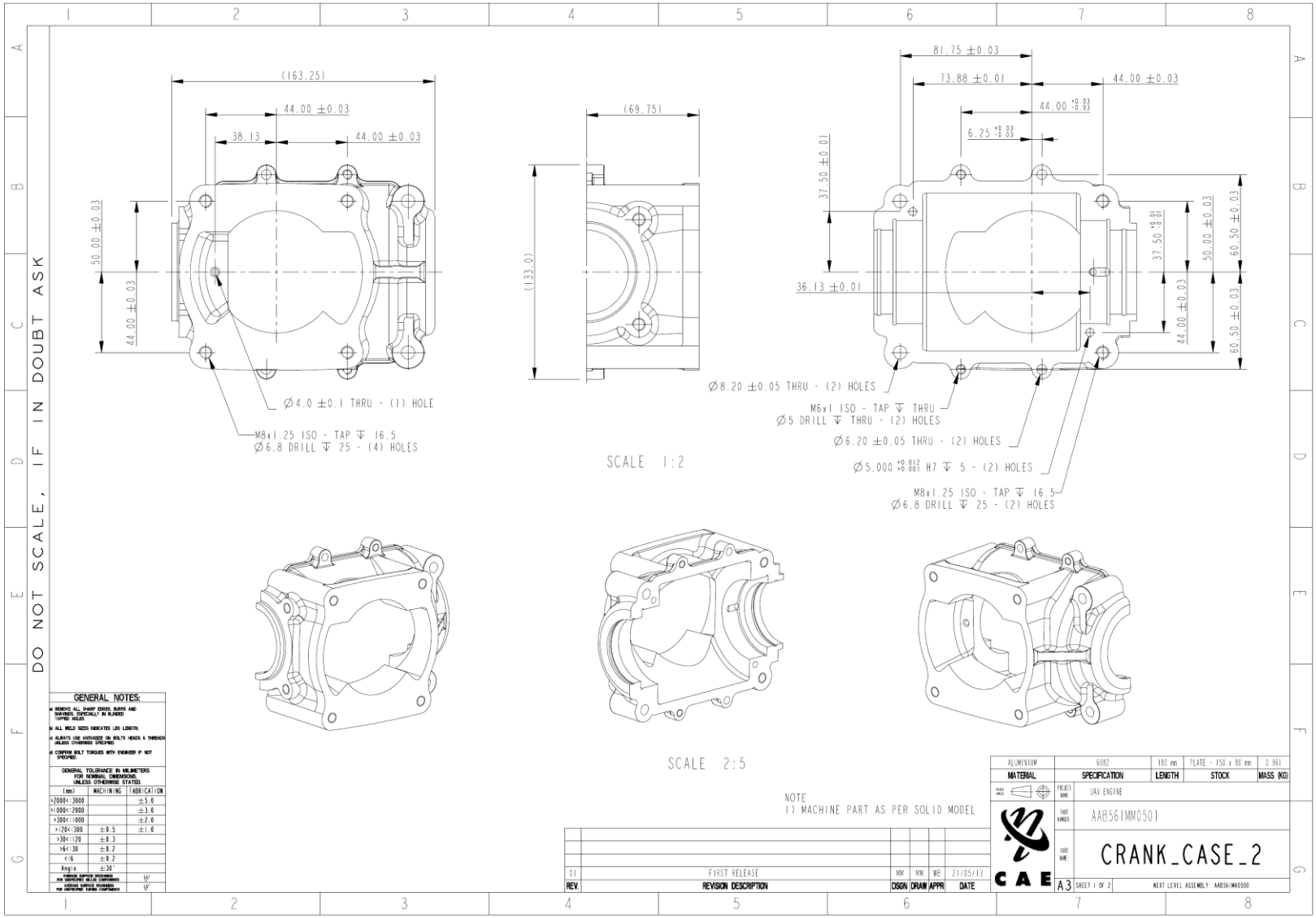
DO NOT SCALE, IF IN DOUBT ASK
(163.25)
44.00 ±0.03
38.13
44.00 ±0.03
50.00 ±0.03
44.00 ±0.03
Ø4.0 ±0.1 THRU - (1) HOLE
M8x1.25 ISO - TAP ↧ 16.5
Ø6.8 DRILL ↧ 25 - (4) HOLES
(69.75)
(133.0)
SCALE 1:2
81.75 ±0.03
73.88 ±0.01
44.00 ±0.03
44.00 +0.03 -0.03
6.25 +0.03 -0.03
37.50 ±0.01
36.13 ±0.01
37.50 +0.01 -0.01
50.00 ±0.03
60.50 ±0.03
44.00 ±0.03
60.50 ±0.03
Ø8.20 ±0.05 THRU - (2) HOLES
M6x1 ISO - TAP ↧ THRU
Ø5 DRILL ↧ THRU - (2) HOLES
Ø6.20 ±0.05 THRU - (2) HOLES
Ø5.000 +0.012 +0.001 H7 ↧ 5 - (2) HOLES
M8x1.25 ISO - TAP ↧ 16.5
Ø6.8 DRILL ↧ 25 - (2) HOLES
SCALE 2:5
GENERAL NOTES:
GENERAL TOLERANCE IN MILIMETERS FOR NOMINAL DIMENSIONS, UNLESS OTHERWISE STATED.
[mm] | MACHINING | FABRICATION
>2000<:3000 | ±5.0
>1000<:2000 | ±3.0
>300<:1000 | ±2.0
>120<:300 | ±0.5 | ±1.0
>30<:120 | ±0.3
>6<:30 | ±0.2
<:6 | ±0.2
Angle | ±30'
NOTE
1) MACHINE PART AS PER SOLID MODEL
01 REV. FIRST RELEASE MM MM WB 21/05/13
REVISION DESCRIPTION DSGN DRAW APPR DATE
ALUMINIUM | 6082 | 180 mm | PLATE - 150 x 80 mm | 0.961
MATERIAL | SPECIFICATION | LENGTH | STOCK | MASS (KG)
PROJECT NAME: UAV ENGINE
PART NUMBER: AAB561MM0501
PART NAME: CRANK_CASE_2
CAE
A3 SHEET 1 OF 2
NEXT LEVEL ASSEMBLY: AAB561MA0500

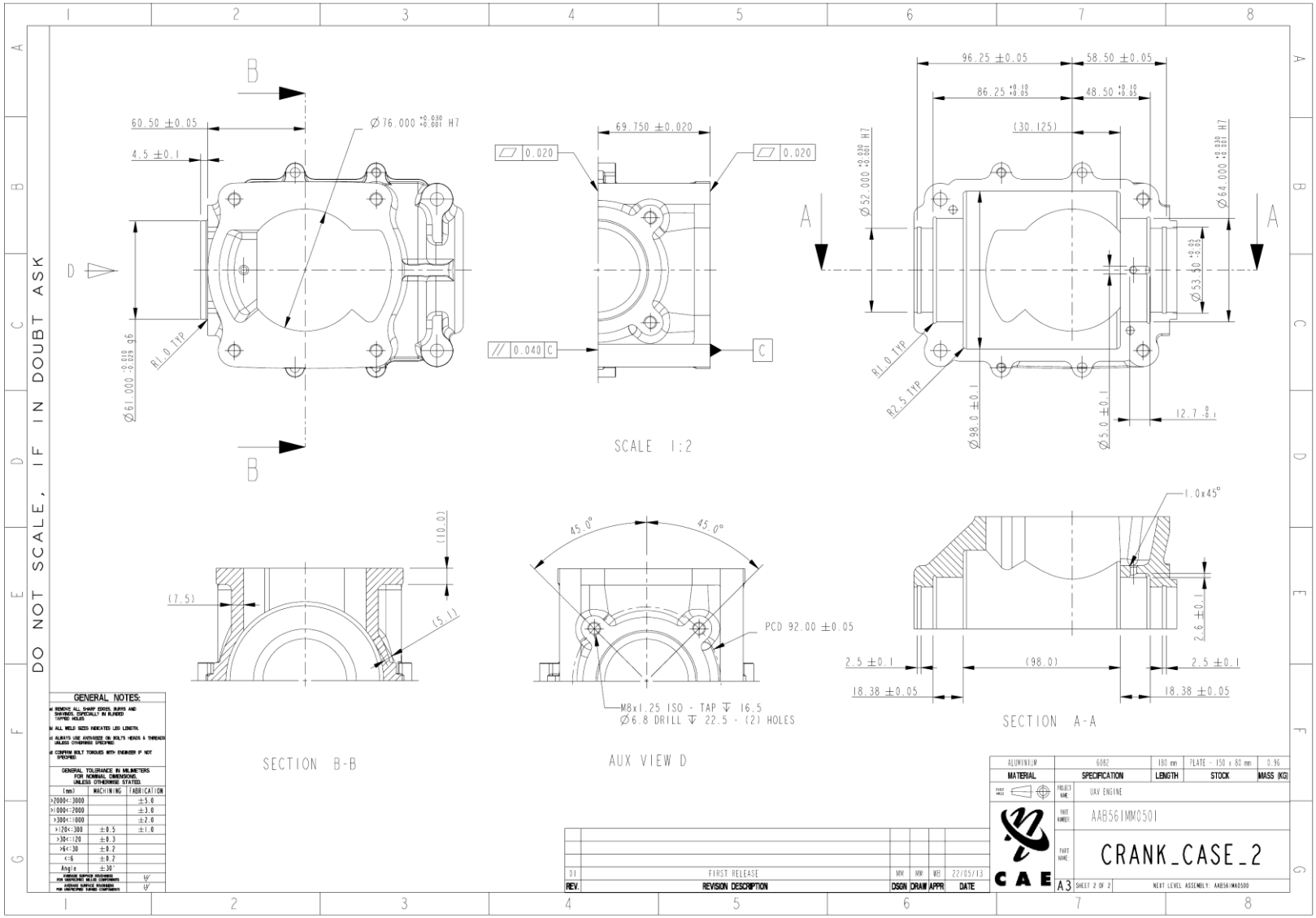
DO NOT SCALE, IF IN DOUBT ASK
SCALE 1:2
SECTION B-B
AUX VIEW D
SECTION A-A
GENERAL NOTES:
ALUMINIUM
6082
180 mm
PLATE - 150 x 80 mm
0.96
MATERIAL
SPECIFICATION
LENGTH
STOCK
MASS (KG)
UAV ENGINE
AAB561MM0501
CRANK_CASE_2
A3
FIRST RELEASE
22/05/13
REVISION DESCRIPTION
DSGN
DRAW
APPR
DATE

F.8 ENGINE MOUNT ASSEMBLY

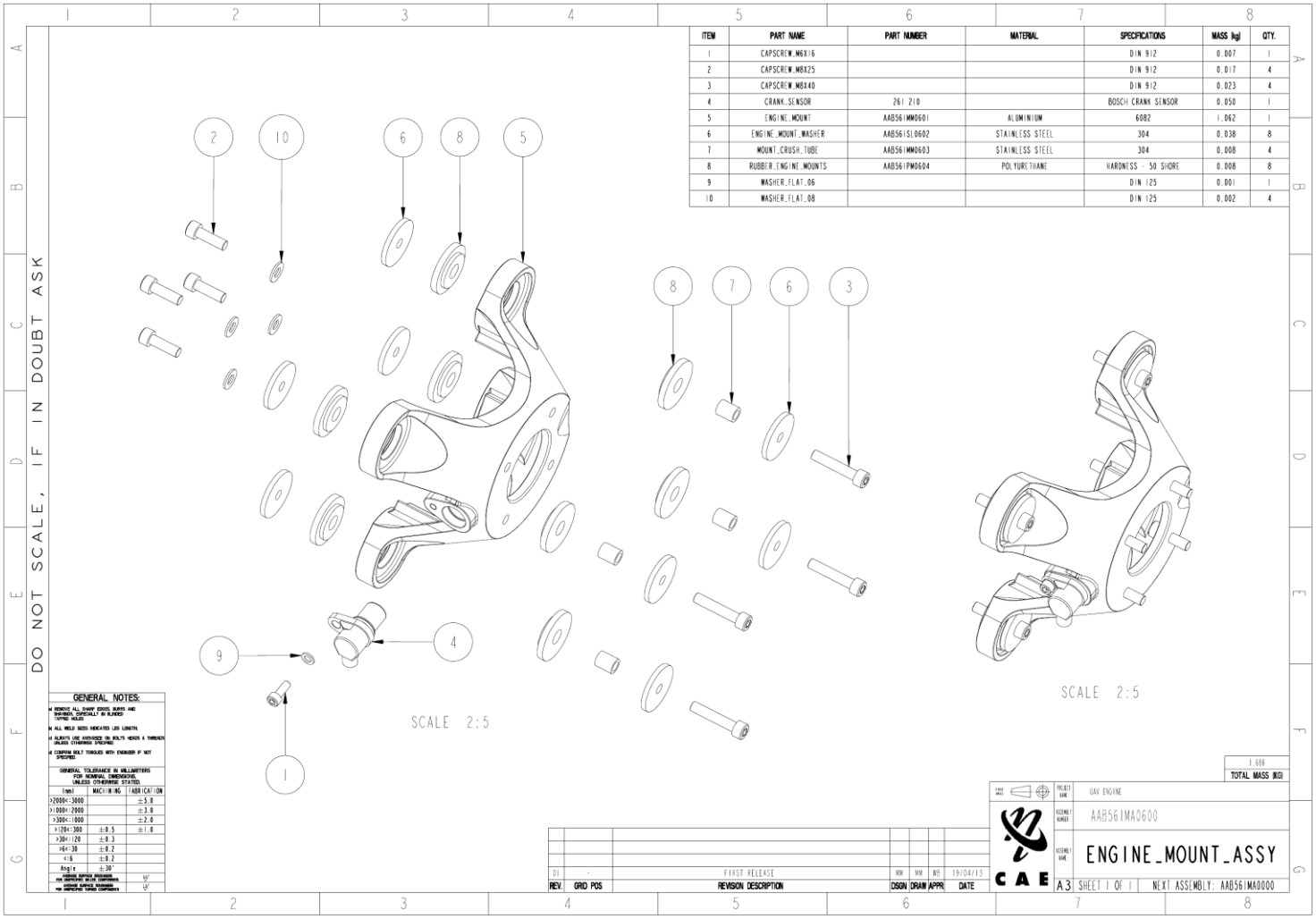

ITEM	PART NAME	PART NUMBER	MATERIAL	SPECIFICATIONS	MASS (kg)	QTY.
1	CAPSCREW_M8X16			DIN 912	0.007	1
2	CAPSCREW_M8X25			DIN 912	0.017	4
3	CAPSCREW_M8X40			DIN 912	0.023	4
4	CRANK_SENSOR	261 210		BOSCH CRANK SENSOR	0.050	1
5	ENGINE_MOUNT	AAB561MM0601	ALUMINIUM	6082	1.062	1
6	ENGINE_MOUNT_WASHER	AAB561SL0602	STAINLESS STEEL	304	0.038	8
7	MOUNT_CRUSH_TUBE	AAB561MM0603	STAINLESS STEEL	304	0.008	4
8	RUBBER_ENGINE_MOUNTS	AAB561PM0604	POLYURETHANE	HARDNESS - 50 SHORE	0.008	8
9	WASHER_FLAT_06			DIN 125	0.001	1
10	WASHER_FLAT_08			DIN 125	0.002	4

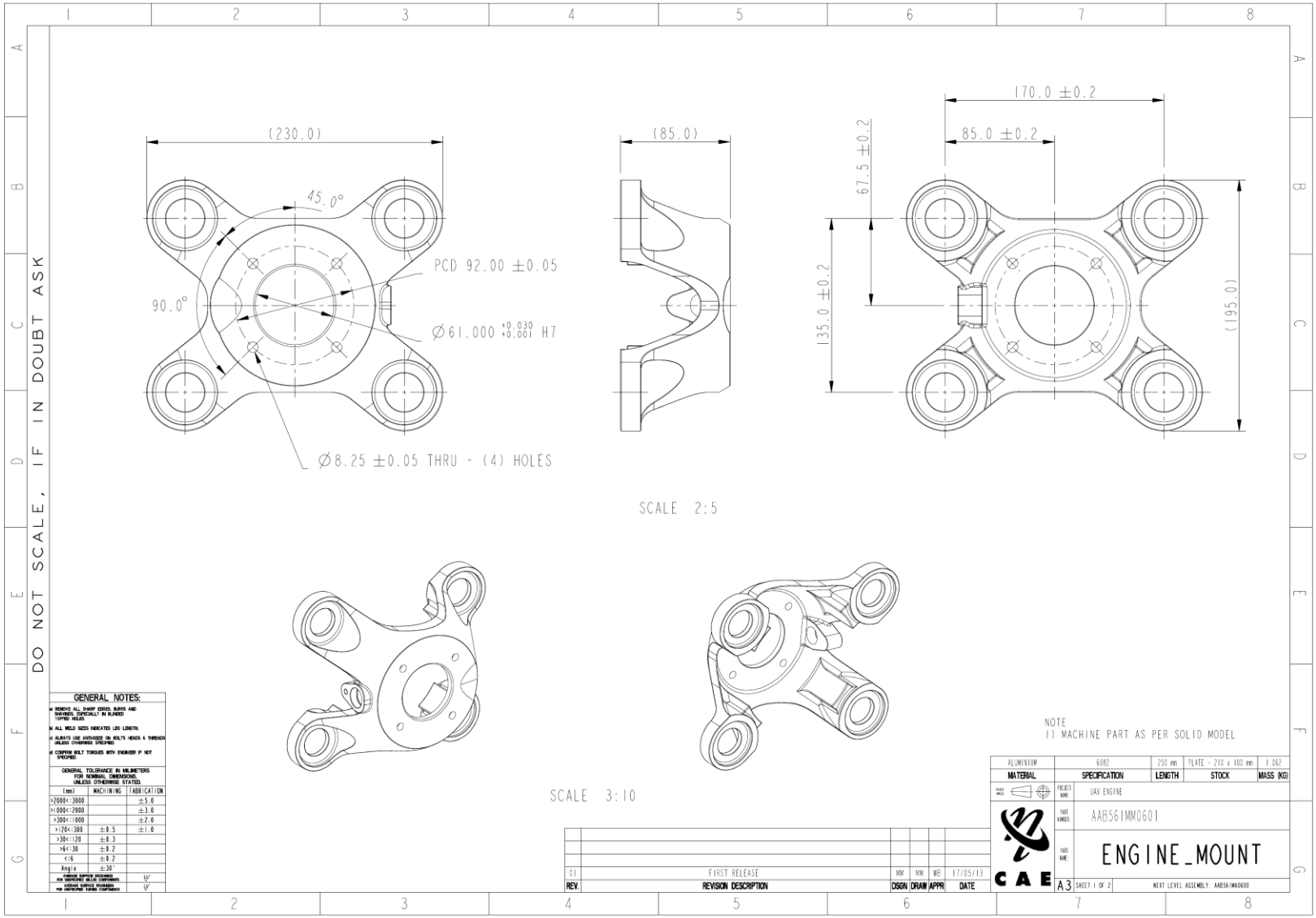
DO NOT SCALE, IF IN DOUBT ASK
(230.0)
45.0°
90.0°
PCD 92.00 ±0.05
Ø61.000 +0.030 +0.001 H7
Ø8.25 ±0.05 THRU - (4) HOLES
(85.0)
170.0 ±0.2
85.0 ±0.2
67.5 ±0.2
135.0 ±0.2
(195.0)
SCALE 2:5
SCALE 3:10
GENERAL NOTES:
GENERAL TOLERANCE IN MILIMETERS FOR NOMINAL DIMENSIONS, UNLESS OTHERWISE STATED.
Item | MACHINING | FABRICATION
>2000<:3000 | | ±5.0
>1000<:2000 | | ±3.0
>300<:1000 | | ±2.0
>120<:300 | ±0.5 | ±1.0
>30<:120 | ±0.3 |
>6<:30 | ±0.2 |
<:6 | ±0.2 |
Angle | ±30'
NOTE
1) MACHINE PART AS PER SOLID MODEL
ALUMINIUM | 6082 | 250 mm | PLATE - 210 x 100 mm | 1.062
MATERIAL | SPECIFICATION | LENGTH | STOCK | MASS (KG)
UAV ENGINE
AAB561MM0601
ENGINE_MOUNT
A3 SHEET 1 OF 2
NEXT LEVEL ASSEMBLY: AAB561MA0600
01 FIRST RELEASE MM MK WB 17/05/13
REV. REVISION DESCRIPTION DSGN DRAW APPR DATE

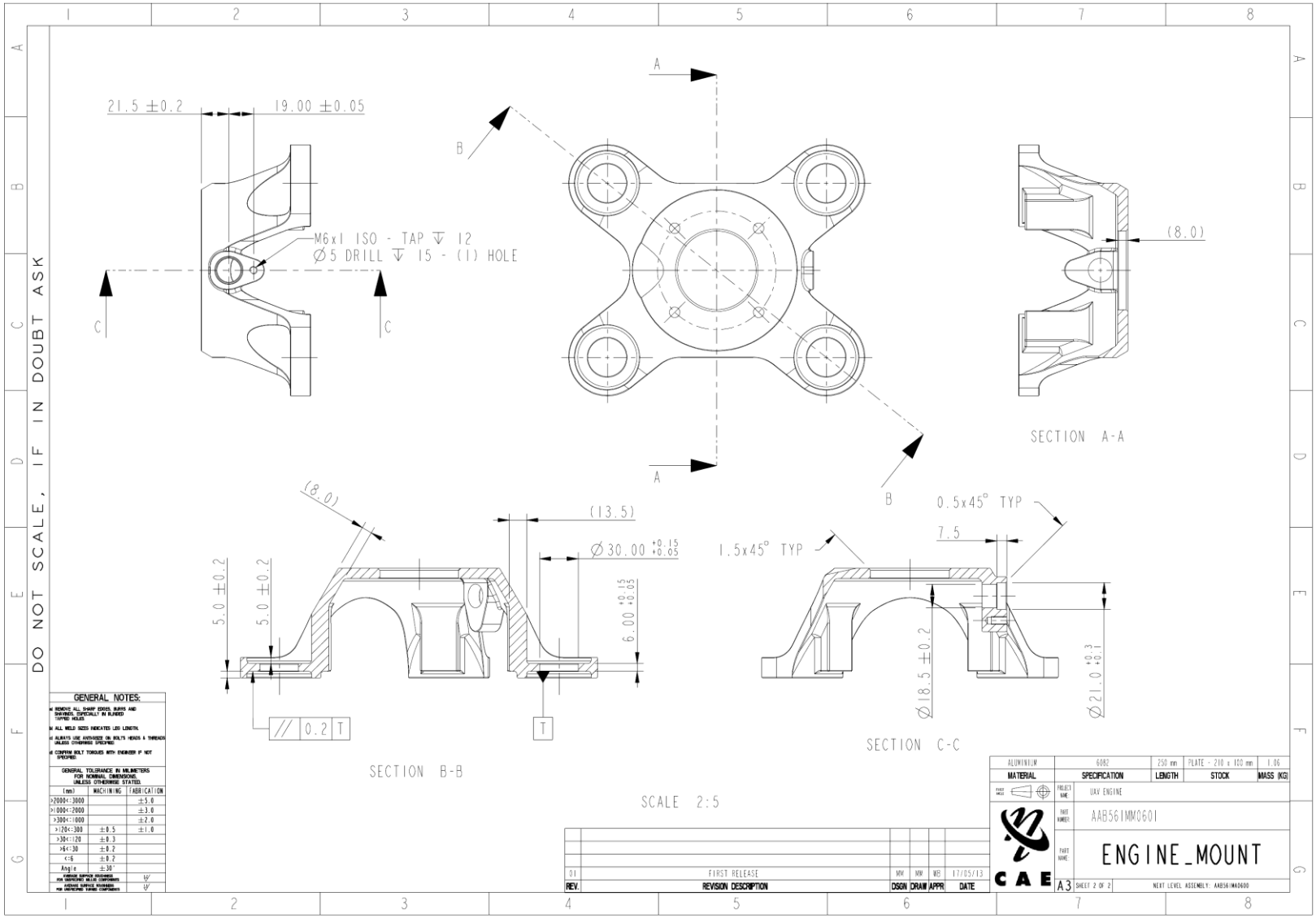
DO NOT SCALE, IF IN DOUBT ASK
21.5 ±0.2
19.00 ±0.05
M6x1 ISO - TAP ↧ 12
Ø5 DRILL ↧ 15 - (1) HOLE
SECTION A-A
(8.0)
(13.5)
Ø30.00 +0.15 +0.05
5.0 ±0.2
5.0 ±0.2
6.00 +0.15 +0.05
// 0.2 T
SECTION B-B
1.5x45° TYP
0.5x45° TYP
7.5
Ø18.5 ±0.2
Ø21.0 +0.3 +0.1
SECTION C-C
SCALE 2:5
GENERAL NOTES:
GENERAL TOLERANCE IN MILIMETERS FOR NOMINAL DIMENSIONS, UNLESS OTHERWISE STATED
Item | MACHINING | FABRICATION
>2000<:3000 | ±5.0
>1000<:2000 | ±3.0
>300<:1000 | ±2.0
>120<:300 | ±0.5 | ±1.0
>30<:120 | ±0.3
>6<:30 | ±0.2
<:6 | ±0.2
Angle | ±30'
REV. | REVISION DESCRIPTION | DSGN | DRAW | APPR | DATE
01 | FIRST RELEASE | MM | MM | WB | 17/05/13
MATERIAL | ALUMINIUM | SPECIFICATION | 6082 | LENGTH | 250 mm | STOCK | PLATE - 210 x 100 mm | MASS (KG) | 1.06
PROJECT NAME | UAV ENGINE
PART NUMBER | AAB561MM0601
PART NAME | ENGINE_MOUNT
A3 | SHEET 2 OF 2 | NEXT LEVEL ASSEMBLY: AAB561MA0600
CAE

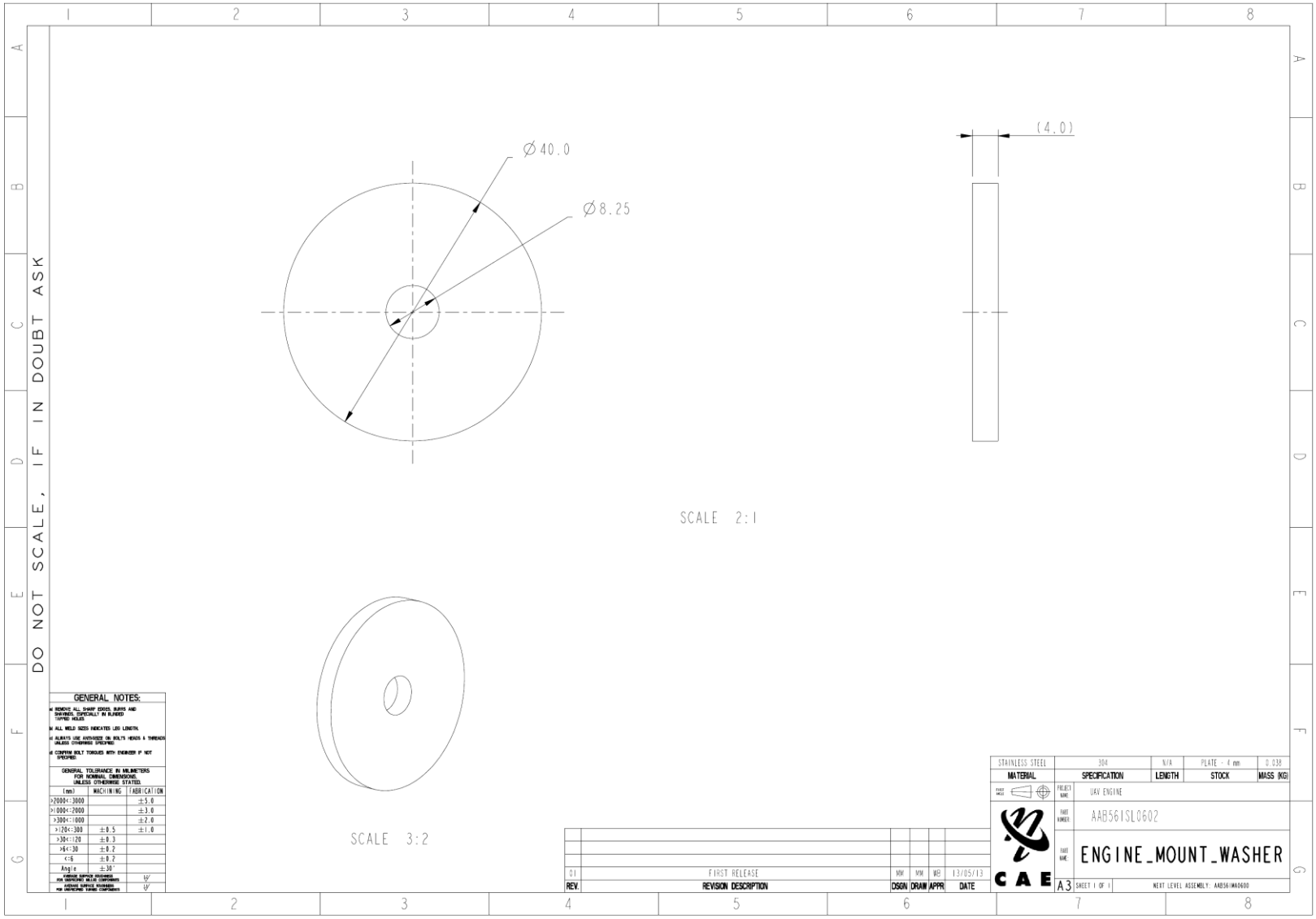
Ø40.0
Ø8.25
(4.0)
SCALE 2:1
SCALE 3:2
DO NOT SCALE, IF IN DOUBT ASK
GENERAL NOTES:
GENERAL TOLERANCE IN MILIMETERS FOR NOMINAL DIMENSIONS, UNLESS OTHERWISE STATED.
STAINLESS STEEL
304
N/A
PLATE - 4 mm
0.038
MATERIAL
SPECIFICATION
LENGTH
STOCK
MASS (KG)
UAV ENGINE
AAB561SL0602
ENGINE_MOUNT_WASHER
CAE
A3
FIRST RELEASE
13/05/13
REVISION DESCRIPTION
DATE

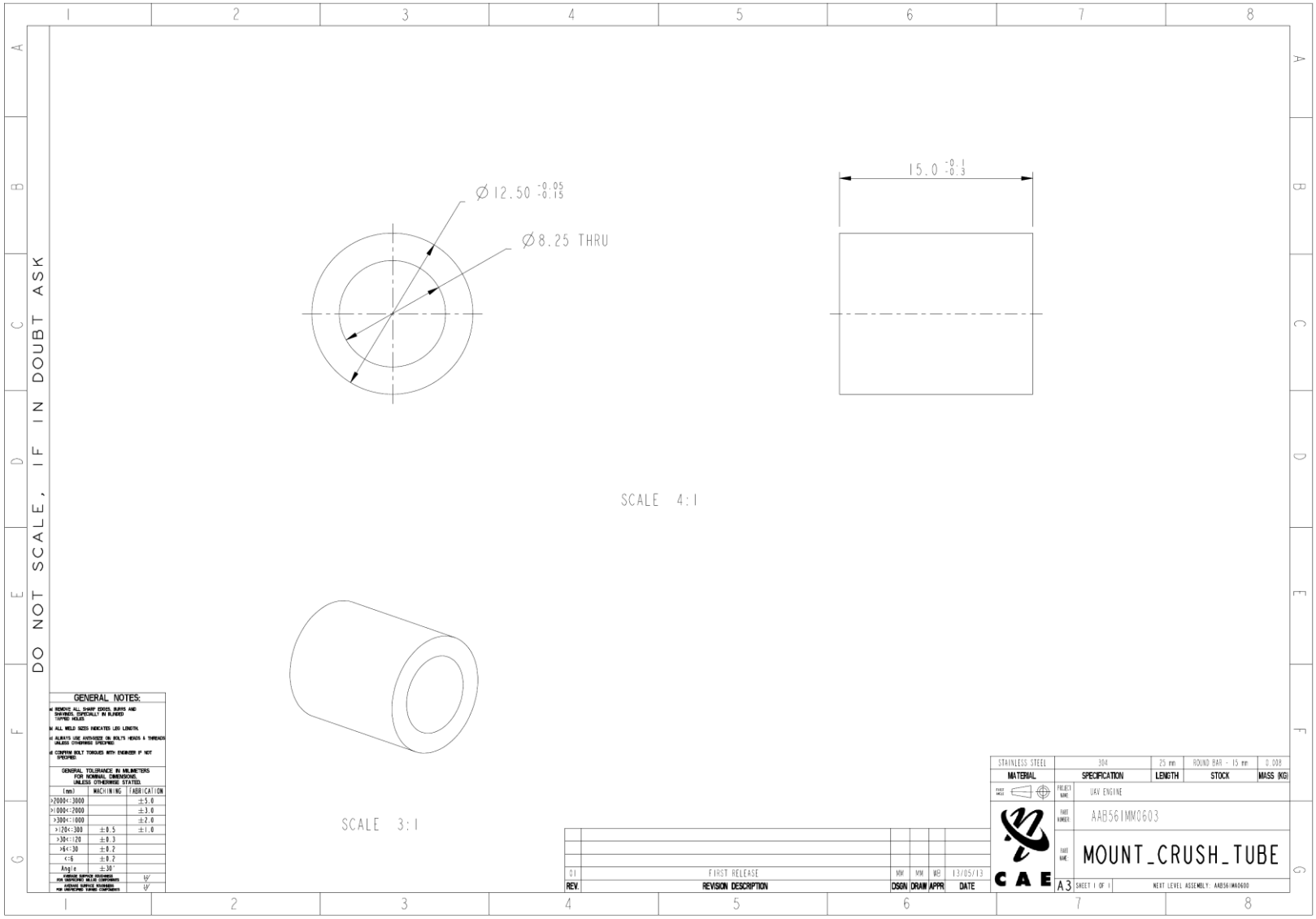
DO NOT SCALE, IF IN DOUBT ASK
Ø12.50 -0.05 -0.15
Ø8.25 THRU
15.0 -0.1 -0.3
SCALE 4:1
SCALE 3:1
GENERAL NOTES:
GENERAL TOLERANCE IN MILIMETERS FOR NOMINAL DIMENSIONS, UNLESS OTHERWISE STATED
[mm] | MACHINING | FABRICATION
>2000<=3000 | ±5.0
>1000<=2000 | ±3.0
>300<=1000 | ±2.0
>120<=300 | ±0.5 | ±1.0
>30<=120 | ±0.3
>6<=30 | ±0.2
<=6 | ±0.2
Angle | ±30'
REV. | REVISION DESCRIPTION | DSGN | DRAW | APPR | DATE
01 | FIRST RELEASE | MM | MM | WB | 13/05/13
STAINLESS STEEL | 304 | 25 mm | ROUND BAR - 15 mm | 0.008
MATERIAL | SPECIFICATION | LENGTH | STOCK | MASS (KG)
PROJECT NAME: UAV ENGINE
PART NUMBER: AAB561MM0603
PART NAME: MOUNT_CRUSH_TUBE
CAE
A3 SHEET 1 OF 1
NEXT LEVEL ASSEMBLY: AAB561MA0600

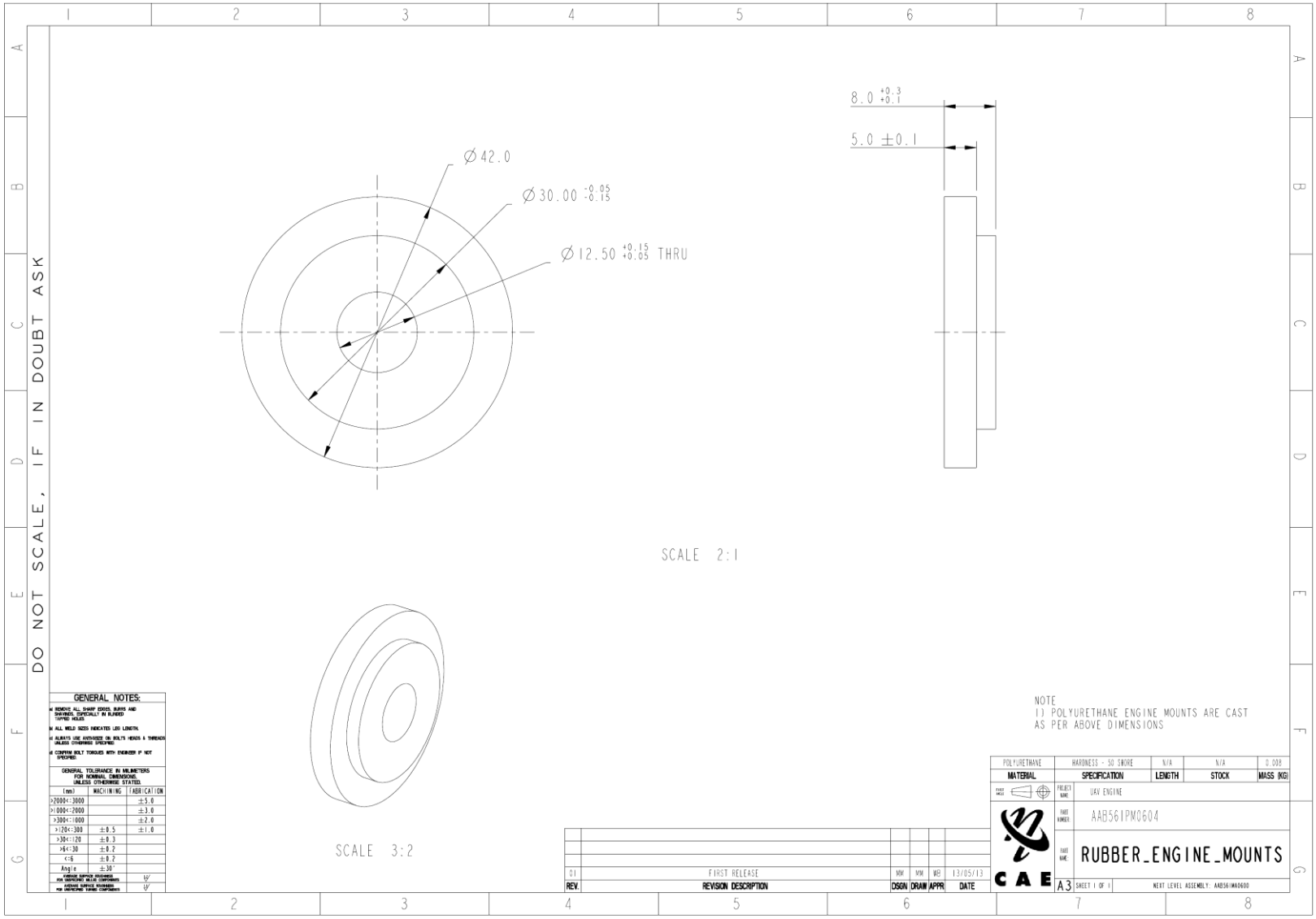
DO NOT SCALE, IF IN DOUBT ASK
Ø42.0
Ø30.00 -0.05 -0.15
Ø12.50 +0.15 +0.05 THRU
8.0 +0.3 +0.1
5.0 ±0.1
SCALE 2:1
SCALE 3:2
GENERAL NOTES:
GENERAL TOLERANCE IN MILIMETERS FOR NOMINAL DIMENSIONS, UNLESS OTHERWISE STATED.
NOTE
1) POLYURETHANE ENGINE MOUNTS ARE CAST AS PER ABOVE DIMENSIONS
POLYURETHANE
HARDNESS - 50 SHORE
N/A
N/A
0.008
MATERIAL
SPECIFICATION
LENGTH
STOCK
MASS (KG)
UAV ENGINE
AAB561PM0604
RUBBER_ENGINE_MOUNTS
CAE
A3
01
FIRST RELEASE
13/05/13
REV.
REVISION DESCRIPTION
DSGN
DRAW
APPR
DATE

F.9 ENCODER WHEEL

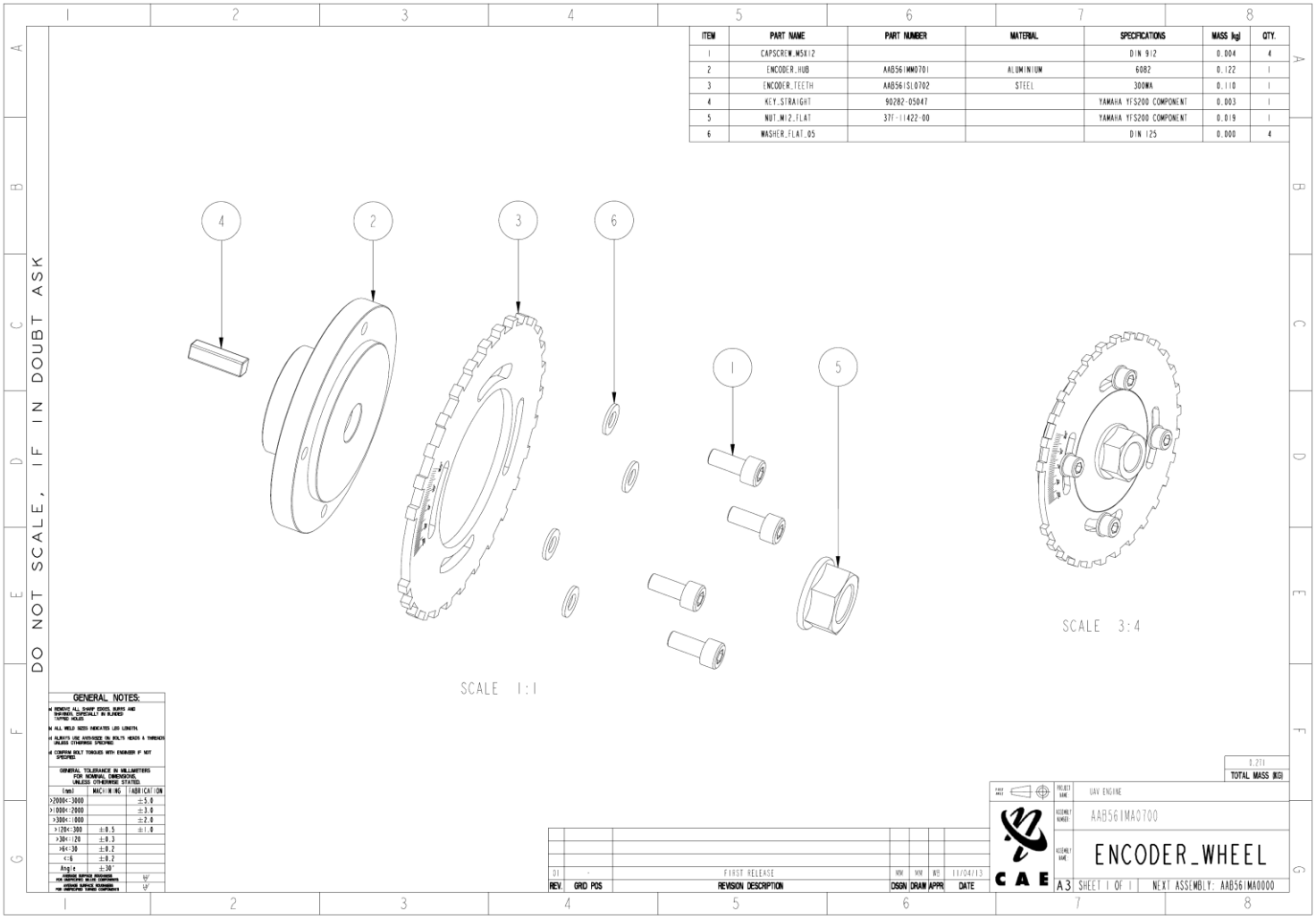

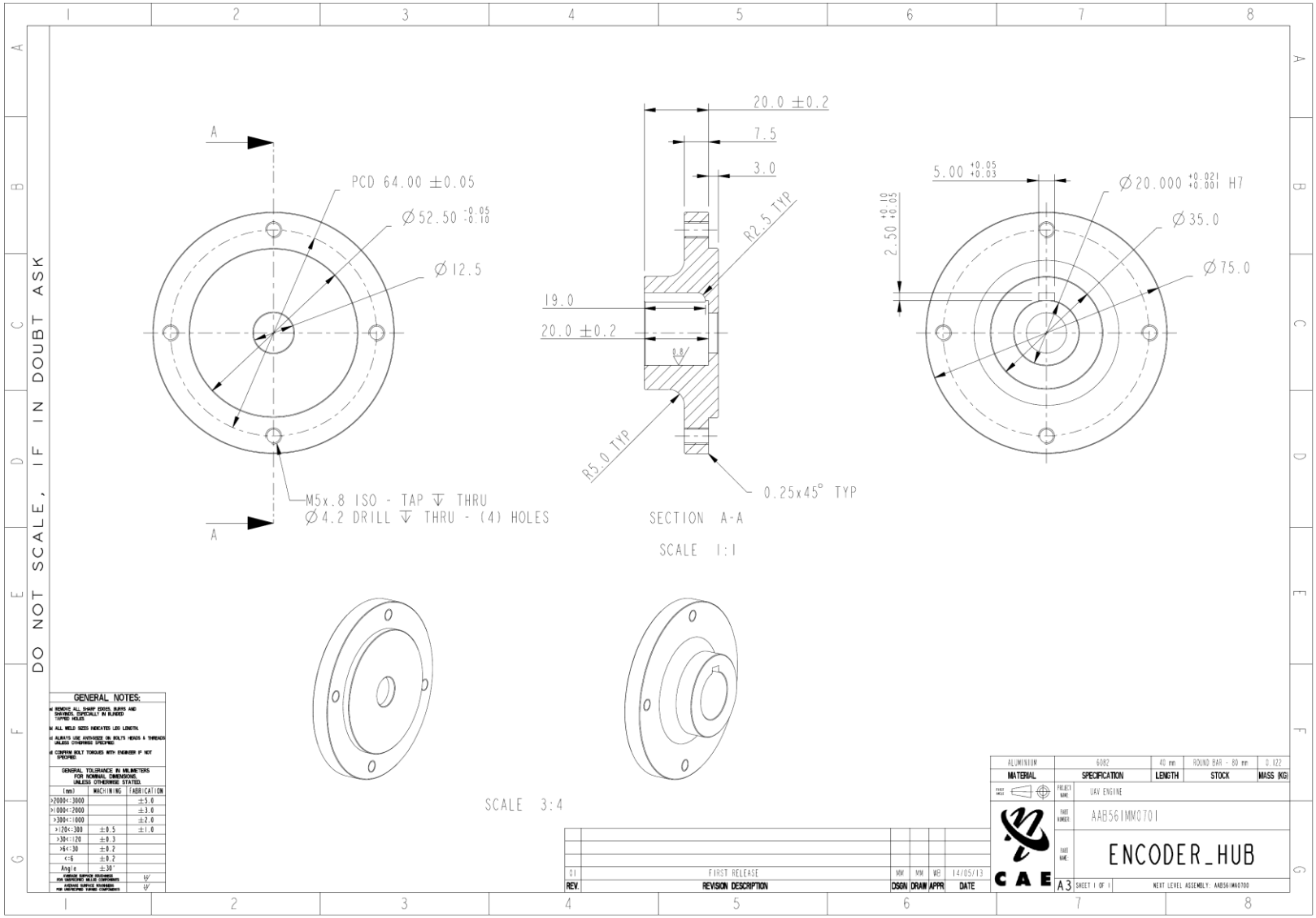
DO NOT SCALE, IF IN DOUBT ASK
PCD 64.00 ±0.05
Ø52.50 -0.05 -0.10
Ø12.5
M5x.8 ISO - TAP ↧ THRU
Ø4.2 DRILL ↧ THRU - (4) HOLES
20.0 ±0.2
7.5
3.0
R2.5 TYP
19.0
20.0 ±0.2
R5.0 TYP
0.25x45° TYP
SECTION A-A
SCALE 1:1
5.00 +0.05 +0.03
2.50 +0.10 +0.05
Ø20.000 +0.021 +0.001 H7
Ø35.0
Ø75.0
SCALE 3:4
GENERAL NOTES:
GENERAL TOLERANCE IN MILIMETERS FOR NOMINAL DIMENSIONS, UNLESS OTHERWISE STATED.
ALUMINIUM
6082
40 mm
ROUND BAR - 80 mm
0.122
MATERIAL
SPECIFICATION
LENGTH
STOCK
MASS (KG)
UAV ENGINE
AAB561MM0701
ENCODER_HUB
CAE
A3
01
FIRST RELEASE
14/05/13
REV.
REVISION DESCRIPTION
DSGN
DRAW
APPR
DATE

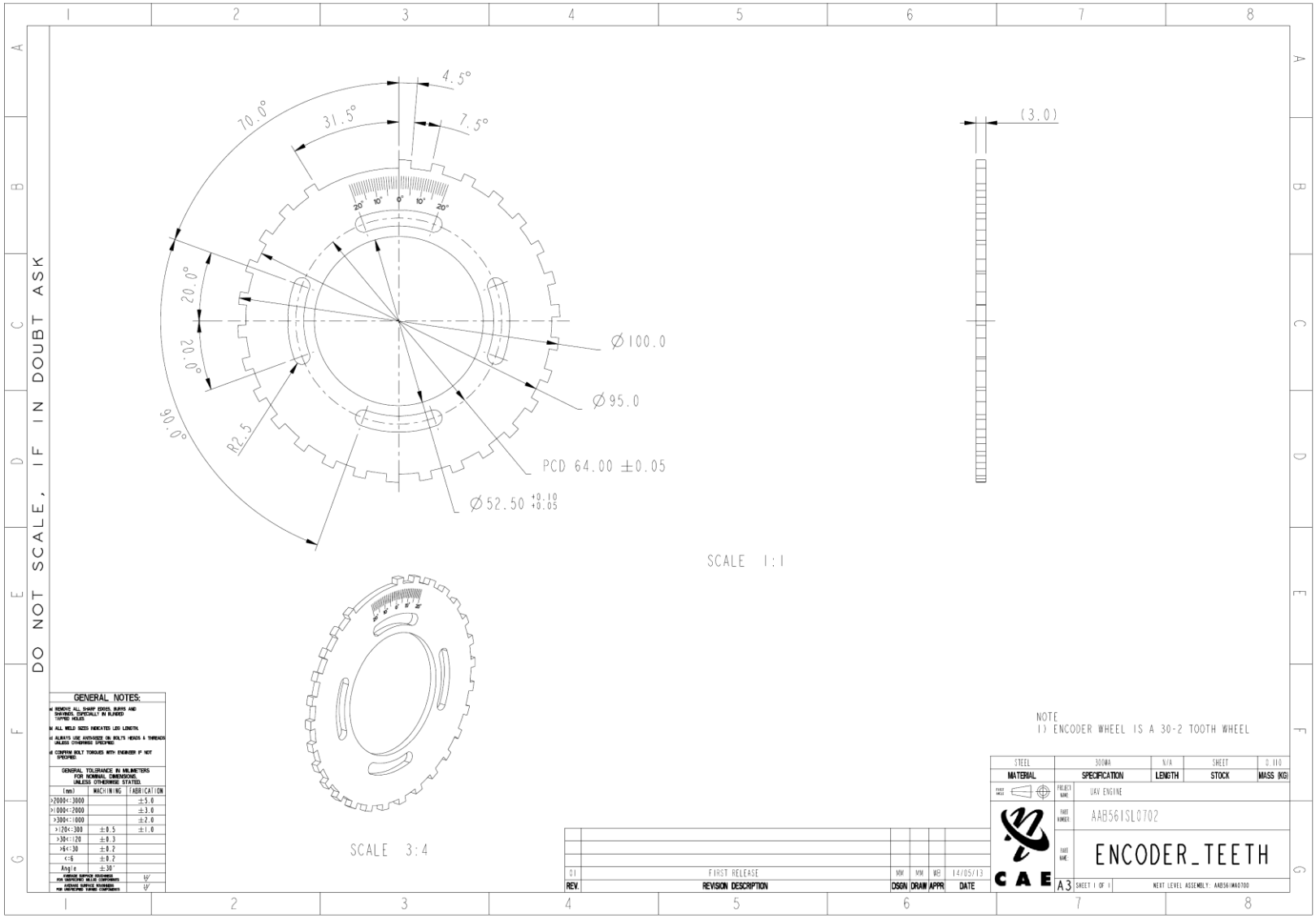
DO NOT SCALE, IF IN DOUBT ASK
4.5°
7.5°
31.5°
70.0°
20.0°
20.0°
90.0°
R2.5
Ø100.0
Ø95.0
PCD 64.00 ±0.05
Ø52.50 +0.10 +0.05
(3.0)
SCALE 1:1
SCALE 3:4
NOTE
1) ENCODER WHEEL IS A 30-2 TOOTH WHEEL
GENERAL NOTES:
GENERAL TOLERANCE IN MILIMETERS FOR NOMINAL DIMENSIONS, UNLESS OTHERWISE STATED
MACHINING
FABRICATION
STEEL
MATERIAL
300WA
SPECIFICATION
N/A
LENGTH
SHEET
STOCK
0.910
MASS (KG)
UAV ENGINE
AAB561SL0702
ENCODER_TEETH
CAE
A3
FIRST RELEASE
REVISION DESCRIPTION
MM
DSGN
MK
DRAW
WB
APPR
14/05/13
DATE

F.10 EXHAUST ASSEMBLY

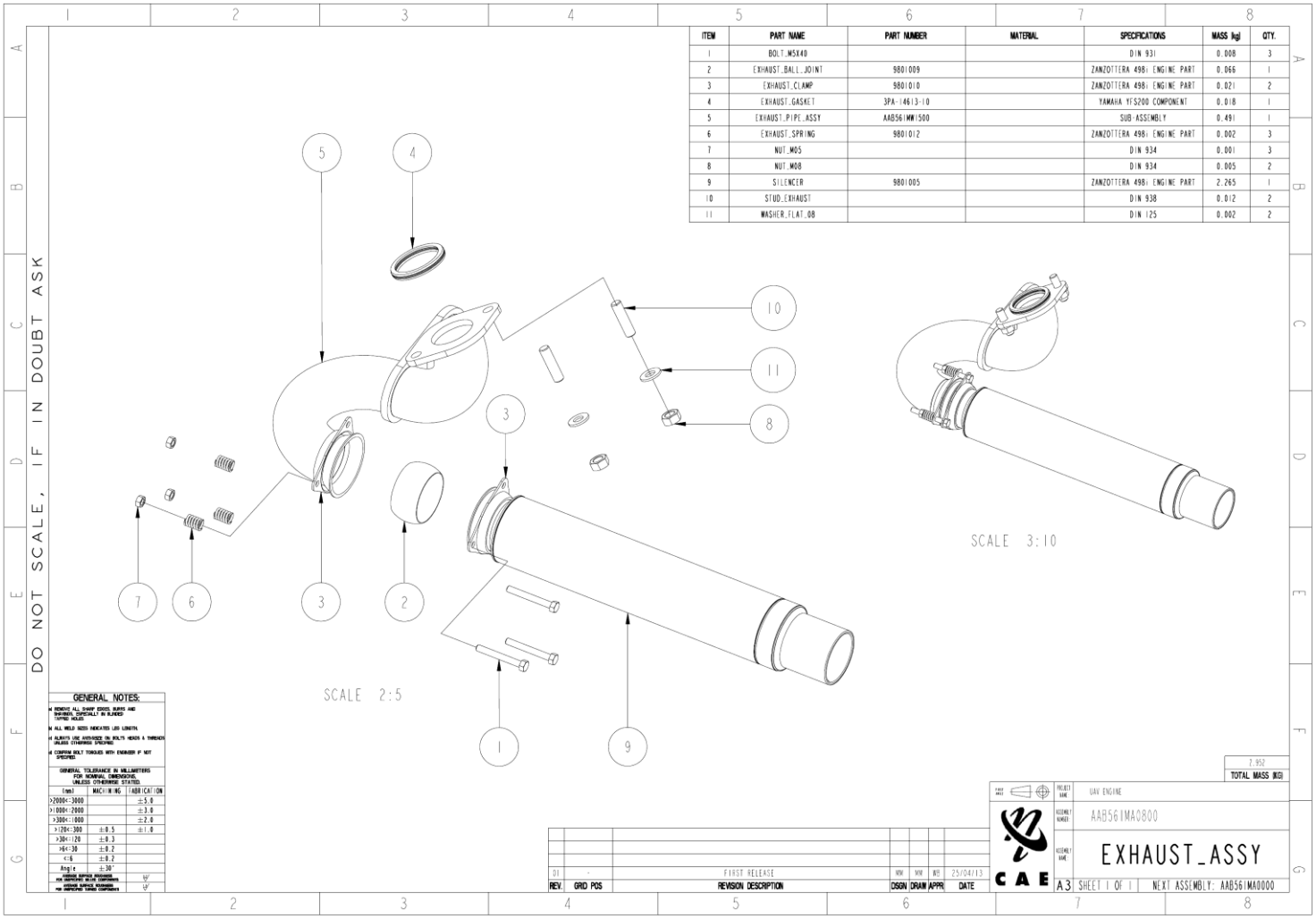

ITEM	PART NAME	PART NUMBER	MATERIAL	SPECIFICATIONS	MASS (kg)	QTY.
1	BOLT_M5X40			DIN 931	0.008	3
2	EXHAUST_BALL_JOINT	9801009		ZANZOTTERA 498i ENGINE PART	0.066	1
3	EXHAUST_CLAMP	9801010		ZANZOTTERA 498i ENGINE PART	0.021	2
4	EXHAUST_GASKET	3PA-14613-10		YAMAHA YFS200 COMPONENT	0.018	1
5	EXHAUST_PIPE_ASSY	AAB561MW1500		SUB-ASSEMBLY	0.491	1
6	EXHAUST_SPRING	9801012		ZANZOTTERA 498i ENGINE PART	0.002	3
7	NUT_M5			DIN 934	0.001	3
8	NUT_M8			DIN 934	0.005	2
9	SILENCER	9801005		ZANZOTTERA 498i ENGINE PART	2.265	1
10	STUD_EXHAUST			DIN 938	0.012	2
11	WASHER_FLAT_M8			DIN 125	0.002	2

GENERAL TOLERANCE IN MILLIMETERS FOR NOMINAL DIMENSIONS UNLESS OTHERWISE STATED		
(mm)	MACHINING	FABRICATION
>2000<:3000		±5.0
>1000<:2000		±3.0
>300<:1000		±2.0
>120<:300	±0.5	±1.0
>30<:120	±0.3	
>6<:30	±0.2	
<:6	±0.2	
Angle	±30'	

F.11 PROPELLER ASSEMBLY

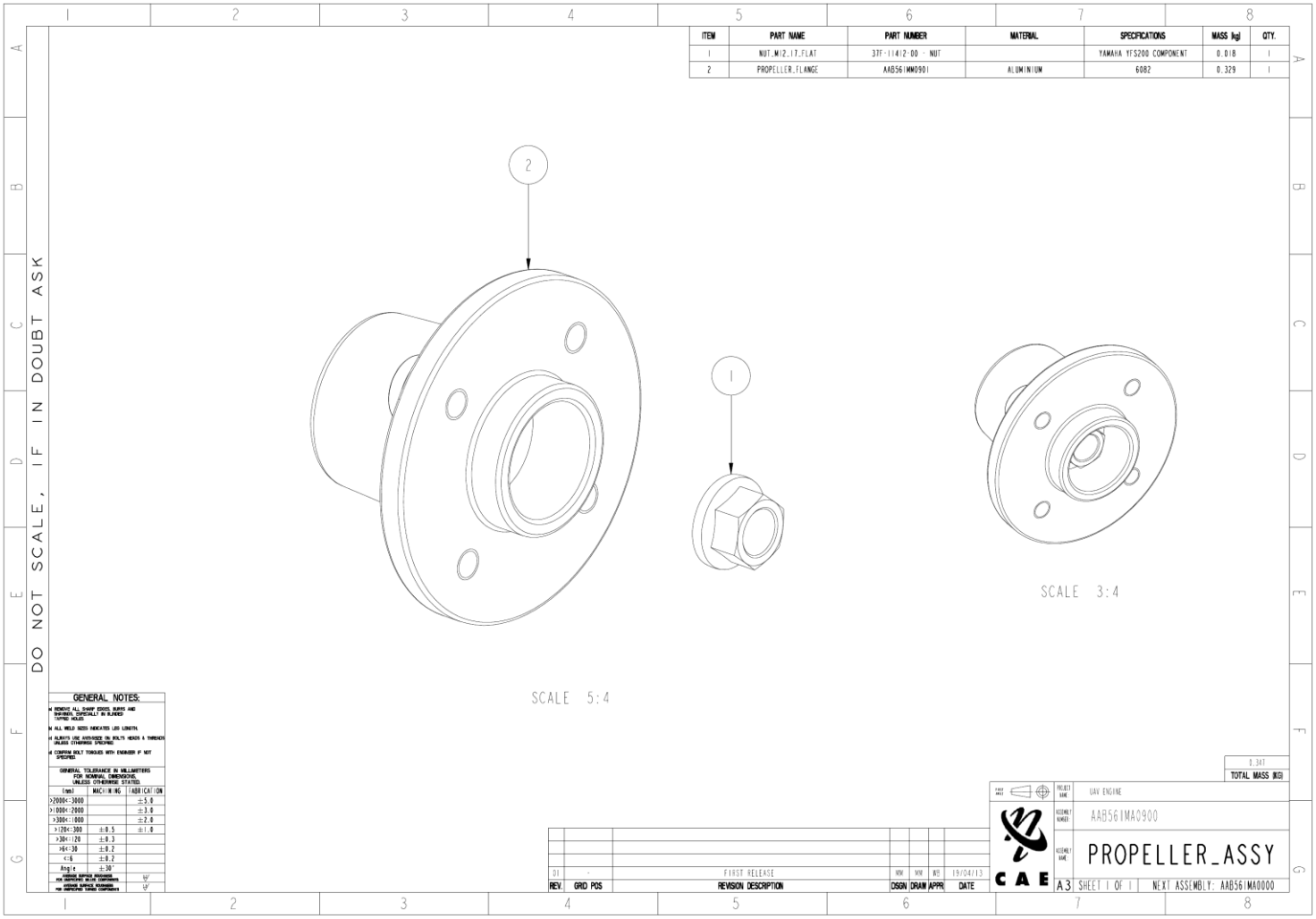

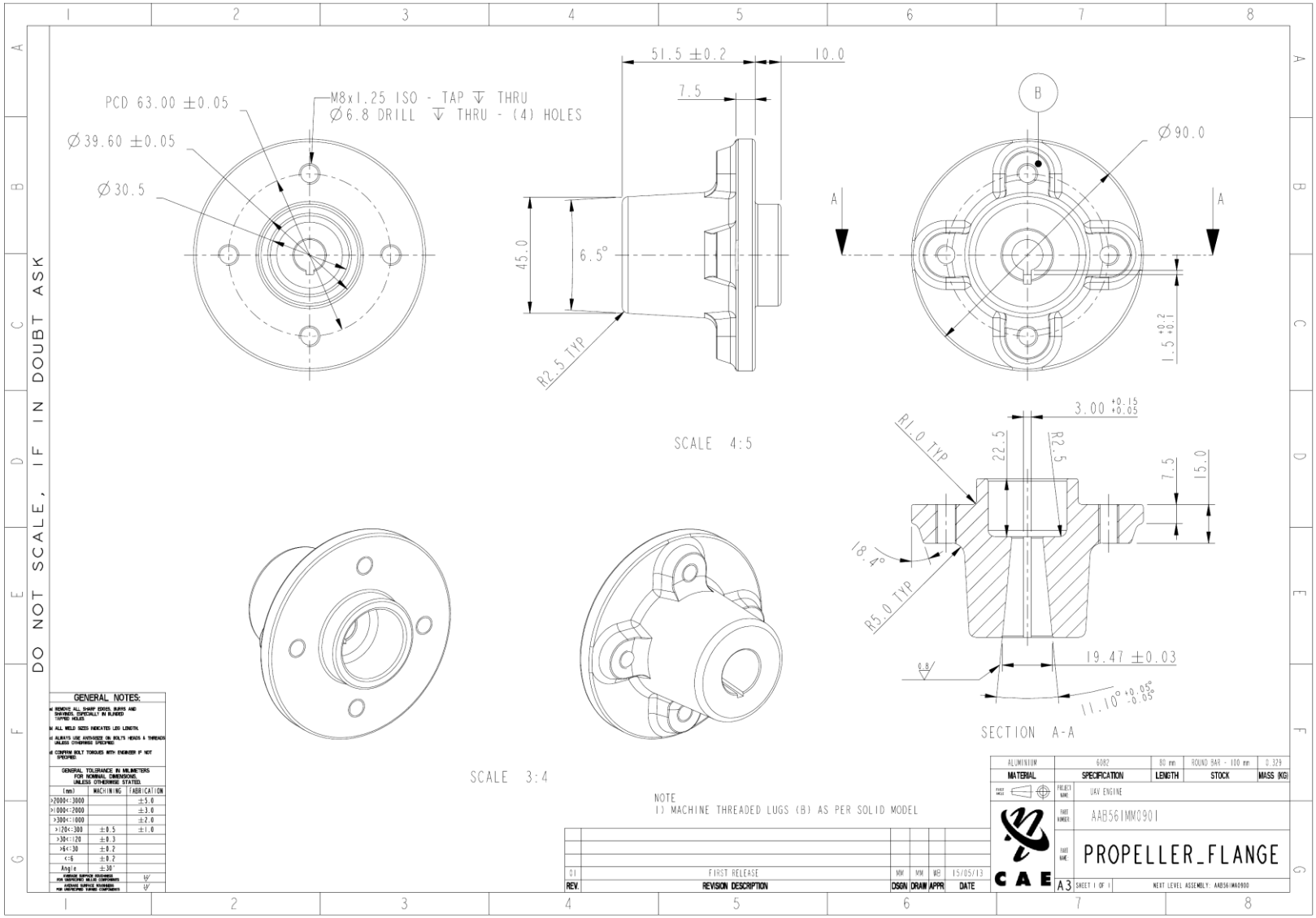
DO NOT SCALE, IF IN DOUBT ASK
PCD 63.00 ±0.05
M8x1.25 ISO - TAP ↧ THRU
Ø6.8 DRILL ↧ THRU - (4) HOLES
Ø39.60 ±0.05
Ø30.5
51.5 ±0.2
10.0
7.5
45.0
6.5°
R2.5 TYP
SCALE 4:5
B
Ø90.0
A
A
1.5 +0.2 +0.1
SCALE 3:4
R1.0 TYP
22.5
R2.5
3.00 +0.15 +0.05
7.5
15.0
18.4°
R5.0 TYP
19.47 ±0.03
11.10° +0.05° -0.05°
SECTION A-A
GENERAL NOTES:
GENERAL TOLERANCE IN MILIMETERS FOR NOMINAL DIMENSIONS, UNLESS OTHERWISE STATED
Item | MACHINING | FABRICATION
>2000<:3000 | ±5.0
>1000<:2000 | ±3.0
>300<:1000 | ±2.0
>120<:300 | ±0.5 | ±1.0
>30<:120 | ±0.3
>6<:30 | ±0.2
<:6 | ±0.2
Angle | ±30'
NOTE
1) MACHINE THREADED LUGS (B) AS PER SOLID MODEL
01 FIRST RELEASE MM MM WB 15/05/13
REV. REVISION DESCRIPTION DSGN DRAW APPR DATE
ALUMINIUM | 6082 | 80 mm | ROUND BAR - 100 mm | 0.329
MATERIAL | SPECIFICATION | LENGTH | STOCK | MASS (KG)
PROJECT NAME: UAV ENGINE
PART NUMBER: AAB561MM0901
PART NAME: PROPELLER_FLANGE
CAE
A3 SHEET 1 OF 1
NEXT LEVEL ASSEMBLY: AAB561MA0900

F.12 REED VALVE ASSEMBLY

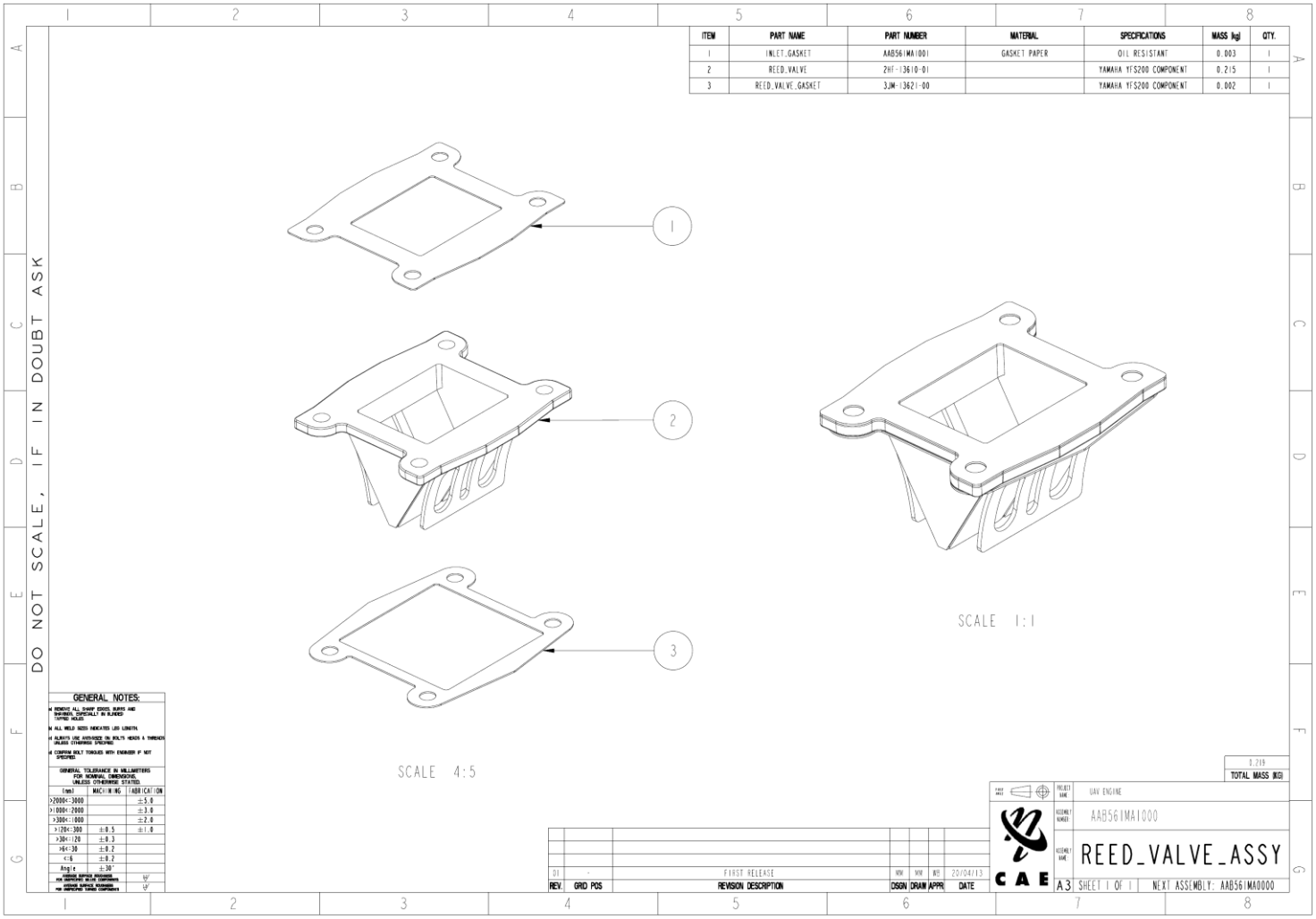

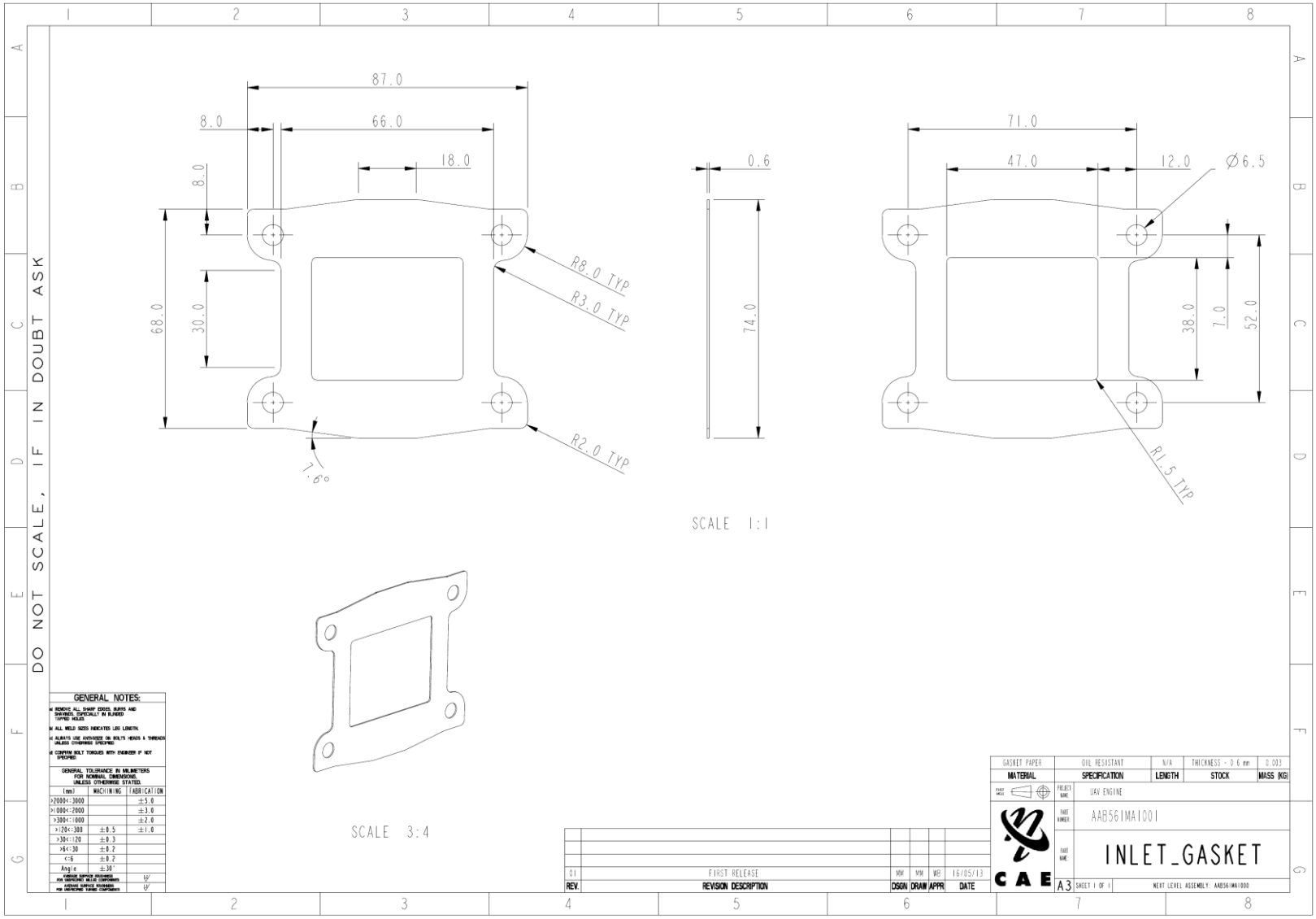
87.0
8.0
66.0
18.0
8.0
68.0
30.0
R8.0 TYP
R3.0 TYP
R2.0 TYP
7.6°
0.6
74.0
71.0
47.0
12.0
Ø6.5
38.0
7.0
52.0
R1.5 TYP
SCALE 1:1
SCALE 3:4
DO NOT SCALE, IF IN DOUBT ASK
GENERAL NOTES:
GENERAL TOLERANCE IN MILIMETERS FOR NOMINAL DIMENSIONS, UNLESS OTHERWISE STATED.
GASKET PAPER
OIL RESISTANT
N/A
THICKNESS - 0.6 mm
0.003
MATERIAL
SPECIFICATION
LENGTH
STOCK
MASS (KG)
UAV ENGINE
AAB561MA1001
INLET_GASKET
A3
01
FIRST RELEASE
16/05/13
REVISION DESCRIPTION
DATE

F.13 INLET MANIFOLD ASSEMBLY

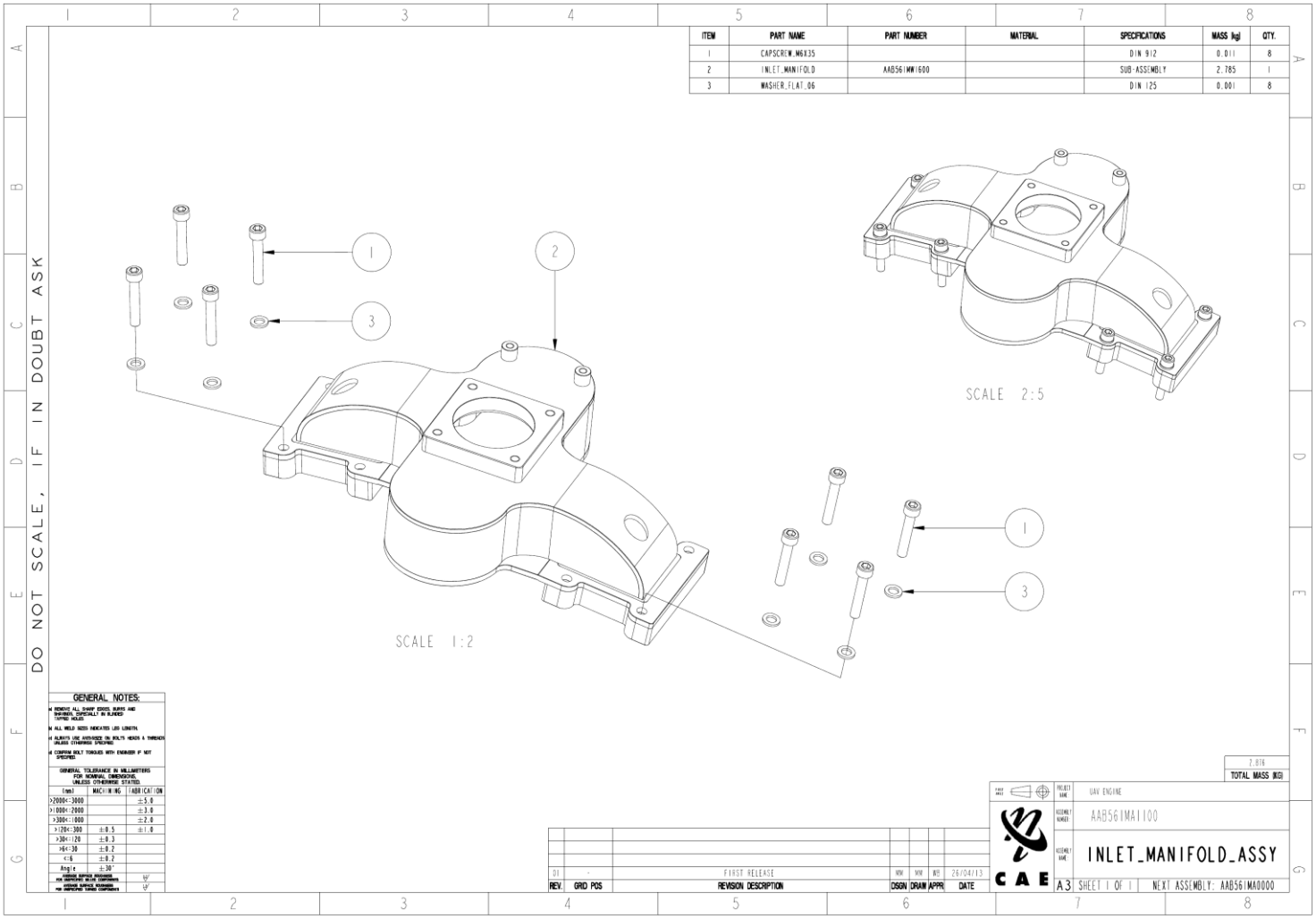

F.14 THROTTLE BODY ASSEMBLY

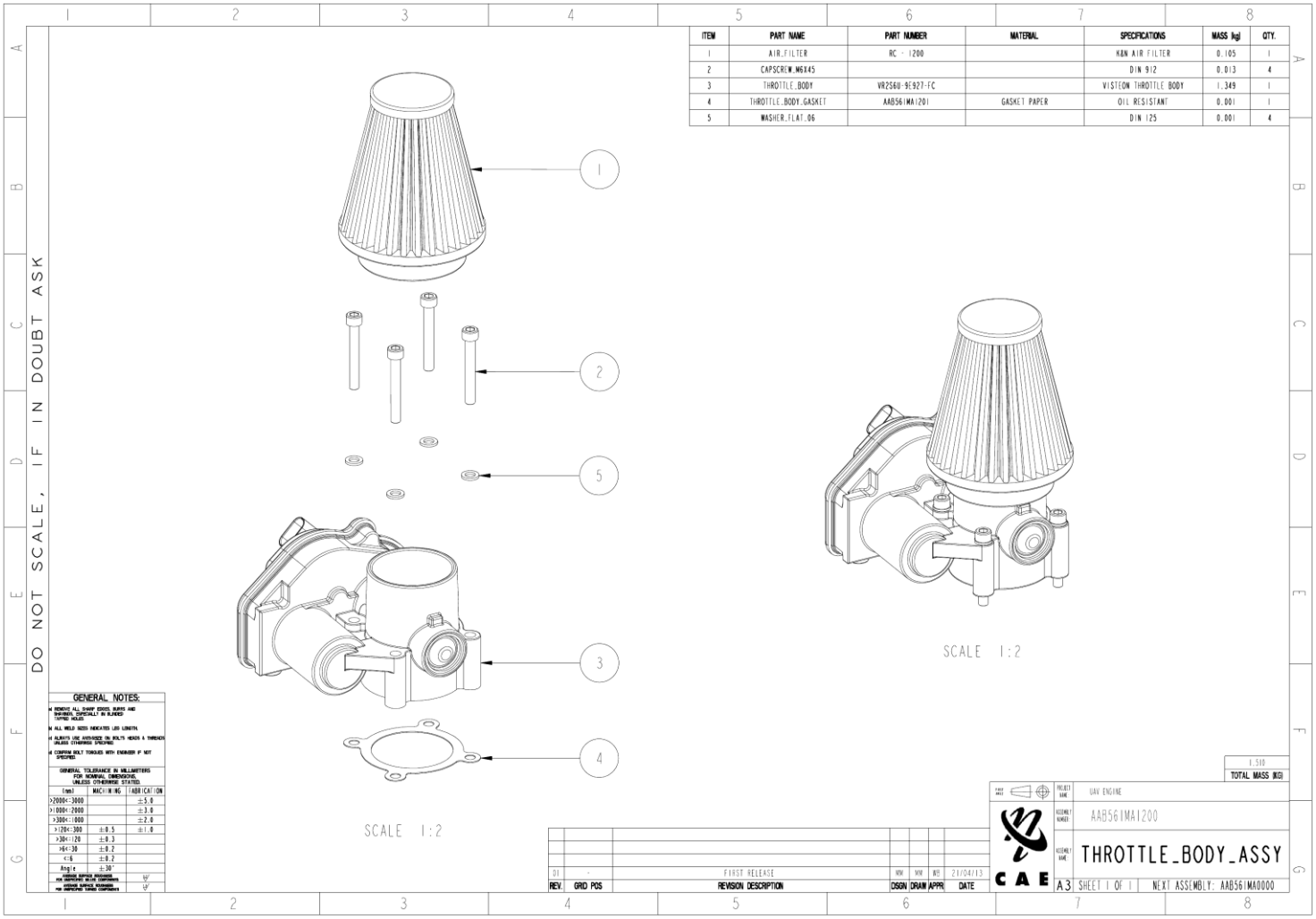

ITEM	PART NAME	PART NUMBER	MATERIAL	SPECIFICATIONS	MASS (kg)	QTY.
1	AIR_FILTER	RC - 1200		K&N AIR FILTER	0.105	1
2	CAPSCREW_M6X45			DIN 912	0.013	4
3	THROTTLE_BODY	VR2560-9E927-FC		VISTEON THROTTLE BODY	1.349	1
4	THROTTLE_BODY_GASKET	AAB561MA1201	GASKET PAPER	OIL RESISTANT	0.001	1
5	WASHER_FLAT_06			DIN 125	0.001	4

(mm)	MACHINING	FABRICATION
>2000<:3000		±5.0
>1000<:2000		±3.0
>300<:1000		±2.0
>120<:300	±0.5	±1.0
>30<:120	±0.3	
>6<:30	±0.2	
<:6	±0.2	
Angle	±30'	

REV.	GRID POS	REVISION DESCRIPTION	DSGN	DRAW	APPR.	DATE
01	-	FIRST RELEASE	MM	MM	MS	21/04/13

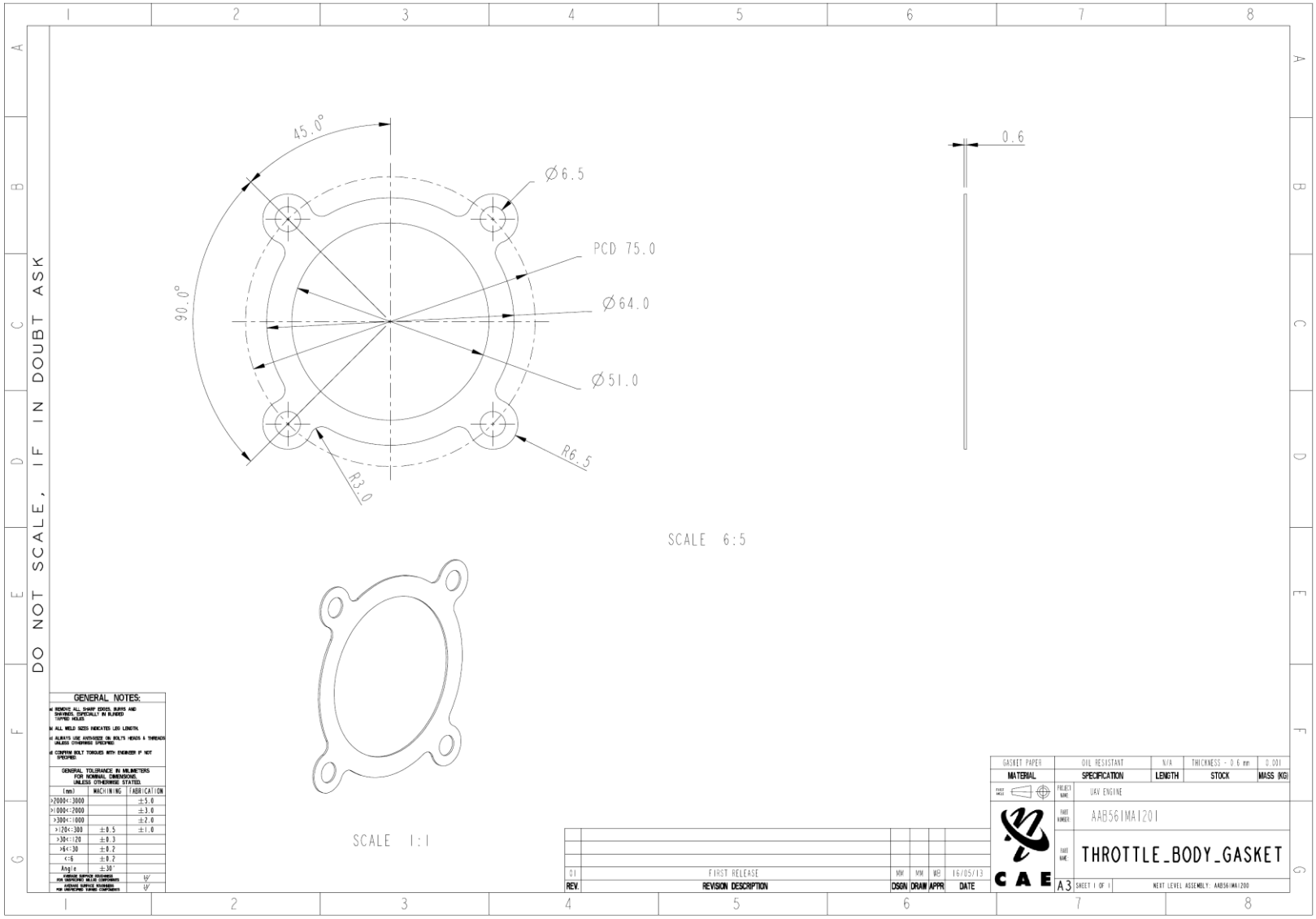
45.0°
90.0°
Ø6.5
PCD 75.0
Ø64.0
Ø51.0
R6.5
R3.0
0.6
SCALE 6:5
SCALE 1:1
DO NOT SCALE, IF IN DOUBT ASK
GENERAL NOTES:
GENERAL TOLERANCE IN MILIMETERS FOR NOMINAL DIMENSIONS, UNLESS OTHERWISE STATED.
MACHINING
FABRICATION
GASKET PAPER
MATERIAL
OIL RESISTANT
SPECIFICATION
N/A
LENGTH
THICKNESS - 0.6 mm
STOCK
0.001
MASS (KG)
UAV ENGINE
AAB561MA1201
THROTTLE_BODY_GASKET
A3
NEXT LEVEL ASSEMBLY: AAB561MA1200
01
FIRST RELEASE
MM
MM
WB
16/05/13
REV.
REVISION DESCRIPTION
DSGN
DRAW
APPR
DATE

F.15 INJECTOR ASSEMBLY

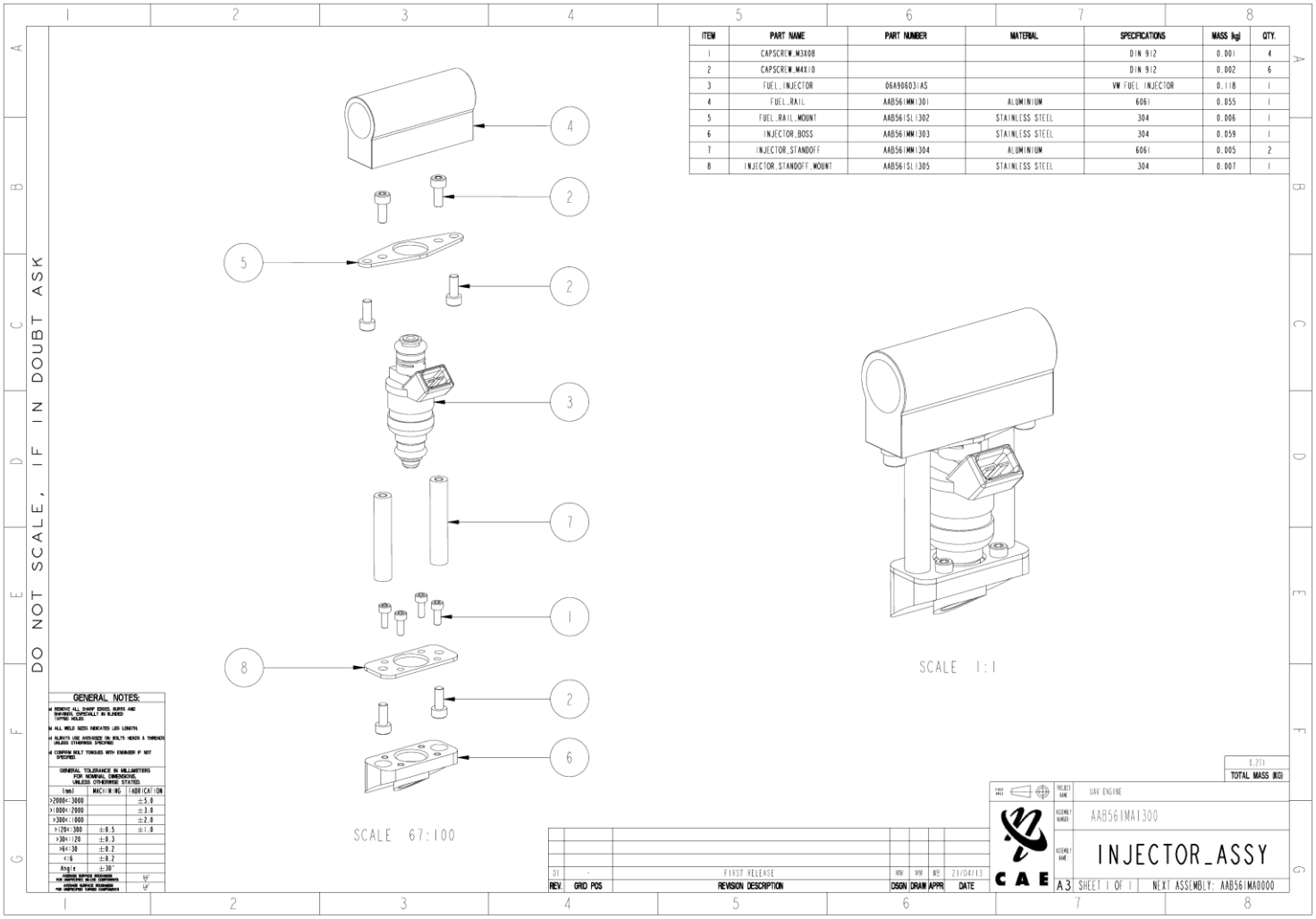

ITEM	PART NAME	PART NUMBER	MATERIAL	SPECIFICATIONS	MASS (kg)	QTY.
1	CAPSCREW_M3X08			DIN 912	0.001	4
2	CAPSCREW_M4X10			DIN 912	0.002	6
3	FUEL_INJECTOR	06A906031AS		VW FUEL INJECTOR	0.118	1
4	FUEL_RAIL	AAB561MM1301	ALUMINIUM	6061	0.055	1
5	FUEL_RAIL_MOUNT	AAB561SL1302	STAINLESS STEEL	304	0.006	1
6	INJECTOR_BOSS	AAB561MM1303	STAINLESS STEEL	304	0.059	1
7	INJECTOR_STANDOFF	AAB561MM1304	ALUMINIUM	6061	0.005	2
8	INJECTOR_STANDOFF_MOUNT	AAB561SL1305	STAINLESS STEEL	304	0.007	1

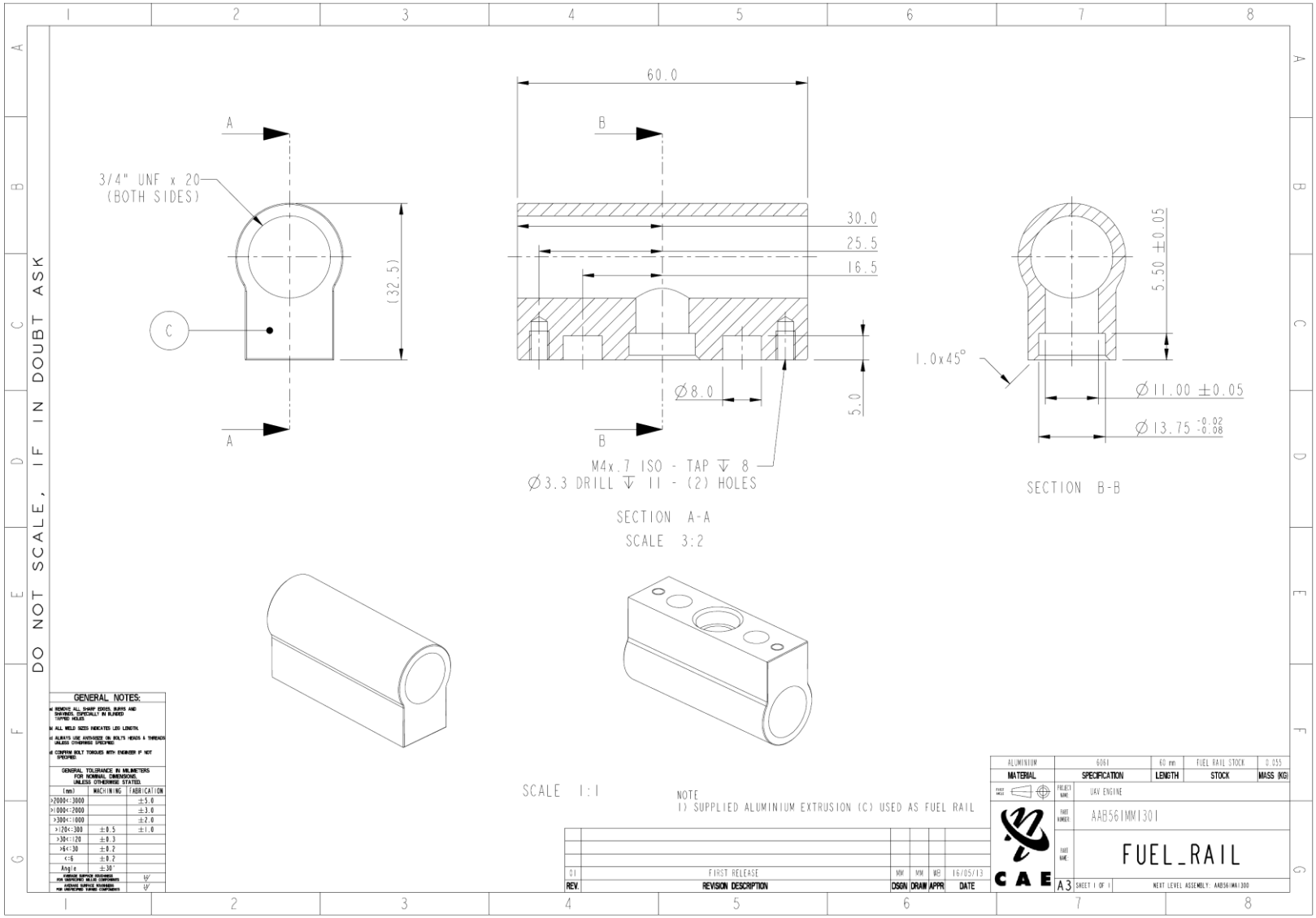
DO NOT SCALE, IF IN DOUBT ASK
3/4" UNF x 20
(BOTH SIDES)
(32.5)
60.0
30.0
25.5
16.5
5.0
Ø8.0
M4x.7 ISO - TAP ↧ 8
Ø3.3 DRILL ↧ 11 - (2) HOLES
SECTION A-A
SCALE 3:2
1.0x45°
5.50 ±0.05
Ø11.00 ±0.05
Ø13.75 -0.02 -0.08
SECTION B-B
SCALE 1:1
NOTE
1) SUPPLIED ALUMINIUM EXTRUSION (C) USED AS FUEL RAIL
GENERAL NOTES:
GENERAL TOLERANCE IN MILIMETERS FOR NOMINAL DIMENSIONS, UNLESS OTHERWISE STATED.
Item | MACHINING | FABRICATION
>2000<=3000 | ±5.0
>1000<=2000 | ±3.0
>300<=1000 | ±2.0
>120<=300 | ±0.5 | ±1.0
>30<=120 | ±0.3
>6<=30 | ±0.2
<=6 | ±0.2
Angle | ±30'
ALUMINIUM | 6061 | 60 mm | FUEL RAIL STOCK | 0.055
MATERIAL | SPECIFICATION | LENGTH | STOCK | MASS (KG)
UAV ENGINE
AAB561MM1301
FUEL_RAIL
A3
01 | FIRST RELEASE | MM | MK | WB | 16/05/13
REV. | REVISION DESCRIPTION | DSGN | DRAW | APPR | DATE

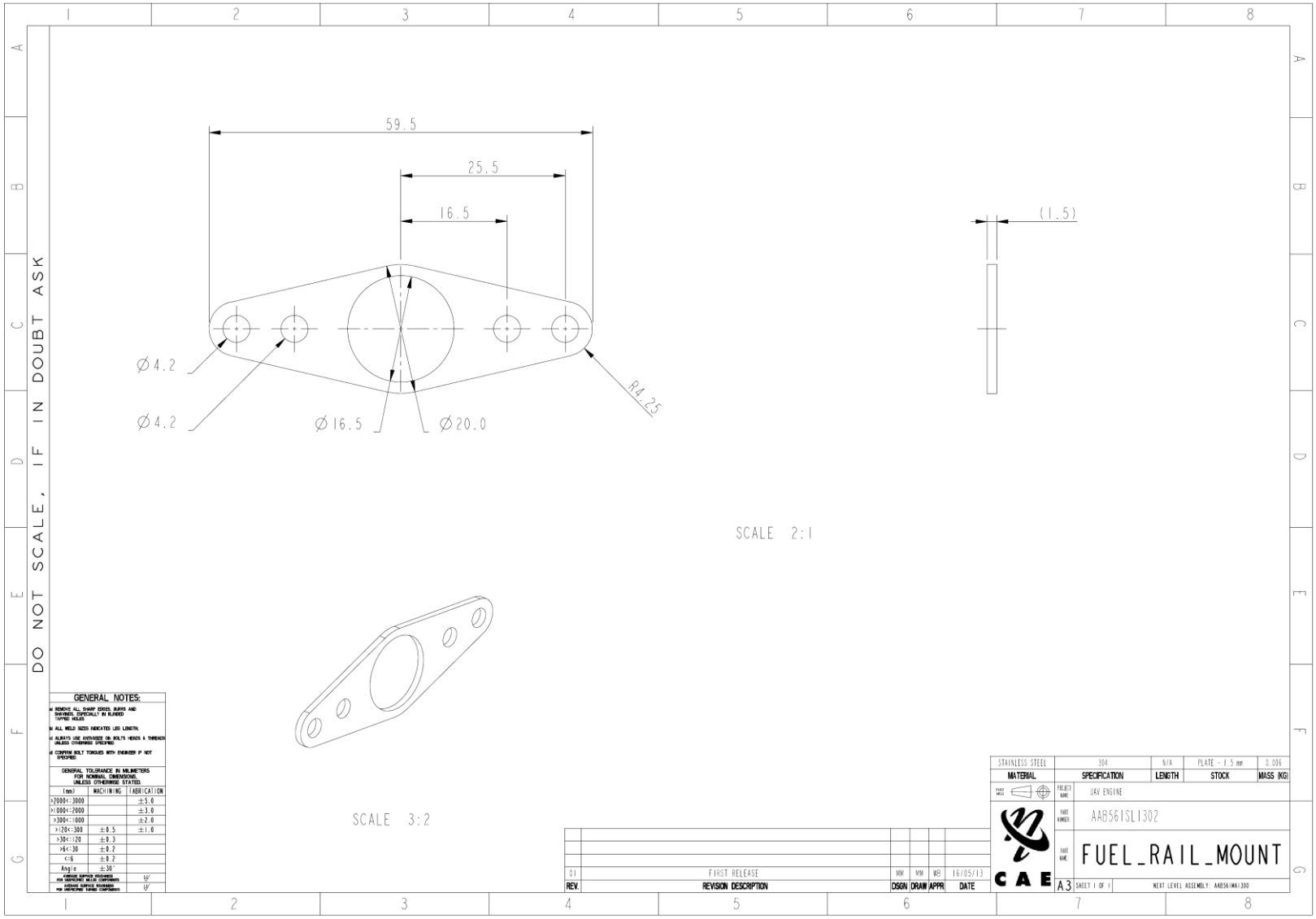
59.5
25.5
16.5
(1.5)
Ø4.2
Ø4.2
Ø16.5
Ø20.0
R4.25
SCALE 2:1
SCALE 3:2
DO NOT SCALE, IF IN DOUBT ASK
GENERAL NOTES:
GENERAL TOLERANCE IN MILIMETERS FOR NOMINAL DIMENSIONS, UNLESS OTHERWISE STATED.
[mm] | MACHINING | FABRICATION
>2000<:3000 | | ±5.0
>1000<:2000 | | ±3.0
>300<:1000 | | ±2.0
>120<:300 | ±0.5 | ±1.0
>30<:120 | ±0.3 |
>6<:30 | ±0.2 |
<:6 | ±0.2 |
Angle | ±30'
STAINLESS STEEL | 304 | N/A | PLATE - 1.5 mm | 0.006
MATERIAL | SPECIFICATION | LENGTH | STOCK | MASS (KG)
PROJECT NAME: UAV ENGINE
PART NUMBER: AAB561SL1302
PART NAME: FUEL_RAIL_MOUNT
CAE
A3 SHEET 1 OF 1
NEXT LEVEL ASSEMBLY: AAB561MA1300
01 | FIRST RELEASE | MM | MM | WB | 16/05/13
REV. | REVISION DESCRIPTION | DSGN | DRAW | APPR | DATE

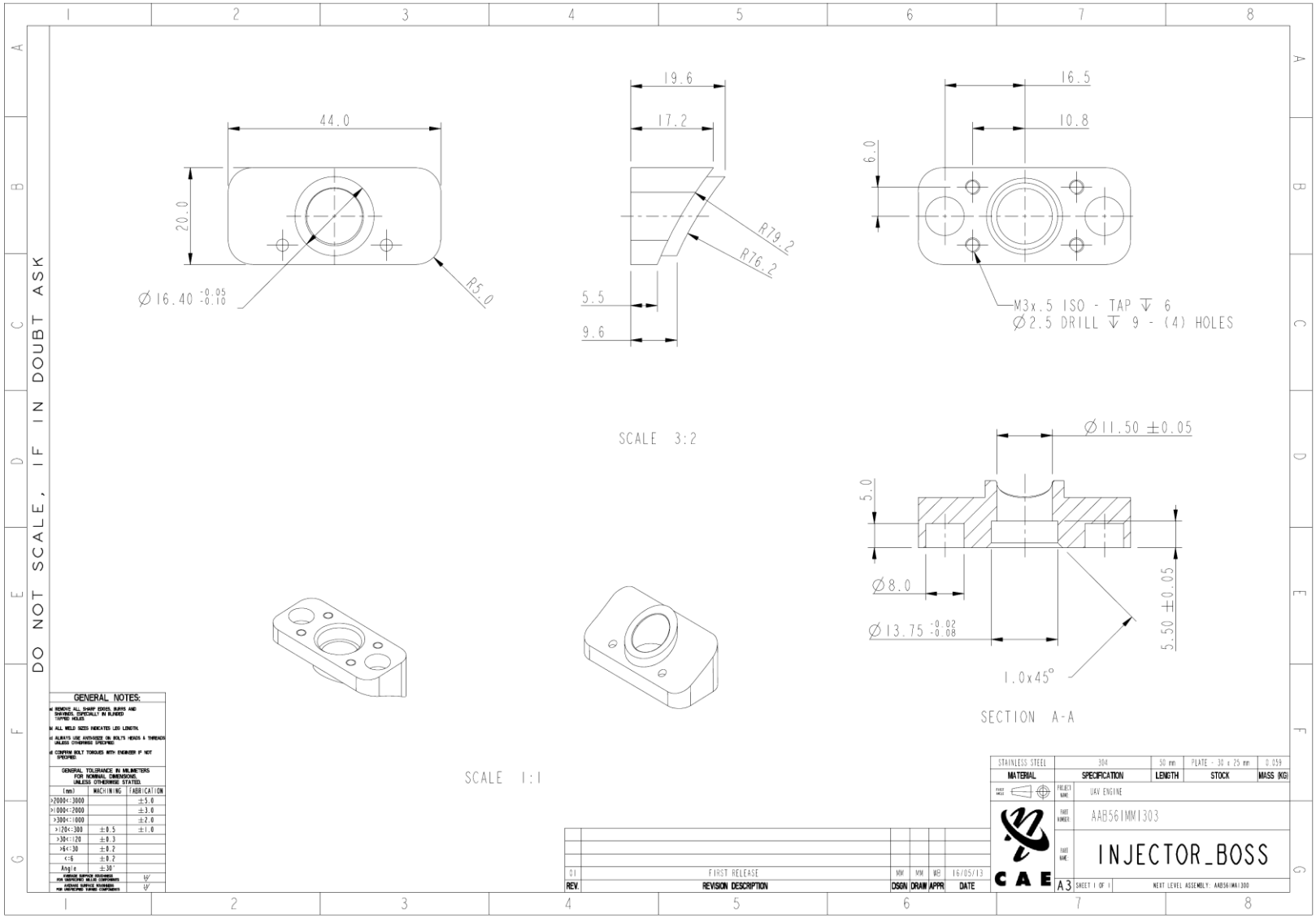
DO NOT SCALE, IF IN DOUBT ASK
44.0
20.0
Ø16.40 -0.05 -0.10
R5.0
19.6
17.2
R79.2
R76.2
5.5
9.6
16.5
10.8
6.0
M3x.5 ISO - TAP ↧ 6
Ø2.5 DRILL ↧ 9 - (4) HOLES
SCALE 3:2
Ø11.50 ±0.05
5.0
Ø8.0
Ø13.75 -0.02 -0.08
5.50 ±0.05
1.0x45°
SECTION A-A
SCALE 1:1
GENERAL NOTES:
GENERAL TOLERANCE IN MILIMETERS FOR NOMINAL DIMENSIONS, UNLESS OTHERWISE STATED
MATERIAL: STAINLESS STEEL
SPECIFICATION: 304
LENGTH: 50 mm
STOCK: PLATE - 30 x 25 mm
MASS (KG): 0.059
PROJECT NAME: UAV ENGINE
PART NUMBER: AAB561MM1303
PART NAME: INJECTOR_BOSS
A3
NEXT LEVEL ASSEMBLY: AAB561MA1300
01 FIRST RELEASE MM MM WB 16/05/13
REV. REVISION DESCRIPTION DSGN DRAW APPR DATE

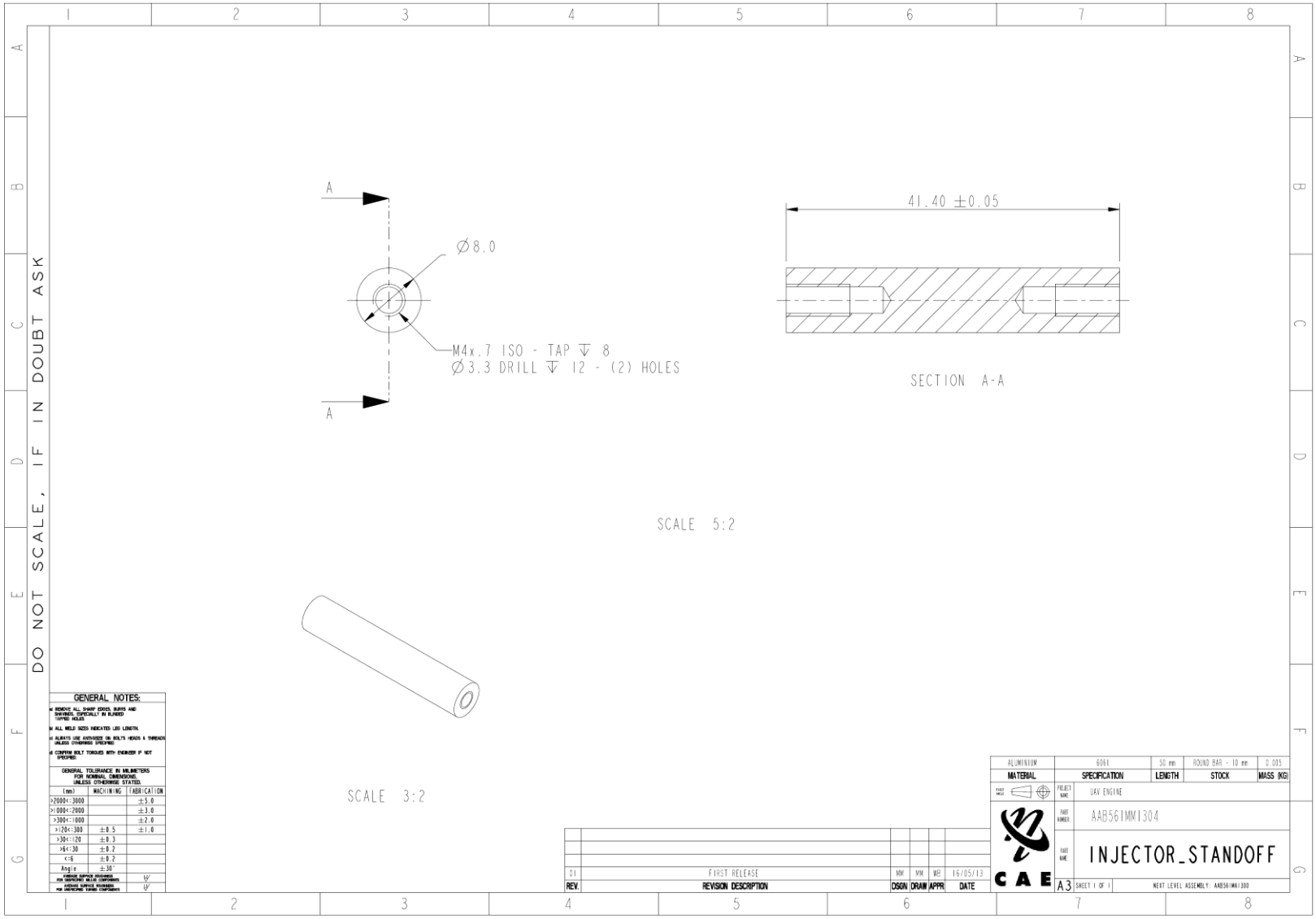
DO NOT SCALE, IF IN DOUBT ASK
A
A
Ø8.0
M4x.7 ISO - TAP ↧ 8
Ø3.3 DRILL ↧ 12 - (2) HOLES
SCALE 5:2
41.40 ±0.05
SECTION A-A
SCALE 3:2
GENERAL NOTES:
GENERAL TOLERANCE IN MILIMETERS FOR NOMINAL DIMENSIONS, UNLESS OTHERWISE STATED.
[mm] | MACHINING | FABRICATION
>2000<=3000 | ±5.0
>1000<=2000 | ±3.0
>300<=1000 | ±2.0
>120<=300 | ±0.5 | ±1.0
>30<=120 | ±0.3
>6<=30 | ±0.2
<=6 | ±0.2
Angle | ±30'
ALUMINIUM | 6061 | 50 mm | ROUND BAR - 10 mm | 0.005
MATERIAL | SPECIFICATION | LENGTH | STOCK | MASS (KG)
PROJECT NAME: UAV ENGINE
PART NUMBER: AAB561MM1304
PART NAME: INJECTOR_STANDOFF
A 3 SHEET 1 OF 1
NEXT LEVEL ASSEMBLY: AAB561MA1300
CAE
01 | FIRST RELEASE | MM | MM | WB | 16/05/13
REV. | REVISION DESCRIPTION | DSGN | DRAW | APPR | DATE

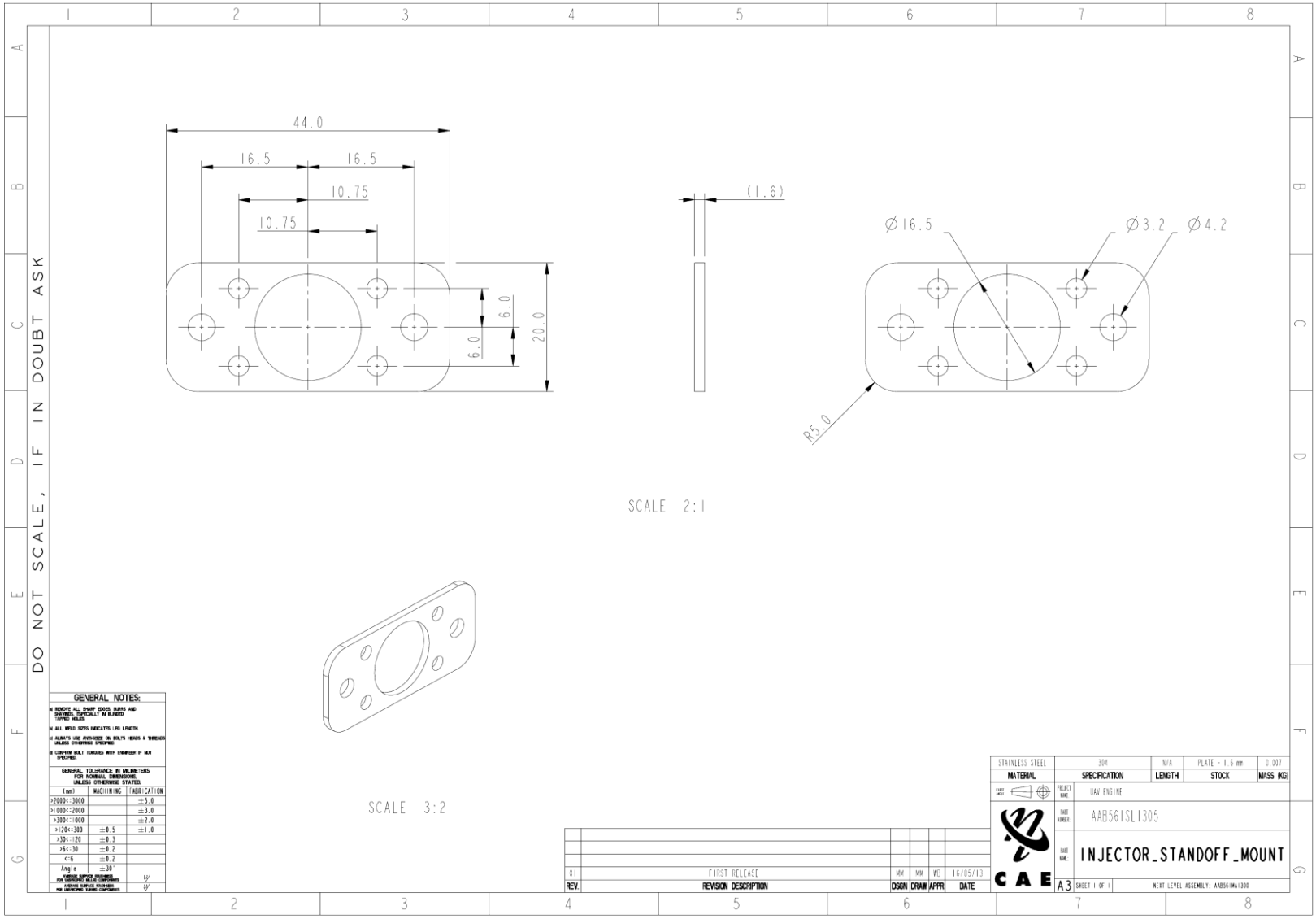
DO NOT SCALE, IF IN DOUBT ASK
44.0
16.5
16.5
10.75
10.75
6.0
6.0
20.0
(1.6)
Ø16.5
Ø3.2
Ø4.2
R5.0
SCALE 2:1
SCALE 3:2
GENERAL NOTES:
GENERAL TOLERANCE IN MILIMETERS FOR NOMINAL DIMENSIONS, UNLESS OTHERWISE STATED.
STAINLESS STEEL
304
N/A
PLATE - 1.6 mm
0.007
MATERIAL
SPECIFICATION
LENGTH
STOCK
MASS (KG)
UAV ENGINE
AAB561SL1305
INJECTOR_STANDOFF_MOUNT
A3
FIRST RELEASE
16/05/13
REVISION DESCRIPTION
DATE

F.16 DRIVESHAFT ASSEMBLY

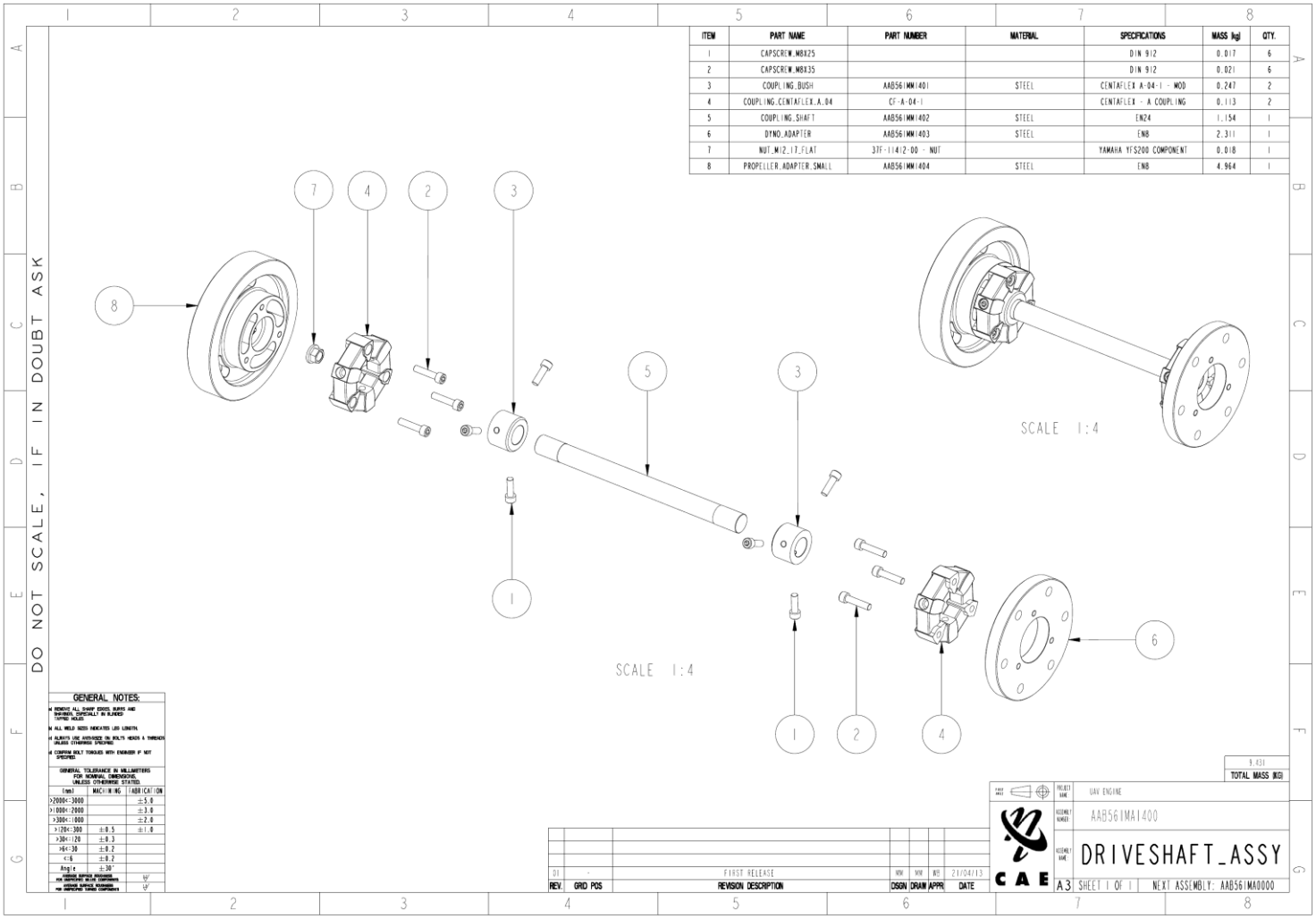

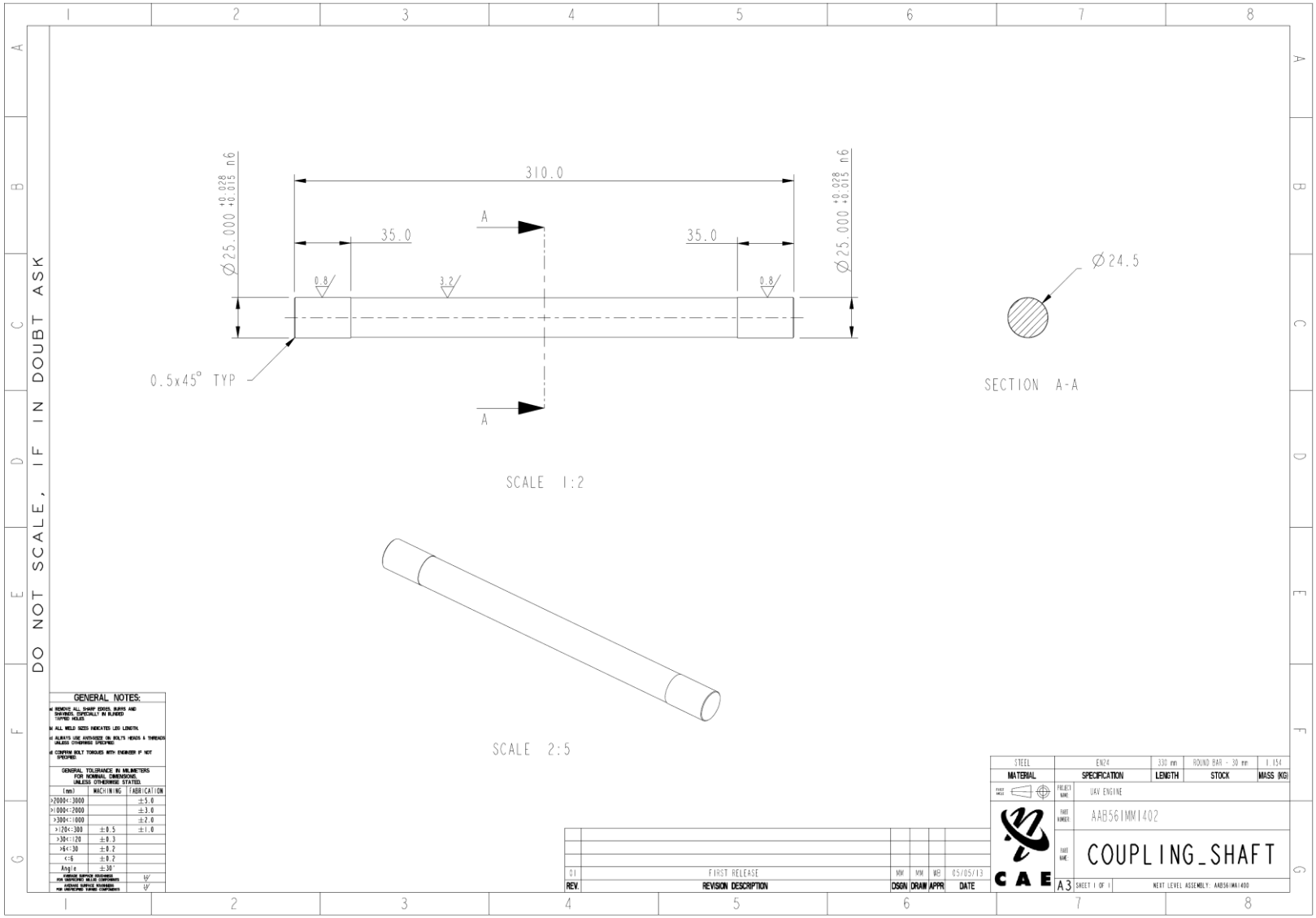
DO NOT SCALE, IF IN DOUBT ASK
310.0
35.0
35.0
Ø25.000 +0.028 +0.015 n6
Ø25.000 +0.028 +0.015 n6
0.8
3.2
0.8
A
A
0.5x45° TYP
SCALE 1:2
Ø24.5
SECTION A-A
SCALE 2:5
GENERAL NOTES:
GENERAL TOLERANCE IN MILIMETERS FOR NOMINAL DIMENSIONS, UNLESS OTHERWISE STATED
STEEL
MATERIAL
EN24
SPECIFICATION
330 mm
LENGTH
ROUND BAR - 30 mm
STOCK
1.054
MASS (KG)
UAV ENGINE
AAB561MM1402
COUPLING_SHAFT
A3
01
FIRST RELEASE
05/05/13
REVISION DESCRIPTION
DATE

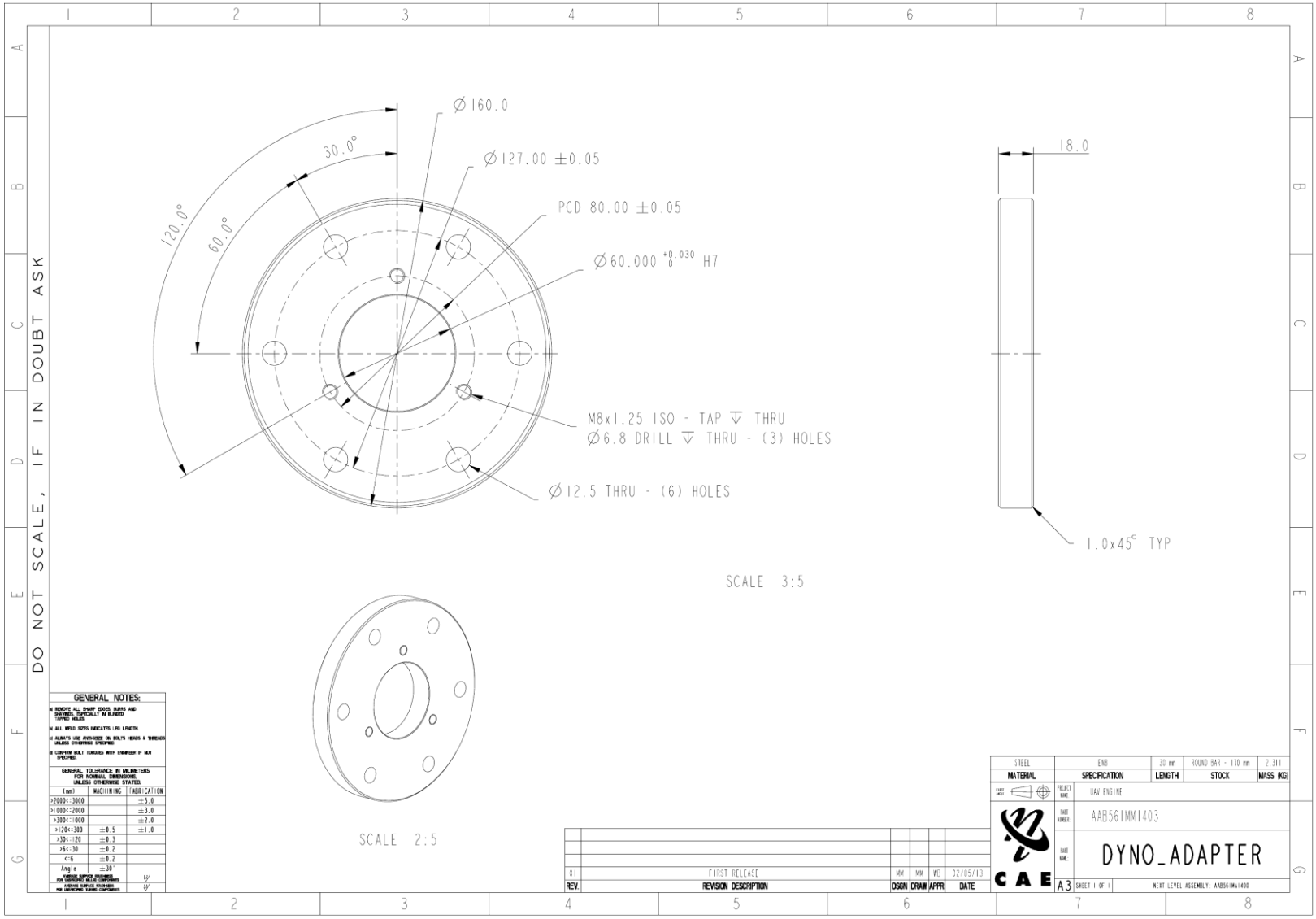
DO NOT SCALE, IF IN DOUBT ASK
Ø160.0
30.0°
120.0°
60.0°
Ø127.00 ±0.05
PCD 80.00 ±0.05
Ø60.000 +0.030 0 H7
M8x1.25 ISO - TAP ↧ THRU
Ø6.8 DRILL ↧ THRU - (3) HOLES
Ø12.5 THRU - (6) HOLES
18.0
1.0x45° TYP
SCALE 3:5
SCALE 2:5
GENERAL NOTES:
GENERAL TOLERANCE IN MILIMETERS FOR NOMINAL DIMENSIONS, UNLESS OTHERWISE STATED.
[mm]	MACHINING	FABRICATION
>2000<:3000		±5.0
>1000<:2000		±3.0
>300<:1000		±2.0
>120<:300	±0.5	±1.0
>30<:120	±0.3	
>6<:30	±0.2	
<:6	±0.2	
Angle	±30'	
01 FIRST RELEASE MM MM WB 02/05/13
REV. REVISION DESCRIPTION DSGN DRAW APPR DATE
STEEL | EN8 | 30 mm | ROUND BAR - 170 mm | 2.3kl
MATERIAL | SPECIFICATION | LENGTH | STOCK | MASS (KG)
PROJECT NAME: UAV ENGINE
PART NUMBER: AAB561MM1403
PART NAME: DYNO_ADAPTER
CAE
A3 SHEET 1 OF 1
NEXT LEVEL ASSEMBLY: AAB561MA1400

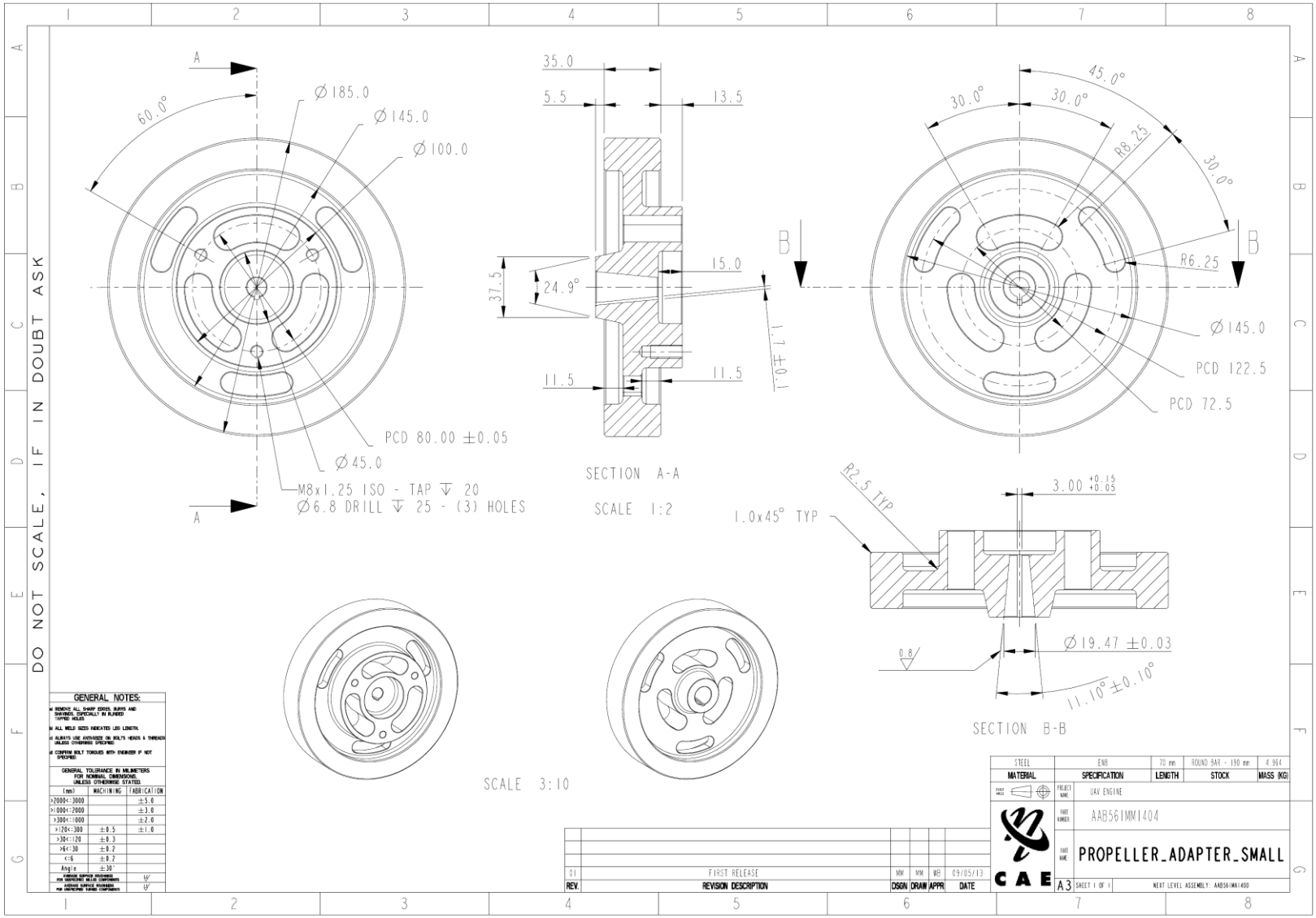
DO NOT SCALE, IF IN DOUBT ASK
Ø185.0
Ø145.0
Ø100.0
60.0°
PCD 80.00 ±0.05
Ø45.0
M8x1.25 ISO - TAP ↧ 20
Ø6.8 DRILL ↧ 25 - (3) HOLES
35.0
5.5
13.5
37.5
24.9°
15.0
11.5
11.5
1.7 ±0.1
SECTION A-A
SCALE 1:2
45.0°
30.0°
30.0°
30.0°
R8.25
R6.25
Ø145.0
PCD 122.5
PCD 72.5
R2.5 TYP
1.0x45° TYP
3.00 +0.15 +0.05
Ø19.47 ±0.03
11.10° ±0.10°
SECTION B-B
SCALE 3:10
GENERAL NOTES:
GENERAL TOLERANCE IN MILIMETERS FOR NOMINAL DIMENSIONS, UNLESS OTHERWISE STATED
STEEL
EN8
70 mm
ROUND BAR - 190 mm
4.964
MATERIAL
SPECIFICATION
LENGTH
STOCK
MASS (KG)
UAV ENGINE
AAB561MM1404
PROPELLER_ADAPTER_SMALL
CAE
A3
NEXT LEVEL ASSEMBLY: AAB561MA1400
01
FIRST RELEASE
09/05/13
REV.
REVISION DESCRIPTION
DSGN
DRAW
APPR
DATE

F.17 EXHAUST PIPE ASSEMBLY

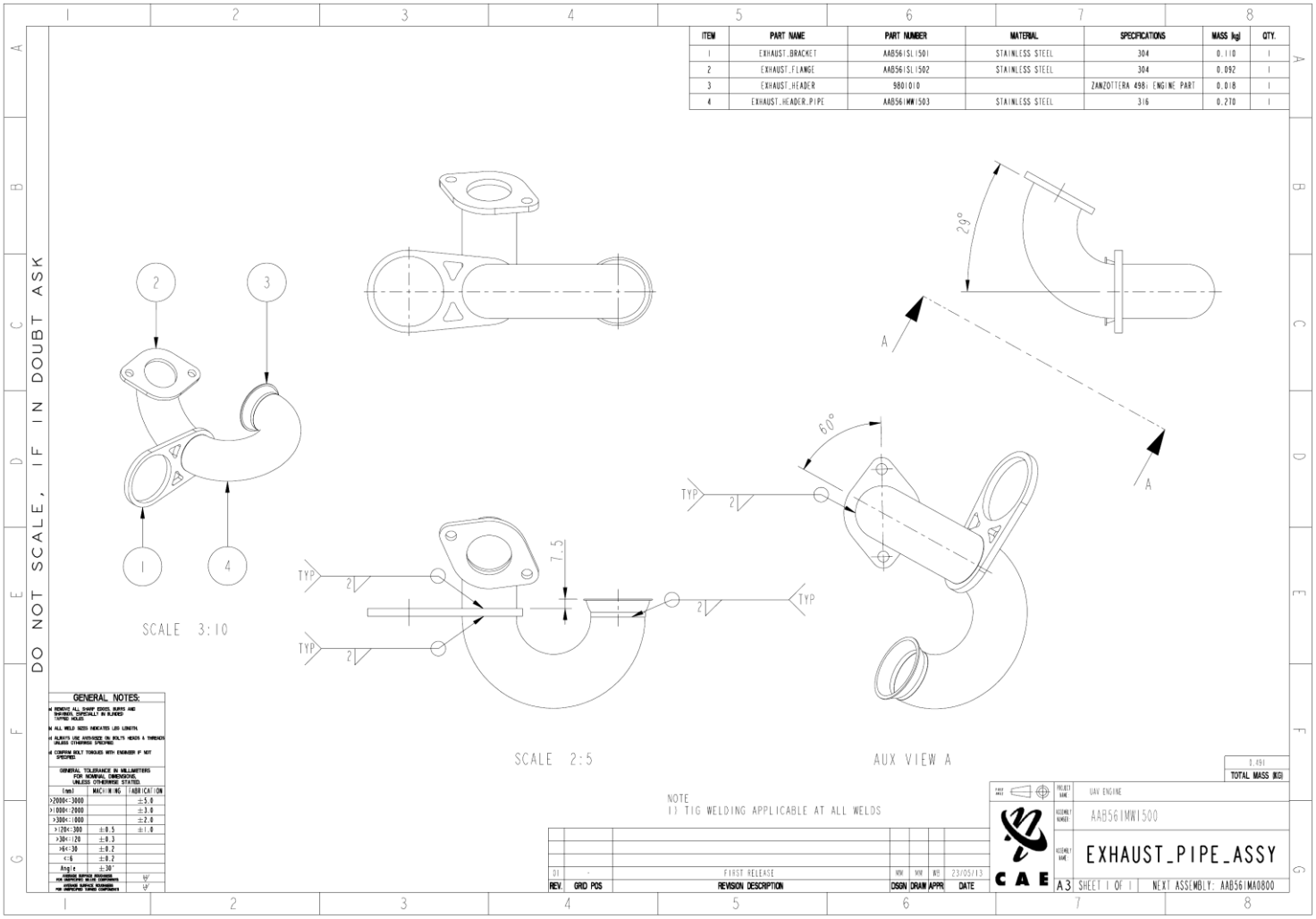

ITEM	PART NAME	PART NUMBER	MATERIAL	SPECIFICATIONS	MASS (kg)	QTY.
1	EXHAUST_BRACKET	AAB561SL1501	STAINLESS STEEL	304	0.110	1
2	EXHAUST_FLANGE	AAB561SL1502	STAINLESS STEEL	304	0.092	1
3	EXHAUST_HEADER	9801010		ZANZOTTERA 498i ENGINE PART	0.018	1
4	EXHAUST_HEADER_PIPE	AAB561MW1503	STAINLESS STEEL	316	0.270	1

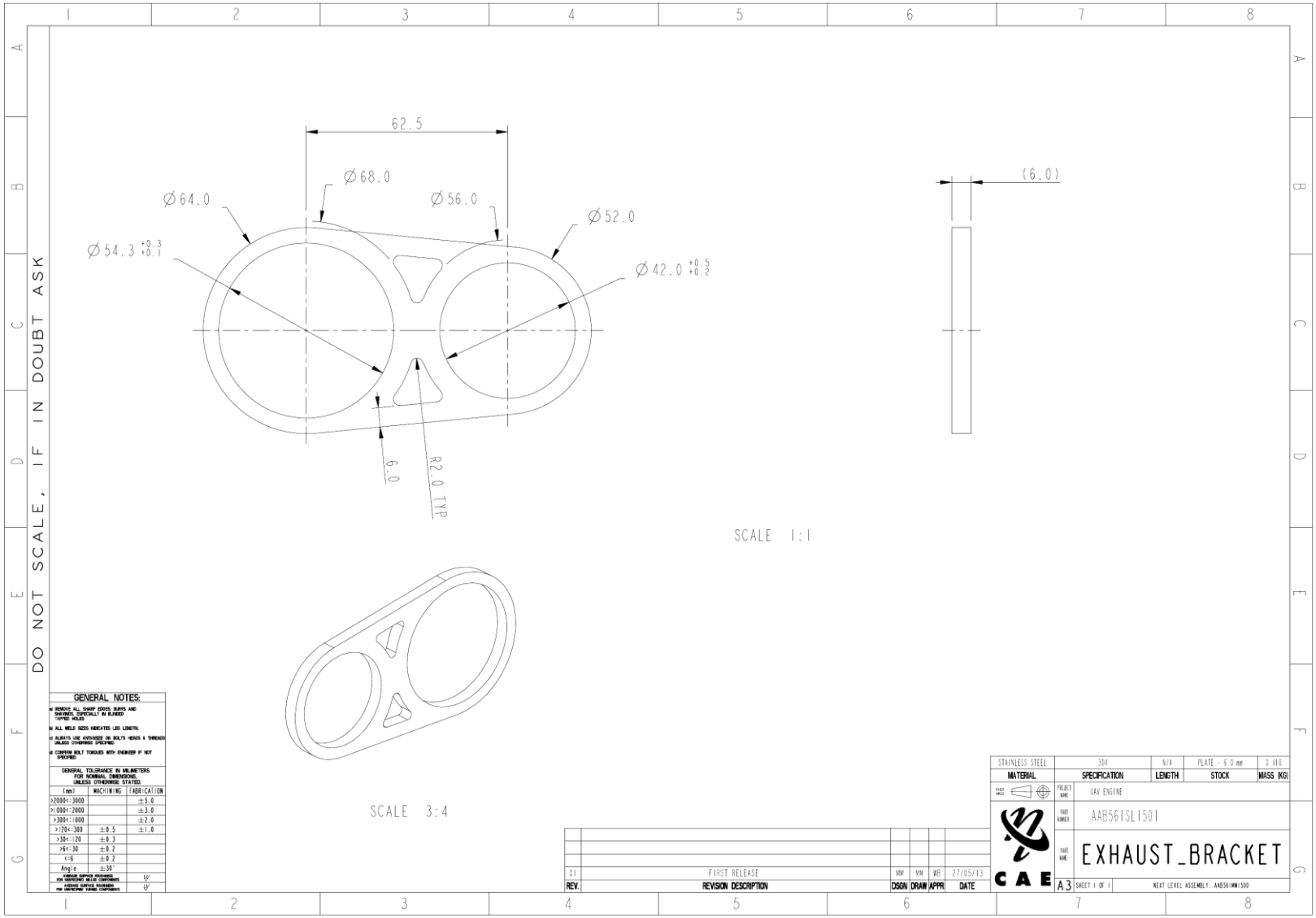
62.5
Ø68.0
Ø64.0
Ø56.0
Ø52.0
Ø54.3 +0.3 +0.1
Ø42.0 +0.5 +0.2
6.0
R2.0 TYP
(6.0)
SCALE 1:1
SCALE 3:4
DO NOT SCALE, IF IN DOUBT ASK
GENERAL NOTES:
GENERAL TOLERANCE IN MILIMETERS FOR NOMINAL DIMENSIONS, UNLESS OTHERWISE STATED.
STAINLESS STEEL
304
N/A
PLATE - 6.0 mm
0.910
MATERIAL
SPECIFICATION
LENGTH
STOCK
MASS (KG)
UAV ENGINE
AAB561SL1501
EXHAUST_BRACKET
CAE
A3
01
FIRST RELEASE
27/05/13
REV.
REVISION DESCRIPTION
DSGN
DRAW
APPR
DATE

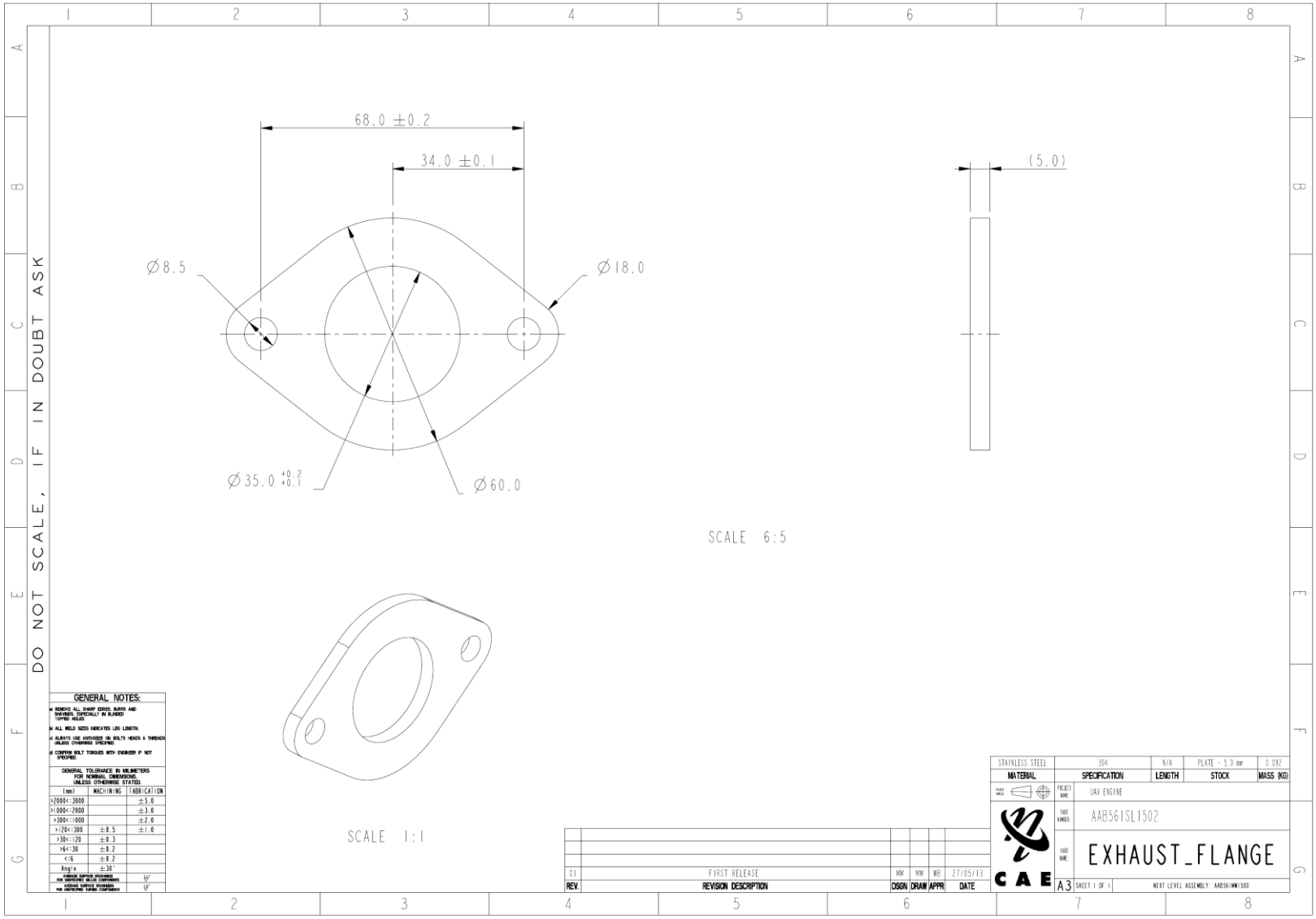
68.0 ±0.2
34.0 ±0.1
(5.0)
Ø8.5
Ø18.0
Ø35.0 +0.2 +0.1
Ø60.0
SCALE 6:5
SCALE 1:1
DO NOT SCALE, IF IN DOUBT ASK
GENERAL NOTES:
GENERAL TOLERANCE IN MILIMETERS FOR NOMINAL DIMENSIONS, UNLESS OTHERWISE STATED.
STAINLESS STEEL
304
N/A
PLATE - 5.0 mm
0.092
MATERIAL
SPECIFICATION
LENGTH
STOCK
MASS (KG)
UAV ENGINE
AAB561SL1502
EXHAUST_FLANGE
A3
FIRST RELEASE
27/05/13
REVISION DESCRIPTION
DATE

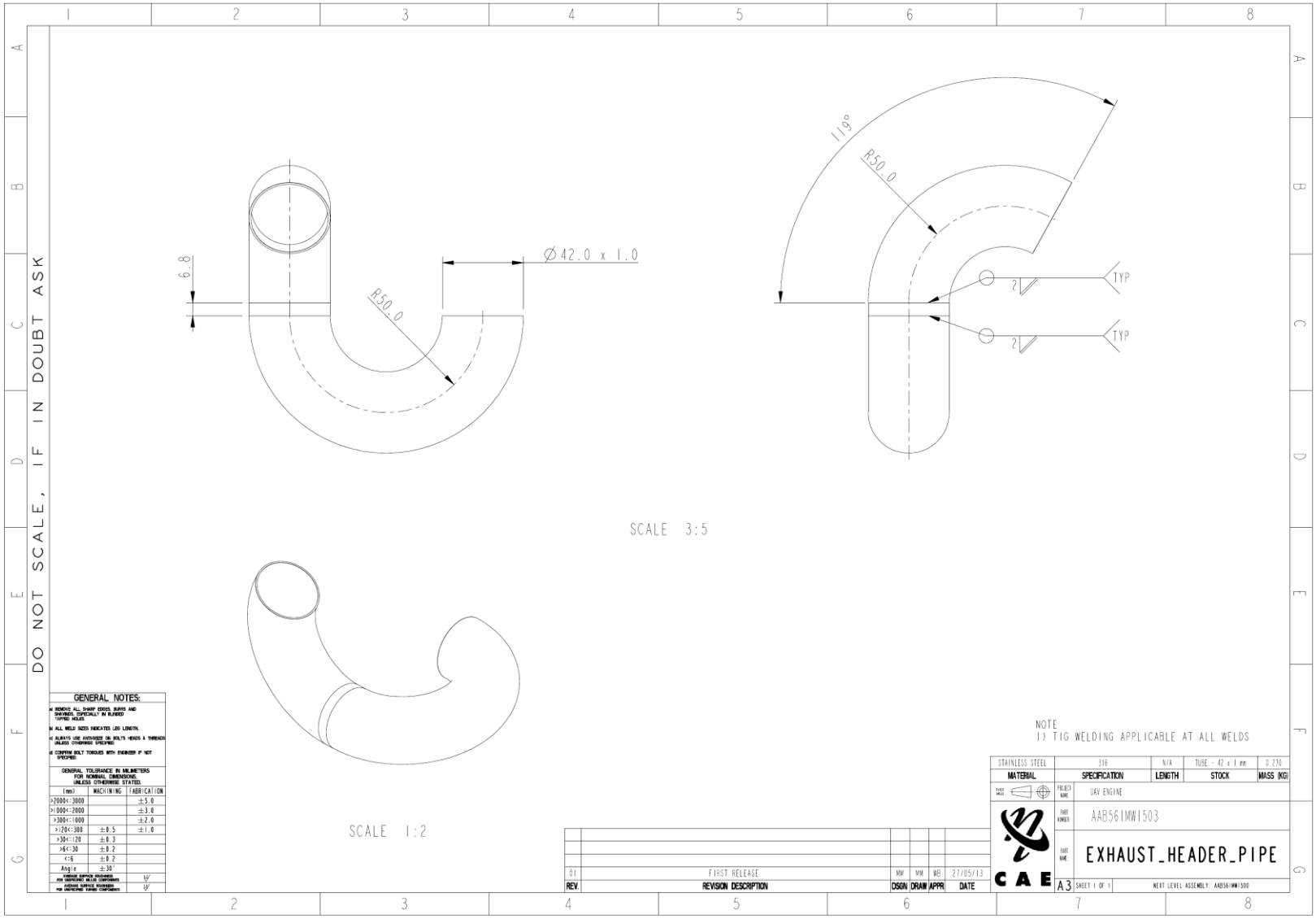
DO NOT SCALE, IF IN DOUBT ASK
6.8
Ø42.0 x 1.0
R50.0
119°
R50.0
TYP
TYP
SCALE 3:5
SCALE 1:2
NOTE
1) TIG WELDING APPLICABLE AT ALL WELDS
GENERAL NOTES:
GENERAL TOLERANCE IN MILIMETERS FOR NOMINAL DIMENSIONS, UNLESS OTHERWISE STATED.
MACHINING
FABRICATION
STAINLESS STEEL
316
N/A
TUBE - 42 x 1 mm
0.270
MATERIAL
SPECIFICATION
LENGTH
STOCK
MASS (KG)
UAV ENGINE
AAB561MW1503
EXHAUST_HEADER_PIPE
A3
01
FIRST RELEASE
27/05/13
REVISION DESCRIPTION
DATE

F.18 INLET MANIFOLD

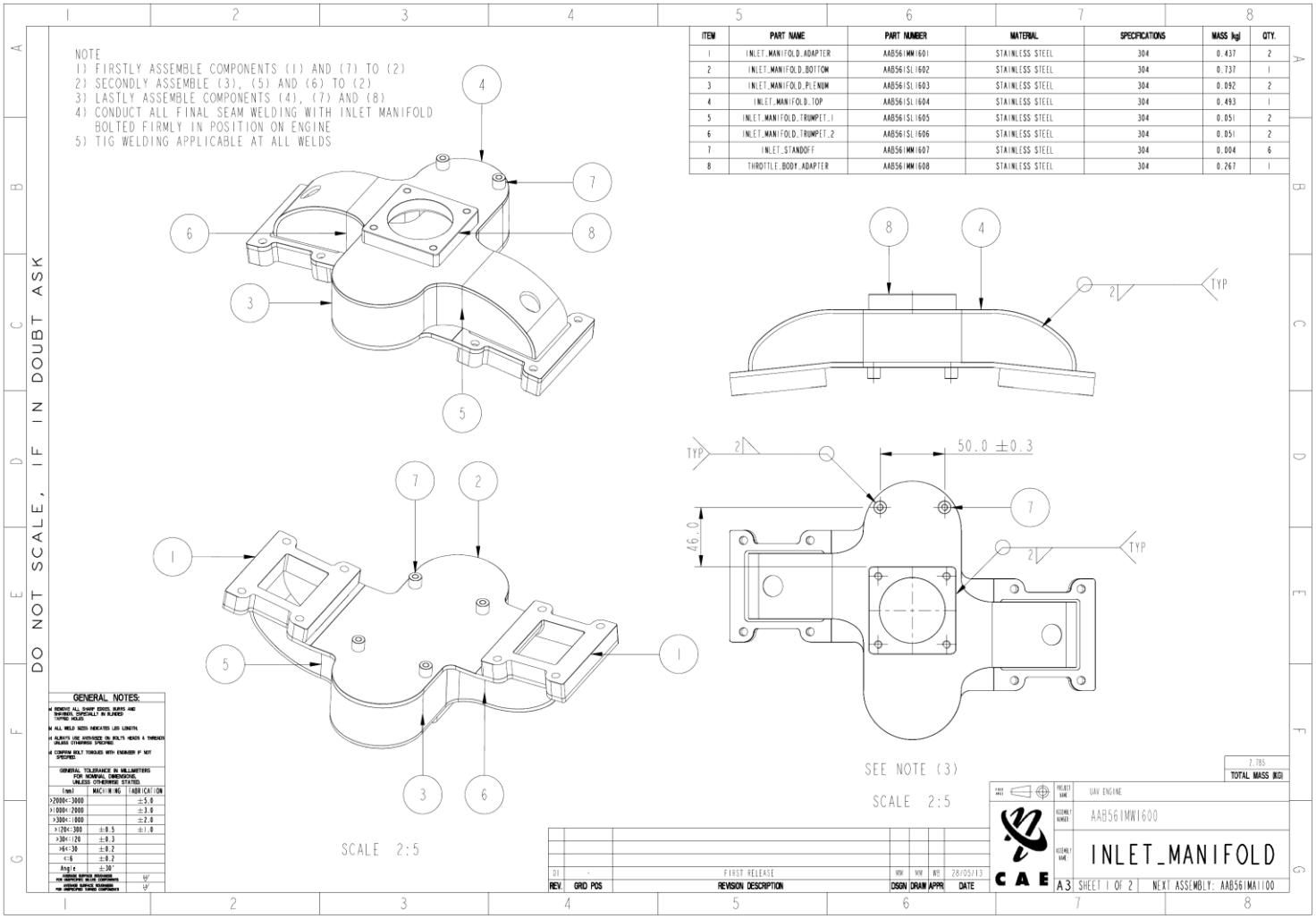

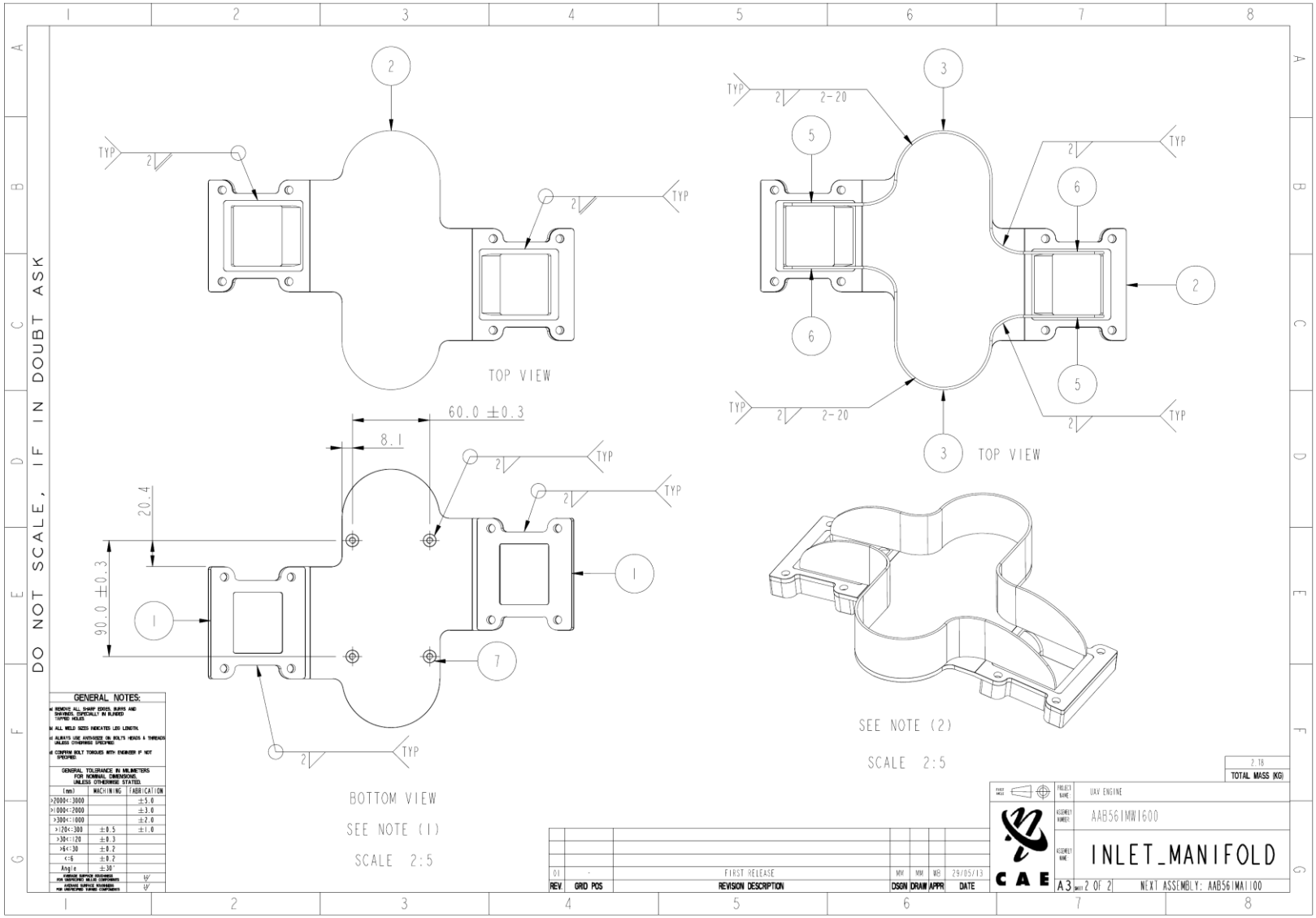
DO NOT SCALE, IF IN DOUBT ASK
TOP VIEW
TOP VIEW
60.0 ±0.3
8.1
20.4
90.0 ±0.3
BOTTOM VIEW
SEE NOTE (1)
SCALE 2:5
SEE NOTE (2)
SCALE 2:5
TYP
2-20
GENERAL NOTES:
GENERAL TOLERANCE IN MILIMETERS FOR NOMINAL DIMENSIONS, UNLESS OTHERWISE STATED.
MACHINING
FABRICATION
Angle ±30'
2.78
TOTAL MASS (KG)
UAV ENGINE
AAB561MW1600
INLET_MANIFOLD
A3 SHEET 2 OF 2
NEXT ASSEMBLY: AAB561MA1100
CAE
01 - FIRST RELEASE MW MM WB 29/05/13
REV. GRD POS REVISION DESCRIPTION DSGN DRAW APPR DATE

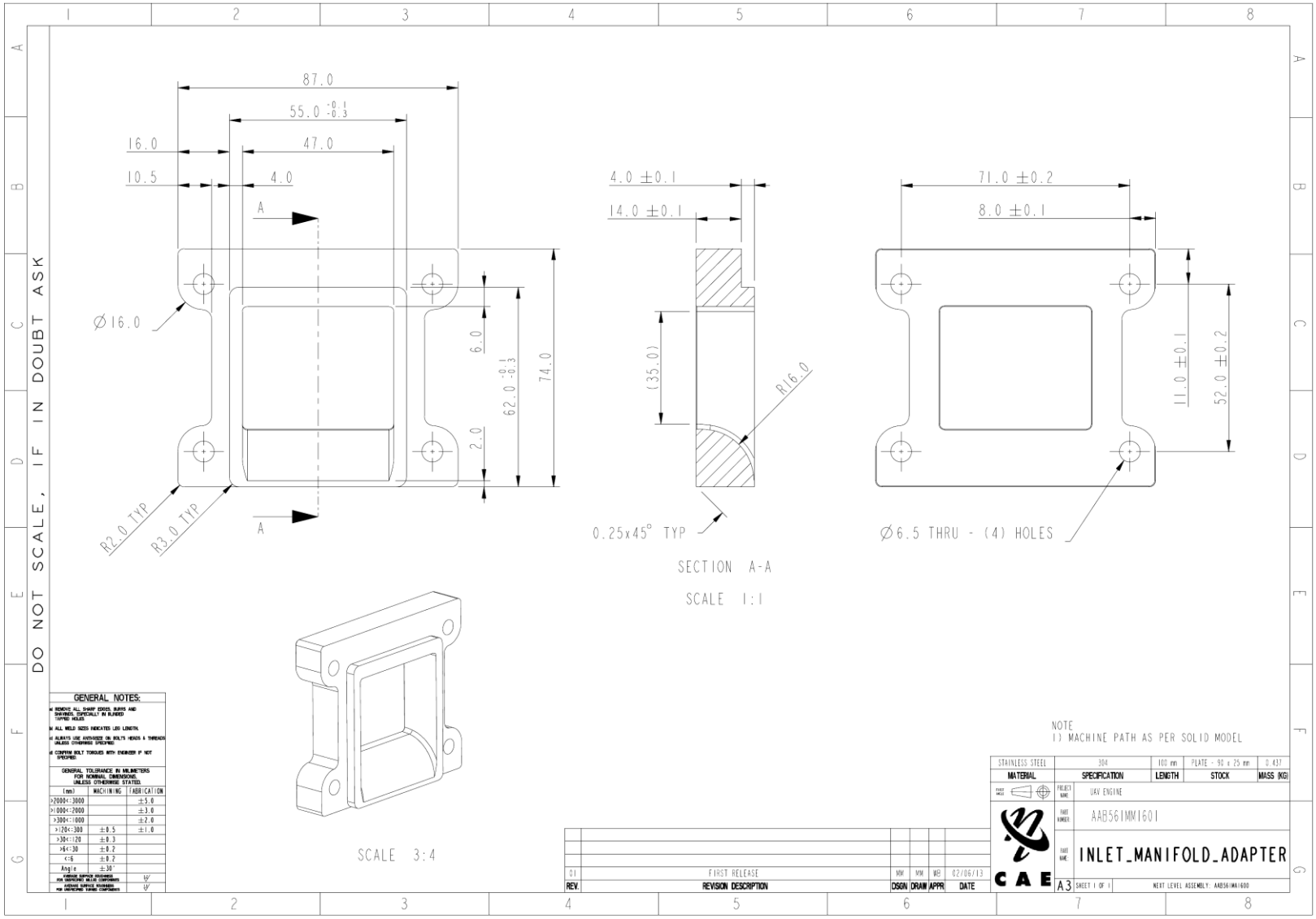
DO NOT SCALE, IF IN DOUBT ASK
87.0
55.0 -0.1 -0.3
16.0
47.0
10.5
4.0
A
Ø16.0
6.0
62.0 -0.1 -0.3
74.0
2.0
R2.0 TYP
R3.0 TYP
4.0 ±0.1
14.0 ±0.1
(35.0)
R16.0
0.25x45° TYP
71.0 ±0.2
8.0 ±0.1
11.0 ±0.1
52.0 ±0.2
Ø6.5 THRU - (4) HOLES
SECTION A-A
SCALE 1:1
SCALE 3:4
NOTE
1) MACHINE PATH AS PER SOLID MODEL
GENERAL NOTES:
GENERAL TOLERANCE IN MILIMETERS FOR NOMINAL DIMENSIONS, UNLESS OTHERWISE STATED
STAINLESS STEEL | 304 | 100 mm | PLATE - 90 x 25 mm | 0.437
MATERIAL | SPECIFICATION | LENGTH | STOCK | MASS (KG)
PROJECT NAME: UAV ENGINE
PART NUMBER: AAB561MM1601
PART NAME: INLET_MANIFOLD_ADAPTER
A3 SHEET 1 OF 1
NEXT LEVEL ASSEMBLY: AAB561MA1600
01 FIRST RELEASE MM MM WB 02/06/13
REV. REVISION DESCRIPTION DSGN DRAW APPR DATE

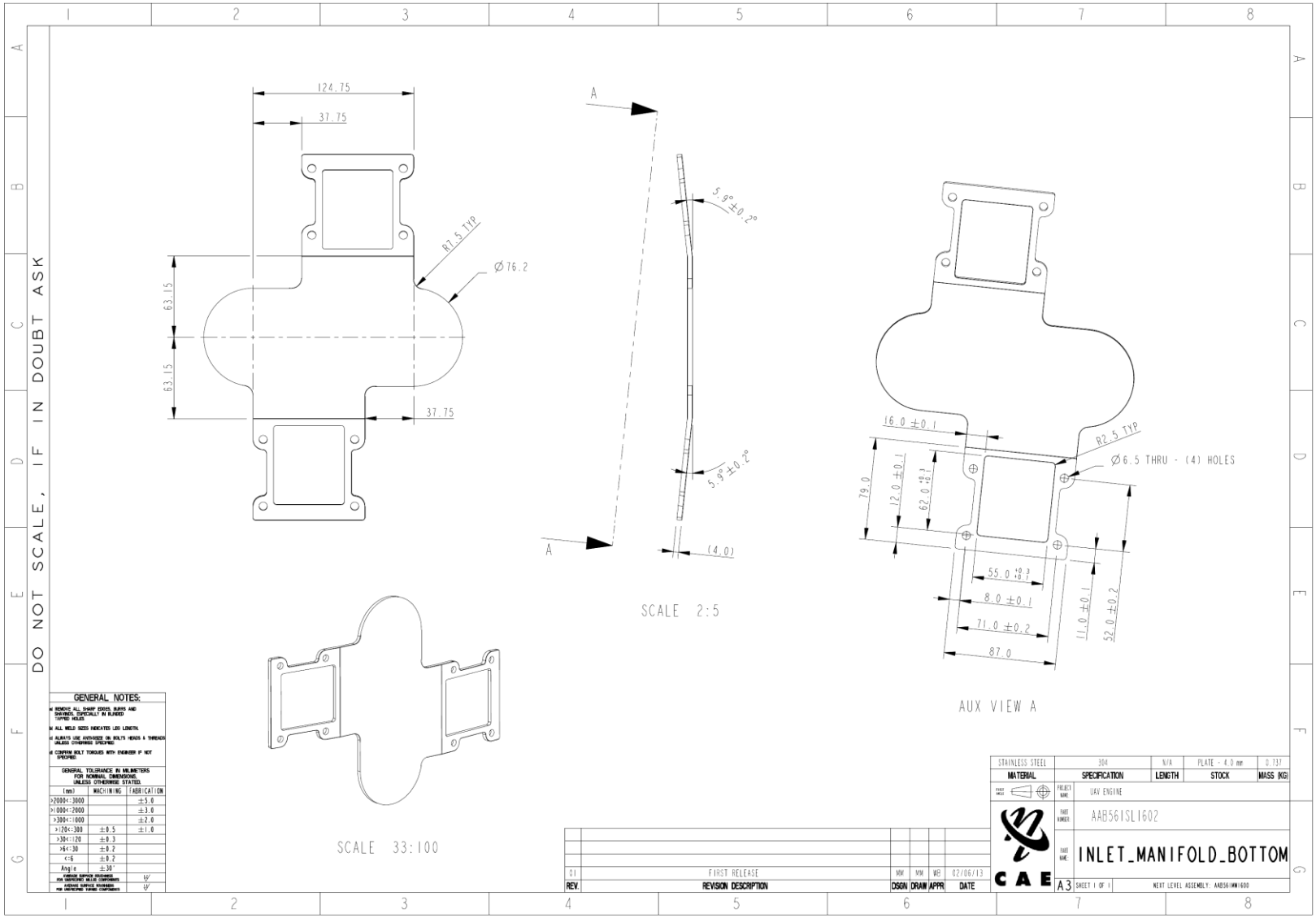
DO NOT SCALE, IF IN DOUBT ASK
124.75
37.75
R7.5 TYP
Ø76.2
63.15
63.15
37.75
A
A
5.9° ±0.2°
5.9° ±0.2°
(4.0)
SCALE 2:5
16.0 ±0.1
R2.5 TYP
Ø6.5 THRU - (4) HOLES
79.0
12.0 ±0.1
62.0 +0.1 -0.1
55.0 +0.3 +0.0
8.0 ±0.1
71.0 ±0.2
87.0
11.0 ±0.1
32.0 ±0.2
AUX VIEW A
SCALE 33:100
GENERAL NOTES:
GENERAL TOLERANCE IN MILIMETERS FOR NOMINAL DIMENSIONS, UNLESS OTHERWISE STATED.
(mm)	MACHINING	FABRICATION
>2000<=3000		±5.0
>1000<=2000		±3.0
>300<=1000		±2.0
>120<=300	±0.5	±1.0
>30<=120	±0.3	
>6<=30	±0.2	
<=6	±0.2	
Angle	±30'	
STAINLESS STEEL | 304 | N/A | PLATE - 4.0 mm | 0.737
MATERIAL | SPECIFICATION | LENGTH | STOCK | MASS (KG)
PROJECT NAME: UAV ENGINE
PART NUMBER: AAB561SL1602
PART NAME: INLET_MANIFOLD_BOTTOM
CAE
A3 SHEET 1 OF 1
NEXT LEVEL ASSEMBLY: AAB561MN1600
01 FIRST RELEASE MM MM WB 02/06/13
REV. REVISION DESCRIPTION DSGN DRAW APPR DATE

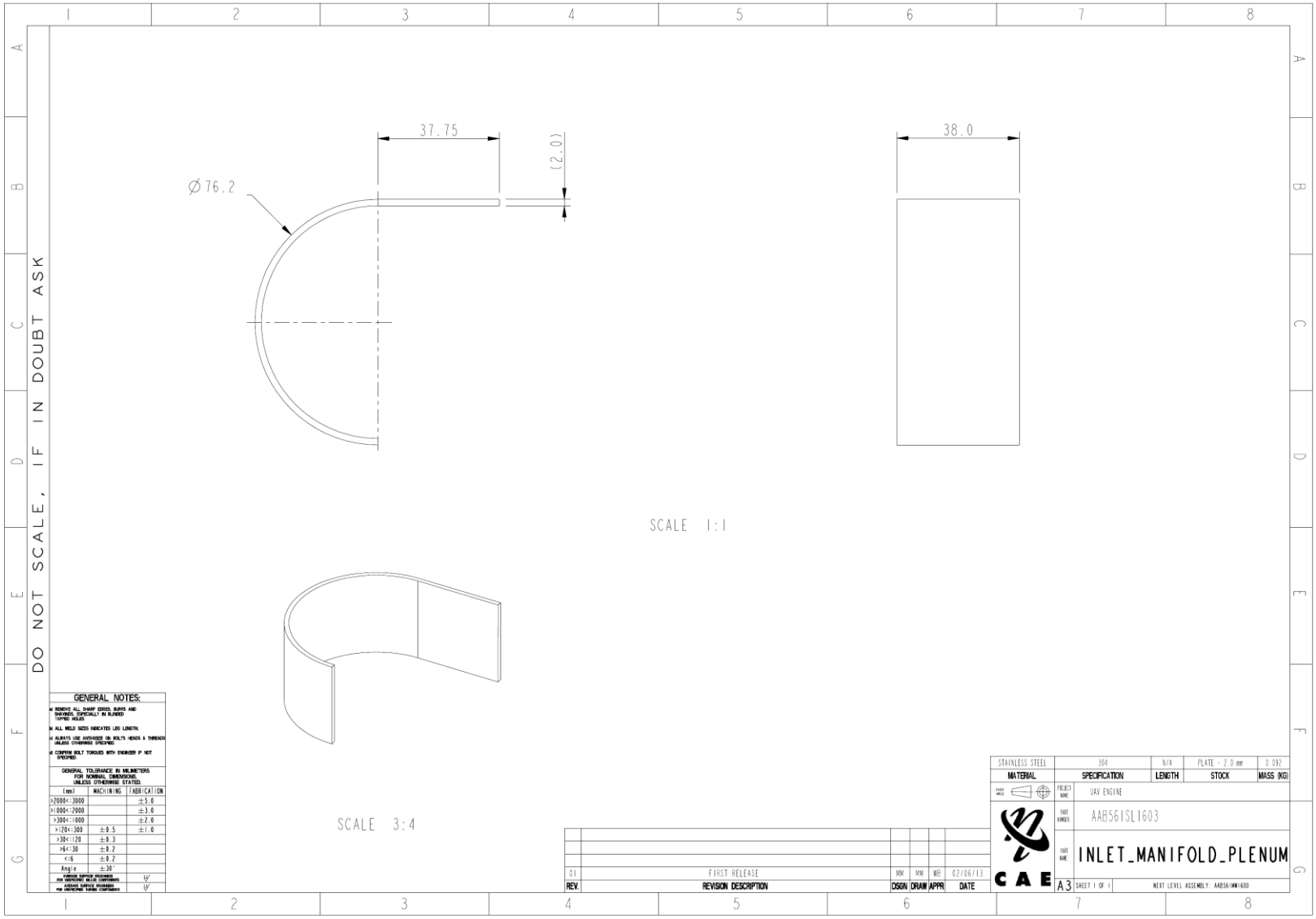
37.75
(2.0)
Ø76.2
38.0
SCALE 1:1
SCALE 3:4
DO NOT SCALE, IF IN DOUBT ASK
GENERAL NOTES:
GENERAL TOLERANCE IN MILIMETERS FOR NOMINAL DIMENSIONS, UNLESS OTHERWISE STATED.
[mm] MACHINING FABRICATION
>2000<=3000 ±5.0
>1000<=2000 ±3.0
>300<=1000 ±2.0
>120<=300 ±0.5 ±1.0
>30<=120 ±0.3
>6<=30 ±0.2
<=6 ±0.2
Angle ±30'
STAINLESS STEEL | 304 | N/A | PLATE - 2.0 mm | 0.092
MATERIAL | SPECIFICATION | LENGTH | STOCK | MASS (KG)
UAV ENGINE
AAB561SL1603
INLET_MANIFOLD_PLENUM
01 FIRST RELEASE MM MK WB 02/06/13
REV. REVISION DESCRIPTION DSGN DRAW APPR DATE
CAE
A3
NEXT LEVEL ASSEMBLY: AAB561MN1600

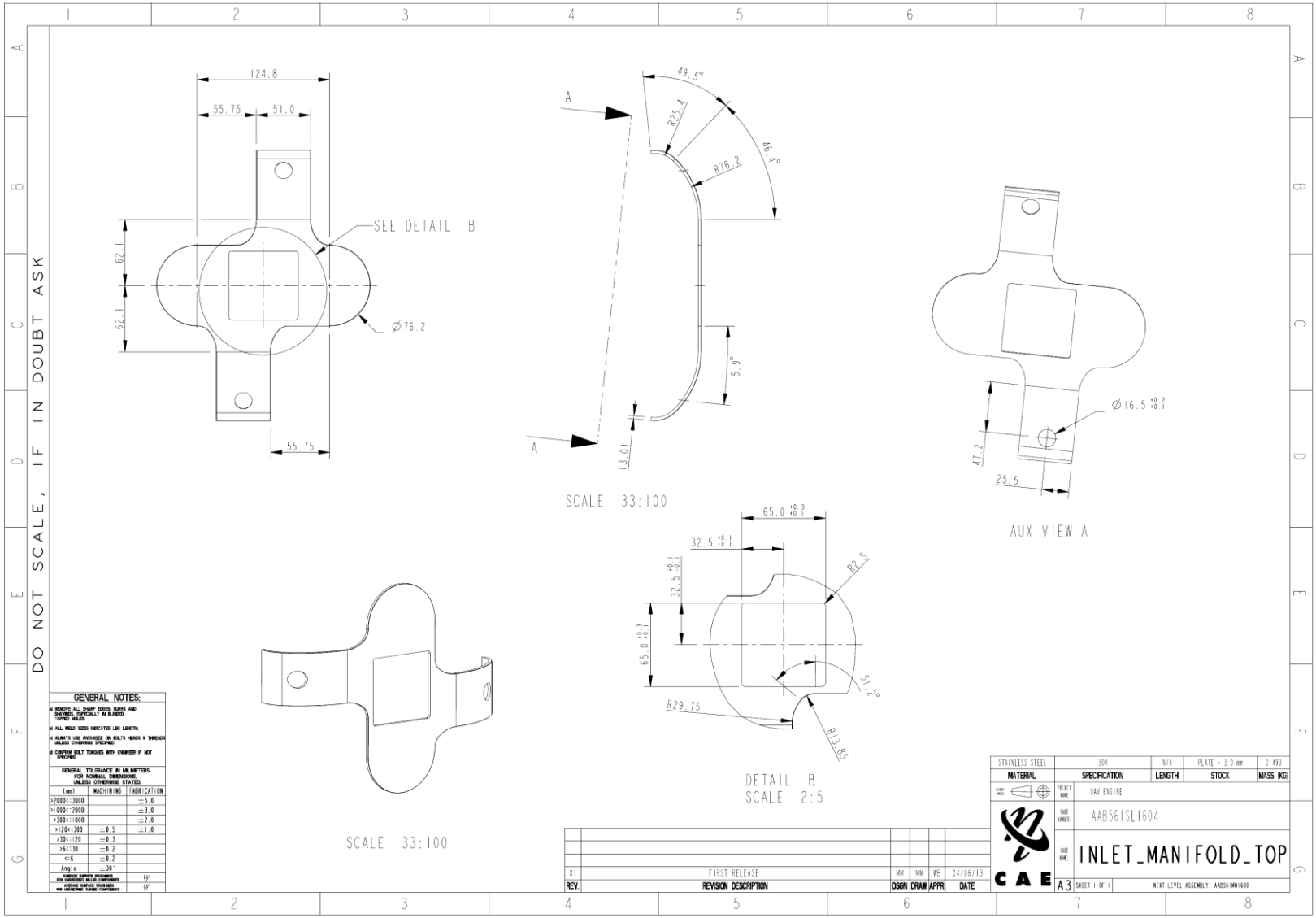
DO NOT SCALE, IF IN DOUBT ASK
124.8
55.75
51.0
SEE DETAIL B
62.1
62.1
Ø76.2
55.75
A
A
49.5°
R25.4
46.4°
R76.2
5.9°
(3.0)
SCALE 33:100
AUX VIEW A
Ø16.5 +0.2 +0.1
47.2
25.5
65.0 +0.3 +0.1
32.5 +0.1 -0.1
32.5 +0.1 -0.1
65.0 +0.3 -0.3
R2.5
51.2°
R29.75
R13.85
DETAIL B
SCALE 2:5
SCALE 33:100
GENERAL NOTES:
GENERAL TOLERANCE IN MILIMETERS FOR NOMINAL DIMENSIONS, UNLESS OTHERWISE STATED.
Item	MACHINING	FABRICATION
>2000<=3000		±5.0
>1000<=2000		±3.0
>300<=1000		±2.0
>120<=300	±0.5	±1.0
>30<=120	±0.3	
>6<=30	±0.2	
<=6	±0.2	
Angle	±30'	
01 FIRST RELEASE MM MM WB 04/06/13
REV. REVISION DESCRIPTION DSGN DRAW APPR DATE
STAINLESS STEEL 304 N/A PLATE - 3.0 mm 0.493
MATERIAL SPECIFICATION LENGTH STOCK MASS (KG)
PROJECT NAME UAV ENGINE
PART NUMBER AAB561SL1604
PART NAME INLET_MANIFOLD_TOP
CAE
A3 SHEET 1 OF 1 NEXT LEVEL ASSEMBLY: AAB561MN1600

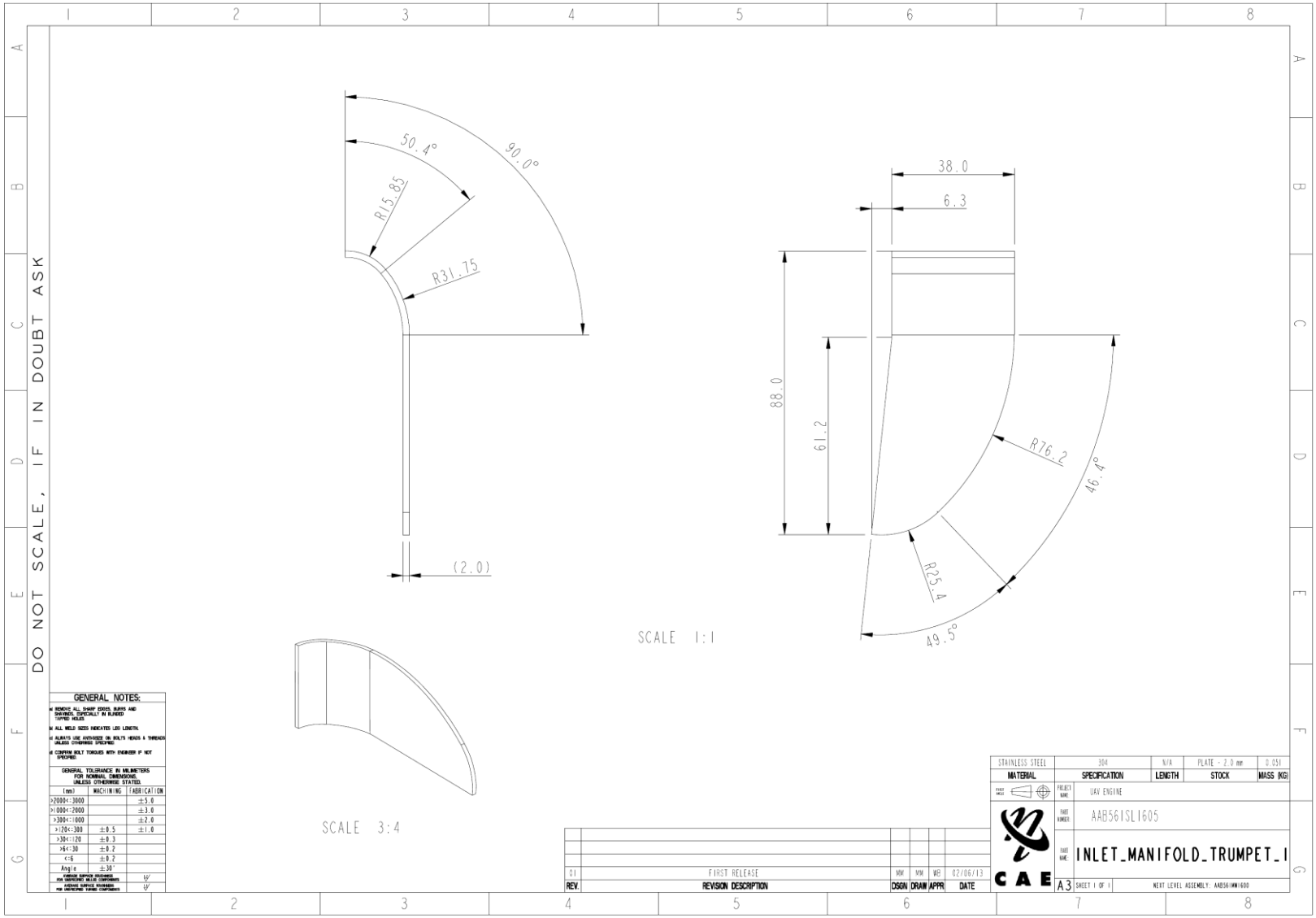
DO NOT SCALE, IF IN DOUBT ASK
50.4°
90.0°
R15.85
R31.75
(2.0)
SCALE 1:1
38.0
6.3
88.0
61.2
R76.2
46.4°
R25.4
49.5°
SCALE 3:4
GENERAL NOTES:
GENERAL TOLERANCE IN MILIMETERS FOR NOMINAL DIMENSIONS, UNLESS OTHERWISE STATED.
[mm] MACHINING FABRICATION
>2000<=3000 ±5.0
>1000<=2000 ±3.0
>300<=1000 ±2.0
>120<=300 ±0.5 ±1.0
>30<=120 ±0.3
>6<=30 ±0.2
<=6 ±0.2
Angle ±30'
STAINLESS STEEL | 304 | N/A | PLATE - 2.0 mm | 0.051
MATERIAL | SPECIFICATION | LENGTH | STOCK | MASS (KG)
PROJECT NAME: UAV ENGINE
PART NUMBER: AAB561SL1605
PART NAME: INLET_MANIFOLD_TRUMPET_1
CAE
A3 SHEET 1 OF 1
NEXT LEVEL ASSEMBLY: AAB561MN1600
01 FIRST RELEASE MM MM WB 02/06/13
REV. REVISION DESCRIPTION DSGN DRAW APPR DATE

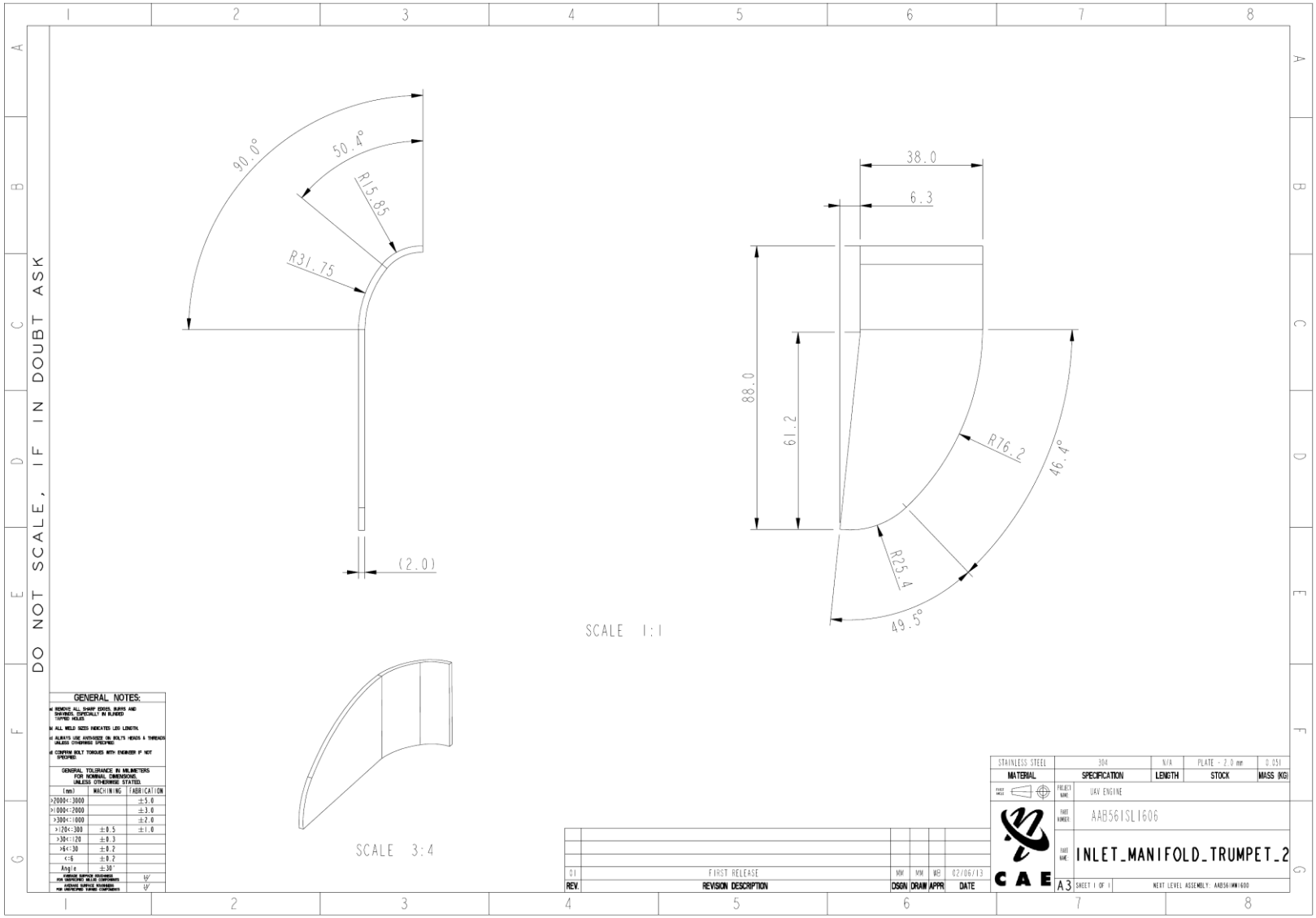
DO NOT SCALE, IF IN DOUBT ASK
90.0°
50.4°
R15.85
R31.75
(2.0)
SCALE 1:1
38.0
6.3
88.0
61.2
R76.2
46.4°
R25.4
49.5°
SCALE 3:4
GENERAL NOTES:
GENERAL TOLERANCE IN MILIMETERS FOR NOMINAL DIMENSIONS, UNLESS OTHERWISE STATED.
[mm] MACHINING FABRICATION
>2000<:3000 ±5.0
>1000<:2000 ±3.0
>300<:1000 ±2.0
>120<:300 ±0.5 ±1.0
>30<:120 ±0.3
>6<:30 ±0.2
<:6 ±0.2
Angle ±30'
STAINLESS STEEL | 304 | N/A | PLATE - 2.0 mm | 0.051
MATERIAL | SPECIFICATION | LENGTH | STOCK | MASS (KG)
PROJECT NAME: UAV ENGINE
PART NUMBER: AAB561SL1606
PART NAME: INLET_MANIFOLD_TRUMPET_2
CAE
A3 SHEET 1 OF 1
NEXT LEVEL ASSEMBLY: AAB561MN1600
01 FIRST RELEASE MM MM WB 02/06/13
REV. REVISION DESCRIPTION DSGN DRAW APPR DATE

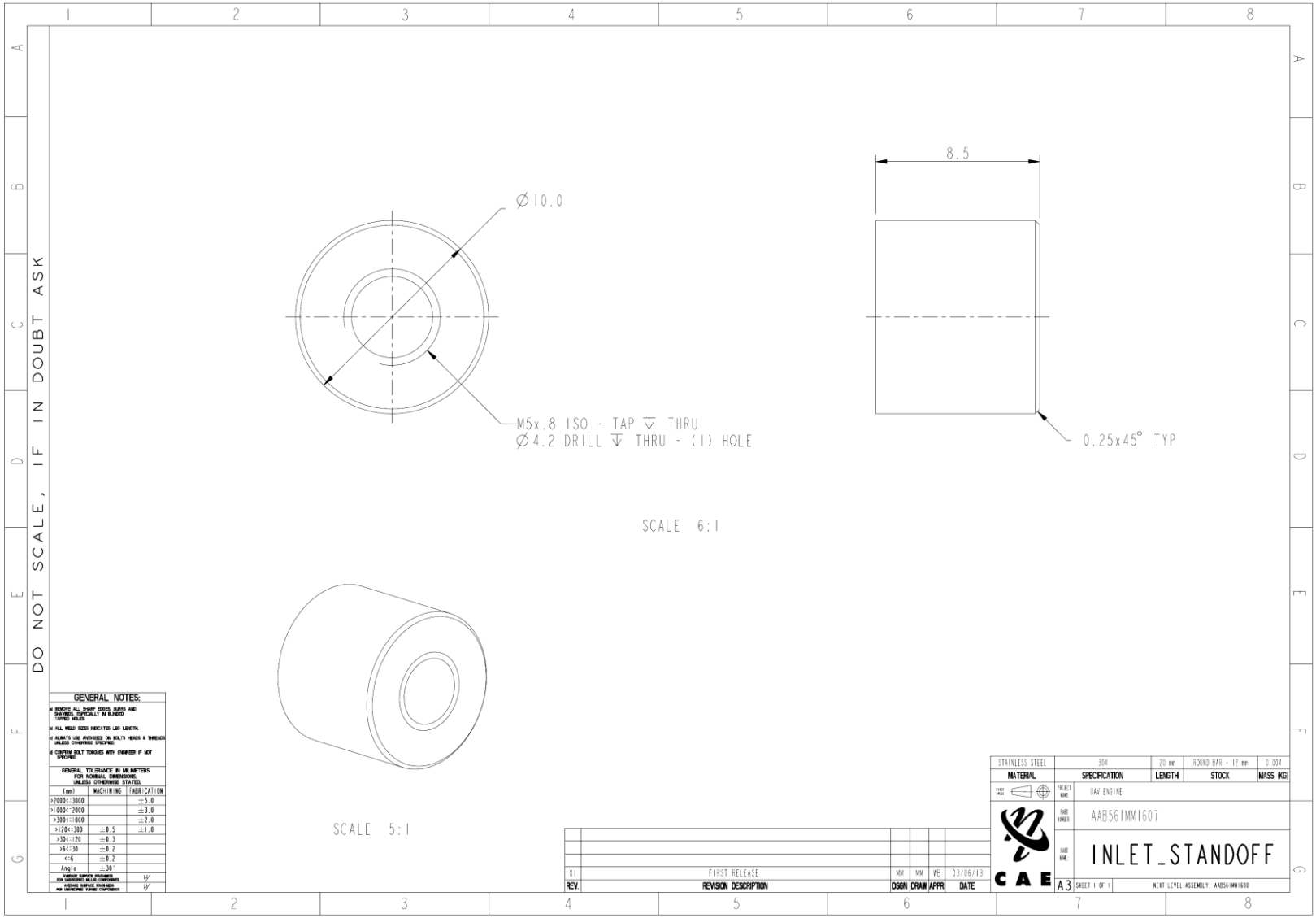
DO NOT SCALE, IF IN DOUBT ASK
Ø10.0
M5x.8 ISO - TAP ↧ THRU
Ø4.2 DRILL ↧ THRU - (1) HOLE
8.5
0.25x45° TYP
SCALE 6:1
SCALE 5:1
GENERAL NOTES:
GENERAL TOLERANCE IN MILIMETERS FOR NOMINAL DIMENSIONS, UNLESS OTHERWISE STATED.
[mm] | MACHINING | FABRICATION
>2000<=3000 | ±5.0
>1000<=2000 | ±3.0
>300<=1000 | ±2.0
>120<=300 | ±0.5 | ±1.0
>30<=120 | ±0.3
>6<=30 | ±0.2
<=6 | ±0.2
Angle | ±30'
01 | FIRST RELEASE | MM | MK | WB | 03/06/13
REV. | REVISION DESCRIPTION | DSGN | DRAW | APPR | DATE
STAINLESS STEEL | 304 | 20 mm | ROUND BAR - 12 mm | 0.004
MATERIAL | SPECIFICATION | LENGTH | STOCK | MASS (KG)
PROJECT NAME: UAV ENGINE
PART NUMBER: AAB561MM1607
PART NAME: INLET_STANDOFF
CAE
A3 SHEET 1 OF 1
NEXT LEVEL ASSEMBLY: AAB561MM1600

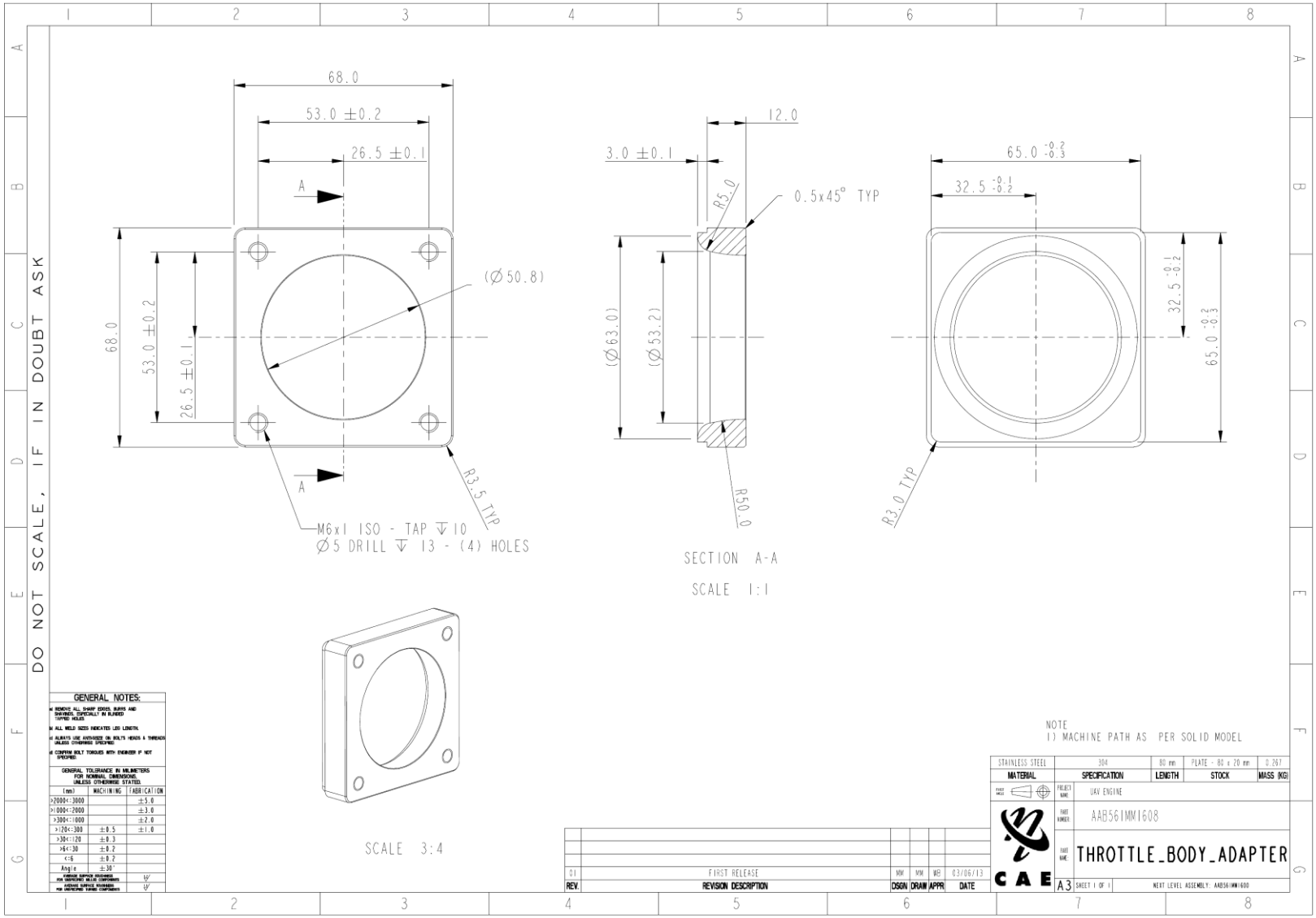
68.0
53.0 ±0.2
26.5 ±0.1
A
(Ø50.8)
68.0
53.0 ±0.2
26.5 ±0.1
R3.5 TYP
M6x1 ISO - TAP ↧10
Ø5 DRILL ↧ 13 - (4) HOLES
12.0
3.0 ±0.1
R5.0
0.5x45° TYP
(Ø63.0)
(Ø53.2)
R50.0
SECTION A-A
SCALE 1:1
65.0 -0.2 -0.3
32.5 -0.1 -0.2
32.5 -0.1 -0.2
65.0 -0.2 -0.3
R3.0 TYP
DO NOT SCALE, IF IN DOUBT ASK
SCALE 3:4
NOTE
1) MACHINE PATH AS PER SOLID MODEL
GENERAL NOTES:
GENERAL TOLERANCE IN MILIMETERS FOR NOMINAL DIMENSIONS, UNLESS OTHERWISE STATED
STAINLESS STEEL | 304 | 80 mm | PLATE - 80 x 20 mm | 0.267
MATERIAL | SPECIFICATION | LENGTH | STOCK | MASS (KG)
PROJECT NAME: UAV ENGINE
PART NUMBER: AAB561MM1608
PART NAME: THROTTLE_BODY_ADAPTER
A3 SHEET 1 OF 1 NEXT LEVEL ASSEMBLY: AAB561MM1600
01 FIRST RELEASE MM MM WB 03/06/13
REV. REVISION DESCRIPTION DSGN DRAW APPR DATE

F.19 ALTERNATIVE DRIVESHAFT ASSEMBLY

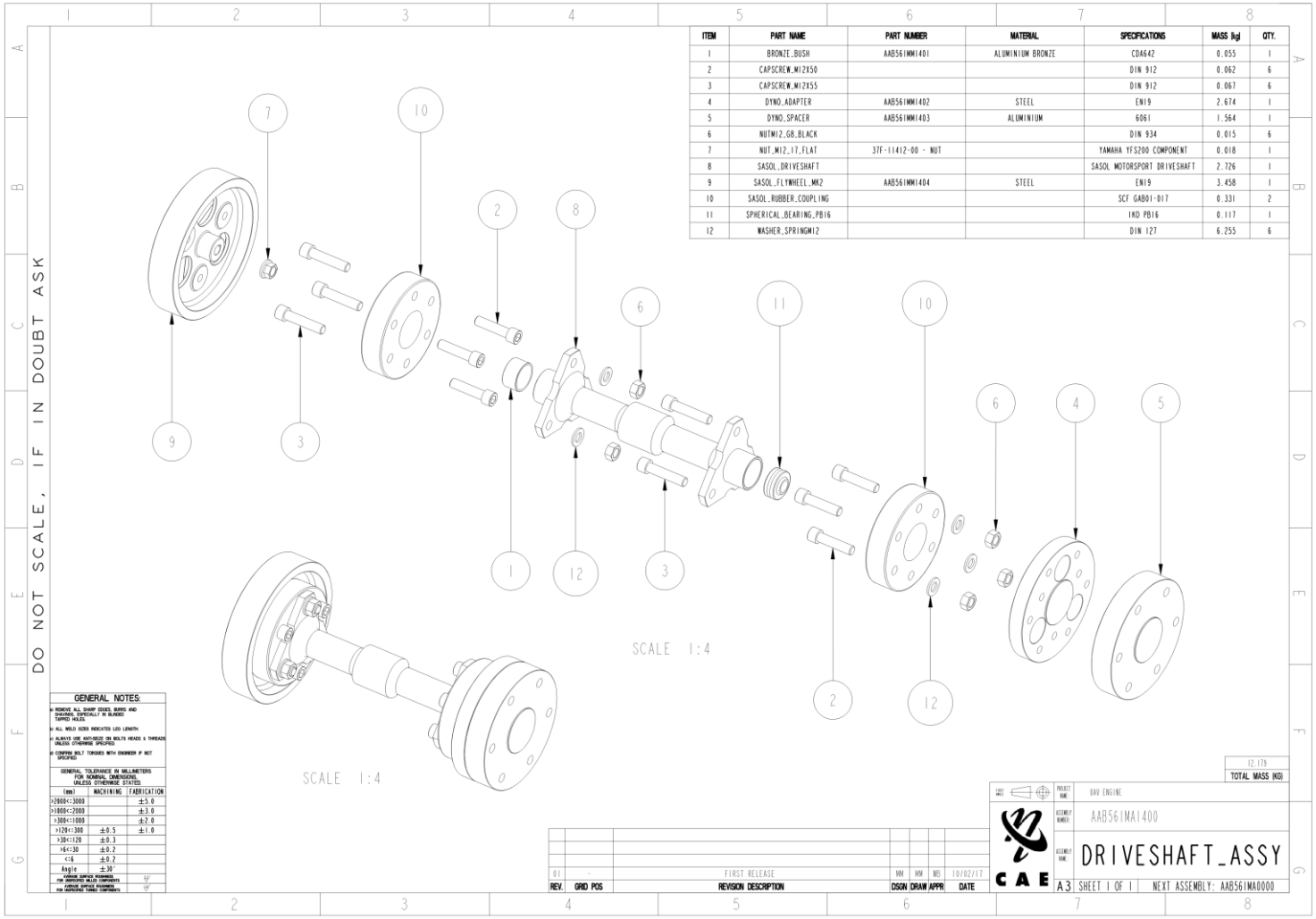

ITEM	PART NAME	PART NUMBER	MATERIAL	SPECIFICATIONS	MASS (kg)	QTY.
1	BRONZE_BUSH	AAB561MM1401	ALUMINIUM BRONZE	CDA642	0.055	1
2	CAPSCREW_M12X50			DIN 912	0.062	6
3	CAPSCREW_M12X55			DIN 912	0.067	6
4	DYNO_ADAPTER	AAB561MM1402	STEEL	EN19	2.674	1
5	DYNO_SPACER	AAB561MM1403	ALUMINIUM	6061	1.564	1
6	NUTM12_G8_BLACK			DIN 934	0.015	6
7	NUT_M12_17_FLAT	37F-11412-00 - NUT		YAMAHA YFS200 COMPONENT	0.018	1
8	SASOL_DRIVESHAFT			SASOL MOTORSPORT DRIVESHAFT	2.726	1
9	SASOL_FLYWHEEL_MK2	AAB561MM1404	STEEL	EN19	3.458	1
10	SASOL_RUBBER_COUPLING			SCF GAB01-017	0.331	2
11	SPHERICAL_BEARING_PB16			IKO PB16	0.117	1
12	WASHER_SPRINGM12			DIN 127	6.255	6

REV.	GRID POS	REVISION DESCRIPTION	DSGN	DRAW	APPR	DATE
01	-	FIRST RELEASE	MM	MM	MS	10/02/17

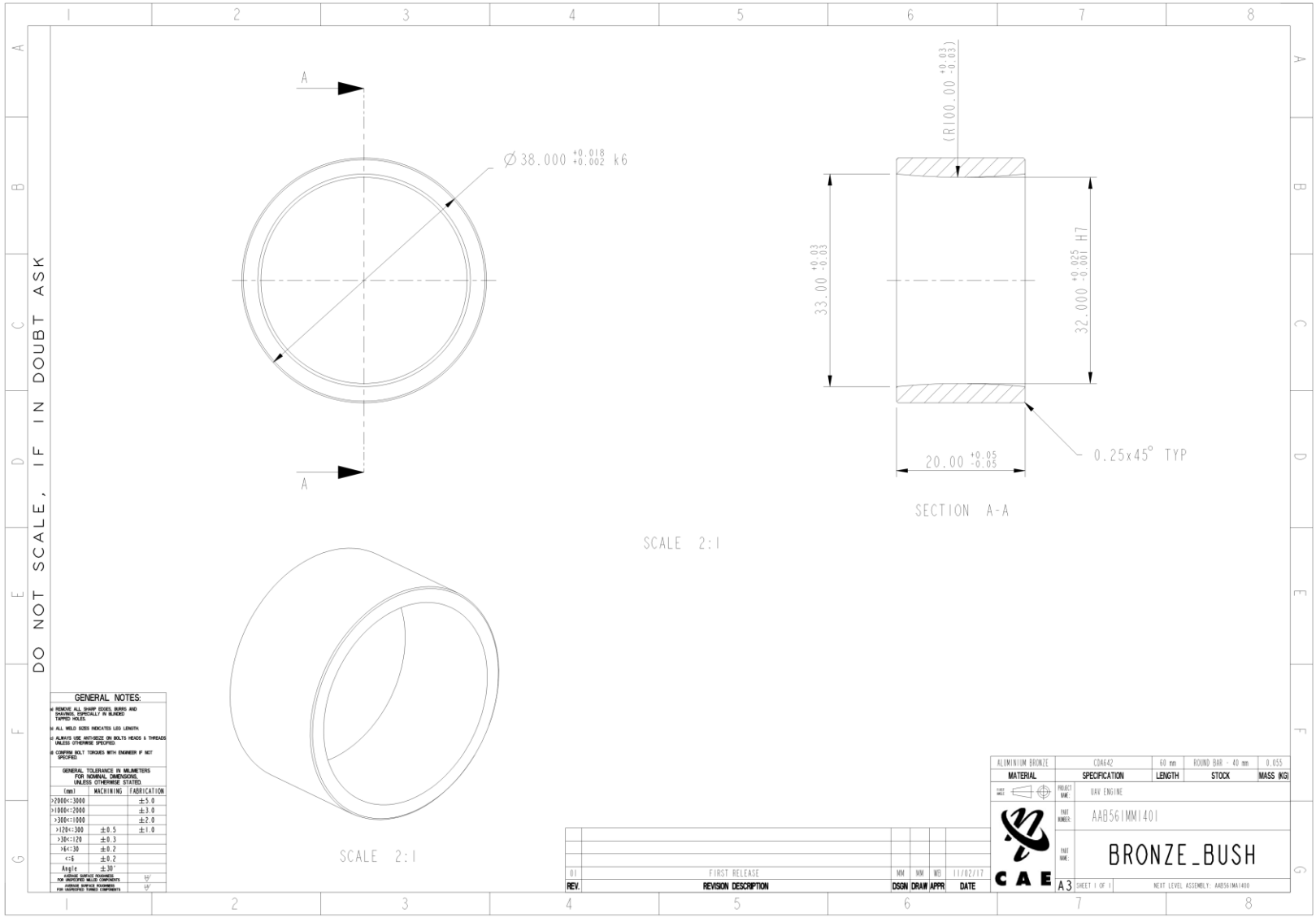
DO NOT SCALE, IF IN DOUBT ASK
A
A
Ø38.000 +0.018 +0.002 k6
SCALE 2:1
(R100.00 +0.03 -0.03)
33.00 +0.03 -0.03
32.000 +0.025 -0.001 H7
20.00 +0.05 -0.05
0.25x45° TYP
SECTION A-A
SCALE 2:1
GENERAL NOTES:
1. REMOVE ALL SHARP EDGES, BURRS AND SWARFS, ESPECIALLY IN BLINDED TAPPED HOLES.
2. ALL WELD SIZES INDICATES LEG LENGTH.
3. ALWAYS USE ANTI-SEIZE ON BOLTS HEADS & THREADS UNLESS OTHERWISE SPECIFIED.
4. CONFIRM BOLT TORQUES WITH ENGINEER IF NOT SPECIFIED.
GENERAL TOLERANCE IN MILIMETERS FOR NOMINAL DIMENSIONS, UNLESS OTHERWISE STATED.
(mm) | MACHINING | FABRICATION
>2000<=3000 | | ±5.0
>1000<=2000 | | ±3.0
>300<=1000 | | ±2.0
>120<=300 | ±0.5 | ±1.0
>30<=120 | ±0.3 |
>6<=30 | ±0.2 |
<=6 | ±0.2 |
Angle | ±30'
AVERAGE SURFACE ROUGHNESS FOR UNSPECIFIED MILLED COMPONENTS | 6.3
AVERAGE SURFACE ROUGHNESS FOR UNSPECIFIED TURNED COMPONENTS | 1.6
ALUMINIUM BRONZE | CDA642 | 60 mm | ROUND BAR - 40 mm | 0.055
MATERIAL | SPECIFICATION | LENGTH | STOCK | MASS (KG)
PROJECT NAME: UAV ENGINE
PART NUMBER: AAB561MM1401
PART NAME: BRONZE_BUSH
CAE
A3 SHEET 1 OF 1 NEXT LEVEL ASSEMBLY: AAB561MA1400
01 FIRST RELEASE MM MM WB 11/02/17
REV. REVISION DESCRIPTION DSGN DRAW APPR. DATE

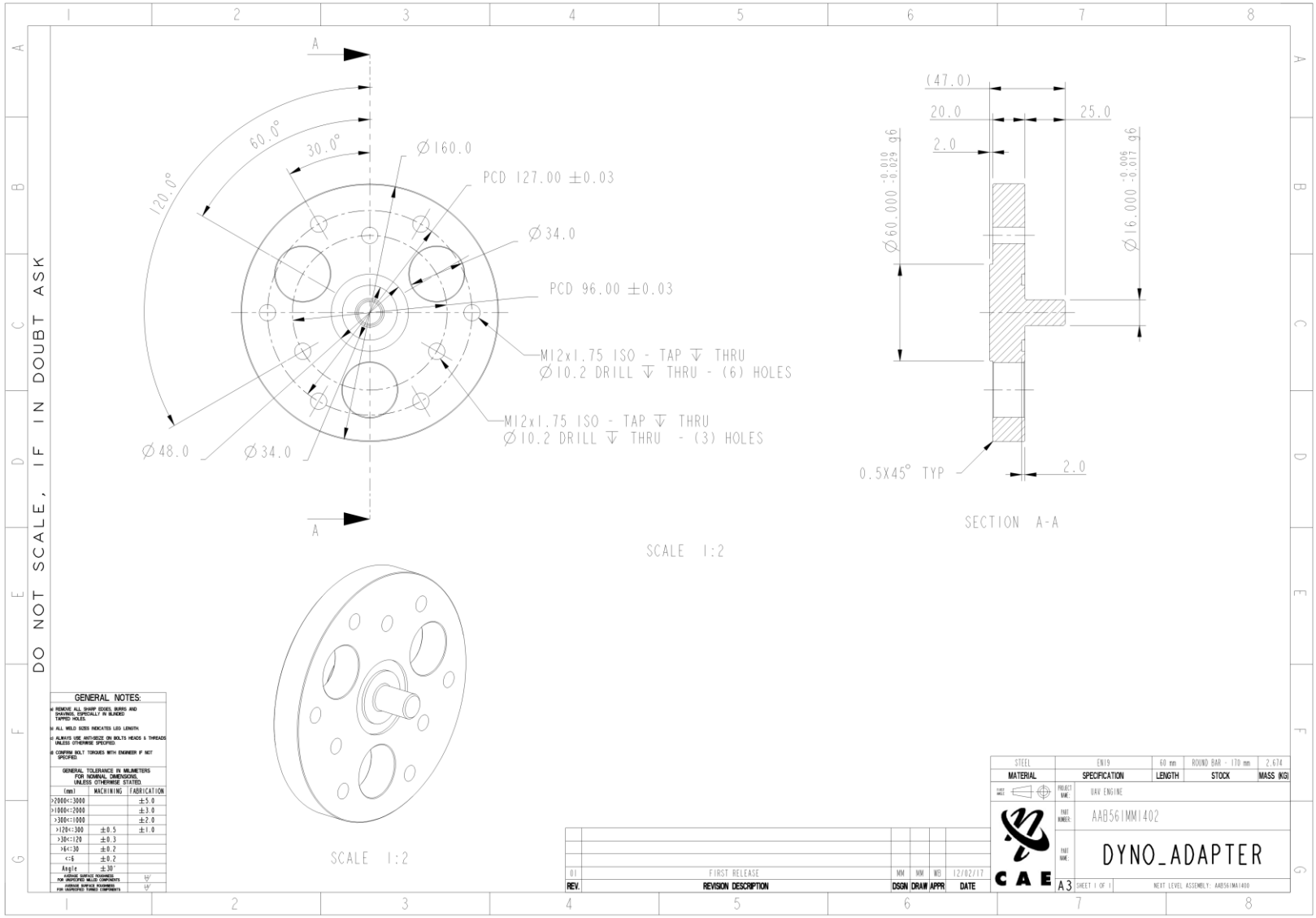
DO NOT SCALE, IF IN DOUBT ASK
A
60.0°
30.0°
120.0°
Ø160.0
PCD 127.00 ±0.03
Ø34.0
PCD 96.00 ±0.03
M12x1.75 ISO - TAP ↧ THRU
Ø10.2 DRILL ↧ THRU - (6) HOLES
M12x1.75 ISO - TAP ↧ THRU
Ø10.2 DRILL ↧ THRU - (3) HOLES
Ø48.0
Ø34.0
SCALE 1:2
(47.0)
20.0
25.0
2.0
Ø60.000 -0.010 -0.029 g6
Ø16.000 -0.006 -0.017 g6
0.5X45° TYP
2.0
SECTION A-A
GENERAL NOTES:
1. REMOVE ALL SHARP EDGES, BURRS AND SHAVINGS, ESPECIALLY IN BLINDED TAPPED HOLES.
2. ALL WELD SIZES INDICATES LEG LENGTH.
3. ALWAYS USE ANTI-SEIZE ON BOLTS HEADS & THREADS UNLESS OTHERWISE SPECIFIED.
4. CONFIRM BOLT TORQUES WITH ENGINEER IF NOT SPECIFIED.
GENERAL TOLERANCE IN MILIMETERS FOR NOMINAL DIMENSIONS, UNLESS OTHERWISE STATED.
(mm) | MACHINING | FABRICATION
>2000<=3000 | | ±5.0
>1000<=2000 | | ±3.0
>300<=1000 | | ±2.0
>120<=300 | ±0.5 | ±1.0
>30<=120 | ±0.3 |
>6<=30 | ±0.2 |
<=6 | ±0.2 |
Angle | ±30'
AVERAGE SURFACE ROUGHNESS FOR UNSPECIFIED MILLED COMPONENTS 6.3
AVERAGE SURFACE ROUGHNESS FOR UNSPECIFIED TURNED COMPONENTS 3.2
SCALE 1:2
REV. | REVISION DESCRIPTION | DSGN | DRAW | APPR | DATE
01 | FIRST RELEASE | MM | MM | WB | 12/02/17
STEEL | EN19 | 60 mm | ROUND BAR - 170 mm | 2.67Kg
MATERIAL | SPECIFICATION | LENGTH | STOCK | MASS (KG)
PROJECT NAME: UAV ENGINE
PART NUMBER: AAB561MM1402
PART NAME: DYNO_ADAPTER
CAE
A3 SHEET 1 OF 1
NEXT LEVEL ASSEMBLY: AAB561MA1400

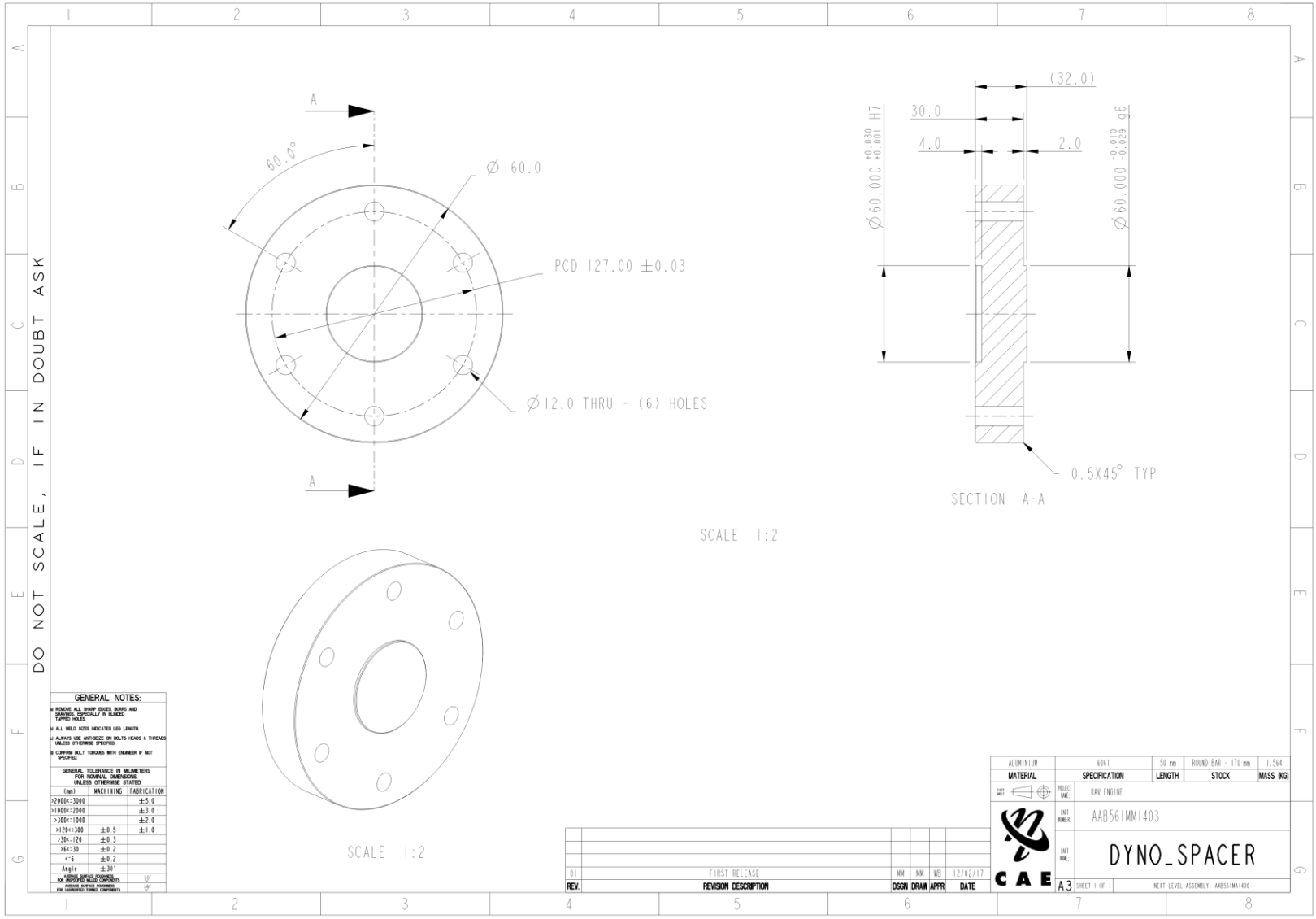
DO NOT SCALE, IF IN DOUBT ASK
A
60.0°
Ø160.0
PCD 127.00 ±0.03
Ø12.0 THRU - (6) HOLES
A
SCALE 1:2
(32.0)
30.0
4.0
2.0
Ø60.000 +0.030 +0.001 H7
Ø60.000 -0.010 -0.029 g6
0.5X45° TYP
SECTION A-A
GENERAL NOTES:
1. REMOVE ALL SHARP EDGES, BURRS AND SHAVINGS, ESPECIALLY IN BLINDED TAPPED HOLES.
2. ALL WELD SIZES INDICATES LEG LENGTH.
3. ALWAYS USE ANTI-SEIZE ON BOLTS HEADS & THREADS UNLESS OTHERWISE SPECIFIED.
4. CONFIRM BOLT TORQUES WITH ENGINEER IF NOT SPECIFIED.
GENERAL TOLERANCE IN MILIMETERS FOR NOMINAL DIMENSIONS, UNLESS OTHERWISE STATED.
(mm) MACHINING FABRICATION
>2000<=3000 ±5.0
>1000<=2000 ±3.0
>300<=1000 ±2.0
>120<=300 ±0.5 ±1.0
>30<=120 ±0.3
>6<=30 ±0.2
<=6 ±0.2
Angle ±30'
AVERAGE SURFACE ROUGHNESS FOR UNSPECIFIED MILLED COMPONENTS
AVERAGE SURFACE ROUGHNESS FOR UNSPECIFIED TURNED COMPONENTS
SCALE 1:2
REV. REVISION DESCRIPTION DSGN DRAW APPR. DATE
01 FIRST RELEASE MM MM WB 12/02/17
ALUMINIUM MATERIAL
6061 SPECIFICATION
50 mm LENGTH
ROUND BAR - 170 mm STOCK
1.564 MASS (KG)
PROJECT NAME: UAV ENGINE
PART NUMBER: AAB561MM1403
PART NAME: DYNO_SPACER
CAE
A3 SHEET 1 OF 1
NEXT LEVEL ASSEMBLY: AAB561MA1400

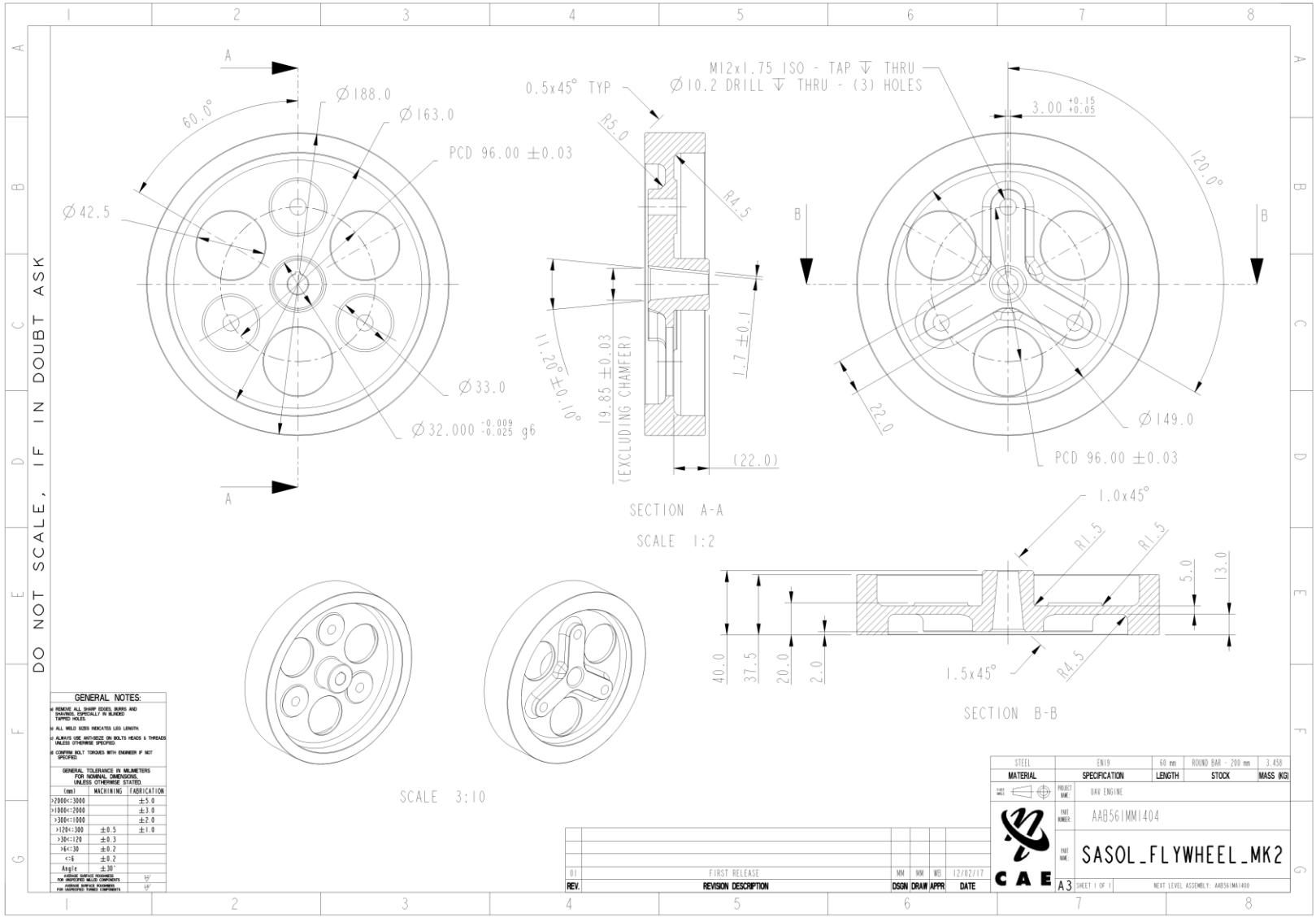
DO NOT SCALE, IF IN DOUBT ASK
Ø188.0
Ø163.0
PCD 96.00 ±0.03
60.0°
Ø42.5
Ø33.0
Ø32.000 -0.009 -0.025 g6
0.5x45° TYP
R5.0
R4.5
11.20° ±0.10°
19.85 ±0.03
(EXCLUDING CHAMFER)
17 ±0.1
(22.0)
SECTION A-A
SCALE 1:2
M12x1.75 ISO - TAP ↧ THRU
Ø10.2 DRILL ↧ THRU - (3) HOLES
3.00 +0.15 +0.05
120.0°
22.0
Ø149.0
PCD 96.00 ±0.03
1.0x45°
R1.5
R1.5
5.0
13.0
40.0
37.5
20.0
2.0
1.5x45°
R4.5
SECTION B-B
SCALE 3:10
GENERAL NOTES:
1. REMOVE ALL SHARP EDGES, BURRS AND SWARFING, ESPECIALLY IN BLINDED TAPPED HOLES.
2. ALL WELD SIZES INDICATES LEG LENGTH.
3. ALWAYS USE ANTI-SEIZE ON BOLTS HEADS & THREADS UNLESS OTHERWISE SPECIFIED.
4. CONFIRM BOLT TORQUES WITH ENGINEER IF NOT SPECIFIED.
GENERAL TOLERANCE IN MILIMETERS FOR NOMINAL DIMENSIONS, UNLESS OTHERWISE STATED.
(mm) | MACHINING | FABRICATION
>2000<=3000 | | ±5.0
>1000<=2000 | | ±3.0
>300<=1000 | | ±2.0
>120<=300 | ±0.5 | ±1.0
>30<=120 | ±0.3 |
>6<=30 | ±0.2 |
<=6 | ±0.2 |
Angle | ±30'
AVERAGE SURFACE ROUGHNESS FOR UNSPECIFIED MILLED COMPONENTS | 6.3
AVERAGE SURFACE ROUGHNESS FOR UNSPECIFIED TURNED COMPONENTS | 1.6
REV. | REVISION DESCRIPTION | DSGN | DRAW | APPR | DATE
01 | FIRST RELEASE | MM | MM | WB | 12/02/17
STEEL | MATERIAL | EN19 | SPECIFICATION | 60 nn | LENGTH | ROUND BAR - 200 nn | STOCK | 3.458 | MASS (KG)
PROJECT NAME: UAV ENGINE
PART NUMBER: AAB561MM1404
PART NAME: SASOL_FLYWHEEL_MK2
CAE
A3 SHEET 1 OF 1
NEXT LEVEL ASSEMBLY: AAB561MA1400

G MATLAB COMPUTER CODE

G.1 DETERMINE MAXIMUM CYLINDER PRESSURE CYCLE

```
% Create data matrix, analyse and plot from binary data file
% Yamaha DT 175, Two-stroke
% 20 April 2014
%
% Recorded data is:
%   Channel 1 - Cylinder pressure pulse
%   Channel 2 - 720 Pulses per revolution (ppr)
%   Channel 3 - Reference pulse (One per revolution)
%   Channel 4 - Exhaust pressure pulse
%
%--------------------------------------------------------------------------%
%
% Additional coding performed - March 2012
%
%   1. Filter final pressure plot (No longer applicable - Apr 2014)
%   2. Apply calibration factor to final pressure plot
%   3. Correct final pressure plot
%   4. Indicate port timing events on final pressure plot
%
%--------------------------------------------------------------------------%
%
% Additional coding performed - January 2014
%
%   Wika pressure transducer in exhaust on longer used to record exhaust
%   pressure pulse. Instead a Kistler quartz pressure transducer is
%   substituted. The text below details the required modification to the
%   code.
%
%   1. Externally measured mean exhaust pressure recorded
%   2. Mean for recorded exhaust pressure calculated
%   3. Difference between 1 and 2 calculated
%   4. Recorded exhaust pressure corrected by 3
%
%--------------------------------------------------------------------------%
%
% Additional coding performed - January 2014
%
%   1. To accommodate the Exhaust paper testing of different types of
%      tune pipes a single Figure is added which consists of filtered data
%      for both the cylinder and exhaust data
%
%--------------------------------------------------------------------------%
%
% Additional coding performed - April 2014
%
%   1. A filter is applied to all the data points for both Channels 1 & 4
%      instead of only filtering 720 data points per revolution for the
%      final chosen maximum amplitude signal
%   2. NOTE: The phase shift inherent with filtering data is negated by use
%      of a filtfilt zero-phase shift digital filter
%
%--------------------------------------------------------------------------%
%
close all
clear all
clc
```

```
%--------------------------------------------------------------------------%
%
%   Required Inputs & Import data
%
%--------------------------------------------------------------------------%
%
%- Required Inputs ------------------------------------------------------%
%
% Cylinder and Exhaust transducer signal calibration factor
%
% Kistler spark plug transducer Serial Number: 937775
% Transducer recorded in 20 bar/V mode
% sig_cal = input('Enter Cylinder transducer signal calibration factor :')
sig_cal = 20.00195;     % Output of AVL amplifier for Cyl transducer[bar/V]
%
% Kistler spark plug transducer Serial Number: 937776
% Transducer recorded in 5 bar/V mode
% exh_cal = input('Enter Exhaust transducer signal calibration factor :')
exh_cal = 5.01365;      % Output of AVL amplifier for Exh transducer[bar/V]
%
% Mean recorded External exhaust pressure (ext_exh)
% Table below is applicable for the complete standard DT 175 exhaust system
ext_exh = [3000    25.0       % [rpm] [mbar]
           3500    31.3
           4000    34.8
           4500    45.7
           5000    72.6
           5500    93.3
           6000    117.1
           6500    135.3];
%
% Cylinder port timing - Determined by use of a degree wheel
%
% Ex_port_o = input('Enter angle ATDC when the Exhaust port opens :');
% Tr_port_o = input('Enter angle ATDC when the Transfer port opens :');
ex_port_o = 92;         % Degrees ATDC
tr_port_o = 121;        % Degrees ATDC
%
% Exhaust and Transfer ports open durations calculated
ex_port_d = 360 - 2*(ex_port_o);
tr_port_d = 360 - 2*(tr_port_o);
%
%- Required Inputs for PV and loglog plots ------------------------------%
%
% Data below for Yamaha DT 175
%
% Bore (B)
B = 66;                 % [mm]
% Stroke (L)
L = 50;                 % [mm]
% Connecting rod length (l)
l = 105;                % [mm]
% Clearance volume (Vc)
Vc = 17.84;             % [ml]
```

```
%- Import data -------------------------------------------------------------%
%
% Input file, specify rpm and number of cycles
%
% file_name = input('Enter file name as \''filename.ext\'': ')
% n = input('Enter the number of cycles to analyse :')
file_name = 'in_5500_100.bin';
n = 50;                  % Number of revolutions - 1. eg. 6-1 = 5 revs
%
% Identify the Rotational speed (rpm) and Throttle position (wot) of run
us = findstr('_',file_name);
dot = findstr('.',file_name);
rpm = str2double(file_name((us(1)+1):(us(2)-1)));
wot = str2double(file_name((us(2)+1):(dot(1)-1)));
%
% Start the program time counter and open the binary file
tic
file_ID = fopen(file_name,'r','ieee-be');
%
% Information about data string length(sls), String length(sl)
sls = fscanf(file_ID,'%c',2);
sl = str2double(sls);
%
% String data(sd): Sampling rate and Number of channels logged
sd = fscanf(file_ID,'%c',sl);
%
% Capture Sampling rate(sr) and channels(c) as real numbers
eq = findstr('=',sd);
com = findstr(',',sd);
sr = str2double(sd(eq(1)+1:(com-1)));
c = str2double(sd(eq(2)+1:end));
%
% Read in all recorded data(read_data)
read_data = fread(file_ID,[c,inf],'single');
data = (read_data');
fclose(file_ID);
%
%-------------------------------------------------------------------------%
%
%   Recorded data filtered and plotted
%
%-------------------------------------------------------------------------%
%
% All 4 recorded channels plotted vs number of sample points
sd = size(data);
sd_x = sd(1);
x = 1:1:sd_x;
figure(1)
subplot(1,1,1)
plot(x,data(1:end,2),'b',x,data(1:end,1),'r',x,data(1:end,3),'k',...
    x,data(1:end,4),'c')
xlabel('Number of data points')
ylabel('Voltage [V]')
legend('720 ppr','Cylinder pressure','Reference pulse','Exhaust pressure')
title(sprintf('Recorded data vs Number of sample points at %d rpm',rpm))
```

```
%- All 4 channels vs time plots ----------------------------------------%
%
% Specified number of cycles (n) of all 4 channels plotted on separate
% subplots vs time
% Generate a time vector for n-1 revolutions
rps = rpm / 60;          % Revolutions per second
spr = sr * (1/rps);      % Samples / revolution(Not normally a whole number)
spr_int = floor(spr);    % Round number to nearest integer to zero
diff = spr - spr_int;    % Check difference
%
if  diff < 0.5           % Minimize error to nearest integer
    spr = spr_int;
else
    spr = spr_int + 1;   % (spr)Samples per revolution
end
%
% Specify data vector lengths according to number of cycles(n) desired
pres = data(spr:spr*n,1);
ppr = data(spr:spr*n,2);
ref = data(spr:spr*n,3);
exh = data(spr:spr*n,4);
%
%-------------------------------------------------------------------------%
%
%   Filters are applied to both the Cylinder pressure (pres) and the
%   Exhaust pressure (exh) entire vectors
%
%-------------------------------------------------------------------------%`
%
% Apply a Butterworth filter to the Cylinder pressure vector (pres)
[BB,A] = butter(4,0.014,'low');
pres = filtfilt(BB,A,pres);
%
% Apply a Butterworth filter to the Exhaust pressure vector (exh)
[BB,A] = butter(4,0.014,'low');
exh = filtfilt(BB,A,exh);
%
%-------------------------------------------------------------------------%
%
%   All 4 channels plotted
%
%-------------------------------------------------------------------------%
%
% Generate X-axis time vector
t = linspace(0,(1/sr)*length(pres),length(pres));
%
figure(2)
subplot(2,2,1)
plot(t,ppr,'b',t,pres,'r',t,ref,'k',t,exh,'c')
xlabel('Time [s]')
ylabel('Voltage [V]')
legend('720 ppr','Cylinder pressure','Reference pulse','Exhaust pressure')
title(sprintf('%d Revolutions of sampled data vs Time at %d rpm',n-1,rpm))
subplot(2,2,2)
plot(t,pres,'r')
xlabel('Time [s]')
ylabel('Voltage [V]')
title(sprintf('%d Cylinder pressure cycles vs Time at %d rpm',n-1,rpm))
```

```
subplot(2,2,3)
plot(t,ref,'k')
xlabel('Time [s]')
ylabel('Voltage [V]')
title(sprintf...
    ('%d Single reference pulses per revolution vs Time at %d rpm',...
    n-1,rpm))
subplot(2,2,4)
plot(t,exh,'c')
xlabel('Time [s]')
ylabel('Voltage [V]')
title(sprintf('%d Exhaust pressure cycles vs Time at %d rpm',n-1,rpm))
%
%--------------------------------------------------------------------------%
%
%   Construct matrix of Reference pulse data per cycle and plot
%
%--------------------------------------------------------------------------%
%
% n Revolutions as per Fig. 2 of the Reference pulse vector (ref)
% are peak picked and compiled into a matrix and all curves plotted
% on the same axis vs time.
%
% Display heading for Data curves printed on screen
disp(sprintf('\t\t\tYAMAHA DT 175 RECORDED DATA\n'))
%
% Allocate correct peak pick parameters to be used for a given engine speed
% ----- 6500 rpm
if rpm == 6500
    disp('6500 rpm Peak picking loop used')
    count = 1;
for a = 2:1:length(ref)
    if  ((ref(a) - ref(a-1)) / (t(a) - t(a-1))) > 15000 ...
            && ref(a-1) < 0.9 && ref(a) > 0.9;  % For poor Ref signal
%           && ref(a-1) < 2 && ref(a) > 2;
        index_p(count) = a; %#ok<AGROW>
        count = count + 1;
    end
end
%
% ----- 6000 rpm
elseif rpm == 6000
    disp('6000 rpm Peak picking loop used')
    count = 1;
for a = 2:1:length(ref)
    if  ((ref(a) - ref(a-1)) / (t(a) - t(a-1))) > 15000 ...
            && ref(a-1) < 1.5 && ref(a) > 1.5;
%           && ref(a-1) < 0.98 && ref(a) > 1.02;  % For poor Ref signal
        index_p(count) = a; %#ok<AGROW>
        count = count + 1;
    end
end
else
```

```
    % ----- Lower engine speeds than 6000rpm
    count = 1;
    disp('Lower engine speeds than 6000rpm Peak picking loop used')
for a = 2:1:length(ref)
    if  ((ref(a) - ref(a-1)) / (t(a) - t(a-1))) > 15000 ...
            && ref(a-1) < 2.0 && ref(a) > 2.0;
        index_p(count) = a; %#ok<AGROW>
        count = count + 1;
    end
end
end
%
% Create an index vector for the starting point of the next 720 ppr cycle
count = 1;
index_s = zeros(1,length(index_p)-1);   % Preallocation
for a = 1:1:length(index_p)-1
    index_s(count) = index_p(a) + 1;
    count = count + 1;
end
index_s = [1,index_s];
%
% Create initial zero matrix equivalent to size of longest data vector
index_z = index_p - index_s;
index_z = index_z + 1;
mat = zeros(max(index_z),length(index_p));  % Preallocation
%
% Generate matrix of each 720 ppr from data vector
for a = 1:length(index_p)
    count = 1;
    for b = index_s(a):index_p(a)
        mat(count,a) = ref(b);
        count = count + 1;
    end
end
%
% Plot all the TDC reference plots(ref_plot) over each other
% The correct length vectors are plotted, all artificial zeros excluded
mat_s = size(mat);
figure(3)
subplot(2,1,1)
hold on
for a = 1:1:mat_s(2)
    ref_plot = mat(:,a);
    plot(ref_plot(1:index_z(a)),'k')
end
xlabel('Number of sample points per single engine revolution')
ylabel('Voltage [V]')
title(sprintf...
('Reference pulse sample points for %d revolutions vs Voltage at %d rpm'...
,n-1,rpm))
hold off
%
% Index matrix data(index_data) and number of Reference pulses picked(rpp)
index_data = [index_s' index_p' index_z'];
size_rpp = size(index_z);
rpp = size_rpp(2);
```

```
%--------------------------------------------------------------------------%
%
%   Correct Reference, Start and Peak vectors
%
%--------------------------------------------------------------------------%
%
% The number of samples per revolution is calculated(spr)
% Set error bands for the Reference matrix column lengths
% Analysis of data showed that a ±3% error band is to be used, all data
% outside that band will be struck from the matrix
%
% Define error band
spr_lo = floor(spr * 0.97);
spr_hi = ceil(spr * 1.03);
count = 1;
counter = 1;
for a = 1:1:rpp
    if index_z(a) < spr_lo || index_z(a) > spr_hi
        index_error(counter) = a; %#ok<NASGU,AGROW>
        index_error_value(counter) = index_z(a); %#ok<AGROW>
        counter = counter + 1;
    else
        indexz(count) = index_z(a); %#ok<AGROW>
        indexp(count) = index_p(a); %#ok<AGROW>
        indexs(count) = index_s(a); %#ok<AGROW>
        count = count + 1;
    end
end
%
% Reference pulses kept(rpk) and Index matrix data(indexdata)
sizerpk = size(indexz);
rpk = sizerpk(2);
disp(sprintf...
('The number of cylinder pressure cycles kept is %d of %d imported',rpk,n))
indexdata = [indexs' indexp' indexz'];
disp(sprintf('\n Index start \t Index end \t String Length'))
disp(indexdata)
%
%--------------------------------------------------------------------------%
%
%   Re-construct matrix of Reference pulse data(matref) per cycle and plot
%
%--------------------------------------------------------------------------%
%
% Create initial zero matrix equivalent to size of longest data vector
matref = zeros(max(indexz),length(indexp)); % Preallocation
%
% Re-create correctly sized Reference matrix(matref)
for a = 1:1:rpk
    count = 1;
    for b = indexs(a):indexp(a)
        matref(count,a) = ref(b);
        count = count + 1;
    end
end
```

```
% Plot re-constructed Reference matrix(matref)
matref_s = size(matref);
subplot(2,1,2)
hold on
for a = 1:1:matref_s(2)
    ref_plot = matref(:,a);
    plot(ref_plot(1:indexz(a)),'k')
end
xlabel('Number of sample points per single engine revolution')
ylabel('Voltage [V]')
title(sprintf...
('Reconstructed Reference pulse for %d revolutions vs Voltage at %d rpm'...
,rpk,rpm))
hold off
%
%--------------------------------------------------------------------------%
%
%   Determine index start(indexs_ppr) for 720 Encoder pulse that
%   correlates to Reference trigger pulse
%
%--------------------------------------------------------------------------%
%
% Determine the locations of the peaks of the 720 ppr encoder signal(ppr)
% NOTE: This is the entire (ppr) signal and must still be discretized
l_indexp = length(indexp);
count = 1;
for a = indexs(1):1:indexp(l_indexp)
    if ppr(a) < 2 && ppr(a+1) > 2
        indexppr(count) = a; %#ok<AGROW>
        count = count + 1;
    end
end
%
% Link the Reference pulse starts(indexs) to the appropriate positions
% within the 720 ppr signal(indexs_ppr)
%
% NOTE: The first value of indexppr(1) must be equated to the first value
%       of indexs(1). The error within this assumption is negligible, one
%       index point at worst, as per the line below.
indexppr(1) = indexs(1);
%
a = 1;  % Initialize the vector counter for the 720 ppr vector
count = 1;
while count <= rpk  % Reference pulses kept(rpk)
    if indexppr(a) == indexs(count) ||...
            indexppr(a) < indexs(count) &&...
            indexppr(a + 1) > indexs(count)
        indexs_ppr_index(count) = indexppr(a); %#ok<AGROW>
        indexs_ppr(count) = a; %#ok<AGROW>
        a = a + 1;
        count = count + 1;
    else
        a = a + 1;
    end
end
```

```
% Compare starting index points for both the Reference and 720 ppr signals
index_error = indexs - indexs_ppr_index;
index_start = [indexs' indexs_ppr_index' index_error'];
disp(sprintf('\n Pulse index \t ppr Index \t spr Error'))
disp(index_start)
%
%--------------------------------------------------------------------------%
%
%   Construct matrices of:  1) Sample index points (matspr)
%                           2) ppr Voltage points (matppr)
%                           3) Cylinder pressure points (matpres) vs
%   720 pulse cycle (Single revolutions)
%                           4) Exhaust pressure points (matexh) vs
%   720 pulse cycle (Single revolutions)
%
%   Plot all Cylinder pressure traces and maximum Cylinder pressure trace
%
%--------------------------------------------------------------------------%
%
% Create initial zero matrix  - 720 rows by length(indexs_ppr)
matspr = zeros(720,length(indexs_ppr)); % Preallocation
matppr = zeros(720,length(indexs_ppr)); % Preallocation
matpres = zeros(720,length(indexs_ppr)); % Preallocation
matexh = zeros(720,length(indexs_ppr)); % Preallocation
%
% Create 720 pulse data matrices
a = 1;
b = 1;
count = 1;
while a <= length(indexs_ppr)
    if count <= 720
        matspr(count,a) = indexppr(b);
        matppr(count,a) = ppr(indexppr(b));
        matpres(count,a) = pres(indexppr(b));
        matexh(count,a) = exh(indexppr(b));
        count = count + 1;
        b = b + 1;
    else
        a = a + 1;
        if a <= length(indexs_ppr)
            b = indexs_ppr(a);
            count = 1;
        end
    end
end
%
% Plot for Pressure trace vs 720 Data points for a single engine revolution
figure(4)
subplot(2,1,1)
for a = 1:1:rpk
    matpres_plot = matpres(:,a);
    plot(matpres_plot,'k')
    hold on
end
xlim([0 720])
xlabel('720 Data points for a single engine revolution')
ylabel('Cylinder pressure in Volts [V]')
```

```
title(sprintf...
    ('Cylinder pressure vs a single revolution for %d cycles at %d rpm'...
    ,rpk,rpm))
hold off
%
% Determine the maximum pressure trace and plot
max_vector = max(matpres);
[pres_max,index_max] = max(max_vector);
disp(sprintf...
    ('\n Maximum pressure occurred during cycle number %d',index_max))
% disp(sprintf('\n Maximum pressure peak is %0.4f [V]',pres_max))
subplot(2,1,2)
plot(matpres(:,index_max),'k')
xlim([0 720])
xlabel('720 Sample points for a single engine revolution')
ylabel('Cylinder pressure in Volts [V]')
title(sprintf...
('Maximum Cylinder pressure vs a single revolution for cycle number %d at %d
rpm'...
,index_max,rpm))
%
%------------------------------------------------------------------------%
%
%   Apply Signal calibration factor (exh_cal) to the Exhaust pressure cycle
%   that corresponds with the Maximum Cylinder pressure cycle.
%   Calculate the mean (vecexh_mean) of the Maximum Exhaust pressure vector
%   (vecexh). Calculate the Exhaust correction factor (exh_cor) and correct
%   the Maximum Exhaust pressure (vecexh) by the factor.
%   Plot the applicable Exhaust pressure curves
%
%------------------------------------------------------------------------%
%
% Create Maximum Exhaust pressure vector
vecexh = matexh(:,index_max);   % [V]
%
% Apply Signal calibration factor (exh_cal) to Maximum Exhaust pressure
% (vecexh)
vecexh = exh_cal * vecexh;      % [bar]
%
% Calculate the Mean Exhaust pressure (vecexh_mean) of the Maximum Exhaust
% pressure vector (vecexh)
vecexh_mean = mean(vecexh);     % [bar]
%
% Plot of recorded Maximum exhaust pressure curve and the calculated
% Mean exhaust pressure trace
figure(5)
subplot(1,1,1)
plot(vecexh,'k:')
hold on
plot([0,720],[vecexh_mean,vecexh_mean],'c:')
hold on
%
% Extract the corresponding Mean recorded External Exhaust pressure
% (ext_exh) for the engine Rotational speed (rpm)
for a = 1:length(ext_exh)
    if rpm == ext_exh(a,1)
        ext_ref = a;
    end
end
```

```
% Calculate the Exhaust correction factor (exh_cor) that is to be added to
% the Maximum Exhaust pressure vector (vecexh)
if vecexh_mean < 0
    exh_cor = abs(vecexh_mean) + (ext_exh(ext_ref,2) / 1000);
else
    exh_cor = (ext_exh(ext_ref,2) / 1000) - vecexh_mean;
end
%
% Apply the Exhaust correction factor (exh_cor) to the Maximum Exhaust
% pressure (vecexh)
vecexh = exh_cor + vecexh;
%
% Plot of corrected Maximum exhaust pressure curve and measured
% Mean exhaust pressure trace
plot(vecexh,'b')
hold on
plot([0,720],[(ext_exh(ext_ref,2) / 1000),(ext_exh(ext_ref,2) / 1000)],'r')
axis([0 720 -0.6 0.8])
xlabel('720 Sample points for a single engine revolution')
ylabel('Exhaust pressure [bar]')
legend...
    ('Measured Exhaust pressure','Calculated Mean Exhaust pressure',...
    'Corrected Exhaust pressure','Measured Mean Exhaust pressure')
title(sprintf...
('Exhaust pressure vs Single engine revolution for cycle number %d at %d rpm'...
,index_max,rpm))
hold off
%
%--------------------------------------------------------------------------%
%
%   Apply Signal calibration factor to Maximum Cylinder pressure cycle.
%   Indicate Port timing events. Correct the signal drift that has occurred
%   in the Cylinder pressure cycle. Graph all three curves
%   (Include TDC indication)
%
%--------------------------------------------------------------------------%
%
% Create Maximum cylinder pressure vector
vecpres = matpres(:,index_max); % [V]
%
% Apply Signal calibration factor (sig_cal) to Maximum Cylinder pressure
% (vecpres)
vecpres = sig_cal * vecpres;    % [bar]
%
% Create degree vector from: BDC(-180°) through TDC(0°) to BDC(179.5°)
% NOTE: The Reference pulse is timed such that it occurs at BDC
deg_np = [-179.5:0.5:180]; %#ok<NBRAK>
%
% Indicate port timing events on Maximum cylinder pressure curve
% Index identification - (For both X and Y axes) - Valid to PV diagram to.
inx_ex_n = 360 - 2 * ex_port_o;
inx_ex_p = 360 + 2 * ex_port_o;
inx_tr_n = 360 - 2 * tr_port_o;
inx_tr_p = 360 + 2 * tr_port_o;
```

```
% Assign X-axis values in degrees to both Exhaust and Transfer port opening
% and closing
xpos_ex_n = deg_np(inx_ex_n);
xpos_ex_p = deg_np(inx_ex_p);
xpos_tr_n = deg_np(inx_tr_n);
xpos_tr_p = deg_np(inx_tr_p);
%
% Assign Y-axis values for the "line" plot command
ypos_ex_n = vecpres(inx_ex_n);
ypos_ex_p = vecpres(inx_ex_p);
ypos_tr_n = vecpres(inx_tr_n);
ypos_tr_p = vecpres(inx_tr_p);
%
% Preallocation of X and Y axis "line" vectors
xline_ex_n = ones(1,3);
xline_ex_p = ones(1,3);
xline_tr_n = ones(1,3);
xline_tr_p = ones(1,3);
yline_ex_n = ones(1,3);
yline_ex_p = ones(1,3);
yline_tr_n = ones(1,3);
yline_tr_p = ones(1,3);
%
% Create "line" plot command vector for X - axis position
for a = 1:3
    xline_ex_n(1,a) = xpos_ex_n;
    xline_ex_p(1,a) = xpos_ex_p;
    xline_tr_n(1,a) = xpos_tr_n;
    xline_tr_p(1,a) = xpos_tr_p;
end
%
% Create "line" plot command vectors for Y - axis position
for a = 1:3
    yline_ex_n(1,a) = ypos_ex_n;
    yline_ex_p(1,a) = ypos_ex_p;
    yline_tr_n(1,a) = ypos_tr_n;
    yline_tr_p(1,a) = ypos_tr_p;
end
%
delta = 2.5;
yline = delta .* [-1 0 1];       % Reference Vector
yline_ex_n = yline_ex_n + yline;
yline_ex_p = yline_ex_p + yline;
yline_tr_n = yline_tr_n + yline;
yline_tr_p = yline_tr_p + yline;
%
% Correct the signal drift that has occurred in the Cylinder pressure
% cycle using the corrected Exhaust pressure cycle (vecexh) as the
% reference signal, linking the two pressures at the point that the
% Transfer port closes
% NOTE: The slope of both the corrected Exhaust pressure and Cylinder
%       pressure cycle are nearly identical and coincident to one another
%       as the Transfer port opens
%
% Determine the pressures in both curves when EC(Exhaust port close) occurs
% Index point on the X-axis known from above section and used
vecpres_ec = vecpres(inx_tr_n);
vecexh_ec = vecexh(inx_tr_n);
```

```
% Code below written to accommodate positive and negative Cylinder pressure
% maxima
if vecpres_ec < 0
    pres_correct = abs(vecpres_ec) + vecexh_ec;
else
    pres_correct = -(vecpres_ec - vecexh_ec);
end
%
% Alter the entire Cylinder pressure curve (vecpres) by the (pres_correct)
% value
vecpres_correct = pres_correct + vecpres;
%
% Plot of Max Cylinder pressure and corrected curves, port events and TDC
figure(6)
subplot(1,1,1)
plot(deg_np,vecpres,'k',deg_np,vecexh,'r',...
    deg_np,vecpres_correct,'b',0,vecpres(360),'ro')
xlim([-180 180])
xlabel('Engine position representation in degrees [°]')
ylabel('Pressure [bar]')
legend...
    ('Measured Cylinder pressure','Corrected Exhaust pressure',...
    'Corrected Cylinder pressure')
title(sprintf...
('Cylinder and Exhaust pressure vs Single engine revolution for cycle number %d at
%d rpm'...
,index_max,rpm))
hold on
line(xline_ex_n,yline_ex_n,'color','r','linewidth',2)
text(xpos_ex_n,(ypos_ex_n + delta*1.2),'EC','horizontalalignment','center')
text(xpos_ex_n,(ypos_ex_n - delta*1.2),sprintf('-%d°',ex_port_o),...
    'horizontalalignment','center')
line(xline_ex_p,(-0.75 + yline_ex_p),'color','r','linewidth',2)
text(xpos_ex_p,(-0.75 + (ypos_ex_p + delta*1.2)),'EO',...
    'horizontalalignment','center')
text(xpos_ex_p,(-0.75 + (ypos_ex_p - delta*1.2)),sprintf('%d°',ex_port_o),...
    'horizontalalignment','center')
line(xline_tr_n,yline_tr_n,'color','b','linewidth',2)
text(xpos_tr_n,(ypos_tr_n + delta*1.2),'IC','horizontalalignment','center')
text(xpos_tr_n,(ypos_tr_n - delta*1.2),sprintf('-%d°',tr_port_o),...
    'horizontalalignment','center')
line(xline_tr_p,yline_tr_p,'color','b','linewidth',2)
text(xpos_tr_p,(ypos_tr_p + delta*1.2),'IO','horizontalalignment','center')
text(xpos_tr_p,(ypos_tr_p - delta*1.2),sprintf('%d°',tr_port_o),...
    'horizontalalignment','center')
text(-10,vecpres(360),'TDC')
hold off
%
%--------------------------------------------------------------------------%
%
%   The vectors of both the Maximum cylinder pressure (vecpres_correct) and
%   the Maximum Exhaust pressure (vecexh) are plotted on the same axis.
%   Figures of both the complete curves (Figure 7) and a magnified view
%   (Figure 8) is plotted
%
%--------------------------------------------------------------------------%
```

```
% Redundant filter code deleted and moved to Line 200 region above
vecpres_filter = vecpres_correct;
vecexh_filter = vecexh;
%
% Plot of filtered Cylinder and Exhaust pressure curves
figure(7)
subplot(1,1,1)
plot(deg_np,vecpres_filter,'k',deg_np,vecexh_filter,'r',...
    0,vecpres_filter(360),'ro')
xlim([-180 180])
xlabel('Engine position representation in degrees [°]')
ylabel('Pressure [bar]')
legend...
    ('Filtered Cylinder pressure','Filtered Exhaust pressure')
title(sprintf...
('Cylinder and Exhaust pressure vs Single engine revolution for cycle number %d at
%d rpm'...
,index_max,rpm))
hold on
yline_cor = pres_correct + yline_ex_n;
line(xline_ex_n,yline_cor,'color','r','linewidth',2)
ypos_cor = pres_correct + (ypos_ex_n + delta*1.2);
text(xpos_ex_n,ypos_cor,'EC','horizontalalignment','center')
ypos_cor = pres_correct + (ypos_ex_n - delta*1.2);
text(xpos_ex_n,ypos_cor,sprintf('-%d°',ex_port_o),...
    'horizontalalignment','center')
yline_cor = (pres_correct + yline_ex_p) - 1.75;
line(xline_ex_p,yline_cor,'color','r','linewidth',2)
ypos_cor = (pres_correct + (ypos_ex_p + delta*1.2)) - 1.75;
text(xpos_ex_p,ypos_cor,'EO','horizontalalignment','center')
ypos_cor = (pres_correct + (ypos_ex_p - delta*1.2)) - 1.75;
text(xpos_ex_p,ypos_cor,sprintf('%d°',ex_port_o),...
    'horizontalalignment','center')
yline_cor = pres_correct + yline_tr_n;
line(xline_tr_n,yline_cor,'color','b','linewidth',2)
ypos_cor = pres_correct + (ypos_tr_n + delta*1.2);
text(xpos_tr_n,ypos_cor,'IC','horizontalalignment','center')
ypos_cor = pres_correct + (ypos_tr_n - delta*1.2);
text(xpos_tr_n,ypos_cor,sprintf('-%d°',tr_port_o),...
    'horizontalalignment','center')
yline_cor = pres_correct + yline_tr_p;
line(xline_tr_p,yline_cor,'color','b','linewidth',2)
ypos_cor = pres_correct + (ypos_tr_p + delta*1.2);
text(xpos_tr_p,ypos_cor,'IO','horizontalalignment','center')
ypos_cor = pres_correct + (ypos_tr_p - delta*1.2);
text(xpos_tr_p,ypos_cor,sprintf('%d°',tr_port_o),...
    'horizontalalignment','center')
text(-10,vecpres_filter(360),'TDC')
hold off
%
% Plot of filtered Cylinder and Exhaust pressure curves magnified
figure(8)
subplot(1,1,1)
plot(deg_np,vecpres_filter,'k',deg_np,vecexh_filter,'r',...
    0,vecpres_filter(360),'ro')
axis([-180 180 -0.6 1.2])
xlabel('Engine position representation in degrees [°]')
ylabel('Pressure [bar]')
```

```
legend...
    ('Filtered Cylinder pressure','Filtered Exhaust pressure')
title(sprintf...
('Cylinder and Exhaust pressure vs Single engine revolution for cycle number %d at
%d rpm'...
,index_max,rpm))
hold on
yline_cor = 2 * (pres_correct + yline_ex_n);
line(xline_ex_n,yline_cor,'color','r','linewidth',2)
text((xpos_ex_n - 5),(-0.26),'EC','horizontalalignment','center')
text((xpos_ex_n - 5),(-0.34),sprintf('-%d°',ex_port_o),...
    'horizontalalignment','center')
yline_cor = 2 * (-pres_correct + yline_ex_p);
line(xline_ex_p,yline_cor,'color','r','linewidth',2)
text((xpos_ex_p - 5),(-0.26),'EO','horizontalalignment','center')
text((xpos_ex_p - 5),(-0.34),sprintf('%d°',ex_port_o),...
    'horizontalalignment','center')
yline_cor = 2 * (pres_correct + yline_tr_n);
line(xline_tr_n,yline_cor,'color','b','linewidth',2)
text((xpos_tr_n - 5),(-0.26),'IC','horizontalalignment','center')
text((xpos_tr_n - 5),(-0.34),sprintf('-%d°',tr_port_o),...
    'horizontalalignment','center')
yline_cor = 2 * (pres_correct + yline_tr_p);
line(xline_tr_p,yline_cor,'color','b','linewidth',2)
text((xpos_tr_p - 5),(-0.26),'IO','horizontalalignment','center')
text((xpos_tr_p - 5),(-0.34),sprintf('%d°',tr_port_o),...
    'horizontalalignment','center')
text(-20,vecpres(360),'TDC')
hold off
%
%--------------------------------------------------------------------------%
%
%   Construct Pressure/Volume(PV) diagram for maximum pressure cycle.
%   Indicate port timing.
%
%--------------------------------------------------------------------------%
%
% Create degree vector from: BDC(180°) - (0.5°)TDC(0°) - BDC(179.5°)
% NOTE: The Reference pulse is timed such that it occurs at BDC(0°)
deg1 = 179.5:-0.5:0;
deg2 = 0.5:0.5:180;
deg = [deg1 deg2];
%
% Indicate port timing events on Corrected and Filtered
% cylinder pressure curve
%
% NOTE: Index and X - Axis position assignment has been completed in
% previous section and still relevant
%
% Assign Y-axis values for the "line" plot command
ypos_ex_n = vecpres_filter(inx_ex_n);
ypos_ex_p = vecpres_filter(inx_ex_p);
ypos_tr_n = vecpres_filter(inx_tr_n);
ypos_tr_p = vecpres_filter(inx_tr_p);
```

```
% Create "line" plot command vector for X - axis position
for a = 1:4
    xline_ex_p(1:a) = xpos_ex_p;
    xline_tr_p(1:a) = xpos_tr_p;
end
%
% Preallocation of Y - axis "line' vectors
yline_ex_p = ones(1,4);
yline_tr_p = ones(1,4);
%
% Enter "line" plot values for the lower "negative" curve for Y - axis
for a = 1:2
    yline_ex_p(1,a) = ypos_ex_n;
    yline_tr_p(1,a) = ypos_tr_n;
end
%
% Enter "line" plot values for the upper "positive" curve for Y - axis
for a = 3:4
    yline_ex_p(1,a) = ypos_ex_p;
    yline_tr_p(1,a) = ypos_tr_p;
end
%
% Extend "line" for Y - axis at the bottom and top of the line
delta = 0.5;
yline = delta .* [-1 0 0 1];       % Reference Vector
yline_ex_p = yline_ex_p + yline;
yline_tr_p = yline_tr_p + yline;
%
% Plot Pressure(vecpres) vs Degrees(deg)
figure(9)
subplot(1,1,1)
plot(deg,vecpres_filter,'k')
axis([-10 190 -1 42.5])
xlabel('Engine position representation in degrees [°]')
ylabel('Cylinder pressure [bar]')
title(sprintf...
('Cylinder pressure trace vs Single engine revolution for cycle number %d'...
,index_max))
hold on
line(xline_ex_p,yline_ex_p,'color','r','linewidth',2)
text(xpos_ex_p,(ypos_ex_p * 1.5),'EO','horizontalalignment','center')
line(xline_tr_p,yline_tr_p,'color','b','linewidth',2)
text(xpos_tr_p,(ypos_tr_p * 2.5),'IO','horizontalalignment','center')
%
% Maximum Pressure peak
disp(sprintf('Maximum pressure peak: %2.2f bar',(pres_max*sig_cal...
    + pres_correct)))
%
%-------------------------------------------------------------------------%
%
%   Calculate the Indicated work done during compression (W_comp),
%   expansion (W_exp) and sum the resultant indicated work (W_i).
%   Calculate the Indicated power (P_i) and Indicated mean torque (Tm_i)
%   Ref: Internal Combustion Engine Fundamentals - J.B. Heywood
%   Chapter 2 - Section 2.4 (Pg 46 to 48)
%
%-------------------------------------------------------------------------%
```

```
% The procedure is documented below:
%   Break the Pressure vector into Compression and Expansion sections and
%   integrate both curves separately over the swept volume, then subtract
%   the Compression curve area from the Expansion curve area. Divide the
%   Work obtained per cycle by the time period required to complete a
%   single engine revolution to obtain Indicated power.
%   Also plot the resultant PV diagram.
%
% Create Crank angle vector 360 elements long, representing 0 to 180
% degrees in both (deg) and (rad)
deg = 0.5:0.5:180;
rad = ((2*pi)/360) * deg;
%
%- Calculated Inputs ----------------------------------------------------%
%
% Convert the input engine values to meters [m]
B = B / 1000;           % [m]
L = L / 1000;           % [m]
l = l / 1000;           % [m]
%
% Crank radius (a)
a = L / 2;              % [m]
%
% Ratio of Connecting rod length to Crank radius
R = l / a;
%
% Area of piston (Ap)
Ap = (pi/4) * B^2;      % [m^2]
%
% Displaced volume (Vd)
Vd = Ap * L;            % [m^3]
%
% Calculate both the Clearance volume (Vc) and Total volume (Vt) in [m^3]
Vc = Vc / 1e6;          % [m^3]
Vt = Vd + Vc;           % [m^3]
%
%-------------------------------------------------------------------------%
%
% Distance between Crank axis and Piston pin axis vs Crank pin angle
s = a * (1 + R - cos(rad) - sqrt(R.^2 - (sin(rad)).^2));        % [m]
%
% Create the Swept Volume vector (Vs) as a function of Crank angle (rad)
Vs = Vc + Ap * s;                   % [m^3]
%
% Convert the loaded Pressure curve from [bar] to [Pa]
Pv = 101325 * vecpres_filter;       % [Pa]
%
% Break the loaded Pressure data curve (vecpres_filter) into the
% Compression stroke (Pcomp) and the Expansion stroke (Pexp) sections
Pexp = Pv(361:720);                 % [Pa]
Pcomp_mirror = Pv(1:360);           % [Pa]
% The Compression data curve (Pcomp) however has to be mirrored to allow
% for integration between the correct limits, a PV diagram
Pcomp = Pcomp_mirror(360:-1:1);     % [Pa]
%
% Display heading for Engine performance printed on screen
disp(sprintf('\n\t\t\tYAMAHA DT 175 ENGINE PERFORMANCE'))
```

```
% Engine operational speed
disp(sprintf('\nEngine operational speed: %d rpm',rpm))
%
% Engine throttle position
disp(sprintf('Engine throttle setting: %d %%',wot))
%
% Integrate both the Compression stroke (Pcomp) and the Expansion stroke
% (Pexp) over the Swept Volume vector (Vs)
W_comp = trapz(Vs,Pcomp);           % [J]
W_exp = trapz(Vs,Pexp);             % [J]
disp(sprintf...
    ('Work done per cycle during compression stroke: %2.2f J',W_comp))
disp(sprintf...
    ('Work done per cycle during expansion stroke: %3.2f J',W_exp))
disp(sprintf...
    ('Compression vs Expansion stroke percentage work done: %2.2f %%',...
    (W_comp/W_exp)*100))
%
% Subtract the Compression area from the Expansion area and obtain Work
% done per cycle (W_i)
W_i = W_exp - W_comp;               % [J]
disp(sprintf('Indicated work per cycle: %3.2f J',W_i))
%
% The Indicated Power (P_i) and Mean indicated torque (Tm_i)
rps = rpm / 60;                     % [rps]
P_i = (W_i / (1/rps)) / 1000;       % [kW]
disp(sprintf('Indicated power for engine: %2.1f kW',P_i))
%
Tm_i = W_i/(2*pi);                  % [Nm]
disp(sprintf('Mean indicated torque for engine: %2.1f Nm',Tm_i))
%
% Plot the PV diagram and indicate the TDC and BDC regions
figure(10)
subplot(1,1,1)
plot(Vs,Pcomp,'k',Vs,Pexp,'k')
axis([0 (max(Vs)+Vc) (min(Pcomp)-25e3) (max(Pexp)+250e3)])
xlabel('Volume [m^3]')
ylabel('Cylinder pressure [Pa]')
title('PV diagram')
line([Vc Vc],[(min(Pcomp)-25e3) 0.1e6],'color','r','linewidth',2)
text(Vc,0.2e6,'TDC','horizontalalignment','center')
line([Vt Vt],[(min(Pcomp)-25e3) 0.1e6],'color','r','linewidth',2)
text(Vt,0.2e6,'BDC','horizontalalignment','center')
%
%--------------------------------------------------------------------------%
%
%   log P vs log V diagram
%   Ref: Internal Combustion Engine Fundamentals - J.B. Heywood
%   Chapter 9 - Section 9.2.2 (Pg 384))
%
%--------------------------------------------------------------------------%
%
% Create log based vectors of both the Swept volume vector (Vs) and the
% Compression (Pcomp) and Expansion pressure vectors (Pexp)
Vs_log = log10(Vs);
Pc_log = log10(Pcomp);
Pe_log = log10(Pexp);
```

```
% Plot log P vs log V
figure(11)
subplot(1,1,1)
plot(Vs_log,Pc_log,'k',Vs_log,Pe_log,'k')
xlabel('Volume')
ylabel('Cylinder pressure')
title('log P vs log V plot')
%
%--------------------------------------------------------------------------%
%
%   Save final filtered cylinder pressure curve (vecpres_filter) and the
%   related crank angle position (deg_np) to be used in determination of
%   maximum force on the bigend and crankshaft bearings. Also export the
%   engine rotational speed of the experiment (rpm) and throttle setting
%   (wot)
%
%--------------------------------------------------------------------------%
%
save prescurve deg_np vecpres_filter rpm wot
%
%--------------------------------------------------------------------------%
%
%   Export selected values to Excel
%
%--------------------------------------------------------------------------%
%
% Identify the rotational test speed of the engine and select the cells
% that are to be populated in Excel
if rpm == 3000
    cell1 = 'C4';
    cell2 = 'C8';
elseif rpm == 3500
    cell1 = 'D4';
    cell2 = 'D8';
elseif rpm == 4000
    cell1 = 'E4';
    cell2 = 'E8';
elseif rpm == 4500
    cell1 = 'F4';
    cell2 = 'F8';
elseif rpm == 5000
    cell1 = 'G4';
    cell2 = 'G8';
elseif rpm == 5500
    cell1 = 'H4';
    cell2 = 'H8';
elseif rpm == 6000
    cell1 = 'I4';
    cell2 = 'I8';
elseif rpm == 6500
    cell1 = 'J4';
    cell2 = 'J8';
end
```

```
% Specify the data that is to be entered into the above stipulated cells
xlswrite('Boxer Maxima.xlsx',wot,'Imported',cell1);
xlswrite('Boxer Maxima.xlsx',(pres_max * sig_cal + pres_correct),...
    'Imported',cell2);
%
%-------------------------------------------------------------------------%
%
tictoc = toc;
disp(sprintf('\n Elapsed time for program run is %0.2f seconds',tictoc))
```

G.2 CALCULATE UAV ENGINE DESIGN PARAMETERS

```
% Engine forces due to engine geometry and combustion pressures
% Engine Performance predictions calculated
% UAV 390cc, Twin Boxer, Two-stroke engine
% Edited: 07 Apr 2015 (12 October 2012)
%
close all
clear all
clc
%
tic
%
%--------------------------------------------------------------------------%
%
%   Required Inputs
%
%--------------------------------------------------------------------------%
%
% Display heading for the general data that is to be printed on screen
disp(sprintf('\t\t\tBOXER ENGINE DATA'))
%
% Number of cylinders
n = 2;
disp(sprintf('\nNumber of cylinders: %d',n))
%
% Bore
B = 66;          % [mm]
disp(sprintf('Bore: %d mm',B))
%
% Stroke
L = 57;          % [mm]
disp(sprintf('Stroke: %d mm',L))
%
% Clearance volume
% Assume the same Geometric Compression ratio (rcg) as the DT 175 of: 10.59
% Clearance volume (Vc) = (Vd) / (rcg - 1) = 20.33 [ml]
Vc = 20.33;      % [ml]
%
% Piston data required:
% 1. Diameter of Piston pin (dp)
% 2. Mass of Piston only (mp)
% 3. Mass of all Piston rings (mpr)
% 4. Mass of both Piston circlips (mpc)
% 5. Mass of Piston pin (mpp)
% 6. Mass of Small end needle bearing (mse)
dp = 16;         % [mm]
mp = 192.98;     % [g]
mpr = 8.06;      % [g]
mpc = 0.56;      % [g]
mpp = 44.97;     % [g]
mse = 18.07;     % [g]
%
% Connecting rod data required:
% 1. Length between centers (l)
% 2. Distance of C of G from Big end center. Measured value (CG)
% 3. Mass without needle roller bearings inserted in either end (mcr)
```

```
l = 110;          % [mm]
CG = 45;          % [mm]
mcr = 139.77;     % [g]
disp(sprintf('Connecting rod length: %d mm',l))
%
% Crankshaft data required:
% 1. Crankpin diameter (d)
% 2. Crankshaft inertia about rotation axis (Jc)
% 3. Mass of crankshaft assembly only (mc)
% 4. Mass of a Connecting rod washer (mw)
% 5. Mass of Big end needle bearing (mbe)
% 6. Propeller inertia for beech wood 32" with a mass of 618g (Jprop)
d = 22;               % [mm]
Jc = 2.815e-3;        % [kgm²]
mc = 3063.8;          % [g]
mw = 5.46;            % [g]
mbe = 21.97;          % [g]
Jprop = 24.31e-3;     % [kgm²]
%
% Load the Maximum Pressure data curve obtained experimentally
% NOTE: 1 - The data curve runs BDC (-179.5°) to BDC (180°)
%       2 - This curve has been passed through a 'low pass' filter
%           (vecpres_filter)
%       3 - The speed at which the test was conducted is also loaded (rpm)
%       4 - The throttle setting for the test (wot)
load ('C:\Documents and Settings\Marcel\My Documents\MATLAB\Masters - Matlab\01 -
UAV - Kistler\prescurve')
% load ('C:\Users\Marcel Mobile\Documents\MATLAB\Masters-Mat\Cylinder Pressure -
09,10-11-2011\Pressure Plot - 21-03-2012\prescurve')
%
% Maximum allowable rotational engine speed
% NOTE: This speed is NOT used to calculate Piston vel. & acc.
N_max = 7000;  % [rpm]
%
%--------------------------------------------------------------------------%
%
%   Calculated Inputs
%   Outputs of selected calculated items stated
%
%--------------------------------------------------------------------------%
%
% Engine capacity (Vdt)
Vd = (pi/4 * (B/1000)^2 * L/1000);      % [m³]
Vdt = (n * Vd) * 1e6;                   % [cc]
disp(sprintf('Engine capacity: %3.2f cc',Vdt))
%
% Geometric Compression ratio (rcg)
Vdcc = Vd * 1e6;                        % [cc]
rcg = (Vdcc + Vc) / Vc;
disp(sprintf('Geometric compression ratio: %2.2f',rcg))
%
% Ratio of Bore to Stroke
Rbs = B/L;
disp(sprintf('Ratio of Bore to Stroke: %1.2f',Rbs))
%
% Crank pin radius
a = L/2;                    % [mm]
disp(sprintf('Crank pin radius: %2.2f mm',a))
```

```
% Ratio of Connecting rod to Crank radius
R = l/a;
disp(sprintf('Ratio of Connecting rod length to Crank radius: %3.2f',R))
%
% Calculate oscillating (ms) and rotating (mb) masses for Connecting rod
mb = (l - CG)/l * mcr;      % [g]
ms = CG/l * mcr;            % [g]
% Percentage mass of total mass of Connecting rod assign to oscillating
% (po) and rotating (pr) masses
po = ms / mcr * 100;        % [%]
pr = mb / mcr * 100;        % [%]
disp(sprintf...
('Percentage of Conrod mass assigned as an oscillating mass %2.2f %%',po))
disp(sprintf...
('Percentage of Conrod mass assigned as a rotating mass %2.2f %%',pr))
%
% Calculate total mass of reciprocating/oscillating (mo) components
mo = mp + mpr + mpc + mpp + mse + ms;       % [g]
disp(sprintf...
('Total mass of reciprocating components per cylinder: %3.2f g',mo))
%
% Calculate total mass of rotating (mr) components
mr = mc + ((2*mw + mbe + mb) * n);          % [g]
disp(sprintf('Total mass of rotating components: %4.2f g',mr))
%
% Imported engine speed in rad/s
rpm_rad = (2*pi*rpm) / 60;          %#ok<USENS> [rad/s]
%
% Maximum allowable engine speed in rad/s
N_max_rad = (2*pi*N_max) / 60;      % [rad/s]
%
%--------------------------------------------------------------------------%
%
%   Calculation of Displacement (s), Velocity (vp) and Acceleration (ap)
%   of Piston vs Crank angle. Plot curves and display maximums.
%   Ref: Theory of Machines - W.G. Green - Section 1 & 2 (Pg 315 - 319)
%   Mean Piston speed at maximum engine speed is also calculated
%
%--------------------------------------------------------------------------%
%
% Create Crank angle vector 720 elements long (deg) and (rad)
deg = 0.5:0.5:360;
rad = ((2*pi)/360) * deg;
%
% State the engine test speed (rpm) and throttle setting (wot) for results
disp(sprintf...
('\nNOTE: All data below recorded at %d rpm and %d %% throttle setting',...
rpm,wot)) %#ok<USENS>
%
% Display heading for Piston data that is to be printed on screen
disp(sprintf('\n\t\t\tPISTON DATA'))
%
% Distance moved from TDC by Piston vs Crank pin angle [mm]
s = a * (1 + R - cos(rad) - sqrt(R.^2 - (sin(rad)).^2));
[s_max,s_max_index] = max(s);
disp(sprintf...
    ('\nMax. Piston displacement is %2.2f mm at a Crank angle of %g°',...
    s_max,(s_max_index/2)))         % NOTE: Crank index is divided by 2
```

```
% Engine speed at which Max Piston Velocity and Acceleration is calculated
disp(sprintf...
    ('Piston vel. and acc. calculated at loaded engine speed of %g rpm',...
    rpm))
%
% Velocity of Piston pin (vp) vs Crank pin angle at loaded speed [m/s]
vp = (rpm_rad * (a/1000)) .* (sin(rad) + ((sin(rad) .* cos(rad)) ./ ...
    (sqrt(R^2 - (sin(rad)).^2))));
[vp_max,vp_max_index] = max(vp);
disp(sprintf...
    ('Max. Piston velocity is %2.2f m/s at a Crank angle of %g°',...
    vp_max,(vp_max_index/2)))       % NOTE: Crank index is divided by 2
%
% Acceleration of Piston pin (ap) vs Crank angle at loaded speed [km/s²]
ap = (rpm_rad^2 .* (a/1000) .* (cos(rad) + ((R^2 .* cos(2.*rad) + ...
     (sin(rad).^4)) ./ ((R^2 - (sin(rad)).^2).^(3/2))))) / 1000;
[ap_max,ap_max_index] = max(ap);
disp(sprintf...
    ('Max. Piston acceleration is %2.2f km/s² at a Crank angle of %g°',...
    ap_max,(ap_max_index/2)))           % NOTE: Crank index is divided by 2
%
% Plots of displacement, velocity and acceleration of piston
figure(1)
subplot(1,1,1)
plot(deg,s,'k',deg,vp,'b',deg,ap,'r')
axis([0 360 -40 90])
grid on
xlabel('Crank angle [°]')
ylabel('Displacement [mm], Velocity [m/s], Acceleration [km/s²] of Piston')
legend('Displacement','Velocity','Acceleration')
title(sprintf...
('Displacement, Velocity & Acceleration of Piston at %d rpm vs Crank angle'...
,rpm))
xline = [0.5 360];
yline = [0 0];
line(xline,yline,'color','k','linewidth',1.0)
%
%--------------------------------------------------------------------------%
%
%   Connecting rod angle (cra) and Angular velocity (crav) vs Crank angle
%   (deg).
%   Ref: Theory of Machines - W.G. Green - Section 3 (Pg 320)
%   The Rubbing velocity at the crank pin (vr) vs Crank angle (deg) and
%   plot results.
%   Ref: Theory of Machines - W.G. Green - Section 17 (Pg 349)
%
%--------------------------------------------------------------------------%
%
% Display heading for Connecting rod data that is to be printed on screen
disp(sprintf('\n\t\t\tCONNECTING ROD DATA'))
%
% Connecting rod Angle (cra) vs Crankshaft pin angle (deg)
cra_rad = asin((a * sin(rad)) / l);             % Rod angle in radians
cra = asin((a * sin(rad)) / l) * (180 / pi);    % From radians to degrees
[cra_max,cra_max_index] = max(cra);
disp(sprintf...
    ('\nMax. Connecting rod angle is %2.2f° at a Crank angle of %g°',...
    cra_max,(cra_max_index/2)))     % NOTE: Crank index is divided by 2
```

```
% Connecting rod Angular velocity (crav) vs Crankshaft pin angle (deg)
crav = (rpm_rad * cos(rad)) ./ (sqrt(R^2 - (sin(rad)).^2)); % [rad/s]
[crav_max,crav_max_index] = max(crav);
disp(sprintf...
('Max. Conrod angular velocity is %2.2f rad/s at a Crank angle of %g°',...
crav_max,(crav_max_index/2)))   % NOTE: Crank index is divided by 2
%
% Calculate the Rubbing velocity at the piston pin (vrp) vs Crank angle
% (deg)
vrp = crav * dp/(2 * 1000);         % [m/s]
[vrp_max,vrp_max_index] = max(vrp);
disp(sprintf...
('Max. Rubbing velocity at piston pin is %2.2f m/s at a Crank angle of %g°',...
vrp_max,(vrp_max_index/2)))     % NOTE: Crank index is divided by 2
%
% Calculate the Relative angular velocity of crank and conrod (rav) and the
% Rubbing velocity at the crank pin (vr) vs Crank angle (deg)
rav = rpm_rad + crav;               % [rad/s]
vr = rav * d/(2 * 1000);            % [m/s]
%
[vr_max,vr_max_index] = max(vr);
disp(sprintf...
('Max. Rubbing velocity at crank pin is %2.2f m/s at a Crank angle of %g°',...
vr_max,(vr_max_index/2)))     % NOTE: Crank index is divided by 2
%
% Plots of Relative angular velocity (rav) and Rubbing velocity (vr) vs.
% Crank angle (deg)
figure(2)
subplot(2,1,1)
plot([0.5 360],[rpm_rad rpm_rad],'b',deg,rav,'k')
axis([0 360 min(rav)-50 max(rav)+50])
xlabel('Crank angle [°]')
ylabel('Angular velocity [rad/s]')
title('Crankshaft and Relative Angular velocity of conrod. vs Crank angle')
legend('Crankshaft','Connecting rod')
%
subplot(2,1,2)
plot(deg,vr,'k',deg,vrp,'b',[0 360],[0 0 ],'k')
axis([0 360 min(vrp)-1 max(vr)+1])
xlabel('Crank angle [°]')
ylabel('Rubbing velocity [m/s]')
title...
('Rubbing velocity on Crank pin and Piston pin surfaces vs Crank angle')
legend('Crank pin','Piston pin')
%
%-------------------------------------------------------------------------%
%
%   Moment arm (CF) and Pin displacement (CF_disp) at any Crank angle (deg)
%   Ref: Theory of Machines - W.G. Green - Section 4 (Pg 321)
%
%-------------------------------------------------------------------------%
%
% Create initial zero vector  - 720 elements (CF)
CF = zeros(1,720);  % Preallocation

% Iterate through crank angle (deg) for a full rotation consisting of 720
% points while calculating Moment arm (CF) in [mm] using 3 specified
% conditions
```

```
count = 1;
for deg = 0.5:0.5:360
    if deg <= 90                % 0 to 90 degrees
        rad = ((2*pi)/360) * deg; %#ok<NASGU>
        CF(count) = (l + a - s(count)) * tan(cra_rad(count));
        % CF(count) = (l + a - s(count)) * tan(asin((1/R)*sin(rad))); %#ok<AGROW>
    elseif deg <= 270           % 90 to 270 degrees
        rad = ((2*pi)/360) * deg;
        CF(count) = (l + a - s(count)) * ((a * sin(pi - rad)) / ...
            ((l + a - s(count)) + (a * cos(pi - rad))));
    else                        % 270 to 360 degrees
        rad = ((2*pi)/360) * deg; %#ok<NASGU>
        CF(count) = (l + a - s(count)) * tan(cra_rad(count));
        % CF(count) = (l + a - s(count)) * tan(asin((1/R)*sin(rad))); %#ok<AGROW>
    end
    count = count + 1;
end
%
% Maximum Moment arm and corresponding Crank angle
[CF_max,deg_CF_max] = max(CF);
disp(sprintf('Max. Moment arm is %2.2f mm at a Crank angle of %g°',...
CF_max,(deg_CF_max/2)))         % NOTE: Crank index is divided by 2
%
% Re-create crank angle vector (deg) and in Radians (rad)
deg = 0.5:0.5:360;
rad = ((2*pi)/360) * deg;
%
% Construct a displacement curve of the Crank pin when viewed from above
CF_disp = a .* sin(rad);        % [mm]
%
% Plot the Moment arm(CF) & Pin displacement(CF_dsip) vs Crank angle (deg)
figure(3)
subplot(1,1,1)
plot(deg,CF,'k',deg,CF_disp,'b')
axis([0 360 -35 35])
grid on
xlabel('Crank angle [°]')
ylabel('Moment arm [mm], Crank Pin displacement [mm]')
legend('Moment arm','Pin displacement')
title('Crankshaft Moment arm and Crank Pin displacement vs Crank angle')
%
%--------------------------------------------------------------------------%
%
%   Using imported Pressure data (vecpres_filter), rearrange Pressure
%   curve (p) for TDC (0°) to TDC (360°) display and plot.
%
%--------------------------------------------------------------------------%
%
% Plot the loaded data as received: Pressure curve vs. Engine position
figure(4)
subplot(2,1,1)
plot(deg_np,vecpres_filter,'k',0,vecpres_filter(360),'ro')
axis([-180 180 -2.5 42.5])
xlabel('Engine position representation in degrees [°]')
ylabel('Cylinder pressure [bar]')
```

```
title(sprintf...
    ('Cylinder pressure data at %d rpm as loaded vs Single revolution',...
    rpm))
text(-17.5,vecpres_filter(360),'TDC')
%
% Rearrange the Pressure curve data vector (vecpres_filter) so that:
%   1 - The last 360 vector points (0.5°:180°) appear first (0.5°:180°)
%   2 - The first 360 vector points (-179.5°:0°) appear last (180.5°:360°)
p = zeros(1,720);           % Preallocation
p(1:360) = vecpres_filter(361:720);
p(361:720) = vecpres_filter(1:360);
%
% Plot the rearranged Pressure curve (p) vs. Engine position (deg)
subplot(2,1,2)
plot(deg,p,'k',180,p(360),'ro')
axis([0 360 -2.5 42.5])
xlabel('Engine position representation in degrees [°]')
ylabel('Cylinder pressure [bar]')
title(sprintf('Cylinder pressure at %d rpm vs Single revolution',rpm))
text(175,2.5,'BDC')
%
%-------------------------------------------------------------------------%
%
%   Calculate Piston crown area (Ap). Then determine the Gross Force on the
%   piston (Fg), the Inertia Force (Fi) to accelerate the reciprocating
%   mass and then calculate the Nett Force or Piston Effort (P).
%   Display maxima and plot single and combined curves.
%   Ref: Theory of Machines - W.G. Green - Section 4 (Pg 321) and Section 5
%   (Pg 323)
%
%-------------------------------------------------------------------------%
%
% Display heading for Piston and Conrod forces that is to be printed on
% screen
disp(sprintf('\n\t\t\tPISTON AND CONNECTING ROD FORCES'))
%
% Calculate Piston crown area (Ap)
Ap = pi/4 * (B/1000)^2;         % [m²]
%
% Calculate Gross Force (Fg) on the Piston crown area (Ap). The Gross Force
% in [Newton] is converted to [kg] for a more "tangible feel" of results
Fg = p * 101325/1 * Ap;         % [N]
Fg_kg = Fg / 9.81;              % [kg]
% The maximum is obtained and displayed in both N and kg
[Fg_max,Fg_max_index] = max(Fg);
[Fg_kg_max,Fg_kg_max_index] = max(Fg_kg);
disp(sprintf...
('\nMax. Gross Force on piston is %4.2f kg at a Crank angle of %3.1f°',...
Fg_kg_max,(Fg_kg_max_index/2))) % NOTE: Crank index is divided by 2
%
% Calculate Inertia Force (Fi) due to total reciprocating mass (mo)
% NOTE: A negative sign is a prefix, true to the equation
Fi = -(mo/1000) * (ap*1000);    % [N]
Fi_kg = Fi / 9.81;              % [kg]
% The maximum is obtained and displayed in both N and kg
[Fi_max,Fi_max_index] = max(abs(Fi));
[Fi_kg_max,Fi_kg_max_index] = max(abs(Fi_kg));
```

```
disp(sprintf...
('Max. Inertia Force on piston is %3.2f kg at a Crank angle of %3.1f°',...
Fi_kg_max,(Fi_kg_max_index/2))) % NOTE: Crank index is divided by 2
%
% Calculate the Piston Effort (P)
% NOTE: The negative sign due to (Fi) is already present in the vector
P = Fg + Fi;                    % [N]
P_kg = P / 9.81;                % [kg]
% The maximum is obtained and displayed in both N and kg
[P_max,P_max_index] = max(P);
[P_kg_max,P_kg_max_index] = max(P_kg);
disp(sprintf...
('Max. Piston Effort is %3.2f kg at a Crank angle of %3.1f°',...
P_kg_max,(P_kg_max_index/2)))   % NOTE: Crank index is divided by 2
%
% The maximum (Fg) and (Fi) when Piston Effort (P) is highest
Fg_max_at_P = Fg(P_max_index);
Fi_max_at_P = abs(Fi(P_max_index));
%
% Plot the Gross Force (Fg), Inertia Force (Fi) and Piston Effort (P) in
% "kg"
figure(5)
subplot(3,1,1)
plot(deg,Fg_kg,'b')
axis([0 360 (min(Fg_kg)-50) (max(Fg_kg)+50)])
xlabel('Engine position representation in degrees [°]')
ylabel('Gross Force [kg]')
title(sprintf('Gross Force on piston at %d rpm vs Single revolution',rpm))
%
subplot(3,1,2)
plot(deg,Fi_kg,'r')
axis([0 360 (min(Fi_kg)-50) (max(Fi_kg)+50)])
xlabel('Engine position representation in degrees [°]')
ylabel('Inertia Force [kg]')
title(sprintf...
('Inertia Force of reciprocating mass at %d rpm vs Single revolution',rpm))
xline = [0.5 360];
yline = [0 0];
line(xline,yline,'color','k','linewidth',1.0)
%
subplot(3,1,3)
plot(deg,P_kg,'k')
axis([0 360 (min(P_kg)-50) (max(P_kg)+50)])
xlabel('Engine position representation in degrees [°]')
ylabel('Piston Effort [kg]')
title(sprintf('Piston Effort at %d rpm vs Single revolution',rpm))
xline = [0.5 360];
yline = [0 0];
line(xline,yline,'color','k','linewidth',1.0)
%
% Plot the Gross Force (Fg), Inertia Force (Fi) and Piston Effort (P) in
% "kg" on the same graph
figure(6)
subplot(1,1,1)
plot(deg,Fg_kg,'b',deg,Fi_kg,'r',deg,P_kg,'k')
axis([0 360 (min(Fi_kg)-50) (max(Fg_kg)+50)])
xlabel('Engine position representation in degrees [°]')
ylabel('Force [kg]')
```

```
title(sprintf...
('Gross / Inertia Force and Piston Effort at %d rpm vs Single revolution'...
,rpm))
legend('Gross Force','Inertia Force','Piston Effort')
xline = [0.5 360];
yline = [0 0];
line(xline,yline,'color','k','linewidth',1.0)
%
%--------------------------------------------------------------------------%
%
%   Calculate the Connecting rod loads (Q) and the Piston side loads (N),
%   using the Piston Effort (P) as the reference force.
%   Plot the resultant curves.
%   Ref: Theory of Machines - W.G. Green - Section 4 (Pg 321)
%
%--------------------------------------------------------------------------%
%
% Calculate the Connecting rod load (Q)
Q = P ./ (cos(cra_rad));        % [N]
Q_kg = Q / 9.81;                % [kg]
% The maximum is obtained and displayed in both N and kg
[Q_max,Q_max_index] = max(Q);
[Q_kg_max,Q_kg_max_index] = max(Q_kg);
disp(sprintf...
    ('Max. Force on Conrod is %3.2f kg at a Crank angle of %3.1f°',...
    Q_kg_max,(Q_kg_max_index/2))) % NOTE: Crank index is divided by 2
%
% Calculate the Piston side load (N)
N = Q .* sin(cra_rad);          % [N]
N_kg = N / 9.81;                % [kg]
% The maximum is obtained and displayed in both N and kg
[N_piston_max,N_max_index] = max(N);
[N_kg_max,N_kg_max_index] = max(N_kg);
disp(sprintf...
    ('Max. Piston side load is %2.2f kg at a Crank angle of %3.1f°',...
    N_kg_max,(N_kg_max_index/2))) % NOTE: Crank index is divided by 2
%
% The maximum Piston side load (N) when Piston effort (P) is highest
N_max_at_P = N(P_max_index);
%
% Plot the Piston side load (N) and Piston effort (P) in "kg", same plot
figure(7)
subplot(1,1,1)
plot(deg,N_kg,'r',deg,P_kg,'b',[0.5 360],[0 0],'k')
axis([0 360 min(P_kg)-50 max(P_kg)+50 ])
xlabel('Engine position representation in degrees [°]')
ylabel('Load [kg]')
title(sprintf...
('Piston side load & Piston effort at %d rpm vs Single revolution',rpm))
legend('Piston side load','Piston effort')
%
% Plot the Connecting rod load (Q) and Piston effort (P) in "kg", same plot
figure(8)
subplot(1,1,1)
plot(deg,Q_kg,'r',deg,P_kg,'b',[0.5 360],[0 0],'k')
axis([0 360 min(Q_kg)-50 max(Q_kg)+50 ])
xlabel('Engine position representation in degrees [°]')
ylabel('Load [kg]')
```

```
title(sprintf...
('Connecting rod load & Piston effort at %d rpm vs Single revolution',rpm))
legend('Connecting rod load','Piston effort')
%
%--------------------------------------------------------------------------%
%
%   Calculate the Gross torque (Tg), Inertia torque (Ti), Nett
%   torque (T) and Mean Indicated torque (Tm) on the crankshaft shaft.
%   Display maxima and plot a single plot indicating all curves.
%   Ref: Theory of Machines - W.G. Green - Section 6 (Pg 325)
%
%--------------------------------------------------------------------------%
%
% Display heading for Crank Moments that is to be printed on screen
disp(sprintf('\n\t\t\tCRANK TORQUE AND SPEED VARIATIONS'))
%
% Calculate Gross torque (Tg) on the crankshaft
Tg = Fg .* (CF./1000);              % [Nm]
% The maximum is obtained and displayed
[Tg_max,Tg_max_index] = max(Tg);
disp(sprintf...
('\nMax. Gross Torque per cyl. is %3.2f Nm at a Crank angle of %3.1f°',...
Tg_max,(Tg_max_index/2))) % NOTE: Crank index is divided by 2
%
% Calculate Inertia torque (Ti) on the crankshaft
Ti = Fi .* (CF./1000);              % [Nm]
% The maximum is obtained and displayed
[Ti_max,Ti_max_index] = max(Ti);
disp(sprintf...
('Max. Inertia Torque per cyl. is %3.2f Nm at a Crank angle of %3.1f°',...
Ti_max,(Ti_max_index/2))) % NOTE: Crank index is divided by 2
%
% Calculate Nett indicated torque (T) on the crankshaft
T = P .* (CF./1000);                % [Nm]
% The maximum is obtained and displayed
[T_max,T_max_index] = max(T);
disp(sprintf...
('Max. Nett Torque per cyl. is %3.2f Nm at a Crank angle of %3.1f°',...
T_max,(T_max_index/2))) % NOTE: Crank index is divided by 2
%
% Calculate the Mean indicated torque (Tm)
Tm = mean(T);
disp(sprintf('Mean Indicated Torque per cyl. is %2.2f Nm',Tm))
%
% Plot the Gross Torque (Tg), Inertia Torque (Ti), Nett Torque (T) and
% Mean Torque (Tm) on the same graph
figure(9)
subplot(1,1,1)
plot(deg,Tg,'b',deg,Ti,'r',deg,T,'k',[0 360],[Tm Tm],'g')
axis([0 360 (min(Ti)-10) (max(Tg)+10)])
xlabel('Engine position representation in degrees [°]')
ylabel('Torque [Nm]')
title(sprintf...
('Gross / Inertia / Nett / Mean Torque per cylinder at %d rpm vs Single
revolution'...
,rpm))
```

```
legend('Gross Torque','Inertia Torque','Nett Torque','Mean Torque')
xline = [0.5 360];
yline = [0 0];
line(xline,yline,'color','k','linewidth',1)
%
%--------------------------------------------------------------------------%
%
%   Calculate the fluctuation of speed (w2) & (w1) that accompanies the
%   variation in turning moment (T) on the crankshaft. NOTE: The
%   approximate method is used - Section 12 (Pg 337)
%   Ref: Theory of Machines - W.G. Green - Section 11 & 12 (Pg 335)
%
%--------------------------------------------------------------------------%
%
% The Nett Torque curve (T) and Mean Torque curve (Tm) values per cylinder
% must be modified to reflect the number of cylinders
% NOTE: The Crankshaft fluctuation of speed calculation is only valid for
%       an engine where all the cylinders fire simultaneously
T = n * T;          % [Nm]
Tm = n * Tm;        % [Nm]
%
% Determine the intercept index points when the Nett Torque curve (T)
% intercepts the Mean Torque curve (Tm)
count = 1;
for x = 1:(720 - 1)
    if T(x) < Tm && T(x+1) > Tm || T(x) > Tm && T(x+1) < Tm
        index(count) = x; %#ok<AGROW>
        count = count + 1;
        index(count) = x; %#ok<AGROW>
        count = count + 1;
    end
end
index = [1 index 720];
l_index = length(index);
%
% Change the offset of the Nett torque (T) curve by subtracting the Mean
% torque (Tm) from the former and plotting the results. This then allows
% the easy integration of the Nett torque (T) above and below the zero line
T_red = T - Tm;
%
% Plot the Redefined Nett torque curve (T_red) vs. Crank angle (deg)
figure(10)
subplot(1,1,1)
plot(deg,T_red,'b',[0 360],[0 0],'k')
axis([0 360 (min(T_red) - 10) (max(T_red) + 10)])
xlabel('Engine position representation in degrees [°]')
ylabel('Torque [Nm]')
title(sprintf...
    ('Redefined Nett Torque curve at %d rpm vs Single revolution'...
    ,rpm))
%
% Create a matrix (mat) for all the areas of the Redefined Nett torque
% curve (T_red) above and below the zero. Also create the corresponding
% X-axis matrix (Mat_rad) in radians.
```

```
c = 1;
for x = 1:(l_index / 2)
    count = 1;
    for y = index(c):index(c + 1)
        mat(count,x) = T_red(y); %#ok<AGROW>
        mat_rad(count,x) = rad(y); %#ok<AGROW>
        l_mat(x) = count; %#ok<AGROW>
        count = count + 1;
    end
    c = c + 2;
end
%
% Calculate the areas above and below the curve using "trapz". Then add the
% first and last enteries in the resultant vector to each other, since both
% linked as an area under the Mean torque.
for x = 1:length(l_mat)
    Int(x) = trapz(mat_rad(1:l_mat(x),x),mat(1:l_mat(x),x)); %#ok<AGROW>
end
I = Int(2:length(l_mat));
I_zero = zeros(1,(length(l_mat)-1));
I_zero(1,(length(l_mat)-1)) = Int(1,1);
I = I + I_zero;
%
% Identify the maximum area above or under the curve (I)
[I_max,I_max_index] = max(abs(I));
%
% Identify the angles within (mat_rad) where the minimum and maximum
% rotational speed occurs, ie. The first (I_index1) and last (I_index2)
% entry of the appropriate column within (mat_rad).
I_index1 = mat_rad(1,(I_max_index + 1));
I_index2 = mat_rad(l_mat(I_max_index + 1),(I_max_index + 1));
I_index = [I_index1 I_index2];
I_index = I_index * (360 / (2*pi));
%
% Calculate the total rotational inertia (Jr) of the Crankshaft.
% This comprises:
% 1. Inertia of balanced Crankshaft for boxer twin (Jc)
% 2. Inertia due to rotating masses at the Crankpin centers (a):
%       2.1 Mass of Connecting rod washers (mw)
%       2.2 Mass of Big end needle bearing (mbe)
%       2.3 Rotating mass contribution of Connecting rod (mb)
% 3. Inertia of 32" wooden propeller was added (Jprop)
Jr = Jc + (((2*mw/1000 + mbe/1000 + mb/1000) * n) * (a/1000)^2) +...
     Jprop;   % [kgm²]
%
% Calculate the rotational speed difference (w) in [rpm]. Then determine
% the maximum and minimum rotational speeds achieved (w2) and (w1). Lastly
% calculate the percentage change in mean speed (p_change)
w = (I_max) / (Jr * rpm_rad) * (60 / (2*pi));
w2 = rpm + w/2;                    % [rpm]
w1 = rpm - w/2;                    % [rpm]
p_change = ((w/2) / rpm) * 100;
%
% The maxima are obtained and displayed and the percentage change with a
% disclaimer
disp...
('NOTE: Values below only valid for all cylinders firing simultaneously')
```

```
disp(sprintf...
('Max. speed of the crankshaft is %4.1f rpm at a Crank angle of %3.1f°',...
w2,I_index(2)))
disp(sprintf...
('Min. speed of the crankshaft is %4.1f rpm at a Crank angle of %3.1f°',...
w1,I_index(1)))
disp(sprintf...
('Percentage variation in rotational speed of %d rpm is approximately %2.1f%%',...
rpm,p_change))
%
%-------------------------------------------------------------------------%
%
%   Engine performance predictions
%   Numerous aspects of the predicted engine performace are calculated and
%   some aspects are calculated speculation
%
%-------------------------------------------------------------------------%
%
% Display heading for Engine performace predictions, printed on screen
disp(sprintf('\n\t\t\tENGINE PERFORMANCE PREDICTIONS'))
%
% Engine operational speed
disp(sprintf('\nEngine operational speed: %d rpm',rpm))
%
% Engine throttle position
disp(sprintf('Engine throttle setting: %d %%',wot))
%
% Mean piston speed (vp_mean) at engine operating speed in [m/s]
vp_mean = 2 * L/1000 * rpm/60;
disp(sprintf...
    ('Mean Piston speed is %2.2f m/s at %g rpm',vp_mean,rpm))
%
% Mean piston speed (vp_mmax) at maximum engine operating speed in [m/s]
vp_mmax = 2 * L/1000 * N_max/60;
disp(sprintf...
    ('Mean Piston speed is %2.2f m/s at %g rpm limit',vp_mmax,N_max))
%
%-------------------------------------------------------------------------%
%
%   Calculate the Indicated work done during compression (W_comp),
%   expansion (W_exp) and sum the resultant indicated work (W_i).
%   Calculate the Indicated power (P_i) and Indicated mean torque (Tm_i)
%   Ref: Internal Combustion Engine Fundamentals - J.B. Heywood
%   Chapter 2 - Section 2.4 (Pg 46 to 48)
%
%-------------------------------------------------------------------------%
%
% The procedure is documented below:
%   Break the Pressure vector into Compression and Expansion sections and
%   integrate both curves seperately over the swept volume, then subtract
%   the Compression curve area from the Expansion curve area. Divide the
%   Work obtained per cycle by the time period required to complete a
%   single engine revolution to obtain Indicated power.
%   Also plot the resultant PV diagram.
%
% Create Crank angle vector 360 elements long, representing 0 to 180
% degrees in both (deg) and (rad)
```

```
deg = 0.5:0.5:180;
rad = ((2*pi)/360) * deg;
%
% Distance between Crank axis and Piston pin axis vs Crank pin angle
s = (a/1000) * (1 + R - cos(rad) - sqrt(R.^2 - (sin(rad)).^2));     % [m]
%
% Calculate both the Clearance volume (Vc) and Total volume (Vt) in [m^3]
% Create the Swept Volume vector (Vs) as a function of Crank angle (rad)
Vc = Vc / 1e6;          % [m^3]
Vt = Vd + Vc;           % [m^3]
Vs = Vc + Ap * s;       % [m^3]
%
% Convert the loaded Pressure curve from [bar] to [Pa]
Pv = 101325 * vecpres_filter;       % [Pa]
%
% Break the loaded Pressure data curve (vecpres_filter) into the
% Compression stroke (Pcomp) and the Expansion stroke (Pexp) sections
Pexp = Pv(361:720);                 % [Pa]
Pcomp_mirror = Pv(1:360);           % [Pa]
% The Compression data curve (Pcomp) however has to be mirrored to allow
% for integration between the correct limits, a PV diagram
Pcomp = Pcomp_mirror(360:-1:1);     % [Pa]
%
% Integrate both the Compression stroke (Pcomp) and the Expansion stroke
% (Pexp) over the Swept Volume vector (Vs)
W_comp = trapz(Vs,Pcomp);           % [J]
W_exp = trapz(Vs,Pexp);             % [J]
disp(sprintf...
('Work done per cycle during compression stroke per cylinder: %2.2f J',...
W_comp))
disp(sprintf...
('Work done per cycle during expansion stroke per cylinder: %3.2f J',...
W_exp))
disp(sprintf...
('Compression vs Expansion stroke percentage work done: %2.2f %%',...
(W_comp/W_exp)*100))
%
% Subtract the Compression area from the Expansion area and obtain Work
% done per cycle (W_i)
W_i = W_exp - W_comp;                   % [J]
disp(sprintf('Indicated work per cycle per cylinder: %3.2f J',W_i))
%
% The Indicated Power (P_i) and Mean indicated torque (Tm_i) for entire
% engine
rps = rpm / 60;                         % [rps]
P_i = n * ((W_i / (1/rps)) / 1000);     % [kW]
disp(sprintf('Indicated power for %d cylinder engine: %2.1f kW',n,P_i))
%
Tm_i = n * (W_i/(2*pi));                % [Nm]
disp(sprintf('Mean indicated torque for %d cylinder engine: %2.1f Nm',...
n,Tm_i))
%
% Plot the PV diagram and indicate the TDC and BDC regions
figure(11)
subplot(1,1,1)
plot(Vs,Pcomp,'k',Vs,Pexp,'k')
axis([0 (max(Vs)+Vc) 0 (max(Pexp)+250e3)])
xlabel('Volume [m^3]')
ylabel('Cylinder pressure [Pa]')
```

```
title('PV diagram')
line([Vc Vc],[0 0.1e6],'color','r','linewidth',2)
text(Vc,0.2e6,'TDC','horizontalalignment','center')
line([Vt Vt],[0 0.1e6],'color','r','linewidth',2)
text(Vt,0.2e6,'BDC','horizontalalignment','center')
%
%--------------------------------------------------------------------------%
%
%   Calculate the Brake power by subtracting experimentally obtained
%   Friction power values from the corresponding Indicated power value
%   Ref: Internal Combustion Engine Fundamentals - J.B. Heywood
%   Chapter 2 - Section 2.5 (Pg 48 to 49)
%
%--------------------------------------------------------------------------%
%
% Friction matrix indicating rotational speed and associsted Friction power
% loss for Yamaha DT 175 while motored through chain drive and gearbox
Fmat = [2000    0.5         % [rpm] [kW]
        2500    0.55
        3000    0.65
        3500    0.85
        4000    0.95
        4500    0.9
        5000    1.1
        5500    1.35
        6000    1.45
        6500    1.7
        7000    1.6];
%
% Assumed Yamaha DT 175 gearbox and chain drive combined efficiency
eff = 0.85;                 % 85%
%
% Adapt the Friction power column in (Fmat) by the stated efficiency
% multiplier (eff)
Fvec = Fmat(:,2) * eff;
%
% Recreated the Speed and Friction matrix with the adapted values (Fvec)
Feffmat = zeros(11,2);      % Preallocation
for x = 1:11
    Feffmat(x,1) = Fmat(x);
    Feffmat(x,2) = Fvec(x);
end
%
% Identify the Friction power (P_f) for the engine operating speed (rpm)
for x = 1:11
    if rpm == Feffmat(x,1)
        ref = x;
    end
end
%
% Additional Friction linear scaling factor related to cylinder
% displacement when compared to the Yamaha DT 175cc
scale = Vd / 1.7106e-004;
%
% Total Friction power
P_f = Feffmat(ref,2);                           % [kW]
P_f = scale * P_f ;                             % [kW]
disp(sprintf('Friction power for %d cylinder engine: %2.1f kW',n,(2*P_f)))
```

```
% Calculate the estimated Brake power (P_b) and Mean brake torque (Tm_b)
P_b = P_i - (n * P_f);                          % [kW]
disp(sprintf('Brake power for %d cylinder engine: %2.1f kW',n,P_b))
Tm_b = (P_b * 1000 * 60) / (2 * pi * rpm);      % [Nm]
disp(sprintf('Mean brake torque for %d cylinder engine: %2.1f Nm',...
n,Tm_b))
%
%--------------------------------------------------------------------------%
%
%   Calculate the Mechanical efficiency (nm) and the Brake mean effective
%   pressure (bmep)
%   Ref: Internal Combustion Engine Fundamentals - J.B. Heywood
%   Chapter 2 - Section 2.5 (Pg 49) and Section 2.7 (Pg 50)
%
%--------------------------------------------------------------------------%
%
% Mechanical efficiency (nm)
nm = (P_b / P_i) * 100;                         % [%]
disp(sprintf('Mechanical efficiency: %2.1f %%',nm))
%
% Brake mean effective pressure (bmep)
bmep = ((P_b*1000) / (2 * Vd * rps)) / 101325;  % [bar]
disp(sprintf('Brake mean effective pressure: %2.1f bar',bmep))
%
%--------------------------------------------------------------------------%
%
%   Save variables required for balancing of the crankshaft (balvar)
%   Save variables required for crankshaft and crankcase forces
%   (boxfor)
%   Save variables required for bearing calculation (bearfor)
%
%--------------------------------------------------------------------------%
%
save balvar a mb rpm rpm_rad mp mpr mpc mpp mse ms mo R
%
save boxfor n rpm wot a l s Fg Fg_kg Fg_kg_max Fg_kg_max_index Q Q_kg...
            Q_kg_max Q_kg_max_index N N_kg N_kg_max N_kg_max_index
%
save bearfor rpm wot a l Q
%
%--------------------------------------------------------------------------%
%
%   Export selected values to Excel
%
%--------------------------------------------------------------------------%
%
% Identify the rotational test speed of the engine and select the cells
% that are to be populated in Excel
if rpm == 3000
    cell1 = 'D9';
    cell2 = 'D49';
elseif rpm == 3500
    cell1 = 'E9';
    cell2 = 'E49';
elseif rpm == 4000
    cell1 = 'F9';
    cell2 = 'F49';
```

```
elseif rpm == 4500
    cell1 = 'G9';
    cell2 = 'G49';
elseif rpm == 5000
    cell1 = 'H9';
    cell2 = 'H49';
elseif rpm == 5500
    cell1 = 'I9';
    cell2 = 'I49';
elseif rpm == 6000
    cell1 = 'J9';
    cell2 = 'J49';
elseif rpm == 6500
    cell1 = 'K9';
    cell2 = 'K49';
end
%
% Generate the matrix (Exmat1) that is to be exported to Excel to display
% "Boxer Engine Data"
Exmat1 = [vp_max;(vp_max_index/2);(ap_max*1000);(ap_max_index/2);...
     crav_max;(crav_max_index/2);vr_max;(vr_max_index/2);...
     vrp_max;(vrp_max_index/2);P_max;(P_max_index/2);Fg_max;...
     (Fg_max_index/2);Fg_max_at_P;Fi_max;(Fi_max_index/2);Fi_max_at_P;...
     Q_max;(Q_max_index/2);N_piston_max;(N_max_index/2);N_max_at_P;...
     T_max;(T_max_index/2);Tg_max;(Tg_max_index/2);Ti_max;...
     (Ti_max_index/2);(Tm/2);W_i;W_exp;W_comp;((W_comp/W_exp)*100);...
     w2;I_index(2);w1;I_index(1);p_change];
%
% Generate the matrix (Exmat2) that is to be exported to Excel to display
% "Engine Performance Predictions"
Exmat2 = [Tm_i;Tm_b;P_i;(n * P_f);P_b;vp_mean;bmep;nm];
%
% Export the data in (Exmat1) and (Exmat2) that is to be imported into
% Excel
xlswrite('Boxer Maxima.xlsx',Exmat1,'Imported',cell1);
xlswrite('Boxer Maxima.xlsx',Exmat2,'Imported',cell2);
%
%--------------------------------------------------------------------------%
%
tictoc = toc;
disp(sprintf('\n Elapsed time for program run is %0.3f seconds',tictoc))
```

G.3 ROTATING AND RECIPROCATING BALANCE

```
% Engine Balancing
% UAV 390cc, Twin Boxer, Two-stroke engine
% 03 October 2012
%
close all
clear all
clc
%
tic
%
%-------------------------------------------------------------------------%
%
%   Required Inputs
%
%-------------------------------------------------------------------------%
%
% Crankshaft dimensions - Reference plane on Bearing 1:
% 1. Length: Reference plane to Counterweight 1
% 2. Length: Reference plane to Cylinder 1
% 3. Length: Reference plane to Cylinder 2
% 4. Length: Reference plane to Counterweight 2
% 5. Length: Reference plane to Bearing 2
l1 = 21.05;          % [mm]
l2 = 36.5;           % [mm]
l3 = 74.25;          % [mm]
l4 = 89.70;          % [mm]
l5 = 110.75;         % [mm]
%
% Crankshaft radii and weights:
% 1. Radius from axis to C.G of Counterweight
% 2. Mass of Counterweight
% 3. Mass of single Connecting rod washer
% 4. Mass of Big end needle bearing
rc = 16.81;          % [mm]
mc = 149.81;         % [g]
mw = 5.46;           % [g]
mbe = 21.97;         % [g]
%
% Removable Crankpin data:
% 1. Length: Crankpin
% 2. Length: Crankpin exposed
% 3. Mass of Crankpin
lcp = 56.5;          % [mm]
lcpe = 19.5;         % [mm]
mcp = 131.16;        % [g]
%
% Crankshaft angles:
% 1. Crankshaft angle (rad)
%   Create Crank angle vector 720 elements long (rad) and (deg)
% 2. Crankpin fixed angle (ph) - Phi
deg = 0.5:0.5:360;           % [rad]
rad = ((2*pi)/360) * deg;    % [deg]
ph = 0;                      % [rad]
```

```
% Load the required variables:
% 1. Crankpin radius (a) in [mm]
% 2. Rotating mass (mb) for Connecting rod in [g]
% 3. Crankshaft rotational speed (rpm) in [rpm]
% 4. Crankshaft rotational speed (rpm_rad) in [rad/s]
% 5. Mass of Piston (mp) in [g]
% 6. Mass of Piston rings (mpr) in [g]
% 7. Mass of Piston circlips (mpc) in [g]
% 8. Mass of Piston pin (mpp) in [g]
% 9. Mass of Small end needle bearing (mse) in [g]
% 10. Oscillating mass of Connecting rod (ms) in [g]
% 11. Total mass of reciprocating components (mo) in [g]
% 12. Ratio of Bore to Stroke (R)
load ('C:\Documents and Settings\Marcel\My Documents\MATLAB\Masters - Matlab\01 -
UAV - Kistler\Matlab - Report\balvar')

%-------------------------------------------------------------------------%
%
%   Calculated Inputs
%
%-------------------------------------------------------------------------%
%
% Mass of "Crankpin exposed"
mcpe = (lcpe/lcp) * mcp;            % [g]
%
% Rotating mass total (mr)
mr = mb + 2*mw + mbe + mcpe;        % [g]
%
%-------------------------------------------------------------------------%
%
%   Crankshaft balance - Static and Dynamic balance
%   Ref: Theory of Machines - W.G. Green - Section 1 & 2 (Pg 372 - 377)
%
%-------------------------------------------------------------------------%
%
% Static balance
sb = (rpm_rad)^2 * ((mc/1000 * rc/1000) - (mr/1000 * a/1000) + ...
    (mr/1000 * a/1000) - (mc/1000 * rc/1000));      % [N]
%
% Dynamic balance
db = (rpm_rad)^2 * (-(mc/1000 * rc/1000 * l1/1000) + ...
    (mr/1000 * a/1000 * l2/1000) - (mr/1000 * a/1000 * l3/1000) + ...
    (mc/1000 * rc/1000 * l4/1000));                 % [Nm]
%
% Display heading for the general data that is to be printed on screen
disp(sprintf('\t\t\tBALANCING OF COMPONENTS\n'))
%
disp(sprintf...
    ('All forces and couples calculated at an engine speed of %g rpm',rpm))
%
% Display heading for the general data that is to be printed on screen
disp(sprintf('\n\t\t\tROTATING COMPONENTS\n'))
%
% Display Static and Dynamic balance outcome
disp(sprintf('Static balance resultant force is %3.2f N',sb))
disp(sprintf('Dynamic balance resultant couple is %3.2f Nm',db))
% Display rotating and the counterweight masses
disp(sprintf('Mass of the rotating parts each are %3.2f g',mr))
disp(sprintf('Mass of the Crankshaft counterweights each are %3.2f g',mc))
```

```
% Approximate Dynamic balance of counterweight
mcapprox = ((mr/1000 * a/1000 * (l2 - l3)) / ((l1 - l4) * rc/1000)) * 1000;
if mc > mcapprox
    mchange = ((mc - mcapprox) / mc) * 100;
    disp(sprintf...
('Reduce the counterweight mass by approximately %3.1f %% to %3.1f g',...
mchange,mcapprox))
else
    mchange = ((mcapprox - mc) / mcapprox) * 100;
    disp(sprintf...
('Increase the counterweight mass by approximately %3.1f %% to %3.1f g',...
mchange,mcapprox))
end
%
%-------------------------------------------------------------------------%
%
%   Engine balance - Primary and Secondary forces
%   Ref: Mechanisms & dynamics of machinery - Mabie - Section 10.6 to 10.9
%   (Pg 516 - 533)
%
%-------------------------------------------------------------------------%
%
% Primary forces - Left bank
Fpl = (mo/1000 * a/1000 * rpm_rad^2) * ...
    (cos(rad) * cos(ph) - sin(rad) * sin(ph));                    % [N]
% Primary forces - Right bank
Fpr = (mo/1000 * a/1000 * rpm_rad^2) * ...
    (cos(rad) * cos(ph) - sin(rad) * sin(ph));                    % [N]
% Primary forces summation and maximum
Fp = Fpl - Fpr;                                                   % [N]
Fpmax = max(Fp);
%
% Secondary forces - Left bank
Fsl = (mo/1000 * a/1000 * rpm_rad^2 * 1/R) * ...
    (cos(2*rad) * cos(2*ph) - sin(2*rad) * sin(2*ph));            % [N]
% Secondary forces - Right bank
Fsr = (mo/1000 * a/1000 * rpm_rad^2 * 1/R) * ...
    (cos(2*rad) * cos(2*ph) - sin(2*rad) * sin(2*ph));            % [N]
% Secondary forces summation and maximum
Fs = Fsl - Fsr;                                                   % [N]
Fsmax = max(Fs);
%
% Primary and Secondary force summation and maximum
F = Fp + Fs;                                                      % [N]
Fmax = max(F);
%
% Display heading for the general data that is to be printed on screen
disp(sprintf('\n\t\t\tRECIPROCATING COMPONENTS\n'))
%
% Display reciprocating masses
disp(sprintf('Mass of the reciprocating parts are %3.2f g',mo))
%
% Display Primary, Secondary and Summation forces
disp(sprintf('Maximum Primary force is %3.2f N',Fpmax))
disp(sprintf('Maximum Secondary force is %3.2f N',Fsmax))
disp(sprintf('Maximum Summation force is %3.2f N',Fmax))
```

```
% Figures of Primary, Secondary and Summation forces
figure(1)
subplot(1,1,1)
plot(deg,Fp,'b',deg,Fs,'r',deg,F,'k')
axis([0 360 -10 10 ])
xlabel('Engine position representation in degrees [°]')
ylabel('Force [N]')
title(sprintf...
('Primary, Secondary and Summation Forces at %d rpm vs Single revolution'...
,rpm))
legend('Primary','Secondary','Summation')
line([180 180],[-10 10],'color','k','linewidth',1.0,'linestyle',':')
%
%--------------------------------------------------------------------------%
%
%   Engine balance - Primary and Secondary couples
%   Ref: Mechanisms & dynamics of machinery - Mabie - Section 10.6 to 10.9
%   (Pg 516 - 533)
%
%--------------------------------------------------------------------------%
%
% Primary couples
% NOTE: Reference plane is Cylinder 1, thus only Cylinder 2 has a couple
Cp = (mo/1000 * a/1000 * rpm_rad^2) * ...
    (cos(rad) * (l3-l2)/1000 * cos(ph) - ...
    sin(rad) * (l3-l2)/1000 * sin(ph));                          % [Nm]
[Cpmax,Cpmax_index] = max(abs(Cp));
%
% Secondary couples
Cs = (mo/1000 * a/1000 * rpm_rad^2 * 1/R) * ...
    (cos(2*rad) * (l3-l2)/1000 * cos(2*ph) - ...
    sin(2*rad) * (l3-l2)/1000 * sin(2*ph));                      % [Nm]
[Csmax,Csmax_index] = max(abs(Cs));
%
% Primary and Secondary couple summation
C = Cp + Cs;                                                     % [Nm]
[Cmax,Cmax_index] = max(abs(C));
%
% Display Primary, Secondary and Summation couples
disp(sprintf...
    ('Maximum Primary couple is %3.2f Nm at a crank angle of %g°',...
    Cpmax,Cpmax_index/2))
disp(sprintf...
    ('Maximum Secondary couple is %3.2f Nm at a crank angle of %g°',...
    Csmax,Csmax_index/2))
disp(sprintf...
    ('Maximum Summation couple is %3.2f Nm at a crank angle of %g°',...
    Cmax,Cmax_index/2))

% Figures of Primary, Secondary and Summation couples
figure(2)
subplot(1,1,1)
plot(deg,Cp,'b',deg,Cs,'r',deg,C,'k')
axis([0 360 -175 175])
xlabel('Crankshaft angular position [°]')
ylabel('Couple [Nm]')
```

```
title(sprintf...
('Primary, Secondary and Summation Couples at %d rpm vs Single revolution'...
,rpm))
legend('Primary','Secondary','Resultant')
line([0 360],[0 0],'color','k','linewidth',1.0,'linestyle',':')
line([180 180],[-200 200],'color','k','linewidth',1.0,'linestyle',':')
%
%--------------------------------------------------------------------------%
%
%   Save variables required for forces and couples imposed on boxer engine
%   (boxbal)
%   Save variables required for bearing calculation (beardis)
%
%--------------------------------------------------------------------------%
%
save boxbal l2 l3 l5 C Cmax Cmax_index
%
save beardis l2 l3 l5 C
%
%--------------------------------------------------------------------------%
%
%   Export selected values to Excel
%
%--------------------------------------------------------------------------%
%
% Identify the rotational test speed of the engine and select the cells
% that are to be populated in Excel
if rpm == 3000
    cell = 'C41';
elseif rpm == 3500
    cell = 'D41';
elseif rpm == 4000
    cell = 'E41';
elseif rpm == 4500
    cell = 'F41';
elseif rpm == 5000
    cell = 'G41';
elseif rpm == 5500
    cell = 'H41';
elseif rpm == 6000
    cell = 'I41';
elseif rpm == 6500
    cell = 'J41';
end
%
% Generate the matrix (Exmat) that is to be exported to Excel to display
% "Balancing of Boxer"
Exmat = [Cmax;Cmax_index/2];
%
% Export the data in (Exmat) that is to be imported into Excel
xlswrite('Boxer Maxima.xlsx',Exmat,'Imported',cell);
%
%--------------------------------------------------------------------------%
%
tictoc = toc;
disp(sprintf('\n Elapsed time for program run is %0.3f seconds',tictoc))
```

G.4 EXPERIMENTAL ENGINE FORCES AND COUPLES

```
% Engine crankcase and crankshaft forces
% UAV 390cc, Boxer twin, Two-stroke engine
% 10 October 2012
%
close all
clear all
clc
%
tic
%
%--------------------------------------------------------------------------%
%
%   Required Inputs
%
%--------------------------------------------------------------------------%
%
% Fastener details:
% 1. Number of bolts on Cylinder lower flange (bcy)
% 2. Number of Crankcase seam bolts (bcr)
bcy = 4;
bcr = 8;
%
% Load the required variables from {Combustion Forces}:
% 1. Number of cylinders (n)
% 2. Connecting rod length between centers (l) in [mm]
% 3. Engine rotational test speed (rpm) in [rpm]
% 4. Throttle setting for test (wot) in [%]
% 5. Crank pin radius (a) in [mm]
% 6. Distance moved from TDC by piston (s) vs Crank pin angle (rad) in [mm]
% 7. Gross force on piston crown (Fg) in [N]
% 8. Gross force on piston crown (Fg_kg)in [kg]
% 9. Maximum gross force on piston crown (Fg_kg_max) in [kg]
% 10. Maximum gross force crank angle (Fg_kg_max_index) in [°]
% 11. Connecting rod load (Q) in [N]
% 12. Connecting rod load (Q_kg) in [kg]
% 13. Maximum connecting rod load (Q_kg_max) in [kg]
% 14. Maximum connecting rod load crank angle (Q_kg_max_index) in [°]
% 15. Piston side load (N) in [N]
% 16. Piston side load (N_kg) in [kg]
% 17. Maximum piston side load (N_kg_max) in [kg]
% 18. Maximum piston side load crank angle (N_kg_max_index) in [°]
load ('C:\Documents and Settings\Marcel\My Documents\MATLAB\Masters - Matlab\01 - UAV
- Kistler\boxfor')
%
% Load the required variables from {Balancing}:
% 1. Length: Bearing 1 to Cylinder 1 (l2) in [mm]
% 2. Length: Bearing 1 to Cylinder 2 (l3) in [mm]
% 3. Length: Bearing 1 to Bearing 2 (l5) in [mm]
% 4. Primary and secondary couple summation (C) in [Nm]
% 5. Maximum summation couple (Cmax) in [Nm]
% 6. Maximum summation couple crank angle (Cmax_index) in [°]
load ('C:\Documents and Settings\Marcel\My Documents\MATLAB\Masters - Matlab\01 - UAV
- Kistler\boxbal')
```

```
%   Create the Crank angle and Connecting rod angle vectors in both [deg]
%   and [rad]. Assign the maximum Force and Couple index point (max) that
%   serves as the reference point for all calculations. State the engine
%   speed and throttle setting
%
%-------------------------------------------------------------------------%
%
% Create Crank angle vector 720 elements long (deg) and (rad)
deg = 0.5:0.5:360;                              % [deg]
rad = ((2*pi)/360) * deg;                       % [rad]
%
% Connecting rod angle (cra) vs Crankshaft pin angle (deg)
cra_rad = asin((a * sin(rad)) / l);             % Rod angle in radians
cra = asin((a * sin(rad)) / l) * (180 / pi);    % From radians to degrees
%
% Maximum Force and Couple index point (max)
% At this index point (ip) in the Crank angle vector (dm) and the
% Connecting rod angle vector (cm) where all calculations will be done
ip = Q_kg_max_index;        % NOTE: Crank index is multiple of 2
dm = deg(ip);               % True maximum Crank angle [deg]
cm = cra(ip);               % True maximum Conrod angle [deg]
%
% Display heading to be printed on screen
disp(sprintf('\t\t\tBOXER ENGINE FORCES\n'))
%
% State the engine test speed (rpm) and throttle setting (wot) used
disp(sprintf...
('Instantaneous forces calculated at %d rpm and %d %% throttle setting',...
rpm,wot))
%
% Display the Crank and Connecting rod angles used for calculations
disp(sprintf('Crank reference angle used: %2.2f °',dm))
disp(sprintf('Corresponding Conrod reference angle: %2.2f °',cm))
%
%-------------------------------------------------------------------------%
%
%   Force (Fg) on the Cylinder flange bolts and Crankcase seam bolts
%
%-------------------------------------------------------------------------%
%
% Display heading of section to be printed on screen
disp(sprintf('\n\t\t\tCYLINDER AND CRANKCASE BOLT FORCES'))
%
% State the reference force: Gross force (Fg) that is used for the
% calculations in this section
disp(sprintf('\nGross force used for calculations: %4.1f kg',Fg_kg(ip)))
%
% Force in the Cylinder flange bolts (Fcy) that bolt the Cylinder to the
% Crankcase
Fcy = Fg(ip) / bcy;                 % [N]
Fcy_kg = Fg_kg(ip) / bcy;           % [kg]
disp(sprintf...
('Max. force per bolt for the Cylinder flange of %d bolts: %3.1f kg',...
bcy,Fcy_kg))
```

```
% Force in the Crankcase seam bolts (Fcr)
Fcr = (Fg(ip) * n) / bcr;          % [N]
Fcr_kg = (Fg_kg(ip) * n) / bcr;    % [kg]
disp(sprintf...
('Max. force per bolt for the Crankcase seam of %d bolts: %3.1f kg',...
bcr,Fcr_kg))
%
%--------------------------------------------------------------------------%
%
%   Force on the bearings due to Connecting rod force (Q)
%
%--------------------------------------------------------------------------%
%
% Display heading of section to be printed on screen
disp(sprintf('\n\t\t\tBEARING FORCES DUE TO CONNECTING ROD FORCES'))
%
% State the reference force: Connecting rod load (Q) and Plane: Connecting
% rod angle (cm) that is used for the calculations in this section
disp(sprintf('\nConnecting rod load used for calculations: %4.1f kg',...
    Q_kg(ip)))
disp(sprintf...
    ('Plane in which Connecting rod forces act on bearings: %1.2f °',cm))
%
% Bearing reaction forces vary dramatically if one or both cylinders fire.
% Both occurances are investigated and corresponding bearing reaction
% forces calculated
%
% CONDITION 1: Both cylinders fire
% Bearing reaction forces when both cylinders fire: (Raq1) and (Raq2)
Raq1 = (Q(ip) * (l3/1000 - l2/1000)) / (l5/1000);   % [N]
Raq1_kg = Raq1 / 9.81;                              % [kg]
disp(sprintf('Bearing 1 reaction force: %3.1f kg (No misfire)',Raq1_kg))
Raq2 = -(Q(ip) * (l3/1000 - l2/1000)) / (l5/1000);  % [N]
Raq2_kg = Raq2 / 9.81;                              % [kg]
disp(sprintf('Bearing 2 reaction force: %3.1f kg (No misfire)',Raq2_kg))
%
% Resultant Bearing reaction forces in the X and Y planes - No misfire
Raq1_x = Raq1 * cos(cra_rad(ip));                   % [N]
Raq1_y = Raq1 * sin(cra_rad(ip));                   % [N]
Raq2_x = Raq2 * cos(cra_rad(ip));                   % [N]
Raq2_y = Raq2 * sin(cra_rad(ip));                   % [N]
%
% CONDITION 2: One cylinder misfires
% Bearing reaction forces when one cylinder misfires: (Ram1) and (Ram2)
Ram1 = (Q(ip) * l3/1000) / (l5/1000);               % [N]
Ram1_kg = Ram1 / 9.81;                              % [kg]
disp(sprintf('Bearing 1 reaction force: %3.1f kg (Misfire)',Ram1_kg))
Ram2 = -(Q(ip) * l2/1000) / (l5/1000);              % [N]
Ram2_kg = Ram2 / 9.81;                              % [kg]
disp(sprintf('Bearing 2 reaction force: %3.1f kg (Misfire)',Ram2_kg))
%
% Resultant Bearing reaction forces in the X and Y planes - Misfire
Ram1_x = Ram1 * cos(cra_rad(ip));                   % [N]
Ram1_y = Ram1 * sin(cra_rad(ip));                   % [N]
Ram2_x = Ram2 * cos(cra_rad(ip));                   % [N]
Ram2_y = Ram2 * sin(cra_rad(ip));                   % [N]
```

```
%-------------------------------------------------------------------------%
%
%   Reaction couple (Tr) on engine mounts due to engine torque
%
%-------------------------------------------------------------------------%
%
% Display heading of section to be printed on screen
disp(sprintf('\n\t\t\tREACTION COUPLE DUE TO ENGINE TORQUE'))
%
% State the reference force: Piston side load (N) is used for the
% calculations in this section
disp(sprintf('\nPiston side load used for calculations: %3.1f kg',...
N_kg(ip)))
%
% CONDITION 1: Both cylinders fire
% Engine mount reaction torque (Tr) due to engine torque generated by the
% Piston side load (N) -
Tr = n * (N(ip) * (a/1000 + l/1000 - s(ceil(ip/2))/1000));  % [Nm]
disp(sprintf('Torque reaction couple: %3.1f Nm (No misfire)',Tr))
%
% CONDITION 2: One cylinder misfires
% Engine mount reaction torque (Trm) due to engine torque generated by the
% Piston side load (N)
Trm = N(ip) * (a/1000 + l/1000 - s(ceil(ip/2))/1000);       % [Nm]
disp(sprintf('Torque reaction couple: %3.1f Nm (Misfire)',Trm))
%
%-------------------------------------------------------------------------%
%
%   Force on the bearings due to Balancing reaction couple (C)
%
%-------------------------------------------------------------------------%
%
% Display heading of section to be printed on screen
disp(sprintf('\n\t\t\tBEARING FORCES DUE TO BALANCING COUPLE'))
%
% State the reference couple:  Primary and Secondary summation couple (C)
% is used for the calculations in this section and Plane
disp(sprintf...
('\nPrimary and Secondary summation couple used: %3.1f Nm',C(ip)))
disp('Plane in which Balancing couples act on bearings: 0 °')
%
% Bearing reaction forces due to Balancing couple (C)
Rac1 = -(C(ip) / (l5/1000));                          % [N]
Rac1_kg = Rac1 / 9.81;                                % [kg]
disp(sprintf('Bearing 1 reaction force: %3.1f kg',Rac1_kg))
Rac2 = C(ip) / (l5/1000);                             % [N]
Rac2_kg = Rac2 / 9.81;                                % [kg]
disp(sprintf('Bearing 2 reaction force: %3.1f kg',Rac2_kg))
%
%-------------------------------------------------------------------------%
%
%   Bearing resultant forces due to Connecting rod force and Balancing
%   reaction couple
%
%-------------------------------------------------------------------------%
%
% Summation of all Bearing reaction forces due to the Connecting rod force
% and Balancing reaction couple
```

```
% Display heading of section to be printed on screen
disp(sprintf('\n\t\t\tBEARING FORCES SUMMATION\n'))
%
% CONDITION 1: Both cylinders fire
R1_x = Raq1_x + Rac1;           % [N]
disp(sprintf('Bearing 1 reaction force - X axis: %3.1f kg (No misfire)',...
    (R1_x / 9.81)))
R1_y = Raq1_y;                  % [N]
disp(sprintf('Bearing 1 reaction force - Y axis: %3.1f kg (No misfire)',...
    (R1_y / 9.81)))
R2_x = Raq2_x + Rac2;           % [N]
disp(sprintf('Bearing 2 reaction force - X axis: %3.1f kg (No misfire)',...
    (R2_x / 9.81)))
R2_y = Raq2_y;                  % [N]
disp(sprintf('Bearing 2 reaction force - Y axis: %3.1f kg (No misfire)',...
    (R2_y / 9.81)))
%
% CONDITION 2: One cylinder misfires
R1m_x = Ram1_x + Rac1;           % [N]
disp(sprintf('\nBearing 1 reaction force - X axis: %3.1f kg (Misfire)',...
    (R1m_x / 9.81)))
R1m_y = Ram1_y;                 % [N]
disp(sprintf('Bearing 1 reaction force - Y axis: %3.1f kg (Misfire)',...
    (R1m_y / 9.81)))
R2m_x = Ram2_x + Rac2;          % [N]
disp(sprintf('Bearing 2 reaction force - X axis: %3.1f kg (Misfire)',...
    (R2m_x / 9.81)))
R2m_y = Ram2_y;                 % [N]
disp(sprintf('Bearing 2 reaction force - Y axis: %3.1f kg (Misfire)',...
    (R2m_y / 9.81)))
%
%-------------------------------------------------------------------------%
%
%   Check integrity/validity of claimed maxima
%
%-------------------------------------------------------------------------%
%
% Plot all used variables on the same plot to check validity of stated
% maxima. Variables used all a function of Crank angle (deg):
%   1. Gross force (Fg)
%   2. Connecting rod load (Q)
%   3. Piston side load (N)
%   4. Balancing couple (C)
%
% Scale all the vectors mentioned above to visulise graph magnitudes
Fg_s = Fg/100;              % [N]
Q_s = Q/100;                % [N]
N_s = N/10;                 % [N]
C_s = C/3;                  % [Nm]
%
figure(1)
subplot(1,1,1)
plot(deg,Fg_s,'b',deg,Q_s,'r',deg,N_s,'k',deg,C_s,'c')
axis([0 360 -60 120])
xlabel('Crankshaft angular position [°]')
ylabel('Magnitude scaled [-]')
title...
('Gross, Conrod, Piston side force and Balancing couple vs Crank angle')
```

```
legend('Gross force','Connecting rod load','Piston side load',...
    'Resultant couple')
line([0 360],[0 0],'color','k','linewidth',1.0,'linestyle',':')
line([180 180],[-60 120],'color','k','linewidth',1.0,'linestyle',':')
line([ip/2 ip/2],[-60 110],'color','r','linewidth',1.0,'linestyle',':')
text((deg(ip)-5),(max(Fg_s)+5),sprintf('IP = %g°',dm),'color','k')
%
% Display heading of section to be printed on screen
disp(sprintf('\n\t\t\tCALCULATION MAXIMA VERIFICATION'))
%
% Calculate the percentage difference due to assigning a maximum to each of
% the four variables using the index point (ip) and the actual maximum
% value of the variables
pd_Fg = ((Fg_kg_max - Fg_kg(ip)) / Fg_kg_max) * 100;    % [%]
disp(sprintf('\nGross force lower by: %2.2f %%',pd_Fg))
pd_Q = ((Q_kg_max - Q_kg(ip)) / Q_kg_max) * 100;        % [%]
disp(sprintf('Conrod force lower by: %2.2f %%',pd_Q))
pd_N = ((N_kg_max - N_kg(ip)) / N_kg_max) * 100;        % [%]
disp(sprintf('Piston side force lower by: %2.2f %%',pd_N))
pd_C = ((Cmax - C(ip)) / Cmax) * 100;                   % [%]
disp(sprintf('Balancing couple lower by: %2.2f %%',pd_C))
%
%--------------------------------------------------------------------------%
%
%   Export selected values to Excel
%
%--------------------------------------------------------------------------%
%
% Identify the rotational test speed of the engine and select the cells
% that are to be populated in Excel
if rpm == 3000
    cell1 = 'C8';
    cell2 = 'C13';
    cell3 = 'C32';
    cell4 = 'C43';
elseif rpm == 3500
    cell1 = 'D8';
    cell2 = 'D13';
    cell3 = 'D32';
    cell4 = 'D43';
elseif rpm == 4000
    cell1 = 'E8';
    cell2 = 'E13';
    cell3 = 'E32';
    cell4 = 'E43';
elseif rpm == 4500
    cell1 = 'F8';
    cell2 = 'F13';
    cell3 = 'F32';
    cell4 = 'F43';
elseif rpm == 5000
    cell1 = 'G8';
    cell2 = 'G13';
    cell3 = 'G32';
    cell4 = 'G43';
```

```
elseif rpm == 5500
    cell1 = 'H8';
    cell2 = 'H13';
    cell3 = 'H32';
    cell4 = 'H43';
elseif rpm == 6000
    cell1 = 'I8';
    cell2 = 'I13';
    cell3 = 'I32';
    cell4 = 'I43';
elseif rpm == 6500
    cell1 = 'J8';
    cell2 = 'J13';
    cell3 = 'J32';
    cell4 = 'J43';
end
%
% Generate the matrix (Exmat1) that is to be exported to Excel to display
% "Reference Angles Used"
Exmat1 = [dm;cm];
%
% Generate the matrix (Exmat2) that is to be exported to Excel to display
% "Forces And Couples At Crank Reference Angle"
Exmat2 = [Fg(ip);Fcy;Fcr;Q(ip);cm;Raq1;Raq2;Ram1;Ram2;N(ip);Tr;Trm;...
    C(ip);0;Rac1;Rac2];
%
% Generate the matrix (Exmat3) that is to be exported to Excel to display
% "Bearing Forces Summation"
Exmat3 = [R1_x;R1_y;R2_x;R2_y;R1m_x;R1m_y;R2m_x;R2m_y];
%
% Generate the matrix (Exmat4) that is to be exported to Excel to display
% "Calculation Maxima Verification"
Exmat4 = [pd_Fg;pd_Q;pd_N;pd_C];
%
% Export the data in (Exmat1), (Exmat2), (Exmat3) and (Exmat4) that is to
% be imported into Excel
xlswrite('Boxer Maxima.xlsx',Exmat1,'Forces',cell1);
xlswrite('Boxer Maxima.xlsx',Exmat2,'Forces',cell2);
xlswrite('Boxer Maxima.xlsx',Exmat3,'Forces',cell3);
xlswrite('Boxer Maxima.xlsx',Exmat4,'Forces',cell4);

%-------------------------------------------------------------------------%
%
tictoc = toc;
disp(sprintf('\n Elapsed time for program run is %0.3f seconds',tictoc))
```

H MANUFACTURER DATASHEETS

H.1 ZANZOTTERA 498H PERFORMANCE CURVES

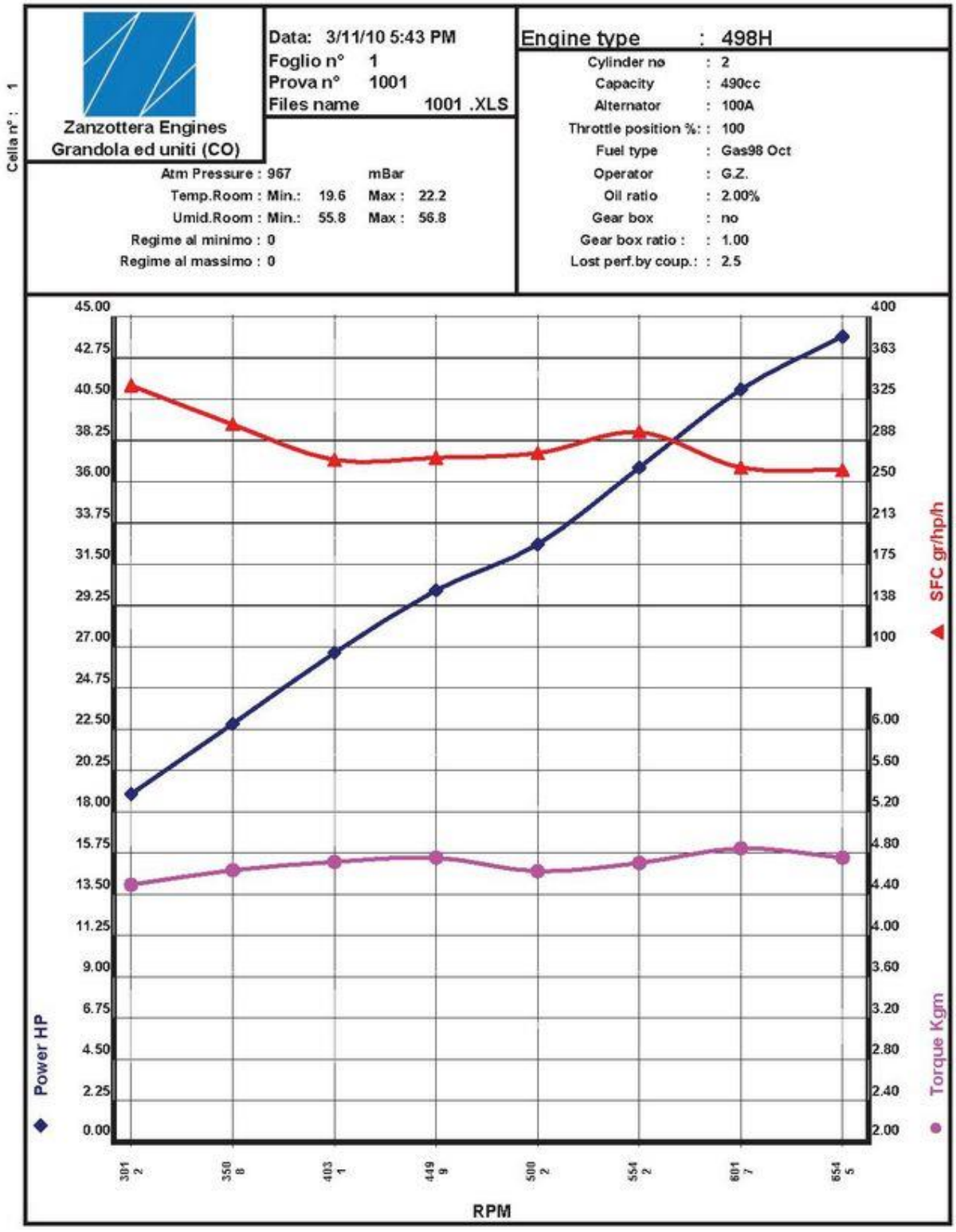

H.2 LIMBACH L550E PERFORMANCE CURVES

LIMBACH Flugmotoren	Operating Manual L 275 E / L 550 E	

6.1.2. L 550 E

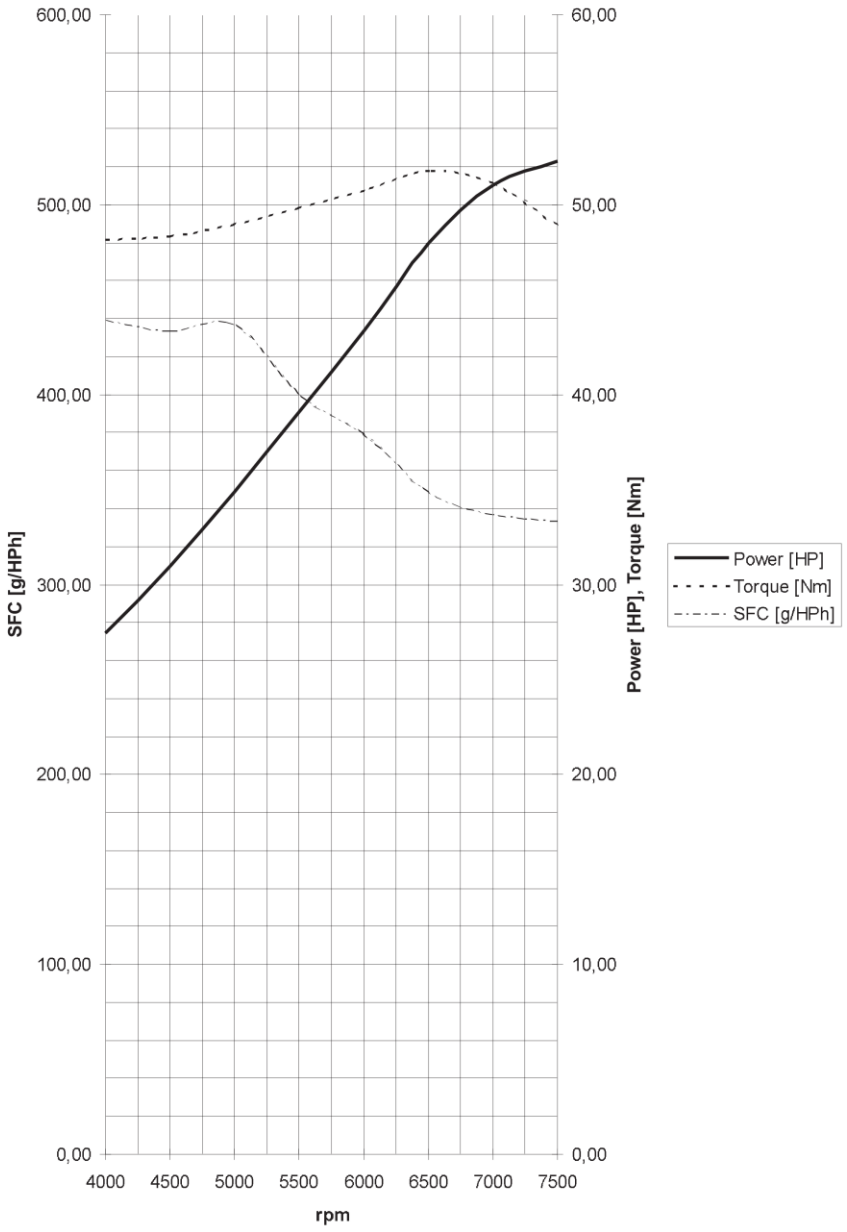

Bearb.: Limbach jr.	Replaces Edition from: 01.04.04	Page : 22
Gepr.:	Edition: 01.08.05	